

DIARENO FUSION TO MODIFY ANTIAROMATICITY AND DIRADICAL
CHARACTER IN *S*-INDACENES AND DICYCLOPENTA[*B,G*]NAPHTHALENES

By

JOSHUA ERVIN BARKER

A DISSERTATION

Presented to the Department of Chemistry and Biochemistry
and the Division of Graduate Studies of the University of Oregon
in partial fulfillment of the requirements
for the degree of
Doctor of Philosophy

June 2021

DISSERTATION APPROVAL PAGE

Student: Joshua Ervin Barker

Title: Diareno Fusion to Modify Antiaromaticity and Diradical Character in *s*-Indacenes and Dicyclopenta[*b,g*]naphthalenes

This dissertation has been accepted and approved in partial fulfillment of the requirements for the Doctor of Philosophy degree in the Department of Chemistry by:

Michael D. Pluth	Chairperson
Michael M. Haley	Advisor
Ramesh Jasti	Core Member
Scott D. Bridgham	Institutional Representative
and	

Andrew Karduna	Interim Vice Provost for Graduate Studies
----------------	---

Original approval signatures are on file with the University of Oregon Division of Graduate Studies.

Degree awarded June 2021

© 2021 Joshua Ervin Barker
This work is licensed under a Creative Commons
Attribution (United States) License



DISSERTATION ABSTRACT

Joshua Ervin Barker

Doctor of Philosophy

Department of Chemistry and Biochemistry

June 2021

Title: Diareno Fusion to Modify Antiaromaticity and Diradical Character in *s*-Indacenes and Dicyclopenta[*b,g*]naphthalenes

Antiaromatic and diradical molecules are emerging both as novel synthetic targets for fundamental studies and as promising materials for next generation organic electronics. In order to properly apply these types of molecules it is important to understand how their properties may be tuned in order to optimize them for device applications. The diradical literature especially suffers from a lack of thorough structure-activity relationship studies. In this dissertation I discuss strategies to tune diradical character and the associated singlet triplet energy gap as well as heteroatom effects in heterocycle-fused *s*-indacenes.

Chapter I is an account of the research the Haley lab has reported in the last five years on tuning strong antiaromaticity and diradical character in a class of indenofluorene-derived molecules. Chapter II describes the synthesis of fluoreno[3,2-*b*]fluorene, a novel quinoidal molecule. Chapter III uses synthetic strategies from Chapter II to fuse benzothiophenes to the Fluorenofluorene structure described in Chapter II which unlocks diradical character in this structure. Chapter IV is an exploration of late-stage modification of benzothiophene-fused indenofluorene and fluorenofluorene derivatives to control their electronics properties. Chapter V revisits the Fluorenofluorene structure from Chapter II and explores how dibenzofusion to this structure changes the diradical character of the core

naphthoquinoidal unit. Finally, Chapter VI explores the heteroatom effects of changing the sulfur atom in the above described benzothiophene fused systems to an oxygen atom through benzofuran fusion.

This dissertation contains previously published and unpublished co-authored material.

CURRICULUM VITAE

NAME OF AUTHOR: Joshua Ervin Barker

GRADUATE AND UNDERGRADUATE SCHOOLS ATTENDED:

University of Oregon, Eugene, OR
Eastern Washington University, Cheney, WA
Olympic College, Bremerton, WA

DEGREES AWARDED:

Doctor of Philosophy, Chemistry, 2021, University of Oregon
Bachelor of Science, Chemistry, 2016, Eastern Washington University
Associate of Arts and High School Diploma, 2013, Olympic College

AREAS OF SPECIAL INTEREST:

Organic Chemistry
Physical Organic Chemistry

PROFESSIONAL EXPERIENCE:

Graduate Employee, University of Oregon, 2016-2021

GRANTS, AWARDS, AND HONORS:

Outstanding Chemistry Senior, Eastern Washington University, 2016

PUBLICATIONS:

Barker, J. E.; Karas, L. J.; Price, T. W.; Kishi, R.; Zakharov, L. N.; MacMillan, S. N.; Gómez-García, C. J.; Nakano, M.; Wu, J. I.; Haley, M. M. A Tale of Two Isomers: Enhanced Antiaromaticity/Diradical Character versus Deleterious Ring-Opening of Benzofuran-fused *s*-Indacenes and Dicyclopenta[*b,g*]naphthalenes. *Angew. Chem.* **2021**, in submission.

Hayashi, H.*; Barker, J. E.*; Valdivia, A. C.*; Kishi, R.; MacMillan, S. N.; Gómez-García, C. J.; Miyauchi, H.; Nakamura, Y.; Nakano, M.; Kato, S.-I.; Haley, M. M.; Casado, J. Monoradicals and Diradicals of Dibenzofluoreno[3,2-*b*]fluorene Isomers: Mechanisms of Electronic Delocalization. *J. Am. Chem. Soc.* **2020**, *142*, 20444-20455.

Dressler, J. J.; Barker, J. E.; Karas, L. J.; Hashimoto, H.; Kishi, R.; Zakharov, L. N.; MacMillan, S. N.; Gómez-García, C. J.; Nakano, M.; Wu, J. I.; Haley, M. M. "Late-Stage Modification of Electronic Properties of Antiaromatic and Diradicaloid Indeno[1,2-*b*]fluorene Analogues via Sulfur Oxidation." *J. Org. Chem.* **2020**, *85*, 10846-10857.

Barker, J. E.; Dressler, J. J.; Valdivia, A. C.; Kishi, R.; Strand, E. T.; Zakharov, L. N.; MacMillan, S. N.; Gómez-García, C. J.; Nakano, M.; Casado, J.; Haley, M. M. "Molecule Isomerism Modulates the Diradical Properties of Stable Singlet Diradicaloids" *J. Am. Chem. Soc.* **2020**, *142*, 1548-1555.

Bard, J. P.; Deng, C. L.; Richardson, H. C.; Odulio, J. M.; Barker, J. E.; Zakharov, L. N.; Cheong, P. H.-Y.; Johnson, D. W.; Haley, M. M. "Synthesis, photophysical properties, and self-dimerization studies of 2- λ 5-phosphaquinolin-2-ones." *Org. Chem. Front.* **2019**, *6*, 1257-1265.

Deng, C.-L.; Bard, J. P.; Lohrman, J. A.; Barker, J. E.; Zakharov, L. N.; Johnson, D. W.; Haley, M. M. "Exploiting the Hydrogen Bond Donor/Acceptor Properties of PN-Heterocycles: Selective Anion Receptors for Hydrogen Sulfate." *Angew. Chem.* **2019**, *131*, 3974-3978; *Angew. Chem. Int. Ed.* **2019**, *58*, 3934-3938.

Barker, J. E.; Kodama, T.; Song, M. K.; Frederickson, C. K.; Jousselein-Oba, T.; Zakharov, L. N.; Marrot, J.; Frigoli, M.; Johnson, R. P.; Haley, M. M. "Serendipitous Rediscovery of the Facile Cyclization of *Z,Z*-3,5-Octadiene-1,7-diyne Derivatives to Afford Stable, Substituted Naphthocyclobutadienes." *ChemPlusChem* **2019**, *84*, 665-672.

Frederickson, C. K.; Barker, J. E.; Dressler, J. J.; Zhou, Z.; Hanks, E. R.; Bard, J. P.; Zakharov, L. N.; Petrukhina, M. A.; Haley, M. M. "Synthesis and Characterization of a Fluorescent Dianthracenoindacene." *Synlett* **2018**, *29*, 2562-2566.

Bateman, C. M.; Beal, H.; Barker, J. E.; Thompson, B. L.; Donovan, D.; Grant, B. J.; Shooter, J.; Arakawa, J. H.; Johnson, S.; Allen, C. J.; Yates, J. L.; Kato, R.; Tinsley, C. W. K.; Zakharov, L. N.; Abbey, E. R. "One-Step Conversion of Potassium Organotrifluoroborates to Metal Organoborohydrides." *Org. Lett.* **2018**, *20*, 3784-3787.

Barker, J. E.; Frederickson, C. K.; Jones, M. H.; Zakharov, L. N.; Haley, M. M. "Synthesis and Properties of Quinoidal Fluorenofluorenes." *Org. Lett.* **2017**, *19*, 5312-5315.

Cardoso, D. S. P.; Sequeira, C. A. C.; Bateman, C. M.; **Barker, J. E.**; Abbey, E.; Santos, D. M. F. "Electroreduction Ability of Organoborohydride Compounds." *J. Electrochem. Soc.* **2017**, *164*, H159-H163.

ACKNOWLEDGMENTS

There are a great number of people without whom my PhD never would have happened. First, I must thank my advisor Mike Haley. On the most basic level Mike gave me a position in his lab to learn about and explore the wide world of PAH chemistry. Beyond that though, Mike has been a great advisor and has been incredibly supportive all along the way. I will miss being able to walk into his office and talk science, life, or departmental politics. I would also like to thank the National Science Foundation (CHE-1565780 and CHE-1954389) for grant funding during my time in Mikes group. I also have appreciated the support and scientific critique from the other members of my committee, Mike Pluth, Ramesh Jasti, and Scott Bridgham.

The next person I want to thank is my undergraduate advisor Eric Abbey. If not for Eric's organic chemistry class I would probably be slaving away in an analytical lab somewhere instead of making cool molecules and learning synthetic organic chemistry. He let me do a bunch of cool stuff in his research lab (including using *t*-BuLi) encouraged me to go to graduate school. I will always be grateful for his mentorship, for inspiring me in my career goals, and for giving me lots of fishing tips.

Next, I would like to thank my family for being supportive all through grad school. I often called Dad on my walk in to campus in the morning and Mom on my walk home in the evening. Their advice on life and interpersonal communications has been invaluable and I couldn't have done any of this without them. I especially want to thank them for raising me to think independently and to have compassion for all the people around me in my life. My Brothers have also been very supportive and I am thankful for their friendship and love.

My church family in Eugene has also been important. For the first two years in Eugene I lived with Don and Lauralyn Martin. I never would have made it without them and the support, counsel, and care that they had for me. In addition to the Martins, Fang Yin, Jack Yang, the Hsu family, and many others from the Church in Eugene have supported me in my time here.

My fellow members in the Haley lab have also been of great support to me. Jeremy and was there with me from the very beginning. I have appreciated their perspective and aspired to his work ethic throughout our time here. Justin Dressler was a great mentor for me starting out in the lab. For the next generation, Gabby, Efrain, Bella, and Nolan, you all going to do great things, and I have loved working with you all. I have also had some great undergraduates and REU students as well as several great rotation students. Virginia, Michael, Nick, Tavis, Tristan, Eric, Efrain, Bella, and Gabby I think I learned as much from all of you as you hopefully learned from me, thank you all for that!

I could go on for a long time, I am incredibly thankful for everyone who has touched my life during my graduate school career. I don't have space to name you all but my PhD would have been real lame without all of you. I would like to conclude by acknowledging Gabrielle Warren. Gabby is my closest friend, my adventure buddy, and my life partner. Without her my life would be incredibly boring. In this last year especially as I spent time teaching a class, writing job proposals, and writing my dissertation she has taken so much care for me that I hope I can make it all up to her at some point. In short, I probably would have fallen completely apart without her. I look forward to our life together and I expect great things from her as she finishes her graduate studies!

Dedicated to all the people I discussed above without whom I wouldn't be here.

TABLE OF CONTENTS

Chapter	Page	
I. RATIONAL DESIGN OF ANTIAROMATIC AND DIRADICALOID		
DIARENO- <i>s</i> - INDACENES, DIARENO-		
DICYCLOPENTA[<i>b,g</i>]NAPHTHALENES, AND DIARENO-		
DICYCLOPENTA[<i>b,i</i>]ANTHRACENES.....		1
1.1 Background.....	1	
1.2 Antiaromaticity.....	6	
1.3 Diradical Character.....	11	
1.4 Conclusions.....	19	
II. SYNTHESIS AND PROPERTIES OF QUINOIDAL FLUORENOFLUORENES		22
2.1 Introduction.....	22	
2.2 Results and Discussion.....	24	
2.3 Conclusions.....	29	
III. MOLECULE ISOMERISM MODULATES THE DIRADICAL PROPERTIES		
OF STABLE SINGLET DIRADICALOIDS.....		30
3.1 Introduction.....	30	
3.2 Results and Discussion.....	34	
3.3 Conclusions.....	43	
IV. LATE-STAGE MODIFICATION OF ELECTRONIC PROPERTIES OF		
ANTIAROMATIC AND DIRADICALOID INDENO[1,2- <i>b</i>]FLUORENE		
ANALOGUES VIA SULFUR OXIDATION.....		45
4.1 Introduction.....	45	

Chapter	Page
4.2 Results and Discussion	48
4.3 Conclusions.....	62
4.4 Experimental Section	63
V. MONORADICALS AND DIRADICALS OF DIBENZOFUORENO[3,2- <i>b</i>]FLUORENE ISOMERS: MECHANISMS OF ELECTRONIC DELOCALIZATION.....	
	70
5.1 Introduction.....	70
5.2 Results and Discussion	75
5.3 Conclusions.....	92
VI. A TALE OF TWO ISOMERS: ENHANCED ANTIAROMATICITY/ DIRADICAL CHARACTER VERSUS DELETERIOUS RING-OPENING OF BENZOFURAN-FUSED <i>s</i> -INDACENES AND DICYCLOPENTA[<i>b,g</i>]NAPHTHALENES.....	
	94
6.1 Introduction.....	94
6.2 Results and Discussion	98
6.3 Conclusion	109
APPENDICES	111
A. SUPPLEMENTARY INFORMATION FOR CHAPTER II.....	111
B. SUPPLEMENTARY INFORMATION FOR CHAPTER III.....	130
C. SUPPLEMENTARY INFORMATION FOR CHAPTER IV	161
D. SUPPLEMENTARY INFORMATION FOR CHAPTER V.....	220
E. SUPPLEMENTARY INFORMATION FOR CHAPTER VI.....	291

Chapter	Page
REFERENCES CITED.....	334

LIST OF FIGURES

Figure	Page
1. Figure 1.1 The five fully-conjugated indenofluorene isomers.....	2
2. Figure 1.2 General strategies for modification of the IF template.....	4
3. Figure 1.3 Illustration of the <i>p</i> -quinodimethide and <i>s</i> -indacene motifs within IF Lower bond order (e.g. through fusion along the highlighted 2,3 bond of Anthracene) favors the <i>p</i> -quinoidal structure. Higher bond order (e.g. through fusion with the highlighted bond of benzothiophene) favors the antiaromatic <i>s</i> -indacene structure	7
4. Figure 1.4 NICS-XY scans of the heterocycle-fused <i>s</i> -indacenes studied by our group.....	8
5. Figure 1.5 Illustration of the electronic structure of a diradical vs. a diradicaloid. In a diradical the orbitals are degenerate. A diradicaloid has orbitals that are close in energy but not degenerate.....	12
6. Figure 1.6 The core diradical motifs contained within FF derivatives (NQD) and DIAn derivatives (AQD).....	15
7. Figure 1.7 (top) SQUID magnetometry data for <i>anti</i> -IIDBT and <i>syn</i> -IIDBT. (bottom) Deuterium labelling experiment to verify the radical character of <i>anti</i> -IIDBT	16
8. Figure 1.8 Structures of the DBFFs and DBDIAns	18
9. Figure 1.9 SQUID magnetometry plots for IIDBTs, <i>syn</i> -IIDBF, the DBFFs and The DBDIAns	20
10. Figure 2.1 Known Fluorenofluorenes and related [3,2-b]FF-containing hydrocarbons.....	23
11. Figure 2.2 Electronic absorbance spectra of 2 (solid red) and 8 (dashed blue) in CH ₂ Cl ₂	26
12. Figure 2.3 (Left) ORTEP showing top view of 8 ; hydrogen atoms omitted for clarity. Ellipsoids drawn at the 50% probability level. (Right) Calculated structures of 2' (top) and 8' (bottom) with selected bonds labeled	27

Figure	Page
13. Figure 2.4 NICS-XY scans of indeno[1,2-b]fluorene 1' and Fluorenofluorenes 2', 5', 5' (OS) and 8'	28
14. Figure 3.1 Chemical structures of anti-IIDBT (1) and syn-IIDBT (2). All canonical forms possess 2,6-naphtho conjugation (bold bonds). In boxes, linear conjugation (left, Li and Lk) vs. cross conjugation (right, Ci and Ck) dispositions of the labeled ijkl atoms where delocalization of the radical centers to the k atoms disrupts thiophene aromaticity.....	31
15. Figure 3.2 Diradical resonance forms of the hydrocarbon core of the two known dibenzoheptazethrene regioisomers.....	33
16. Figure 3.3 <i>Anti</i> and <i>syn</i> IIDBT derivatives studied in this work.....	34
17. Figure 3.4 Odd-electron density maps for 1a (left) and 2a (right) with contour value 0.0005 a.u. calculated at the tuned-LC-RBLYP-CASCI(2,2)/6-311G* level. Mulliken population analysis for the odd-electron density on the relevant carbon and sulfur atoms of the linear and cross conjugated paths is shown on top.	36
18. Figure 3.5 (a) Molecular packing of 2b with the ellipsoids drawn with 50% probability level; hydrogens are omitted for clarity. (b) Experimental (black) bond lengths for the core motifs of 2b and 1a along with the calculated (blue) values for 2a and 1a	38
19. Figure 3.6 Bis phenylenyl-fused indacene (6) and indenoindene (7) for comparison.....	39
20. Figure 3.7 Electronic absorption (in CH ₂ Cl ₂ , top) and Raman spectra (in solid	

Figure	Page
state with 1064 nm laser excitation, bottom) of 1a (red) and 2a (blue). Raman spectrum of aromatized 2cH2 is in black.	40
21. Figure 3.8 (top) Variable temperature ¹ H NMR spectra (in 1,2-C ₆ D ₄ Cl ₂) of 2a . (bottom) SQUID magnetometry data of 1a-1b and 2a-2b ; for 1b and 2b the data for the heating and cooling curves are denoted by squares and circles, respectively.	42
22. Figure 4.1 New IDBTs 1 and 2 , known IIDBTs 3 and 4 , their sulfone analogues 5-8 , and decomposition product 9	47
23. Figure 4.2 (a) Proton NMR spectra of the aromatic region of IDBTs 1 and 2 and the corresponding sulfones 5 and 6 . The central proton (*) displayed in bold in the structures on the left can be used to roughly assess antiaromaticity. (b) NICS-XY scans for IDBTs 1 and 2 and sulfones 5 and 6 along with the scan for the parent s-indacene, in order of most to least paratropic; for clarity the ring labels are shown above in the structure of 5	51
24. Figure 4.3 Selected resonance forms for the hydrocarbon dianion reference analogues of (a) syn-IDBT 2 and (b) anti-IDBT 1 ; boxed structures are the dominant resonance forms recognized by NBO.	53
25. Figure 4.4 Natural population analyses (NPA) charges for s-indacene.	54
26. Figure 4.5 Electronic absorption spectra of the three stable sulfones 5 , 6 , and 8 and their parent thiophenes 1 , 2 , and 4 , in CHCl ₃ at room temperature. The spectrum of each sulfone is a similar color to the parent compound, with the sulfone having the lighter hue.	55

Figure	Page
27. Figure 4.6 Cyclic voltammograms of 5 , 6 , and 8	56
28. Figure 4.7 X-ray structures of (left to right) sulfone derivatives 5-Mes , 6 , and 8 and decomposition product 9 with selected bond lengths (Å; experimental values in black, calculated values in blue); ellipsoids drawn at the 50% probability level. Experimental numbers for 6 represent the average value from two crystallographically independent molecules.	58
29. Figure 4.8 (a) Generalized structures displaying the “normal” bonding pattern observed in most indeno[1,2- <i>b</i>]fluorene-based molecules and the “flipped” bonding pattern observed for sulfones 5 , 6 , and 8 . (b) NICS-XY scans of both <i>anti</i> -IDBT-S geometries where 5 is the observed bond-flipped orientation and 5* is the normally observed bonding pattern.	59
30. Figure 5.1 (top left) Strategies for tuning diradical character showing the “chemical approach” using an expansion in the quinoidal conjugation path in indenofluorene congeners (A , B and C for benzo-, naphtho- and anthraceno- quinodimethanes, respectively). (top right) The arrows and boxes denote the variation that the $y_0/\Delta E_{ST}$ points might undergo with altering the lateral Ar substituents. The B region targets fluorenofluorenes 1-5 reported in this study. (bottom) Literature examples of the DBDIAn/C series with different fused Ar groups illustrating that the Ar motif exhibits secondary control (fine tuning) of $y_0/\Delta E_{ST}$, i.e., the “physical approach”. In all instances, only the conjugated diradical cores are shown without the bulky alkyl and/or pendant aryl groups used to protect the radical centers.	73

Figure	Page
31. Figure 5.2 (a) Structures of target molecules FF 1 , DBFFs 2-4 , and TBFF 5 with (b) the two viable core moieties (<i>t</i> -Mes = 4- <i>t</i> -butyl-2,6-dimethylphenyl).....	74
32. Figure 5.3 (left) Variation of the diradical character index y_0 and ΔE_{ST} from calculations for the DIAn derivatives (white box) and FF derivatives (blue box) at the same level of theory. Green line denotes the generalized behavior of the function of equation (2). (right) Variation of the $U/2$ and t_{ab} as a function of the diradical character.	77
33. Figure 5.4 Top) Coupling mode (see blue arrows) of the HONO natural orbitals of the constituting fragments (2,6-dimethylene-2,6-dihydronaphthalene and naphthalene). Bottom) HONO and LUNO of the given compounds 2-4 . All single particle orbitals are illustrated schematically by the contribution of each atom. Notice that the HOMO and LUMO of the compounds are not necessarily built by the combination of the HOMOs of the fragments.	78
34. Figure 5.5 VT ^1H NMR spectra of (a) anti-DBFF 4 in $o\text{-CD}_2\text{Cl}_4$ and (b) TBFF 5 in $1,1,2,2\text{-C}_2\text{D}_2\text{Cl}_4$	81
35. Figure 5.6 X-ray crystal structures of FF 1 and the DBFFs 2-4 . Bond lengths from the crystal structures are in black, bond lengths from the calculated structures are in blue.	82
36. Figure 5.7 (left) UV-vis spectra of FF 1 , linear-DBFF 2 , syn-DBFF 3 , anti-DBFF 4 , and TDFFF 5 recorded at room temperature in CH_2Cl_2 . (middle) Solid state vibrational Raman spectra at room temperature of the same compounds together with the hydrogenated precursors of 2 (10a) and 4 (10c) as grey lines. (right)	

Figure	Page
<p>Thermal variation of the $\chi_m T$ product for compounds 1-5 in the heating (dark colors) and cooling scans (light colors). Solid lines are the corresponding fits to the Bleaney-Bowers model.</p>	84
<p>37. Figure 5.8 (top) Cyclic voltammetry of <i>linear</i>-DBFF 2 recorded in CH₂Cl₂ solution 0.1 M TBAPF₆ at room temperature (blue, first oxidation; and red, first reduction); see SI for detail; and UV-Vis-NIR absorption spectra of <i>linear</i>-DBFF 2 recorded in the above electrochemical conditions during the oxidation and reduction waves on the first oxidation (blue shaded) and reduction (red shaded) processes of <i>linear</i>-DBFF 2. (Bottom) NICS_{πzz(1.7)} scan values for the neutral, radical anion, and radical cation of <i>linear</i>-DBFF 2' at the tuned-LC-UBLYP/6-311G* level.....</p>	86
<p>38. Figure 5.9 (left) Molecular structure from solid state x-ray diffraction data of the radical cation of <i>syn</i>-DBFF (3⁺·SbCl₆⁻) with thermal ellipsoids at 50% probability. Hydrogen atoms, methyl and <i>tert</i>-butyl groups are omitted for clarity. (right) Core CC carbon bond length differences in Å (neutral minus radical cation).....</p>	88
<p>39. Figure 5.10 (top) UV-Vis-NIR electronic absorption spectra of the radical anions (left) and radical cations (right) of the DBFF series (black lines) and of the DBDIAn series (red lines) recorded electrochemically in CH₂Cl₂ solution 0.1 M TBAPF₆ at room temperature. (bottom left) Representation as a function of the diradical character index of the singlet-triplet gap of the neutrals and of the optical gap in the radical anions and radical cations from the lowest energy absorption band of the UV-Vis-NIR spectra for both series of DBFFs and DBDIAns. Energy values are all in kcal mol⁻¹. (bottom right) UV-Vis-NIR electronic absorption spectra</p>	

Figure	Page
of the radical anion, neutral and radical cation of TBFF 5 generated electrochemically in CH ₂ Cl ₂ /0.1 M TBAPF ₆ at room temperature.	89
40. Figure 5.11 (top) Lowest energy absorption bands of <i>linear</i> -DBFF 2 radical cation and anion. FWHM = full width at half maximum. (bottom) Pictorial view of the main structures in the radical anion and cation of <i>linear</i> -DBFF 2 as a representative example.....	91
41. Figure 6.1 Previously synthesized BT-fused PAAHs (1-5) by our group, and the IDBFs (6-7) and IIDBFs (8-9) described in this paper. *As the reader will discover below, compound 9 is not isolable.	95
42. Figure 6.2 NICS-XY scans of <i>s</i> -indacene, IDBFs 6'-7', and the IDBT analogues 1'-2'. Dashed lines represent the path of the ghost atoms used in the NICS calculations. Computations were performed without bulky mesityl groups to reduce cost. Legend is ordered from most paratropic to least paratropic.	98
43. Figure 6.3 Partial ¹ H NMR spectra (500 MHz, CD ₂ Cl ₂ , 25 °C) of compounds 1 , 2 , 6 , and 7 , which illustrate the shifting of the core ¹ H resonance as the antiaromaticity of the core <i>s</i> -indacene unit changes. Spectra are ordered by increasing paratropicity.....	101
44. Figure 6.4 Resonance structures of the hydrocarbon dianion analogues of a) <i>syn</i> -IDBF and b) <i>anti</i> -IDBF. Boxed structures indicate the dominant resonance form identified by NRT calculations. c) Computed NPA charges of the <i>s</i> -indacene core.....	102
45. Figure 6.5 X-ray crystal structures of IDBFs 6 and 7 , and <i>syn</i> -IIDBF 8 . Bond lengths from the crystal structures are in black and bond lengths from the	

Figure	Page
calculated structures are in blue. Ellipsoids were drawn at 50% probability. Hydrogens and mesityl groups are omitted for clarity.....	103
46. Figure 6.6 a) Resonance structures and orbital representations of the closed-shell singlet state (left), open-shell diradical singlet state (middle), and open-shell diradical triplet state (right); all canonical forms possess 2,6-naphtho conjugation (bold bonds). b) Cross conjugation (C and C', top) vs. linear conjugation (L and L', bottom) orientation of the heteroatom where delocalization of the radical centers to the lower carbon atom disrupts heterocycle aromaticity; X = S or O. c) VT-NMR spectra of 8 in 1,1,2,2-tetrachloroethane- <i>d</i> ₂ ; d) SQUID magnetometry plot of 8; lines (red – heating, blue – cooling) represent the Bleaney-Blowers fit to the data.	104
47. Figure 6.7 a) Electronic absorption spectra of the IDBFs (6-7) and <i>syn</i> -IIDBF (8); b) Cyclic voltammograms of <i>syn</i> -IDBF (6) and <i>syn</i> -IIDBF (8).....	107

LIST OF TABLES

Table	Page
1. Table 1.1 Electrochemical, optical, and NMR data for the heterocycle-fused- <i>s</i> -indacenes	10
2. Table 1.2 Collected computational and experimental data for FF and DIAn based diradicaloids.....	19
3. Table 2.1 Selected bond lengths (Å). ^a All geometries were calculated at the RB3LYP/6-31++G(d,p) level of theory, mesityl groups omitted for computational simplification	27
4. Table 3.1 Theoretically Estimated γ and ΔE_{ST} Values Together with the Main Physical Parameters.	35
5. Table 4.1 Cyclic Voltammetry Data for Thiophenes 1, 2, and 4 and Sulfones 5, 6, and 8. CVs were recorded at a scan rate of 50 mV s ⁻¹ with a glassy carbon working electrode, Pt coil counter electrode and Ag wire pseudo-reference. All data were collected in degassed CH ₂ Cl ₂ and ferrocene was used as an internal reference. Potentials were referenced to SCE by using the Fc/Fc ⁺ half-wave potential (Fc/Fc ⁺ = 0.46 V vs. SCE).	57
6. Table 5.1 Summary of computational parameters and experimental values of ΔE_{ST} for fluorenofluorenes 1' - 5' . ^a Computational data for 1' from reference 44. ^b Calculated at the PUHF/6-311G*//RB3LYP/6-311G* level. ^c Calculated at the spin-flip noncollinear TD-DFT PBE50/6-311G*//RB3LYP/6-311G* level. ^d Calculated at the tuned-LC-RBLYP CASCI(2,2)/6-311G*//RB3LYP/6-311G* level. Computational details are given in the SI.	76
7. Table 6.1 Theoretically estimated γ and ΔE_{ST} values together with the main	

physical parameters. [a] Geometry optimization for the singlet/triplet states and frequency analyses were performed at the R- and UB3LYP/6-311G* levels, respectively. [b] Calculated at the PUHF/ 6-311G*. [c] Adiabatic ΔE_{ST} value calculated at the spin-flip non-collinear (SF-NC)-TDDFT-PBE5050/6-311G* level along with R- or UB3LYP/6-311G* zero-point vibrational energy correction for each spin state. [d] Estimated at the CASCI(2,2)/6-311G* level using the (tuned-)LC-RBLYP MOs (denoted as tuned-LC-RBLYP-CASCI(2,2)/6-311G*). Additional details are given in the Supporting Information.	105
8. Table 6.2 Cyclic voltammetry and absorbance data for IDBTs (1-2), IDBFs (6-7), <i>syn</i> -IIDBT 3 , and <i>syn</i> -IIDBF 8^a . [a] CVs were recorded at a scan rate of 50 mV s ⁻¹ with a glassy carbon working electrode, Pt coil counter electrode, and Ag wire pseudoreference. All data were collected in degassed CH ₂ Cl ₂ , and ferrocene was used as an internal reference. Potentials were referenced to the SCE by using the Fc/Fc ⁺ half-wave potential (Fc/Fc ⁺ = 0.46 V vs. SCE).....	108

LIST OF SCHEMES

Scheme	Page
1. Scheme 1.1 Synthetic routes to various IF analogues.....	3
2. Scheme 1.2 Synthesis of fluoreno[3,2- <i>b</i>]fluorene.....	14
6. Scheme 2.1 Synthesis of Fluoreno[3,2- <i>b</i>]fluorene 2	24
7. Scheme 2.2 Synthesis of Fluoreno[4,3- <i>c</i>]fluorene 8	25
8. Scheme 3.1 Synthesis of <i>syn</i> -IIDBTs 2	35
9. Scheme 4.1 Synthesis of IDBTs 1 , 2 , and IIDBTs 3 , 4 and their conversion to the respective sulfones 5-8 along with formation of decomposition product 9	50
10. Scheme 5.1 Synthesis of FF 1 , DBFFs 2-4 and TBFF 5 along with the isolated diketone decomposition products 11 and 12	80
11. Scheme 6.1 Synthesis of <i>syn</i> -IDBF (6) and <i>syn</i> -IIDBF (8) as well as the ring- Opened products 22-23 derived from <i>anti</i> -IDBF (7) and <i>anti</i> -IIDBF (9), respectively	99

CHAPTER I

SYNTHESIS AND PROPERTIES OF QUINOIDAL FLUORENOFLUORENES

This chapter is an un-published review to be submitted to *Accounts of Chemical Research* by Barker, J. E.; Warren G. I.; Haley, M. M. entitled: Rational Design of Antiaromatic and Diradicaloid Diareno-*s*-indacenes, Diareno-dicyclopenta[*b,g*]naphthalenes, and Diareno-dicyclopenta[*b,i*]anthracenes. This manuscript was written by Joshua E. Barker with assistance from Gabrielle I. Warren and Prof. Michael M. Haley.

1.1 Introduction

In 2011 we reported the synthesis of 5,6,11,12-tetraethynylindeno[1,2-*b*]fluorenes (IF, **1**).¹ This study began as a simple rotation project for a first-year graduate student who wanted to try something different other than the current lab projects at the time.² Ten years and ~40 papers later, what began as a rotation project to synthesize a new organic semiconductor has blossomed into a fruitful and thorough study of structure-activity relationships at the intersection of antiaromaticity and diradical character. Initial efforts in our group^{1,3} coincided with similar work from the Tobe^{4,5} group examining the synthesis of different indenofluorene isomers (**2-4**, Figure 1) which culminated in 2017 in the synthesis of indeno[1,2-*a*]fluorene⁶ (**5**), the last unreported indenofluorene isomer.

Perhaps the greatest draw to the seemingly simple IF scaffold is its use as a template. The initial synthesis based on work by the Swager group⁷ was not modular or high-yielding and

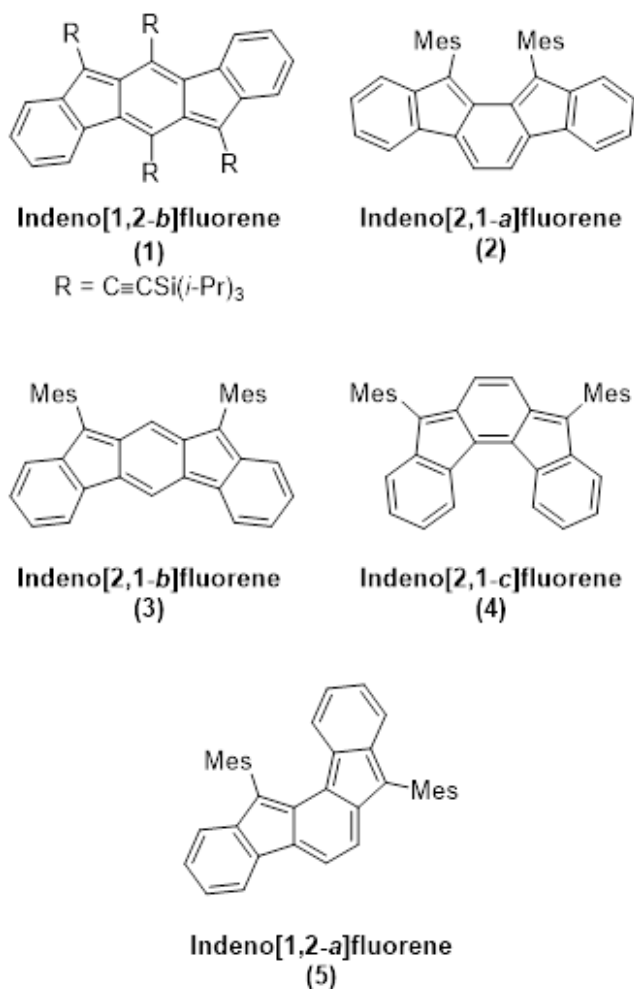
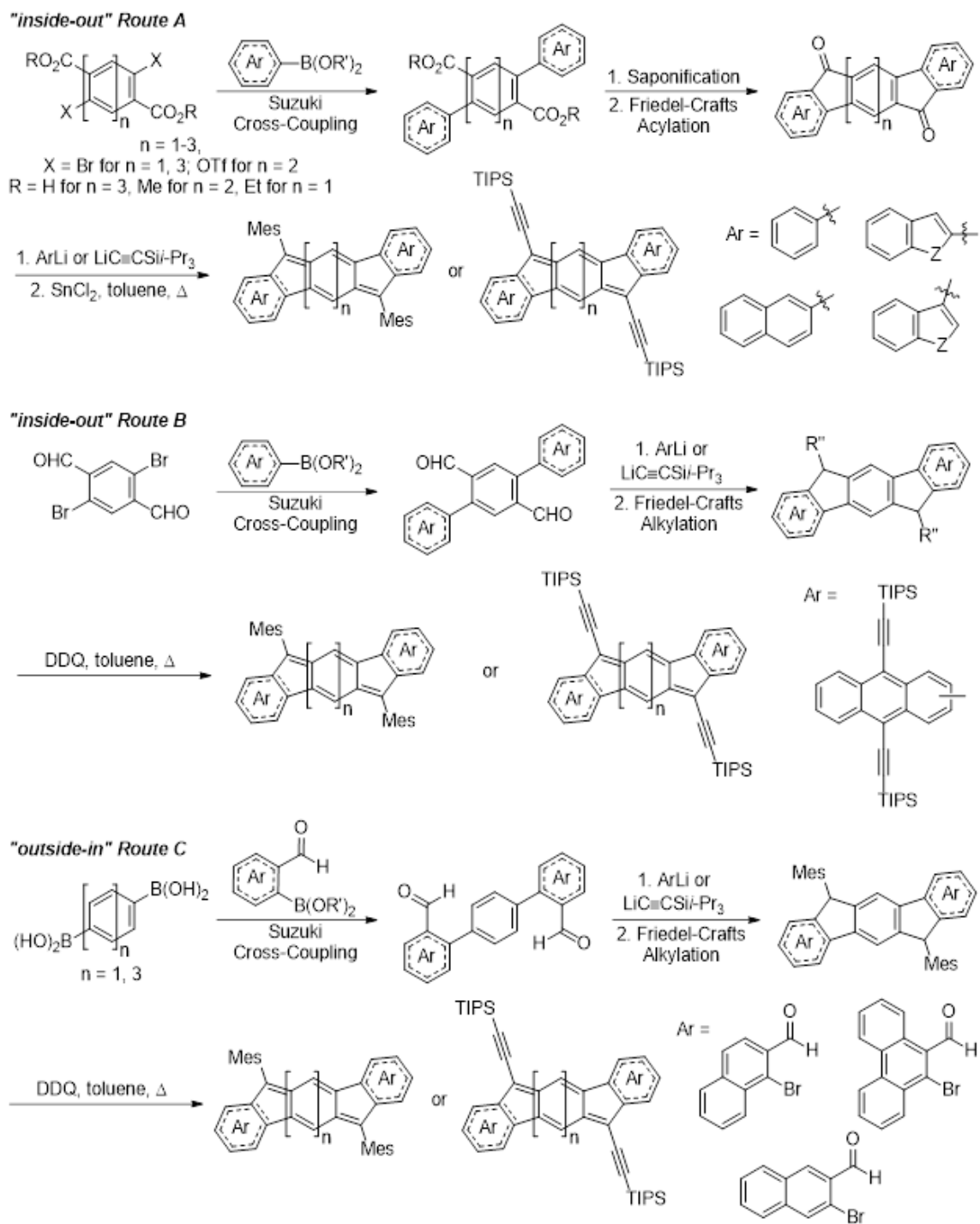


Figure 1.1 The five fully-conjugated indenofluorene isomers.

we quickly developed a synthetic scheme, derived from the Deuschel^{8,9} and Wang¹⁰ routes to indeno[1,2-*b*]fluorene diketones, which could be used to make a wide range of IF-type structures. This scheme is enacted through two possible paths, either an “inside-out” route (Scheme 1A and 1B) or an “outside in route” (Scheme 1C). In both cases, a symmetrically functionalized aryl core is coupled with the desired external aryl rings through a Suzuki cross-coupling reaction. After *p*-terphenyl formation, the next steps depend on the identity of the carbonyl group. If it is an ester, then saponification followed by Friedel-Crafts acylation yield the key diketone intermediate. The diketone is then subjected to an addition using either an aryl Grignard reagent, an aryl-lithiate, or an



Scheme 1.1 Synthetic routes to various IF analogues.

acetylide anion followed by reductive dearomatization using tin (II) chloride to yield the final conjugated product. On the other hand, if the carbonyl is an aldehyde, the first step

after the cross-coupling is to perform the addition reaction followed by a Friedel-Crafts alkylation to generate dihydro-precursor to the final compound. In this case, oxidative dearomatization using DDQ yields the desired product. As graduate students in the Haley group performed the first studies using these methods they envisioned a wide range of IF analogues that were now accessible.

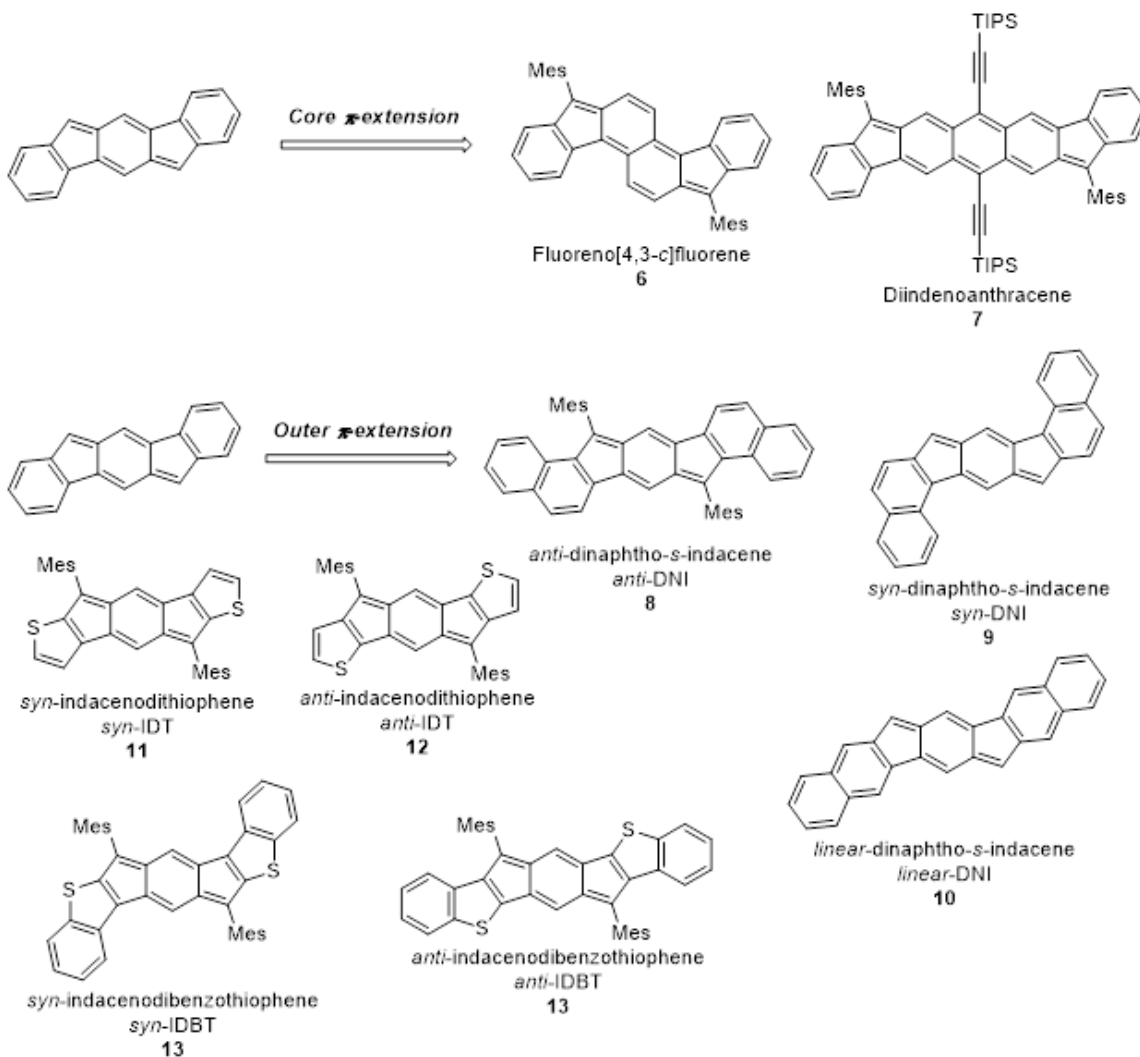


Figure 1.2 General strategies for modification of the IF-template.

The first steps into the chemical space around the IF template involved two main strategies that the group has followed through to this day. The first involved π -extension of the quinoidal core (Figure 2), seen in the synthesis of fluoreno[4,3-*c*]fluorene ([4,3-*c*]FF,

6) which possessed a quinoidal naphthalene core in contrast to the benzoquinoidal IF.¹¹ While this molecule exhibited closed shell quinoidal character similar to IF, serendipity struck with the synthesis of the anthracenoquinoidal analogue diindenoanthracene (DIAn, **7**). Synthesized in 2016 by graduate student Gabe Rudebusch, DIAn demonstrated strong diradical character with a thermally accessible singlet-triplet energy transition.¹² At the time it was known that [2,1-*b*]IF (**3**) was a diradicaloid and that the as-yet unreported [1,2-*a*]IF (**5**) had an extremely high calculated diradical character. However, while diradical resonance structures can be drawn for any IF derivative, no indication of diradical behavior had been exhibited by IFs **1**, **2** and **4** or by [4,3-*c*]FF **6**. Thus, the discovery of diradical character in DIAn **7** opened the question of how to further promote this interesting property in other IF-derived structures; a question which will be explored in detail in the coming pages.

The second strategy for modifying the IF template involves modification of the outer π -system. A study by graduate student Conerd Frederickson used fused naphthalenes to create the dinaphtho-*s*-indacenes (DNIs, **8-10**), which allowed for control over the electronic structure of the core π -system on the basis of the bond order of the naphthalene-*s*-indacene fusion bond (Figure 3).¹³ A variation on this modification was introduced by graduate students Brian Young and Jon Marshall who worked on the synthesis of thiophene-fused *s*-indacenes. The indacenodithiophenes (IDTs, **11** and **12**) or indacenodibenzothiophenes (IDBTs, **13** and **14**) can be viewed as analogues of the IF scaffold where thiophenes or benzothiophenes are fused to the core of the molecule instead of the outer fused benzene rings of IF **1**.¹⁴ Motivation for this work came from the use of anthradithiophene as a more stable analogue to pentacene, but in contrast to the

anthradithiophene/pentacene relationship, the IDBTs and IDTs have smaller HOMO-LUMO energy gaps than IF **1**. Further investigation uncovered the reason for the decrease in the HOMO-LUMO energy gap, namely, that synthesis of the thiophene-fused *s*-indacene structures enhances the *s*-indacene electronic structure in contrast to the quinoidal structure observed in **1**.^{14,15} Increasing the double bond character of the fusion bond moving from IDT to IDBT results in a more antiaromatic *s*-indacene core to the point that the molecules are effectively a phenyl-substituted *s*-indacene core fused with a thioether linkage.¹⁵

1.2 Antiaromaticity

One of the notable characteristics of indenofluorenes and their analogues is that they all possess $4n-\pi$ -electrons making them formally antiaromatic. Indenofluorenes themselves possess 20 π -electrons and each additional benzenoid ring added to the core adds 4 π -electrons, while each additional aromatic ring fused to the outside of the molecule adds 8 π -electrons. While IF is formally antiaromatic, it is better viewed as an interface between different π -systems. Figure 3 shows a schematic of IF highlighting the *p*-quinodimethane core of IF vs. the embedded *s*-indacene motif. Through the use of NICS-XY scans¹⁶ it is observed that the outer benzene rings retain their aromaticity while the five-membered rings and central benzenoid ring exhibit moderate paratropicity typical of quinoidal π -systems. As discussed above, through outer fusion of different carbocycles or heterocycles, this quinoidal behavior can be modulated such that in the case of the IDBTs, the *s*-indacene character of the core can be enhanced over the quinoidal character. The synthesis of the DNIs illustrated that this interplay broadly depends on the bond order of the fusion bond. Through fusion along different bonds of naphthalene it was seen that a higher bond order (1,2-bond = 1.66 bond order) increased the *s*-indacene character and the

core became more paratropic than **1**. Fusion along the 2,3-bond (1.33 bond order) resulted in the central π -system becoming less paratropic than IF **1**. Finally, extension of the core of the molecule leads to an increase in quinoidal conjugation and thus a decrease in overall antiaromaticity relative to less-extended analogues.^{12,17}

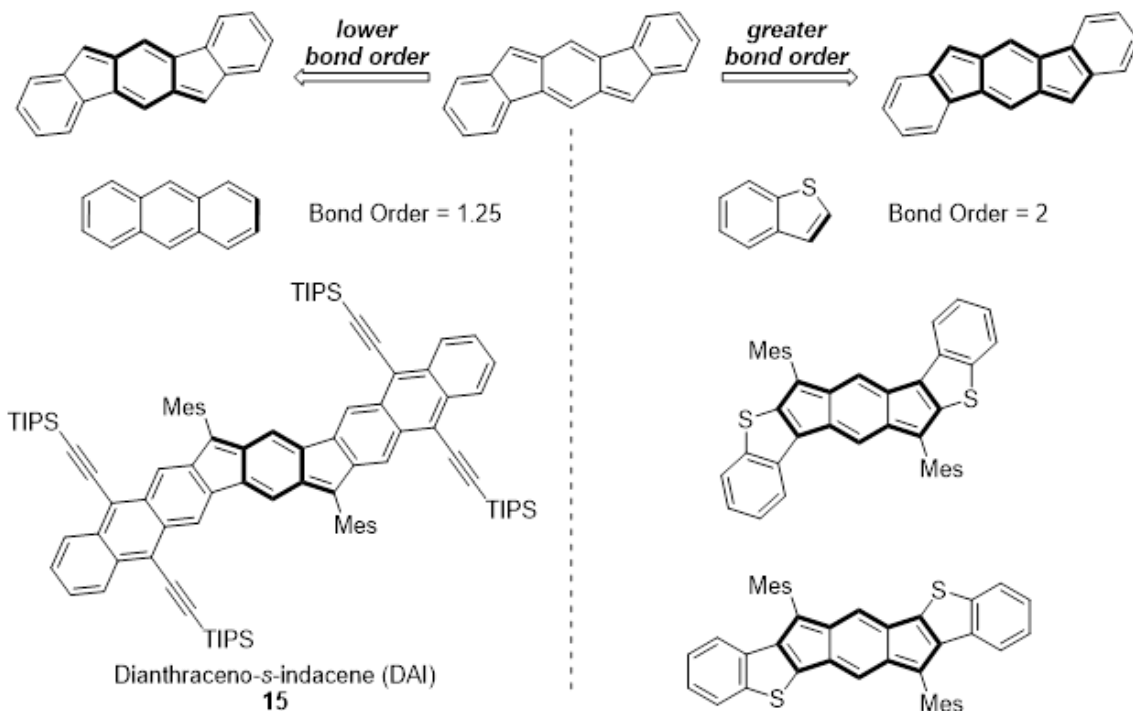


Figure 1.3 Illustration of the *p*-quinodimethide and *s*-indacene motifs within IF. Lower bond order (e.g. through fusion along the highlighted 2,3 bond of anthracene) favors the *p*-quinoidal structure. Higher bond order (e.g. through fusion with the highlighted bond of benzothiophene) favors the antiaromatic *s*-indacene structure.

We recently showed an extreme case of the bond order fusion phenomenon with the synthesis of a dianthraceno-*s*-indacene (DAI, **15**, Figure 3) that was fused along the 2,3-bond of anthracene.¹⁸ The 2,3-bond of anthracene is assigned a bond order of 1.25 by a simple resonance structure scheme where the 2,3-bond is a double bond in 1 out of 5 possible resonance structures for anthracene. As a result of this lower bond order, we expected the paratropicity of the *s*-indacene core to be essentially extinguished leading to a molecule that would behave like a *p*-quinodimethide fused to two anthracenes. Synthesis

of this molecule resulted in a downfield shift of the core ^1H singlet by 0.33 ppm. The most striking feature of the decreased paratropicity was that **15** exhibited weak orange fluorescence. IFs and other antiaromatic/quinooidal systems generally are non-emissive due to an intersystem crossing between the S_0 and S_1 states leading to non-radiative decay of the excited state. The fluorescence of **15** therefore provided compelling evidence that, due to the decrease in paratropicity, the barrier between the S_0 and S_1 states had been raised sufficiently to allow for weak emission from the excited state.

Considering the other extreme of paratropicity, high antiaromaticity, in the core of the IF-template, our only forays had been the DNIs and the IDBTs. While the DNIs showed a method to modulate core paratropicity, they still only exhibited moderate paratropicity as shown through NICS-XY scans and ^1H NMR analysis. Only the IDBTs approached the antiaromaticity of *s*-indacene, according to NICS values (Figure 4a).¹⁵

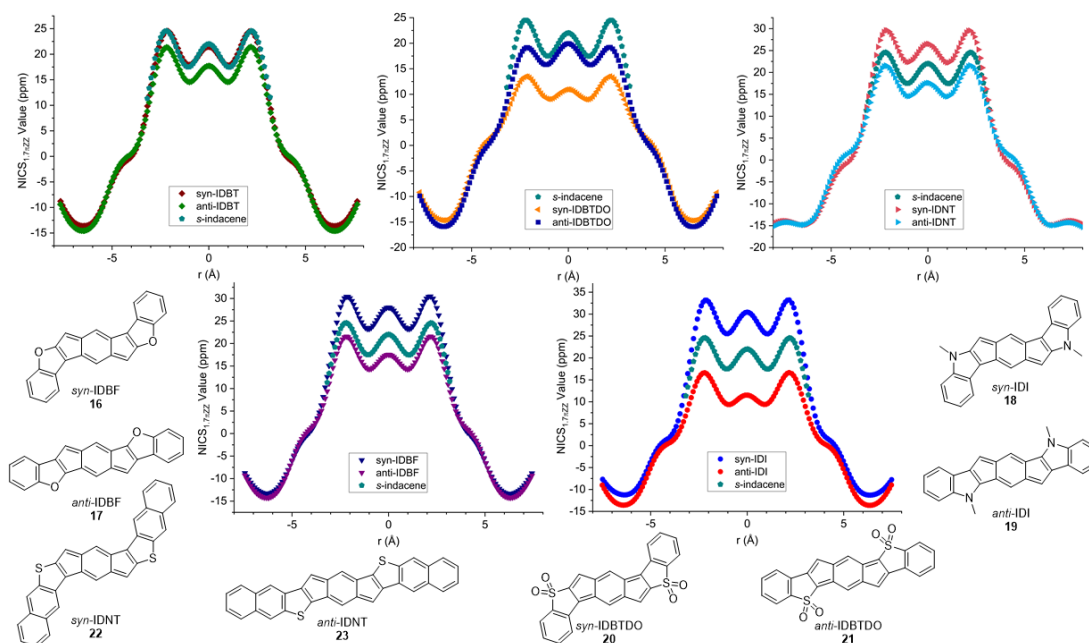


Figure 1.4 NICS-XY scans of the heterocycle-fused *s*-indacenes studied by our group.

s-Indacene presents an interesting challenge from a theoretical point of view. While it possesses 12 π -electrons, suggestive of strong antiaromaticity, it exhibits delocalized

bond lengths in the solid state^{19,20} and computational methods have disagreed on its classification as antiaromatic, aromatic, or non-aromatic.²¹⁻²³ This disagreement arises from the two possible electronic structures indicated by computations, which are either a delocalized D_{2h} structure or a bond-alternant C_{2h} structure.

The DNI and IDBT studies showed that we could access an s-indacene motif within our molecules that would approximate the C_{2h} structure in contrast with the previously isolated D_{2h} s-indacenes. This was not completely appreciated until we recently began examining the effects of other heterocycle fusions analogous to the IDBTs. “When are you going to look at benzofuran (BF) fusion in place of the benzothiophenes in the IDBTs?” had been a common question directed at M.M.H. from colleagues as well as audience members at conferences and professional meetings for many years. More projects than students had kept us from studying the indacenodibenzofurans (IDBFs, **16** and **17**) until a rotation project once again provided a spark. In the fall of 2018, J.E.B. had been tasked with creating a project for an incoming rotation student to work on during the 10-week fall term. After running some predictive NICS-XY calculations he realized that changing the heteroatom in the fused heterocycle had a dramatic effect on the antiaromatic s-indacene core. The tested molecules included not only the IDBFs, but also indacenediindoles (IDIs, **18** and **19**) and indacenodibenzothiophene dioxides (IDBTDOs, **20** and **21**, also common targets proffered by conference attendees)²⁴ where the sulfur atoms of the IDBT had been oxidized to sulfones. These computations (Figures 4b-d) showed that paratropicity of the syn-isomers of IDBF (**16**) and IDI (**18**) (syn- vs. anti- denotes the relationship of the heteroatom with respect to the apical carbon of the five-membered ring) would exceed that

of *s*-indacene. Synthesis of the IDBFs²⁵ and IDIs therefore commenced in the fume hood of J.E.B. with rotation students Tavis Price and Nick Gallman, while fellow lab member

Table 1.1 Electrochemical, optical, and NMR data for the heterocycle-fused-*s*-indacenes.

	HOMO (eV)	LUMO (eV)	E_{gap} (eV)	λ_{max} (nm)	^1H shift (ppm)
13	-5.54	-3.93	1.61	632	6.06
14	-5.52	-3.81	1.71	624	6.08
16	-5.55	-3.97	1.58	642	5.60
17	–	–	–	584	6.14
20	-6.28	-4.51	1.77	624	6.91
21	-6.12	-4.46	1.67	587	6.03
22	-5.49	-4.08	1.41	697	5.99
23	-5.43	-3.83	1.60	665	6.09

Justin Dressler (J.J.D. hereafter) began the work of synthesizing the IDBTDOs.²⁶ A final wrinkle was added during the winter term when, prompted by work from the Tovar group examining the effects of naphthothiophene-fusion on borepin aromaticity, M.M.H. wondered about the effects of the same fusion on the *s*-indacene core. Then a rotation student, Gabrielle Warren was tasked with the synthesis of the indacenodinaphthothiophenes (IDNTs, **22**, and **23**) which she continued as a full-member of the Haley group and has recently reported.²⁷

These recent studies have revealed a great deal. Perhaps the best illustration of the changes in paratropicity of the *s*-indacene core between these compounds is from the singlet proton NMR shift attributed to the proton located on the *s*-indacene core common to these molecules. Increasing antiaromaticity will result in an upfield shift of the core

proton shift. This is observed in the ^1H NMR spectra of the *syn*-isomers **13**, **16**, and **22** (6.06, 5.99, and 5.60 ppm, respectively) as they become more paratropic. Conversely the *anti*-isomers show a slightly decreasing trend in paratropicity (6.11, 6.14, and 6.91 ppm for **14**, **17**, and **23**, respectively). Molecules **20** and **21** show a reversed trend with *anti*-IDBTDO **21** being the most paratropic (6.03 ppm vs. 6.09 ppm for **20**), which is attributed to a change in electronegativity in the oxidized sulfur atom.²⁶ Cyclic voltammetry measurements also corroborate the strong antiaromaticity of these molecules which manifests in deep HOMO (−6.28 to −5.43 eV vs. vacuum) and LUMO levels (−4.51 to −3.81 eV vs. vacuum) as well as low HOMO-LUMO energy gaps (1.41 to 1.77 eV). Similar trends are observed in the low energy absorbance maxima (Table 1) for all compounds, where red-shifting is observed in correlation with increased antiaromaticity and π -extension. All optical and electrochemical data are summarized in Table 1 along with the core proton NMR shift. The final evidence in favor of antiaromatic *s*-indacene cores in these molecules comes in the form of their x-ray crystal structures which universally show bond-alternant cores consistent with the C_{2h} structure of *s*-indacene. A novel variation on this electronic structure was found in the case of the IDBTDOs, which had strong bond alternation in the core but the opposite bonding pattern compared to all other derivatives. A computational investigation determined that for the IDBTDOs the standard bond alternation existed as a local minimum on the potential energy surface while the observed pattern resulted in a structure that was slightly lower in energy due to a slightly less paratropic *s*-indacene core.

1.3 Diradical character

The discovery of diradical character in DIAn **7** sparked a great deal of interest in

our group as to whether this property could be induced in other IF homologues. Before discussing this topic too extensively though, several terms should be defined. For the purposes of consistency, we will use the definition found in the IUPAC “Gold Book” for diradicals which states that diradicals are “Molecular species having two unpaired electrons, in which at least two different electronic states with different multiplicities [electron-paired (singlet state) or electron-unpaired (triplet state)] can be identified.²⁸ In terms of orbital energies pure diradicals are described as molecules in which two electrons occupy two degenerate non-bonding molecular orbitals, while the term diradicaloids is used to identify diradical-like molecules in which the two molecular orbitals are nearly degenerate (Figure 6).

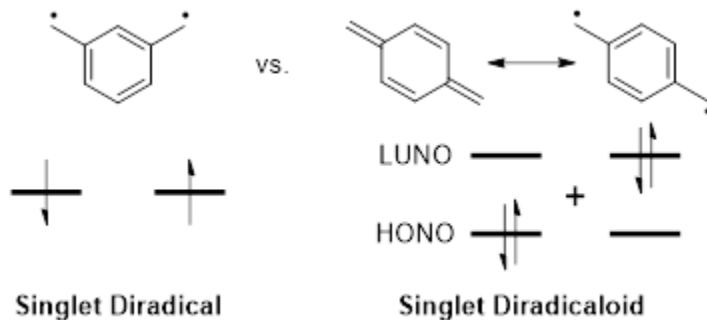


Figure 1.5 Illustration of the electronic structure of a diradical vs. a diradicaloid. In a diradical the orbitals are degenerate. A diradicaloid has orbitals that are close in energy but not degenerate.

Quantum chemical calculations are indispensable to any study of diradicaloids for determining the effects responsible for changes in diradical character. Standard diradical calculations involve determination of the diradical index value (y_0) which represents the % occupation of the lowest unoccupied natural orbital (LUNO) according to natural orbital occupation number (NOON) analysis. In this scheme $y_0 = 1$ represents pure diradical character while $y_0 = 0$ is taken to represent a pure closed-shell system.²⁹ Compounds with intermediate values are predicted to be diradicaloids and the magnitude of the y_0 value is

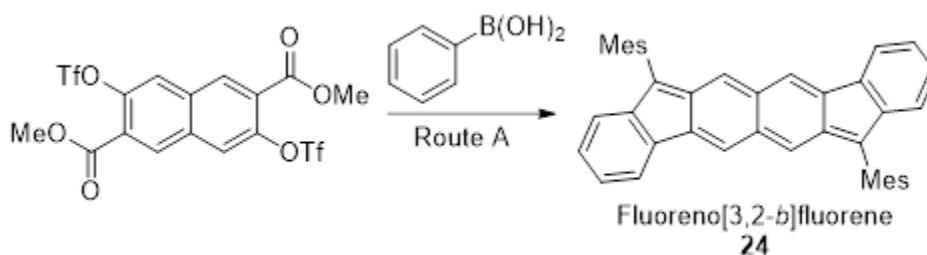
used as an indicator for the likelihood that a molecule will exhibit diradical-like properties. It is important to note that y_0 value calculations depend heavily on functional selection and as a result they can only be reliably compared when the functional and basis set are the same. The energy gap between the singlet state and triplet state (ΔE_{ST}) in diradicaloids is another important property that is often calculated and is the only unambiguous experimentally measurable phenomenon related to diradical character. Our collaborators in the Nakano group at Osaka University have used calculations of the various parameters that contribute to ΔE_{ST} to probe the effects of different aryl-fusions on diradical character. According to the two-electrons in two-sites model of diradical character, ΔE_{ST} can be calculated according to Equations 1 and 2 where a and b represent the two electrons in localized natural orbitals and the key terms are U (the difference between on- and intersite Coulomb repulsions), t_{ab} (the transfer integral) and K_{ab} (the direct exchange orbital). These calculations have proven invaluable to our understanding of the theoretical explanations for observed changes in diradical character across the families of molecules that we have studied.

$$(1) \Delta E_{ST} = \frac{U}{2} \left[1 - \frac{1}{\sqrt{y(2-y)}} \right] + 2k_{ab}$$

$$(2) y = 1 - \frac{1}{\sqrt{1 + \left(\frac{U}{4t_{ab}}\right)^2}}$$

Along with DIAn another long time synthetic target in our group was fluoreno[3,2-*b*]fluorene (FF, **24**), the naphthoquinoidal analogue of IF. Considering the diradical character of DIAn we were interested in determining whether or not FF, being the intermediate structure between IF and DIAn, would exhibit the diradical character of the

latter or the quinoidal structure of the former. Unfortunately, our efforts towards this target remained largely unsuccessful for many years due to the difficulty in generating an appropriately functionalized naphthalene precursor. A report by the McCulloch group on naphthacenedithiophenes led us to a key bistriflate precursor which enabled the successful synthesis of FF.¹⁷ Upon completing the synthesis of FF it was found that FF exhibits mostly closed-shell quinoidal properties comparable to IF with no indication of diradical character despite an intermediate y_0 value ($y_0 = 0.492$).



Scheme 1.2 Synthesis of fluoreno[3,2-*b*]fluorene

With FF finally reported our interest turned to modifying the FF and DIAn in similar ways to the IF scaffold. Given that increased antiaromaticity in molecules with a diradical motif will lead to stronger diradical character, we reasoned that making analogous compounds to the DNIs or IDBTs using the FF and DIAn templates would modulate the antiaromaticity and thereby the diradical character. Achieving a level of control over diradical character is desirable because of the associated singlet-triplet energy gap. The ability to controllably transition from the diamagnetic spin-paired singlet state to the paramagnetic spin-parallel makes diradicaloids interesting targets for magnetic materials.³⁰⁻³² Unfortunately, while the diradical literature has seen many recent reports of interesting diradicaloid structures, there have been few thorough structure-activity relationship studies that examine the optimization of ΔE_{ST} . As we began synthesizing various derivatives based on FF and DIAn we realized that we had a unique opportunity to

examine diradical character and tune ΔE_{ST} . By applying the synthetic schemes from Scheme 1 it is possible to synthesize a diverse family of diradicaloids that have a common diradical core. In the case of FF-derived structures, the core of the molecule is a dicyclopenta[*b,g*]naphthalene (DCN) that possesses a 2,6-naphthoquinodimethide (NQD) diradical motif. The DIAn-type structures contain a dicyclopenta[*b,i*]anthracene (DCA) core and possess a 2,6-anthraquinoidimethide (AQD) diradical unit. The common NQD and AQD units between derivatives allow us to directly compare experimental results and draw conclusions about the effects of changing the fused aryl group or isomerism on diradical character.

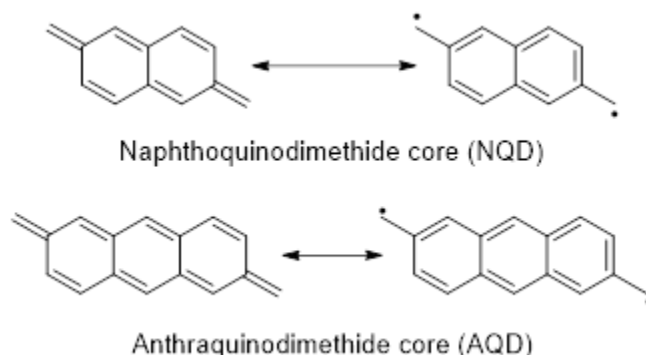


Figure 1.6 The core diradical motifs contained within FF derivatives (NQD) and DIAn derivatives (AQD).

Our first step after DIAn involved functionalization of the DCN motif with benzothiophenes. Given the increase in antiaromaticity seen in the IDBTs relative to IF, J.J.D. hypothesized that a similar increase in paratropicity would occur in the DCN core relative to FF and might unlock diradical character in the resultant *anti*-indenoindenodibenzothiophene (IIDBT, **25**).³³ The increase in diradical character could be expected as it would relieve the paratropicity in the core by re-aromatizing the central naphthalene unit (Figure 6). Diradical character resulting from the generation of a larger number of Clar sextets (i.e., a more aromatic resonance structure) is commonly seen in the

diradical literature relating to carbon-centered PAH-type diradicaloids.³⁴ Computational analysis supported this hypothesis with **25** ($y_0 = 0.61$) having a comparable diradical index to DIAn ($y_0 = 0.62$). Upon successfully synthesizing the *anti*-IIDBT isomer, it was not initially clear that this molecule had strong diradical character. VT-NMR experiments performed in 1,1,2,2-tetrachloroethane-*d*₂ did not show significant thermal broadening which indicated that the paramagnetic triplet state was not being populated even at 125 °C. On the other hand, the x-ray structure showed an elongated bond (1.424 Å) between the naphthalene core and the apical carbon of the five-membered ring, which indicated

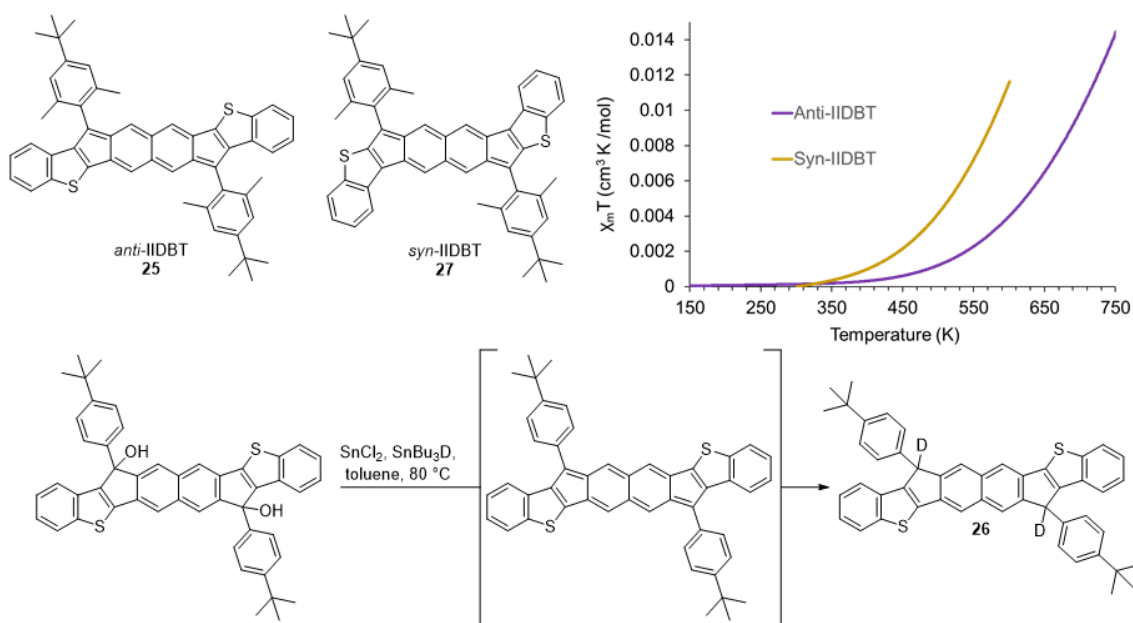


Figure 1.7 (top) SQUID magnetometry data for *anti*-IIDBT and *syn*-IIDBT. (bottom) Deuterium labelling experiment to verify the radical character of *anti*-IIDBT.

increased single-bond character implying an open-shell structure. Radical labelling experiments using tri-*n*-butyltin deuteride and a less-bulky aryl substituent on the five-membered ring resulted in dideutero compound **26** (Scheme 3) indicating radical character at the expected positions of highest spin-density. The crucial piece of evidence was finally obtained from collaborators in Spain who performed a high-temperature superconducting

quantum interference device (SQUID) measurement which showed definitively that **25** had a thermally accessible triplet state ($\Delta E_{ST} = -8.0 \text{ kcal mol}^{-1}$), indicating that it was a singlet diradicaloid.

As this study was being completed J.E.B. wondered what differences would be observed between **25** and the *syn*-IIDBT isomer (**27**).³⁵ According to the trends seen in the IDBTs, **27** should be more antiaromatic than **25**, which would favor increased diradical character due to aromatization of the naphthalene core. Simple resonance structure analysis (Figure 7) also provided a hypothesis that with the sulfur cross-conjugated to the NQD core increased spin delocalization to the outer benzene rings was possible. This was confirmed by computations which showed that (1) spin density was predicted to exist on the outer benzene rings of **27** but was non-existent in **25**, (2) the U term from Equation 1 was smaller for **27** than for **25** indicating less electronic repulsion between the sulfur atom and the radical as a result of the radical conjugation path, and (3) as a result of the first two points, the diradical index value for **27** was larger than **25** (0.66 and 0.61, respectively) and the calculated ΔE_{ST} was smaller (-8.06 for **27** vs. $-8.77 \text{ kcal mol}^{-1}$ for **25**). Gratifyingly, these predictions were borne out experimentally as the measured ΔE_{ST} value for **27** was $-6.9 \text{ kcal mol}^{-1}$ which represented a $1.1 \text{ kcal mol}^{-1}$ difference in ΔE_{ST} compared with **25** ($\Delta E_{ST} = -8.0 \text{ kcal mol}^{-1}$). The singlet-triplet energy gap could be further tuned by following the heteroatom effects of the IDBTs and IDBFs. *Syn*-fusion of benzofurans (*syn*-indenoindenodibenzofuran, *syn*-IIDBF, **28**) instead of the benzothiophenes led to a further enhancement of diradical character ($y_0 = 0.68$) and an associated reduction in ΔE_{ST} (-7.68 calculated, $-6.0 \text{ kcal mol}^{-1}$ experimental) due to the increased electronegativity of the heteroatom.²⁵ Unfortunately *anti*-IIDBF was not successfully synthesized due to an

unexpected ring-opening of the furan ring during the final reductive dearomatization step.

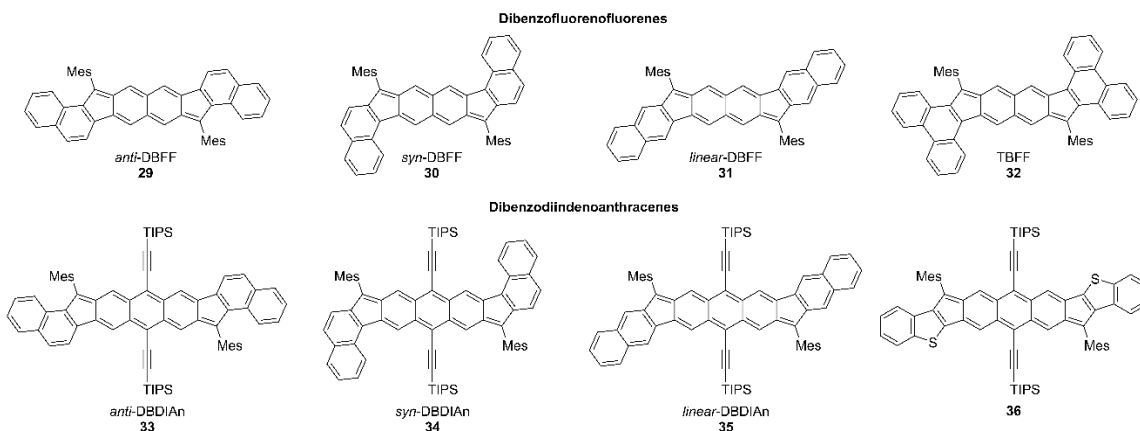


Figure 1.8 Structures of the DBFFs and DBDIAn.

With the IIDBTs the main theoretical effect of modifying the diradical character was the difference in U between the two isomers. Through further computations we realized that we could leverage the second part of the U/t_{ab} term from Equation 1 by performing the naphthalene fusion strategy seen in the DNIs with the FF and DIAn templates. Fusion of naphthalene along the 1,2 bond to the FF core gives either *anti*-dibenzofluorenofluorene (*anti*-DBFF, **29**) or *syn*-DBFF (**30**) and we denote fusion along the 2,3-bond of naphthalene as *linear*-DBFF (**31**).³⁶ Fusion of a phenanthrene increases the fusion bond order to 1.8 and gives tetrabenzofluorenofluorene (TBFF, **32**). Analogous fusions with the DIAn core yield *anti*-dibenzodiindenoanthracene (*anti*-DBDIAn, **33**), *syn*-DBDIAn (**34**), *linear*-DBDIAn (**35**), and *anti*-fusion of benzothiophene is named *anti*-dicyclopenta[*b,i*]anthracenodibenzothiophene (**36**).³⁷ According to the two-electrons in two-sites calculations (Table 2), y_0 varies between 0.51 (*linear*-DBFF) and 0.63 (TBFF) for the DBFF series and 0.64 (*linear*-DBDIAn) to 0.82 (**35**) for the DBDIAn series. ΔE_{ST} varies in a similar manner within these series and generally decreases in correlation with increasing fusion bond order. These two series of molecules contrast with the IIDBTs in

that the change transfer integral (t_{ab}) is the larger effect responsible for the tuning of ΔE_{ST} . As a result of the difference in t_{ab} between isomers we are able to tune ΔE_{ST} in small increments across each series with the variance between the DBFFs and TBFF being -7.6 to -9.6 kcal mol $^{-1}$ and the variance between the DBDIAn isomers and **35** being -4.8 to -3.2 kcal mol $^{-1}$. Tuning y_0 and ΔE_{ST} in such small increments has previously not been seen in isomeric series of diradicaloids. The lack of similar studies in the literature highlights the importance of the common diradical cores within these molecules that enabled connection of structural differences to changes in ΔE_{ST} . These studies lay the groundwork for future SAR investigations of diradical molecules which is an important step towards their optimization for materials applications.

Table 1.2 Collected computational and experimental data for FF and DIAn based diradicaloids.

^a Geometries optimized at the R- and UB3LYP/6-311G* levels. ^b Estimated at the CASCI(2,2)6-311G* level using the (tuned-)LC-RBLYP MOs (denoted as tuned-LC-RBLYP-CASCI(2,2)/6-311G*). ^c Calculated at the PUHF/6-311G* level. ^d Adiabatic ΔE_{ST} value calculated at the spin-flip noncollinear (SF-NC)-TDDFT PBE5050/6-311G* level along with R- or UB3LYP/6-311G* zero-point vibrational energy correction for each spin state.

	$U/2$ (eV) ^{a,b}	t_{ab} (eV) ^{a,b}	y_0 ^{a,c}	ΔE_{STcalc} (kcal mol $^{-1}$) ^{a,d}	ΔE_{STexpt} (kcal mol $^{-1}$)
7	1.435	0.916	0.62	-4.71	-4.2
24	1.446	1.163	0.49	-10.25	-9.3
25	1.563	1.031	0.61	-8.77	-8.0
27	1.404	0.905	0.66	-8.06	-6.8
28	1.380	0.865	0.68	-7.68	-6.0
29	1.336	1.012	0.60	-8.61	-7.8
30	1.352	1.055	0.56	-9.63	-8.7
31	1.315	1.143	0.51	-10.03	-9.6
32	1.349	0.960	0.63	-7.90	-7.6
33	1.377	0.781	0.71	-3.45	-3.2
34	1.378	0.818	0.69	-4.16	-3.8
35	1.348	0.905	0.64	-5.09	-4.8
36	1.572	0.774	0.82	-3.41	-3.4

1.4 Conclusions

In our previous Account² we brought “the fully conjugated indenofluorene scaffold

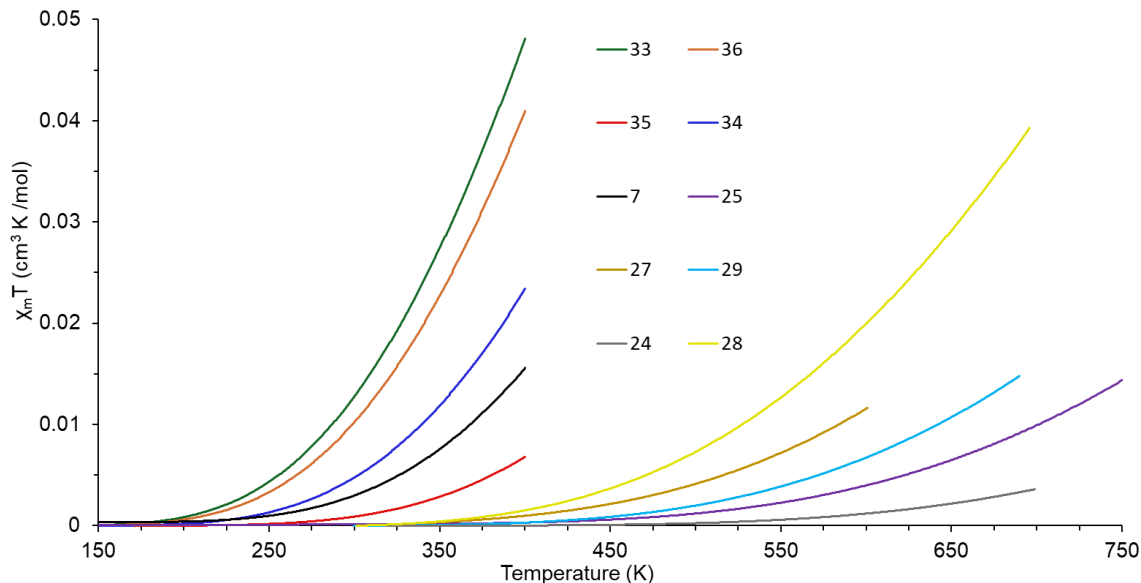


Figure 1.9 SQUID magnetometry plots for IIDBTs, *syn*-IIDBF, the DBFFs, and the DBDIAnS.

out of the unknown and into the toolbox of organic materials available for study”. In this Account we describe our further utilization of the IF template to guide fundamental studies of antiaromaticity in heterocycle fused *s*-indacenes and diradical character in diareno-fused FF and DIAn derivatives. Continued development of our synthetic schemes has enabled access to a wide range of IF, FF, and DIAn homologues allowing us to fine-tune their optical, electronic, and magnetic properties. Specifically, with regards to diradical character, we have described how extension of the quinoidal core from IF to FF to DIAn serves as a “coarse-shim” to transition from strong paratropicity to strong diradical character which relieves that paratropicity. The “fine-shim” (Figure 9) then comes from the outer fused arenes which can be used to modulate the diradical character based on increased or decreased conjugation pathways which influence t_{ab} or heterocycle-fusion which modulates U . Both of these theoretical “handles” provide us with a means to predict new structures and explain the magnetic phenomena we observe. Such studies have seldom been seen in the diradical literature but they are increasingly necessary if these novel

molecules are to be applied. The IF template has proven to be a truly fascinating study and has provided the inspiration for a diverse family of related molecules. There is still much work to do though and we look forward to further fundamental studies as well as semiconductor applications of this interesting class of hydrocarbons.

CHAPTER II

SYNTHESIS AND PROPERTIES OF QUINOIDAL FLUORENOFLUORENES

This chapter includes previously published and co-authored material from Barker, J. E.; Frederickson, C. K.; Jones, M. H.; Zakharov, L. N.; Haley, M. M. Synthesis and Properties of Quinoidal Fluorenofluorenes. *Org. Lett.* **2017**, *19*, 5312-5315. This manuscript was written by Joshua E. Barker with assistance from Conerd K. Frederickson and Prof. Michael M. Haley. The project in this chapter was conceived by Prof. Michael M. Haley. The experimental work in this chapter was performed by Joshua E. Barker. The computational work in this chapter was performed by Conerd K. Frederickson.

2.1 Introduction

Polycyclic antiaromatic hydrocarbons (PAAHs) have seen increasing interest as potential small molecule semiconductors for use in organic electronic and optical devices.¹ PAAHs are intriguing candidates for such applications because of their low HOMO-LUMO gaps compared with prominent acene-type polycyclic aromatic hydrocarbons (PAHs).² PAAHs historically have been difficult to study because they are less stable than their aromatic counterparts; however, kinetic stabilization for these compounds has been achieved through either the addition of bulky groups at reactive sites or fusion of aromatic rings to the antiaromatic core. This has enabled further investigation into PAAH properties and their fitness for use in devices.³

Our interest in PAAHs began some years ago with the report of stable, fully conjugated

indeno[1,2-*b*]fluorene derivatives⁴ (e.g., **1**, Figure 2.1), which proved to be the impetus for further study of indenofluorene (IF) scaffolds and related conjugated systems.⁵ Several indenofluorene regioisomers have since been reported,⁶ and recent work from our laboratory has turned to expanded structures⁷ and analogues containing heterocycles.⁸ Along with probing the antiaromaticity of these systems,^{7,8c} interest has grown in the open shell (OS) character exhibited by several derivatives.^{6b-c,9} Fusion of indene moieties with acenes to make IF homologues has recently been shown to be an effective strategy for tuning the OS character and aromaticity of IF-type structures. A most notable example, reported last year,^{9a} is based on a diindenoanthracene core (e.g., **3**). This molecule exhibited remarkable kinetic stability for an OS species, with a half-life of ~2 months in solution.

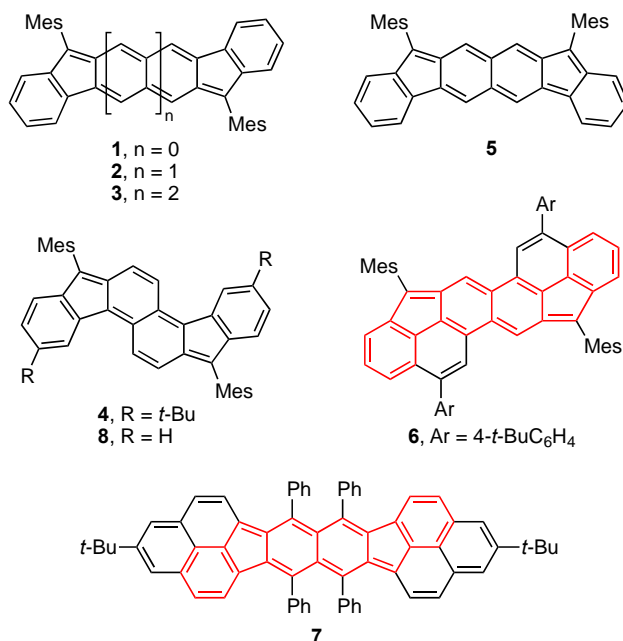


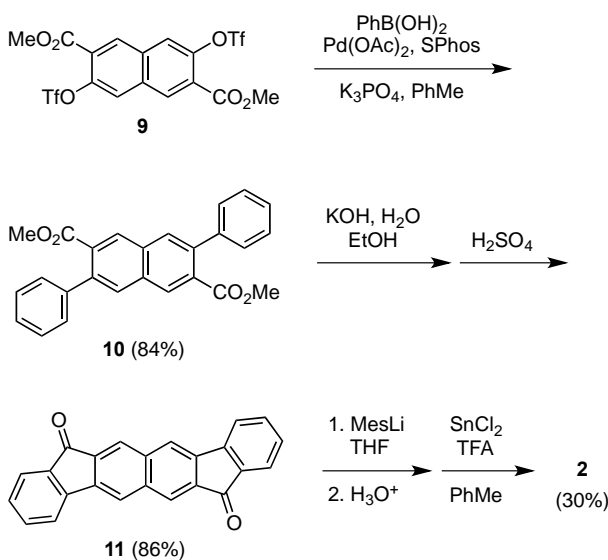
Figure 2.1 Known Fluorenofluorenes and related [3,2-*b*]FF-containing hydrocarbons.

Despite this resurgence in PAAH chemistry, IF analogues containing a naphthalene core, known as fluorenofluorenes (FF, e.g., **2**), are quite rare. The first reported FF regioisomer was fluoreno[4,3-*c*]fluorene **4** in 2012.¹⁰ Solution and solid-state analysis suggested the molecule to be closed shell (CS) as no evidence of a thermally accessible

triplet state was observed. Subsequent theoretical examination of several IF isomers and two FF analogues suggested that different modes of fusion of the indene moieties with the naphthalene core could yield greater open shell character.¹¹ Tobe and co-workers very recently reported the synthesis of fluoreno[2,3-*b*]fluorene **5**, which was found to have significant OS character in confirmation of the computational predictions.¹² Although fluoreno[3,2-*b*]fluorene **2** is unknown, this core unit is contained within two larger, known hydrocarbons, namely picene derivative **6**¹³ and bis-phenalenyl **7**,¹⁴ which display pronounced CS and OS character, respectively. In fact, the authors of the former very recent publication remarked that [3,2-*b*]FF **2** “is still elusive”.¹³ This is no longer the case for herein we disclose the successful preparation of **2** along with a new synthesis of [4,3-*c*]FF **8**, as well as discuss their resultant optoelectronic and structural properties.

2.2 Results and Discussion

The synthesis of **2** initially proved somewhat daunting because it was necessary to use an “inside-out” strategy to promote ring closure to afford the correct molecule geometry.⁵

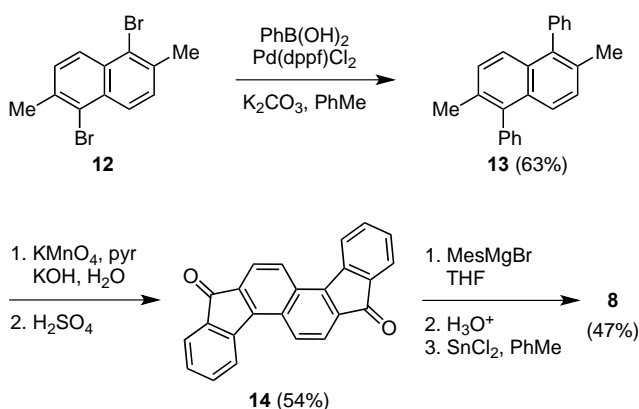


Scheme 2.1 Synthesis of Fluoreno[3,2-*b*]fluorene **2**.

Determining the best method for creating an appropriately substituted naphthalene

intermediate was not trivial.¹⁵ Fortuitously McCulloch and co-workers reported bis-triflate **9** (Scheme 2.1) as an intermediate in their recent report of naphthacenedithiophene-based polymers,¹⁶ from which **9** could be prepared in multigram quantities. Suzuki cross-coupling of **9** with phenylboronic acid gave diester **10** in 84% yield. Compound **10** was converted to **11** via hydrolysis of the ester groups followed by intramolecular Friedel-Crafts acylation, which afforded the poorly soluble, bright red dione in 86% yield. Treatment of **11** with mesityllithium followed by reductive dearomatization with SnCl₂ furnished **2** as a blue-purple solid in a modest 30% yield.

In addition to [3,2-*b*]FF **2** we prepared the parent hydrocarbon core of previously



Scheme 2.2 Synthesis of Fluoreno[4,3-*c*]fluorene **8**.

reported [4,3-*c*]FF **4**. Beginning from dibromide **12** (Scheme 2.2),¹⁷ Suzuki cross-coupling again with phenylboronic acid gave naphthalene **13** in good yield. Oxidation of the methyl groups using KMnO₄ and subsequent Friedel-Crafts acylation provided dione **14** in satisfactory yield. The conversion of **14** to **8** was similar to the analogous synthesis for **2** with the exception that catalytic TFA was not used for the reductive dearomatization. [4,3-*c*]FF **8** was isolated as a dark blue crystalline solid in 47% yield.

The electronic absorption spectra for **2** and **8** (Figure 2.2) show similar higher energy transitions in the 300-350 nm range, with the λ_{max} of the lowest energy transitions being

600 and 637 nm, respectively. TD-DFT calculations afford λ_{max} values in excellent agreement (607 and 631 nm, respectively).¹⁸ FF **2** and **8** tail off at around 725 and 800 nm, which correspond to optically determined energy gaps of ca. 1.71 and 1.55 eV, respectively. This latter, very low energy feature is common for molecules that have some OS singlet contribution to the ground state (*vide infra*).¹⁹

Crystals of **8** suitable for X-ray diffraction were obtained by layering CH₃CN on a

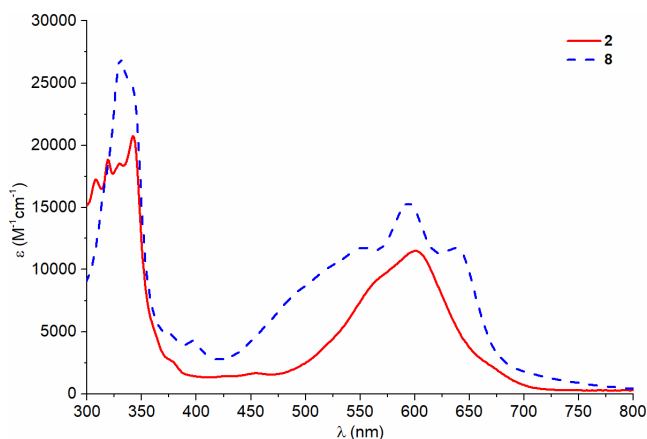


Figure 2.2 Electronic absorbance spectra of **2** (solid red) and **8** (dashed blue) in CH₂Cl₂. saturated CHCl₃ solution of **8**. Unfortunately, X-ray quality crystals of **2** were not secured; therefore, the structure was analyzed computationally.¹⁸ The molecular structure of **8** is shown in Figure 2.3 and notable bond lengths are given in Table 2.1, along with the theoretical bond lengths for computational analogues **2**^ˆ and **8**^ˆ. As expected **8** adopts a planar geometry (rms deviation of 0.026 Å) with nearly orthogonal mesityl groups (75°). The former naphthalene core displays a pronounced quinoidal arrangement as suggested by the alternating long (1.431–1.449 Å, bonds 2, 4, and 7) and short (1.347–1.381 Å, bonds 1, 3, and 5) bond lengths, indicating minimal OS character. The bond lengths of **8** are well replicated by those predicted for **8**^ˆ. The calculated bond lengths of **2**^ˆ would suggest that it too should exhibit a quinoidal core and therefore the CS form would dominate. In stark contrast, the X-ray structure of [2,3-*b*]FF **5** clearly implicates an OS system as the bond

lengths within the central core resemble a rearomatized naphthalene unit. In addition, the bond from this core to the apical carbon (bond 1) is considerably elongated (1.437 Å) compared to the same bond in **8** (1.380 Å).¹²

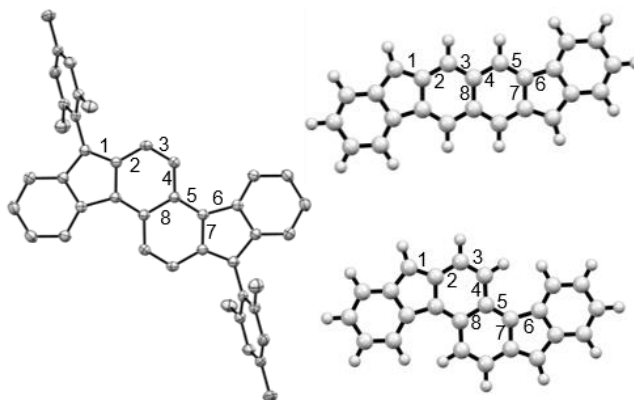


Figure 2.3 (Left) ORTEP showing top view of **8**; hydrogen atoms omitted for clarity. Ellipsoids drawn at the 50% probability level. (Right) Calculated structures of **2'** (top) and **8'** (bottom) with selected bonds labeled.

bond	8 (X-ray)	8' (calc) ^a	2' (calc) ^a
1	1.380(3)	1.378	1.387
2	1.431(3)	1.430	1.420
3	1.347(3)	1.359	1.384
4	1.442(3)	1.448	1.444
5	1.381(3)	1.387	1.361
6	1.484(3)	1.482	1.464
7	1.449(3)	1.460	1.466
8	1.474(4)	1.482	1.467

Table 2.1 Selected bond lengths (Å). ^aAll geometries were calculated at the RB3LYP/6-31++G(d,p) level of theory, mesityl groups omitted for computational simplification.

To compare the effects of antiaromaticity and biradical character, fluorenofluorenes **2**, **5**, and **8** as well as indeno[1,2-*b*]fluorene **1** were examined with NICS-XY scan²⁰ and biradical character index computations.²¹ Parent versions of each compound without the bulky mesityl groups on the five-membered rings were used to simplify comparisons as well as make the most efficient use of computational resources. FFs **2'** and **8'** show similar NICS-XY scans (Figure 2.4) to the parent indeno[1,2-*b*]fluorene **1'**, with NICS_{πZZ} values

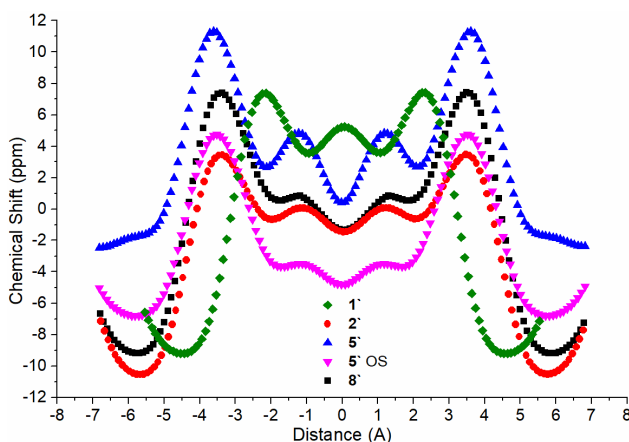


Figure 2.4 NICS-XY scans of indeno[1,2-*b*]fluorene **1'** and Fluorenofluorenes **2'**, **5'**, **5'** (OS) and **8'**.

reaching a maximum over the five-membered rings and being within 4 ppm of each other (3.5, 7.4, and 7.4 ppm, respectively), suggesting only modest antiaromaticity. All exhibit little variation in their NICS-XY scans when they are performed using an open shell method (Figure A3). In contrast, significant differences in chemical shifts are observed in the NICS-XY scans of **5'** when performed with closed and open shell methods. FF **5'** shows peak NICS _{π ZZ} values over the five-membered ring of 11.3 and 4.7 ppm calculated with the closed and open shell methods, respectively. The NICS scans of FF **5'** also show significant differences in the NICS values over the outer six-membered rings between the closed and open shell forms. The CS form of FF **5'** is consistent with the resonance structure depicted in Figure 2.1 where one of the outer rings is dearomatized (−2 ppm). In contrast, the OS form has a NICS _{π ZZ} value for the outer six-membered ring (−7 ppm) closer to those of FF **2'** (−10 ppm) and **8'** (−9 ppm), rings that are fully aromatic in both the open and closed shell forms. The inner six-membered rings of FF **2'** and **8'** are essentially atropic, whereas in FF **5'** (OS) the naphthalene has regained modest aromatic character (−4 to −5 ppm). The NICS results are corroborated by the biradical character indices calculated for FF **2'**, **5'** and **8'**, which are $y = 0.434$, 0.732 and 0.377 , respectively. Together, all of these data are

consistent with quinoidal FF **2** and **8** possessing modest biradical character and FF **5** having substantial biradical character.

2.3 Conclusions

In summary, we report the addition of polycyclic antiaromatic hydrocarbons **2** and **8** to the fluorenofluorene family. The observed structural properties of **8** are consistent with a quinoidal core, which is corroborated by the calculated geometries, NICS-XY scans, and the modest calculated biradical characters for **2** and **8**. Our report of **2** and **8** should allow for a more thorough examination of how π -extension of the indenofluorene core affects intrinsic optical and electronic properties, such as biradical character and antiaromaticity, as well as permit a comparison of related fluorenofluorene regioisomers to determine the effects of different ring fusions on these properties. We will also explore further derivatization for possible device applications of these molecules.

CHAPTER III

MOLECULE ISOMERISM MODULATES THE DIRADICAL PROPERTIES OF STABLE SINGLET DIRADICALOIDS

This chapter includes previously published and co-authored material from Barker, J. E.; Dressler, J. J.; Valdivia, A. C.; Kishi, R.; Strand, E. T.; Zakharov, L. N.; MacMillan, S. N.; Gómez-García, C. J.; Nakano, M.; Casado, J.; Haley, M. M. Molecule Isomerism Modulates the Diradical Properties of Stable Singlet Diradicaloids. *J. Am. Chem. Soc.* **2020**, *142*, 1548-1555. This manuscript was written by Joshua E. Barker and Justin J. Dressler with assistance from Prof. Michael M. Haley, Prof. Juan Casado, and Prof. Masayoshi Nakano. The project in this chapter was conceived by Michael M. Haley, Joshua Barker, and Justin J. Dressler. The experimental work in this chapter was performed by Joshua E. Barker, Justin J. Dressler, Abel Cárdenas Valdivia, and Eric T. Strand. The computational work in this chapter was performed by Ryohei Kishi, and Prof. Masayoshi Nakano.

3.1 Introduction

The subject of open-shell character and its interplay with the fundamental properties in polycyclic hydrocarbons¹ is a topic of high relevance to organic electronics.² Among molecules possessing open-shell character, diradicals³ in particular have garnered substantial attention as they have been proposed as candidates for a variety of materials applications, such as ambipolar organic field effect transistors, singlet fission in organic

photovoltaics, organic spintronics, etc.⁴ The design of Kekuléan diradicals is mainly based on a quinoidal core that upon recovery of aromaticity stabilizes the open-shell form (Figure 3.1).⁵ Depending upon the length of the quinoidal motif, the diradical character index (γ)⁶ and its closely related observable property, the singlet-triplet energy gap (ΔE_{ST}), can be broadly modulated. Though there are other structural features, such as the presence of donor and acceptor groups,⁷ the flexibility of the rearomatized core,⁸ etc., this quinoidal strategy represents the first and simplest method for tuning the electronic and magnetic properties of diradicaloids and has resulted in a wide range of ΔE_{ST} values in the literature.⁵ Adherence to this strategy has resulted in a shotgun approach focused on the synthesis of diversiform quinoidal topologies for the design of Kekuléan diradicaloids.⁵ A more deliberate tactic for tuning ΔE_{ST} requires consideration of additional electronic factors that could provide further improvement of the broader quinoidal strategy. We posit that a “*structure refinement approach*”, based on subtle/minor alteration of molecular geometry yet with retention of the same quinoidal/diradical core might allow a more rational

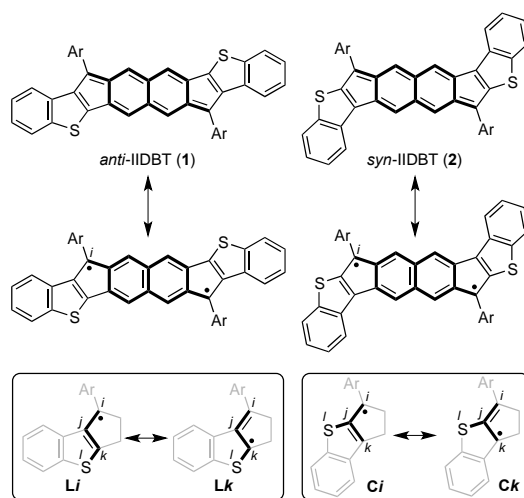


Figure 3.1 Chemical structures of anti-IIDBT (1) and syn-IIDBT (2). All canonical forms possess 2,6-naphtho conjugation (bold bonds). In boxes, linear conjugation (left, Li and Lk) vs. cross conjugation (right, Ci and Ck) dispositions of the labeled ijkl atoms where delocalization of the radical centers to the k atoms disrupts thiophene aromaticity.

modulation of ΔE_{ST} .

We recently reported the *anti*-indenoindenodibenzothiophene diradicaloid **1** (*anti*-IIDBT, Figure 3.1)⁹ with a medium-large y value (0.61; PUHF/6-311G* level of theory) and a large ΔE_{ST} (-8.0 kcal mol⁻¹; experimental magnetic susceptibility measurements). Theoretical examination of the molecular parameters involved in the y - ΔE_{ST} connection found that the position of the sulfur atom (i.e., its lone π -electron pair) relative to the radical center plays a key role increasing ΔE_{ST} at constant y . Analysis of the *syn*-IIDBT (**2**) regioisomer therefore became necessary to confirm the theoretical conclusions. In the IIDBTs *anti*- and *syn*- denote the position of the sulfur atom relative to the apical carbon (carbon i , Figure 3.1) of the 5-membered ring, where the radical can delocalize from i to atom k in each isomer (canonical forms **Li** – **Lk** and **Ci** – **Ck**). It is important to note that the 2,6-naphtho conjugation path of the radicals is consistent in both **1** and **2** enabling direct comparison of the effects of the sulfur positioning. Linear conjugation of the sulfur and the radical along the path $ijkl$ (**Li** and **Lk**) in **1** is in contrast to cross-conjugation along ijk in **2** (**Ci** and **Ck**), and in forms **Lk** and **Ck** the thiophene aromaticity is broken, all of which highlight the changing role of the sulfur to act electronically on the radical centers. As a result, this scenario could offer the desired “tuning” of ΔE_{ST} consisting of: (i) the relative through-bond separation between the sulfur and the radical center that are three and one atoms apart in **Li** and **Lk** (Figure 3.1, **1**) compared to two atoms apart in **Ci** and **Ck** (Figure 3.1, **2**) and (ii) the change in the conjugation mode (linear vs. cross) between the S lone pair and the radical as discussed above.

Previously reported carbon-based diradicaloid regioisomers have illustrated stark differences in properties that result from making small geometric changes to a molecule;

however, in most of these existing cases, structural isomerism concomitantly changes the conjugation pattern, thus altering the diradical character based on the quinoidal character of the molecule.¹⁰ For instance, the known dibenzoheptazethrene isomers (Figure 3.2) exhibit a marked difference in magnetic properties: whereas the 5,6:13,14-regioisomer displays pronounced open shell character, the 1,2:9,10-isomer is closed shell.^{10d} This difference is exacerbated in the indenofluorene family^{11,12} as there is the possibility of either para, meta, or ortho conjugation between the radical centers (Figure B1), which imparts significant changes in the magnetic structure to the extent that, from one isomer to another, the ground electronic state can even change from singlet to triplet.^{11e,13} Furthermore, substituent type and placement on the hydrocarbon backbone very often varies within the isomer series, thus diminishing meaningful comparison of molecule electronic and magnetic properties.^{10d,f-i} Structural isomerism in nitrogen- (verdazyl) and oxygen-based (nitroxide) diradicals has also been reported, but in these cases there is little effect on magnetic properties as the radical centers are not conjugated to the backbone.¹⁴

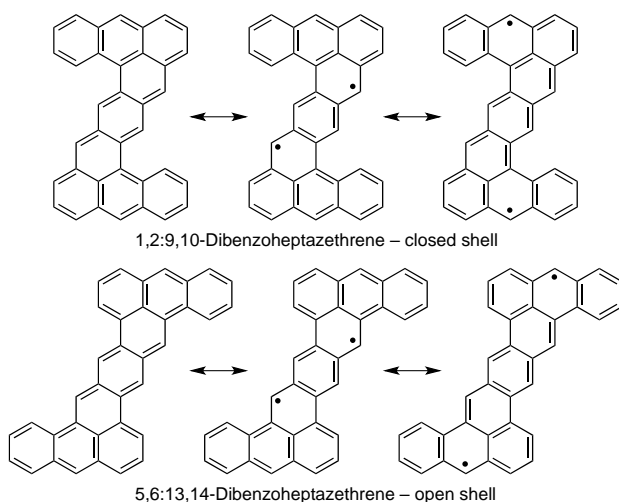


Figure 3.2 Diradical resonance forms of the hydrocarbon core of the two known dibenzoheptazethrene regioisomers.

Unlike previous examples, the relationship of the radical centers in this current

study, namely 2,6-conjugation, as well as the bond of benzothiophene fusion (*jk* in Figure 3.1) are identical in both **1** and **2**, thus meaning that only a single parameter that could influence magnetic properties is altered. Herein we report the synthesis of the *syn*-IIDBT isomers **2a**, **2b** and **2cH₂** as well as new *anti*-IIDBT **1b** (Figure 3.3) and computationally and experimentally corroborate that varying the benzothiophene subunit from *anti* to *syn* orientation in the IIDBT scaffold is an efficient strategy to modulate ΔE_{ST} .⁶ In addition, we demonstrate that these molecules are stable singlet diradicaloids at room temperature and only access the triplet state at elevated temperatures, where they are stable upwards of 375-

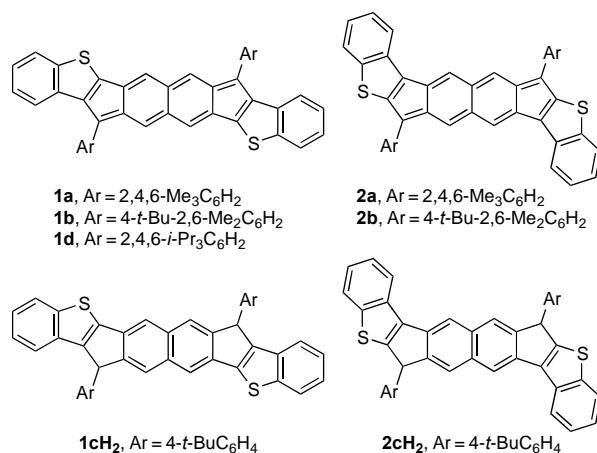


Figure 3.3 *Anti* and *syn* IIDBT derivatives studied in this work.

400 °C.

3.2 Results and Discussion

Quantum chemical calculations have been performed to explore the validity of our hypothesis. Equation 1 provides, in the two-electron diradical model, in terms of U (the difference between on- and inter-site Coulomb repulsions), t_{ab} (the transfer integral) and K_{ab} (direct exchange integral), where a and b define the electrons in the localized natural orbitals. Table 3.1 summarizes the main theoretical data for both **1** and **2** (see Appendix B for additional details in Table B1).

$$\Delta E_{ST} = \frac{U}{2} \left[1 - \frac{1}{\sqrt{y(2-y)}} \right] + 2K_{ab} = \frac{U}{2} f_{ST}(y) + 2K_{ab} \quad (1)$$

$$y = 1 - \frac{1}{\sqrt{1 + \left(\frac{U}{4t_{ab}}\right)^2}} \quad (2)$$

	y^{ab}	ΔE_{ST}^{ac} (kcal mol ⁻¹)	$U/2^{ad}$ (eV)	$ t_{ab} ^{ad}$ (eV)	$2K_{ab}^{ad}$ (eV)
1	0.613	-8.77	1.563	1.031	0.165
2	0.658	-8.06	1.404	0.905	0.130

Table 3.1 Theoretically Estimated y and ΔE_{ST} Values Together with the Main Physical Parameters.

The computational results reveal that *anti*→*syn* isomerism slightly increases y and decreases ΔE_{ST} , the mechanism of which can be discussed by evaluating the integral parameters (see Appendix B, Table B1 for details of the integral evaluations). For proper disjoint orbitals, such as in our case, $K_{ab} \ll \frac{U}{2} f_{ST}(y)$; hence, according to the values in Table 1, the term containing U and t_{ab} is the dominant factor as far as ΔE_{ST} is concerned. Thus, the increase in U/t_{ab} in **2** (3.10) compared to U/t_{ab} in **1** (3.03) anticipates a moderate increase of y in the *syn* isomer and a concomitant decrease in ΔE_{ST} . The $U_{syn} < U_{anti}$ reveals that the repulsive terms between the radical and the sulfur decrease in **2**, which can be explained by the location of the radical center relative to the sulfur in cross conjugation compared to linear conjugation in **1** (see bold paths in the boxes of Figure 3.1). In addition, $t_{ab-syn} < t_{ab-anti}$ is due to enlargement of the interaction distance between the two radicals in the delocalized forms **Lk** and **Ck**. Form **Ck** is possible in **2** because of the same cross conjugation effect, while in the case of **1**, this delocalized form is less feasible due to geminal repulsion between the radical and the sulfur. To further corroborate this description, Figure 3.3 shows the odd-electron density maps for **1** and **2**, which indicate

very little amplitude on the S atom of **2** yet rather large amplitude in the same heteroatom in **1** (see Figure B2 for the HONO/LUNO orbitals and Figure B3 for the Mulliken population analysis). This illustrates the effect of the cross-conjugation mode in the *syn* isomer, which isolates the sulfur from the radical conjugation paths. All these factors contribute to a suitable modulation of ΔE_{ST} , thus fulfilling our purposes in this study.

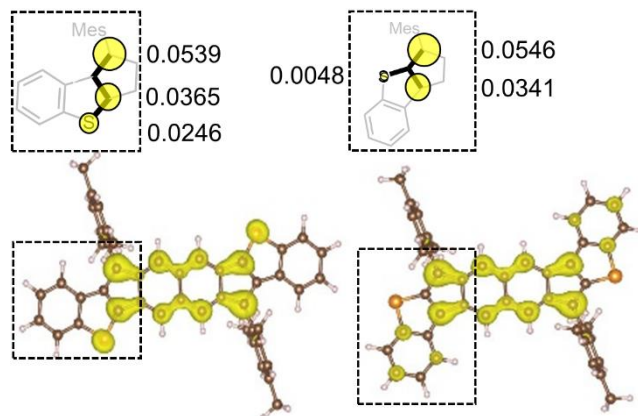
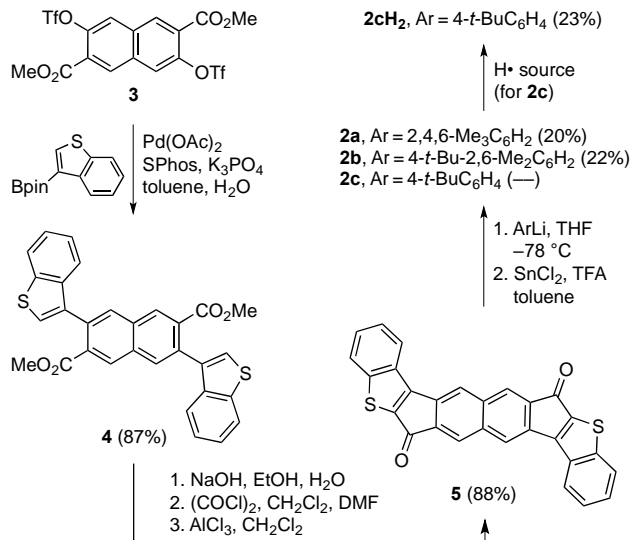


Figure 3.4 Odd-electron density maps for **1a** (left) and **2a** (right) with contour value 0.0005 a.u. calculated at the tuned-LC-RBLYP-CASCI(2,2)/6-311G* level. Mulliken population analysis for the odd-electron density on the relevant carbon and sulfur atoms of the linear and cross conjugated paths is shown on top.

In solid state physics, the Hubbard model¹⁵ successfully accounts for the electronic properties of conductive and semiconducting π -conjugated materials in which two basic electronic parameters are considered among the interacting electrons, namely the transfer integral, t , and the repulsion term U . One prediction of the model is that the semiconducting energy gap increases with increasing U and decreases with increasing t (a nice case of this U versus t balance is the Mott metal-insulator transition¹⁶). This description is very similar to that employed in the two-electron model for our case. Here, though t_{ab} is not equal for both isomers, the increase of electronic repulsion U in **1** compared to **2** enlarges the observed magnetic ΔE_{ST} gap on **2** \rightarrow **1**. This comparison nicely discloses the close correspondence between solid-state physics and molecular physics to address closely

related phenomena.



Scheme 3.1 Synthesis of *syn*-IIDBTs **2**.

Encouraged by the promising theoretical predictions, the *syn*-IIDBTs **2** were prepared via a similar synthetic route used for **1**. Starting from known bistriflate **3**¹⁷ (Scheme 3.1), Suzuki-Miyaura cross-coupling with benzothiophene 3-boronpinacolate ester¹⁸ furnished diester **4** in an 88% yield. Saponification of **4** followed by acyl chloride formation and then intramolecular Friedel-Crafts acylation yielded essentially insoluble dione **5**. Reaction of **5** with mesityllithium at -78°C gave the penultimate diol, which is then reductively dearomatized using SnCl_2 in rigorously anaerobic and anhydrous reaction conditions to afford fully conjugated, deep green **2a** in modest yield. Use instead of 2,6-dimethyl-4-*t*-butylphenyllithium or 4-*t*-butylphenyllithium gave *syn*-IIDBTs **2b** and **2cH₂**, respectively, with the latter structure gaining two hydrogen atoms because of the reduced steric protection of the radical centers, in analogy to formation of **1cH₂**.⁹ Additionally, treatment of the known *anti*-IIDBT dione⁹ with 2,6-dimethyl-4-*t*-butylphenyllithium followed by SnCl_2 furnished the new *anti*-IIDBT **1b**.

Dark green crystals suitable for X-ray diffraction were obtained by slow evaporation of a solution of **2b** in a 10:1 mixture of CHCl₃ and CH₃CN. The resultant X-ray structure along with the relevant experimentally- and computationally-determined bond lengths for **1** and **2** are given in Figure 4. The X-ray data revealed that the carbon-carbon bond length from the apical carbon to the naphthalene core is 1.419(4) Å, which is comparable in length to the analogous bond in the crystal structures of **1a** (1.424(4) Å)⁹ and **1d** (1.426(5) Å; see Figure B5 in Appendix B). All three values are roughly the same within experimental error and suggest a pronounced open-shell character of the IIDBT scaffold. In contrast, the analogous CC bond in closed-shell molecules is usually in the range of 1.38-1.40 Å.^{11a,c,12b} Interestingly, these ~1.42 Å values also show that the steric bulk of the aryl group attached to the apical carbon has little to no effect on this bond length (e.g., **1d**), as might be expected given their orthogonality with respect to the plane of the

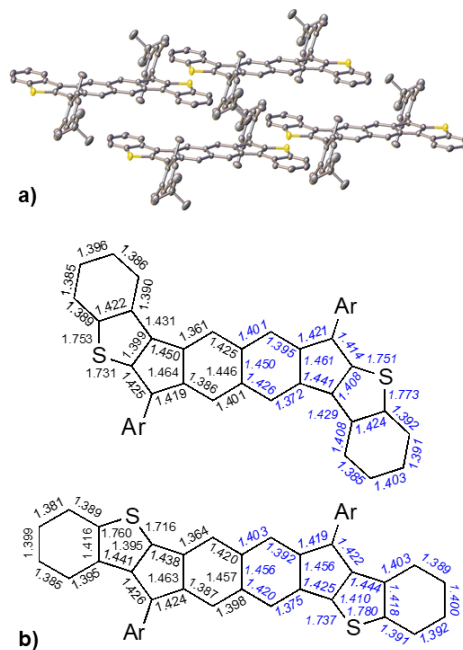


Figure 3.5 (a) Molecular packing of **2b** with the ellipsoids drawn with 50% probability level; hydrogens are omitted for clarity. (b) Experimental (black) bond lengths for the core motifs of **2b** and **1a** along with the calculated (blue) values for **2a** and **1a**.

IIDBT framework. The biggest disparity between the structures of **1a/d** and **2b** resides in

the thiophene rings, where there is a marked difference in the C–S bond lengths—1.731 / 1.753 Å for **2b** vs. 1.716 / 1.760 Å for **1a**, reflecting the differences in S orientation, i.e., the linear conjugation vs. cross conjugation arguments. The computational bond lengths do an excellent job replicating the aforementioned trends (Figures 3.5 and B4-B5).

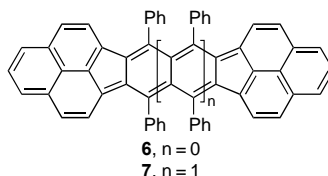


Figure 3.6 Bis phenylenyl-fused indacene (**6**) and indenoindene (**7**) for comparison.

In the crystal lattice, **2b** packs as dimeric pairs where one of the outer benzene ring overlaps with the same ring of its nearest neighbor with intermolecular π – π distances of 3.47–3.51 Å. Although the odd-electron density map in Figure 3.4 does show some spin density on three of the benzene carbons of **2a**, these particular carbons overlap with the three benzene carbons that have no spin density; thus, the likelihood of magnetic interactions between neighboring molecules in the solid state is minimal. This result is in sharp contrast with Kubo’s related bisphenalenyl-fused indacene (**6**)¹⁹ and indenoindene (**7**)²⁰ molecules that do display multiple close π – π contacts between carbons of high spin density of the phenalenyl groups (e.g., 3.10–3.23 Å for **7**), suggestive of strong π -dimer formation in the solid state. In the case of **1a** there are only two close π – π contacts (3.49 and 3.53 Å), whereas in **1d** the analogous distances are all >3.7 Å; however, the outer benzenes possess no spin density (Figure 3.4), indicating no intermolecular magnetic interactions are present within these IIDBT scaffolds in the solid state.

The electronic absorption spectra (Figure 3.7, top) depict a redshift of +25 nm from 724 to 749 nm going from **1a** to **2a**, indicating a reduction of the optical gap even though the two compounds are compositionally identical. Quantum chemical calculations (TD-

UB3LYP/6-311G* level) also predict a similar redshift from 703 nm for **1a** to 741 nm for **2a** (see Tables B2-B3) of the main lowest energy lying theoretical excitation, which corresponds to a HOMO-LUMO transition. In the lowest energy part of these strong absorptions, weak shoulders can also be observed that are typical of diradical molecules and are associated with double excitations. This is related with the $t_{ab-syn} < t_{ab-anti}$ discussion above and, as such, it is explained in terms of an extended conjugational path in **2** between the two radical centers due to cross conjugation, which limits the effect of the sulfurs on it.

The solid-state Raman spectra of **1a** and **2a** at room temperature are shown in Figure 3.7 (bottom). The characteristic C=C stretching mode of the central naphthalene

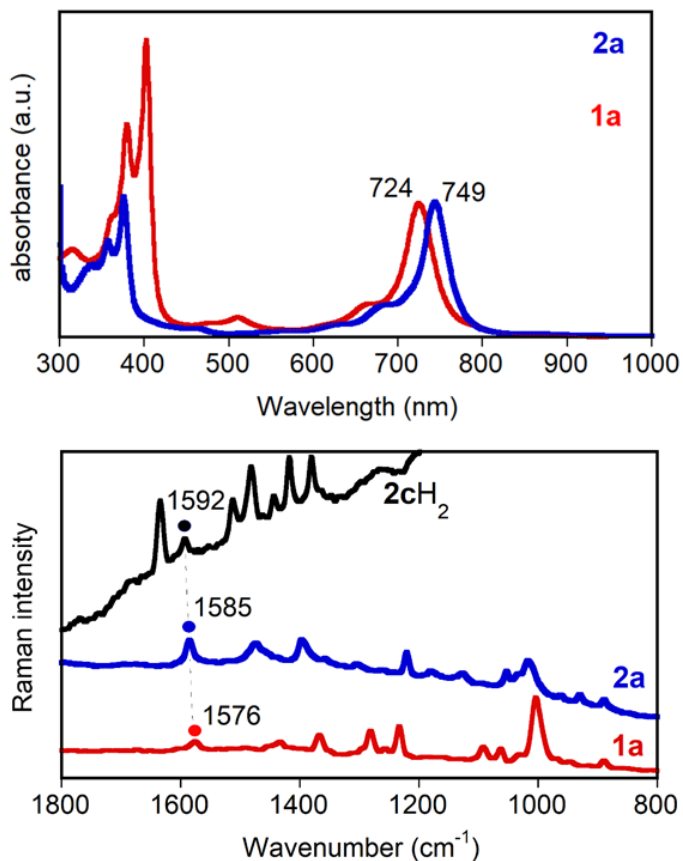


Figure 3.7 Electronic absorption (in CH_2Cl_2 , top) and Raman spectra (in solid state with 1064 nm laser excitation, bottom) of **1a** (red) and **2a** (blue). Raman spectrum of aromatized **2cH2** is in black.

unit in **1a** appears at 1576 cm^{-1} and is representative of a transitional structure from quinoidal to aromatic for this core. This is in agreement with a medium diradical index of $y = 0.61$, confirming that aromaticity recovery is the main driving force for diradical formation, although it is not fully completed.^{5c,9} In the case of **2a** ($y = 0.66$), the same yet more intense Raman band emerges at 1585 cm^{-1} , upshifted by $+9\text{ cm}^{-1}$, indicating an additional gain of aromatization of the naphthalene core in this isomer. In addition, this band is only $+7\text{ cm}^{-1}$ away from the same stretching mode in **2cH₂** (1592 cm^{-1}), a molecule that contains a fully aromatized naphthalene (note that in **1a** \rightarrow **1cH₂** the upshift is $+11\text{ cm}^{-1}$). The emerging interpretation is that the contribution of the 2,6-naphthoquinoidal conjugation to ΔE_{ST} does not arise separately from cross-conjugation of the sulfur lone pair and the radical, but there is a synergy between the two. We mean that delocalization of the radical to *k* in form **Ck** of Figure 3.1 enlarges/weakens the distance/interaction between the two radicals which simultaneously reinforces the aromatic character of the central naphthalene.

The ^1H NMR spectra of **2a** as a function of the temperature are shown in Figure 3.8 (top). At room temperature, the spectrum is clearly resolved with all peaks assignable to the structure of **2a**. At higher temperatures these peaks have broadened as is clearly observed at $130\text{ }^\circ\text{C}$. While this behavior was observed for **1a**, the onset of peak broadening in **2a** occurs at a considerably lower temperature ($75\text{ }^\circ\text{C}$) compared to that for **1a** ($125\text{ }^\circ\text{C}$), suggesting a smaller singlet-triplet energy gap.

In the solid state, SQUID measurements for **2a** (Figure 3.8, bottom) show a clear increase of the molar susceptibility from low to high temperature that is typical behavior of singlet low-spin ground electronic state from which a high-spin triplet excited state is

populated thermally. Fitting the data to the Bleany-Bowers equation²¹ yields a singlet-triplet energy gap of -6.9 kcal mol⁻¹, which agrees well with the ΔE_{ST} predicted from calculations (-8.06 kcal mol⁻¹). Furthermore, the matching of the experimental data to a Bleany-Bowers dimer model confirms the rather small spin-spin intermolecular interaction in the solid such as revealed by the large π - π distances in the X-ray data. This ~ 1 kcal mol⁻¹ modulation of ΔE_{ST} in **2a** demonstrates the finer tuning of ΔE_{ST} in the closely related IIDBT regioisomers. This result stands in contrast to the much larger range of ΔE_{ST} values that result from variation of the size of the acene diradical core (i.e., the number of fused rings). For example, in the family of bis-phenalenyl-fused molecules, ΔE_{ST} varies from -7.2 kcal mol⁻¹ for **6** to -4.5 kcal mol⁻¹ for **7** and -2.9 kcal mol⁻¹ for the analogue possessing

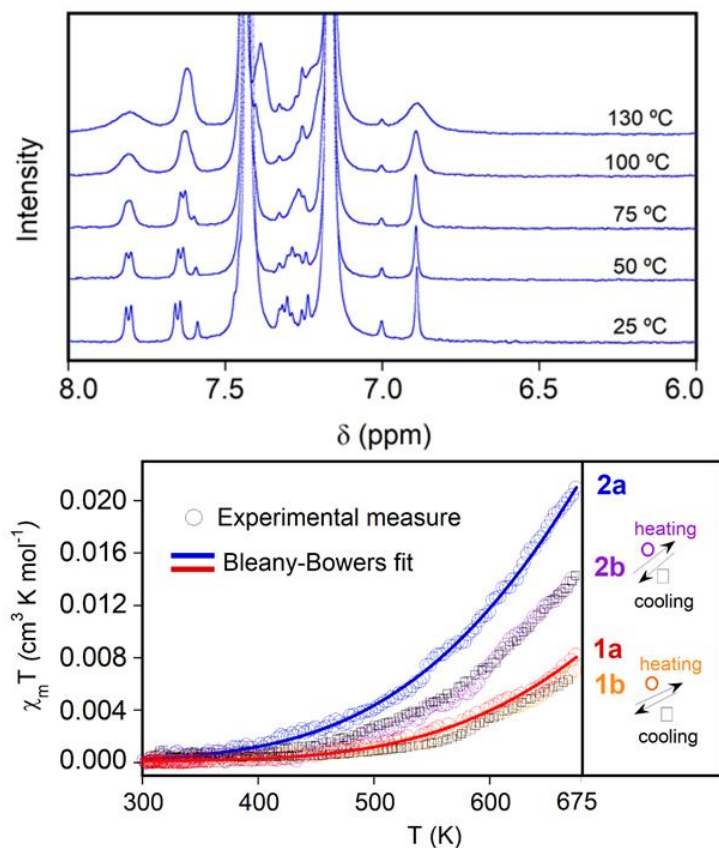


Figure 3.8 (top) Variable temperature ¹H NMR spectra (in 1,2-C₆D₄Cl₂) of **2a**. (bottom) SQUID magnetometry data of **1a-1b** and **2a-2b**; for **1b** and **2b** the data for the heating and cooling curves are denoted by squares and circles, respectively.

an anthracene core.²²

One of the unique attributes of the IIDBTs is the need for pronounced heating in order to populate the triplet state, which then raises the question of the thermal stability of the scaffold. Thermogravimetric analysis (TGA, Figures B6-B9) of both sets of isomers reveals that the onset of decomposition is ~ 375 °C with significant mass loss above 400 °C. Examination of the data for **1a** indicates that the first two events are sequential loss of the mesityl groups followed by decomposition of the conjugated core at higher temperatures (>450 °C). Heating samples of **1b** and **2b** in the SQUID up to 675-700 K and then cooling back to room temperature (Figures 3.8 and B10-11) afford ΔE_{ST} values (**1b**: H -8.2 /C -8.4 kcal mol⁻¹; **2b**: H -7.2 /C -7.0 kcal mol⁻¹) that are in very good agreement with those obtained by only heating SQUID samples of **1a** and **2a** (-8.0 and -6.9 kcal mol⁻¹, respectively), further corroborating the thermal stability of the IIDBT family of diradicaloids.

3.3 Conclusions

In summary, we have demonstrated a finer, rational adjustment of ΔE_{ST} by *anti* \rightarrow *syn* isomerism of the IIDBT framework. The two constitutional isomers have a common 2,6-naphtho core that contributes the greater amount to ΔE_{ST} whereas *anti/syn* flip modulates this value within ~ 1 kcal mol⁻¹, which we attribute to the combination of change in the relative position of the radical and of the S atom together with the change from linear to cross conjugation. Importantly, we have shown that IIDBTs **1** and **2** are stable singlet diradicaloids at room temperature and only access the triplet state at elevated temperatures, where they are stable upwards of 375-400 °C as revealed by TGA analysis as well as by the reversibility of the high temperature SQUID measurements.

With this study we have posited the question of the necessary fine control of ΔE_{ST} in a stable diradical as the way to design tailored open-shell molecules with control of their emerging properties. While most published studies employ a more qualitative approach to varying ΔE_{ST} without much emphasis on the actual ΔE_{ST} outcome, knowledge of how to subtly tune the singlet-triplet energy gap as well as understanding of what diradical parameter one is altering will be essential for future design and use of diradicals in materials applications. Practical diradicals are those with intermediate diradical character (i.e., greater stability, efficient non-linear optical response, capability of photonic control, etc.) where the tailored design of ΔE_{ST} becomes mandatory. Additional efforts to accomplish this tailoring via a “structural refinement approach” will be the subject of future studies.

CHAPTER IV

LATE-STAGE MODIFICATION OF ELECTRONIC PROPERTIES OF ANTIAROMATIC AND DIRADICALOID INDENO[1,2-*b*]FLUORENE ANALOGUES VIA SULFUR OXIDATION

This chapter includes previously published and co-authored material from Dressler, J. J.; Barker, J. E.; Hashimoto, H. E.; Karas, L. J.; Kishi, R. Zakharov, L. N.; MacMillan, S. N.; Gómez-García, C. J.; Nakano, M.; Wu, J. I.; Haley, M. M. Late-stage modification of Electronic Properties of Antiaromatic and Diradicaloid Indeno[1,2-*b*]fluorene Analogues via Sulfur Oxidation. *J. Org. Chem.* **2020**, *85*, 10846-10857. This manuscript was written by Justin Dressler with assistance from Joshua E. Barker and Prof. Michael M. Haley. The project in this chapter was conceived by Justin Dressler. The experimental work in this chapter was performed by Justin J. Dressler, Joshua E. Barker, and Hannah E. Hashimoto. The computational work in this chapter was performed by Joshua Barker, Lucas Karas with assistance from Prof. Judy I. Wu, and Ryohei Kishi with assistance from Prof. Masayoshi Nakano.

4.1 Introduction

Recently there has been resurgent interest in polycyclic conjugated hydrocarbons (PCHs) that possess unique properties for application in organic electronics. The earliest and most promising PCH targets were acenes;¹⁻⁴ however, these compounds are prone to oxidative degradation.^{3,5,6} In an attempt to develop suitable acene alternatives with

decreased aromaticity and yet retain the π -conjugation integral to the high charge carrier mobility of acenes, PCHs that possess antiaromatic character have become fruitful avenues of research.⁷ Defined as cyclic, planar, fully conjugated systems with $(4n)$ π -electrons,⁸ antiaromatic molecules often display properties such as decreased delocalization, narrow HOMO-LUMO energy gaps,⁹⁻¹¹ paratropic proton NMR chemical shifts, as well as concomitant large positive nucleus independent chemical shift (NICS) values.^{12,13} A common strategy to generate antiaromatic hydrocarbons that are closely related to acenes is to replace one or more six-membered ring with either a four- or five-membered carbonaceous ring.⁷ This approach over the past decade has resulted in a wide range of antiaromatic compounds based mainly on pentalenes,¹⁴⁻²² cyclobutadienes,²³⁻²⁶ and indacenes,²⁷⁻³³ among others. The research on such molecules was in part fueled by the Breslow group's hypothesis that reduced aromaticity/antiaromaticity has the potential to increase molecular conductivity.³⁴⁻³⁷ Very recent studies support this notion as organic field effect transistors (OFETs) with antiaromatic molecules as the semiconducting layer can now exhibit average hole-mobilities that are $> 1 \text{ cm}^2 \text{ V}^{-1} \text{ s}^{-1}$.^{23,25,38,39}

Another group of PCHs accruing interest are those that display diradical character. The recent increase in reports of carbon-based diradicaloids has also been driven by their potential applications both in organic electronics^{40,41} and as magnetic materials.⁴²⁻⁴⁵ The desire to gain a better fundamental understanding of these compounds, which possess a unique set of properties (e.g., narrow HOMO-LUMO gaps,⁴⁰ low-lying doubly excited electronic energy absorptions^{46,47} and electronic spin resonance (ESR) signals⁴⁸), has led to synthesis of various families of diradicaloids based on bisphenalenyls,^{41,49-51} zethrenes,⁵²⁻⁵⁵ indenofluorenes^{56,57} and closely related diindenoacenes,⁵⁸⁻⁶⁵ among others.

Through the study of these different classes of diradicals, a common theme has been unearthed, that the two concepts of antiaromaticity and diradical character are interrelated. In many cases antiaromatic molecules, once π -expanded, reveal a tendency to assume an aromatic, open shell resonance structure in the ground state to relieve the antiaromaticity of the conjugated, closed shell core.⁶⁶

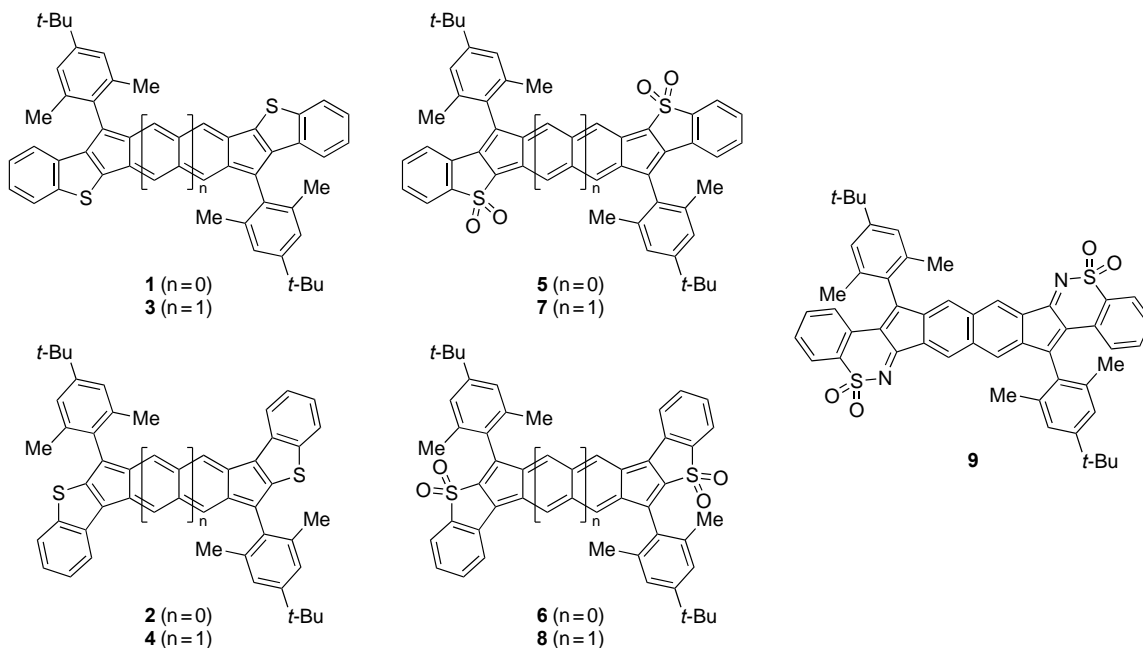


Figure 4.1 New IDBTs **1** and **2**, known IIDBTs **3** and **4**, their sulfone analogues **5-8**, and decomposition product **9**.

Utilizing the indeno[1,2-*b*]fluorene framework, our group in recent years has aspired to tune both antiaromaticity (in benzene core molecules) and diradical character (naphthalene and larger aromatic cores) through two different approaches, either by changing the fusion bond order on both sides of the *s*-indacene core^{28,63} or by adding benzothiophene units in the same position (*anti* or *syn* to the apical carbon in the five-membered ring, e.g., **1-4** in Figure 4.1) to modulate electronic properties.^{27,60,62,67} These studies have provided key insights into what electronic factors can be altered to tune either the antiaromaticity (i.e., fusion bond order)^{27,28} and/or the diradical character (i.e.,

electronic repulsion factor and the transfer integral term)^{60,62} in a series of structurally related molecules.⁶⁸ Such approaches have relied heavily on early synthetic modification to impart changes in the chemical connectivity to drive a concomitant change in properties. These modifications are manifested either by π -extending the acene core requiring a change to the synthetic route very early on or through altering the outer fused rings that required synthetic changes during the key carbon-carbon bond forming steps; nonetheless, the amount of synthetic work needed to tune these properties was demanding, often requiring entirely new preparative routes.

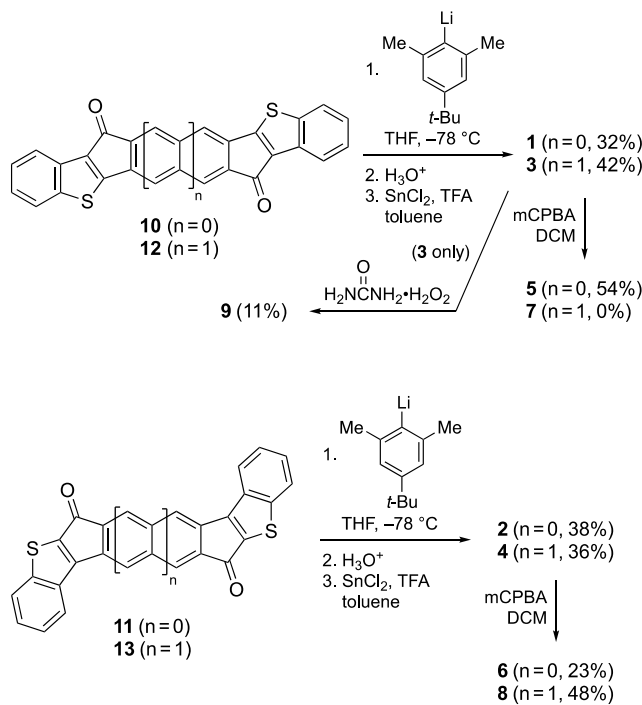
Our recent studies on indacenodibenzothiophenes^{27,67} (IDBTs, e.g. **1**, **2**) and indenoindenodibenzothiophenes^{60,62} (IIDBTs, e.g. **3**, **4**) provide a unique opportunity for late-stage modification of the electronics of our molecules, from electron-rich to electron-poor through the conversion of the sulfur atoms to fully oxidized sulfones (e.g., IDBT-S **5-6** and IIDBT-S **7-8**). A relevant report from the Campos group,⁶⁹ among others,⁷⁰⁻⁷³ has shown that oxidation of sulfur in polythiophene lowers the LUMO energy level and thus affords an overall change in the properties of the bulk material. Herein we report the synthesis and detailed characterization of sulfones **5**, **6** and **8** and computationally corroborate that changing the oxidation state of the sulfur has profound effects on the antiaromaticity and diradical character of the molecules. This work looks to highlight the ability to impart overall large-scale electronic modification to the molecules, tuning the targeted properties, utilizing a non-arduous synthetic route.

4.2 Results and Discussion

Our initial efforts started with the known mesityl (2,4,6-trimethylphenyl) analogues of **1** and **2**.²⁷ While we successfully oxidized the former to **5-Mes** (see Experimental

Section for details), oxidation of the latter afforded an insoluble and uncharacterizable violet solid. We then switched to 2,6-dimethyl-4-*t*-butylphenyl units (which we have coined *t*-Mes) on the apical carbons as these confer considerably improved solubility. Reacting 2,6-dimethyl-4-*t*-butylphenyllithium with diones **10** and **11** (Scheme 4.1) followed by an acidic aqueous workup gave intermediate diols (not shown) that were reductively dearomatized using SnCl₂ and catalytic trifluoroacetic acid (TFA) to furnish the fully conjugated IDBTs **1** and **2**, respectively. IIDBTs **3** and **4** were prepared analogously from diones **12** and **13** as previously reported.^{60,62} Oxidation of the fully conjugated scaffolds utilizing mCPBA successfully resulted in purple sulfones **5**, **6** and **8** in modest to moderate yields. Surprisingly, oxidation of *anti*-IIDBT **3** with mCPBA did not furnish sulfone **7** but rather an uncharacterizable orange solid whose absorption spectrum lacked the characteristic low energy bands > 500 nm (Figure S8), suggestive of a system with less than expected π -conjugation. We explored other oxidizing reagents such as H₂O₂, oxone, and urea-hydrogen peroxide (UHP). Only the reaction of **3** with UHP proceeded to afford a purple solid in low yield, which we initially believed to be the desired sulfone as the compound possessed low energy transitions out to ~640 nm (Figure S9) and an appropriate ¹H NMR spectrum (see Supporting Information); however, the structure obtained by X-ray diffraction (vide infra) revealed it to be molecule **9** as shown in Figure 1. This structure suggests that compound **7** likely was formed during the reaction but the oxidized ring hydrolyzed/cleaved (ArSO₂⁻ is a reasonable leaving group), urea next condensed onto the newly formed ketone carbonyls, and then the system recycled in some manner to afford **9**. Regardless of how **9** is generated, we never observed direct evidence of **7**. Out of chemical curiosity, less π -conjugated *anti*-IDBT **1** was subjected to oxidation

conditions using UHP, which furnished only a trace amount of an analogous sulfonamide (as detected by mass spectrometry). This outcome suggests that the *anti*-orientation of the pro-aromatic core of **7** is prone to degradation to regain naphthalene aromaticity as found in **9**, something we have not observed in any of our prior IIDBT studies.



Scheme 4.1 Synthesis of IDBTs **1**, **2**, and IIDBTs **3**, **4** and their conversion to the respective sulfones **5-8** along with formation of decomposition product **9**.

Because the central protons on the IDBTs are directly attached to the *s*-indacene core, one would expect these protons to be sensitive to the paratropic environment and experience an upfield chemical shift. Indeed this is the case—whereas the ^1H NMR chemical shift of the central six-membered ring protons of the parent indeno[1,2-*b*]fluorene is 6.85 ppm, these analogous protons in the previously reported Mes-substituted *anti*-IDBT and *syn*-IDBT appear at 6.11 and 6.06 ppm, respectively, in line with the claim of increased antiaromaticity of the *s*-indacene core of the IDBTs.²⁷ In the current study, substitution with *t*-Mes affords values of 6.09 and 6.06 ppm for **1** and **2**, respectively (Figure 2a). In

both cases, the *syn* derivative is slightly more upfield than the *anti* isomer, indicating the *syn* is slightly more paratropic, a result corroborated by NICS-XY scan calculations (vide infra).²⁷ Intriguingly, after sulfone formation this trend is reversed, the core singlet for *syn*-IDBT-S **6** appears at 6.91 ppm and for *anti*-IDBT-S **5** at 6.03 ppm, the latter result suggesting that the paratropic core of **5** is comparable to **1** and **2**.

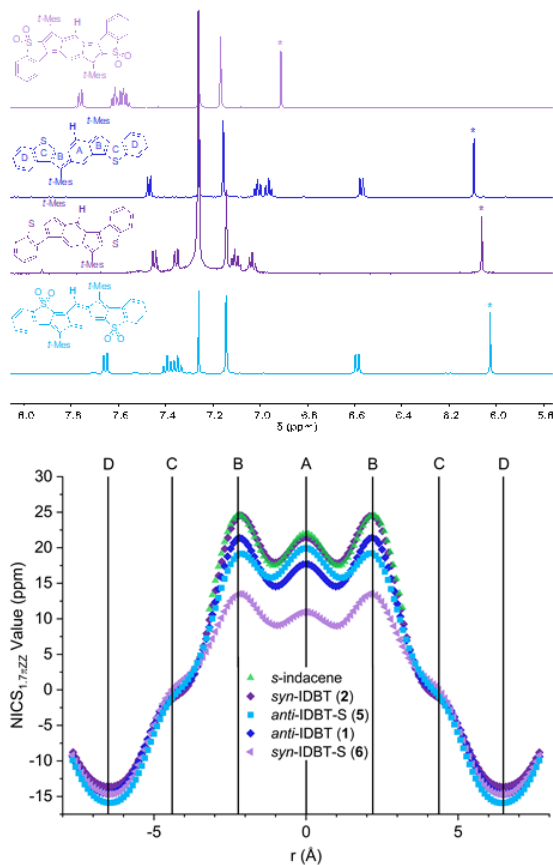


Figure 4.2 (a) Proton NMR spectra of the aromatic region of IDBTs **1** and **2** and the corresponding sulfones **5** and **6**. The central proton (*) displayed in bold in the structures on the left can be used to roughly assess antiaromaticity. (b) NICS-XY scans for IDBTs **1** and **2** and sulfones **5** and **6** along with the scan for the parent s-indacene, in order of most to least paratropic; for clarity the ring labels are shown above in the structure of **5**.

Given the difficulty of assessing aromaticity/antiaromaticity based solely on relatively small changes of NMR chemical shifts, we explored computationally the ring currents of IDBT-S **5** and **6** using NICS-XY scans, as these allow us to explore areas of the

molecule that possess both paratropic and diatropic ring currents within the same system.^{74,75} All calculations were performed with the unsubstituted structures to decrease computational cost as exclusion of the mesityl groups has been shown to have a negligible impact on the NICS-XY results.²⁸ Notably all the IDBT derivatives possess a paratropic *s*-indacene-like core (Figure 4.2, rings A and B). The NICS scans (Figure 4.2b) replicate our prior studies that showed that the *syn*-IDBT core of **2** is nearly as antiaromatic (21-24 ppm, dark purple) as *s*-indacene itself (22-25 ppm, green), whereas the *anti*-IDBT core of **1** is slightly less paratropic (18-21 ppm, dark blue). In all cases the thiophene rings (C) appear to be atropic (0 to -1 ppm) regardless of sulfur oxidation state, and similarly the outer benzene rings (D) all possess strong aromaticity with minimal variation (-14 to -16 ppm). Interestingly, oxidation reverses the *syn/anti* ordering, where *syn*-IDBT-S **6** has weaker paratropicity (11-13 ppm, light purple) compared to IDBTs **1** and **2**, and *anti*-IDBT-S **5** shows comparable paratropicity (19-20 ppm, light blue) to **1**. In fact, the NICS values for ring A are essentially the same for **2** and **5**, which support their near identical chemical shifts in the aforementioned proton NMR experiments.

Further calculations suggest there are two competing effects that influence the antiaromatic characters of the parent IDBTs (**1** vs. **2**) and the corresponding sulfones (**5** vs. **6**)—a “Clar sextet-effect” and a “charge-effect”, respectively (vide infra). When a Clar sextet-effect dominates, the compound with more quinoidal character will have a smaller HOMO-LUMO energy gap (e.g., *syn*-IDBT **2**). When a charge-effect dominates, the less charge-stabilized compound will have a smaller HOMO-LUMO gap (e.g., *anti*-IDBT-S **5**). A smaller HOMO-LUMO gap often translates to greater antiaromatic character, since the HOMO-LUMO gap is a denominator in the paramagnetic term of the equation used to

compute magnetic shielding. Whether a Clar sextet-effect or charge-effect dominates depends on the electronegativity of the heteroatom(s).

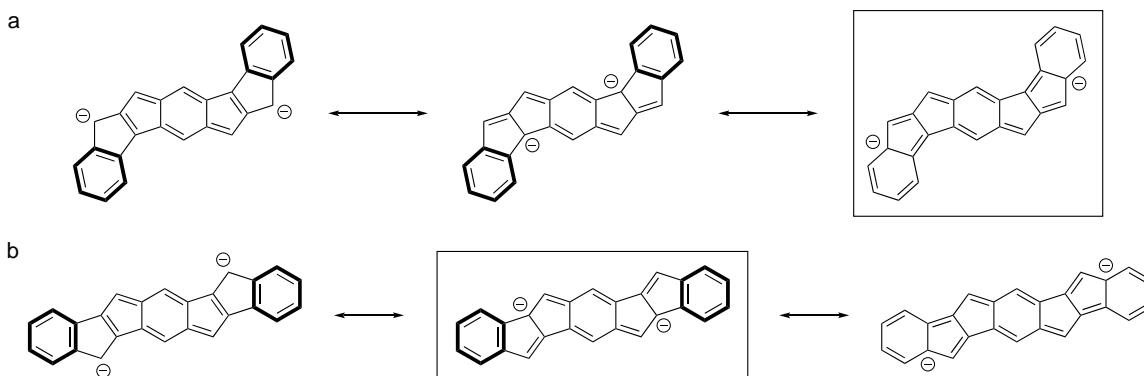


Figure 4.3 Selected resonance forms for the hydrocarbon dianion reference analogues of (a) *syn*-IDBT **2** and (b) *anti*-IDBT **1**; boxed structures are the dominant resonance forms recognized by NBO.

Calculations suggest that the stronger paratropicity of **2** (dark purple curve, Figure 4.2b) vs. **1** (dark blue) is the result of a less aromatic resonance structure (i.e., a “Clar sextet-effect”). Computed natural bond orbital (NBO) analyses for the isoelectronic hydrocarbon “dianion” reference analogues of the benzothiophene-fused *s*-indacenes (i.e., *syn*- and *anti*-IDBT) show that the dominant resonance form of the *syn*-IDBT reference is a quinoidal resonance structure (boxed structure in Figure 4.3a and Figure C24 for the NBO output), while that of the *anti*- reference displays two Clar sextets in the terminal benzenoid rings (boxed structure in Figure 4.3b and Figure C25 for the NBO output).⁷⁶ In concert, the computed NICS(1.7)_{πzz} values show a less negative value for **2** (−14 ppm) and a more negative value for **1** (−15 ppm) at the terminal benzene rings (ring D in Figure 4.2b). The more paratropic *syn*-IDBT also has a smaller computed HOMO-LUMO gap (1.84 eV) compared to *anti*-IDBT (1.96 eV).

As shown experimentally, IDBT-S **5** and **6** display the opposite trend, i.e., a “charge-effect” dominates. Sulfone **5** (light blue trace in Figure 4.2b) is significantly more

paratropic than **6** (light purple) because the electronegative sulfone (SO₂) groups are placed at topologically disfavored positions, resulting in a narrower HOMO-LUMO gap and increased antiaromatic character. As shown in Figure 4.4, computed natural population analyses (NPA) charges for *s*-indacene are the most negative at carbons 2 and 6. Because of this charge distribution, fused ring arrangements that stabilize negative charges at carbons 2 and 6 will stabilize the *s*-indacene core. When SO₂ groups are fused to *s*-indacene in a *syn* arrangement, the electronegative SO₂ groups are placed at positions that help stabilize negative charges at carbons 2 and 6. For this reason, **6** exhibits a larger HOMO-LUMO gap (1.95 eV, Table C1) and decreased paratropicity. When SO₂ groups are fused to *s*-indacene in an *anti* arrangement, the SO₂ groups are connected to carbons 3 and 7 (the least negatively charged positions), and this stabilizes the *s*-indacene core to a lesser extent. As a result, *anti*-IDBT-S **5** exhibits a narrower HOMO-LUMO gap (1.65 eV), i.e., increased paratropicity. The charge-effect described here is akin to the rule of topological charge stabilization, first proposed by Gimarc to explain how the placement of heteroatoms in hydrocarbon frameworks affect the relative stabilities of the possible isomers.⁷⁷

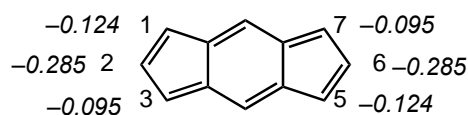


Figure 4.4 Natural population analyses (NPA) charges for *s*-indacene.

It is worth noting that even though both Clar sextet-effects and charge-effects are present in the parent and sulfone compounds, differences in the antiaromatic characters of *syn* vs. *anti*-IDBT are dominated by the Clar sextet-effect, while the *syn*- vs. *anti*-sulfones set is influenced more so by the charge-effect because of the stronger electronegativity of the sulfones. To further illustrate the competing Clar sextet- and charge-effects, the NICS-XY scans of *syn*- and *anti*-IDT and *syn*- and *anti*-IDT-S were performed at the same level

of theory (Figures C21-C22). The scans showed that without the terminal benzene rings (no Clar sextet-effect), both the IDT and IDT-S compounds show a more paratropic *anti*-form due to a dominating charge-effect. It is also worth noting the more pronounced difference in paratropicity for the IDT-S pair (Figure C22).

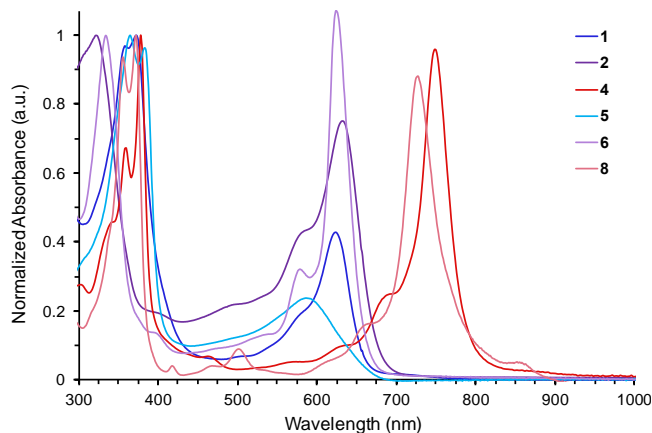


Figure 4.5 Electronic absorption spectra of the three stable sulfones **5**, **6**, and **8** and their parent thiophenes **1**, **2**, and **4**, in CHCl_3 at room temperature. The spectrum of each sulfone is a similar color to the parent compound, with the sulfone having the lighter hue.

Sulfones **5**, **6** and **8** exhibit UV-Vis-NIR absorption spectra (Figure 4.5) very similar to their respective thiophene parents (**1**, **2**, **4**). All of the molecules possess strong absorptions in the range of 300-400 nm. Interestingly the main difference between the thiophene and sulfone compounds is displayed in the low energy absorptions, where all of the sulfones show a blue-shift of the main low energy absorption anywhere from 8 nm in compound **6** to as large as 37 nm in **5**. While the π -extended nature of the IIDBTs redshifts the low energy absorption appreciably (~ 100 nm), IIDBT-S **8** also is blue-shifted 24 nm compared to parent **4**, suggesting all three sulfones possess slightly larger optical energy gaps. Gratifyingly, the TD-DFT generated absorption spectra (Figures C4-C7) corroborate these changes for all sulfones; specifically, the calculations replicate that *anti*-**5** would display a greater blue shift in the low energy absorption than *syn*-**6**, a trend also predicted

for the naphthalene series (*anti*-**7** vs. *syn*-**8**) as well. Another interesting feature observed for compounds **4** and **8** is a weak absorption shoulder (852 and 866 nm, respectively) on the low energy absorption due to a low-lying doubly excited electronic configuration, a common occurrence in molecules with appreciable open shell character (*vide infra*).^{46,47}

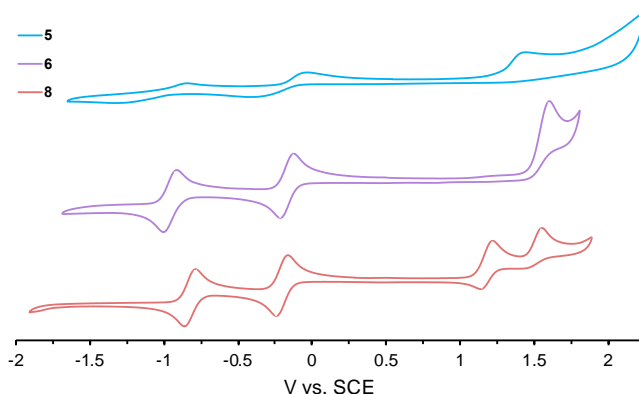


Figure 4.6 Cyclic voltammograms of **5**, **6**, and **8**.

To further probe their electronic properties, cyclic voltammetry of sulfones **5/6/8** was carried out in CH₂Cl₂ (Figure 4.6). The redox behavior of the sulfones compared to their thiophene precursors are shown in Figures C10-C12, with the results compiled in Table 4.1. All of the sulfones undergo a reversible first reduction in solution along with a second reduction that is reversible for **6** and **8** and pseudo-reversible for **5**. IDBT-S **5** and **6** exhibit one irreversible oxidation, while IIDBT-S **8** displays one reversible oxidation followed by a second irreversible oxidation. E_{red}^1 values range from -0.17 to -0.22 V vs. SCE and E_{ox}^1 values range from 1.18 to 1.60 V vs. SCE. In our prior studies, comparison of the electrochemistry of parent IDBTs (**1** and **2**) showed that the *syn*-IDBT had the narrower HOMO-LUMO energy gap, in agreement with the fact that **2** was more antiaromatic.²⁷ Whereas the HOMO levels of **1** and **2** are comparable, **2** has a lower LUMO leading to the decreased energy gap. In the case of the IDBT-S, the trend is reversed—the LUMOs of **5** and **6** are essentially equal in energy but it is the higher in energy HOMO that

leads to the decreased electrochemical energy gap in **5**. Given that HOMO-LUMO energy gaps generally narrow with increased antiaromaticity, this supports the finding that once oxidized **5** is the more antiaromatic of the two. These experimental observations are well reproduced by quantum chemical calculations (Table C1). Gratifyingly, the electrochemical data for **8** matches DFT calculations well in that the HOMO-LUMO energy gap is calculated to be approximately 1.52 eV and the experimental value was 1.38 eV. As with the benzene-core sulfones the HOMO and LUMO energy levels experimentally and computationally are overall lower (more negative) for *syn*-IIDBT-S **8** when compared to the parent *syn*-IIDBT **4**. A general trend from these studies that all three sulfones possess overall lower energy HOMO and LUMO levels (HOMO < -5.8 eV, LUMO < -4.4 eV) relative to the parent thiophenes (HOMO < -5.3 eV, LUMO < -3.8 eV).

cmpd	$E_{\text{red}2}$ (V)	$E_{\text{red}1}$ (V)	$E_{\text{ox}1}$ (V)	$E_{\text{ox}2}$ (V)	E_{HOMO} (eV)	E_{LUMO} (eV)	E_{gap} (eV)
<i>anti</i> -IDBT (1)	-1.72	-0.87	0.84	1.32	-5.52	-3.81	1.71
<i>anti</i> -IDBT-S (5)	-1.08	-0.22	1.44	-	-6.12	-4.46	1.67
<i>syn</i> -IDBT (2)	-1.37	-0.75	0.86	1.57	-5.54	-3.93	1.61
<i>syn</i> -IDBT-S (6)	-0.96	-0.17	1.60	-	-6.28	-4.51	1.77
<i>syn</i> -IIDBT (4)	-1.23	-0.67	0.66	1.09	-5.34	-4.01	1.33
<i>syn</i> -IIDBT-S (8)	-0.82	-0.20	1.18	1.55	-5.86	-4.48	1.38

Table 4.1 Cyclic Voltammetry Data for Thiophenes 1, 2, and 4 and Sulfones 5, 6, and 8. CVs were recorded at a scan rate of 50 mV s⁻¹ with a glassy carbon working electrode, Pt coil counter electrode and Ag wire pseudo-reference. All data were collected in degassed CH₂Cl₂ and ferrocene was used as an internal reference. Potentials were referenced to SCE by using the Fc/Fc⁺ half-wave potential (Fc/Fc⁺ = 0.46 C vs. SCE).

To gain insight into the molecular structure of the electronically altered sulfones, single crystal X-ray diffraction (XRD) and subsequent bond length analysis of the structures was performed. Slow diffusion of CH₃CN into CHCl₃ gave deep violet crystals of **5-Mes** and **9**, whereas to attain strongly diffracting crystals for **6** and **8**, 3-5 mg of the

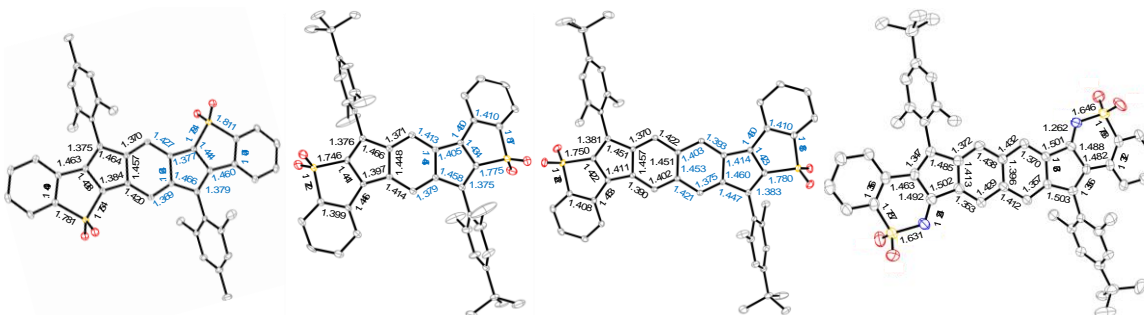


Figure 4.7 X-ray structures of (left to right) sulfone derivatives **5-Mes**, **6**, and **8** and decomposition product **9** with selected bond lengths (Å; experimental values in black, calculated values in blue); ellipsoids drawn at the 50% probability level. Experimental numbers for **6** represent the average value from two crystallographically independent molecules.

target compound was dissolved in a 15:1 mixture of CHCl_3 and CH_3CN , which then slowly evaporated over several weeks to obtain suitable crystals for XRD.⁷⁸ The resultant structures as well as calculated geometries (Figures C27-C30) are shown in Figure 4.7.

Whereas molecules of **5-Mes** pack roughly as 1D stacks with a distance of 3.51 Å between the average planes of the central fragments (Figure C14), **6**, **8** and **9** pack as isolated molecules with no close π - π contacts because of the orientation of the bulky *t*-Mes groups and/or the presence of solvent molecules (Figures C16, C18, C20). As is typical of benzene- and naphthalene-based quinoidal systems, the molecules show distinct bond alternation about the antiaromatic core. Surprisingly, the bonding pattern in both the IDBT-S and IIDBT-S is flipped as a result of oxidation, as depicted in Figure 4.8. In fact, out of 50+ X-ray structures of our quinoidal molecules obtained over the past decade,²⁹ the three sulfones are the only molecules to have this flipped arrangement. Nonetheless, the experimental bond lengths (black numbers in Figure 4.7) of the hydrocarbon cores are all in relatively good agreement with the predicted values (< 0.01 Å, blue numbers). All four structures possess bond lengths suggesting that two external six-membered rings behave as isolated benzenes, in line with the NICS-XY scans. The three sulfone structures all

display asymmetric carbon-sulfur bond lengths on either side of the S atom where the shorter bond is from the sulfone to the core. Interestingly, the computations overestimate all of the C–S bond lengths by ~ 0.03 Å. The bond lengths for **9**, which are only experimental numbers, are typical of those found in a ring-fused naphthalene.

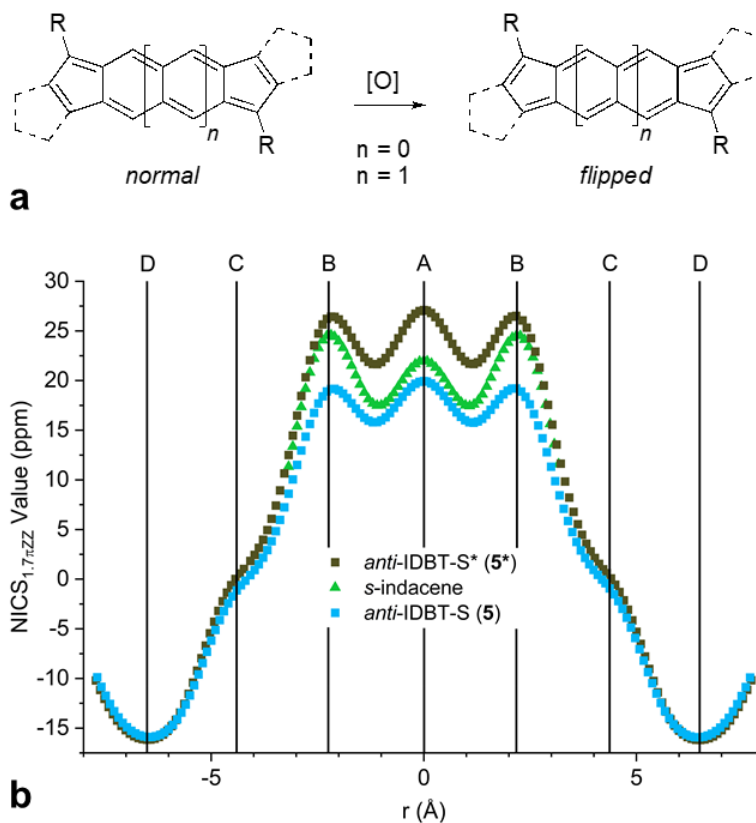


Figure 4.8 (a) Generalized structures displaying the “normal” bonding pattern observed in most indeno[1,2-*b*]fluorene-based molecules and the “flipped” bonding pattern observed for sulfones **5**, **6**, and **8**. (b) NICS-XY scans of both *anti*-IDBT-S geometries where **5** is the observed bond-flipped orientation and **5*** is the normally observed bonding pattern.

As depicted in Figure 4.8a, the bond alternation pattern in all three sulfones changes from the “normal” arrangement (left) to the “flipped” arrangement (right), and the computations corroborate these findings. Plunkett and co-workers discovered a similar bonding pattern reversal for an acenaphthylene-fused pentalene, but their rationale, i.e., the [5]radialene orientation of the double bonds similar to C₆₀ and related “buckybowls”,²⁰ is

clearly not applicable for our molecules. While calculations identified only a bond flipped structure for **6**, two minima structures were found for **5**—a higher energy structure with the normal bond alternation pattern and a flipped structure that was 1.5 kcal mol⁻¹ lower in energy.⁷⁹ NICS-XY scan calculations of **5** and its normal bonding pattern isomer **5*** provide a plausible explanation (Figure 4.8b) for the bond-flipped behavior: whereas the NICS scan of **5** shows reduced paratropicity compared to *s*-indacene, the NICS scan of **5*** suggests that a normal bond alternation arrangement would afford a molecule with greater paratropicity than *s*-indacene. Since antiaromaticity is a destabilizing feature, the sulfones simply adopt a bond alternation pattern to minimize their paratropicity and thus maximize their overall stability. Computational reevaluation of the Plunkett group's pentalene using NICS-XY scans (Figure C23) reveals that flipping of the bond alternation pattern results in a significant reduction in paratropicity compared to normal pentalene bonding, a result consistent with the above arguments.

We recently disclosed the synthesis and characterization of IIDBTs **3** and **4**, which are rare examples of singlet ground-state diradicaloids that required heating to 100-150 °C in order to access their triplet spin state.^{60,62} The uniquely large singlet-triplet energy gaps (7-8 kcal mol⁻¹) that the IIDBTs display are in part explained by the electronic repulsion of the lone pairs on the sulfur atoms. If we were to remove participation of the sulfur lone pairs by changing them into sulfones as in **7** and **8**, we would expect an accompanying change in the singlet-triplet energy gap (ΔE_{ST}) and the diradical character index (y). As shown in Table C2, the computational results reveal that sulfone formation slightly decreases y (*anti* -0.012, *syn* -0.006) and increases ΔE_{ST} , more so for the *anti* isomers (**3** → **7**, $\Delta\Delta E_{ST} = 0.88$ kcal mol⁻¹) than the *syn* isomers (**4** → **8**, $\Delta\Delta E_{ST} = 0.23$ kcal mol⁻¹).

These results are also in line with the linear (**3** / **7**) versus cross conjugation (**4** / **8**) arguments of the S atom with respect to the radical center accounting for the differences in IIDBT magnetic properties, i.e., cross conjugated **4** / **8** should be affected less than linearly conjugated **3** / **7**.

Although isolation of *anti*-IIDBT-S **7** proved elusive, we explored the diradical nature of *syn*-sulfone **8** first by variable temperature (VT) proton NMR spectroscopy. Based on its calculated ΔE_{ST} (-8.29 kcal mol⁻¹), one would expect the need for slightly higher temperatures to populate the triplet state when compared to *syn*-IIDBT **4** (-8.06 kcal mol⁻¹). Like its parent thiophene, sulfone **8** also displayed solubility issues at room temperature in either 1,1,2,2-tetrachloroethane-*d*₂ (Figure C1) or 1,2-dichlorobenzene-*d*₄ (Figure C2). As was the case with **4**, thermal broadening of the aromatic proton NMR signals of **8** (Figures 4.9a and C3) began at 75 °C and resolution of the signals was almost lost by 125-130 °C. Interestingly, once the sample was cooled back to 25 °C, the solubility of **8** was greatly enhanced and the signals could be completely assigned. Similar to the computations, these qualitative results suggest that compounds **4** and **8** have very similar singlet-triplet energy gaps.

To experimentally examine the magnetic properties of the sole open-shell sulfone, superconducting quantum interference device (SQUID) magnetometry was performed on a sample of **8**. The magnetic properties of **8** were measured up to ~580 K (Figure 4.9b), as the compound was shown by TGA to be stable at elevated temperatures (Figure C31). The SQUID signal was subjected to the Bleaney-Bowers fitting⁸⁰ from which the singlet-triplet energy gap was calculated to be -6.5 kcal mol⁻¹, the average of two sets of heating and cooling experiments. With changes of < 3% between the heating and cooling runs, these

results are indicative of the thermal resilience of **8** at high temperatures. Although somewhat lower than the calculated ΔE_{ST} ($-8.29 \text{ kcal mol}^{-1}$), the experimental value, much like in the case of IIDBTs **3** and **4**, support the hypothesis of an open shell molecule with a ground state singlet and an accessible triplet state only at elevated temperatures.

4.3 Conclusions

A small family of benzothiophene-derived sulfones has been synthesized and fully characterized using a late-stage modification approach. Through the use of a single chemical transformation, we are able to alter the antiaromaticity in our IDBTs and the diradical character and related properties in *syn*-IIDBT. This work highlights the development of late stage modification methods to impart meaningful change in properties without time-consuming synthetic modification. These resulting changes in antiaromaticity are trackable through proton NMR spectroscopy, NICS-XY scan calculations, and electrochemistry. The CV data show that while such modification increases the HOMO-LUMO energy gaps to a small degree, it lowers the HOMO and LUMO energy levels by 0.5-0.6 eV. The most significant change upon sulfone formation is flipping of the bond alternation pattern within the indacene core, as this relieves the potential destabilizing effects of enhanced paratropicity if the bond alternation were to retain a normal pattern. Notably, late-stage modification has provided an additional way to tune the diradical character and singlet-triplet energy gap of our ever-expanding series of diradicaloids,^{58,60,62,63} garnering new hope for the implementation of diradicals into organic devices. Work is under way to develop additional late stage modification approaches to fine-tune antiaromaticity and diradical character and related properties in our indeno[1,2-*b*]fluorene-derived scaffolds, as well as to integrate some of these molecules into OFETs.

4.4 Experimental Section

General procedures. All air-sensitive manipulations were carried out under an inert nitrogen gas using standard Schlenk technique. For moisture sensitive reactions, THF and toluene were refluxed with Na benzophenone ketyl for 24 h prior to distillation and use. Silica gel (240-300 mesh) was used for column chromatography. All other reagents were purchased and used as received. NMR spectra were recorded on a Bruker Avance III HD 500 equipped with a Prodigy multinuclear cryoprobe (^1H : 500 MHz) or Bruker Avance III HD 600 equipped with a Prodigy multinuclear cryoprobe (^1H : 600 MHz, ^{13}C : 151 MHz) NMR spectrometer at room temperature (unless otherwise noted). ^1H and ^{13}C NMR chemical shifts (δ) are expressed in ppm relative to the residual non-deuterated solvent reference (CDCl_3 : ^1H 7.26 ppm, ^{13}C 77.16 ppm; CD_2Cl_2 : ^1H 5.32 ppm, ^{13}C 53.84 ppm; $\text{DMSO}-d_6$: ^1H 2.50 ppm, ^{13}C 39.52 ppm). UV-Vis spectra were recorded on an Agilent Technologies Cary 60 UV-Vis spectrometer in HPLC grade CHCl_3 . 4-*tert*-Butyl-2,6-dimethylbromobenzene,⁸¹ diones **10-11**,^{27,67} diones **12-13**,^{60,62} and **1-Mes**^{27,67} were prepared according to the literature.

General Procedure A: Preparation of Quinoidal Compounds 1-4. A flame-dried round bottom flask was charged with 4-*tert*-butyl-2,6-dimethylbromobenzene (6 equiv.) dissolved in dry THF that was then cooled to $-78\text{ }^\circ\text{C}$. Once at temperature, *n*-BuLi (5.5 equiv.) was added dropwise and the organolithiate was stirred at $-78\text{ }^\circ\text{C}$ for 1 h. Meanwhile in a separate flame-dried round bottom flask a suspension of dione (1 equiv.) in dry THF was also cooled to $-78\text{ }^\circ\text{C}$ to which the organolithiate was transferred via cannula. The reaction was gradually warmed to room temperature overnight. The reaction was quenched with sat. NH_4Cl solution and the organics were extracted with DCM (3x). The combined

organic layer was then washed with H₂O and brine, dried (MgSO₄) and concentrated *in vacuo*. A short plug over SiO₂ purified the resultant diols which were carried onto the reductive dearomatization without further purification or characterization.

In a round-bottom flask the crude diol (1 equiv.) and anhydrous SnCl₂ (4 equiv.) were dissolved in dry toluene. Trifluoroacetic acid (3 drops, catalytic) was added to the mixture which was then stirred for 4 h. The reaction was monitored via TLC (9:1 hexanes/DCM). Once the reaction was complete, the mixture was concentrated to ~10 mL and then poured over a silica plug eluting with 1:1 hexanes/DCM to collect the crude reduced compounds. Column chromatography using an eluant of hexanes and DCM (see each compound for specific details) afforded the purified title compounds.

General Procedure B: Preparation of Sulfones. A flame-dried, foil wrapped round bottom flask equipped with a Claisen head was charged with compounds **1-4** (1 equiv.) and dry DCM. To this mCPBA (6 equiv.) was added in 3 portions over a 30 min period. After stirring at room temperature for 21 h, the reaction was quenched with a 10% KOH solution and the organics were extracted using DCM (3x). The combined organic layers were washed with brine, dried (MgSO₄), and then concentrated to dryness. Column chromatography using a mixture of hexanes and DCM as eluant (see each compound for specific details) afforded the purified title compounds.

anti-IDBT 1. Following General Procedure A, the lithiate generated from 4-*tert*-butyl-2,6-dimethylbromobenzene (0.92 g, 3.80 mmol) in THF (10 mL) and *n*-BuLi (2.2 mL, 3.49 mmol) was added to dione **10** (0.25 g, 0.63 mmol) in THF (20 mL) to produce the intermediate diol. A short SiO₂ plug using hexanes removed the non-polar impurities, followed by 1:3 DCM/hexanes to collect the first diastereomer and pure DCM to collect

the second diastereomer.

Following General Procedure A, the diol mixture and SnCl₂ (0.30 g, 4 equiv.) were reacted in rigorously degassed and dry toluene (40 mL). After the initial plug, column chromatography on SiO₂ using 15% DCM/hexanes gave **1** (138 mg, 32% from dione) as a deep purple solid. ¹H NMR (600 MHz, CDCl₃) δ 7.47 (d, *J* = 7.9 Hz, 2H), 7.16 (s, 4H), 7.01 (t, *J* = 6.9 Hz, 2H), 6.96 (t, *J* = 7.5 Hz, 2H), 6.57 (dd, *J* = 8.0, 1.3 Hz, 2H), 6.09 (s, 2H), 2.36 (s, 12H), 1.39 (s, 18H). ¹³C{¹H} NMR (151 MHz, CDCl₃) δ 150.9, 148.1, 147.6, 143.7, 143.0, 136.7, 136.0, 133.0, 131.5, 129.8, 125.9, 125.4, 124.4, 123.8, 123.5, 120.6, 34.4, 31.4, 20.9. HRMS (TOF ES⁺) (*m/z*) calculated for C₄₈H₄₅S₂ (M+H)⁺ 685.2963, found 685.2939.

anti-IDBT-sulfone 5. Following general procedure B, **1** (90 mg, 0.13 mmol) was reacted with mCPBA (135 mg, 0.79 mmol) in dry DCM (15 mL). After the basic aqueous work-up, the crude sulfone was purified by flash column chromatography using 45% DCM/hexanes as the eluant to give **5** (41 mg, 54%) as a vibrant purple solid with a blue sheen. ¹H NMR (500 MHz, CDCl₃) δ 7.66 (d, *J* = 8.2 Hz, 2H), 7.38 (t, *J* = 8.0 Hz, 2H), 7.35 (td, *J* = 7.5, 1.2 Hz, 2H), 7.14 (s, 4H), 6.59 (d, *J* = 7.5 Hz, 2H), 6.03 (s, 2H), 2.34 (s, 12H), 1.38 (s, 18H). ¹³C{¹H} NMR (126 MHz, CDCl₃) δ 152.2, 146.6, 146.4, 144.9, 142.3, 140.7, 135.7, 133.5, 130.73, 130.70, 129.3, 128.0, 126.9, 125.0, 122.0, 121.8, 34.5, 31.2, 20.8. HRMS (TOF ES⁺) (*m/z*) calculated for C₄₈H₄₅O₄S₂ (M+H)⁺ 749.2759, found 749.2747.

anti-IDBT-sulfone 5-Mes. Following general procedure B, **1-Mes** (81 mg, 0.13 mmol) was reacted with mCPBA (135 mg, 0.79 mmol) in dry DCM (10 mL). After the basic aqueous work-up, the crude sulfone was purified by flash column chromatography

using 4:1 DCM/hexanes as the eluant (due to lower solubility of the mesityl groups) to give **5-Mes** (52 mg, 58%) as a deep purple solid. ^1H NMR (600 MHz, CDCl_3) δ 7.65 (d, $J = 7.6$ Hz, 2H), 7.39 (t, $J = 7.6$ Hz, 2H), 7.34 (t, $J = 7.7$ Hz, 2H), 6.97 (s, 4H), 6.59 (d, $J = 7.7$ Hz, 2H), 6.01 (s, 2H), 2.36 (s, 6H), 2.31 (s, 12H). $^{13}\text{C}\{^1\text{H}\}$ NMR (151 MHz, CDCl_3) δ 146.7, 146.4, 145.2, 142.6, 140.9, 139.3, 136.4, 133.7, 130.9, 130.8, 129.5, 128.9, 128.1, 127.1, 122.1, 122.0, 21.3, 20.6. HRMS (TOF ES^+) (m/z) calculated for $\text{C}_{42}\text{H}_{33}\text{O}_4\text{S}_2$ ($\text{M}+\text{H}$) $^+$ 665.1821, found 665.1812.

syn-IDBT 2. Following General Procedure A, the lithiate generated from 4-*tert*-butyl-2,6-dimethylbromobenzene (0.92 g, 3.80 mmol) in THF (10 mL) and *n*-BuLi (2.2 mL, 3.49 mmol) was added to dione **11** (0.25 g, 0.63 mmol) in THF (20 mL) to produce the intermediate diol. A short SiO_2 plug using hexanes removed non-polar impurities, followed by 30% DCM/hexanes to collect the first diastereomer and pure DCM to collect the second diastereomer.

Following General Procedure A, the diol mixture and SnCl_2 (0.39 g, 4 equiv.) were reacted in rigorously degassed and dry toluene (45 mL). After the initial plug using 1:9 DCM/hexanes, preparatory TLC (1:3 DCM/hexanes) afforded **2** (164 mg, 38% from the dione) as a teal solid. Due to the low solubility of the title compound (peaks are the same magnitude of the ^{13}C satellite peaks), the residual solvent peaks are greatly exaggerated. ^1H NMR (600 MHz, CDCl_3) δ 7.45 (d, $J = 8.1$ Hz, 2H), 7.36 (d, $J = 8.0$ Hz, 2H), 7.14 (s, 4H), 7.11 (t, $J = 7.2$ Hz, 4H), 7.04 (t, $J = 7.3$ Hz, 2H), 6.06 (s, 2H), 2.45 (s, 12H), 1.39 (s, 18H). $^{13}\text{C}\{^1\text{H}\}$ NMR (151 MHz, CDCl_3) δ 151.2, 148.1, 147.1, 146.6, 140.9, 137.5, 136.1, 134.9, 133.4, 129.4, 125.2, 124.7, 124.4, 124.3, 123.9, 121.8, 34.5, 31.4, 21.0. HRMS (TOF ASAP^+) (m/z) calculated for $\text{C}_{48}\text{H}_{45}\text{S}_2$ ($\text{M}+\text{H}$) $^+$ 685.2963, found 685.2931.

***syn*-IDBT-sulfone 6.** Following General Procedure B, **2** (0.27 g, 0.40 mmol) was reacted with mCPBA (275 mg, 1.59 mmol) in dry DCM (40 mL). After the basic aqueous work-up, the crude sulfone was purified by flash column chromatography using 2:1 DCM/hexanes as the eluant to give **6** (72 mg, 23%) as a bluish-violet solid. ^1H NMR (600 MHz, CDCl_3) δ 7.76 (dd, $J = 7.2, 1.5$ Hz, 2H), 7.62 (td, $J = 6.6, 1.5$ Hz, 2H), 7.60–7.55 (m, 4H), 7.17 (s, 4H), 6.91 (s, 2H), 2.40 (s, 12H), 1.38 (s, 18H). $^{13}\text{C}\{^1\text{H}\}$ NMR (151 MHz, CDCl_3) δ 152.3, 147.9, 147.4, 146.8, 143.5, 138.7, 136.7, 133.7, 132.6, 131.6, 128.9, 126.8, 125.9, 125.6, 125.1, 122.9, 34.9, 31.7, 21.2. HRMS (TOF ES^+) (m/z) calculated for $\text{C}_{48}\text{H}_{45}\text{O}_4\text{S}_2$ ($\text{M}+\text{H}$) $^+$ 749.2759, found 749.2749.

***anti*-IIDBT 3.** Following General Procedure A, the lithiate generated from 4-*tert*-butyl-2,6-dimethylbromobenzene (0.61 g, 2.52 mmol) in THF (20 mL) and *n*-BuLi (1.5 mL, 2.36 mmol) was added to dione **12**³ (0.14 g, 0.32 mmol) in THF (20 mL) to produce the intermediate diol. A short SiO_2 plug using hexanes removed non-polar impurities, followed by 2:3 DCM/hexanes to collect the first diastereomer and pure DCM to collect the second diastereomer.

Following General Procedure A, the diol mixture and SnCl_2 (0.20 g, 4 equiv.) were reacted in rigorously degassed and dry toluene (40 mL). After the initial plug using 1:9 DCM/hexanes, the filtrate was concentrated. The solid was rinsed with cold MeCN (3x) and **3** was isolated as a deep purple solid (97 mg, 42% from the dione). NMR spectra and mass spectrum matched the data previously reported.⁶²

Benzothiazine dioxide 9. Compound **3** (0.18 g, 0.25 mmol, 1 equiv.), urea-hydrogen peroxide (UHP) (0.24 g, 2.52 mmol, 10 equiv.) and phthalic anhydride (0.37 g, 2.52 mmol, 10 equiv.) were added to a flame-dried round bottom flask equipped with a

reflux condenser under an N₂ atmosphere. Dry EtOAc (25 mL) was added and the reaction was heated in a sand-filled heating mantle to 90 °C for 24 h. The reaction was quenched with saturated Na₂SO₃ solution and then the organics were extracted with DCM (3x). The organics were washed sequentially with 1 M NaOH, H₂O and brine, dried (MgSO₄) and concentrated *in vacuo*. Purification by preparatory TLC (DCM) and collecting the vibrant purple band with an R_f of 0.5. furnished **9** (22 mg, 11%) as a purplish-red solid. ¹H NMR (600 MHz, CDCl₃) δ 8.09 (s, 2H), 8.05 (d, *J* = 7.8 Hz, 2H), 7.48 (t, *J* = 7.5 Hz, 2H), 7.33–7.27 (m, 6H), 7.13 (s, 2H), 6.94 (d, *J* = 8.2 Hz, 2H), 2.15 (s, 12H), 1.44 (s, 18H). ¹³C{¹H} NMR (151 MHz, CDCl₃) δ 171.2, 157.9, 153.4, 142.4, 138.1, 134.6, 134.2, 133.2, 130.2, 128.5, 127.5, 126.4, 126.1, 125.1, 124.9, 120.9, 35.1, 31.7, 20.5. MS (TOF ES⁺) (*m/z*) calculated for C₅₂H₄₇N₂O₄S₂ (M+H)⁺ 827.2977, found 827.2997.

***syn*-IIDBT 4.** Following General Procedure A, the lithiate generated from 4-*tert*-butyl-2,6-dimethylbromobenzene (0.82 g, 3.37 mmol) in THF (10 mL) and *n*-BuLi (1.9 mL, 3.09 mmol) was added to dione **13**³ (0.25 g, 0.56 mmol) in THF (20 mL) to produce the intermediate diol. A short SiO₂ plug using hexanes removed non-polar impurities, followed by 45% DCM/hexanes to collect the first diastereomer and pure EtOAc to collect the second diastereomer.

Following General Procedure A, the diol mixture and SnCl₂ (0.39 g, 4 equiv.) were reacted in rigorously degassed and dry toluene (45 mL). After the initial plug using 1:9 DCM/hexanes, preparatory TLC of the crude material using 1:3 DCM/hexanes as eluant gave **4** (149 mg, 36% from the dione) as a green solid. NMR spectra and mass spectrum matched the previously reported compound.⁶²

***syn*-IIDBT-sulfone 8.** Following General Procedure B, **4** (0.11 g, 0.15 mmol) was

reacted with mCPBA (210 mg, 1.21 mmol) in dry DCM (20 mL). After the basic aqueous work-up, the crude sulfone was purified by flash column chromatography using 2:1 DCM/hexanes as the eluant to give **8** (58 mg, 48%) as a greyish-purple solid. (¹H NMR (500 MHz, CDCl₃) δ 7.83 (s, 2H), 7.76–7.73 (m (overlapping dd), 4H), 7.58 (td, *J* = 7.7, 1.1 Hz, 2H), 7.48 (t, *J* = 7.4 Hz, 2H), 7.24 (s, 2H), 7.16 (s, 4H), 2.29 (s, 12H), 1.38 (s, 18H). ¹³C{¹H} NMR (151 MHz, CDCl₃) δ 152.1, 145.8, 142.3, 142.1, 141.4, 140.1, 136.9, 136.5, 135.4, 133.8, 131.1, 130.2, 130.0, 127.4, 127.1, 125.0, 124.0, 123.0, 34.9, 31.7, 21.0. HRMS (TOF ES⁺) (*m/z*) calculated for C₅₂H₄₆O₄S₂ (M)⁺ 798.2838, found 798.2831.

CHAPTER V

MONORADICALS AND DIRADICALS OF DIBENZOFUORENO[3,2-*b*]FLUORENE ISOMERS: MECHANISMS OF ELECTRONIC DELOCALIZATION

This chapter includes previously published and co-authored material from Hayashi, H.; Barker, J. E.; Valdivia, A. C.; Kishi, R.; MacMillan, S. N.; Gómez-García, C. J.; Miyauchi, H.; Nakamura, Y.; Nakano, M.; Kato, S.-I.; Haley, M. M.; Casado, J. Monoradicals and Diradicals of Dibenzofluoreno[3,2-*b*]fluorene Isomers: Mechanisms of Electronic Delocalization. *J. Am. Chem. Soc.* **2020**, *142*, 20444-20455. This manuscript was written by Joshua E. Barker and Abel Cárdenas Valdivia with assistance from Prof. Juan Casado and Prof. Michael M. Haley. The project in this chapter was conceived by Joshua E. Barker and Prof. Michael Haley. The experimental work in this chapter was performed by Hideki Hayashi, Joshua E. Barker, and Abel Cárdenas Valdivia. The computational work in this chapter was performed by Ryohei Kishi with assistance from Prof. Masayoshi Nakano.

5.1 Introduction

Carbon-based diradicaloids are fundamentally interesting molecules that have received a great deal of attention over the last decade.¹⁻⁴ These novel conjugated polycyclic hydrocarbons (CPHs) promise use in many organic electronic (OE) applications⁵⁻⁷ and as magnetic materials;^{8,9} however, an inherent shortcoming in such open-shell constructs is

instability. Bulky groups installed at positions of high reactivity have enabled the isolation of kinetically stable diradicaloids, which have advanced the field beyond novel syntheses. With the advent of increased stability, attention has turned to careful tuning of diradical properties with a goal towards application in OEs.¹⁰⁻¹⁶

An inherent property of diradicaloids is their ability to switch spins from a spin-paired singlet state to a spin-parallel triplet state. Controllable transition between these states can be achieved through heating or cooling, and variable temperature (VT) measurements using SQUID magnetometry or ESR spectroscopy can determine the singlet-triplet energy gap (ΔE_{ST}). For the application of this class of molecules to be fully realized, it is essential to uncover the underlying geometric/structural and theoretical parameters that can be modulated to optimize ΔE_{ST} , in other words, to understand the basis of electronic diradical and spin delocalization.¹⁷

With this goal in mind, several groups have reported different strategies for tuning ΔE_{ST} . Broadly, in what could be considered a “chemical approach”, extending quinoidal conjugation (Figure 5.1 top, e.g., $\mathbf{A} \rightarrow \mathbf{B} \rightarrow \mathbf{C}$)¹⁸⁻²⁵ or changing the conjugation pattern entirely²⁶⁻⁴⁰ (e.g., from *para*- to *meta*-) can yield large scale changes in ΔE_{ST} .⁴¹⁻⁴³ This often correlates with a strong increase in the diradical character index (y_0 , with $y_0 \rightarrow 0$, a compound becomes more closed shell and with $y \rightarrow 1$, a compound becomes more open-shell) resulting from a greater driving force to aromatize the central quinoidal unit and create more Clar aromatic sextets.^{2,26,28,29,31,38,40} Recently our group has explored changing diradical character and tuning ΔE_{ST} through a contrasting “physical approach”, coupling synthetic modulation with physical methods.⁴⁴⁻⁴⁶ The “two electrons in two sites” model of diradicals provides the framework for this strategy through consideration of the effects

of U (the on-site electron-electron repulsion term)^{44,45} and t_{ab} (the transfer integral, an electron delocalization term).⁴⁶ Equation 1 provides, in the two-site diradical model, the dependence of y (defined in Equation 2) in terms of U and t_{ab} .

$$y_0 = 1 - \frac{1}{\sqrt{1 + \left(\frac{U}{4t_{ab}}\right)^2}} \quad (1)$$

with:

$$\Delta E_{ST} = \frac{U}{2} \left[1 - \frac{1}{\sqrt{y_0(2 - y_0)}} \right] + 2K_{ab} = \frac{U}{2} f_{ST}(y_0) + 2K_{ab} \quad (2)$$

Equation 2 further accounts for the ΔE_{ST} in terms of y_0 and K_{ab} (direct exchange integral), where a and b define the electrons in the localized natural orbitals. For most organic diradicaloids, K_{ab} is expected to be much smaller than the first term, and thus ΔE_{ST} is primarily determined by the first term. Given that y_0 is expressed as a function of U/t_{ab} by Equation 1, ΔE_{ST} is determined from the balance of U and U/t_{ab} . Specifically, in diindenoanthracene-based diradicaloids (DIAnS, Figure 5.1 bottom), we have observed that for an isomeric series of dibenzo-fused DIAn (DBDIAn) diradicaloids, the same chemical hydrocarbon composition causes the repulsion U term to be similar among them, and the differences in diradical character result from a large change in t_{ab} .⁴⁶

The current study focuses on the quinoidal approach. Figure 5.1 illustrates the generalized representation of ΔE_{ST} versus y_0 (blue curve, defined above in eq. 2) for the quinoidal diindenoacene family **A-C** with two assumptions: (i) lateral fusion with different Ar groups in a symmetric manner, and (ii) these Ar groups do not become the main stabilizing force of the diradical (as would be the case of fused phenalenyls); thus, the fused arenes always represent secondary stabilization motifs and impart fine tuning of the

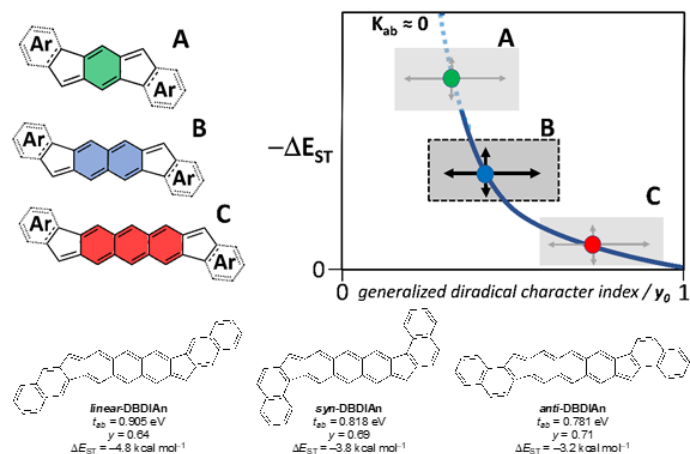


Figure 5.1 (top left) Strategies for tuning diradical character showing the “chemical approach” using an expansion in the quinoidal conjugation path in indenofluorene congeners (A, B and C for benzo-, naphtho- and anthraceno-quinodimethanes, respectively). (top right) The arrows and boxes denote the variation that the $y_0/\Delta E_{ST}$ points might undergo with altering the lateral Ar substituents. The B region targets fluorenofluorenes 1-5 reported in this study. (bottom) Literature examples of the DBDIAn/C series with different fused Ar groups illustrating that the Ar motif exhibits secondary control (fine tuning) of $y_0/\Delta E_{ST}$, i.e., the “physical approach”. In all instances, only the conjugated diradical cores are shown without the bulky alkyl and/or pendant aryl groups used to protect the radical centers.

magnetic properties around the main points such as highlighted as the expanding arrows in the boxes also in Figure 5.1. As a result, the main changes among molecules all lie along the generalized ΔE_{ST} - y curve that is dictated by the benzo-, naphtho- and anthraceno-quinodimethane cores of A-C shown in Figure 5.1. The use of the “chemical approach” to reduce the quinoidal central motif from anthracenoquinodimethane to naphthoquinodimethane affords fluoreno[3,2-*b*]fluorene (FF, **1**). As depicted in Figure 5.2, inclusion of additional benzene rings to each side of the core FF structure gives the representative dibenzofluorenofluorenes (DBFFs, **2-4**) and tetrabenzofluorenofluorene (TBFF, **5**). Alternatively, these derivatives can also be viewed as fusion along the 1,2-bond or 2,3-bond of naphthalene to a dicyclopenta[*b,g*]naphthalene (DCN, **6**) core. This new series of compounds provides an avenue for predicting the change in diradical index based

on U/t_{ab} in molecules with larger/smaller $\Delta E_{ST}/y_0$. Given that the structural alteration consists of changing the fusion-orientation along the 2,3-bond of DCN (6), it should be

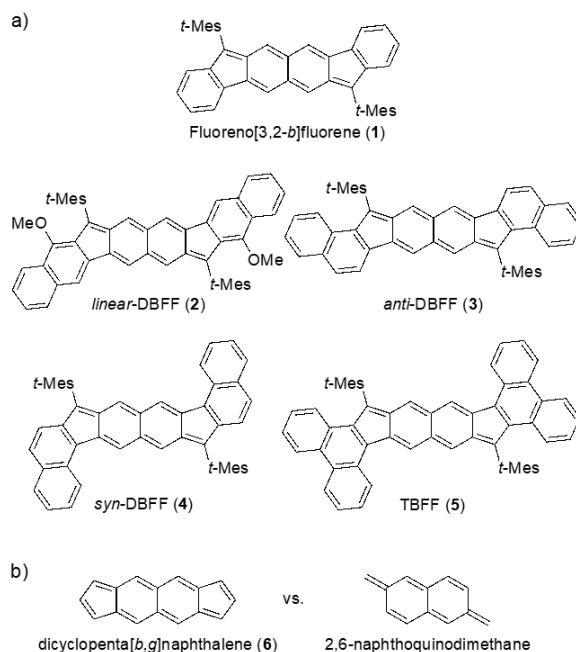


Figure 5.2 (a) Structures of target molecules FF **1**, DBFFs **2-4**, and TBFF **5** with (b) the two viable core moieties (t-Mes = 4-t-butyl-2,6-dimethylphenyl).

possible to connect the variation of the bond-order of the fusion bond with the value of diradical parameters to evaluate the interdependence of ΔE_{ST} and y_0 in molecules possessing intermediate values of y . This is in contrast to the case of diradicals with larger y_0 , such as the dibenzoDIAn derivatives.⁴⁶ Finally, in addition to the comparative study of neutral diradicals, both DBFF and DBDIAn are amphoteric redox molecules that nicely stabilize cations or anions, which become the monoradical versions of the neutral diradicals. This offers the possibility of a second comparative study of mono- and diradicals in the DBFF and DBDIAn series to obtain insight into the similarities and differences in electron delocalization between isomers within each series. Surprisingly, when comparing the neutral diradicals and in the radical cations, the electron delocalization is inherently the

same, but in the anions some variation is seen.

5.2 Results and Discussion

Calculations have been carried out on model compounds **1'**-**5'** (Mes replacing *t*-Mes) and the main theoretical data are summarized in Table 5.1 (see Table D1-D3 for additional data and Figure D1 for optimized geometries). We should note that Table 5.1 contains two-types of computational results for $y_0/\Delta E_{ST}$, namely, spin-projected spin-unrestricted Hartree-Fock/spin-flip-noncollinear time-dependent density functional theory (PUHF/SF-NC-TDDFT) results that are useful and reliable for (semi-)quantitative comparison with several other systems as well as with experimental results (for ΔE_{ST}), and complete active space configuration-interaction method combined with tuned-long-range-corrected Kohn-Sham DFT (tuned-LC-RBLYP CASCI) results that are used for qualitative discussion on the basis of the “two electrons in two sites” model (for details, see the Computational Details in Appendix D). Calculations predict U/t_{ab} values to vary among the studied compounds as 2.30 in **2'**, 2.56 in **3'**, 2.64 in **4'**, and 2.81 in **5'**, in good agreement with the change of diradical character at the PUHF level. The evolution of y_0 can be further simplified since its change is concomitant with the decrease in the series of t_{ab} alone. In fact, this variation of the t_{ab} term is in accordance with the deduced reduction of the HOMO-LUMO energy gap in the series (*vide infra*). U conversely increases and decreases modestly on **2'** → **3'** → **4'** → **5'**, a non-constant behavior that will play a secondary role in the modulation of y_0 .

Figure 5.3 compares the variation of the diradical character index y_0 and ΔE_{ST} from calculations for the DBDIAn and DBFF series at the same level of theory in both cases. We observe that DIAn and FF both show similar behavior of ΔE_{ST} gap versus y_0 (predicted

by eq. 2 and delineated by the green-dotted curve in Figure 5.3 left). It is predicted that dibenzo substitution of the FF core produces an incremental decrease of $y_0/\Delta E_{ST}$ of 0.083/1.42 kcal mol⁻¹ from *linear*-DBFF **2'** to *anti*-DBFF **4'** while these variations are 0.073/1.64 kcal mol⁻¹ going from *linear*-DBDIAn to *anti*-DBDIAn,⁴⁶ revealing different degrees of tuning of the two parameters by “isomerization” of the fused arenes. Thus, though the large-scale change in ΔE_{ST} and y_0 is attributable to the difference between naphthoquinodimethane to anthracenoquinodimethane in Figure 5.3 (left), dibenzo-fusion and its bond orientation play an important fine-tuning role that we now analyze in detail.

	FF (1') ^a	<i>linear</i> -DBFF (2')	<i>syn</i> -DBFF (3')	<i>anti</i> -DBFF (4')	TBFF (5')
y_0 (PUHF) (-) ^b	0.492	0.512	0.559	0.595	0.629
Vertical ΔE_{ST} (kcal mol ⁻¹) ^c	-17.46	-17.52	-	-13.68	-12.68
Adiabatic ΔE_{ST} (+ZPVE)	-10.25	-10.03	-9.63	-8.61	-7.90
Experimental ΔE_{ST} (kcal	-9.3	-9.6	-8.7	-7.8	-7.6
y_0 (CASCI) (-) ^d	0.151	0.133	0.158	0.166	0.182
Vertical ΔE_{ST} (CASCI)	-27.9	-28.8	-24.3	-22.4	-20.2
$U/ t_{ab} $ (-) ^d	2.487	2.301	2.563	2.640	2.810
$ t_{ab} $ (eV) ^d	1.163	1.143	1.055	1.012	0.960
$f_{ST}(y)$ (-) ^d	-0.894	-1.006	-0.854	-0.815	-0.740
$U/2 = K_{gu}^M$ (eV) ^d	1.446	1.315	1.352	1.336	1.349
$2K_{ab}$ (eV) ^d	0.082	0.073	0.102	0.116	0.123

Table 5.1 Summary of computational parameters and experimental values of ΔE_{ST} for fluorenofluorenes **1'**-**5'**. ^aComputational data for **1'** from reference 44. ^bCalculated at the PUHF/6-311G**/RB3LYP/6-311G* level. ^cCalculated at the spin-flip noncollinear TD-DFT PBE50/6-311G**/RB3LYP/6-311G* level. ^dCalculated at the tuned-LC-RBLYP CASCI(2,2)/6-311G**/RB3LYP/6-311G* level. Computational details are given in the SI.

The variation of U in Figure 5.3 (right) is much smaller than the variation of t_{ab} in the DBFF and DIAn series, suggesting the latter is the physical reason for the modulation within the series of ΔE_{ST} and y_0 . This is reasonable due to the dependence of U on the

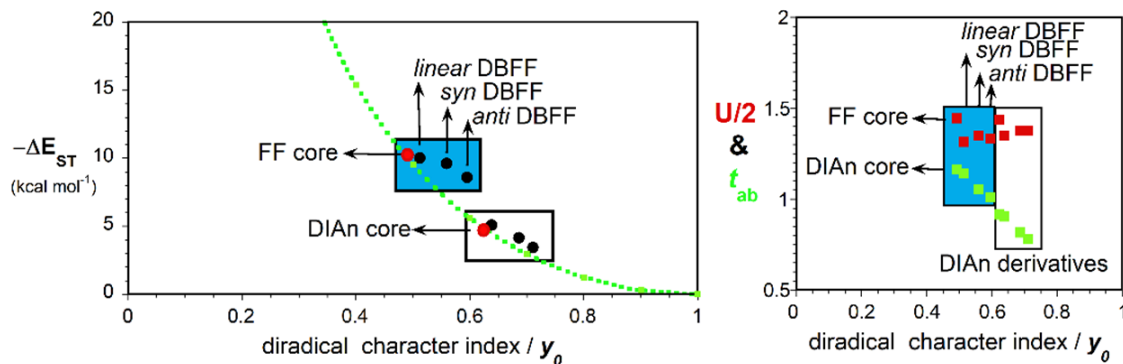


Figure 5.3 (left) Variation of the diradical character index y_0 and ΔE_{ST} from calculations for the DIAn derivatives (white box) and FF derivatives (blue box) at the same level of theory. Green line denotes the generalized behavior of the function of equation (2). (right) Variation of the $U/2$ and t_{ab} as a function of the diradical character.

chemical composition, given that both series are hydrocarbon-based compounds (U is more dependent on the presence of heteroatoms, which is not the case herein).^{44,45} Furthermore, the variation of t_{ab} is similar in both series reflecting the change in fusion bond-order. In absolute terms, the values of t_{ab} are larger in the DBFFs compared to the DBDIAn derivatives because of the smaller central naphthalene core. This in turn strengthens the inter-radical bonding, increasing the HOMO-LUMO energy gap and t_{ab} . Nonetheless, despite the larger effect on t_{ab} being dictated by the central pro-aromatic core, there is a part which is modulated by the external fusion and should result from the radical centers being delocalized on the external naphthalenes. This is further corroborated by the unpaired electron density distribution which partially diffuses out on the external rings in different ways depending on the fusion orientation (Figure 5.4).

The diradical character index is based on the evaluation of the occupation numbers of the natural orbitals. Typically, in our diradicaloid molecules, y_0 is based on the highest occupied natural orbital (HONO) and lowest unoccupied natural orbitals (LUNO), provided these HONO and LUNO are those with fractional occupation numbers (different for 1 and 0). Figure 5.4 displays the amplitudes and phases of the HONOs of the starting

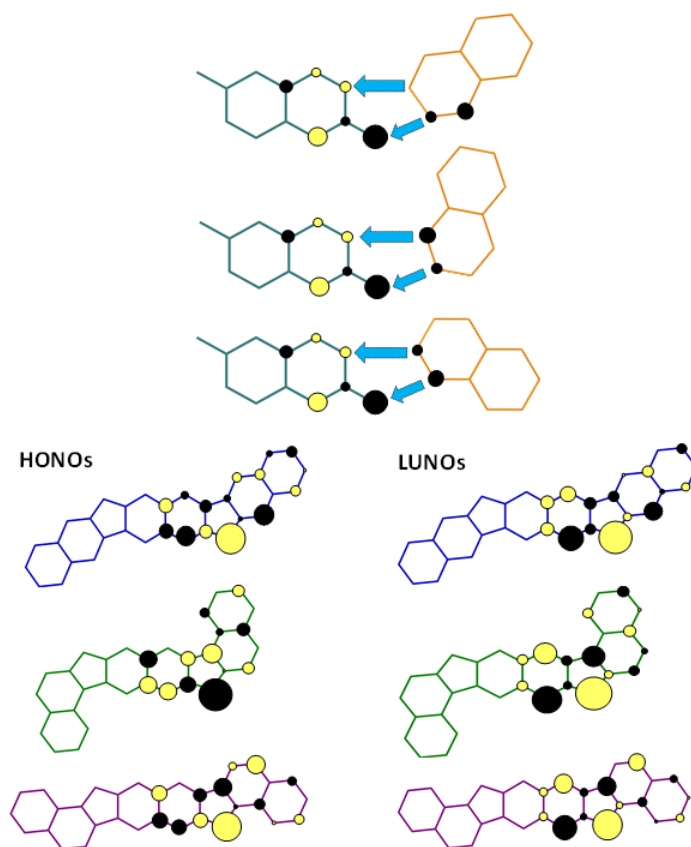
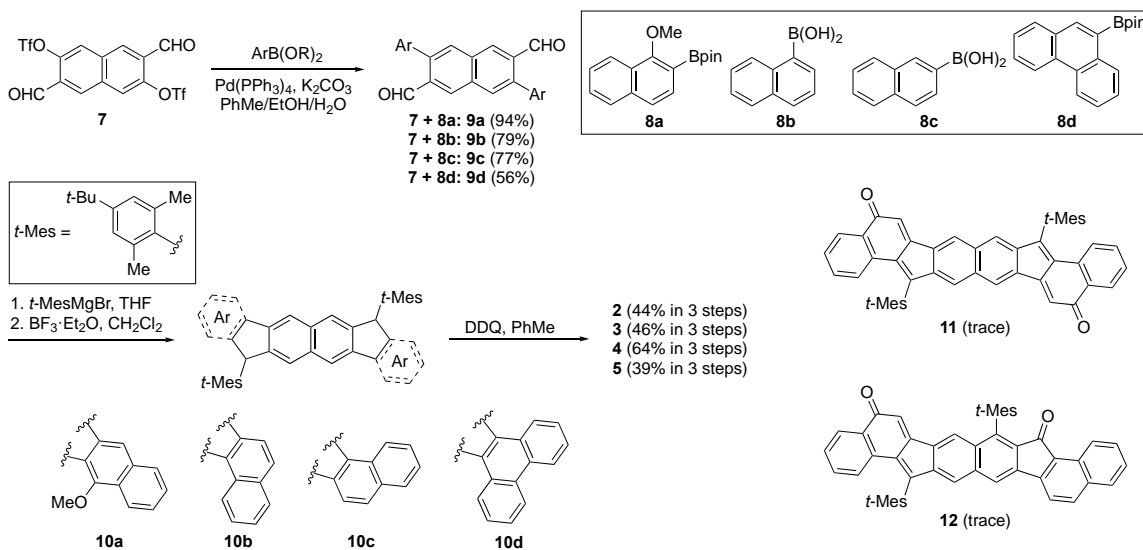


Figure 5.4 Top) Coupling mode (see blue arrows) of the HONO natural orbitals of the constituting fragments (2,6-dimethylene-2,6-dihydronaphthalene and naphthalene). Bottom) HONO and LUNO of the given compounds **2-4**. All single particle orbitals are illustrated schematically by the contribution of each atom. Notice that the HOMO and LUMO of the compounds are not necessarily built by the combination of the HOMOs of the fragments.

naphthalene and 2,6-dimethylene-2,6-dihydronaphthalene fragments (see Figure D2 and Figure D3 for the precise combinations to produce the natural orbitals of the **2-4** compounds). Though the natural orbitals of **2-4** do not necessarily result from mixing of the HONOs of the constituting fragments in Figure 4, the particular shape of the HONO of naphthalene relative to that of the HONO of 2,6-dimethylene-2,6-dihydronaphthalene serve to show that the orientation along the fusion bond of the two fragments has distinctive implications in the electronic properties of the resulting isomers. The diradical character index is based on the evaluation of the occupation numbers of the natural orbitals.

Typically, in our diradicaloid molecules, y_0 is based on the highest occupied natural orbital (HONO) and lowest unoccupied natural orbitals (LUNO), provided these HONO and LUNO are those with fractional occupation numbers (different for 1 and 0). Figure 5.4 displays the amplitudes and phases of the HONOs of the starting naphthalene and 2,6-dimethylene-2,6-dihydronaphthalene fragments (see Figure D2 and Figure D3 for the precise combinations to produce the natural orbitals of the **2-4** compounds). Though the natural orbitals of **2-4** necessarily do not result from mixing of the HONOs of the constituting fragments in Figure 5.4, the particular shape of the HONO of naphthalene relative to that of the HONO of 2,6-dimethylene-2,6-dihydronaphthalene serve to show that the orientation along the fusion bond of the two fragments has distinctive implications in the electronic properties of the resulting isomers. Going to the precise shape of the HONO and LUNO of compounds **2-4** in Figure 5.4 (see Figure D2 for all molecules), we observe that the fusion of the two fragments produces the emergence of several features: (i) it gives rise to atomic coefficients with significant contributions in the peripheral naphthalenes (absent in the starting naphthalene) in accordance with the delocalization effects at the origin of the variation of t_{ab} . (ii) The nature of the atomic coefficients in the HONO and LUNO natural orbitals in the atoms of the fusion bond of 2,6-dimethylene-2,6-dihydronaphthalene and naphthalene reveals the changes with isomerization and their values notably change in the parent molecules. (iii) In the case of TBFF **5**, the enlargement of the external π -system from naphthalene to phenanthrene reduces its t_{ab} due to the expansion of the delocalization in a greater π -system. Additional theoretical data for neutral **1-5** (including NICS calculations and ACID plots, Figures D4-D5) as well as for the models (Figures D6-D7 and Table D4) are provided in Appendix D.



Scheme 5.1 Synthesis of FF **1**, DBFFs **2-4** and TBFF **5** along with the isolated diketone decomposition products **11** and **12**.

For the preparation of the FF congeners, it is essential to use an “inside-out” cyclization strategy (i.e., Friedel-Crafts closure onto the outer ring system, Scheme 5.1 and Scheme D1) because of the preferential electrophilic aromatic substitution reactivity of naphthalene at the 1/4/5/8-positions. Thus, it is important to begin with a symmetrically functionalized naphthalene starting material to form the core of the FF structure. Starting with known bis-triflate **7**,²⁷ we utilized a modular synthesis to obtain the desired FF derivatives. Suzuki cross-coupling of **7** with the requisite boronic acids/esters **8a-d** yields dialdehydes **9a-d**. Addition of an aryl nucleophile to the carbonyl group followed by Friedel-Crafts alkylation provides dihydro-DBFF/TBFF intermediates **10a-d** in good yields. Finally, oxidative dearomatization with DDQ furnishes FF derivatives **2-5** in moderate to very good yields. To properly compare these compounds with the parent fluoreno[3,2-*b*]fluorene, we re-synthesized **1** with *t*-Mes groups on the apical carbons according to the previous procedure (Scheme D2).²² To obtain *linear*-DBFF **2** it was necessary to block the C1 position to ensure closure at C3 and thus avoid reproducing *anti*-

DBFF **4**. Use of **8a** as the aryl coupling partner in the initial cross-coupling step enabled the successful synthesis of MeO-substituted *linear*-DBFF **2**. Unfortunately, the use of Me groups afforded highly insoluble products. Despite inherent naphthalene reactivity, the synthesis of *syn*-DBFF **3** proceeded with respectable yields without evidence of ring-closure at the C8 position of naphthalene, which would form the expected octazethrene product.²⁷ Interestingly, oxidative dearomatization of **10c** to give *anti*-DBFF **4** also yielded diketone decomposition product **11**, supporting the notion of increased delocalization onto the outer naphthalenes (*vide supra*). In addition, we obtained dione **12** as a side product using an alternative synthesis of **4** via an intermediate *anti*-DBFF dione (Scheme D3). Both dione side-products were characterized by x-ray crystallography (Figures D8-D9) despite being obtained in only trace amounts. Similar degradation products have been previously observed by the Wu group,²⁷ where the oxygen can add at sites of appreciable spin density (e.g., **11**) and/or the aryl nucleophile can add in a conjugate manner (e.g., right *t*-Mes group in **12**). NMR spectra of all products are provided in Appendix D.

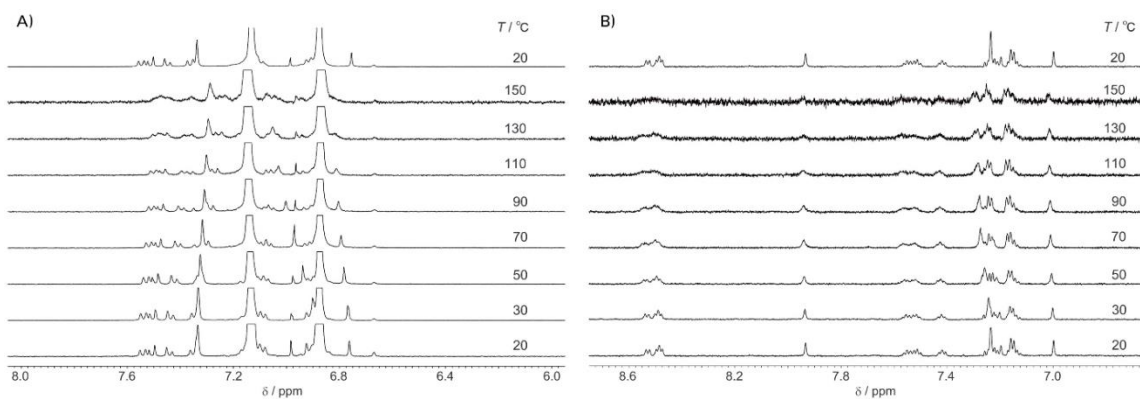


Figure 5.5 VT ¹H NMR spectra of (a) *anti*-DBFF **4** in *o*-CD₂Cl₄ and (b) TBFF **5** in 1,1,2,2-C₂D₂Cl₄.

Variable temperature (VT) ¹H NMR spectroscopy was performed with each of the DBFF/TBFF derivatives to begin probing the diradical character. All compounds have

sharp, well defined peaks in their ^1H NMR spectra at room temperature (see Appendix D), implying singlet ground states as expected. Considering the diradical index value and predicted ΔE_{ST} for each of the FF derivatives, it would be expected that *linear*-DBFF **2** should be comparable to FF **1** with minimal broadening of peaks even at elevated temperatures (~ 150 °C) whereas *syn*-DBFF **3**, *anti*-DBFF **4**, and TBFF **5** should show onset of triplet population at lower temperatures. Confirming these predictions, significant broadening of peaks is observed in the ^1H NMR spectra of **4** and **5** (Figure 5.5). The onset of peak broadening, implying population of the paramagnetic triplet state, is observed at ~ 90 °C for TBFF **5**, and ~ 130 °C for *anti*-DBFF **4**. The ^1H NMR spectra of *syn*-DBFF **3** show only minimal broadening at 150 °C, whereas *linear*-DBFF **2** displays a sharpening of peaks rather than broadening, likely due to enhanced solubility at higher temperatures. The samples did not undergo any noticeable decomposition, and upon cooling the spectra appeared identical to the initial spectra taken at room temperature.

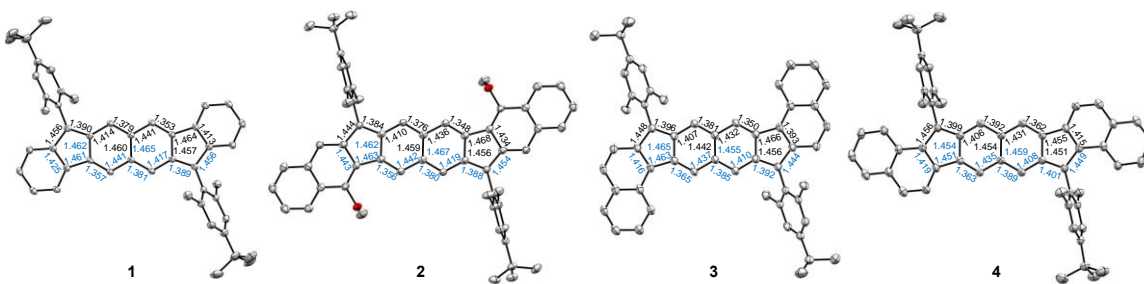


Figure 5.6 X-ray crystal structures of FF **1** and the DBFFs **2-4**. Bond lengths from the crystal structures are in black, bond lengths from the calculated structures are in blue.

Single crystals suitable for analysis by X-ray crystallography were obtained for neutral compounds **1-4** from CH_2Cl_2 /hexane solutions and for the radical cation of **3**, $\mathbf{3}^+\cdot\text{SbCl}_6^-$. The respective experimental and calculated (Figure D1) bond lengths are given in Figure 5.6, which show good agreement between the two sets of numbers; additional structural data including bond length esd values are given in Figures D10-D14.

Unfortunately, we were unable to secure diffraction quality crystals of **5**. According to the above discussion, the relevant CC bond distance from the naphthalene core to the apical carbon of the five-membered ring should correlate with the strength of the diradical character, i.e., the longer the bond the more diradical the molecule is.⁴⁶ Based on the calculations, **4** should possess the longest CC distance while **2** should exhibit the smallest among the four compounds. Gratifyingly, this is the observed trend, where the distance of 1.384(2) Å for **2** is the shortest among the derivatives, **1** is slightly longer at 1.390(2) Å, and **3** and **4** show similar distances of 1.396(3) and 1.399(4) Å, respectively. This trend (1.384-1.399 Å) in general is analogous to that observed in the DIAn derivatives (1.391-1.412 Å),⁴⁶ with the latter congeners exhibiting slightly longer apical bond lengths (e.g., 1.399(4) Å for **4** vs. 1.412(5) Å for *anti*-DIAn) than the corresponding DBFF analogues because of their increase diradicaloid character.

Figure 5.7 shows the electronic absorption spectra of compounds **1-5** (Figure D15 for calculated spectra). All compounds exhibit two sets of bands at 350-400 nm and 550-700 nm. The latter group is composed of two well-resolved vibronic components each. There is a continuous red-shift of the wavelengths of these bands from FF **1** (600 nm) → *linear*-DBFF **2** (629 nm) → *syn*-DBFF **3** (688 nm) → *anti*-DBFF **4** (697 nm) → TBFF **5** (738 nm). Considering the variation in t_{ab} , the trend in the low energy absorbance maxima agrees quite well since the trend in t_{ab} values directly correlates with the HOMO-LUMO energy gap, which is what the optical spectra reveal.

It is interesting to note that fully quinoidal molecules always possess larger wavelength absorption maxima than their aromatic counterparts because of the smaller HOMO-LUMO energy gap in the former, and this is generally true for comparison between

closed-shell molecules. The situation here is just the opposite since the more diradicaloid the molecule is, the more aromatic the central cores becomes and thus the greater redshift of the bands. To account for this behavior, it is well known that the appearance of diradical character provokes a strong reorganization of the energies of the bright and dark electronic excited states that exhibits a contrasting behavior when compared with that in classical closed-shell entities.^{2,13} A consequence of this reorganization in diradicaloid molecules is the detection of a weak band, often appearing as a low energy shoulder of the main band, which corresponds to the double exciton state fully absent in the closed-shell analogue molecules.

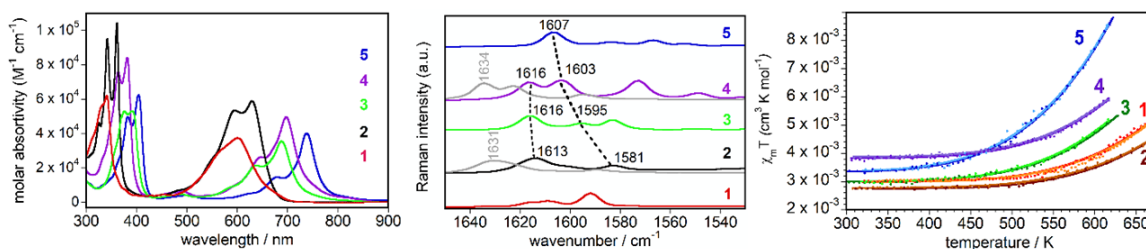


Figure 5.7 (left) UV-vis spectra of FF 1, linear-DBFF 2, syn-DBFF 3, anti-DBFF 4, and TDF 5 recorded at room temperature in CH_2Cl_2 . (middle) Solid state vibrational Raman spectra at room temperature of the same compounds together with the hydrogenated precursors of 2 (10a) and 4 (10c) as grey lines. (right) Thermal variation of the $\chi_m T$ product for compounds 1-5 in the heating (dark colors) and cooling scans (light colors). Solid lines are the corresponding fits to the Bleaney-Bowers model.

FT-Raman spectra of the five molecules have been obtained in the state and are shown in Figure 5.7 (center). The Raman spectra of the diradical samples reveal two main groups of bands in the region of the aromatic CC stretching vibrations (i.e., $\nu(\text{CC})$) assignable to vibrational modes placed either in the outer and innermost naphthalenes. According to the correlations (marked by broken lines in Figure 5.7), the bands around 1615 cm^{-1} that undergo small changes in the series can be attributed to $\nu(\text{CC})$ on the external naphthalenes (see assignments in Figures D16-D17). Further corroboration of this

assignment is that the main Raman band in the aromatic precursors **10a** and **10c** (comprised of three independent aromatic naphthalenes) is ca. 1630 cm^{-1} , more similar to the 1615 cm^{-1} above.

The $\nu(\text{CC})$ band of the central diradical-bearing fused naphthalenes is at 1581 cm^{-1} for *linear*-DBFF **2**, 1595 cm^{-1} for *syn*-DBFF **3**, and 1603 cm^{-1} for *anti*-DBFF **4**, which experiences a wavenumber upshift revealing a progressive increase of the aromatization of this moiety in line with the differences of diradical character, y_0 . In fact, the largest change of these values is going from *linear*-DBFF **2** to *syn*-DBFF **3** where the largest change of y_0 is predicted. In TBFF **5**, the molecular symmetry changes and the spectrum is simplified with only one emerging band (composed of several contributions) that can be nicely correlated with the inner naphthalene $\nu(\text{CC})$ band; thus, the higher wavenumber value of this band at 1607 cm^{-1} in TBFF **5** agrees with the largest y_0 .

Figure 5.7 shows the SQUID data from magnetometry experiments as a function of the temperature up to 600-660 K (depending on the sample) for FFs **1-5**. The five compounds show similar behaviors, although with some differences noted below. The $\chi_m T$ product (χ_m is the molar magnetic susceptibility) depicts very low values at low temperatures and a smooth increase as the temperature increases because of thermal population of the $S = 1$ spin state. These measurements, therefore, provide direct evidence of a low spin to high spin thermal transition through a singlet-triplet spin crossover process dictated by a singlet-triplet gap, ΔE_{ST} . As shown in Figure 5.7, the measurements are reversible in a heating-cooling cycle, confirming the robustness of the diradical molecules in the solid state, in agreement with the thermogravimetric measurements (Figures D18-D22). To estimate the singlet-triplet gap, we have fit both the heating and cooling scans to

the classical Bleaney-Bowers $S = \frac{1}{2}$ dimer model.⁴⁷ This model produces a set of ΔE_{ST} values between -7.6 and -9.6 kcal mol⁻¹ (with a value of $g = 2.0$ and paramagnetic contribution attributed to monoradicals smaller than 1%) for the five molecules, in very good one-to-one agreement with the calculated ΔE_{ST} values (Table 5.1) in the studied molecules with some small theory/experiment differences that can be attributed to the estimated error of the experimental values given the low susceptibility values.

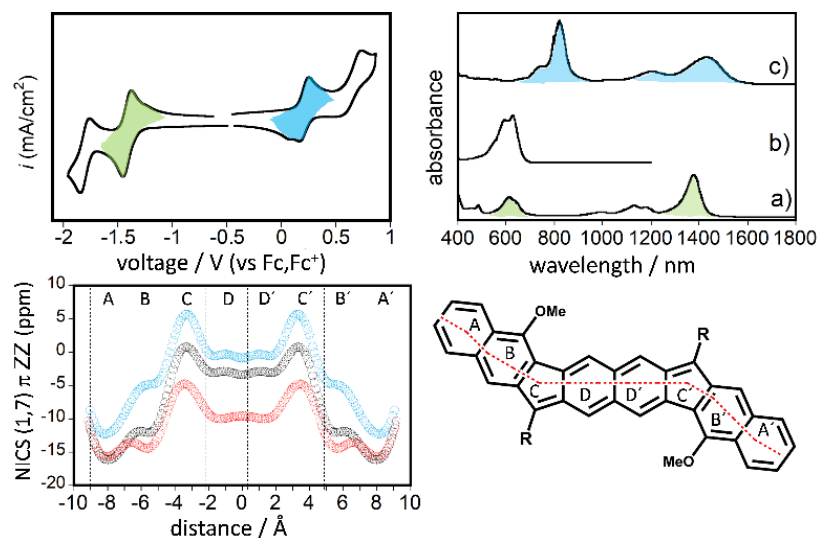


Figure 5.8 (top) Cyclic voltammetry of linear-DBFF 2 recorded in CH₂Cl₂ solution 0.1 M TBAPF₆ at room temperature (blue, first oxidation; and red, first reduction); see SI for detail; and UV-Vis-NIR absorption spectra of linear-DBFF 2 recorded in the above electrochemical conditions during the oxidation and reduction waves on the first oxidation (blue shaded) and reduction (red shaded) processes of linear-DBFF 2. (Bottom) NICS_{πZZ}(1,7) scan values for the neutral, radical anion, and radical cation of linear-DBFF 2' at the tuned-LC-UBLYP/6-311G* level.

The cyclic voltammetry of *linear*-DBFF 2, as an example, is shown in Figure 5.8 and those of the remaining compounds are in Figure D23. These display one-electron quasi-reversible first oxidation and reduction waves, revealing the stability of their radical cations and anions. Second one-electron reductions and oxidations are also observed for the five compounds with varying degree of irreversibility. From the CV data the electrochemical gaps can be deduced, which follow the same trend as the optical gaps for the UV-Vis

absorption spectra (Table D5).

We have also recorded the UV-Vis-NIR absorption spectra of the first produced redox species, radical cations and radical anions upon electrolysis. Figure 5.8 shows these spectra for *linear*-DBFF **2** together with the NICS scan values obtained for its neutral, radical anion and radical cation (see Figure D24 for the theoretical UV-Vis-NIR spectra and Figure D25 for the NICS scan values of the rest of the compounds). The radical cation and anion species are characterized by the presence of two bands each (shaded bands in Figure 5.8 for *linear*-DBFF **2**). The wavelengths of the band maxima are at smaller wavelengths in the anions than in the cations, revealing a larger optical gap in the former.

The evolution of the spectroscopic data can be indirectly interpreted by relation to the trend in the aromatic character as estimated by the NICS among the redox species of *linear*-DBFF **2**. First, we notice that the largest changes of the NICS values take place in the central core between the two five-membered rings (i.e., 5MRs) indicating that the injected charge (either electron or hole) is significantly stabilized by the central DCN core. However, for the radical anions, the NICS values in this DCN molecular fragment become more negative (more aromatic) than in the neutral while in the radical cations, these values become more positive (less aromatic or non-aromatic). From anions to cations, we observe a narrowing of the optical gap which agrees with the destabilization of the central DCN according to the more positive NICS values. In addition, this different behavior upon charging also reveals a rather different electron delocalization scenario in the two distonic radicals (see next section). Regarding the changes in the external naphthalenes, these also modify their electronic structure upon charging, particularly in the cations where their NICS values display larger variations regarding the neutral than these in the anions. This

more marked structure alteration in the external naphthalenes in the cations might highlight a further delocalization of the charge on them, which is not the case of the anions.

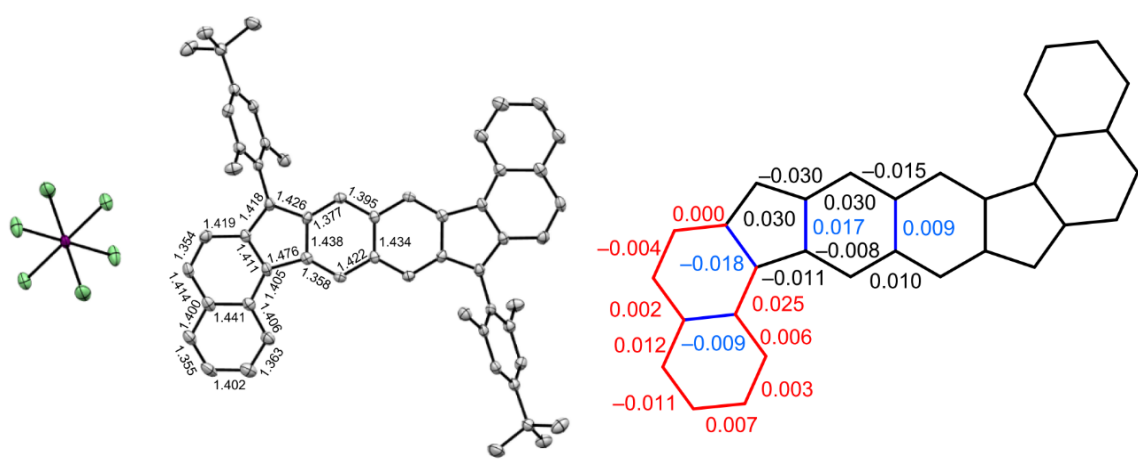


Figure 5.9 (left) Molecular structure from solid state x-ray diffraction data of the radical cation of *syn*-DBFF ($3^{2+} \cdot \text{SbCl}_6^-$) with thermal ellipsoids at 50% probability. Hydrogen atoms, methyl and tert-butyl groups are omitted for clarity. (right) Core CC carbon bond length differences in Å (neutral minus radical cation).

To prove the alteration of the external naphthalenes upon oxidation, the radical cation $3^{2+} \cdot \text{SbCl}_6^-$ was prepared (Scheme D4) chemically by treatment of *syn*-DBFF **3** with “magic blue” ($(p\text{-BrC}_6\text{H}_4)_3\text{N}^+ \cdot \text{SbCl}_6^-$) and characterized by EPR (Figure S26) and UV-Vis-NIR absorption (Figure D27) spectroscopies. Single crystals suitable for x-ray diffraction were obtained and the resultant structure is shown in Figure 9 and Figure S14 along with the differences of the CC bond distances between neutral *syn*-DBFF **3** and its radical cation. The main changes affect those bonds around the apical carbons of the 5MRs with changes of ± 0.030 Å in the CC bonds connecting to the naphthalenes and to the central DCN motif (Figure S28 for the theoretical charge distribution). It is clearly seen that the external naphthalenes are noticeably affected due to the delocalization of the charge on them.

Figure 5.10 collects the spectra of the radical cations and anions of the DBFF and DBDIAn compounds (Figure D29 for additional spectra and processes). Comparing the

same redox species of same isomer in the two series, the wavelengths of the maxima of the lowest energy bands are more red-shifted in the DBIAN analogues^{46,48} due to the main role of the naphthoquinodimethane to anthroquinodimethane substitution. Among the anions and cations of the two series, the red-shift is larger for the cations of the DBFF compounds due to the larger stabilization in these cations by the peripheral naphthalenes than what was observed in the DBDIAn series due to the dominant role of the central core. In Figure 10, the behavior as a function of the diradical character, y_0 , of ΔE_{ST} in the neutral compounds and of the energy of the lowest energy intervalence charge transfer band of the radical

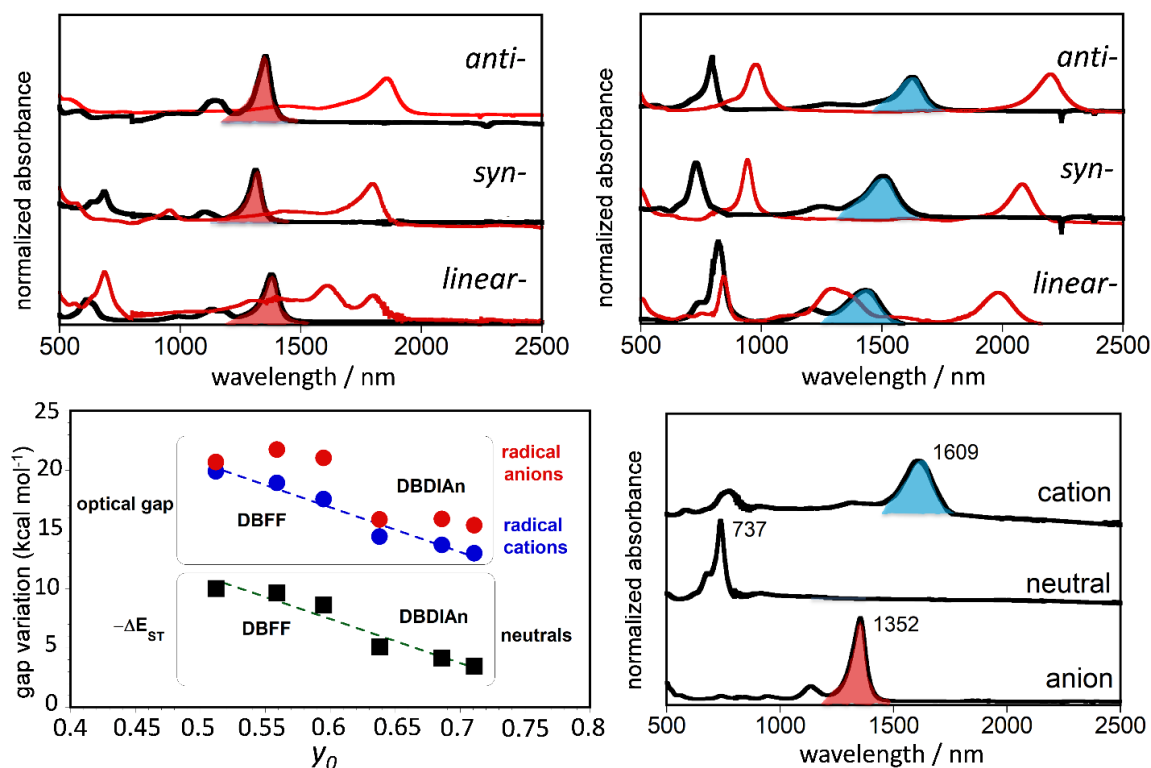


Figure 5.10 (top) UV-Vis-NIR electronic absorption spectra of the radical anions (left) and radical cations (right) of the DBFF series (black lines) and of the DBDIAn series (red lines) recorded electrochemically in CH_2Cl_2 solution 0.1 M TBAPF_6 at room temperature. (bottom left) Representation as a function of the diradical character index of the singlet-triplet gap of the neutrals and of the optical gap in the radical anions and radical cations from the lowest energy absorption band of the UV-Vis-NIR spectra for both series of DBFFs and DBDIAns. Energy values are all in kcal mol^{-1} . (bottom right) UV-Vis-NIR electronic absorption spectra of the radical anion, neutral and radical cation of TBFF 5 generated electrochemically in $\text{CH}_2\text{Cl}_2/0.1 \text{ M TBAPF}_6$ at room temperature.

cations and anions in the two series are compared. Interestingly, the rate of evolution in both series of the two magnitudes for the neutrals diradicals and for radical cations is very similar; thus, it is revealed that changing the geometry of the external naphthalenes marks the evolution of both quantities and that the mechanism producing such changes might be very similar, in both neutrals and cations. Conversely, the evolution of the values in the radical anions is significantly different in line with a different mode of stabilization. The UV-Vis-NIR spectra of the radical cation and anion of TBFF **5** in Figure 5.10 (Figure D29) show that the main features described in its parent compounds are valid. There is an overall red-shift of the TBFF **5** absorption wavelength maxima regarding the DBFF analogs due to the enlargement of the path from naphthalene to phenanthrene also in agreement with the decrease of the ΔE_{ST} magnetic gap upon tetrabenzo-substitution such a discussed in a previous section.

In the framework of the mixed valence theory, these lowest energy lying absorption bands in the monovalent redox states are assigned to the so-called inter-valence charge transfer bands^{49,50} and according to these our radical species can be classified.⁵¹ A complete analysis of the parameters determining the mixed valence behavior of these species is beyond the scope of the present work. It is well known that dications of donor disubstituted π -conjugated oligomers show diradicaloid character and open-shell structure when the conformation or length of the bridge reverts the quinoidal shape typical of these oligomer bipolarons.⁵²⁻⁵⁶ These diradicaloid dications upon one electron reduction develop radical cations which are class II or mixed valent localized species (Figure D30). Conversely, dications with full closed-shell quinoidal structure have associated radical cations with class III delocalized mixed valent character.⁵⁷⁻⁶⁰ Though the DBFF and DBDIAn compounds are

not formally composed by electron donor or electron acceptor groups connected through a conjugated bridge, once singly charged, they can develop the mixed valence function. Considering the medium-large diradical character developed by the neutral DBFF and DBDIAn diradicaloids, the question of whether they develop delocalized or localized monoradicals species is very pertinent. Furthermore, in contrast with conventional donor or acceptor disubstituted dication/dianion diradicaloids, that produced either monoradical cations or anions, but not both, each of our compounds do give way to both redox monovalent species allowing to directly compare them since both are supported by the same skeleton with the same chemical composition.

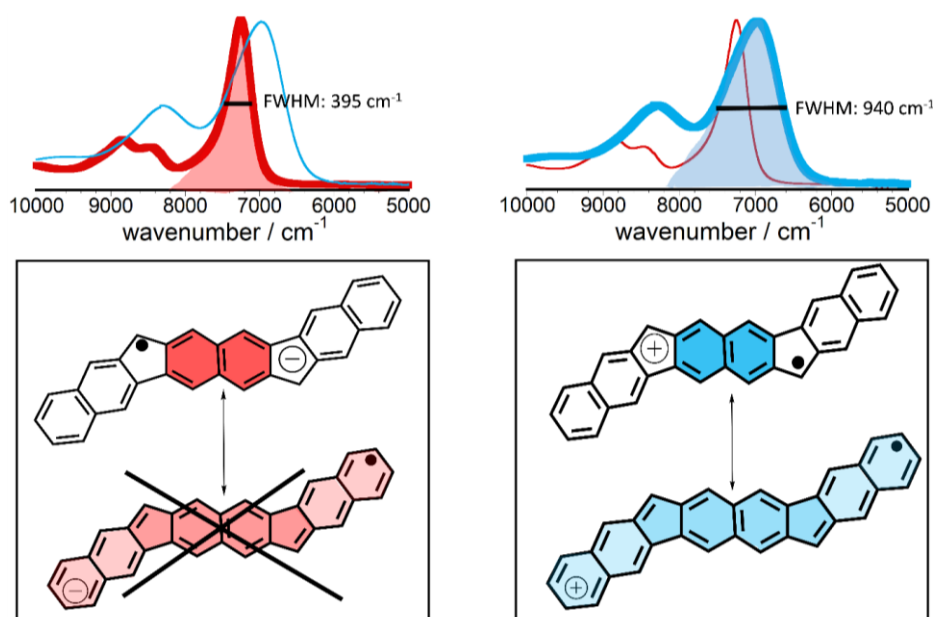


Figure 5.11 (top) Lowest energy absorption bands of linear-DBFF **2** radical cation and anion. FWHM = full width at half maximum. (bottom) Pictorial view of the main structures in the radical anion and cation of linear-DBFF **2** as a representative example.

Quantum chemical calculation of the radical cation and anion of in *linear*-DBFF **2** as isolated entities (Figure D31-D33), with functionals with different HF contents (Figure D34), and with solvent effects, always predict a full delocalized charge symmetrically distributed in the conjugated backbone indicating that, either cation and anions, are class

III delocalized species (see resonance forms in Figure 5.11). The alteration of the CC bond distances in *syn*-DBFF ($3^{+\cdot}\cdot\text{SbCl}_6^-$) from the crystalline structures also agrees with the above assignment. Nonetheless, the above correlation in Figure 5.10 between the y_0 and the optical band gap clearly suggests that cations and anions, in despite of being of the same mixed valence class, behave differently. This distinction between the two redox species is also supported by the shape of their inter-valence CT bands in Figure 5.11: that of the anion being sharp (for instance, in *linear*-DBFF **2**, a FWHM of 395 cm^{-1} is measured) and slightly asymmetric, whereas those of the radical cation appear much broader (for instance, FWHM of 940 cm^{-1} in *linear*-DBFF **2**) and gaussian-like. This significantly different inhomogeneous spectral broadening indicates the different shape of the potential energy surfaces of the ground and excited states in both redox forms. It is possible these originate from different modes of charge stabilization: (i) in the radical anion, there is an exclusive aromatic stabilization/delocalization of the charge in the naphthalene segment between the two 5MRs; however, (ii) in the radical cations, there are additional effects by delocalization onto the peripheral naphthalenes such as schematized in the canonical forms in Figure 5.11. Since aromatization, as the driving force for the stabilization of the anion, mostly occurs in the central DCN core, the external sites play a minor role.

5.3 Conclusions

In conclusion, we have reported the synthesis, characterization, and computational analysis of a new series of diradicaloids related to fluoreno[3,2-*b*]fluorene bearing moderate diradical character. The behavior has been compared with that reported for an analogous series based on anthraquinodimethane with larger diradical character. While the replacement of anthracene by naphthalene accounts for the main change in the electronic

properties, the variation of bond-fusion of the peripheral naphthalenes plays the fine-tuning role required to adjust them. An explanation of the behavior of all the properties has been proposed on the basis of a “physical approach” in which the emerging properties are understood by consideration of two parameters, U and t_{ab} . Attempts to unify the behavior of related series of diradicals in a common footing are scarce and the case here serves as a model to face these valuable comparative studies. Another novelty of this study is the analysis of the redox species generated by reduction and oxidation in the two isomeric series. We have been able to describe all cation and anion redox products as delocalized class III species with two different mechanisms of charge stabilization in the DBFF series in which the radical anions are stabilized by the aromatization of the central core while the radical cations are further stabilized by resonance over the external naphthalenes. Interestingly, the delocalization of the cation radicals over the external rings goes by means of the same mechanism by which the radical centers are extended on these rings in the neutral diradicals. This connects the stability and delocalization modes in diradicals and related radicals revealing rather unknown aspects in this class of polycyclic conjugated compounds.

CHAPTER VI

A TALE OF TWO ISOMERS: ENHANCED ANTIAROMATICITY/DIRADICAL CHARACTER VERSUS DELETERIOUS RING-OPENING OF BENZOFURAN-FUSED *s*-INDACENES AND DICYCLOPENTA[*b,g*]NAPHTHALENES

This chapter includes unpublished material from Barker, J. E.; Price, T. W.; Karas, L. J.; Kishi, R.; MacMillan, S. N.; Zakharov, L. N.; Gómez-García, C. J.; Wu, J. I.; Nakano, M.; Haley, M. M. A Tale of Two Isomers: Enhanced Antiaromaticity/Diradical Character versus Deleterious Ring-Opening of Benzofuran-fused *s*-Indacenes and Dicyclopenta[*b,g*]naphthalenes. *Angew. Chem. Int. Ed.* **2021**, Submitted. This manuscript was written by Joshua E. Barker with assistance from Prof. Michael M. Haley. The project in this chapter was conceived by Joshua E. Barker and Prof. Michael Haley. The experimental work in this chapter was performed by Joshua E. Barker, and Tavis W. Price. The computational work in this chapter was performed by Joshua E. Barker, Lucas J. Karas, and Ryohei Kishi with assistance from Prof. Judy I. Wu and Prof. Masayoshi Nakano.

6.1 Introduction

Heteroatom doping is a useful strategy for adjusting the energetics of conjugated organic molecules. In the field of polycyclic aromatic hydrocarbons (PAHs), fusion of heterocycles or fixation of heteroatoms at key positions through bottom-up synthesis can have a significant effect on electronic properties. This is especially important in the field

of nanographenes where the use of heteroatoms to cause precise defects can increase conductivity.^[1-4] Similarly, heteroatoms can be used to perturb polycyclic antiaromatic hydrocarbons (PAAHs) or quinoidal π -systems and can further decrease the low HOMO-LUMO energy gaps for which these motifs are known. Studies of structure-activity relationships advance this field by building a framework where the properties resulting from inclusion of specific heteroatoms can be predicted and used to fine-tune electrochemical activity,^[4] charge transport,^[2] or stability.^[5-8]

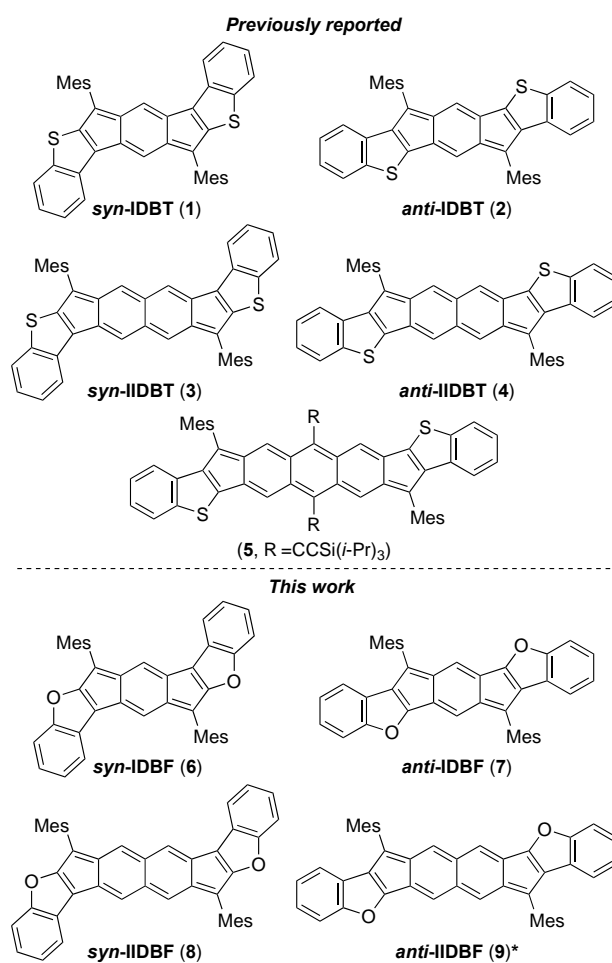


Figure 6.1 Previously synthesized BT-fused PAAHs (1-5) by our group, and the IDBFs (6-7) and IIDBFs (8-9) described in this paper. *As the reader will discover below, compound 9 is not isolable.

Antiaromatic molecules are desirable scaffolds for structure-activity studies

involving variation of heteroatoms or fused heterocycles. PAAHs are defined as having $4n$ π -electrons^[9] and exhibit strong bond-length alternation, paratropicity, and small HOMO-LUMO energy gaps.^[9-11] This latter property makes PAAHs interesting synthetic targets for electronics applications,^[12,13] as recent reports of organic field effect transistors fabricated with PAAHs have shown good hole mobilities ($>1 \text{ cm}^2 \cdot \text{V}^{-1} \cdot \text{s}^{-1}$).^[14-17] A strategy for stabilization of antiaromatic moieties, that also enables greater functionalization within SAR studies, is to fuse aryl groups, specifically heterocycles, to reactive positions of the antiaromatic structure. Examples of this strategy include studies of pentalenes,^[5,18-20] *s*-indacenes,^[21-26] and even the synthesis of planar antiaromatic cyclooctatetraene derivatives.^[7,8] Fusion of thieno-heterocycles have dominated these reports and as a result there has been limited exploration of the effects of changing the heteroatoms in these systems.

Diradical character is a related property found in some PAAHs that is also affected by heteroatom doping or heterocycle fusion.^[27-29] In this context incorporation of heteroatoms can modify the diradical character of these systems, which is described by the diradical index value (y_0)^[30] where $y_0 = 0$ describes a closed shell system, and $y_0 = 1$ describes a purely open shell system. The extent of influence that heteroatoms have on y_0 is visible in changes to the key experimental characteristic of diradical character, which is the singlet-triplet energy gap ΔE_{ST} , resulting from magnetic interactions between the radical centers. The Zheng and Würthner groups each described recently examples of the effects of varying heteroatoms on diradical character of phenoxyl radicals, where inclusion of furan, thiophene, and selenophene heterocycles within the quinoidal backbone yielded decreasing y_0 and increasing ΔE_{ST} , respectively.^[31,32] Beyond this report, studies linking

changes in heteroatoms to changes in diradical character across a common diradicaloid scaffold are rare.

Our group described the synthesis and properties of benzothiophene-fused *s*-indacenes (IDBTs, **1-2**, Figure 6.1)^[21,23] that exhibited strong antiaromaticity comparable with the parent *s*-indacene molecule. Extending the quinoidal conjugation to make benzothiophene-fused dicyclopenta[*b,g*]naphthalenes yields indenoindenodibenzothiophene isomers (IIDBTs, **3-4**),^[33,34] as well as a dicyclopenta[*b,i*]anthracene derivative (**5**).^[35] These π -extended systems show significant diradical character that is dramatically increased relative to their carbocyclic analogues.^[36-38] Alternating the orientation of the fused benzothiophene (e.g., **3** vs. **4**) was also determined to be a strategy by which to fine-tune the effect of the heteroatom by modifying its conjugation in relation to the antiaromatic or diradical motif.^[34]

Considering our results from the incorporation of BT units in the IDBT and IIDBT systems, our interest turned to variations on the heterocyclic moiety. Fusion of benzofuran (BF) with the *s*-indacene or dicyclopenta[*b,g*]naphthalene core would elucidate the effects of switching to a more electronegative heteroatom with stronger π -donation into the antiaromatic core. To provide some direction to our study, NICS-XY scans^[39] were performed on the two possible indacenodibenzofuran (IDBF) isomers, *syn*-IDBF (**6**) and *anti*-IDBF (**7**), where *syn* and *anti* refer to the relationship of the heteroatom to the apical carbon of the five-membered ring. Comparison of the resulting plots with those of *s*-indacene and the IDBTs (Figure 6.2) showed that *syn*-fusion of BF increased the paratropicity of the core over 5 ppm beyond that of *s*-indacene. Fusion of the BF in the *anti*-orientation led to similar paratropicity relative to *anti*-IDBT. Assuming the same trend

would translate to the relationship between the IIBDTs and indenoindenodibenzo-furans (IIBDFs), it could also lead to increased diradical character in these π -extended derivatives due to the diradical structure relieving the increased antiaromaticity.^[29] Inspired by the computational results, we undertook the synthesis and characterization of the IDBF and IIBDF isomers reported below.

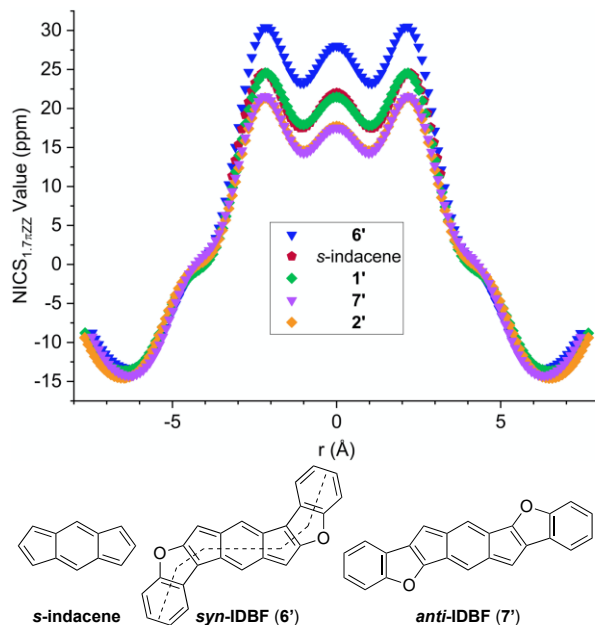
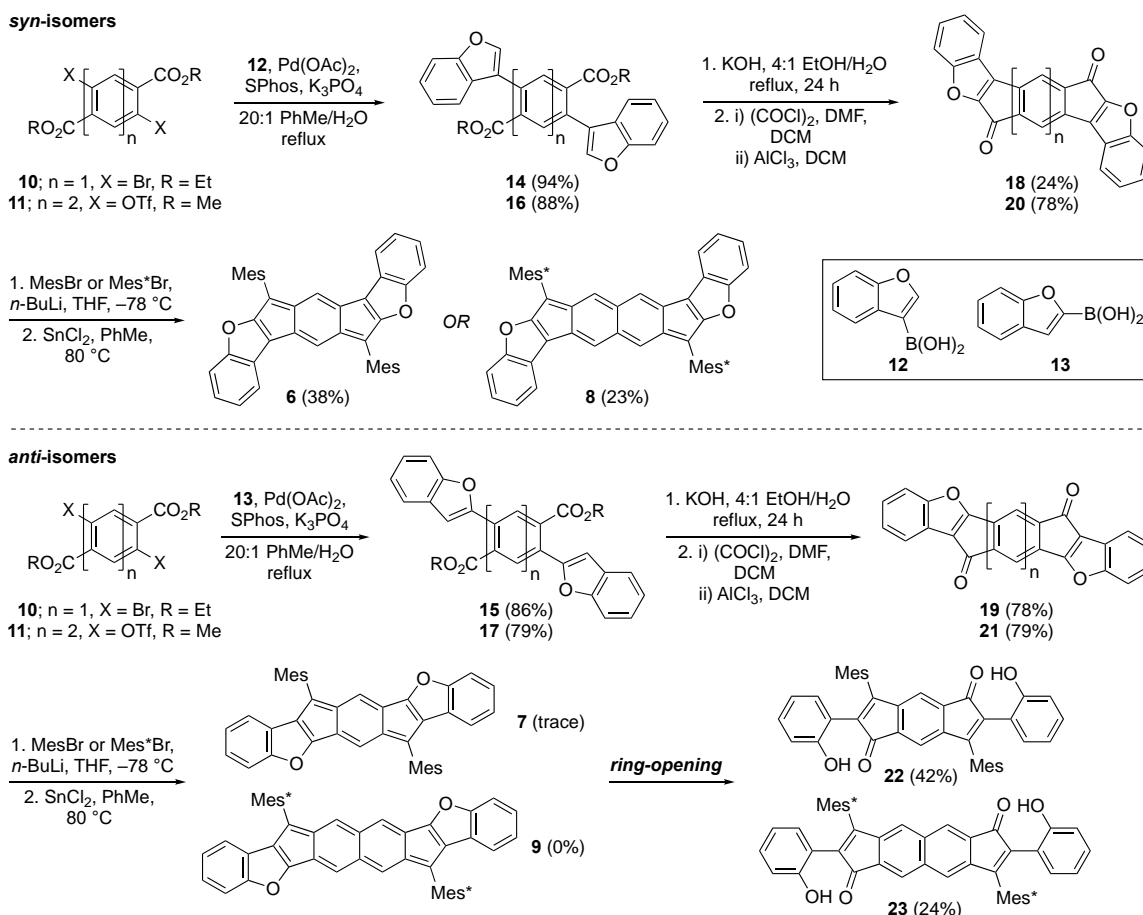


Figure 6.2 NICS-XY scans of *s*-indacene, IDBFs 6'-7', and the IDBT analogues 1'-2'. Dashed lines represent the path of the ghost atoms used in the NICS calculations. Computations were performed without bulky mesityl groups to reduce cost. Legend is ordered from most paratropic to least paratropic.

6.2 Results and Discussion

The syntheses of the IDBFs and IIBDFs begin from dibromoterephthalate **10** and bistriflate **11**,^[40] respectively (Scheme 6.1). Suzuki cross-coupling with either 3-benzofuran-boronic acid (**12**) or 2-benzofuranboronic acid (**13**) yielded diesters **14-17**. These were saponified and subjected to Friedel-Crafts acylation conditions to make diketones **18-21** in modest to very good yields. IDBF precursors **18** and **19** were treated with mesityllithium to install mesityl groups as kinetic protecting groups for the final

IDBFs (**6** and **7**). Reaction of the addition products with SnCl₂ in a reductive dearomatization successfully yielded **6** as a dark blue solid whereas **7** was isolated only in trace amounts as it instead underwent ring-opening of the furans to form phenol-substituted diketone **22**. Another fraction of **22** was separated from the reaction mixture as the major product (42%). Repeated attempts to synthesize pure **7** were unsuccessful under basic and acidic conditions despite use of rigorously dried solvents and careful purification (see Supporting Information).



Scheme 6.1 Synthesis of syn-IDBF (**6**) and syn-IIDBF (**8**) as well as the ring-opened products **22-23** derived from anti-IDBF (**7**) and anti-IIDBF (**9**), respectively.

To prepare the IIDBFs, 2-bromo-5-tert-butyl-1,3-dimethylbenzene (Mes*) was treated with *n*-butyllithium to generate the aryl lithiate that was added to diketones **20** and

21. We found that use of this substituent in the IIDBTs greatly improved their solubility compared to their poorly soluble mesityl-substituted analogues. Reductive dearomatization of the addition product of **19** and **21** yielded syn-IIDBF (**8**) in 23% yield as a deep teal solid. Unfortunately, the dearomatization to create anti-IIDBF (**9**) failed to yield the desired product; rather, in similar fashion to the dearomatization of **7**, diketone **23** was isolated as the sole product. A plausible mechanism for the ring-opening of the anti-isomers is shown Scheme E2: coordination of the Lewis acidic SnCl₂ to the hydroxyl groups activates it to leave, followed by a traditional hydrolysis of an oxocarbenium ion, leads to cleavage of the furan rings. While a somewhat disappointing result, importantly we see no evidence of this pathway in the syn-isomers, which are predicted to be the more interesting molecules of the series (vide supra).

Within the heterocycle-fused s-indacenes the proton located on the central benzenoid ring provides a convenient reporter by which to evaluate the antiaromaticity of the s-indacene core. As the antiaromaticity increases or decreases this proton would be expected to shift upfield or downfield, respectively. By this reasoning, the resonance associated with this proton in **6** should be observed upfield of its position in the IDBTs. Indeed, upon comparison of the ¹H spectra of **1** and **2** to that of **6** (Figure 6.3) we observed that the proton assigned to the core of the molecule was shifted significantly upfield (5.60 ppm) from **1** (6.06 ppm) and **2** (6.08 ppm). A spectrum of a crude sample of **7** also revealed decreased antiaromaticity based on a downfield shift of the core proton (6.14 ppm). The singlets assigned to the core protons in **3**, **4**, and **8** show similar variance (Figure E3) with those of **8** being found farther upfield by 0.13–0.33 ppm relative to those of **3** and **4**. All results match well with the NICS-XY calculations, confirming that there is much stronger

paratropicity in the core of **6** than in **1**, **2**, or **7**. It is worth noting that the core protons could experience a shielding effect from the orthogonal mesityl group. Since this substituent is common to all derivatives, however, the same effect should be present in all derivatives; therefore, it is reasonable to attribute the change in chemical shift of the ^1H resonance solely to the changing antiaromaticity of the core π -system.

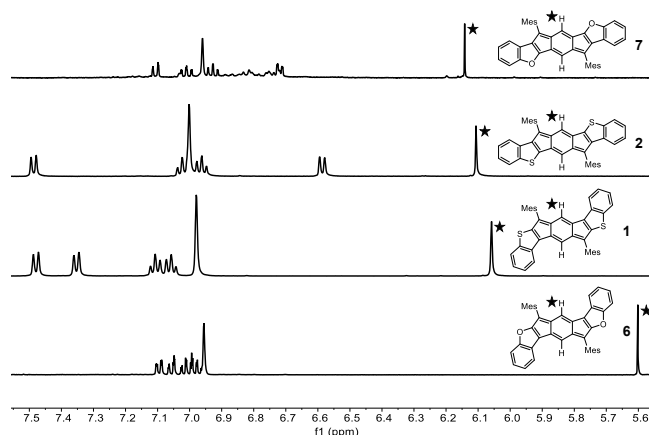


Figure 6.3 Partial ^1H NMR spectra (500 MHz, CD_2Cl_2 , 25 $^\circ\text{C}$) of compounds **1**, **2**, **6**, and **7**, which illustrate the shifting of the core ^1H resonance as the antiaromaticity of the core *s*-indacene unit changes. Spectra are ordered by increasing paratropicity.

Intrigued by the significant increase in antiaromaticity in the *syn*-fused BF compounds, natural bond orbital (NBO) computations were performed to provide a theoretical explanation. As recently described in the report of sulfone-functionalized IDBTs,^[26] stronger antiaromaticity of *syn*- vs. *anti*- fused derivatives can arise due to a “Clar sextet-effect,” which can be seen through natural resonance theory (NRT) analyses of the isoelectronic hydrocarbon dianion analogues of the IDBTs/IDBFs.^[26] Based on NRT analyses, the dominant resonance structure of the *syn*-dianion (Figure 6.4a) possesses a quinoidal core with no Clar sextets. In contrast, the dominant resonance form of the *anti*-dianion (Figure 6.4b) exhibits two Clar sextets in the terminal benzenoid rings, and this feature of the π -system weakens antiaromatic character. Importantly, placements of

heteroatoms can direct the annelation pattern of PAAHs, and in this way, modulate antiaromaticity.

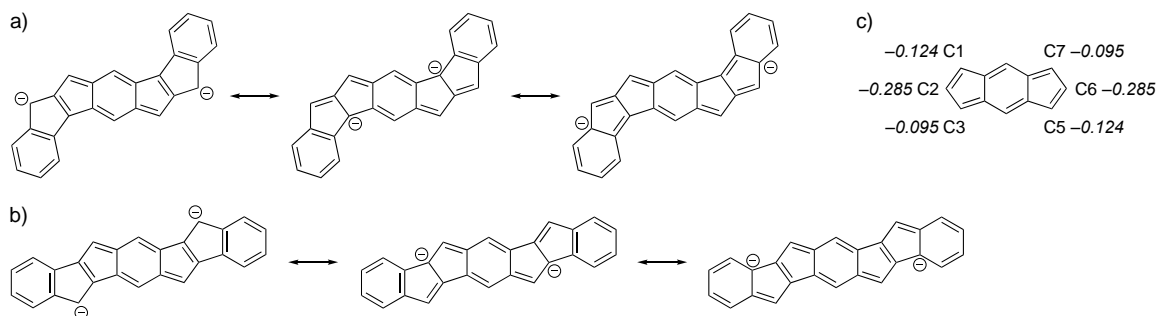


Figure 6.4 Resonance structures of the hydrocarbon dianion analogues of a) *syn*-IDBF and b) *anti*-IDBF. Boxed structures indicate the dominant resonance form identified by NRT calculations. c) Computed NPA charges of the *s*-indacene core.

Comparing *syn*-IDBF to *syn*-IDBT, stronger antiaromaticity of the BF-fused derivative can be explained by differences in the negative charge stabilizing ability of O vs. S atoms. Computed natural population analysis (NPA) charges for the *s*-indacene core (Figure 4c) show pronounced partial negative charges at carbons 2 and 6, which are stabilized more so by *syn*-fused S atoms than by *syn*-fused O atoms at these positions, due to the greater negative charge stabilizing ability of sulfur. For this reason, *syn*-IDBT has a more stabilized *s*-indacene core, larger HOMO-LUMO gap, and weaker paratropicity compared to the *syn*-IDBF. This charge-effect is similar to the topological charge stabilization rule proposed by Gimarc,^[41] which describes how variation of the location of heteroatoms in π -systems can affect the stabilities of isomers.

To characterize the molecular structures of **6** and **8**, single crystals suitable for x-ray diffraction were grown from mixtures of CHCl_3 and CH_3CN either by slow evaporation (10:1 $\text{CHCl}_3/\text{CH}_3\text{CN}$) or by layering the latter over the former (1:3 $\text{CHCl}_3/\text{CH}_3\text{CN}$) and allowing them to slowly diffuse together at $-40\text{ }^\circ\text{C}$. Gratifyingly, despite the difficulty in its isolation/purification, a single crystal of **7** was obtained from a crude mixture by the

layering procedure described above and its structure secured. Finally, x-ray structures of diketones **22** and **23** were obtained to fully characterize these unexpected side products (Figures E7-E8). The experimental and calculated bond lengths of **6**, **7**, and **8** (Figure 6.5) show good agreement. IDBF **6** adopts a herringbone packing motif, while **7** packs in a 3D chain with a distance between the average planes of 3.55 Å. IIDBF **8** on the other hand packs as isolated molecules with no close contacts due to the presence of solvent molecules and the orientation of the bulky Mes* groups. The bond length alternation of the conjugated core of **6** and **7** is comparable to their IDBT analogues and is consistent with a quinoidal/antiaromatic *s*-indacene motif. Interestingly though, within the BF series, the short bonds are shorter and the long bonds are longer in *syn*-**6** versus *anti*-**7** compared to the structural differences in the BT isomers. On the other hand, **8** shows a different bond length alternation pattern indicative of its strong diradical character. Most notable is the bond length between the naphthalene core and the apical carbon of the five-membered ring which is elongated (1.443 Å) as would be expected if this molecule exists as an open-shell singlet diradical (Figure 6.6a). In addition to this, the central naphthalene core shows bond-length alternation consistent with a fully aromatized naphthalene unit, supporting the existence of this molecule as a diradical.

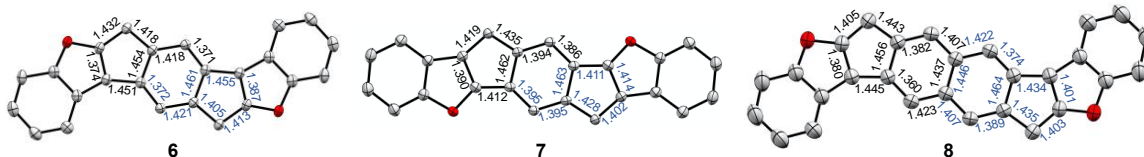


Figure 6.5 X-ray crystal structures of IDBFs **6** and **7**, and *syn*-IIDBF **8**. Bond lengths from the crystal structures are in black and bond lengths from the calculated structures are in blue. Ellipsoids were drawn at 50% probability. Hydrogens and mesityl groups are omitted for clarity.

Figure 6.6a shows simplified representations of the possible electronic structures of *syn*-IIDBT **8**. Considering the pronounced diradical character of the IIDBTs, we expected that

8 should also possess measurable diradical character. In the related IIDBTs, *syn*-fusion of the BT units leads to cross-conjugation between the sulfur atoms and the radical centers (Figure 6.6b) but allows greater delocalization of spin onto the outer benzene rings of the BT.^[34] In contrast to this, *anti*-fusion yields linear conjugation of the radicals with the sulfur atoms (Figure 6.6b) that prevents delocalization of spin density and leads to repulsive interactions between the sulfur and the radical center. Calculations of diradical character (y_0) and singlet-triplet energy gap (ΔE_{ST}) were in agreement with these

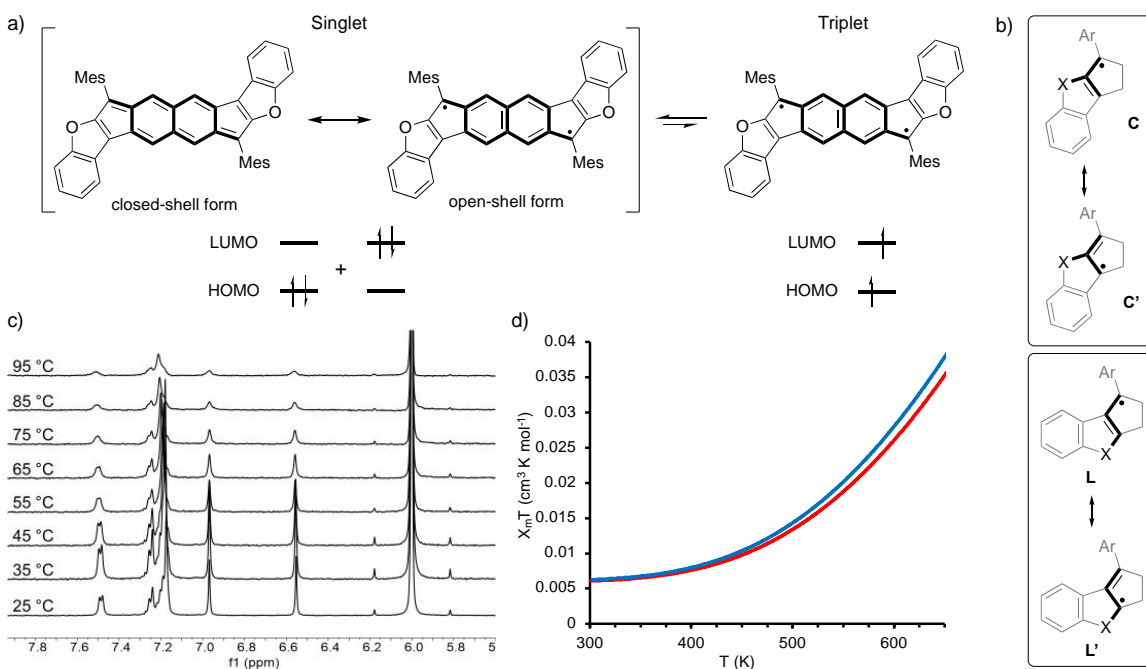


Figure 6.6 a) Resonance structures and orbital representations of the closed-shell singlet state (left), open-shell diradical singlet state (middle), and open-shell diradical triplet state (right); all canonical forms possess 2,6-naphtho conjugation (bold bonds). b) Cross conjugation (**C** and **C'**, top) vs. linear conjugation (**L** and **L'**, bottom) orientation of the heteroatom where delocalization of the radical centers to the lower carbon atom disrupts heterocycle aromaticity; X = S or O. c) VT-NMR spectra of **8** in 1,1,2,2-tetrachloroethane-*d*₂; d) SQUID magnetometry plot of **8**; lines (red – heating, blue – cooling) represent the Bleaney-Blowers fit to the data.

descriptions and indicated that *syn*-fusion in **3** led to increased y_0 and decreased ΔE_{ST} relative to **4**. We expected to see similar results from the IIDBFs with the increased

paratropicity of *syn*-IIDBF **8** contributing to an increase in y_0 and decrease of ΔE_{ST} due to relief of antiaromaticity afforded in the diradical structure (Figure 6.6a).

Table 6.1 Theoretically estimated y and ΔE_{ST} values together with the main physical parameters. [a] Geometry optimization for the singlet/triplet states and frequency analyses were performed at the R- and UB3LYP/6-311G* levels, respectively. [b] Calculated at the PUHF/ 6-311G*. [c] Adiabatic ΔE_{ST} value calculated at the spin-flip non-collinear (SF-NC)-TDDFT PBE5050/6-311G* level along with R- or UB3LYP/6-311G* zero-point vibrational energy correction for each spin state. [d] Estimated at the CASCI(2,2)/6-311G* level using the (tuned-)LC-RBLYP MOs (denoted as tuned-LC-RBLYP-CASCI(2,2)/6-311G*). Additional details are given in the Supporting Information.

cmpd	$y^{[a,b]}$	$\Delta E_{ST}^{[a,c]}$ (kcal mol ⁻¹)	$U/2^{[a,d]}$ (eV)	$It_{ab}^{[a,d]}$ (eV)	$2K_{ab}^{[a,d]}$ (eV)
<i>syn</i> -IIDBT 3	0.658	-8.06	1.404	0.905	0.130
<i>anti</i> -IIDBT 4	0.613	-8.77	1.563	1.031	0.165
<i>syn</i> -IIDBF 8	0.682	-7.68	1.380	0.865	0.133
<i>anti</i> -IIDBF 9	0.623	-9.10	1.677	1.058	0.151

Using the two-electron diradical model, analogous to our prior studies,^[33-36] the quantum chemical calculations shown in Tables 6.1 and E3 support our hypothesis. Admittedly, the variation in y_0 (0.682 for **8** vs. 0.658 for **3**, 0.623 for **9** vs. 0.613 for **4**) is quite small and susceptible to the calculation conditions. More important are the differences in ΔE_{ST} , numbers that are measurable. Whereas the calculated singlet-triplet energy gap for *syn*-IIDBF has slightly decreased (-7.68 for **8** vs. -8.06 kcal mol⁻¹ for **3**), the reverse holds true for the *anti* isomer (-9.10 for **9** vs. -8.77 kcal mol⁻¹ for **4**). Comparison of the values between *anti*-IIDBF and *anti*-IIDBT suggest that the larger singlet-triplet energy gap of **9** could be because of its larger U term than in *anti*-IIDBT **4**, whereas in **8** the U term is smaller than in *syn*-IIDBT **3**. Because ΔE_{ST} is expressed by

$f(y)U/2 + 2K_{ab}$, even though y values are similar in both systems, the difference of U should determine the difference in and the order of ΔE_{ST} . We believe this variation again is due to the fusion mode of the heterocycle. *syn*-Fusion of the BF motifs, while only cross-conjugated between the more electronegative oxygen atoms and the radical centers (Figure 6.6b), provides even greater delocalization of spin onto the outer benzene ring of the BF (Figure E12), thus lowering ΔE_{ST} . Conversely, *anti*-fusion and the resultant linear conjugation of the radicals with the greater electron donating oxygen atoms (Figure 6.6b) results in even stronger repulsive interactions between the oxygen and the radical center, increasing ΔE_{ST} in **9**.

Experimental verification of these properties was obtained through two types of magnetic measurements. A variable temperature NMR (VT-NMR, Figure 6.6c) experiment of **8** provided qualitative information about the transition from the diamagnetic singlet state to the paramagnetic triplet state. Considering the ΔE_{ST} of *syn*-IIDBF was predicted to be lower than that of *syn*-IIDBT, triplet population should be seen at a lower temperature. Heating a sample of **8** in 1,1,2,2-tetrachloroethane- d_2 revealed significant broadening of the proton signals beginning at 55 °C which is ~20 °C lower than the onset of thermal broadening in *syn*-IIDBT. With this initial confirmation of the lower ΔE_{ST} of **8**, a quantitative measurement was performed in the form of superconducting quantum interference device magnetometry (SQUID, Figure 6.6d). According to TGA (Figure E1), the sample was stable at elevated temperatures, so the magnetic properties of **8** were measured by SQUID up to ~650 K. Data was collected both during heating and cooling to provide an additional test for compound stability. The SQUID signal was then fit to the Bleaney–Bowers equation to yield the experimental ΔE_{ST} . The average of the heating and

cooling data yielded a singlet-triplet energy gap of $-6.0 \text{ kcal mol}^{-1}$ which is lower than the experimental value of $-6.8 \text{ kcal mol}^{-1}$ for *syn*-IIDBT. These measurements illustrate that altering the heteroatom is a viable method for tuning the singlet-triplet energy gap in the DCN diradicaloid core.

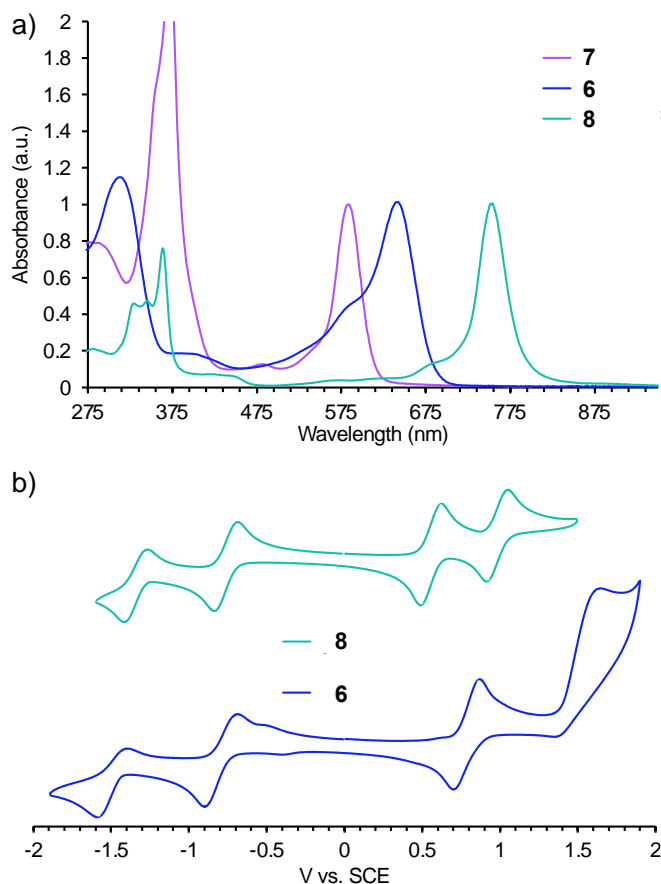


Figure 6.7 a) Electronic absorption spectra of the IDBFs (6-7) and *syn*-IIDBF (8); b) Cyclic voltammograms of *syn*-IDBF (6) and *syn*-IIDBF (8).

Figure 6.7a shows the electronic absorption spectra of the IDBFs and *syn*-IIDBF and the absorbance maxima are listed in Table 6.2. These compounds all exhibit similar UV-Vis absorption spectra to the IDBTs and IIDBTs with a major absorbance in the ~ 300 – 400 nm range and a broad low-energy absorbance feature. Compared with the IDBTs, the low-energy absorbance of **6** is red-shifted (642 nm) whereas that of **7** is blue-shifted (584 nm), which is in agreement with the expected trends in HOMO-LUMO energy gap based

on computed values as well as the predicted changes in antiaromaticity. Similarly, the low-energy absorbance of **8** is also slightly red shifted (753 nm) from that of *syn*-IIDBT (748 nm). According to TD-DFT calculations (Table E2) the primary transition responsible for the low-energy absorbance is the HOMO-1→LUMO transition, which is commonly seen in the heterocycle-fused *s*-indacenes. TD-DFT calculations also reproduce the shift in absorbance between the BF-fused derivatives with respect to the BT-fused systems. As is generally the case in singlet-diradical compounds, **8** also presents a broad but weak absorption in the ~900 nm range attributed to the low-lying doubly excited electronic configuration (Figure 6.6a, middle) giving further evidence of its strong diradical character.

Table 6.2 Cyclic voltammetry and absorbance data for IDBTs (**1-2**), IDBFs (**6-7**), *syn*-IIDBT **3**, and *syn*-IIDBF **8**^a. [a] CVs were recorded at a scan rate of 50 mV s⁻¹ with a glassy carbon working electrode, Pt coil counter electrode, and Ag wire pseudoreference. All data were collected in degassed CH₂Cl₂, and ferrocene was used as an internal reference. Potentials were referenced to the SCE by using the Fc/Fc⁺ half-wave potential (Fc/Fc⁺ = 0.46 V vs. SCE).

cmpd	$E_{\text{red}2}$ (V)	$E_{\text{red}1}$ (V)	$E_{\text{ox}1}$ (V)	$E_{\text{ox}2}$ (V)	HOMO (eV)	LUMO (eV)	E_{gap} (eV)	λ_{max} (nm)
<i>syn</i> - IDBT (1)	-1.37	-0.75	0.86	1.57	-5.54	-3.93	1.61	632
<i>anti</i> - IDBT (2)	-1.72	-0.87	0.84	1.32	-5.52	-3.81	1.71	624
<i>syn</i> - IDBF (6)	-1.40	-0.71	0.87	1.73	-5.55	-3.97	1.58	642
<i>anti</i> - IDBF (7)	—	—	—	—	—	—	—	584
<i>syn</i> - IIDBT (3)	-1.23	-0.67	0.66	1.09	-5.34	-4.01	1.33	748
<i>syn</i> - IIDBF (8)	-1.25	-0.67	0.64	1.14	-5.32	-4.01	1.32	753

The electrochemical properties of **6** and **8** were investigated by cyclic voltammetry. Unfortunately, as stated above, **7** was only isolable in trace-crude amounts that precluded its analysis by this technique. Both *syn*-isomers show two oxidations and two reductions (Figure 6.7b and Table 6.2). In the case of **6**, the first oxidation and reduction events are reversible, while the second oxidation is irreversible, and the second reduction is pseudo-reversible. For **8** all oxidations and reductions are reversible which is comparable to the analogous *syn*-IIDBT. The HOMO-LUMO energy gap in both **6** (1.58 eV) and **8** (1.32 eV) is narrowed only slightly compared with the sulfur-containing analogues (1.61 eV for **1** and 1.33 eV for **3**). While narrowed HOMO-LUMO energy gaps are generally correlated with increasing antiaromaticity, across a series of analogous molecules, the change in these derivatives appears to be only incremental. Notably in both BT-fused and BF-fused systems, the HOMO and LUMO levels are essentially the same between each pair of analogous compounds. In fact, between *syn*-IIDBT **3** and *syn*-IIDBF **8**, all reductions and oxidations are within 0.05 eV of one another. The separation is almost as close between *syn*-IDBT **1**, and *syn*-IIDBF **6** (0.01–0.04 V) with the exception that the second reduction (1.57 V vs. SCE for **1** and 1.73 V vs. SCE for **6**) is not as close.

6.3 Conclusion

As shown by spectroscopic and computational analysis we have tuned the antiaromaticity of the *s*-indacene core through changing the heteroatom in fused heterocycles from sulfur to oxygen. This small structural change yielded a fine-tuning of experimental properties as shown by a slightly lower electrochemical HOMO-LUMO energy gap, red-shifted absorbances, and upfield-shifted core proton NMR resonances. Computational analysis through NICS-XY scans corroborated the high antiaromaticity of

this scaffold. NBO calculations showed that a “Clar-sextet” effect causes the difference in antiaromaticity between *syn*-BT/BF-fused and *anti*-BT/BF-fused isomers, while NPA charges indicated that a charge-stabilization effect is responsible for the increased antiaromaticity of *syn*-IDBF relative to *syn*-IDBT. Synthesis of *anti*-IDBF was only possible in trace amounts; however, some comparison of isomers was possible through NMR spectrometry, UV-Vis spectroscopy, and the solid-state X-ray crystal structures.

Additionally, we were able to synthesize *syn*-IIDBF which is a new singlet-diradicaloid similar to the IIDBTs we have recently reported. *syn*-IIDBF possesses a significantly lowered singlet-triplet energy gap relative to the IIDBTs and shows that it is possible to further tune this property of diradicaloids through heteroatom doping. Indeed, the temperature range of the singlet-triplet transition for *syn*-IIDBF is approaching a range that would be usable in practical applications, indicating that further heteroatom doping studies should be performed with this scaffold to further tune the ΔE_{ST} property. Unfortunately, in similar fashion to *anti*-IDBF, attempts to synthesize *anti*-IIDBF resulted in a ring-opened diketone product; nonetheless, computations suggested the *syn*-IDBF/IIDBF isomers were more fundamentally interesting molecules, which was verified experimentally.

In summary, we have shown how variation of the heteroatom in heteroatom-doped antiaromatic molecules can be used to fine-tune their properties. The use of NBO and NPA charge calculations could be applied to similar scaffolds along with our synthetic strategy to identify key positions where heterocycle fusion can cause similar effects. Efforts are underway in our group to follow this strategy and expand the family of heterocycle-fused *s*-indacenes and dicyclopenta[*b,g*]naphthalenes to push the extremes of antiaromaticity and diradical character within these scaffolds.

APPENDIX A

SUPPLEMENTARY INFORMATION FOR CHAPTER II

Appendix A is the supplementary information for Chapter II of this dissertation. It includes experimental details, other experimental data, spectra, and computational details relevant to the content in Chapter II.

Experimental Details

General. ^1H and ^{13}C NMR spectra were recorded in CDCl_3 at room temperature using either a Bruker Avance III HD 500 equipped with a Prodigy multinuclear cryoprobe (^1H : 500 MHz, ^{13}C : 126 MHz) or Bruker Avance III HD 600 MHz (^1H : 600.02 MHz, ^{13}C : 150.89 MHz) NMR spectrometer with Prodigy multinuclear broadband cryoprobe. Chemical shifts (δ) are expressed in ppm relative to the residual non-deuterated solvent (CDCl_3 , ^1H : 7.26 ppm, ^{13}C : 77.16 ppm). UV-Vis spectra were recorded on an HP 8453 UV-Vis spectrometer. THF and toluene were distilled from Na/benzophenone ketyl under nitrogen prior to use. Compounds **9**¹ and **12**² were prepared according to literature procedures. Unless stated otherwise, all solvents and reagents were used as received.

Diphenyl diester 10. Phenylboronic acid (270.7 mg, 2.22 mmol), ditriflate **9** (200 mg, 0.370 mmol), and K_3PO_4 (235.6 mg, 1.11 mmol) were dissolved in dry toluene (25 mL) and the mixture was sparged with N_2 for 1 h. $\text{Pd}(\text{OAc})_2$ (3.3 mg, 0.0148 mmol) and SPhos (12.2 mg, 0.0296 mmol) were then added. After sparging for an additional 20 min

the reaction mixture was heated to reflux overnight. After cooling, the mixture was quenched with H₂O and extracted with Et₂O. The organic layer was washed with water and brine solution, and then dried (MgSO₄). The crude reaction mixture was purified via column chromatography on SiO₂ (3:2 hexanes:EtOAc) to yield **10** (123 g, 84 %) as an off-white solid. ¹H NMR (600 MHz, CDCl₃) δ 8.38 (s, 2H), 7.92 (s, 2H), 7.48–7.39 (m, 10H), 3.71 (s, 6H). ¹³C NMR (126 MHz, CDCl₃) δ 168.90, 140.98, 139.70, 132.60, 131.62, 130.67, 130.31, 128.58, 128.34, 52.38. HRMS (ESI) for C₂₆H₂₀O₄ [M+H]⁺: calcd 397.1440, found 397.1448.

Dione 11. A mixture of diester **10** (400 mg, 1.01 mmol), EtOH (96 mL), H₂O (24 mL), and KOH (906 mg) was refluxed overnight. The reaction was concentrated to remove the EtOH and the resulting aqueous mixture was acidified carefully by dropwise addition of concentrated HCl solution. The resulting precipitate was collected, washed with H₂O, and then dried in an oven to give the diacid as a beige solid. The diacid was then stirred in concentrated H₂SO₄ overnight. The reaction mixture was poured over ice and stirred for 5 min. The product was filtered and washed with H₂O, hexanes, and acetone to yield dione **11** (251 mg, 86%) as a bright red solid. Due to very poor solubility, NMR data for **11** could not be obtained. HRMS (EI+) for C₂₄H₁₄O₂ [M]⁺: calcd 332.0837, found 332.0825.

Fluoreno[3,2-*b*]fluorene 2. An oven dried flask containing THF (15 mL) and mesityl bromide (0.127 mL, 0.831 mmol) was cooled to –78 °C and then *n*-BuLi (0.312 mL, 2.5 M solution, 0.779 mmol) was added slowly. The reaction was stirred for 30 min and then added slowly to a THF solution of dione **11** (59 mg, 0.104 mmol) under N₂ at –78 °C. After warming the solution to room temperature overnight, the reaction was

quenched with saturated NH_4Cl solution, and extracted with CH_2Cl_2 . The organic phase was washed with water and then brine solution. The organic layer was dried (MgSO_4) and the volatiles removed to give a crude yellow solid that was used without further purification.

Under N_2 the crude diol (~50 mg, ~0.174 mmol) and SnCl_2 (185 mg, 0.699 mmol) were dissolved in toluene (20 mL). Immediately 10 drops of trifluoroacetic acid (TFA) were added and the solution became a deep blue color. Upon completion (ca. 2-4 h), the mixture was passed through a SiO_2 plug eluting with 1:1 hexanes: CH_2Cl_2 . The solution was concentrated to dryness then dissolved in minimal CH_2Cl_2 and layered with CH_3CN and cooled in the freezer. The precipitated product was filtered to yield **2** (17 mg, 30%) as a dark blue-purple solid. ^1H NMR (500 MHz, CDCl_3) δ 7.56 (d, $J = 6.8$ Hz, 2H), 7.38 (s, 2H), 7.13–7.09 (m, 2H), 7.09–7.06 (m, 2H), 7.02 (s, 4H), 6.95 (s, 2H), 6.86 (d, $J = 7.0$ Hz, 2H), 2.39 (s, 6H), 2.12 (s, 12H). ^{13}C NMR (151 MHz, CDCl_3) δ 143.97, 137.64, 137.41, 137.40, 137.00, 134.90, 131.69, 130.42, 128.37, 128.08, 127.64, 126.70, 124.92, 122.08, 120.76, 21.35, 20.46. UV-Vis (CH_2Cl_2) λ_{max} (ϵ) 342 (20,860), 561 sh (8820), 600 (11,640) nm. HRMS (EI+) for $\text{C}_{42}\text{H}_{34} [\text{M}]^+$: calcd 538.2661, found 538.2677. Note: the poor solubility of **2** hindered the acquisition of good NMR spectra, as the poor solubility has the side effect of greatly exaggerating impurities present in the CDCl_3 of H-grease impurities present in the samples from our Schlenk line.

Diphenyl 13. To a mixture of phenylboronic acid (6.01 g, 44.3 mmol), dibromide **12**² (5.00 g, 15.9 mmol), $\text{Pd}(\text{dppf})\text{Cl}_2$ (229 mg, 0.39 mmol), and K_2CO_3 (6.02 g, 60.8 mmol) in a 350 mL heavy-walled flask was added dry toluene (60 mL). After degassing the mixture with N_2 for 30 min, the reaction was sealed and heated to reflux overnight.

After cooling to r.t. the reaction was filtered to remove solid impurities and the filter cake was washed with CH₂Cl₂. The filtrate was concentrated under reduced pressure and recrystallized from toluene to yield **13** (3.12 g, 63%) as fine white needles. ¹H NMR (600 MHz, CDCl₃) δ 7.52 (t, *J* = 7.4 Hz, 4H), 7.45 (t, *J* = 7.4 Hz, 2H), 7.35 (d, *J* = 8.6 Hz, 2H), 7.32–7.30 (m, 4H), 7.27 (d, *J* = 8.6 Hz, 2H), 2.20 (s, 6H). ¹³C NMR (151 MHz, CDCl₃) δ 140.24, 138.11, 132.12, 131.51, 130.33, 128.60, 128.52, 127.08, 125.60, 20.73. HRMS (ESI) for C₂₄H₂₀ [M+H]⁺: calcd 309.1643, found 309.1647.

Dione 14. Diphenyl **13** (0.503 g, 1.6 mmol), KOH (0.972 g, 17.3 mmol), and pyridine (15 mL) were heated to reflux. Once the mixture was at reflux, KMnO₄ (3 g, 19 mmol) and water (8.7 mL) were added portionwise over 4 h. After refluxing overnight, the reaction mixture was cooled and then filtered through a celite plug with a hot solution of 10% aqueous KOH. The filtrate was acidified with concentrated HCl upon which a precipitate formed. Filtration yielded the mono-acid side product as an off-white solid. Further acidification of this filtrate yielded the crude diacid as a white flaky solid, which was subsequently dissolved in concentrated H₂SO₄ (10 mL) and stirred overnight. The reaction was quenched by pouring over ice to give a bright red precipitate. The solid was filtered and washed with acetone to yield dione **14** (248 mg, 54%). ¹H NMR (500 MHz, CDCl₃) δ 8.57 (d, *J* = 8.4 Hz, 2H), 8.10 (d, *J* = 7.5 Hz, 2H), 7.92 (d, *J* = 8.4 Hz, 2H), 7.79–7.73 (m, 2H), 7.64–7.57 (m, 2H), 7.40 (d, *J* = 7.3 Hz, 2H). Due to poor solubility, ¹³C NMR data of **14** could not be obtained. HRMS (EI+) for C₂₄H₁₄O₂ [M]⁺: calcd 332.0837, found 332.0831.

Fluoreno[4,3-*c*]fluorene 8. To an oven-dried flask containing dione **14** (150 mg, 0.45 mmol) dissolved in THF under N₂ was added mesitylmagnesium bromide (4 mL, 1.0

M solution, 4 mmol) was added at 0 °C. The reaction solution was stirred overnight and transitioned from a dark reddish-brown color to a turquoise color. The reaction was quenched with saturated NH₄Cl solution, extracted with CH₂Cl₂, and the organic phase was washed with water and then brine solution. The organic layer was dried (MgSO₄) and the volatiles removed. The resulting crude solid was used without further purification.

Under N₂ the crude diol was dissolved in degassed toluene (20 mL) and anhydrous SnCl₂ (809 mg, 4.3 mmol) was added. The reaction was stirred for 16 h at room temperature at which time the solution had turned a deep purple color. The reaction solution was evaporated and the crude product was purified on a silica gel plug eluting with 4:1 hexanes:CH₂Cl₂. The crude product was recrystallized by layering CH₃CN over a saturated solution in CHCl₃. The solid was collected by filtration to yield **8** (128 mg, 47%) as dark blue crystal. ¹H NMR (600 MHz, CDCl₃) δ 7.85 (d, *J* = 7.6 Hz, 2H), 7.57 (d, *J* = 9.4 Hz, 2H), 7.11 (t, *J* = 7.5 Hz, 2H), 7.04 (t, *J* = 7.3 Hz, 2H), 7.00 (s, 4H), 6.80 (d, *J* = 7.3 Hz, 2H), 6.70 (d, *J* = 9.3 Hz, 2H), 2.38 (s, 6H), 2.13 (s, 12H). ¹³C NMR (151 MHz, CDCl₃) δ 144.00, 143.84, 138.09, 137.68, 137.26, 136.99, 134.15, 132.92, 130.12, 128.35, 127.88, 126.92, 125.41, 124.99, 122.47, 122.12, 21.34, 20.41. UV-Vis (CH₂Cl₂) λ_{max} (ε) 331 (34,160), 554 sh (14,950), 594 (19,480), 637 (14,970) nm. HRMS (ESI) for C₄₂H₃₄ [M+H]⁺: calcd 539.2736, found 539.2739.

X-ray Crystallographic Data

General. Diffraction intensities for **8** were collected at 173 K on a Bruker Apex2 CCD diffractometer using a *Incoatec* Cu *IμS* source, CuKα radiation, 1.54178 Å. Space group was determined based on intensity statistics. Absorption correction was applied by

SADABS.³ Structure was solved by direct methods and Fourier techniques and refined on F^2 using full matrix least-squares procedures. All non-H atoms were refined with anisotropic thermal parameters. H atoms were treated in calculated positions in a rigid group model. All calculations were performed by the SHELXL-2014/7 packages.⁴

Crystallographic Data for 8: C₄₂H₃₄, M = 538.69, 0.09 × 0.08 × 0.06 mm, T = 173(2) K, Triclinic, space group *P*-1, $a = 7.1561(6)$ Å, $b = 8.0619(6)$ Å, $c = 12.8650(10)$ Å, $\alpha = 87.837(4)^\circ$, $\beta = 88.161(4)^\circ$, $\gamma = 75.494(4)^\circ$, $V = 717.84(10)$ Å³, $Z = 1$, $Z' = 0.5$, $D_c = 1.246$ Mg m⁻³, $\mu(\text{Cu}) = 0.529$ mm⁻¹, $F(000) = 286$, $2\theta_{\text{max}} = 133.00^\circ$, 8275 reflections, 2481 independent reflections [Rint = 0.0454], R1 = 0.0621, wR2 = 0.1733 and GOF = 1.065 for 2481 reflections (190 parameters) with $I > 2\sigma(I)$, R1 = 0.0677, wR2 = 0.1778 and

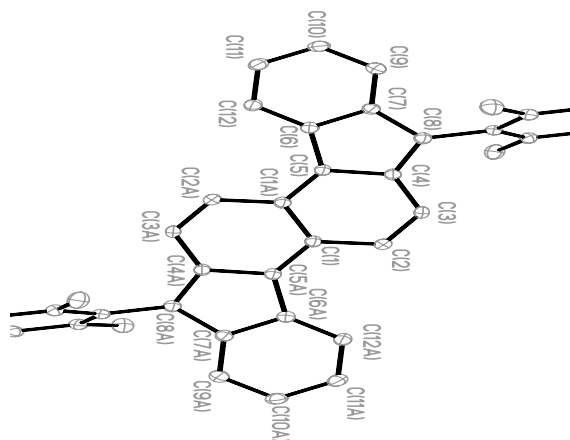


Figure A1. Molecular structure and atom labeling for fluoreno[4,3-*c*]fluorene **8**; ellipsoids at the 50% probability level.

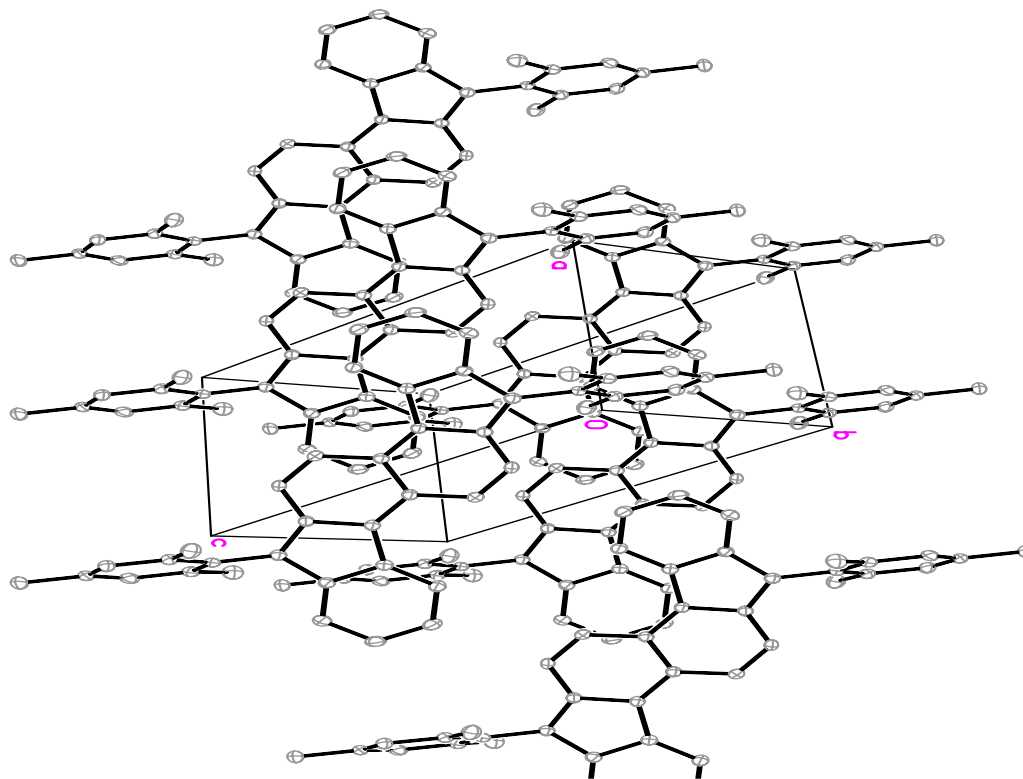


Figure A2. Molecular packing of fluoreno[4,2-*c*]fluorene **8**.

Computational Details

All calculations related were performed using Gaussian 09.⁵ Geometries and TD-DFT calculations were optimized using RB3LYP/6-31++G(d,p) level of theory and the structures were verified as global minima by the absence of imaginary frequencies. All NICS-XY scans were carried out with the Aroma package⁶ with the B3LYP/6-311+G* level of theory following the established procedures as a singlet in either the open or closed shell regime as stated in the plot. Biradical character index values were calculated using an unrestricted long range corrected method with a range separating parameter μ of 0.33 bohr^{-1} similar to that used by the Nakano group for calculating the biradical character of indenofluorenes.⁷

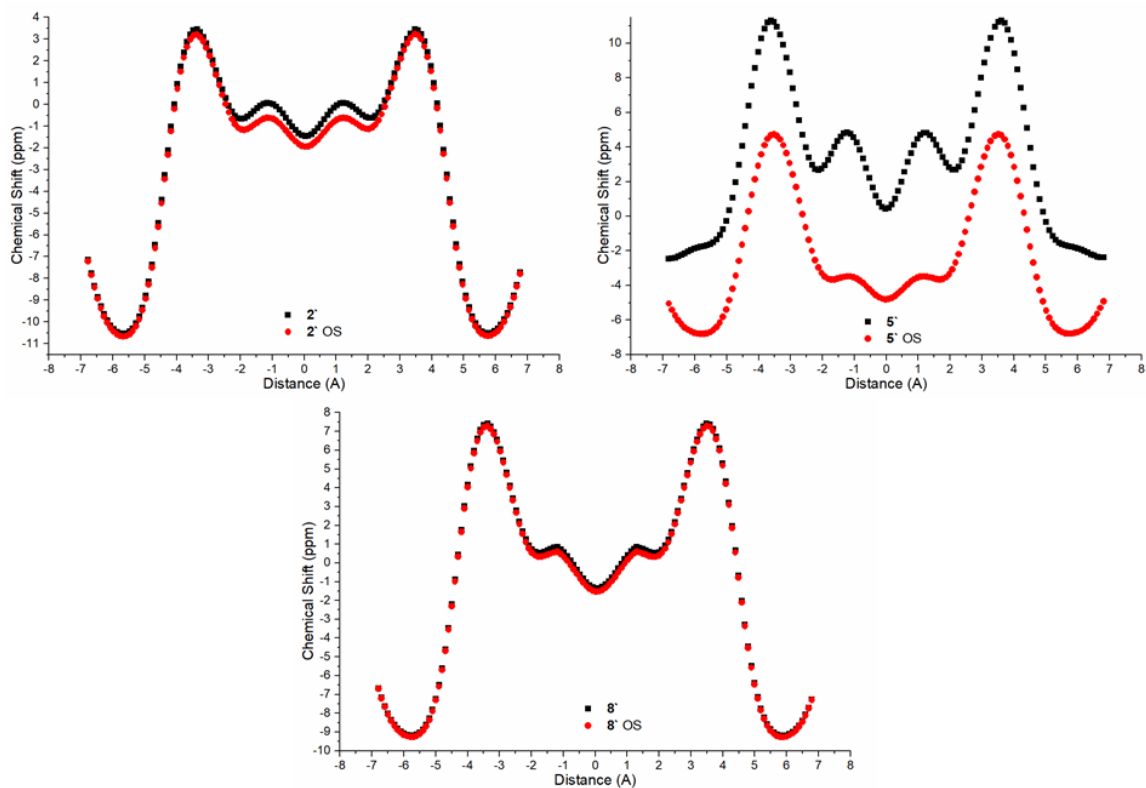


Figure A3. Comparison of the NICS-XY scans of the open and closed shell structures for fluorenofluorene isomers $2'$, $5'$, and $8'$.

Calculated Geometries

$1'$

Zero-point correction=	0.251575 (Hartree/Particle)
Thermal correction to Energy=	0.264910
Thermal correction to Enthalpy=	0.265854
Thermal correction to Gibbs Free Energy=	0.212308
Sum of electronic and zero-point Energies=	-769.141567
Sum of electronic and thermal Energies=	-769.128233
Sum of electronic and thermal Enthalpies=	-769.127288
Sum of electronic and thermal Free Energies=	-769.180834

H	-2.43941	3.46846	0.
H	2.34832	4.94205	0.
H	2.43941	-3.46846	0.
H	-2.34832	-4.94205	0.
H	1.85782	-5.8825	0.
H	-0.50516	-6.61454	0.
H	0.50516	6.61454	0.
H	-1.85782	5.8825	0.

H	2.42643	-0.74692	0.
H	-2.42643	0.74692	0.
C	0.37194	-1.36626	0.
C	1.38063	-0.44883	0.
C	1.03666	0.94686	0.
C	-0.37194	1.36626	0.
C	-1.38063	0.44883	0.
C	-1.03666	-0.94686	0.
C	1.83487	2.07039	0.
C	0.99155	3.25502	0.
C	-0.37194	2.83469	0.
C	0.37194	-2.83469	0.
C	-1.83487	-2.07039	0.
C	-0.99155	-3.25502	0.
C	-1.39683	3.77515	0.
C	1.31193	4.61521	0.
C	1.39683	-3.77515	0.
C	-1.31193	-4.61521	0.
C	1.06593	-5.13921	0.
C	-0.27243	-5.55371	0.
C	0.27243	5.55371	0.
C	-1.06593	5.13921	0.
H	2.91968	2.08058	0.
H	-2.91968	-2.08058	0.

2`

Zero-point correction=	0.297931 (Hartree/Particle)
Thermal correction to Energy=	0.313994
Thermal correction to Enthalpy=	0.314938
Thermal correction to Gibbs Free Energy=	0.254485
Sum of electronic and zero-point Energies=	-922.737573
Sum of electronic and thermal Energies=	-922.721510
Sum of electronic and thermal Enthalpies=	-922.720566
Sum of electronic and thermal Free Energies=	-922.781018

C	-1.7309	-1.86858	0.
C	-2.46988	-0.60267	0.
C	-1.7539	0.62373	0.
C	-0.36975	0.63339	0.
C	0.36976	-0.6334	0.
C	-0.36975	-1.87376	0.
C	0.36976	1.87376	0.
C	1.73091	1.86857	0.
C	2.46989	0.60267	0.

C	1.75391	-0.62373	0.
C	2.72993	2.93887	0.
C	4.01528	2.312	0.
C	3.82893	0.87735	0.
C	-2.72994	-2.93887	0.
C	-4.01528	-2.31199	0.
C	-3.82892	-0.87734	0.
C	-2.62251	-4.32709	0.
C	-3.79325	-5.09751	0.
C	-5.05672	-4.4855	0.
C	-5.17858	-3.0934	0.
C	2.6225	4.32709	0.
C	3.79323	5.09752	0.
C	5.05671	4.48551	0.
C	5.17858	3.09341	0.
H	-2.29666	1.56648	0.
H	0.19296	-2.80484	0.
H	-0.19296	2.80483	0.
H	2.29666	-1.56648	0.
H	4.62811	0.14461	0.
H	-4.6281	-0.14461	0.
H	-1.65073	-4.81359	0.
H	-3.72245	-6.18124	0.
H	-5.95005	-5.10328	0.
H	-6.15983	-2.62657	0.
H	1.65072	4.81358	0.
H	3.72243	6.18124	0.
H	5.95004	5.1033	0.
H	6.15984	2.62659	0.

5`

Zero-point correction=	0.297026 (Hartree/Particle)
Thermal correction to Energy=	0.313139
Thermal correction to Enthalpy=	0.314083
Thermal correction to Gibbs Free Energy=	0.253581
Sum of electronic and zero-point Energies=	-922.724625
Sum of electronic and thermal Energies=	-922.708512
Sum of electronic and thermal Enthalpies=	-922.707567
Sum of electronic and thermal Free Energies=	-922.768070

C	2.43509	-1.26102	0.
---	---------	----------	----

C	2.43427	0.19625	0.
C	1.23944	0.89124	0.
C	0.	0.20425	0.
C	-0.00017	-1.24923	0.
C	1.22698	-1.95349	0.
C	-1.23952	0.89145	0.
C	-2.43433	0.19662	0.
C	-2.43534	-1.26073	0.
C	-1.22722	-1.95334	0.
C	-3.81453	0.61	0.
C	-4.6281	-0.58692	0.
C	-3.77839	-1.71837	0.
C	3.77794	-1.71905	0.
C	4.62805	-0.5878	0.
C	3.81456	0.60948	0.
C	-4.42848	1.87175	0.
C	-5.81686	1.94771	0.
C	-6.6189	0.77726	0.
C	-6.04078	-0.47985	0.
C	6.04074	-0.48095	0.
C	6.61915	0.77599	0.
C	5.81734	1.94663	0.
C	4.42898	1.87103	0.
H	1.23019	1.9794	0.
H	1.21179	-3.04155	0.
H	-1.23002	1.97961	0.
H	-1.2122	-3.04139	0.
H	-4.09665	-2.75433	0.
H	4.09576	-2.75515	0.
H	-3.83191	2.77998	0.
H	-6.30091	2.92012	0.
H	-7.70041	0.87631	0.
H	-6.65792	-1.37423	0.
H	6.65766	-1.37548	0.
H	7.70068	0.87477	0.
H	6.30155	2.91896	0.
H	3.83275	2.7795	0.

8`

Zero-point correction=	0.297946 (Hartree/Particle)
Thermal correction to Energy=	0.314284

Thermal correction to Enthalpy=	0.315228
Thermal correction to Gibbs Free Energy=	0.253709
Sum of electronic and zero-point Energies=	-922.727065
Sum of electronic and thermal Energies=	-922.710728
Sum of electronic and thermal Enthalpies=	-922.709783
Sum of electronic and thermal Free Energies=	-922.771303

C	-2.46518	0.74896	0.
C	-1.66871	1.93717	0.
C	-0.21186	1.84626	0.
C	0.41918	0.61128	0.
C	-0.41918	-0.61128	0.
C	-1.85981	-0.46798	0.
C	1.85981	0.46798	0.
C	2.46518	-0.74896	0.
C	1.66871	-1.93717	0.
C	0.21186	-1.84626	0.
C	2.05271	-3.26025	0.
C	0.86689	-4.0911	0.
C	-0.28592	-3.24179	0.
C	-2.05271	3.26025	0.
C	-0.86689	4.0911	0.
C	0.28592	3.24179	0.
C	-0.74292	5.48093	0.
C	0.53696	6.04946	0.
C	1.66871	5.23022	0.
C	1.55093	3.82957	0.
C	0.74292	-5.48093	0.
C	-0.53696	-6.04946	0.
C	-1.66871	-5.23022	0.
C	-1.55093	-3.82957	0.
H	-3.54887	0.82873	0.
H	-2.4685	-1.35977	0.
H	2.4685	1.35977	0.
H	3.54887	-0.82873	0.
H	3.07285	-3.62769	0.
H	-3.07285	3.62769	0.
H	-1.62727	6.11254	0.
H	0.65034	7.12956	0.
H	2.65833	5.67755	0.
H	2.45938	3.2406	0.
H	1.62727	-6.11254	0.
H	-0.65034	-7.12956	0.

H -2.65833 -5.67755 0.
H -2.45938 -3.2406 0.

Table S1. TD-DFT calculated transitions for model fluorenofluorenes **2'** and **8'**.

FF 2'			
Excited state 1	HOMO-1 to LUMO	647.41 nm	Oscillator strength f = 0
Excited state 2	HOMO-2 to LUMO	606.55 nm	Oscillator strength f = 0.6830
	HOMO to LUMO		
Excited state 3	HOMO to LUMO+1	466.36 nm	Oscillator strength f = 0.0000
Excited state 4	HOMO to LUMO+3	410.18 nm	Oscillator strength f = 0.0000
	HOMO-2 to LUMO		
Excited state 5	HOMO-3 to LUMO	404.68 nm	Oscillator strength f = 0.0296
FF 8'			
Excited state 1	HOMO-1 to LUMO	765.20 nm	Oscillator strength f = 0
Excited state 2	HOMO-2 to LUMO	631.05 nm	Oscillator strength f = 0.3892
	HOMO to LUMO		
	HOMO-1 to LUMO+1		
Excited state 3	HOMO-2 to LUMO	486.65 nm	Oscillator strength f = 0.2611
	HOMO to LUMO		
	HOMO-1 to LUMO+1		

References

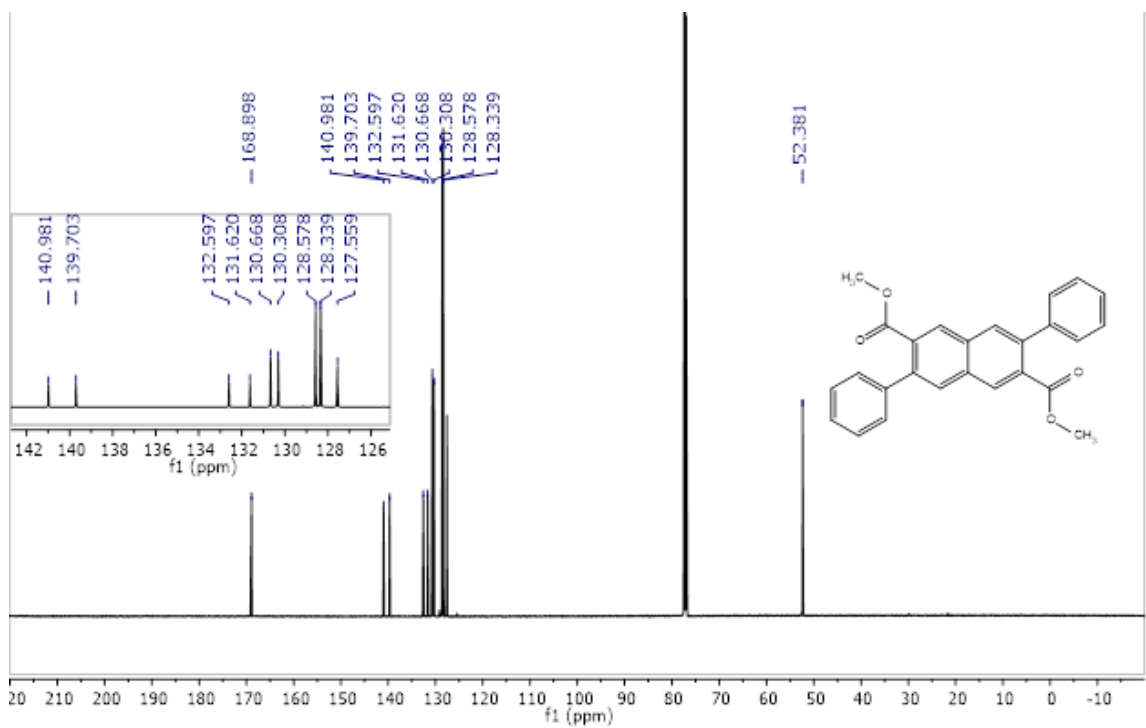
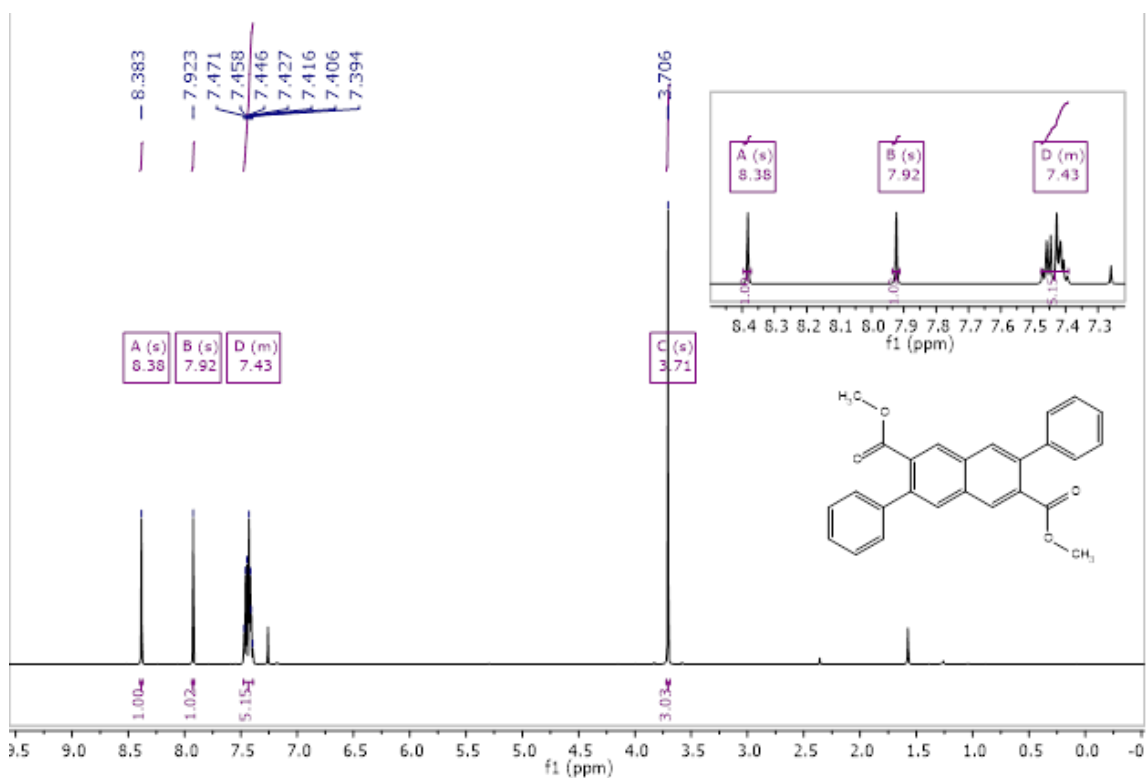
- Knall, A.-C.; Ashraf, R. S.; Nikolka, M.; Nielsen, C. B.; Purushothaman, B.; Sadhanala, A.; Hurhangee, M.; Broch, K.; Harkin, D. J.; Novák, J.; Neophytou, M.; Hayoz, P.; Sirringhaus, H.; McCulloch, I. *Adv. Funct. Mater.* **2016**, *26*, 6961–6969.
- Anton, U.; Adam, M.; Wagner, M.; Qi-Liu, Z.; Müllen, K. *Chem. Ber.* **1993**, *126*, 517–521.
- Sheldrick, G. M. *Bruker/Siemens Area Detector Absorption Correction Program*, Bruker AXS, Madison, WI, 1998.
- Sheldrick, G. M. *Acta Cryst. C* **2015**, *71*, 3–8.
- Frisch, M. J.; Trucks, G. W.; Schlegel, H. B.; Scuseria, G. E.; Robb, M. A.; Cheeseman, J. R.; Scalmani, G.; Barone, V.; Men-nucci, B.; Petersson, G. A.; Nakatsuji, H.; Caricato, M.; Li, X.; Hratchian, H. P.; Izmaylov, A. F.; Bloino, J.; Zheng, G.; Son-

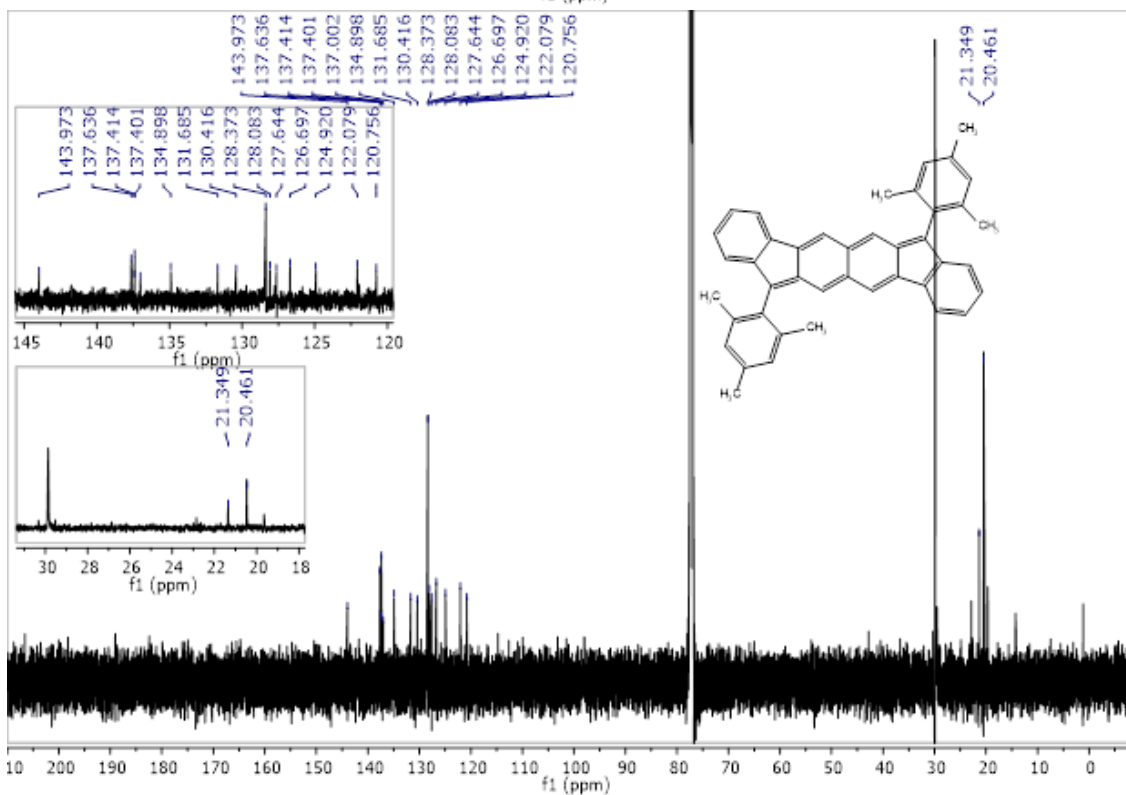
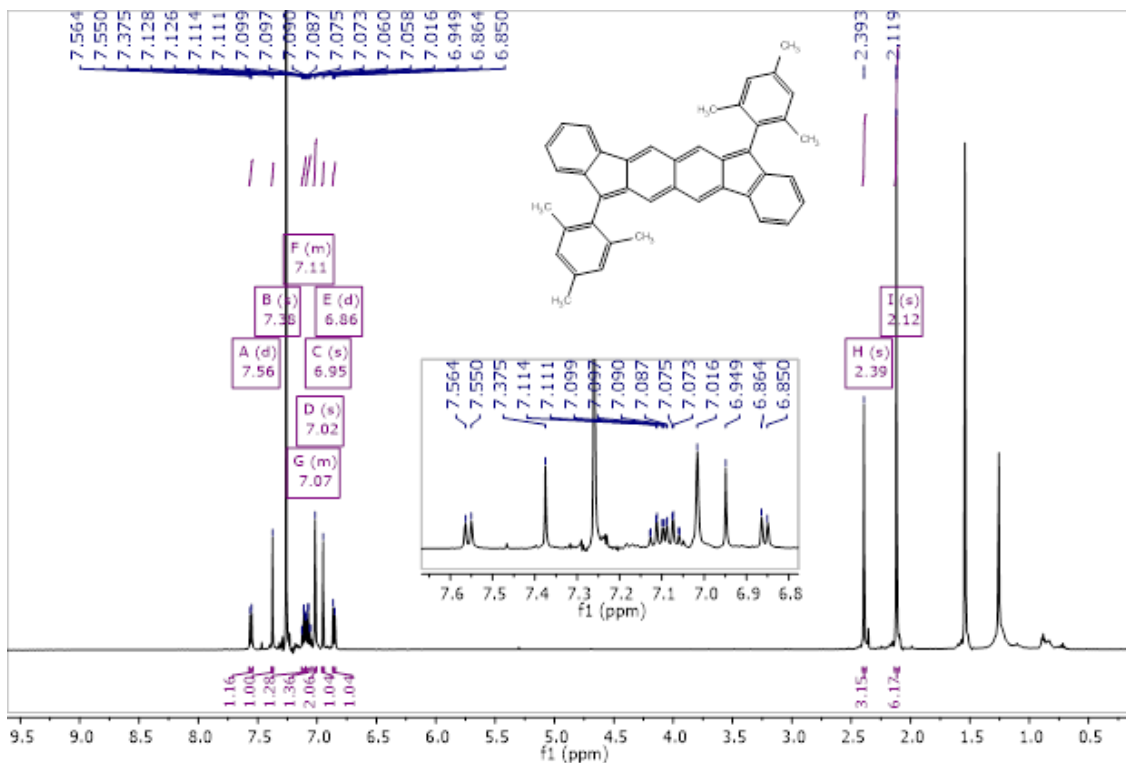
nenberg, J. L.; Hada, M.; Ehara, M.; Toyota, K.; Fukuda, R.; Hasegawa, J.; Ishida, M.; Nakajima, T.; Honda, Y.; Kitao, O.; Nakai, H.; Vreven, T.; Montgomery, J. A., Jr.; Peralta, J. E.; Ogliaro, F.; Bearpark, M.; Heyd, J. J.; Brothers, E.; Kudin, K. N.; Staroverov, V. N.; Kobayashi, R.; Normand, J.; Raghavachari, K.; Rendell, A.; Burant, J. C.; Iyengar, S. S.; Tomasi, J.; Cossi, M.; Rega, N.; Millam, N. J.; Klene, M.; Knox, J. E.; Cross, J. B.; Bakken, V.; Adamo, C.; Jaramillo, J.; Gomperts, R.; Stratmann, R. E.; Yazyev, O.; Austin, A. J.; Cammi, R.; Pomelli, C.; Ochterski, J. W.; Martin, R. L.; Morokuma, K.; Zakrzewski, V. G.; Voth, G. A.; Salvador, P.; Dannenberg, J. J.; Dapprich, S.; Daniels, A. D.; Farkas, Ö.; Foresman, J. B.; Ortiz, J. V.; Cioslowski, J.; Fox, D. J. Gaussian 09, Revision D.01; Gaussian Inc.: Wallingford, CT, 2010.

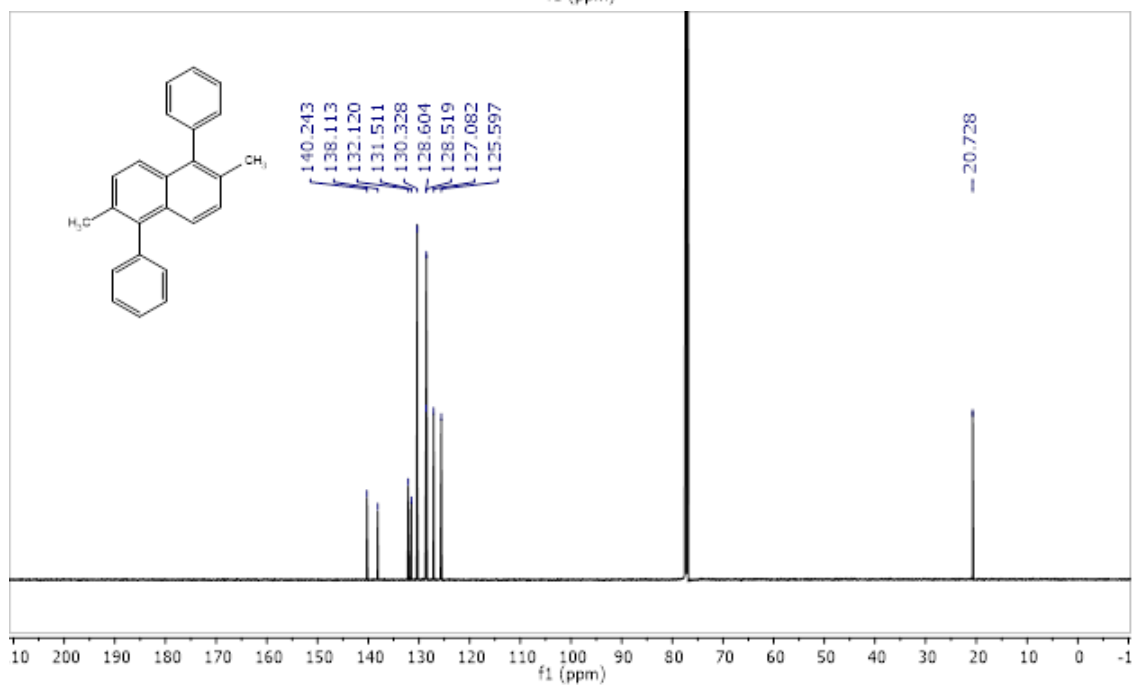
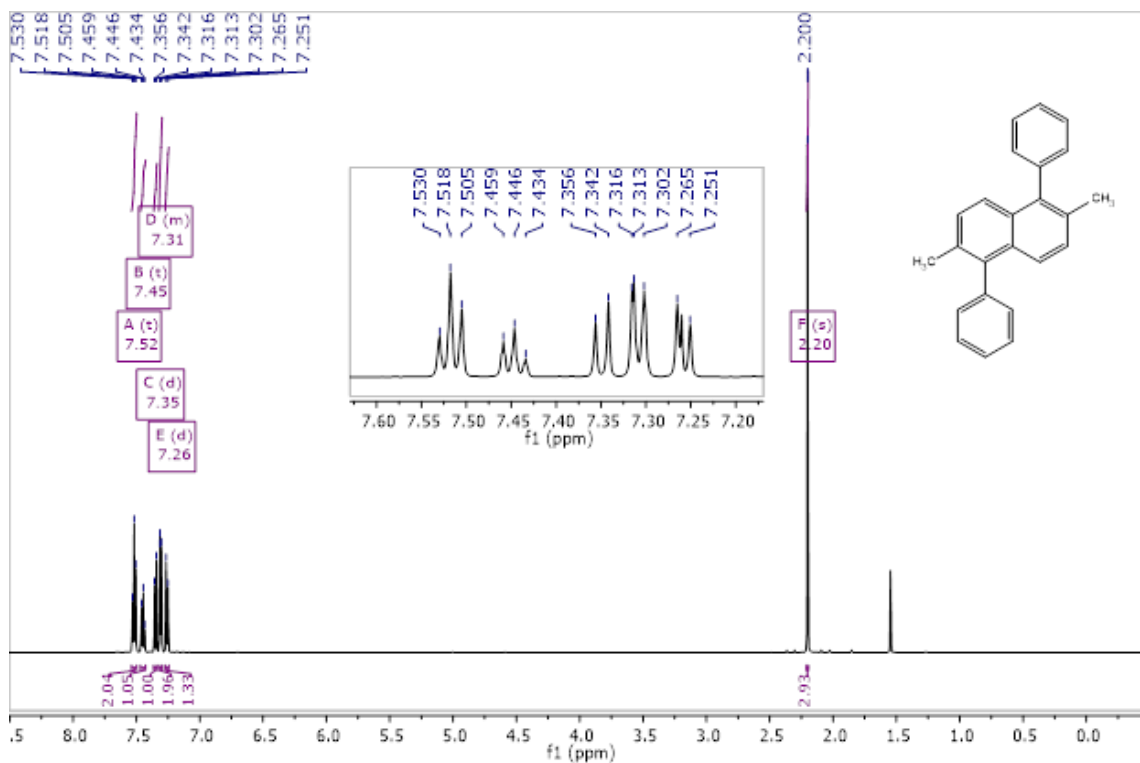
6. Rahalkar, A.; Stanger, A. "Aroma", <http://chemistry.technion.ac.il/members/amnon-stanger/>

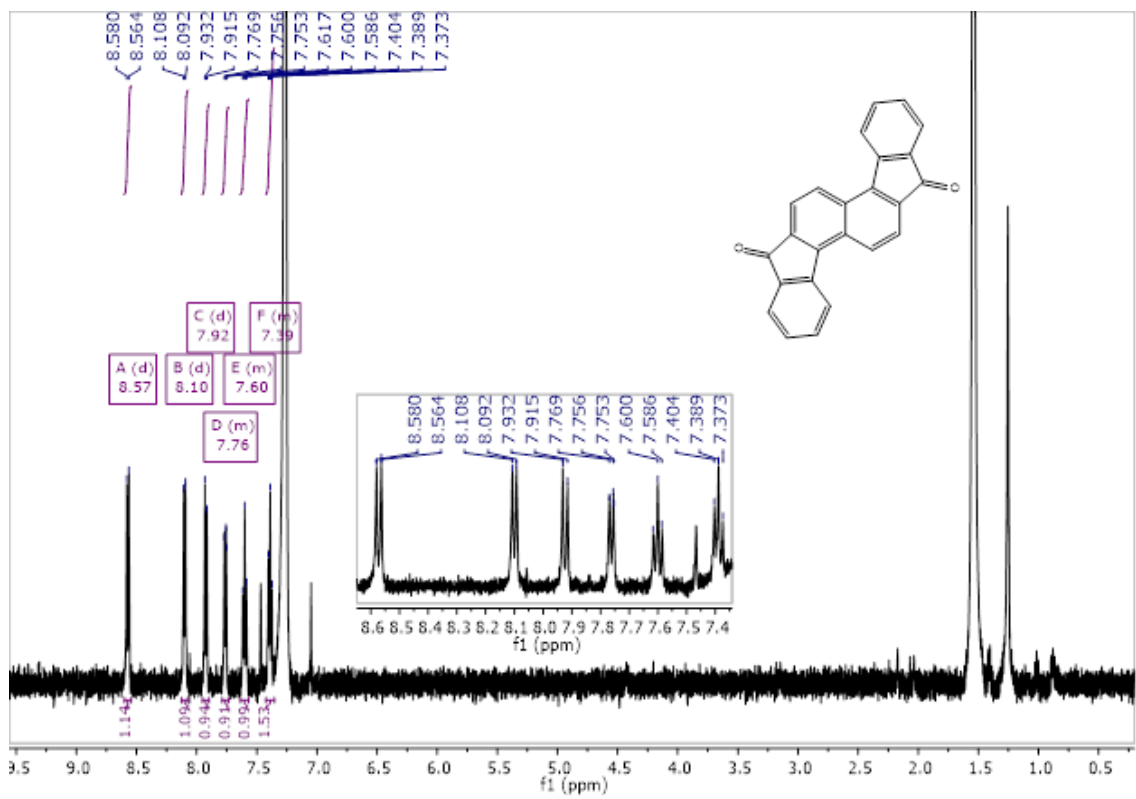
7. Fukuda, K.; Nagumi, T.; Fujiyoshi, J.-Y.; Nakano, M. *J. Phys. Chem. A* **2015**, *119*, 10620–10627.

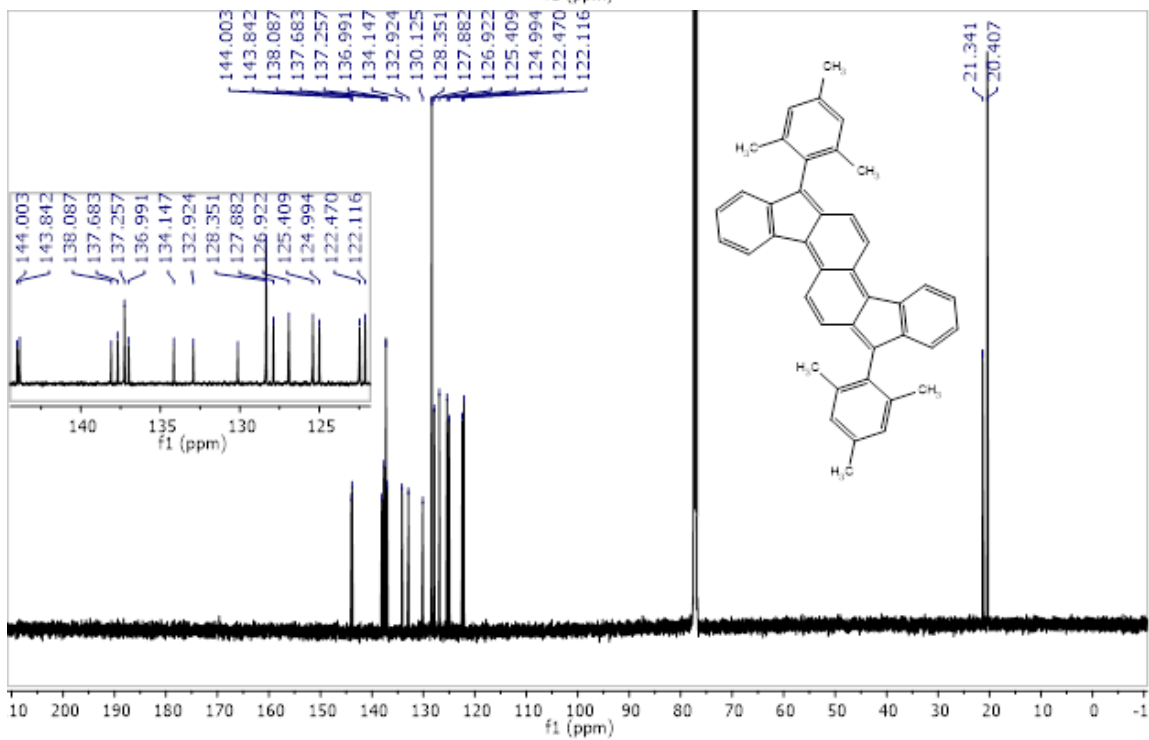
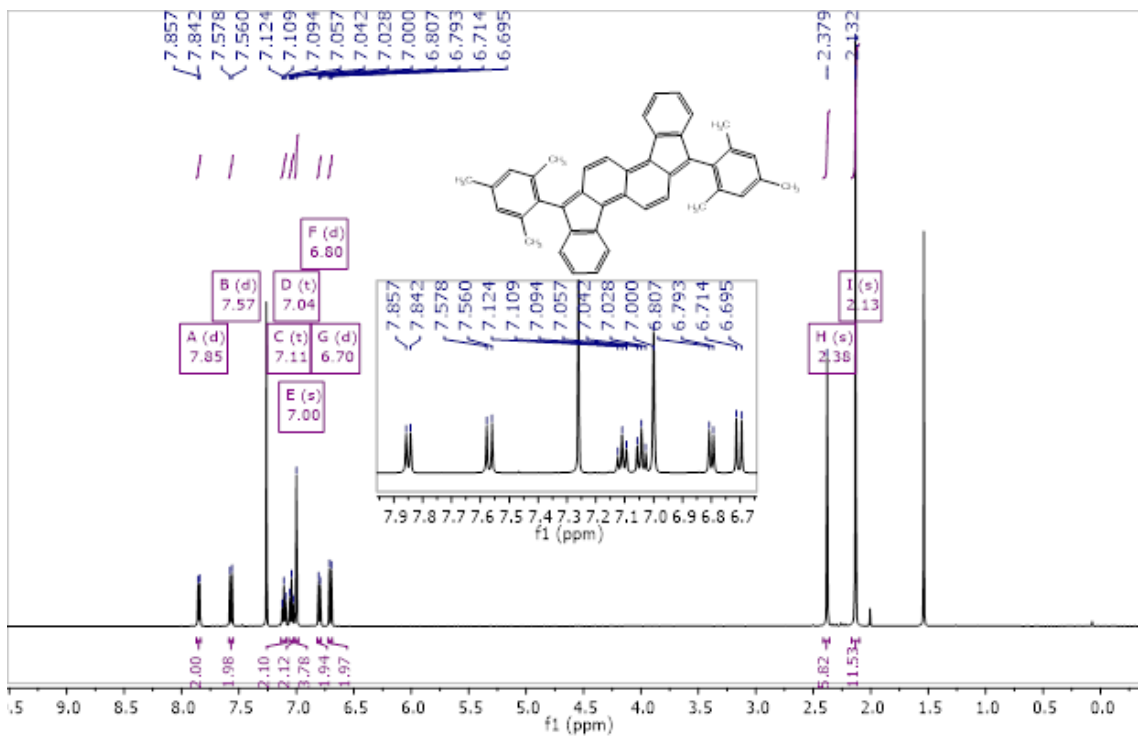
Copies of NMR Spectra











APPENDIX B

SUPPLEMENTARY INFORMATION FOR CHAPTER III

Appendix B is the supplementary information for Chapter III of this dissertation. It includes experimental details, other experimental data, spectra, and computational details relevant to the content in Chapter III.

Indenofluorenes Figure

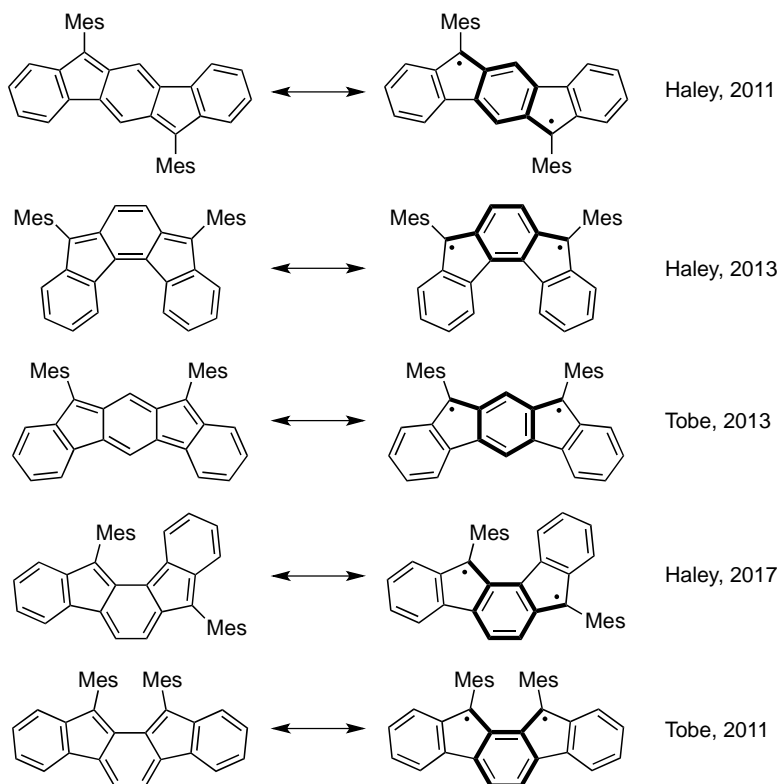


Figure B1. Quinoidal and diradical resonance forms of the five regioisomeric indenofluorenes.

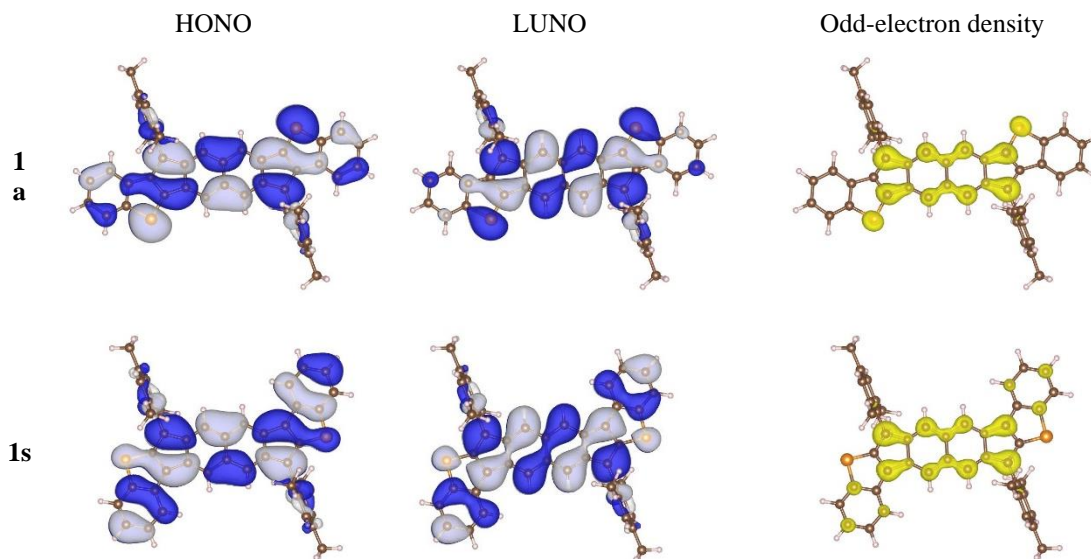
Computational Details

Geometry optimization and frequency analysis for the singlet and triplet states were

performed at the RB3LYP and UB3LYP levels, respectively, using the 6-311G* basis set. Vertical and adiabatic ΔE_{ST} values were evaluated at the spin-flip non-collinear (SF-NC-)TDDFT PBE5050/6-311G* level,^{1,2} where zero-point vibrational energy (ZPVE) corrections for the singlet and triplet states were estimated from the results of the frequency analysis calculations at the RB3LYP and UB3LYP levels, respectively. Excitation energies were evaluated at the TD-UB3LYP/6-311G* level. CASCI(2,2) calculations for the estimations of VCI parameters were performed using the molecular orbitals obtained at the tuned-LC-RBLYP/6-311G* level, where an optimal range-separating parameter μ for each system was determined by IP-tuning scheme for N -electron system.³ These calculations were performed using Gaussian 09 (geometry optimization and excitation energy),⁴ GAMESS-US (CASCI),⁵ and Q-Chem 4.2 (ΔE_{ST})⁶ program packages. Diradical characters y were evaluated at the PUHF/6-311G* [denoted as $y(\text{PUHF})$] and tuned-LC-RBLYP-CASCI(2,2)/6-311G* [denoted as $y(\text{CASCI})$] levels.⁷

Table B1. Summary of calculation results for **1a** and **1s**.

	1a	2a
y (PUHF) [-]	0.613	0.658
Vertical ΔE_{ST} [kcal mol ⁻¹]	-11.65	-11.09
Adiabatic ΔE_{ST} [kcal mol ⁻¹]	-9.37	-8.84
Adiabatic ΔE_{ST} (+ZPVE) [kcal mol ⁻¹]	-8.77	-8.06
<hr/>		
Tuned value of μ [bohr ⁻¹]	0.1444	0.1434
y (CASCI) [-]	0.203	0.210
Vertical ΔE_{ST} (CASCI) [kcal mol ⁻¹]	-19.8	-17.5
$ t_{ab} $ [eV]	1.031	0.905
$f_{ST}(y)$ [-]	-0.655	-0.632
$U/2 = K_{gu}^M$ [eV]	1.563	1.404
$(U/2)f_{ST}(y)$ [eV]	-1.025	-0.887
J_{gg}^M [eV]	4.417	4.225
J_{uu}^M [eV]	4.755	4.394
J_{gu}^M [eV]	4.420	4.179
$2K_{ab}$ [eV]	0.165	0.130

**Figure B2.** Spatial distributions of natural orbitals (NOs) and odd-electron density calculated at the tuned-LC-RBLYP-CASCI(2,2)/6-311G* level. White and blue meshes for NO maps represent the isosurfaces with the contour values of ± 0.01 a.u. Yellow mesh for odd-electron density maps represents the isosurface with the contour value of 0.0005 a.u.

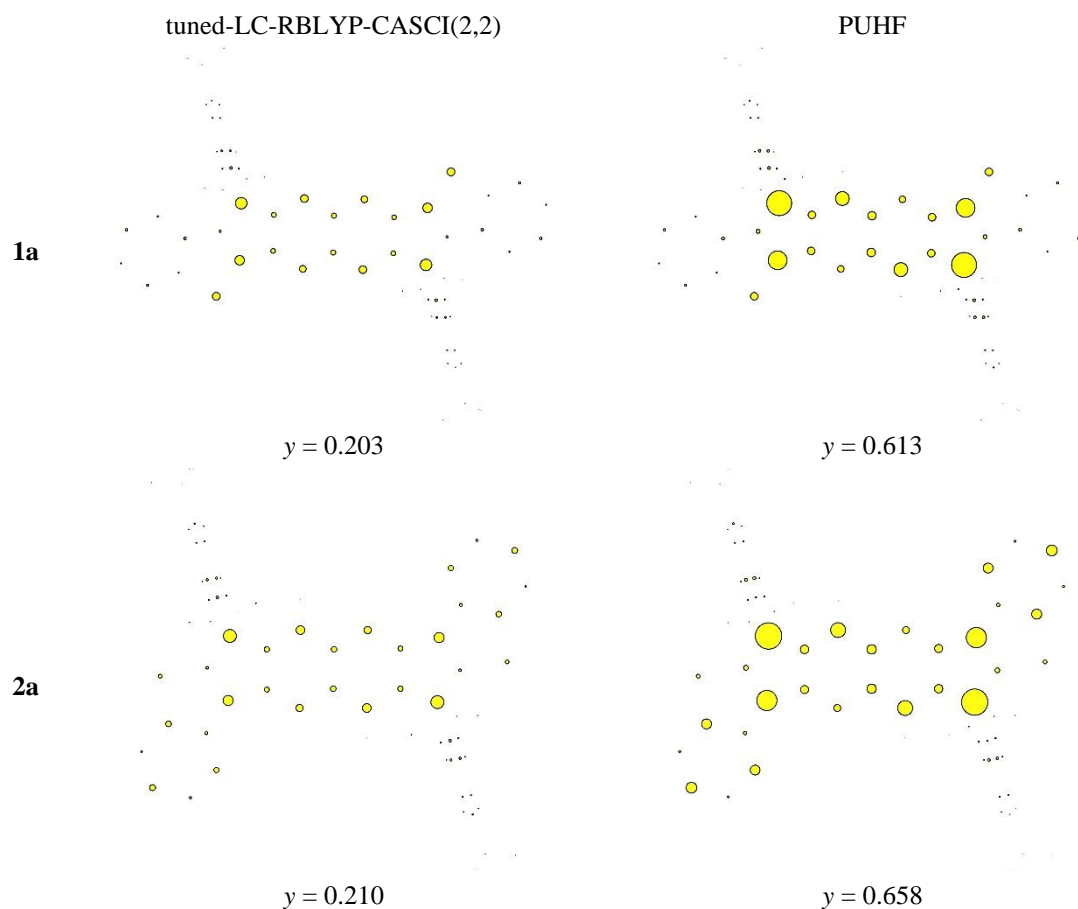


Figure B3. Mulliken population analysis for the odd-electron density calculated at the tuned-LC-RBLYP-CASCI(2,2)/6-311G* and PUHF/6-311G* levels. Note that the sum of odd-electron populations (odd-electron number) corresponds to $2y$ at the given level of approximation.⁷

Table B2. Excitation energies of **1a** calculated at the TD-UB3LYP/6-311G* level.

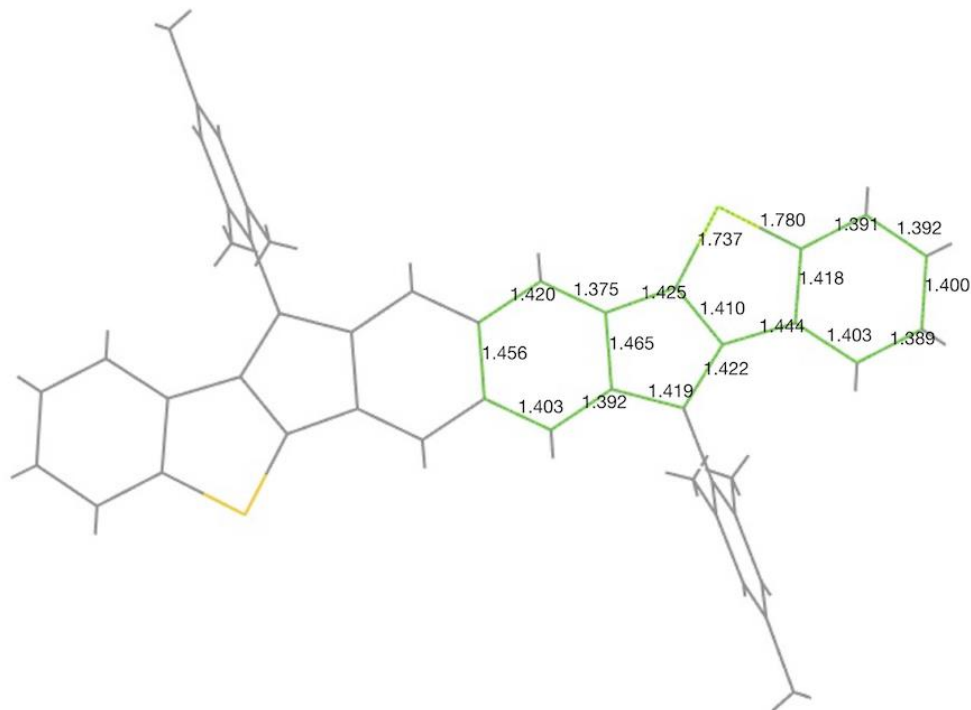
Excited state	Excitation energy [eV] (wavelength [nm])	Excitation amplitudes ^a	$\langle S^2 \rangle^b$	Oscillator strength
1	0.752 (1649)	0.724 (H α \rightarrow L α) 0.724 (H β \rightarrow L β) 0.184 (H α \leftarrow L α) 0.184 (H β \leftarrow L β)	1.081	0.0000
2	1.414 (877)	0.700 (H-1 α \rightarrow L α) -0.700 (H-1 β \rightarrow L β)	1.788	0.0005
3	1.508 (822)	0.687 (H-1 α \rightarrow L α) 0.687 (H-1 β \rightarrow L β) 0.109 (H-3 α \rightarrow L α) 0.109 (H-3 β \rightarrow L β)	0.290	0.0000
4	1.765 (703)	0.681 (H α \rightarrow L α) -0.681 (H β \rightarrow L β) -0.186 (H-1 α \rightarrow L+1 α) 0.186 (H-1 β \rightarrow L+1 β) -0.110 (H α \leftarrow L α) 0.110 (H β \leftarrow L β)	0.005	0.5447
5	2.192 (566)	-0.668 (H α \rightarrow L+1 α) 0.668 (H β \rightarrow L+1 β) -0.172 (H-1 α \rightarrow L α) 0.172 (H-1 β \rightarrow L β)	1.742	0.0007

^a H and L represent HOMO and LUMO, respectively. Excitations with amplitudes larger than 0.1 are shown. ^b $\langle S^2 \rangle$ of the ground state at the UB3LYP/6-311G* level is 0.376.

Table B3. Excitation energies of **2a** calculated at the TD-UB3LYP/6-311G* level.

Excited state	Excitation energy [eV] (wavelength [nm])	Excitation amplitudes ^a	$\langle S^2 \rangle^b$	Oscillator strength
1	0.687 (1806)	0.726 (H α \rightarrow L α) 0.726 (H β \rightarrow L β) 0.190 (H α \leftarrow L α) 0.190 (H β \leftarrow L β)	1.118	0.0000
2	1.165 (1064)	-0.701 (H-1 α \rightarrow L α) 0.701 (H-1 β \rightarrow L β)	1.801	0.0022
3	1.326 (935)	0.690 (H-1 α \rightarrow L α) 0.690 (H-1 β \rightarrow L β) 0.111 (H-2 α \rightarrow L α) 0.111 (H-2 β \rightarrow L β)	0.289	0.0000
4	1.673 (741)	-0.695 (H α \rightarrow L α) 0.695 (H β \rightarrow L β) -0.156 (H-1 α \rightarrow L+1 α) 0.156 (H-1 β \rightarrow L+1 β) 0.121 (H α \leftarrow L α) -0.121 (H β \leftarrow L β)	-0.029	0.6684
5	2.192 (566)	0.667 (H α \rightarrow L+1 α) 0.667 (H β \rightarrow L+1 β) -0.120 (H-1 α \rightarrow L α) -0.120 (H-1 β \rightarrow L β) -0.105 (H-9 α \rightarrow L α) -0.105 (H-9 β \rightarrow L β)	1.739	0.0000

^a H and L represent HOMO and LUMO, respectively. Excitations with amplitudes larger than 0.1 are shown. ^b $\langle S^2 \rangle$ of the ground state at the UB3LYP/6-311G* level is 0.363.

1a

2a

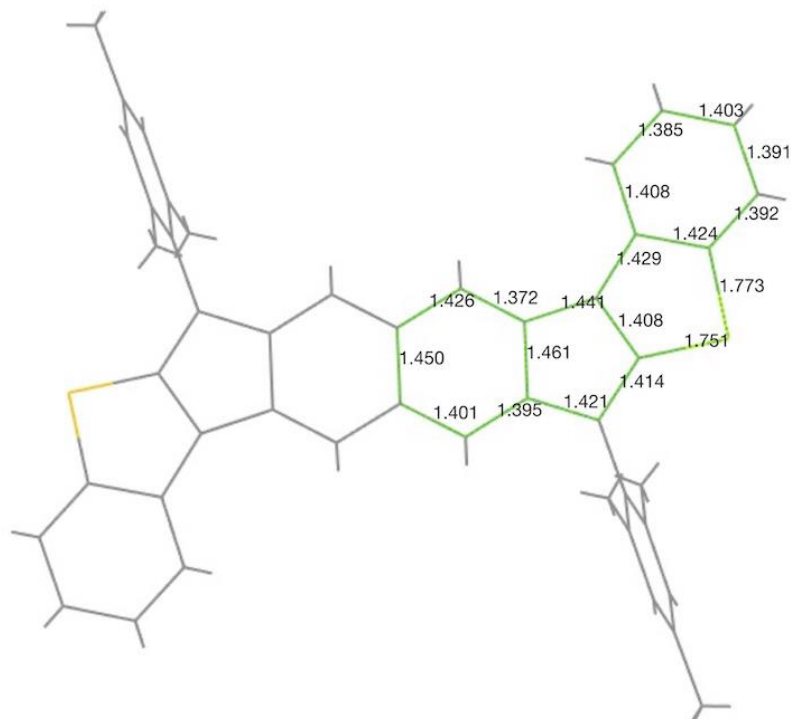


Figure B4. Selected bond lengths (Å) for the singlet state calculated at the RB3LYP/6-311G* level.

Cartesian Coordinates of Optimized Geometries

Table B4. Optimized geometry for singlet **1a** at the RB3LYP/6-311G* level (Total energy: -2570.18389983 Hartree, lowest frequency: 16.0370 cm^{-1}).

	X	Y	Z		X	Y	Z
C	1.513760	1.100368	0.081290	H	-0.612356	2.724543	0.016981
C	0.167989	0.707925	0.017368	C	-4.693523	-1.571907	-0.232430
C	2.532057	0.151436	0.114482	C	-4.897541	-2.219356	-1.468371
C	-0.167989	-0.707925	-0.017368	C	-5.211173	-2.137340	0.950068
C	2.190320	-1.273070	0.074742	C	-5.609431	-3.419748	-1.495402
C	0.875545	-1.670148	0.012150	C	-5.916208	-3.340660	0.875197
H	0.612356	-2.724543	-0.016981	H	-5.768712	-3.912626	-2.451400
H	1.758645	2.159206	0.105069	H	-6.311972	-3.773396	1.790635
C	-3.438018	1.959391	-0.113967	C	-6.124861	-4.000250	-0.335826
C	-3.942210	-0.292372	-0.177323	C	4.693523	1.571907	0.232430
C	3.942210	0.292372	0.177323	C	4.897541	2.219356	1.468371
C	3.438018	-1.959391	0.113967	C	5.211173	2.137340	-0.950068
C	4.488416	-1.020781	0.175192	C	5.609431	3.419748	1.495402
C	-4.488416	1.020781	-0.175192	C	5.916208	3.340660	-0.875197
C	7.070012	-1.075795	0.295234	H	5.768712	3.912626	2.451400
C	6.797949	-3.882831	0.228789	H	6.311972	3.773396	-1.790635
C	-6.797949	3.882831	-0.228789	C	6.124861	4.000250	0.335826
C	-7.070012	1.075795	-0.295234	C	-4.378168	-1.621714	-2.755227
C	8.188671	-1.898524	0.331260	H	-3.289361	-1.522069	-2.747392
C	8.056259	-3.292212	0.297724	H	-4.651423	-2.240432	-3.612299
C	-8.056259	3.292212	-0.297724	H	-4.782064	-0.619079	-2.923287
C	-8.188671	1.898524	-0.331260	C	-5.017499	-1.458330	2.285641
H	7.179371	0.002574	0.323110	H	-5.519570	-0.486800	2.320031
H	9.177701	-1.455643	0.386543	H	-5.418570	-2.068480	3.097361
H	8.940401	-3.920463	0.326401	H	-3.960539	-1.272318	2.494456
H	6.695496	-4.962668	0.204108	C	-6.862203	-5.316357	-0.390154
H	-7.179371	-0.002574	-0.323110	H	-7.452342	-5.409582	-1.305424
H	-9.177701	1.455643	-0.386543	H	-6.165309	-6.161616	-0.368678
H	-8.940401	3.920463	-0.326401	H	-7.539842	-5.433648	0.458689
H	-6.695496	4.962668	-0.204108	C	5.017499	1.458330	-2.285641
S	3.987989	-3.607156	0.109552	H	5.519570	0.486800	-2.320031
C	5.789373	-1.644430	0.224300	H	3.960539	1.272318	-2.494456
C	-5.678400	3.057268	-0.193311	H	5.418570	2.068480	-3.097361
C	-5.789373	1.644430	-0.224300	C	4.378168	1.621714	2.755227
C	5.678400	-3.057268	0.193311	H	3.289361	1.522069	2.747392
S	-3.987989	3.607156	-0.109552	H	4.782064	0.619079	2.923287
C	-1.513760	-1.100368	-0.081290	H	4.651423	2.240432	3.612299
C	-0.875545	1.670148	-0.012150	C	6.862203	5.316357	0.390154
C	-2.190320	1.273070	-0.074742	H	7.452342	5.409582	1.305424
C	-2.532057	-0.151436	-0.114482	H	7.539842	5.433648	-0.458689
H	-1.758645	-2.159206	-0.105069	H	6.165309	6.161616	0.368678

Table B5. Optimized geometry for triplet **1a** at the UB3LYP/6-311G* level (Total energy: -2723.86336623 Hartree, lowest frequency: 8.6876 cm^{-1}).

	X	Y	Z		X	Y	Z
S	4.258406	-3.268707	-0.179031	S	-4.258406	3.268707	0.179031
C	0.106184	0.710650	-0.041536	C	-0.106184	-0.710650	0.041536
C	1.430519	1.215549	-0.165365	C	-1.430519	-1.215549	0.165365
H	1.583899	2.288927	-0.233009	H	-1.583899	-2.288927	0.233009
C	2.503419	0.353490	-0.200669	C	-2.503419	-0.353490	0.200669
C	3.933109	0.607814	-0.326959	C	-3.933109	-0.607814	0.326959
C	4.568125	-0.655073	-0.328048	C	-4.568125	0.655073	0.328048
C	5.910295	-1.186610	-0.400034	C	-5.910295	1.186610	0.400034
C	7.143476	-0.529153	-0.514986	C	-7.143476	0.529153	0.514986
H	7.173509	0.553759	-0.560305	H	-7.173509	-0.553759	0.560305
C	8.317803	-1.270381	-0.564692	C	-8.317803	1.270381	0.564692
H	9.270615	-0.758853	-0.653201	H	-9.270615	0.758853	0.653201
C	8.287247	-2.668611	-0.500872	C	-8.287247	2.668611	0.500872
H	9.213413	-3.232300	-0.541297	H	-9.213413	3.232300	0.541297
C	7.076924	-3.346316	-0.384261	C	-7.076924	3.346316	0.384261
H	7.053272	-4.429758	-0.332753	H	-7.053272	4.429758	0.332753
C	5.902731	-2.602000	-0.334184	C	-5.902731	2.602000	0.334184
C	3.594704	-1.667814	-0.204373	C	-3.594704	1.667814	0.204373
C	2.283532	-1.077272	-0.122568	C	-2.283532	1.077272	0.122568
C	1.012838	-1.587441	-0.004115	C	-1.012838	1.587441	0.004115
H	0.842242	-2.658805	0.053975	H	-0.842242	2.658805	-0.053975
C	4.566682	1.942867	-0.438011	C	-4.566682	-1.942867	0.438011
C	4.978916	2.427348	-1.694782	C	-4.978916	-2.427348	1.694782
C	5.572260	3.690315	-1.775112	C	-5.572260	-3.690315	1.775112
H	5.883408	4.061421	-2.748302	H	-5.883408	-4.061421	2.748302
C	5.769566	4.486278	-0.648381	C	-5.769566	-4.486278	0.648381
C	5.352443	3.987949	0.587907	C	-5.352443	-3.987949	-0.587907
H	5.500669	4.591459	1.480326	H	-5.500669	-4.591459	-1.480326
C	4.754485	2.734695	0.715771	C	-4.754485	-2.734695	-0.715771
C	4.782815	1.606812	-2.948125	C	-4.782815	-1.606812	2.948125
H	3.749704	1.263279	-3.047572	H	-3.749704	-1.263279	3.047572
H	5.031584	2.187514	-3.838698	H	-5.031584	-2.187514	3.838698
H	5.413386	0.712284	-2.949676	H	-5.413386	-0.712284	2.949676
C	6.417840	5.845847	-0.750357	C	-6.417840	-5.845847	0.750357
H	6.619515	6.118336	-1.788391	H	-6.619515	-6.118336	1.788391
H	5.782126	6.625663	-0.319921	H	-5.782126	-6.625663	0.319921
H	7.369779	5.875231	-0.210231	H	-7.369779	-5.875231	0.210231
C	4.340446	2.231649	2.079024	C	-4.340446	-2.231649	-2.079024
H	4.809399	1.271122	2.310799	H	-4.809399	-1.271122	-2.310799
H	4.623154	2.939853	2.860394	H	-4.623154	-2.939853	-2.860394
H	3.259973	2.075784	2.144952	H	-3.259973	-2.075784	-2.144952

Table B6. Optimized geometry for singlet **2a** at the RB3LYP/6-311G* level (Total energy: -2570.19601268 Hartree, lowest frequency: 14.3984 cm^{-1}).

	X	Y	Z		X	Y	Z
C	1.531045	1.068760	0.008266	H	-4.748046	-0.574016	2.604359
C	0.179232	0.702210	-0.015421	H	-4.788594	-2.199900	3.293975
C	2.530876	0.097779	0.057145	H	-3.336339	-1.607194	2.484770
C	-0.179233	-0.702210	0.015421	C	-7.008652	-5.164529	-0.026052
C	2.172441	-1.317828	0.093187	H	-8.080878	-4.947580	0.035273
C	0.850824	-1.686291	0.070911	H	-6.851182	-5.755452	-0.931867
H	0.558548	-2.732227	0.096733	H	-6.755903	-5.791992	0.831884
H	1.799810	2.121860	-0.011351	C	4.429504	1.608526	-2.449441
C	-3.412952	2.047757	-0.153009	H	4.748051	0.574009	-2.604360
C	-3.945516	-0.226197	-0.093540	H	3.336342	1.607186	-2.484776
C	3.945516	0.226197	0.093540	H	4.788598	2.199892	-3.293980
C	3.412952	-2.047757	0.153012	C	5.005498	1.318564	2.596664
C	4.447888	-1.093761	0.154050	H	3.940357	1.154812	2.782405
C	-4.447888	1.093760	-0.154049	H	5.483928	0.335278	2.625893
C	-1.531045	-1.068760	-0.008266	H	5.404849	1.906164	3.425574
C	-0.850825	1.686291	-0.070911	C	7.008653	5.164529	0.026042
C	-2.172441	1.317828	-0.093187	H	8.080879	4.947580	-0.035282
C	-2.530876	-0.097779	-0.057145	H	6.755904	5.791990	-0.831897
H	-1.799810	-2.121860	0.011350	H	6.851181	5.755455	0.931854
H	-0.558548	2.732227	-0.096732	S	6.044246	-1.810628	0.211216
C	-4.726856	-1.486553	-0.074449	S	-6.044246	1.810627	-0.211217
C	-5.240066	-2.015473	-1.276808	C	3.893510	-3.392905	0.205196
C	-4.951096	-2.160430	1.142893	C	5.316668	-3.426901	0.243726
C	-5.961770	-3.209146	-1.237814	C	3.196462	-4.615580	0.223379
C	-5.680723	-3.351041	1.133172	C	6.016409	-4.629239	0.298772
H	-6.348710	-3.617621	-2.168125	C	3.895713	-5.810284	0.278343
H	-5.854057	-3.866291	2.074642	H	2.112315	-4.621483	0.195028
C	-6.195906	-3.892678	-0.044071	C	5.298332	-5.819917	0.316112
C	4.726857	1.486552	0.074446	H	7.100945	-4.639038	0.327584
C	5.240066	2.015476	1.276804	H	3.353623	-6.750085	0.292721
C	4.951097	2.160427	-1.142898	H	5.830200	-6.764535	0.359418
C	5.961770	3.209149	1.237808	C	-3.893510	3.392905	-0.205191
C	5.680725	3.351038	-1.133179	C	-3.196463	4.615580	-0.223370
H	6.348708	3.617627	2.168118	C	-5.316668	3.426901	-0.243719
H	5.854060	3.866285	-2.074650	C	-3.895714	5.810284	-0.278330
C	6.195907	3.892678	0.044063	H	-2.112315	4.621483	-0.195019
C	-5.005501	-1.318557	-2.596666	C	-6.016410	4.629239	-0.298761
H	-3.940360	-1.154802	-2.782408	C	-5.298333	5.819917	-0.316097
H	-5.404851	-1.906155	-3.425578	H	-3.353625	6.750085	-0.292705
H	-5.483932	-0.335271	-2.625891	H	-7.100946	4.639037	-0.327573
C	-4.429500	-1.608533	2.449437	H	-5.830202	6.764535	-0.359401

Table B7. Optimized geometry for triplet **2a** at the UB3LYP/6-311G* level (Total energy: -2570.18606481 Hartree, lowest frequency: 14.5734 cm^{-1}).

	X	Y	Z		X	Y	Z
C	1.550284	1.066269	0.004515	H	-4.834923	-0.611353	2.635790
C	0.176380	0.694965	-0.017089	H	-4.726557	-2.250668	3.283976
C	2.527893	0.099981	0.052986	H	-3.351555	-1.527982	2.444106
C	-0.176380	-0.694965	0.017090	C	-6.997416	-5.190412	-0.028710
C	2.173017	-1.301661	0.092006	H	-8.070735	-4.985784	0.052939
C	0.852282	-1.678855	0.073674	H	-6.848844	-5.769870	-0.943354
H	0.564195	-2.725130	0.103853	H	-6.723729	-5.824215	0.818112
H	1.815796	2.119552	-0.016693	C	4.441741	1.613990	-2.444091
C	-3.424852	2.038418	-0.155118	H	4.834916	0.611353	-2.635789
C	-3.985621	-0.223480	-0.092247	H	3.351552	1.527988	-2.444106
C	3.985621	0.223479	0.092247	H	4.726558	2.250667	-3.283975
C	3.424852	-2.038418	0.155118	C	5.051709	1.311184	2.594610
C	4.470422	-1.086397	0.156884	H	3.990274	1.123271	2.779030
C	-4.470422	1.086397	-0.156884	H	5.552929	0.339252	2.622580
C	-1.550284	-1.066269	-0.004514	H	5.436286	1.906026	3.425367
C	-0.852282	1.678855	-0.073673	C	6.997416	5.190412	0.028710
C	-2.173017	1.301661	-0.092006	H	8.070736	4.985783	-0.052937
C	-2.527893	-0.099981	-0.052986	H	6.723731	5.824214	-0.818113
H	-1.815796	-2.119552	0.016694	H	6.848844	5.769870	0.943353
H	-0.564195	2.725130	-0.103852	S	6.061463	-1.822654	0.219378
C	-4.756765	-1.487566	-0.075144	S	-6.061463	1.822654	-0.219378
C	-5.271676	-2.016464	-1.276585	C	3.890631	-3.382180	0.209428
C	-4.963445	-2.171037	1.140213	C	5.315817	-3.431746	0.251752
C	-5.980797	-3.217778	-1.238295	C	3.178466	-4.598378	0.226413
C	-5.679949	-3.369117	1.130085	C	6.000165	-4.640963	0.309355
H	-6.369404	-3.626228	-2.167917	C	3.864651	-5.799969	0.283970
H	-5.839867	-3.891467	2.070031	H	2.094702	-4.590924	0.194877
C	-6.198754	-3.909701	-0.046378	C	5.267244	-5.824380	0.325548
C	4.756765	1.487566	0.075144	H	7.084375	-4.664317	0.340972
C	5.271676	2.016463	1.276585	H	3.312862	-6.734061	0.297383
C	4.963444	2.171037	-1.140212	H	5.788544	-6.774753	0.370805
C	5.980797	3.217778	1.238296	C	-3.890631	3.382180	-0.209428
C	5.679949	3.369116	-1.130085	C	-3.178466	4.598379	-0.226414
H	6.369405	3.626227	2.167917	C	-5.315817	3.431746	-0.251753
H	5.839866	3.891467	-2.070031	C	-3.864651	5.799969	-0.283971
C	6.198755	3.909701	0.046378	H	-2.094702	4.590924	-0.194877
C	-5.051707	-1.311185	-2.594610	C	-6.000165	4.640963	-0.309356
H	-3.990271	-1.123277	-2.779031	C	-5.267244	5.824380	-0.325550
H	-5.436289	-1.906024	-3.425366	H	-3.312862	6.734061	-0.297384
H	-5.552922	-0.339249	-2.622578	H	-7.084375	4.664317	-0.340973
C	-4.441743	-1.613989	2.444092	H	-5.788544	6.774753	-0.370807

Experimental Details

General. All air-sensitive manipulations were carried out under an inert atmosphere using standard Schlenk technique. For moisture sensitive reactions, THF and toluene were refluxed with Na benzophenone ketyl for 24 h prior to distillation and use. Silica gel (240-300 mesh) was used for column chromatography. All other reagents were purchased and used as received. NMR spectra were recorded on a Bruker Avance III HD 500 equipped with a Prodigy multinuclear cryoprobe (^1H : 500 MHz, ^2D : 77 MHz) or Bruker Avance III HD 600 equipped with a Prodigy multinuclear cryoprobe (^1H : 600 MHz, ^{13}C : 151 MHz) NMR spectrometer at room temperature (unless otherwise noted). ^1H and ^{13}C NMR chemical shifts (δ) are expressed in ppm relative to the residual non-deuterated solvent reference (CDCl_3 : ^1H 7.26 ppm, ^{13}C 77.16 ppm; CD_2Cl_2 : ^1H 5.32 ppm, ^{13}C 53.84 ppm; $\text{DMSO}-d_6$: ^1H 2.50 ppm, ^{13}C 39.52 ppm). UV-Vis spectra were recorded on an Agilent Technologies Cary 60 UV-Vis spectrometer in HPLC grade CH_2Cl_2 . *anti*-Dione,⁸ compound **3**⁹ and 3-(4,4,5,5-tetramethyl-1,3,2-dioxaborolan-2-yl)benzo[*b*]thiophene¹⁰ were prepared according to literature procedures.

Diester 4. A two-neck round-bottom flask fitted with a condenser was charged with bistriflate **3**⁹ (0.500 g, 0.925 mmol, 1 equiv.), benzothiophene 3-boronpinacolate ester¹⁰ (0.601 g, 2.31 mmol, 2.5 equiv.), K_3PO_4 (0.589 g, 2.78 mmol, 3 equiv.), $\text{Pd}(\text{OAc})_2$ (8.3 mg, 0.037 mmol, 0.04 equiv.), and SPhos (30.4 mg, 0.074 mmol, 0.08 equiv.). These solids were then placed under N_2 atmosphere and dissolved in toluene (40 mL) and H_2O (1 mL) that had been sparged with N_2 for 1.5 h. After refluxing overnight and cooling to room temperature, the reaction was quenched with H_2O and poured over filter paper. The precipitate was washed with H_2O and MeOH to yield diester **4** (409 mg, 87%) as a yellow

solid. ^1H NMR (500 MHz, CDCl_3 , 25 °C) δ 8.54 (s, 2H), 8.09 (s, 2H), 7.94 (d, $J = 8.0$ Hz, 2H), 7.51 (d, $J = 7.8$ Hz, 2H), 7.46 (s, 2H), 7.39 (t, $J = 7.3$ Hz, 2H), 7.35 (t, $J = 7.4$ Hz, 2H), 3.53 (s, 6H); ^{13}C NMR (151 MHz, CDCl_3 , 25 °C) δ (ppm) 168.02, 139.82, 139.21, 136.80, 133.61, 133.24, 132.05, 131.58, 131.07, 124.58, 123.93, 123.02, 122.32, 52.50; HRMS (ES^+) (m/z), calculated for $\text{C}_{30}\text{H}_{20}\text{O}_4\text{NaS}_2$ ($\text{M}+\text{Na}$) $^+$ 531.0701, found 531.0654.

syn-Dione 5. A round-bottom flask fitted with a condenser was charged with diester **3** (0.400 g, 0.786 mmol, 1 equiv.), KOH (0.706 g, 12.6 mmol, 16 equiv.), EtOH (60 mL), and H_2O (15 mL). After refluxing the flask overnight, the reaction was cooled and the EtOH evaporated. Concentrated HCl was slowly added to the aqueous solution and a precipitate formed, which was isolated and washed with H_2O to yield the diacid intermediate as a yellow solid that was carried on without further purification.

To a suspension of the diacid (0.345 g, 0.718 mmol, 1 equiv.) in CH_2Cl_2 (40 mL) was added 3 drops of DMF followed by oxalyl chloride (0.24 mL, 2.87 mmol, 4.0 equiv.). After 12 h, the volatiles were removed under reduced pressure. The crude acid chloride was dissolved in CH_2Cl_2 (40 mL) and solid AlCl_3 (0.479 g, 3.59 mmol, 5 equiv.) was added to the flask. The reaction was stirred overnight and then poured into an HCl-ice mixture, precipitating the dione. The solid was filtered and washed successively with H_2O , CH_2Cl_2 and acetone to afford dione **5** as a purple solid (0.302 g, 88%) that was too insoluble to obtain NMR spectra. HRMS (ES^+) (m/z), calculated for $\text{C}_{28}\text{H}_{13}\text{O}_2\text{S}_2$ ($\text{M}+\text{H}$) $^+$ 445.0351, found 445.0352.

syn-IIDBT 2a. In an oven-dried round bottom flask, a suspension of dione **5** (0.195 g, 0.439 mmol, 1 equiv.) in dry THF (20 mL) was cooled to -78 °C under a N_2 atmosphere. In a separate oven-dried round bottom flask, 2-bromomesitylene (0.537 mL, 3.51 mmol, 8

equiv.) was dissolved in dry THF (20 mL), cooled to $-78\text{ }^{\circ}\text{C}$ under a N_2 atmosphere, and *n*-BuLi (2.5 M in hexanes, 1.32 mL, 3.29 mmol, 7.5 equiv.) was added dropwise. After stirring the mixture at $-78\text{ }^{\circ}\text{C}$ for 1 h, the aryl lithiate was transferred via cannula to the flask containing the dione. This reaction mixture was stirred for 4 h at $-78\text{ }^{\circ}\text{C}$, then slowly warmed to room temperature overnight with stirring. The reaction was then quenched with a saturated aq. NH_4Cl solution and extracted with CH_2Cl_2 (3 \times). The combined organic layer was washed with brine, dried (MgSO_4) and concentrated in vacuo. The resulting crude residue was passed through a silica plug eluting with hexanes, followed by a CH_2Cl_2 wash, to provide the desired diol that was carried onto the reductive dearomatization step without further purification.

In a single-neck round-bottom flask the crude diol (0.140 g, 0.204 mmol, 1 equiv.) and anhydrous SnCl_2 (0.154 g, 0.84 mmol, 4 equiv.) were dissolved in dry degassed toluene (60 mL). Trifluoroacetic acid (5 drops) was added and this mixture was then vigorously stirred. The reaction was monitored via TLC (9:1 hexanes/ CH_2Cl_2). After 3 h, the solvent was evaporated and the solid was washed with cold MeCN to remove trace impurities. The remaining solid was redissolved in CHCl_3 and MeCN was layered over the solution to furnish *syn*-IIDBT **2a** as a deep green solid (0.055 mg, 20% from **5**). Unfortunately, **2a** proved to be poorly soluble so that only its proton NMR spectra could be obtained. ^1H NMR (500 MHz, CDCl_3 , $25\text{ }^{\circ}\text{C}$) δ (ppm) 7.71 (d, $J = 7.9\text{ Hz}$, 2H), 7.55 (d, $J = 8.0\text{ Hz}$, 2H), 7.24 (m, 2H), 7.17–7.13 (m, 4H), 6.99 (s, 4H), 6.64 (s, 2H), 2.37 (s, 6H), 2.28 (s, 12H); HRMS (ES^+) (m/z), calculated for $\text{C}_{46}\text{H}_{35}\text{S}_2$ ($\text{M}+\text{H}$) $^+$ 651.2175, found 651.2174.

***syn*-IIDBT 2b.** Following the procedure described above for **2a**, dione **5** (0.115 g, 0.26 mmol, 1 equiv.), 2-bromo-5-*t*-butyl-1,3-dimethylbenzene (0.625 g, 2.59 mmol, 10

equiv.), and *n*-BuLi (2.5 M in hexanes, 0.984 mL, 2.46 mmol, 9.5 equiv.) were reacted to give the crude diol. Dearomatization of the crude diol (0.130 g, 0.17 mmol, 1 equiv.) with anhydrous SnCl₂ (0.125 g, 0.68 mmol, 4 equiv.) gave a deep green solution which was reacted for 4 h and then filtered through a pad of celite. The filtrate was concentrated, triturated with MeCN, and filtered to yield *syn*-IIDBT **2b** as a deep green solid (40 mg, 22% from **5**). ¹H NMR (600 MHz, CD₂Cl₂, 25 °C) δ 7.74 (d, *J* = 6.8 Hz, 2H), 7.58 (d, *J* = 8.0 Hz, 2H), 7.30–7.26 (m, 2H), 7.23–7.16 (m, 8H), 6.67 (s, 2H), 2.31 (s, 12H), 1.38 (s, 18H); ¹³C NMR (126 MHz, CD₂Cl₂, 25 °C) δ (ppm) 151.20, 147.70, 146.77, 140.84, 140.04, 138.98, 136.47, 133.37, 132.35, 131.93, 129.76, 129.22, 128.29, 125.57, 125.35, 124.70, 123.99, 122.21, 34.36, 31.09, 20.56; HRMS (ASAP) (*m/z*) calculated for C₅₂H₄₇S₂ (M+H)⁺ 735.3119, found 735.3119.

DihydroIIDBT 2cH₂. Following the procedure described above for **2a**, dione **5** (0.1 g, 0.225 mmol, 1 equiv.) and 1-bromo-4-*tert*-butylbenzene (0.39 mL, 2.25 mmol, 10 equiv.), and *n*-BuLi (1.6 M in hexanes, 1.34 mL, 2.14 mmol, 9.5 equiv.) were reacted to yield the crude diol. The diol (0.1 g, 0.14 mmol, 1 equiv.) and SnCl₂ (0.107 g, 0.56 mmol, 4 equiv.) were reacted at 70 °C. After 4 h, the mixture was poured over a silica plug and washed with hexanes. Switching to 3:1 hexanes/CH₂Cl₂ eluted the crude product. The dihydro product was further purified using preparative TLC using 2:1 hexanes/CH₂Cl₂ as eluent to furnish **2cH₂** (21 mg, 23% from **5**) as a pale yellow solid. ¹H NMR (500 MHz, CD₂Cl₂, 25 °C) δ (ppm) 8.29 (d, *J* = 7.9 Hz, 2H), 8.15 (s, 2H), 7.90 (d, *J* = 7.9 Hz, 2H), 7.82 (s, 2H), 7.55 (t, *J* = 7.6 Hz, 2H), 7.41 (t, *J* = 7.6 Hz, 2H), 7.36 (d, *J* = 7.9 Hz, 4H), 7.17 (d, *J* = 7.9 Hz, 4H), 5.36 (s, 2H), 1.31 (s, 18H); ¹³C NMR (126 MHz, CD₂Cl₂, 25 °C) δ (ppm) 152.32, 150.37, 149.92, 145.22, 139.70, 137.68, 136.40, 132.90, 131.54, 127.47,

125.86, 124.98, 124.32, 123.85, 123.68, 122.24, 116.91, 53.85, 53.63, 53.41, 53.20, 52.98, 51.91, 34.40, 31.07, 29.68; HRMS (ASAP) (m/z) calculated for $C_{48}H_{40}S_2$ ($M+H$)⁺ 680.2572, found 680.2539.

***anti*-IIDBT 1b.** Following the procedure described above for **2a**, *anti*-dione⁸ (0.140 g, 0.32 mmol, 1 equiv.) and 2-bromo-5-*t*-butyl-1,3-dimethylbenzene (0.608 g, 2.52 mmol, 8 equiv.), and *n*-BuLi (1.6 M in hexanes, 1.50 mL, 2.36 mmol, 7.5 equiv.) were reacted to give the crude diol. Dearomatization of the crude diol (0.201 g, 0.261 mmol, 1 equiv.) with anhydrous SnCl₂ (0.198 g, 1.05 mmol, 4 equiv.) gave a deep green solution which was reacted for 4 h and then filtered through a pad of celite. The filtrate was concentrated, triturated with MeCN, and filtered to yield *syn*-IIDBT **1b** (0.074 g, 42% from *anti*-dione) as a deep green solid. ¹H NMR (500 MHz, CD₂Cl₂, 25 °C) δ (ppm) 7.61 (d, $J = 7.7$ Hz, 2H), 7.24–7.13 (m, overlapping singlets and a triplet, 8H), 7.08 (s, 2H), 6.92 (d, $J = 7.8$ Hz, 2H), 6.86 (s, 2H), 2.23 (s, 12H), 1.41 (s, 18H); ¹³C NMR (126 MHz, CD₂Cl₂, 25 °C) δ (ppm) 150.94, 145.30, 144.75, 142.54, 138.76, 138.25, 136.66, 133.00, 131.87, 130.93, 130.59, 130.18, 127.59, 125.54, 125.21, 124.64, 123.88, 122.07, 34.65, 31.62, 20.96; HRMS (ASAP) (m/z) calculated for $C_{52}H_{47}S_2$ ($M+H$)⁺ 735.3119, found 735.3076.

Variable Temperature NMR Experiments. Approximately 10 mg of IIDBT **2a** was dissolved in 1,2-dichlorobenzene-*d*₄ and transferred to an NMR tube. Proton NMR spectra were acquired in a Varian Inova 500 MHz spectrometer that was heated to 50, 75, 100, 130, 140, then cooled back to 25 °C.

General Details for X-ray Structures. Diffraction intensities for **1d** were collected at 173 K on a Bruker Apex2 CCD diffractometer using CuK α radiation, $\lambda = 1.54178$ Å. Space group was determined based on intensity statistics. Absorption

correction was applied by SADABS.¹¹ Structure was solved by direct methods and Fourier techniques and refined on F^2 using full matrix least-squares procedures. All non-H atoms were refined with anisotropic thermal parameters. H atoms in all structures were refined in calculated positions in a rigid group model. Solvent molecule, CH₃CN, is highly disordered over three or four positions. Some of these positions are related by an inversion center. This solvent molecule was treated by SQUEEZE.¹² The correction of the X-ray data by SQUEEZE was 51 electron/cell; the expected number of electrons is 44 electrons/cell. Crystals of **1d** were very thin plates that did not provide visible reflections at high angles. Even using a strong *Incoatec I μ S* Cu source it was possible to collect diffraction data only up to $2\theta_{\max} = 101.25^\circ$. The collected data provide 2737 reflections per 271 refined parameters. All calculations were performed by the Bruker SHELXL-2014 package.¹³

X-ray diffraction data for **2b** were collected on a Rigaku XtaLAB Synergy diffractometer coupled to a Rigaku Hypix detector with Cu K α radiation ($\lambda = 1.54184 \text{ \AA}$), from a PhotonJet micro-focus X-ray source at 200 K. The diffraction images were processed and scaled using the CrysAlisPro software.¹⁴ The structures were solved through intrinsic phasing using SHELXT¹³ and refined against F^2 on all data by full-matrix least squares with SHELXL¹⁵ following established refinement strategies.¹⁶ All non-hydrogen atoms were refined anisotropically. All hydrogen atoms bound to carbon were included in the model at geometrically calculated positions and refined using a riding model. The isotropic displacement parameters of all hydrogen atoms were fixed to 1.2 times the U_{eq} value of the atoms they are linked to (1.5 times for Me groups).

Crystallographic Data for 1d. C₆₂H₆₄N₂S₂, C₅₈H₅₈S₂•2(CH₃CN), M = 901.27, 0.12 x 0.09 x 0.01 mm, T = 173(2) K, Triclinic, space group *P*-1, $a = 9.0360(6) \text{ \AA}$, $b =$

10.7067(7) Å, $c = 14.4033(10)$ Å, $\alpha = 77.940(4)^\circ$, $\beta = 85.741(5)^\circ$, $\gamma = 74.769(4)^\circ$, $V = 1314.56(16)$ Å³, $Z = 1$, $D_c = 1.138$ Mg/m³, $\mu(\text{Cu}) = 1.210$ mm⁻¹, $F(000) = 482$, $2\theta_{\text{max}} = 101.25^\circ$, 9539 reflections, 2737 independent reflections [$R_{\text{int}} = 0.0436$], $R1 = 0.0545$, $wR2 = 0.1503$ and $\text{GOF} = 1.068$ for 2737 reflections (271 parameters) with $I > 2\sigma(I)$, $R1 = 0.0755$, $wR2 = 0.1593$ and $\text{GOF} = 1.068$ for all reflections, max/min residual electron density $+0.337/-0.166$ eÅ⁻³. CCDC 1589136.

Crystallographic Data for 2b. C₅₄H₄₈Cl₆S₂, C₅₂H₄₆S₂•2(CHCl₃), $M = 973.74$, $0.185 \times 0.073 \times 0.037$ mm³, $T = 200.00(10)$ K, Monoclinic, space group P2₁/c, $a = 8.11560(10)$ Å, $b = 9.97380(10)$ Å, $c = 29.2458(3)$ Å, $\alpha = 90^\circ$, $\beta = 94.8550(10)^\circ$, $\gamma = 90^\circ$, $V = 2358.76(4)$ Å³, $Z = 2$, $D_c = 1.371$ Mg/m³, $\mu(\text{Cu}) = 4.432$ mm⁻¹, $F(000) = 1012$, $2\theta_{\text{max}} = 67.723^\circ$, 29112 reflections, 4271 independent reflections [$R(\text{int}) = 0.0397$], $R1 = 0.0847$, $wR2 = 0.2315$ and $\text{GOF} = 1.041$ for all reflections, max/min residual electron density $+1.232/-0.929$ eÅ⁻³. CCDC 1949404.

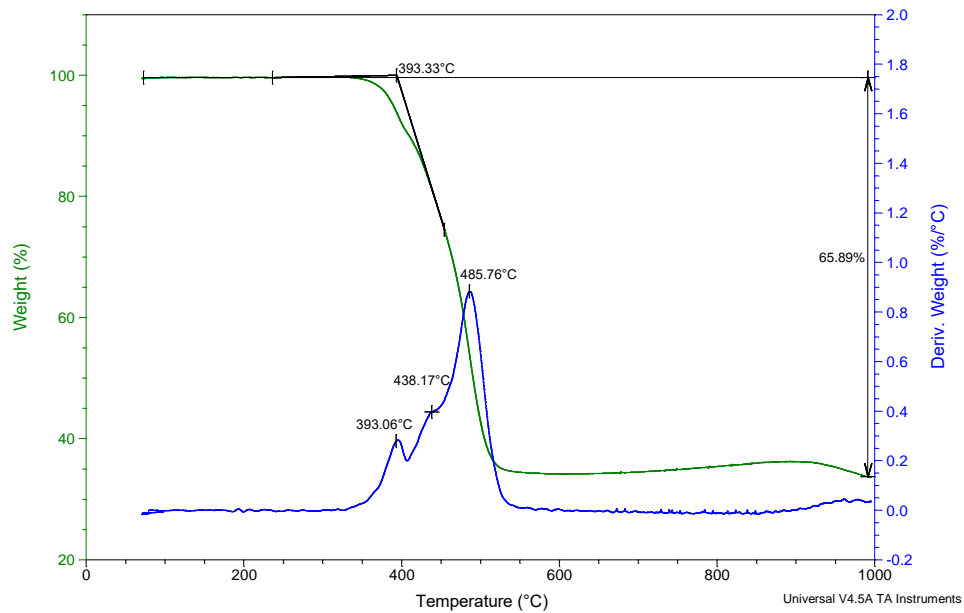


Figure B6. TGA plot for *anti*-IIDBT **1a**.

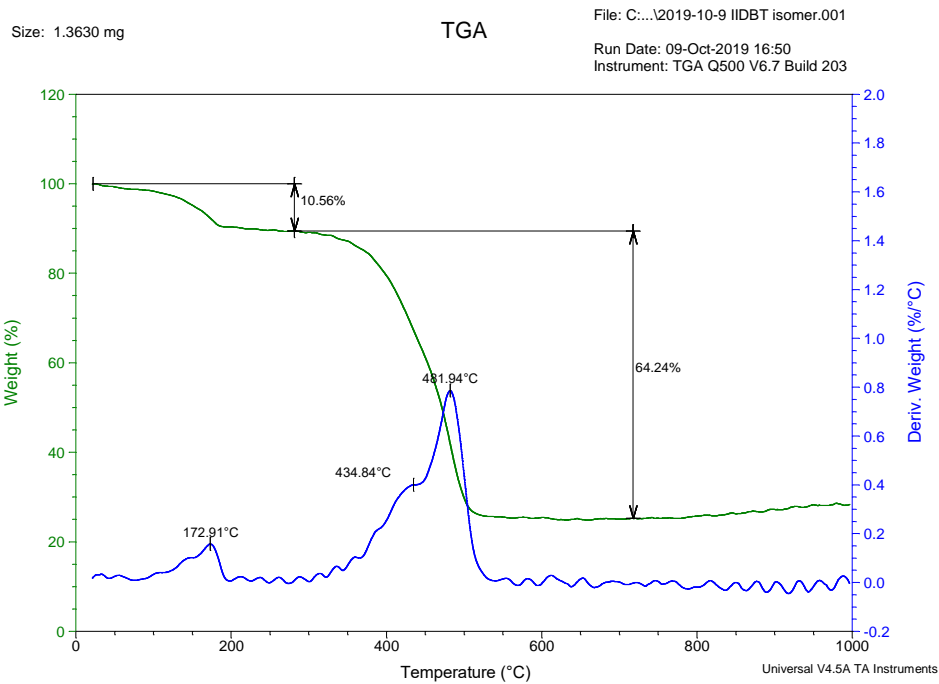


Figure B7. TGA plot for *anti*-IIDBT **1b**. The small, initial weight loss corresponds to 1,2-dichlorobenzene solvent.

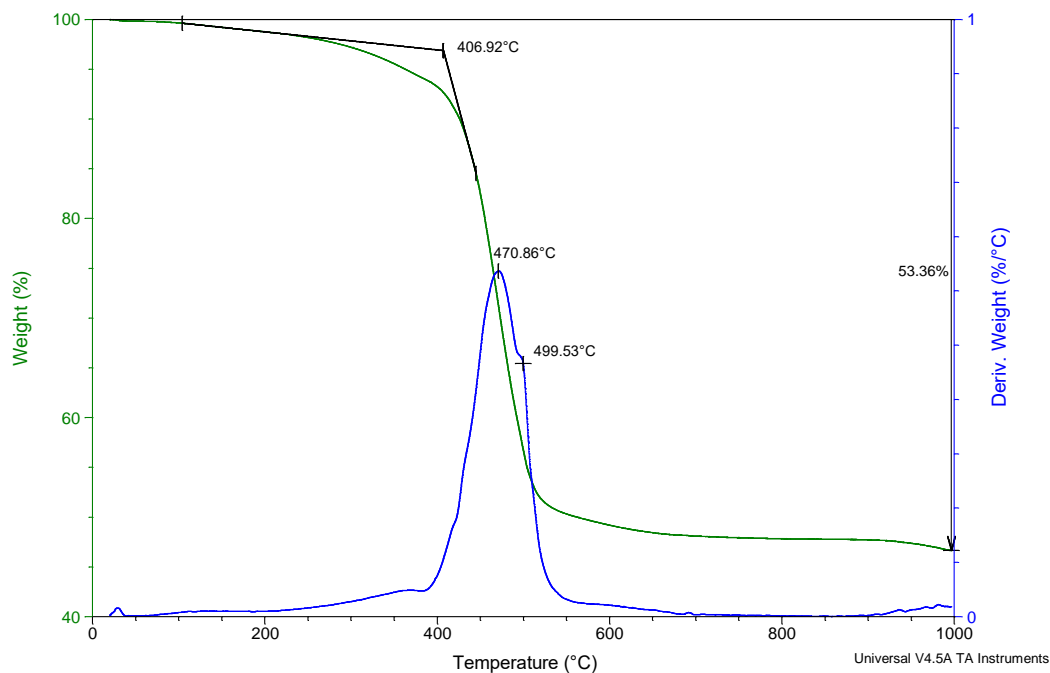


Figure B8. TGA plot for *syn*-IIDBT 2a.

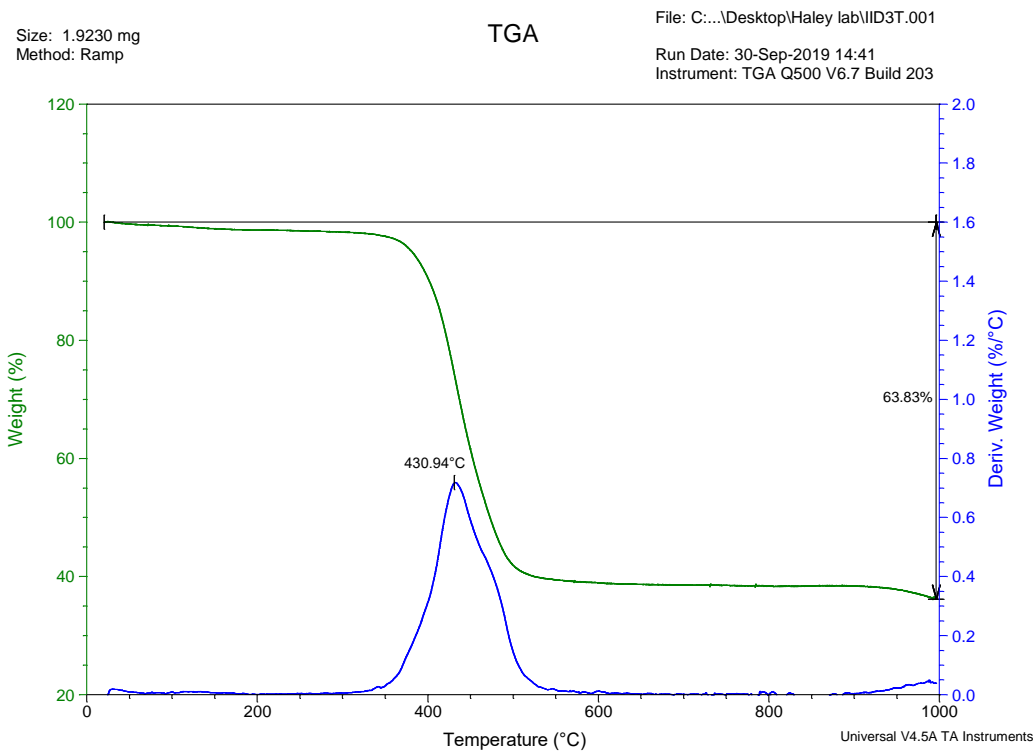


Figure B9. TGA plot for *syn*-IIDBT 2b.

SQUID measurements. Magnetic susceptibility measurements were performed with a Quantum Design MPMS-XL-7 SQUID susceptometer equipped with a sample space oven reaching a maximum temperature of 800 K. The magnetic measurements were performed in the 300-700 K temperature range with an applied field of 1 T using a sample space oven with the samples inserted in a 1.5 mm diameter aluminium foil cylinder. The sample masses used for the magnetic measurements are 11.665, 3.868 and 1.469 mg for **2a**, **1b** and **2b**, respectively. The susceptibility data were corrected for the same sample holder previously measured using the same conditions and for the diamagnetic contributions of the compound as deduced by using Pascal's constant tables.¹⁷ The magnetic measurements were fitted using the classical Bleaney-Bowers model for an antiferromagnetic $S = \frac{1}{2}$ dimer.¹⁸ This model reproduces satisfactorily the magnetic properties of **2a** with $g = 2.0(1)$, $J = -3479$ K and a paramagnetic $S = \frac{1}{2}$ impurity (ρ) of *ca.* 0.6% with a regression factor, $R = 0.99877$ (the Hamiltonian is written as $H = -JS_1S_2$). This J value corresponds to a ΔE_{ST} of *ca.* -6.9 kcal mol⁻¹.

Compounds **1b** and **2b** were measured in the heating and cooling scans in order to verify stability. The magnetic measurements of **1b** and **2b** were also fitted to the classical Bleaney-Bowers model.¹⁸ This model for **1b** gives (solid lines in Figure S8): $g = 2.0(1)$, $J = -4141$ K and $\rho \approx 0.1\%$ in the heating scan ($R = 0.9991$) and $g = 2.0(1)$, $J = -4227$ K and $\rho \approx 0.1\%$ in the cooling scan ($R = 0.9985$). These J values correspond to ΔE_{ST} of *ca.* -8.2 and -8.4 kcal mol⁻¹, for the heating and cooling scans, respectively. For **2b** we obtain (solid lines in Figure S9): $g = 2.0(1)$, $J = -3652$ K and $\rho \approx 0.1\%$ in the heating scan ($R = 0.9994$) and $g = 2.0(1)$, $J = -3533$ K and $\rho \approx 0.2\%$ in the cooling scan ($R = 0.9979$).

These J values correspond to ΔE_{ST} of *ca.* -7.2 and -7.0 kcal mol⁻¹, for the heating and cooling scans, respectively.

In all cases the paramagnetic impurities may come from a small fraction of mono-radical present in the sample. Given the low magnetic signal, the J value obtained presents an uncertainty of around 10%, as this error corresponds to the error in the $\chi_m T$ values (and, therefore in the g values that are directly related to them). For the estimated ΔE_{ST} values from the fit to the Bleaney-Bowers model, however, the ΔE_{ST} value mainly depends on the curvature of the plot as T increases; thus, the error in ΔE_{ST} can be evaluated to be around 0.2 kcal mol⁻¹, which is more like 2-3%.

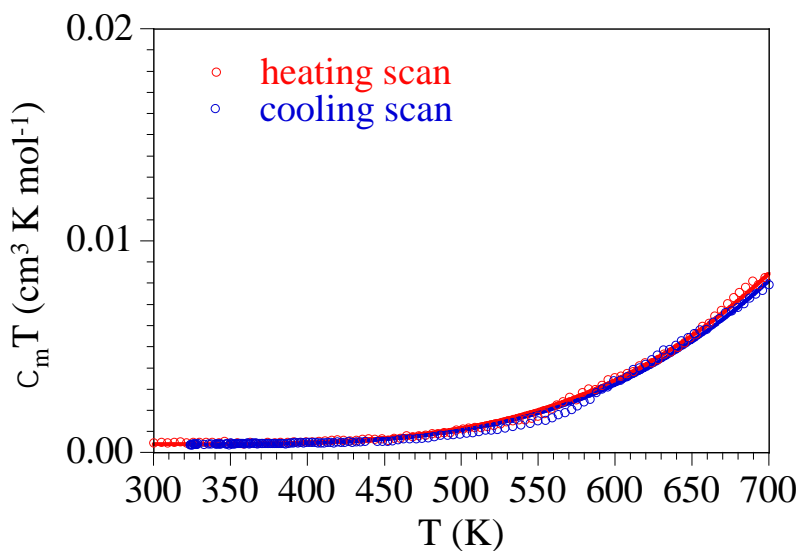


Figure B10. Variable temperature SQUID measurement of *anti*-IIDBT **1b** in the heating (red points) and cooling scans (blue points). Solid lines are the best fit to the Bleaney-Bowers dimer model.

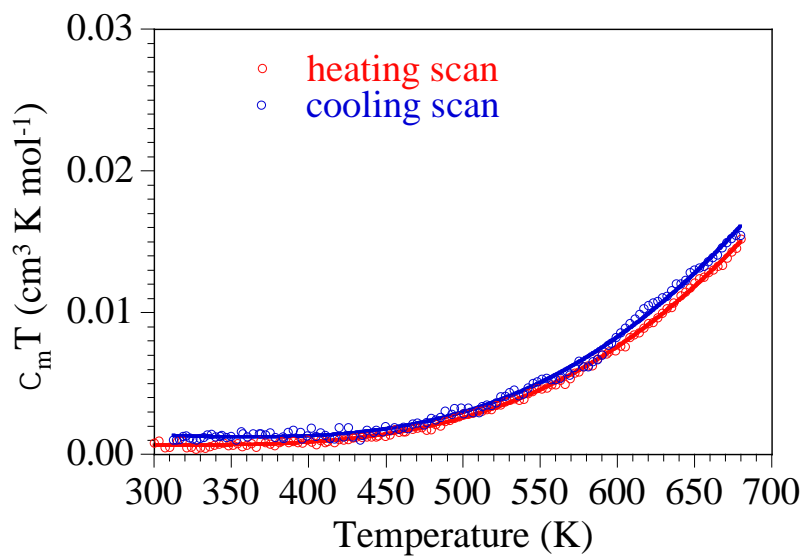
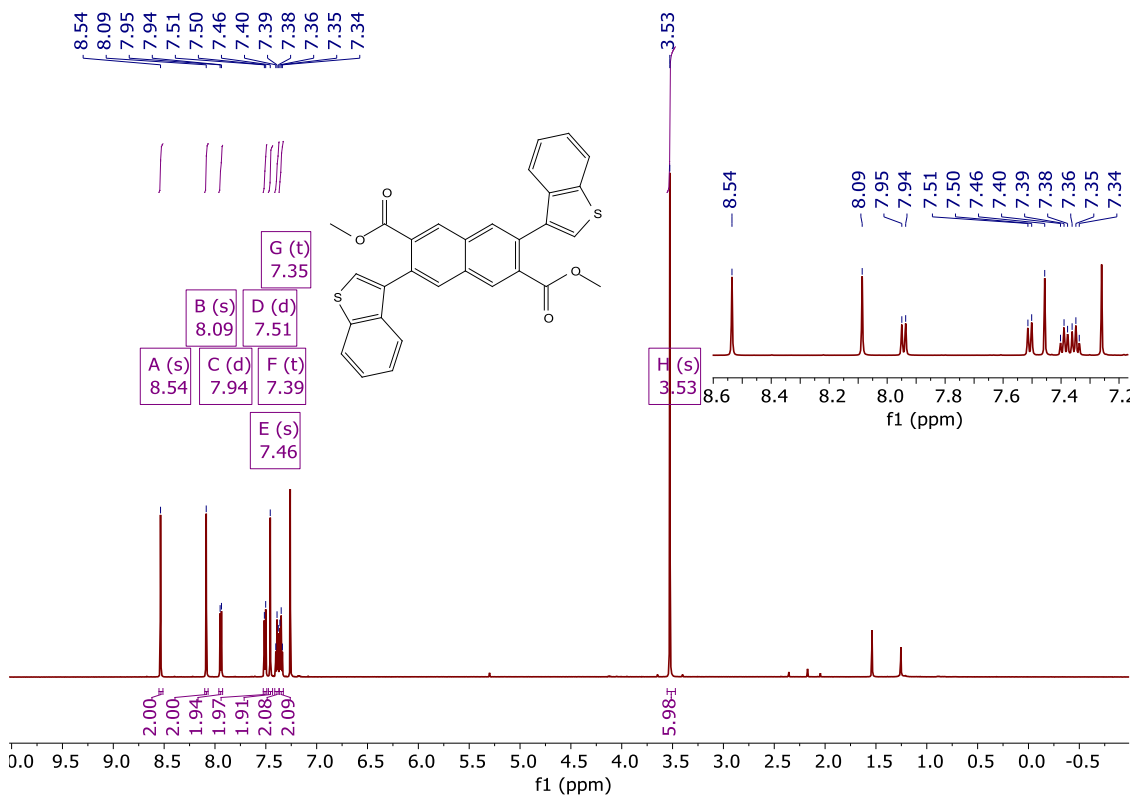
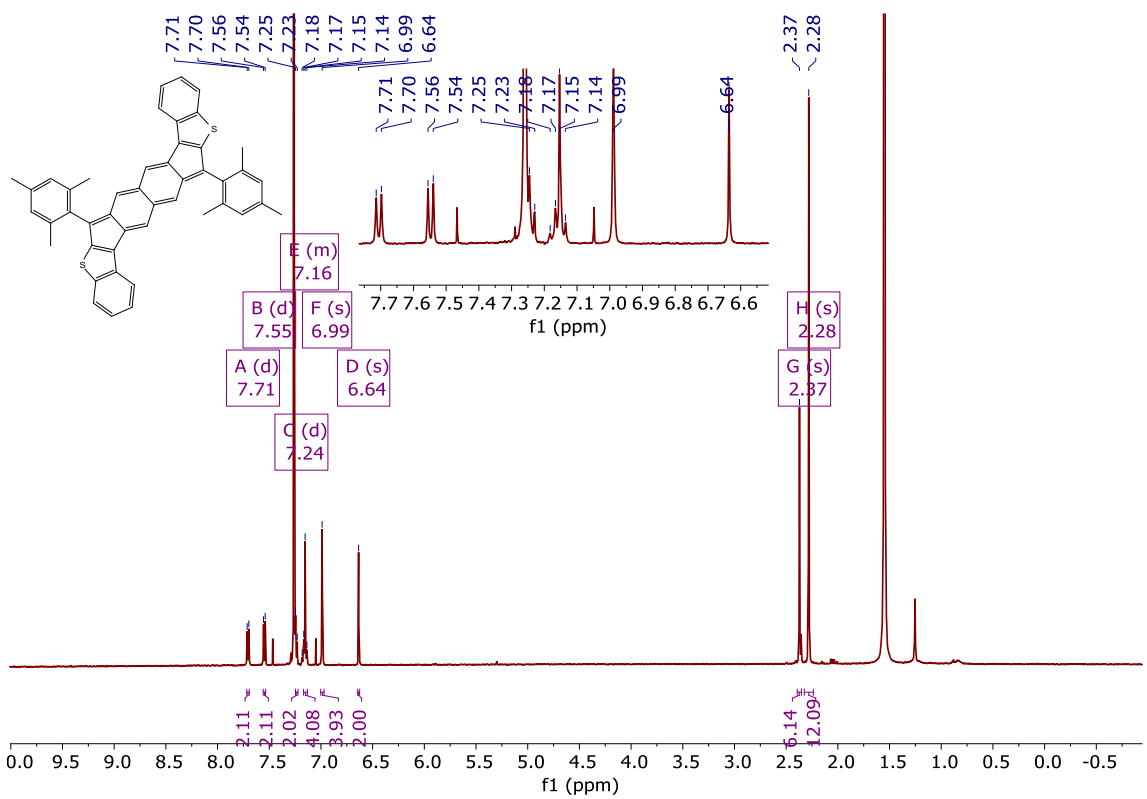
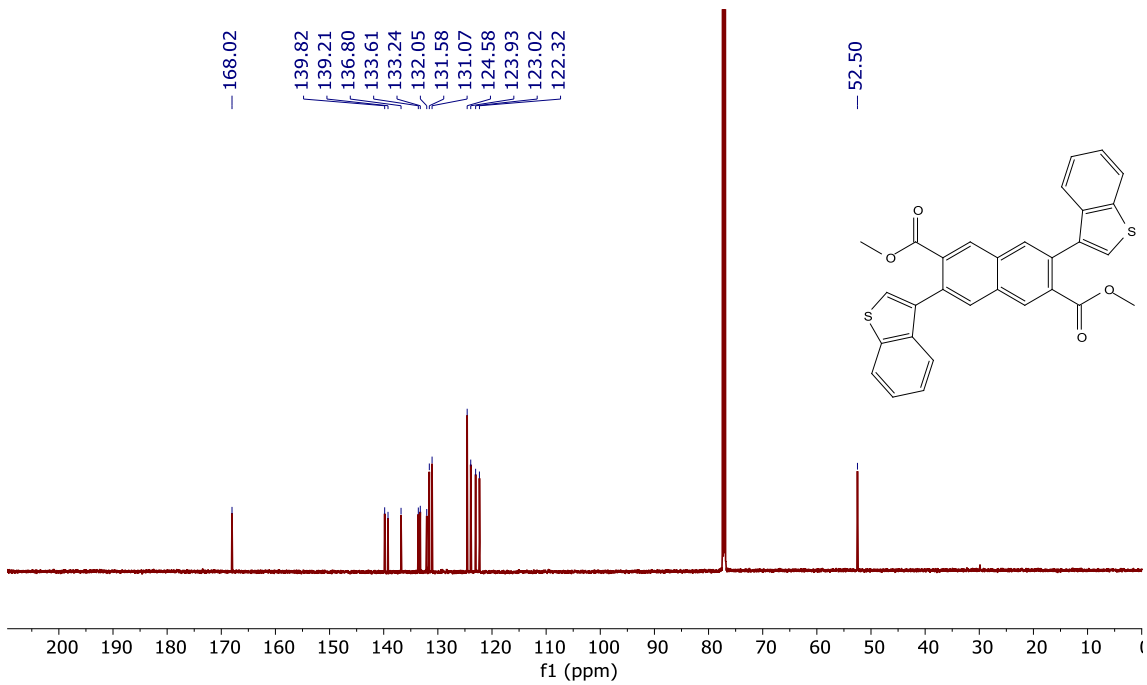
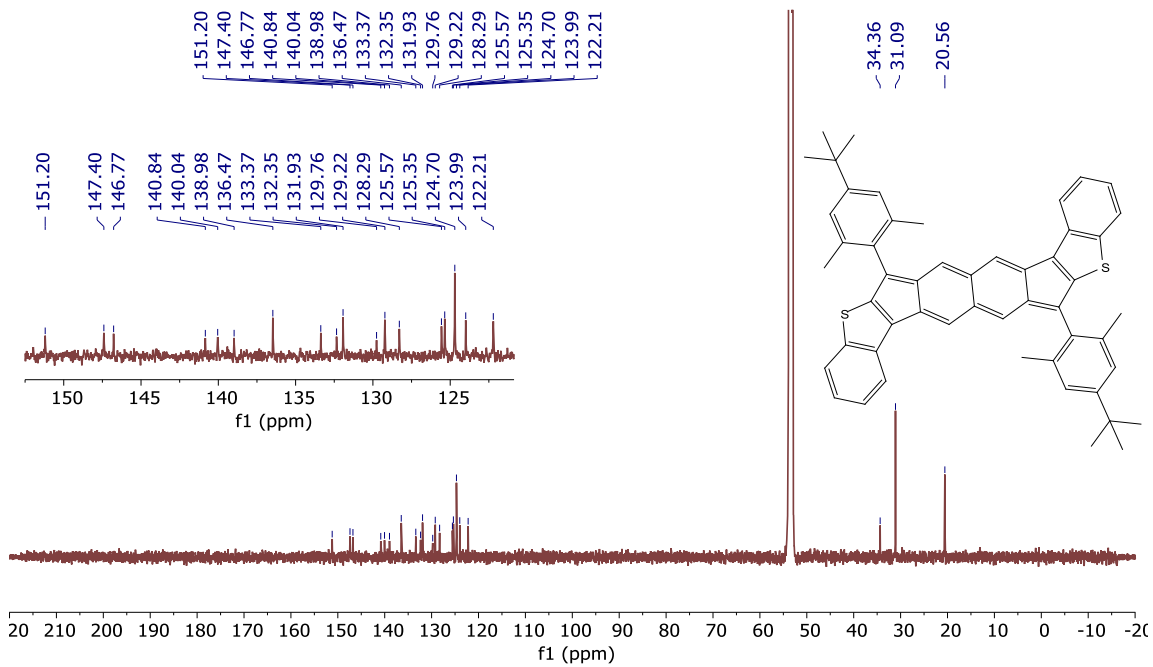
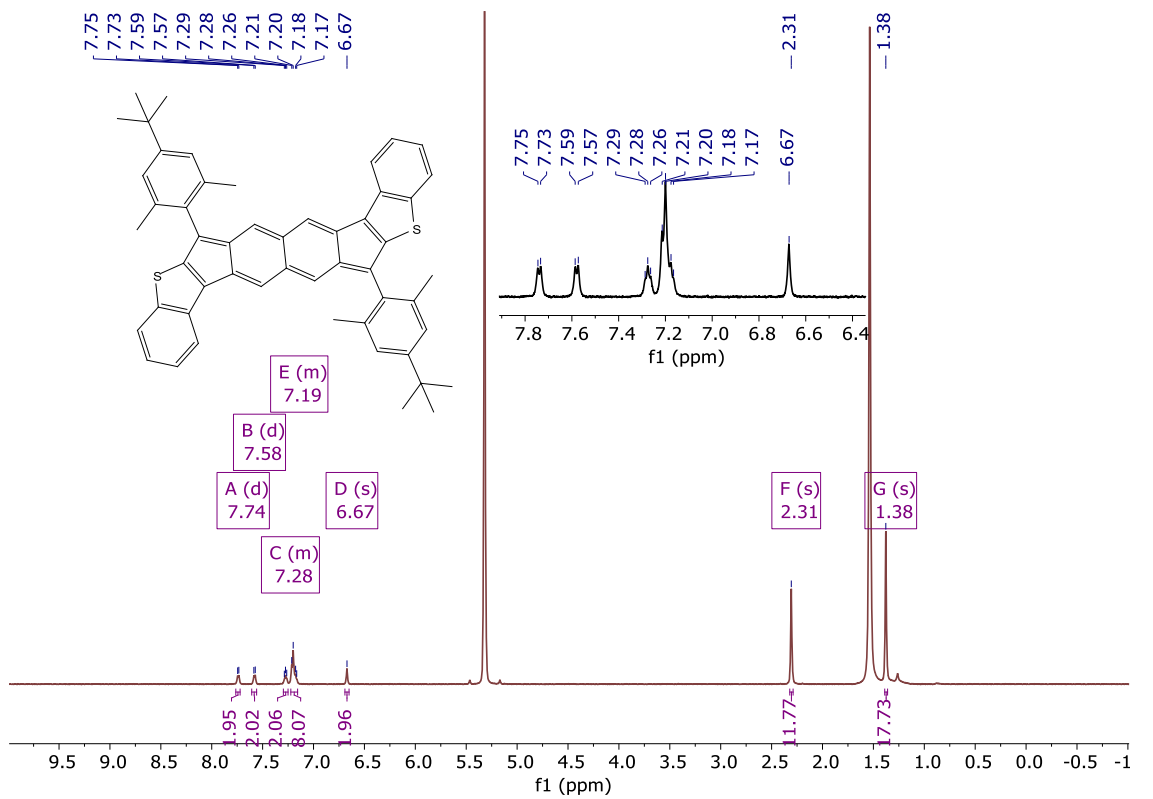


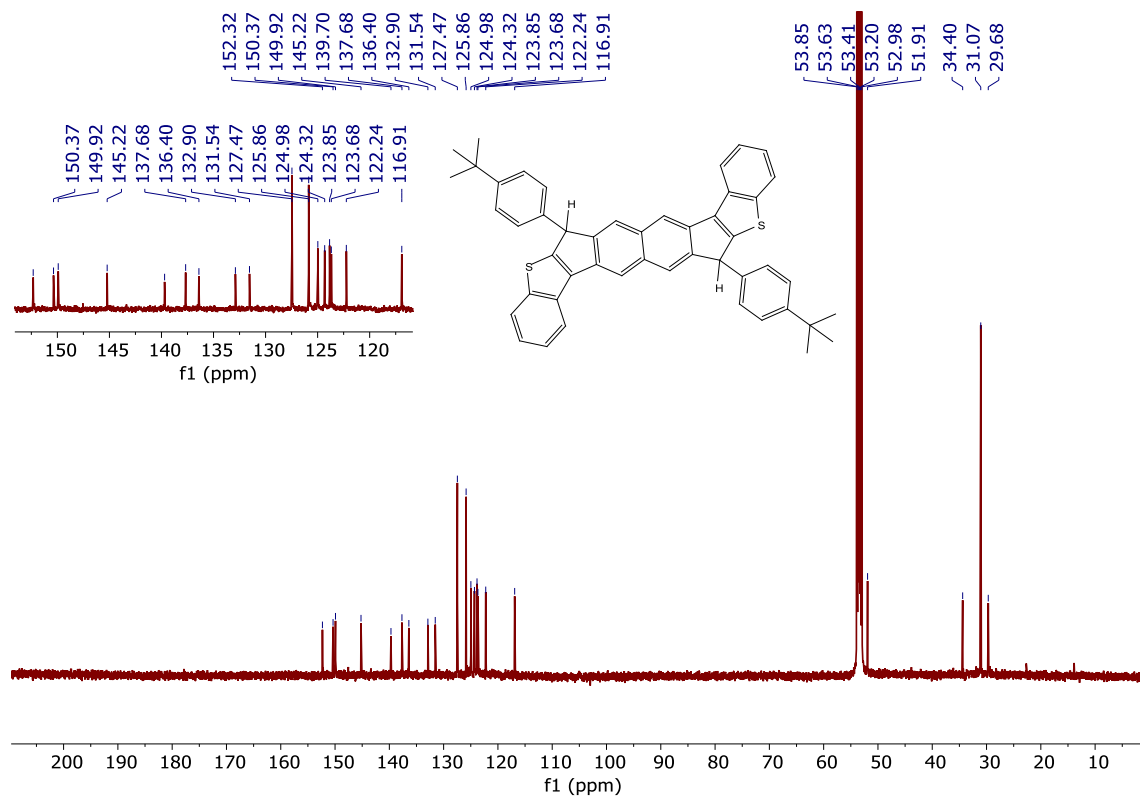
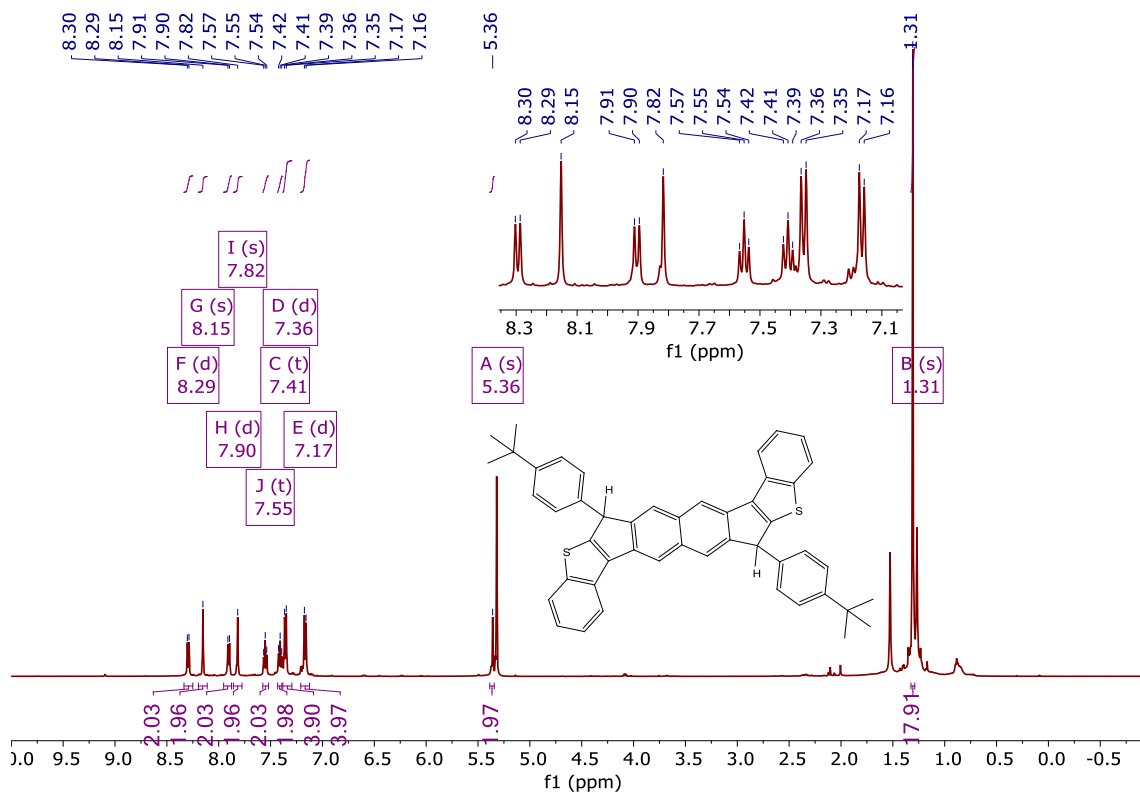
Figure B11. Variable temperature SQUID measurement of *syn*-IIDBT **2b** in the heating (red points) and cooling scans (blue points). Solid lines are the best fit to the Bleaney-Bowers dimer model.

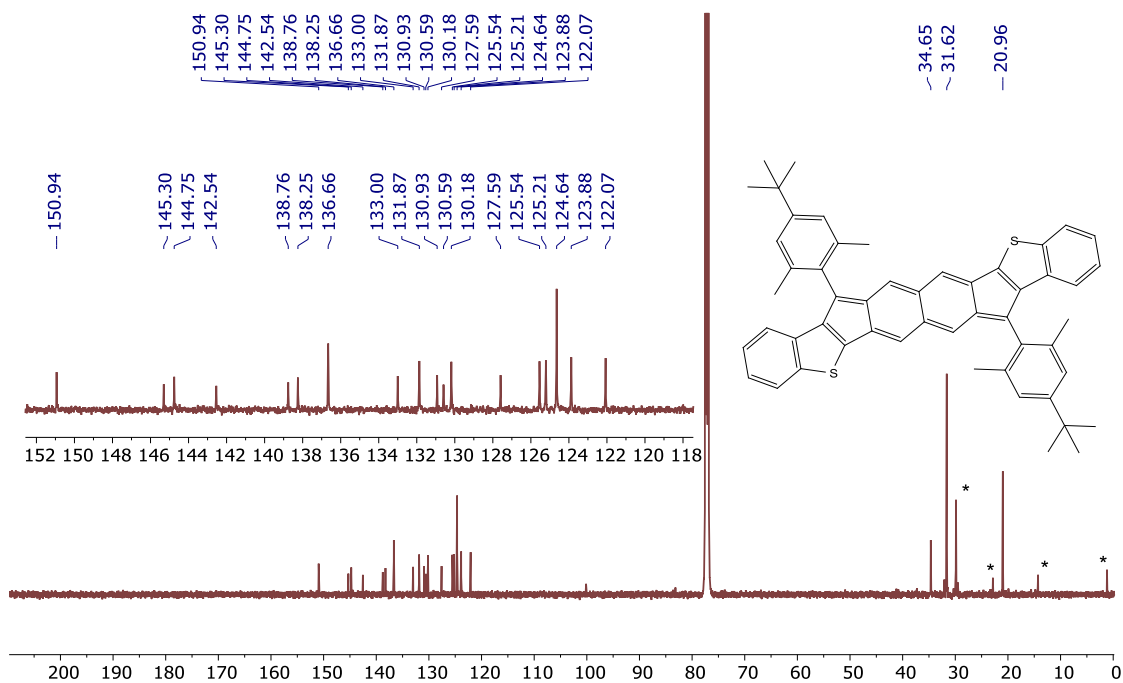
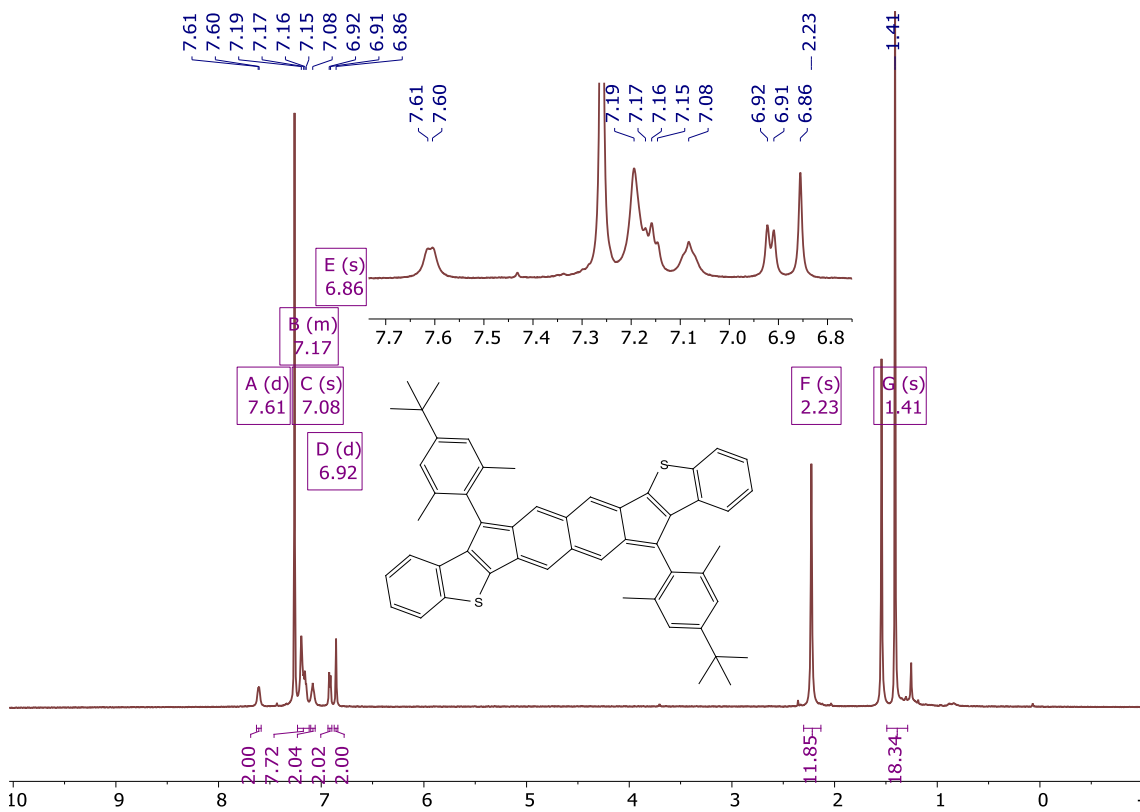
Copies of NMR Spectra











References

- (1) Shao, Y.; Head-Gordon, M.; Krylov, A. I. *J. Chem. Phys.* **2003**, *118*, 4807.
- (2) (a) Wang, F.; Ziegler, T. *J. Chem. Phys.* **2004**, *121*, 12191; (b) Wang, F.; Ziegler, T. *J. Chem. Phys.* **2005**, *122*, 074109. c) Wang, F.; Ziegler, T. *Int. J. Quantum Chem.* **2006**, *106*, 2545.
- (3) Stein, T.; Eisenberg, H.; Kronik, L.; Baer, R. *Phys. Rev. Lett.* **2010**, *105*, 266802.
- (4) Frisch, M. J.; Trucks, G. W.; Schlegel, H. B.; Scuseria, G. E.; Robb, M. A.; Cheeseman, J. R.; Scalmani, G.; Barone, V.; Mennucci, B.; Petersson, G. A.; Nakatsuji, H.; Caricato, M.; Li, X.; Hratchian, H. P.; Izmaylov, A. F.; Bloino, J.; Zheng, G.; Sonnenberg, J. L.; Hada, M.; Ehara, M.; Toyota, K.; Fukuda, R.; Hasegawa, J.; Ishida, M.; Nakajima, T.; Honda, Y.; Kitao, O.; Nakai, H.; Vreven, T.; Montgomery, J. A., J.; Peralta, J. E.; Ogliaro, F.; Bearpark, M.; Heyd, J. J.; Brothers, E.; Kudin, K. N.; Staroverov, V. N.; Kobayashi, R.; Normand, J.; Raghavachari, K.; Rendell, A.; Burant, J. C.; Iyengar, S. S.; Tomasi, J.; Cossi, M.; Rega, N.; Millam, J. M.; Klene, M.; Knox, J. E.; Cross, J. B.; Bakken, V.; Adamo, C.; Jaramillo, J.; Gomperts, R.; Stratmann, R. E.; Yazyev, O.; Austin, A. J.; Cammi, R.; Pomelli, C.; Ochterski, J. W.; Martin, R. L.; Morokuma, K.; Zakrzewski, V. G.; Voth, G. A.; Salvador, P.; Dannenberg, J. J.; Dapprich, S.; Daniels, A. D.; Farkas, Ö.; Foresman, J. B.; Ortiz, J. V.; Cioslowski, J.; Fox, D. J. *Gaussian 09*; Revision D.01; Gaussian, Inc.: Wallingford CT, 2009.
- (5) Schmidt, M. W.; Baldridge, K. K.; Boatz, J. A.; Elbert, S. T.; Gordon, M. S.; Jensen, J. H.; Koseki, S.; Matsunaga, N.; Nguyen, K. A.; Su, S.; Windus, T. L.; Dupuis, M.; Montgomery, J. A. *J. Comput. Chem.* **1993**, *14*, 1347.
- (6) Shao, Y.; Gan, Z.; Epifanovsky, E.; Gilbert, A. T. B.; Wormit, M.; Kussmann, J.;

Lange, A. W.; Behn, A.; Deng, J.; Feng, X.; Ghosh, D.; Goldey, M.; Horn, P. R.;
Jacobson, L. D.; Kaliman, I.; Khaliullin, R. Z.; Kuś, T.; Landau, A.; Liu, J.; Proynov, E.
I.; Rhee, Y. M.; Richard, R. M.; Rohrdanz, M. A.; Steele, R. P.; Sundstrom, E. J.;
Woodcock, H. L.; Zimmerman, P. M.; Zuev, D.; Albrecht, B.; Alguire, E.; Austin, B.;
Beran, G. J. O.; Bernard, Y. A.; Berquist, E.; Brandhorst, K.; Bravaya, K. B.; Brown, S.
T.; Casanova, D.; Chang, C.-M.; Chen, Y.; Chien, S. H.; Closser, K. D.; Crittenden, D.
L.; Diedenhofen, M.; DiStasio, R. A.; Do, H.; Dutoi, A. D.; Edgar, R. G.; Fatehi, S.;
Fusti-Molnar, L.; Ghysels, A.; Golubeva-Zadorozhnaya, A.; Gomes, J.; Hanson-Heine,
M. W. D.; Harbach, P.H.P.; Hauser, A. W. ; Hohenstein, E. G.; Holden, Z. C.; Jagau, T.-
C.; Ji, H.; Kaduk, B.n; Khistyayev, K.; Kim, J.; Kim, J.; King, R. A.; Klunzinger, P.;
Kosenkov, D.; Kowalczyk, T.; Krauter, C. M.; Lao, K. U.; Laurent, A. D.; Lawler, K. V.;
Levchenko, S. V.; Lin, C. Y.; Liu, F.; Livshits, E.; Lochan, R. C.; Luenser, A.; Manohar,
P.; Manzer, S. F.; Mao, S.-P.; Mardirossian, N.; Marenich, A. V.; Maurer, S. A.; Mayhall,
N. J.; Neuscamman, E.; Oana, C. M.; Olivares-Amaya, R.; O'Neill, D. P.; Parkhill, J. A.;
Perrine, T. M.; Peverati, R.; Prociuk, A.; Rehn, D. R.; Rosta, E.; Russ, N. J.; Sharada, S.
M.; Sharma, S.; Small, D. W.; Sodt, A.; Stein, T.; Stück, D.; Su, Y.-C.; Thom, A. J. W.;
Tsuchimochi, T.; Vanovschi, V.; Vogt, L.; Vydrov, O.; Wang, T.; Watson, M. A.;
Wenzel, J.; White, A.; Williams, C. F.; Yang, J.; Yeganeh, S.; Yost, S. R.; You, Z.-Q.;
Zhang, I. Y.; Zhang, X.; Zhao, Y.; Brooks, B. R.; Chan, G. K. L.; Chipman, D. M.;
Cramer, C. J.; Goddard, W. A.; Gordon, M. S.; Hehre, W. J.; Klamt, A.; Schaefer, H. F.;
Schmidt, M. W.; Sherrill, C. D.; Truhlar, D. G.; Warshel, A.; Xu, X.; Aspuru-Guzik, A.;
Baer, R.; Bell, A. T.; Besley, N. A.; Chai, J.-D.; Dreuw, A.; Dunietz, B. D.; Furlani, T.
R.; Gwaltney, S. R.; Hsu, C.-P.; Jung, Y.; Kong, J.; Lambrecht, D. S.; Liang, W.;

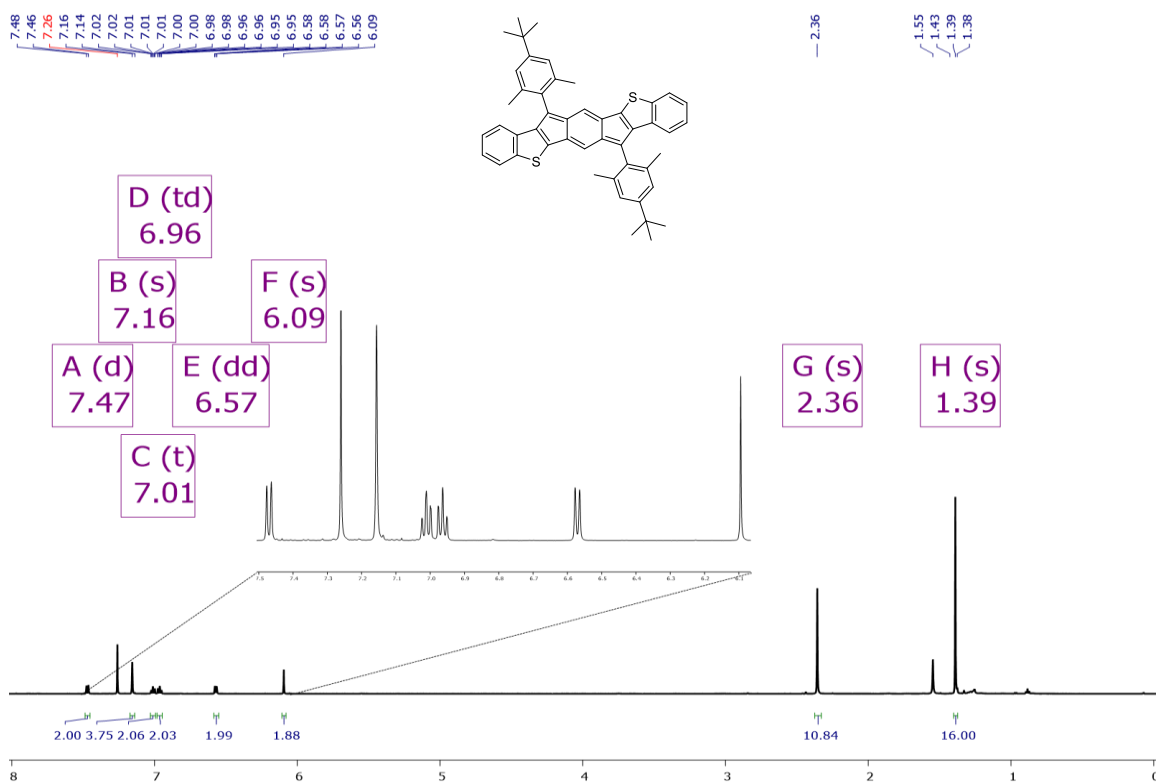
- Ochsenfeld, C.; Rassolov, V. A.; Slipchenko, L. V.; Subotnik, J. E.; Voorhis, T. V.; Herbert, J. M.; Krylov, A. I.; Gill, P. M. W.; Head-Gordon, M. *Mol. Phys.* **2015**, *113*, 184.
- (7) Nakano, M.; Fukui, H.; Minami, T.; Yoneda, K.; Shigeta, Y.; Kishi, R.; Champagne, B.; Botek, E.; Kubo, T.; Ohta, K. *Theor. Chem. Acc.* **2011**, *130*, 711.
- (8) Dressler, J. J.; Teraoka, M.; Espejo, G. L.; Kishi, R.; Takamuku, S.; Gómez-García, C. J.; Zakharov, L. N.; Nakano, M.; Casado, J.; Haley, M. M. *Nat. Chem.* **2018**, *10*, 1134–1140.
- (9) Knall, A.-C.; Ashraf, R. S.; Nikolka, M.; Nielsen, C. B.; Purushothaman, B.; Sadhanala, A.; Hurhangee, M.; Broch, K.; Harkin, D. J.; Novák, J.; Neophytou, M.; Hayoz, P.; Sirringhaus, H.; McCulloch, I. *Adv. Funct. Mater.* **2016**, *26*, 6961–6969.
- (10) Nakagawa, H.; Kawai, S.; Nakashima, T.; Kawai, T. *Org. Lett.* **2009**, *11*, 1475–1478.
- (11) Sheldrick, G. M. *Bruker/Siemens Area Detector Absorption Correction Program*, Bruker AXS, Madison, WI, 1998.
- (12) Spek, A. L. *Acta Cryst., Sect. C* **2015**, *C71*, 9–18.
- (13) Sheldrick, G. M. *Acta Cryst., Sect. C* **2015**, *C71*, 3–8.
- (14) CrysAlisPro, Rigaku OD, The Woodlands, TX, 2015.
- (15) Sheldrick, G. M. *Acta Cryst., Sect. A* **2008**, *A64*, 112–122.
- (16) Müller, P. *Crystallogr. Rev.* **2009**, *15*, 57–83.
- (17) Bain, G. A.; Berry, J. F. Diamagnetic corrections and Pascal's constants. *J. Chem. Educ.* **2008**, *85*, 532–536.
- (18) Bleaney, B.; Bowers, K. D. Anomalous Paramagnetism of Copper Acetate. *Proc. R. Soc. Lond. A.* **1952**, *214*, 451–465.

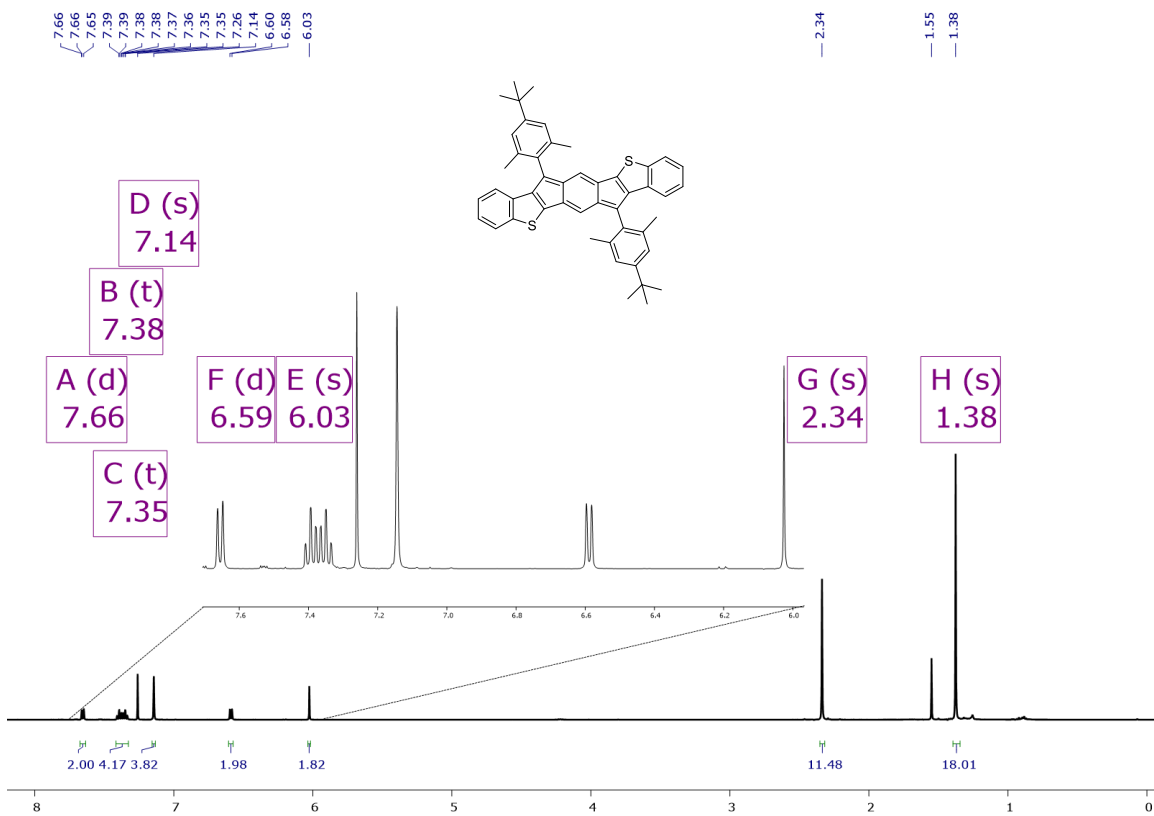
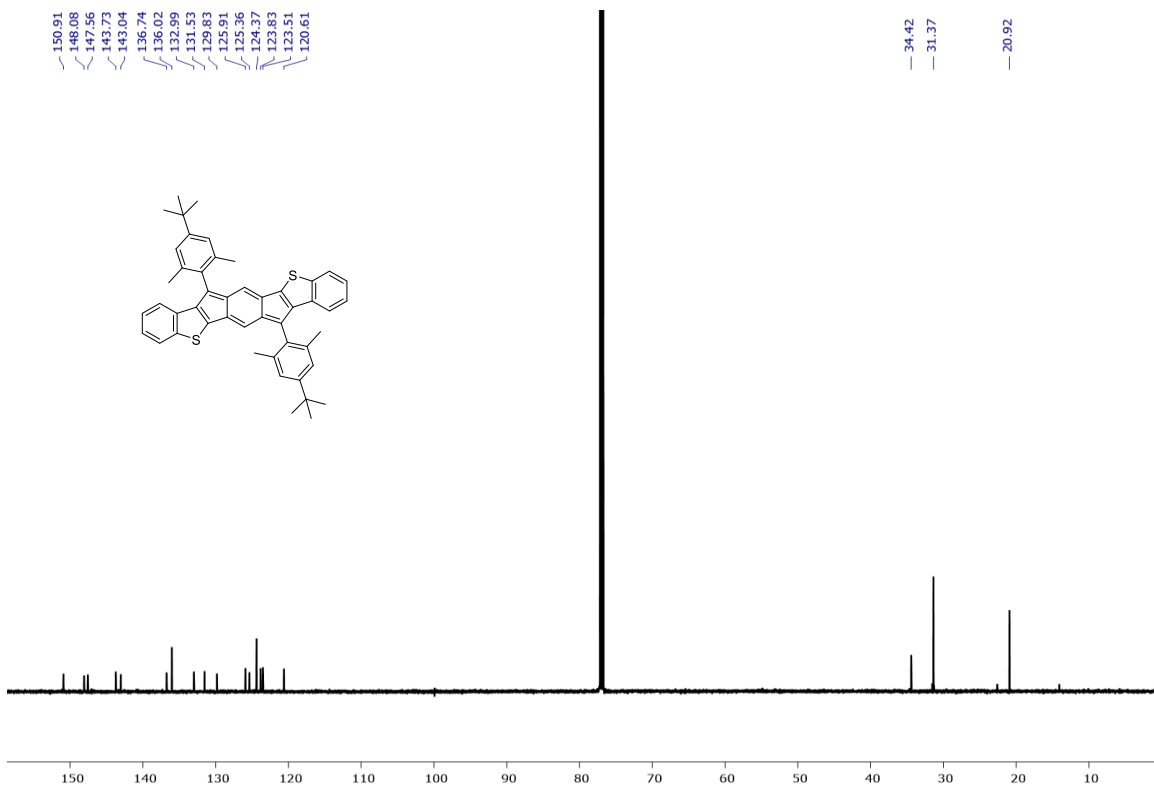
APPENDIX C

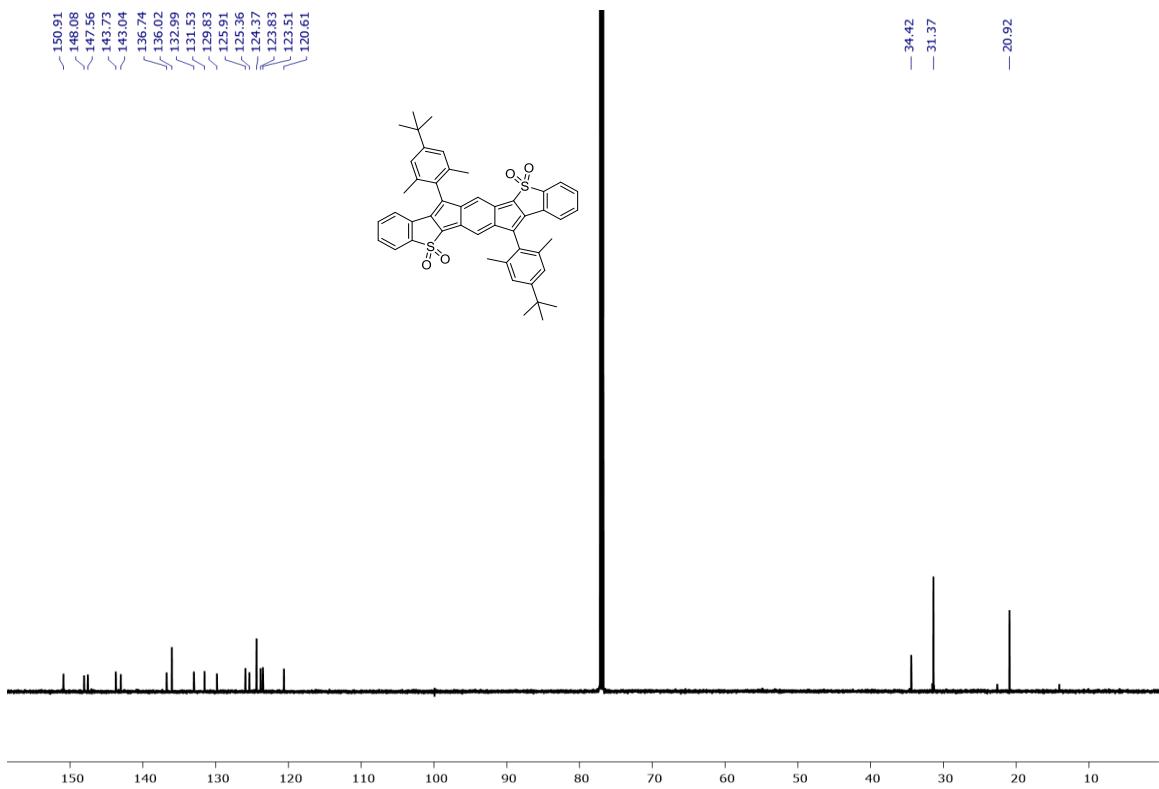
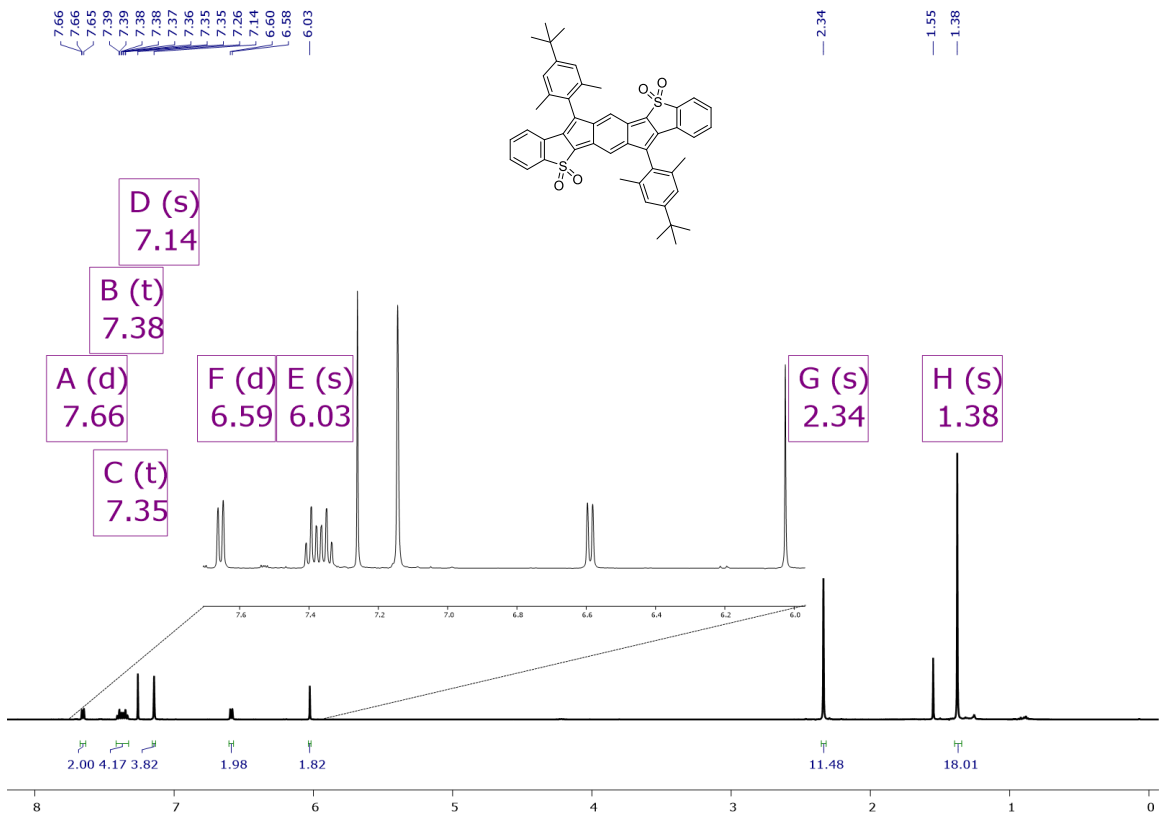
SUPPLEMENTARY INFORMATION FOR CHAPTER IV

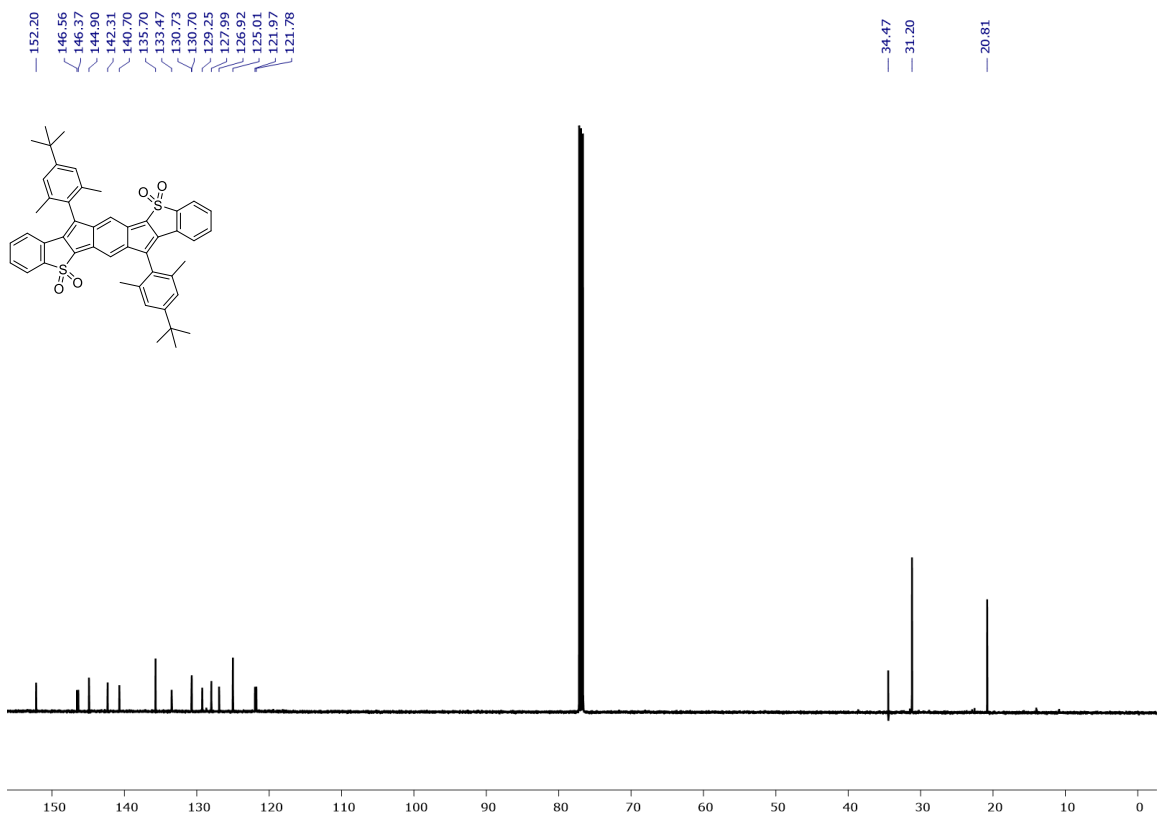
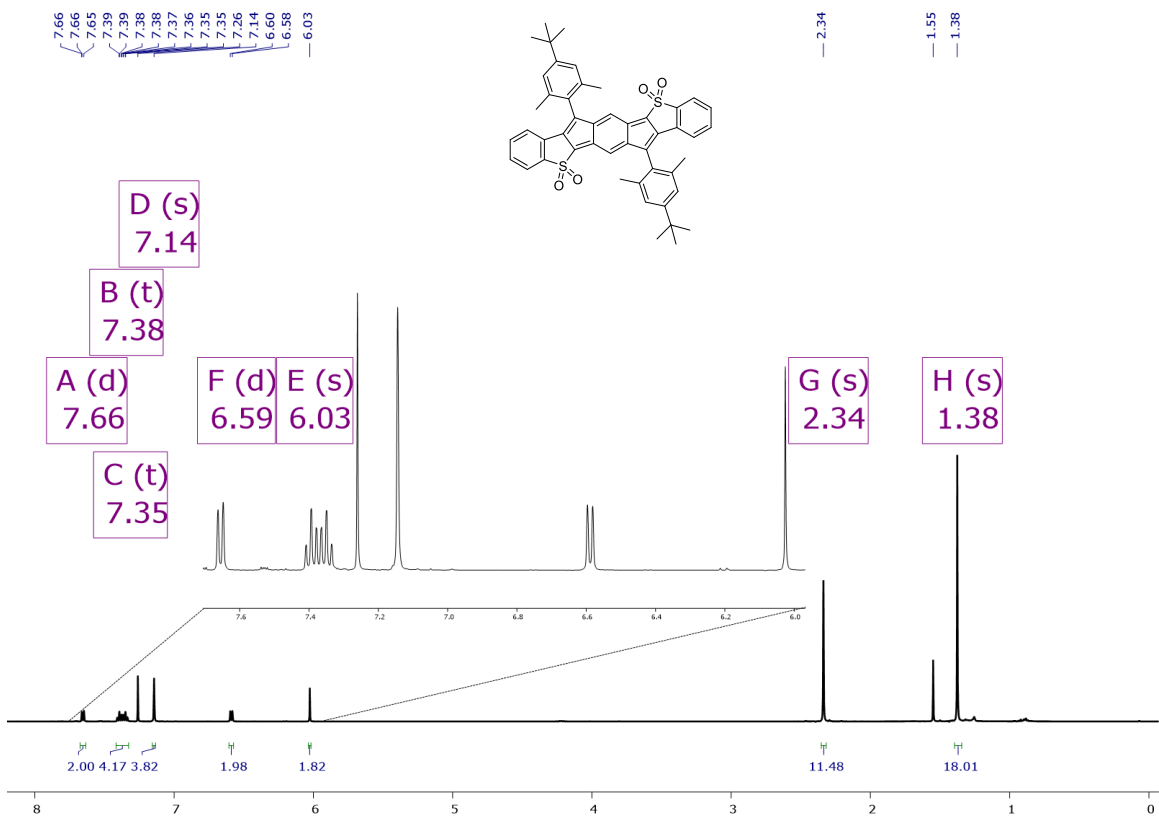
Appendix C is the supplementary information for Chapter IV of this dissertation. It includes experimental details, other experimental data, spectra, and computational details relevant to the content in Chapter IV.

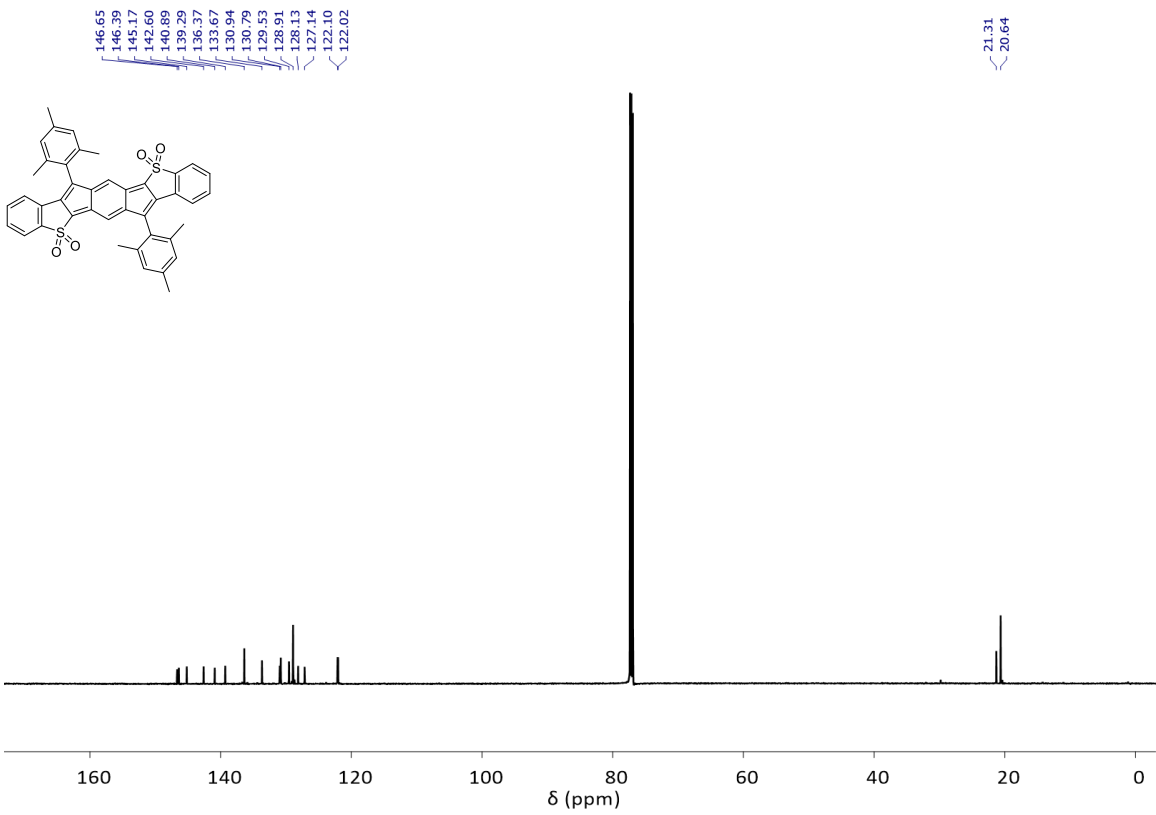
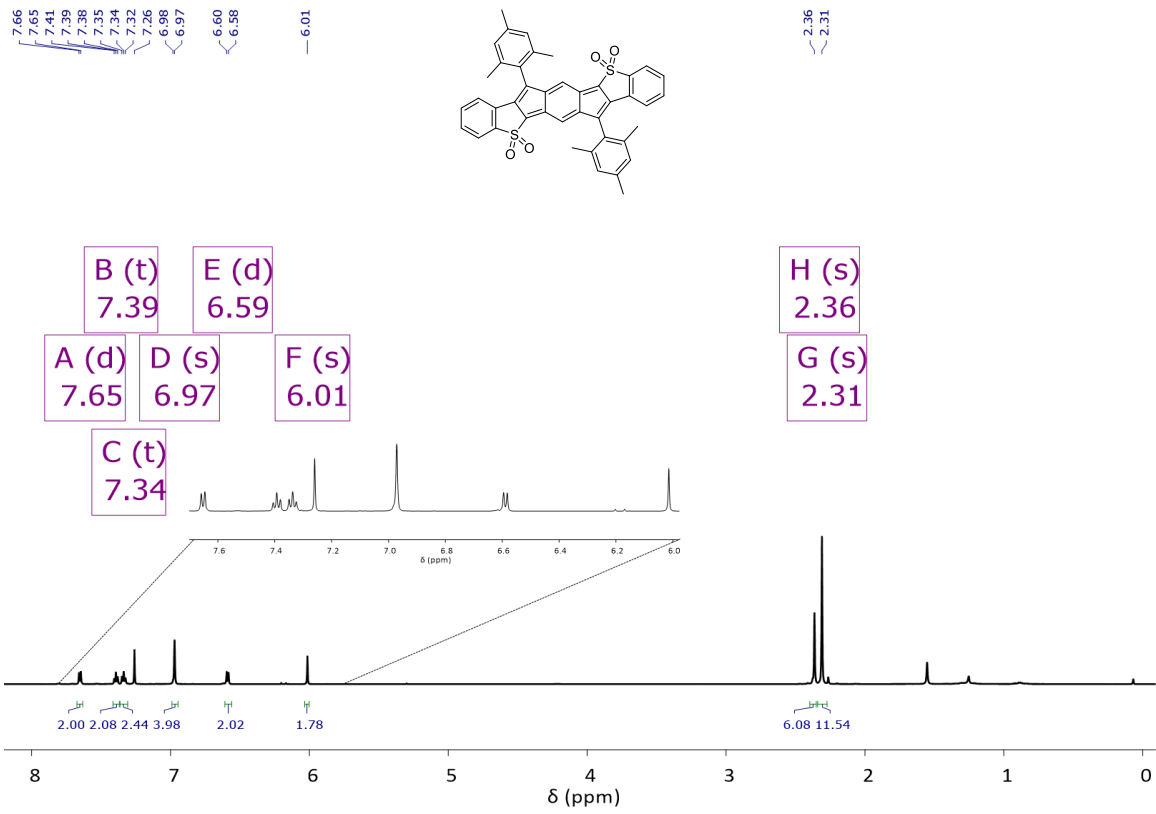
1. Copies of NMR Spectra

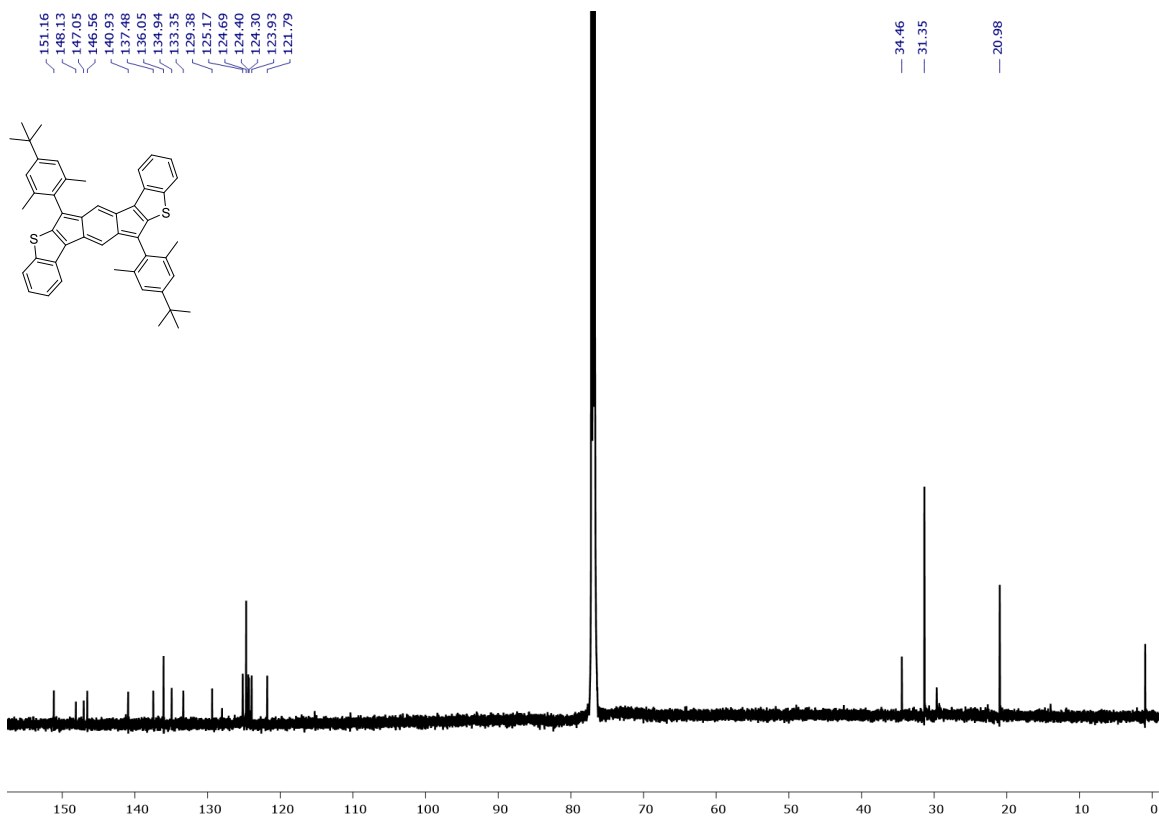
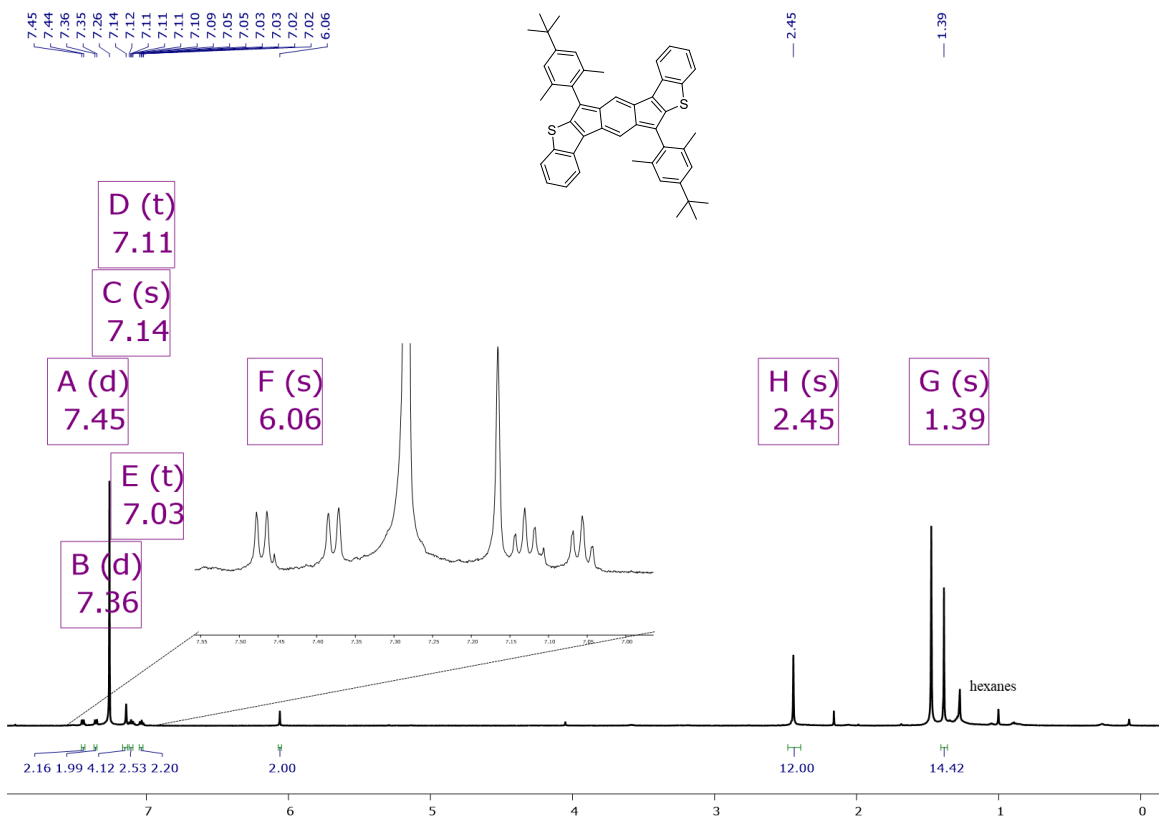


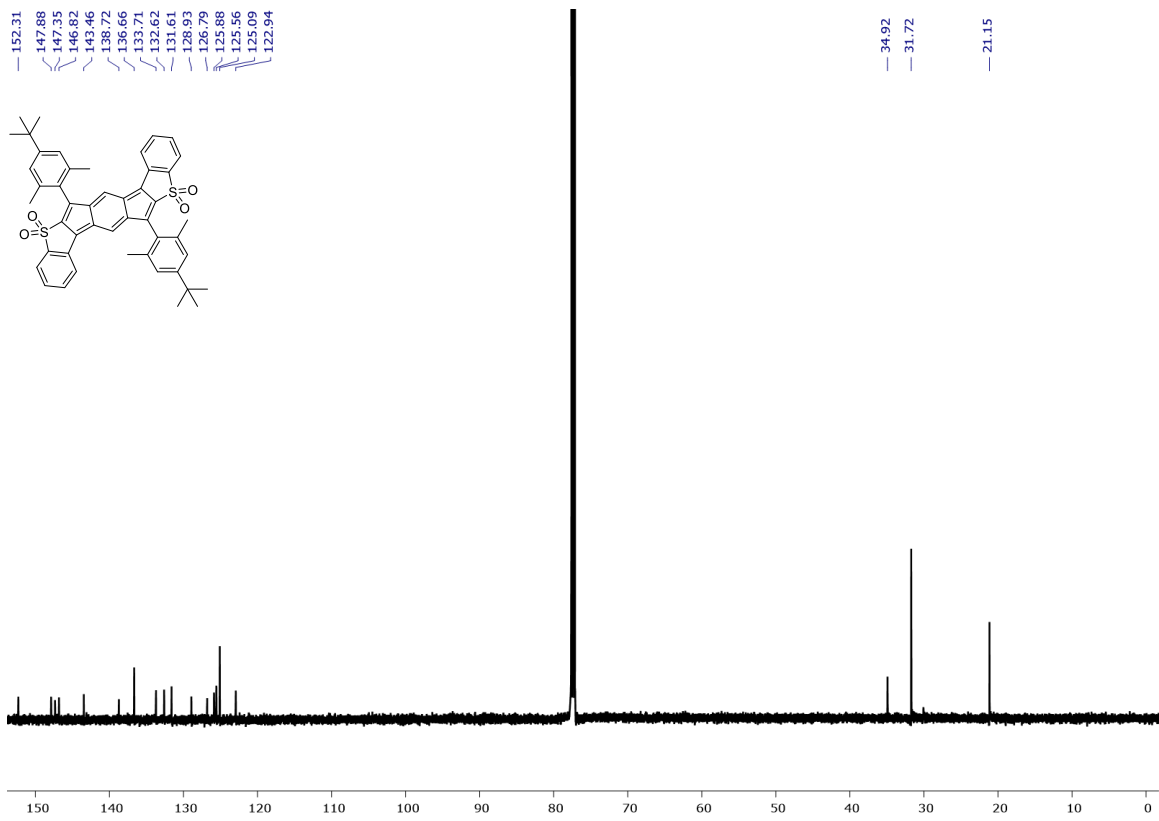
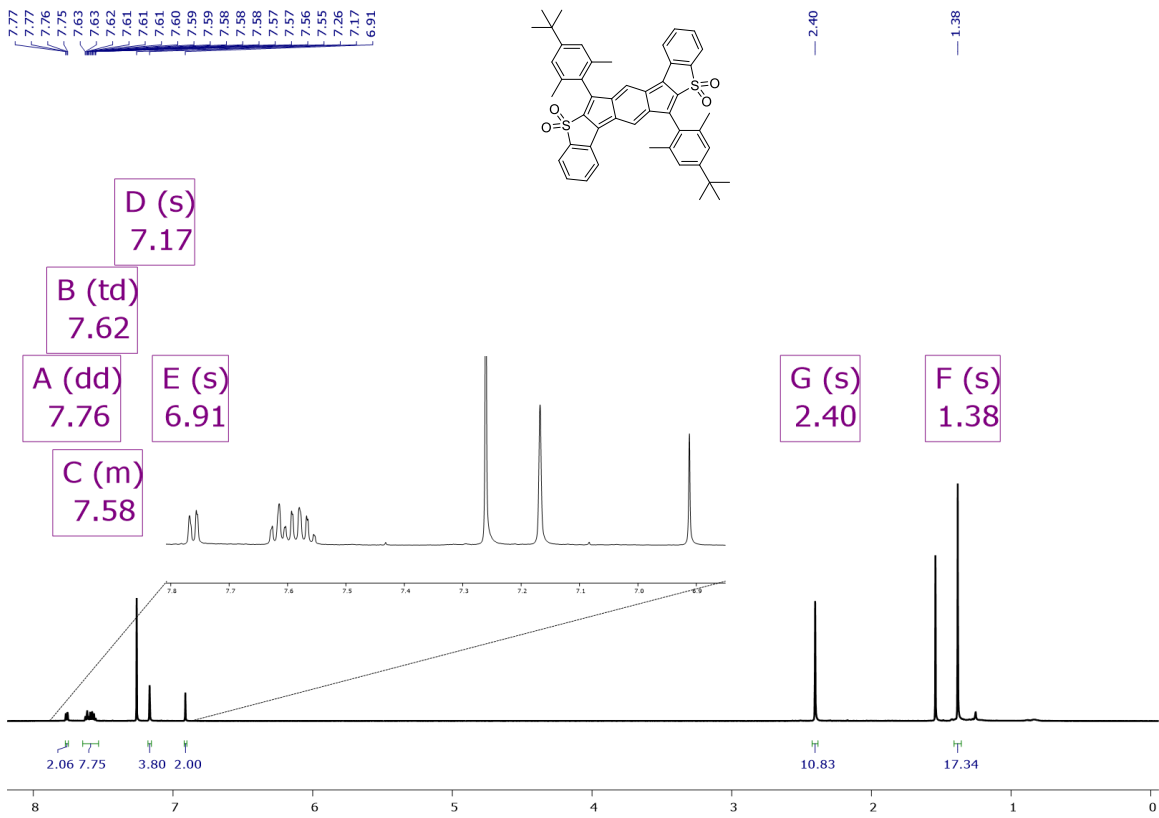


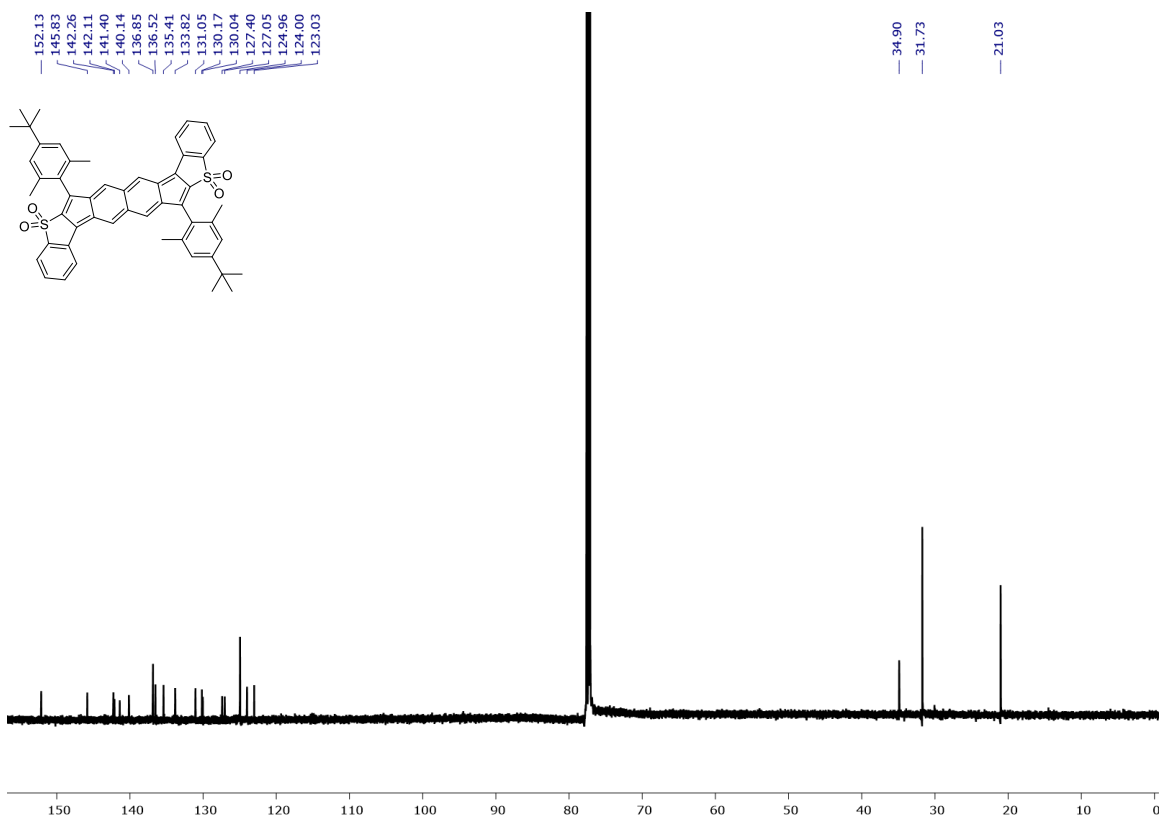
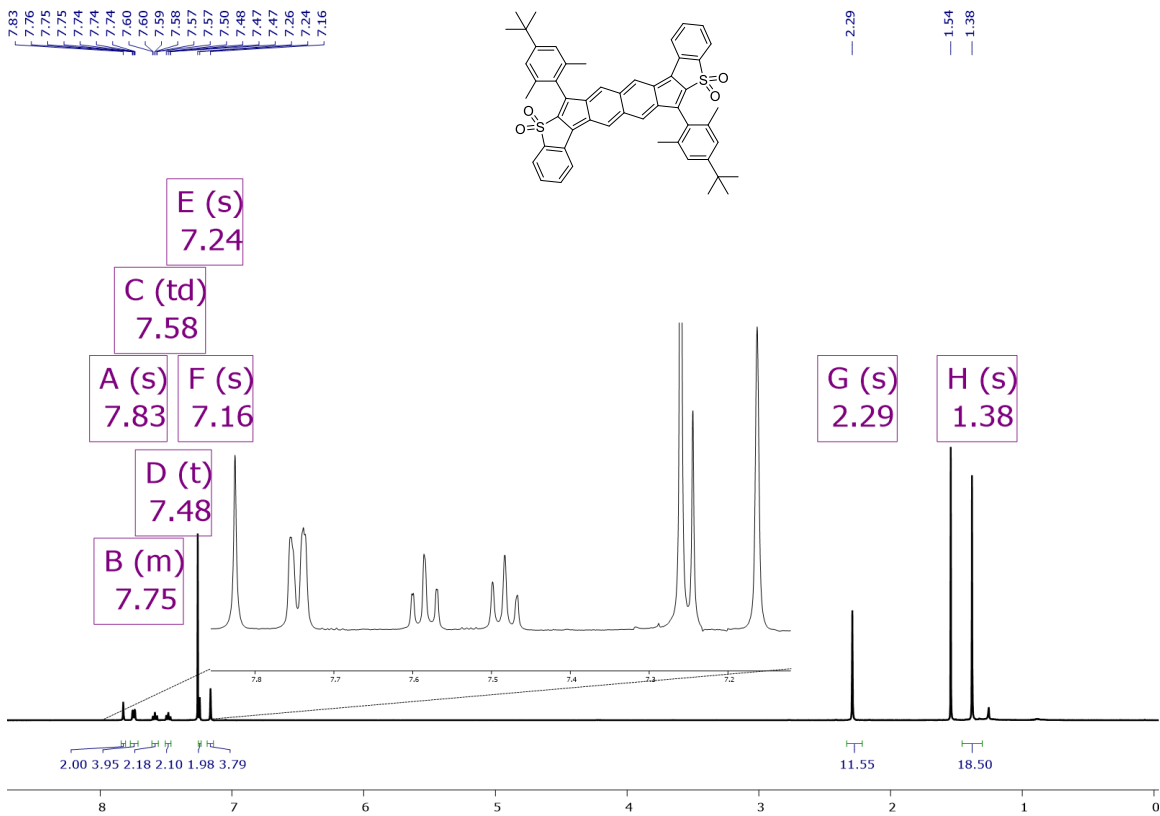


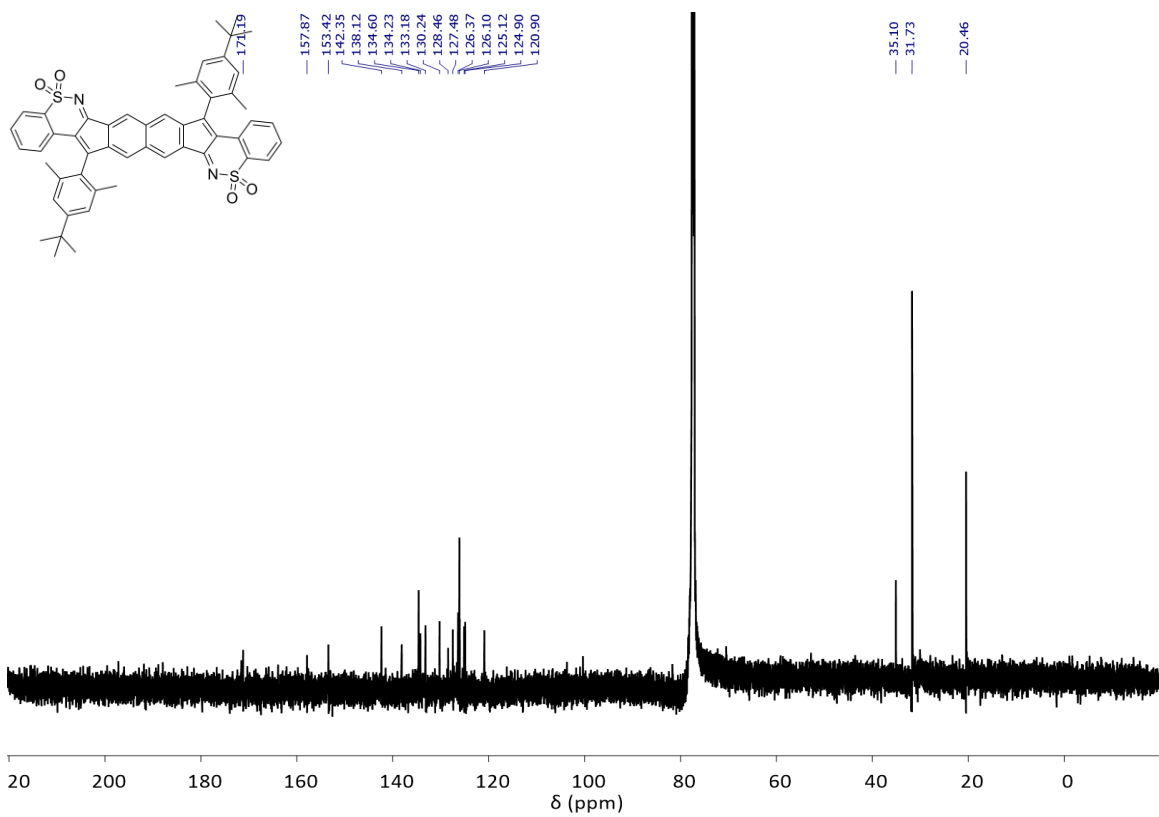
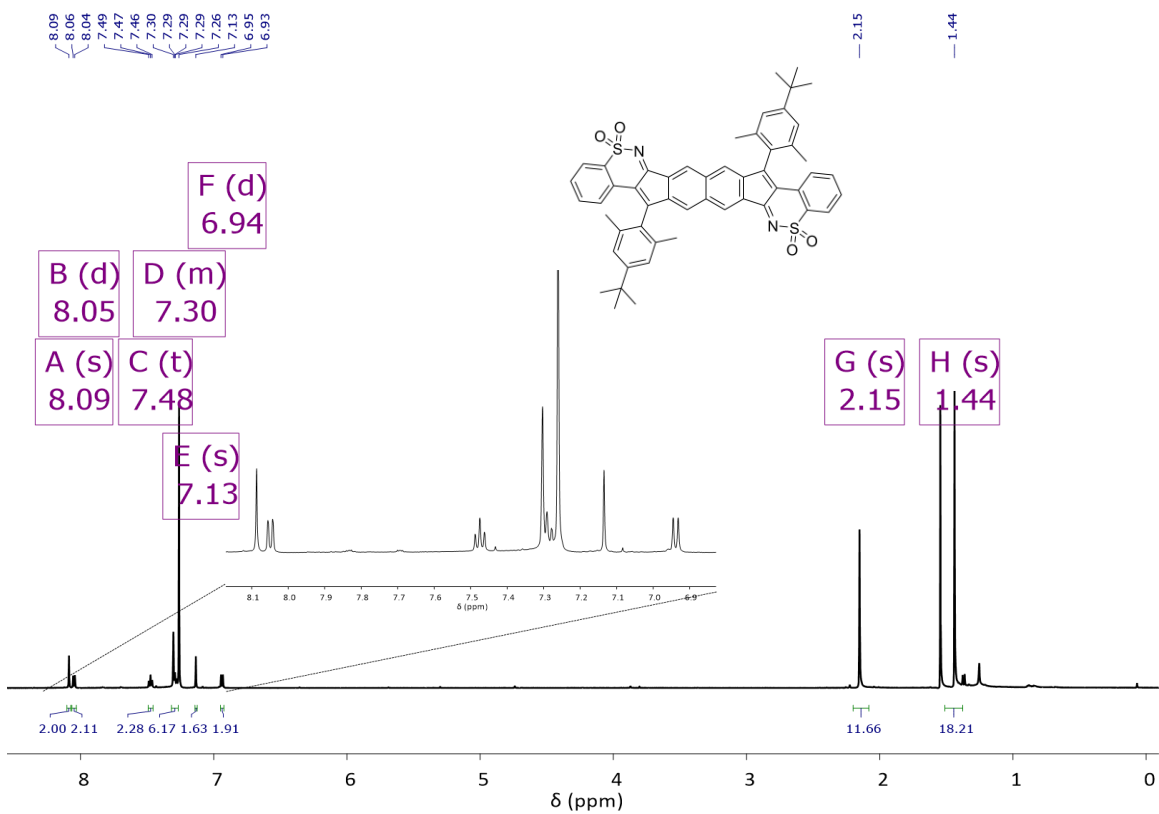












2. Additional Variable Temperature NMR Experiments

Approximately 5 mg of *syn*-IIDBT-sulfone (**8**) was placed in an NMR tube with different NMR solvents and the spectra were collected at different temperatures. The spectra were acquired on a Bruker 500 MHz spectrometer that was heated to the maximum temperature range of each NMR solvent.

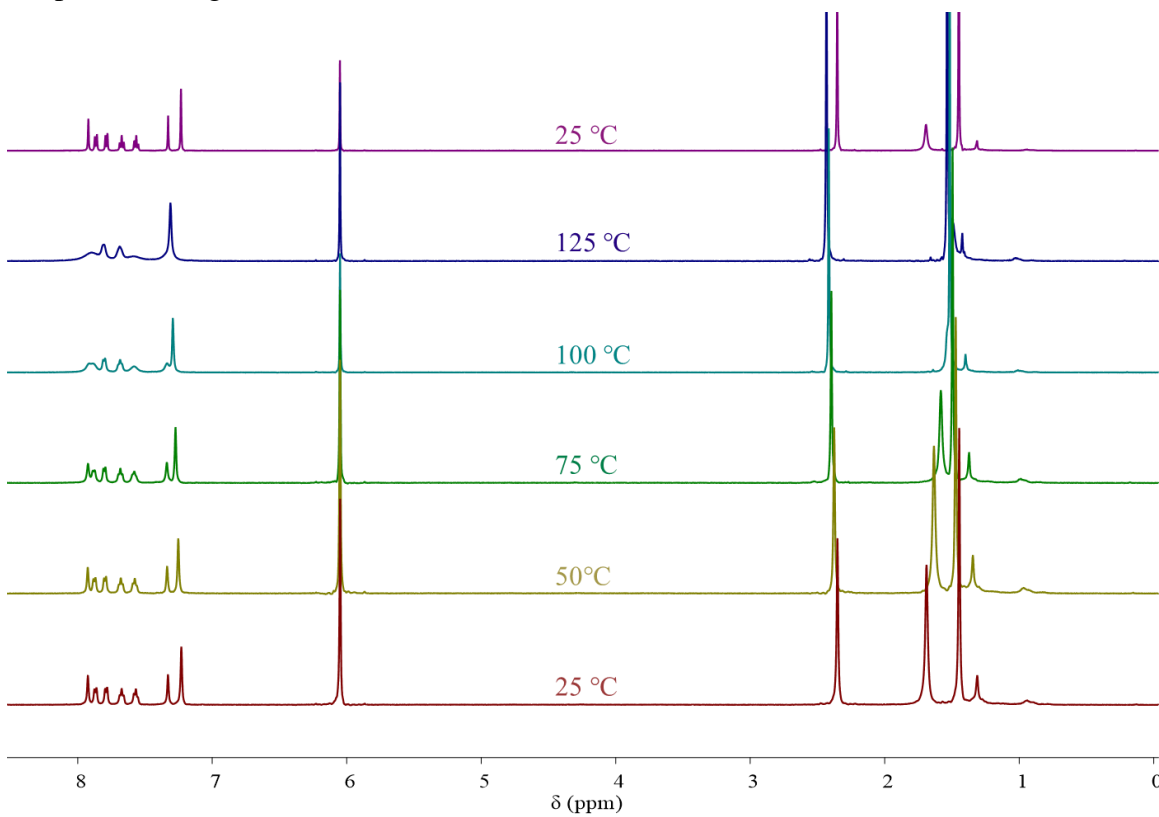


Figure C1. VT ¹H NMR full spectra of **8** in 1,1,2,2-tetrachloroethane-*d*₂ showing thermal population of the paramagnetic triplet state at elevated temperatures.

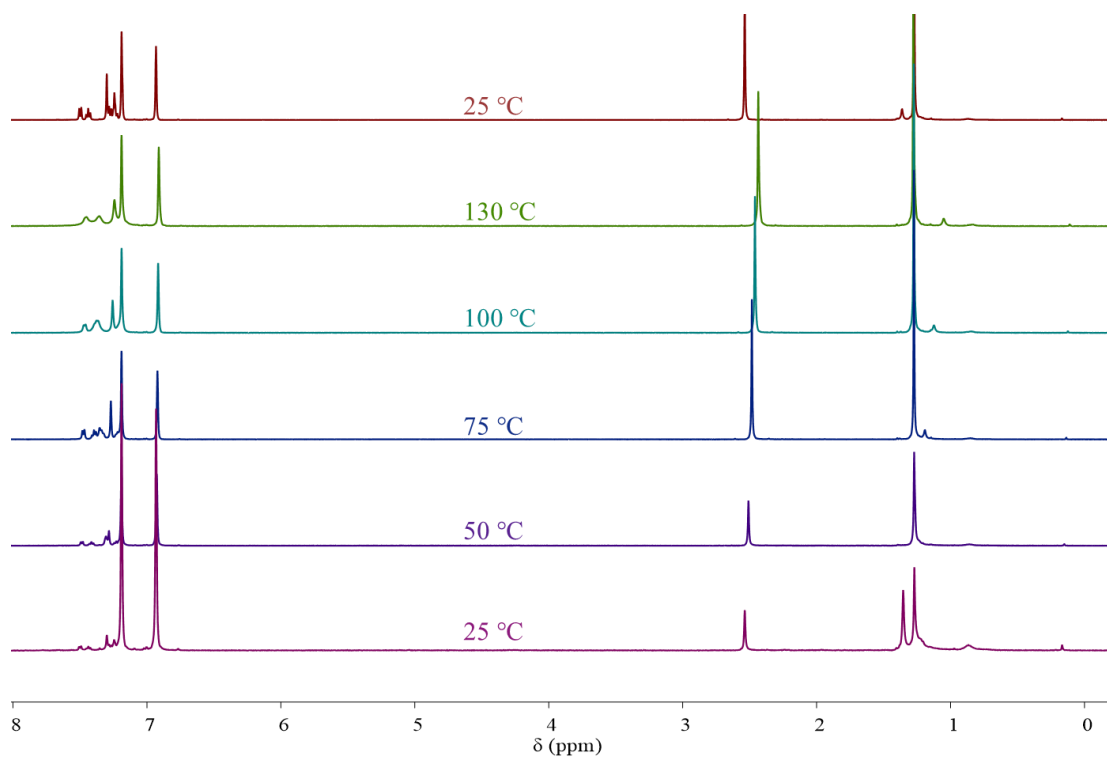


Figure C2. VT ^1H NMR full spectra of **8** in 1,2-dichlorobenzene- d_4 showing thermal population of the paramagnetic triplet state at elevated temperatures.

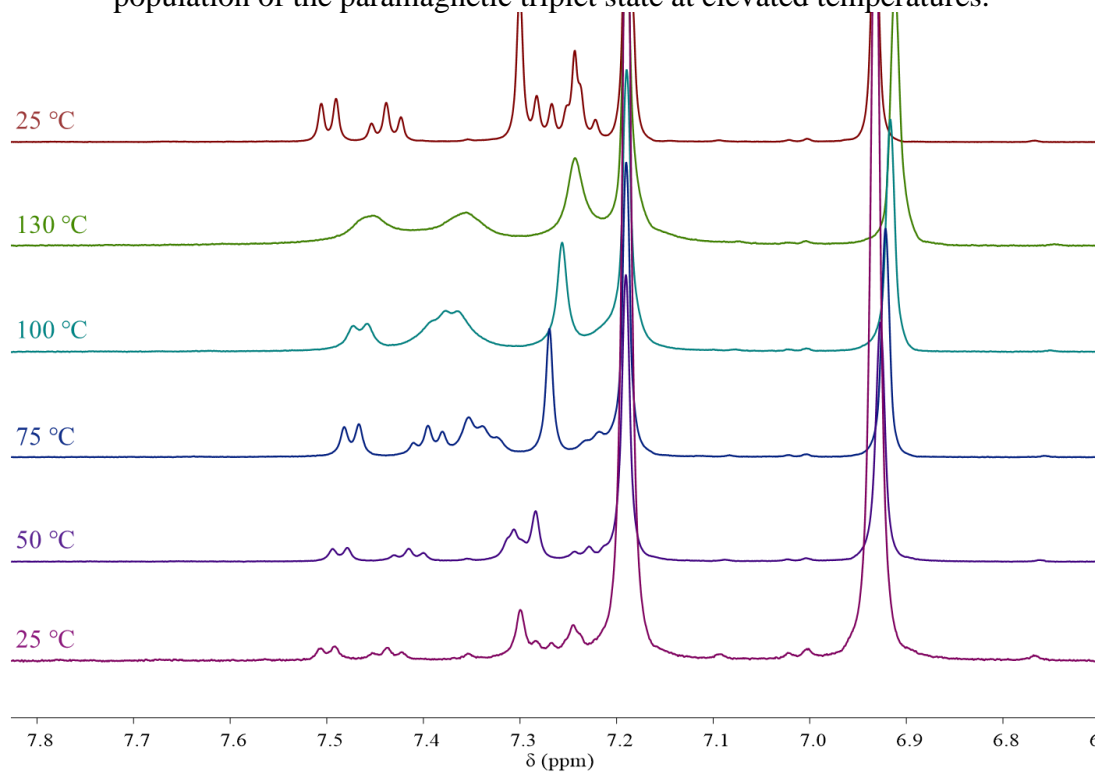


Figure C3. VT ^1H NMR of the aromatic region of **8** in 1,2-dichlorobenzene- d_4 showing thermal population of the paramagnetic triplet state at elevated temperatures.

3. TD-DFT Calculations for UV-Vis Spectra

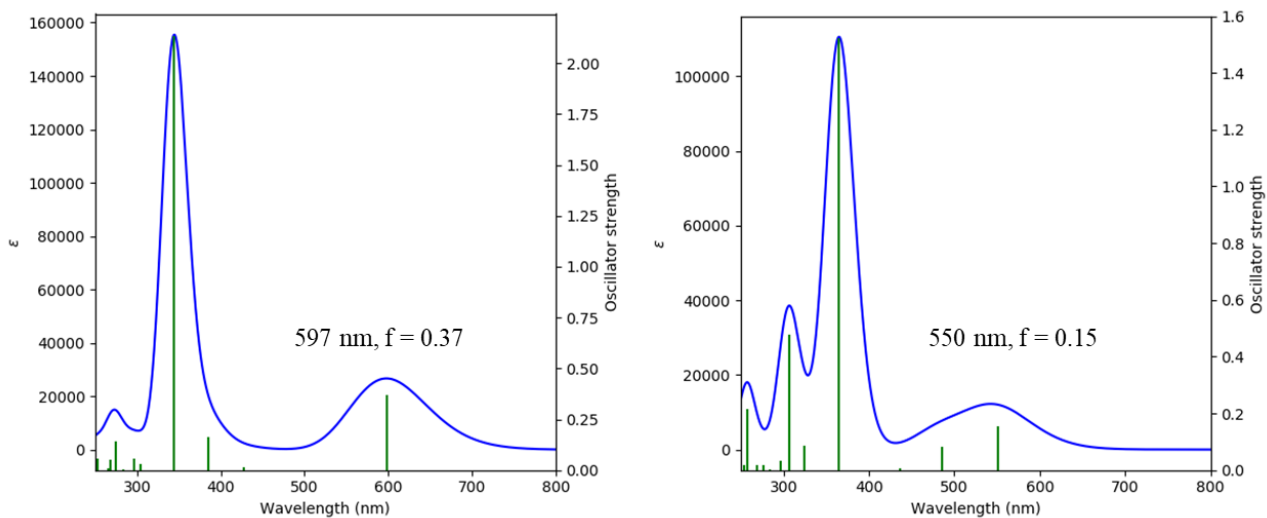


Figure C4. TD-DFT predicted UV-Vis spectra for (left) *anti*-IDBT (**1**) and for (right) *anti*-IDBT-sulfone (**5**) calculated at the TD-B3LYP/6-311++G** level of theory.

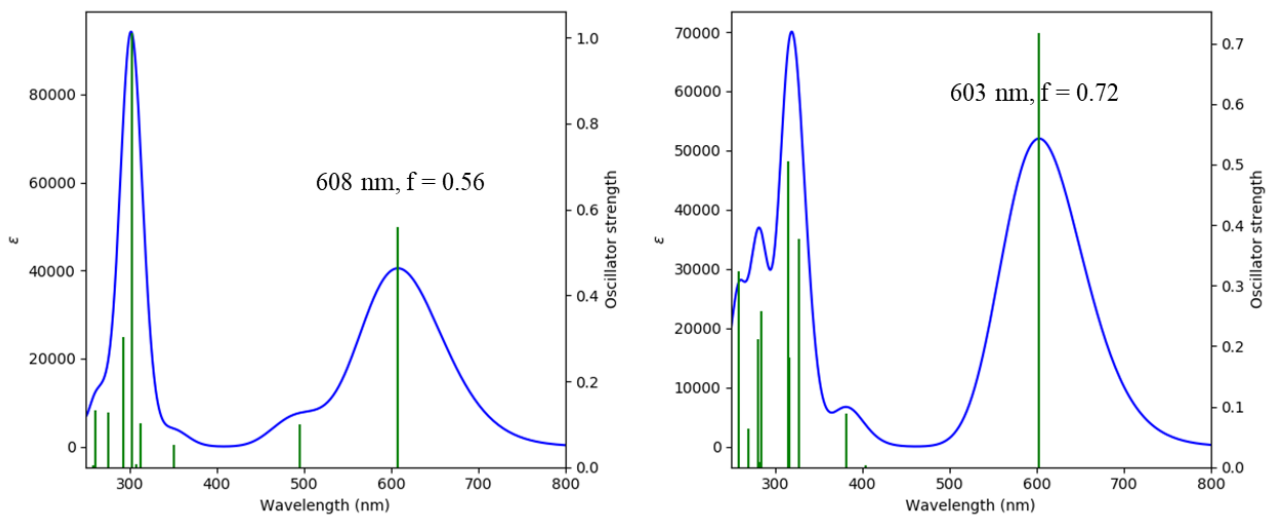


Figure C5. TD-DFT predicted UV-Vis spectra for (left) *syn*-IDBT (**2**) and for (right) *syn*-IDBT-sulfone (**6**) calculated at the TD-B3LYP/6-311++G** level of theory.

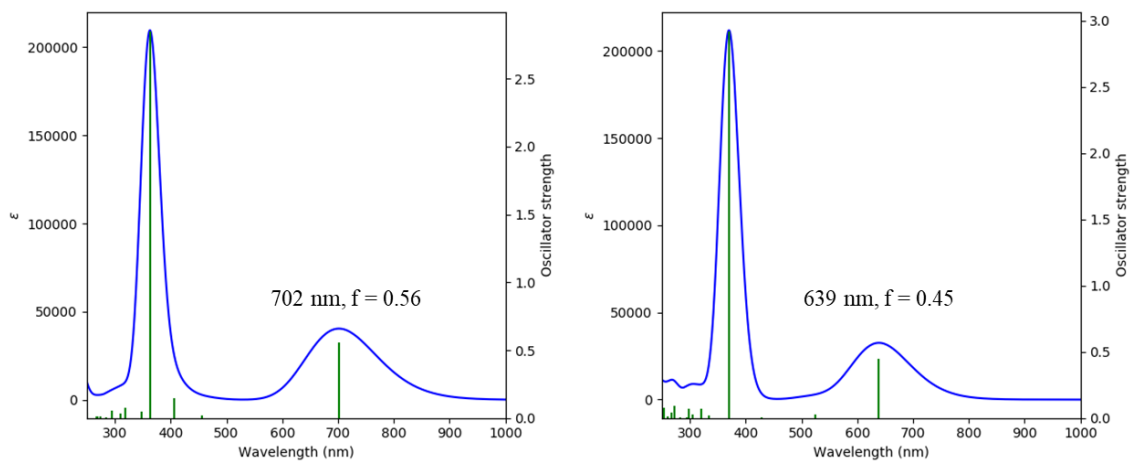


Figure C6. TD-DFT predicted UV-Vis spectra for (left) *anti*-IIDBT (**3**) and for (right) *anti*-IIDBT-sulfone (**7**) calculated at the TD-B3LYP/6-311+G* level of theory.

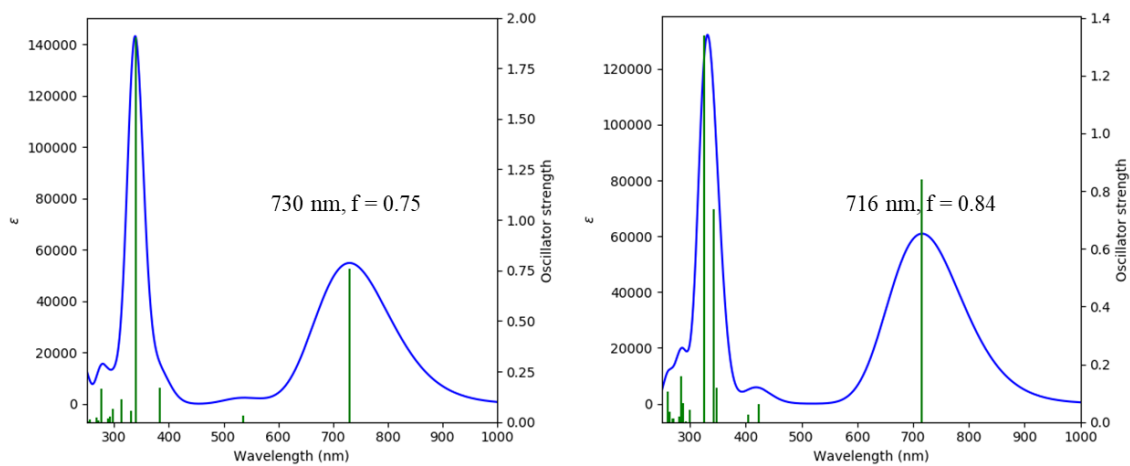


Figure C7. TD-DFT predicted UV-Vis spectra for (left) *syn*-IIDBT (**4**) and for (right) *syn*-IIDBT-sulfone (**8**) calculated at the TD-B3LYP/6-311+G* level of theory.

4. Additional Electronic Absorption Measurements

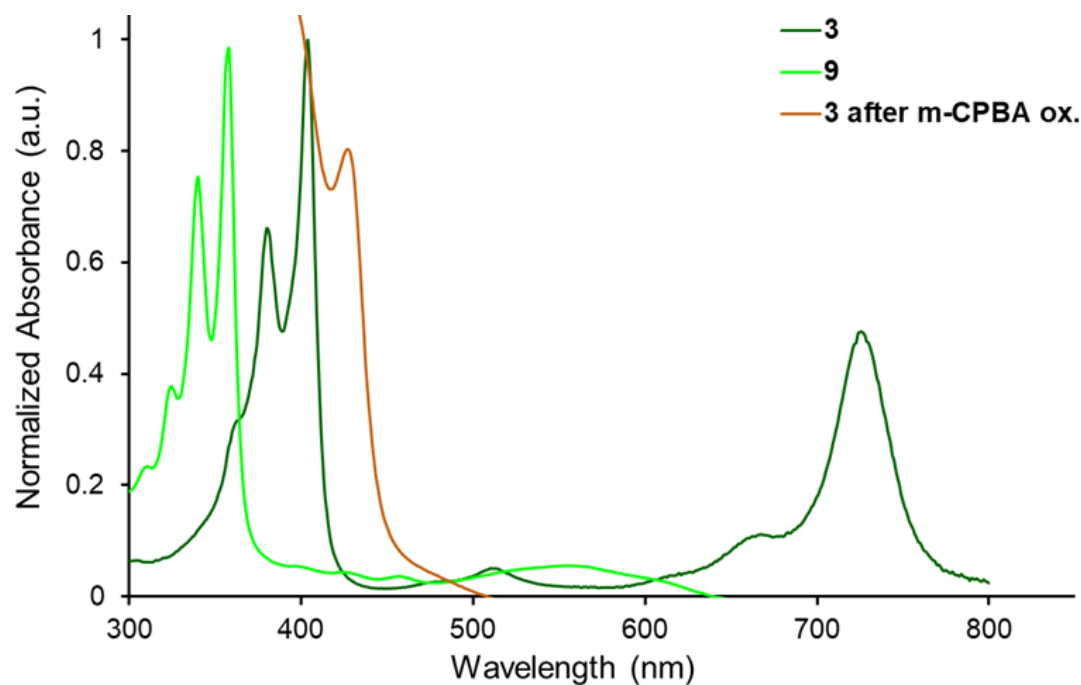


Figure C8. Electronic absorption spectra for *anti*-IIDBT (**3**), the sulfonamide side product **9** from the reaction of **3** with UHP, and the orange colored decomposition product that was the result of the unsuccessful oxidation of **3** with mCPBA.

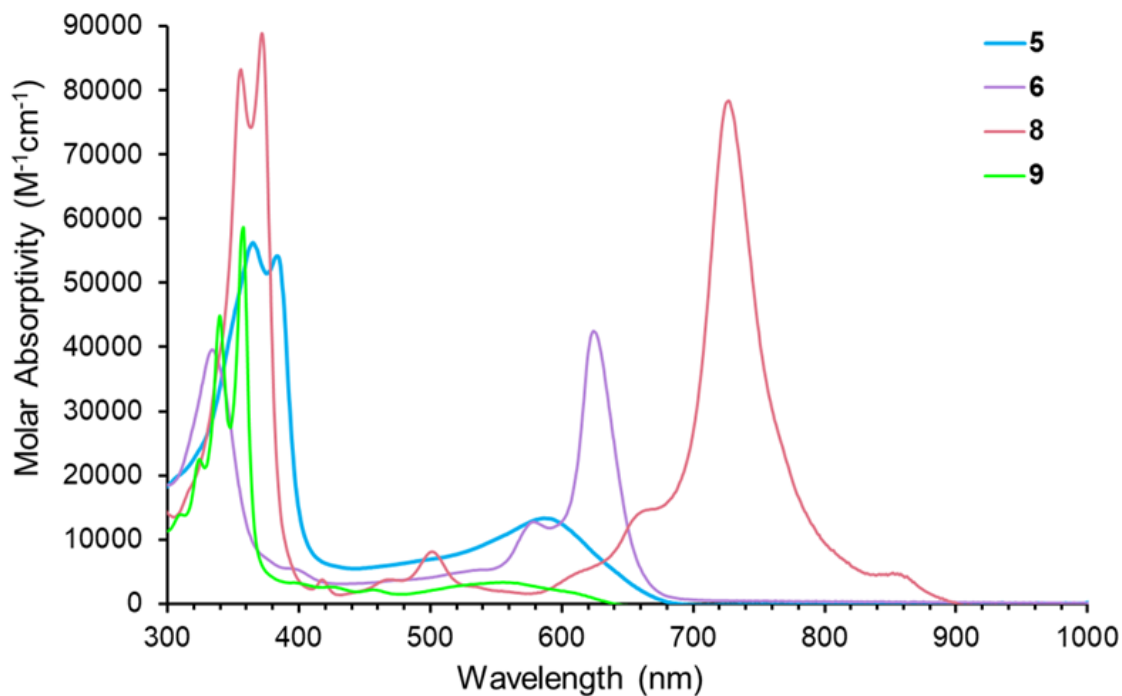


Figure C9. Plot of wavelength vs. molar absorptivity for the three successfully synthesized sulfone compounds (**5**, **6**, **8**), and the sulfonamide side product **9**.

5. Cyclic Voltammetry

General. All electrochemical experiments were conducted with traditional 3-electrode geometry using a Biologic SP-50 potentiostat. Electrolyte solutions (0.1 M) were prepared from anhydrous, degassed HPLC grade CH_2Cl_2 and anhydrous Bu_4NPF_6 . The working electrode was a glassy carbon electrode (3-mm diameter), with a Pt-coil counter electrode and a Ag wire pseudo reference. The ferrocene/ferrocenium (Fc/Fc^+) couple was used as an internal standard following each experiment. Potential values were re-referenced to SCE using a value of 0.46 (V vs. SCE) for the Fc/Fc^+ couple in CH_2Cl_2 . LUMO and HOMO levels were approximated using $\text{SCE} = -4.68 \text{ eV vs. vacuum}$. CV experiments were conducted in a three-neck flask that had been evacuated and backfilled with nitrogen for three cycles using standard Schlenk-line technique. Voltammograms were recorded at a sweep rates of 50 mV s^{-1} . $E_{1/2}$ values were calculated assuming $E_{1/2} \approx E_{o'} = (E_{\text{anodic}} + E_{\text{cathodic}})/2$ based on these observations for reversible couples; for irreversible couples the $E_{o'}$ value is estimated as the potential at peak current. Analyte concentrations were ca. 1-5 mM.

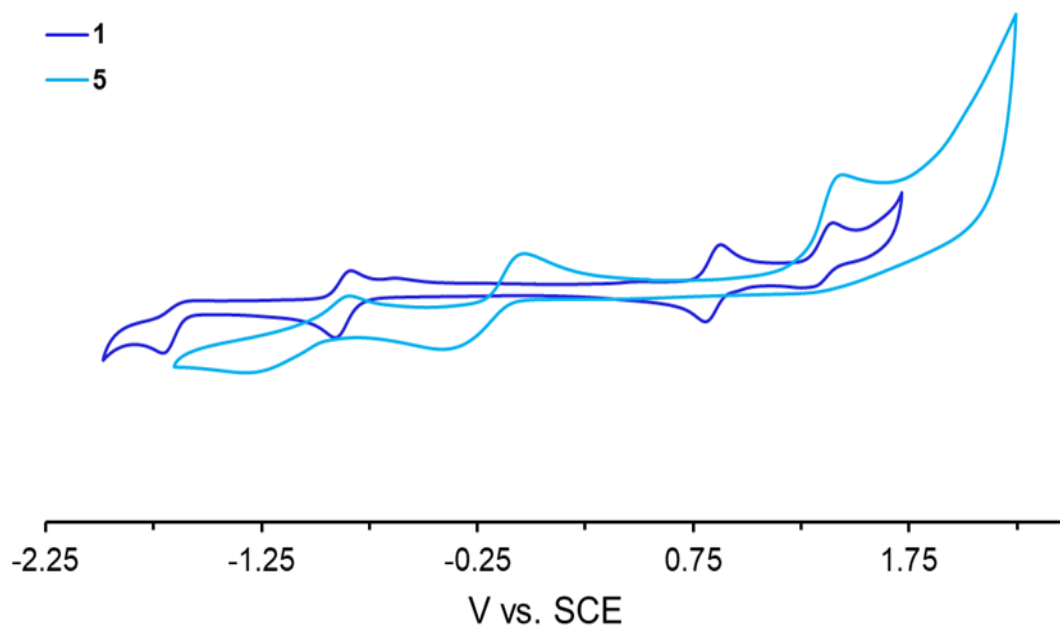


Figure C10. Cyclic voltammograms of **1** and **5**.

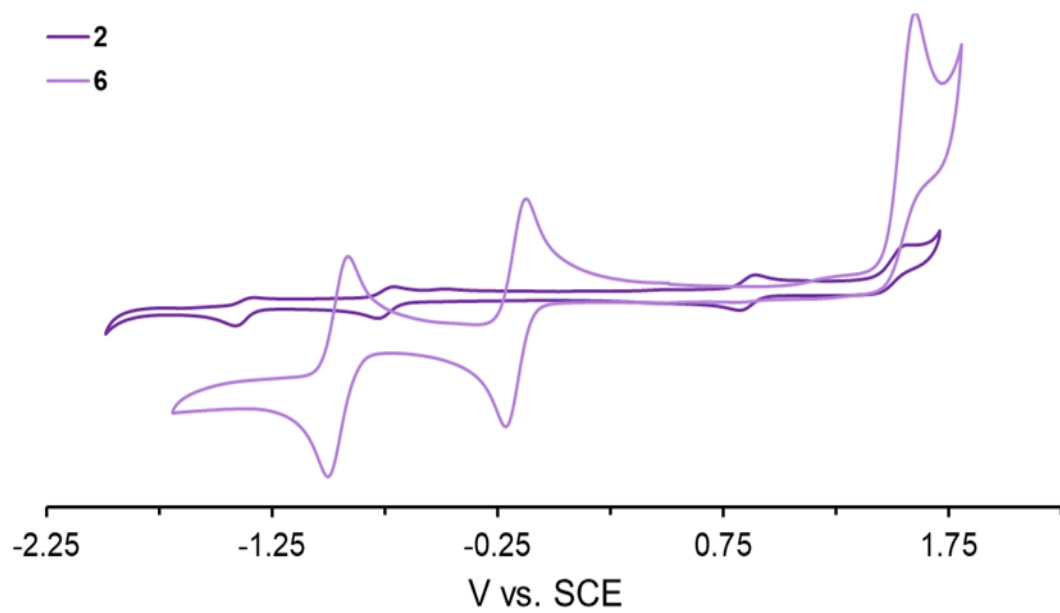


Figure C11. Cyclic voltammograms of **2** and **6**.

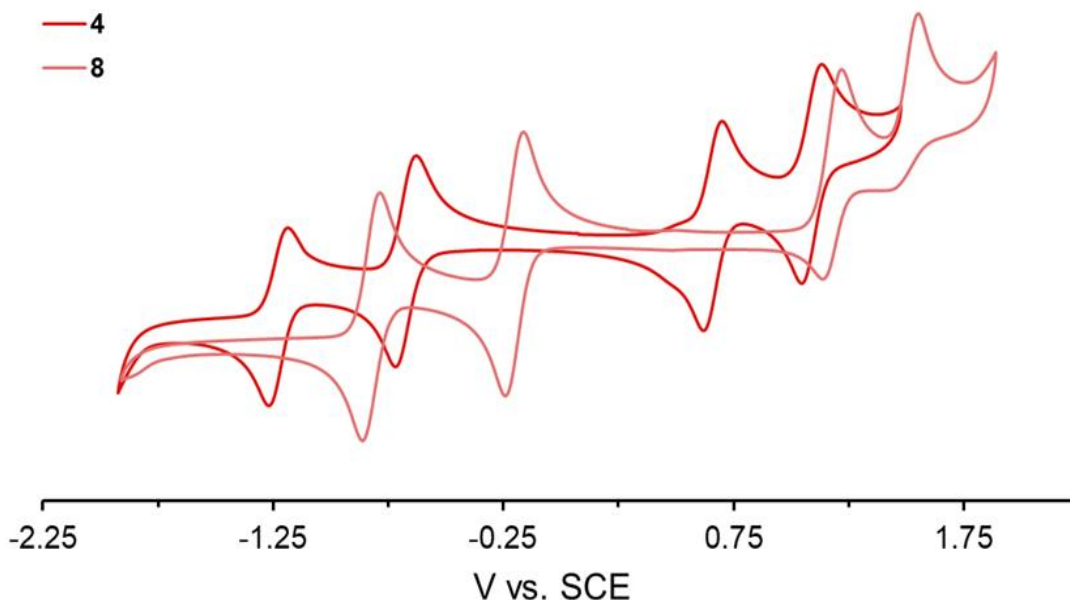


Figure C12. Cyclic voltammograms of **4** and **8**.

6. X-ray Diffraction

General. Diffraction intensities were collected at 173 K on a Bruker Apex2 CCD diffractometer using CuK α ($\lambda = 1.54178$ Å, **5-Mes** and **9**) or MoK α ($\lambda = 0.71073$ Å, **6**) radiation. Space groups were determined based on systematic absences (**9**) and intensity statistics (**5-Mes** and **6**). Absorption corrections were applied by SADABS.¹ Structures were solved by direct methods and Fourier techniques and refined on F^2 using full matrix least-squares procedures. All non-H atoms were refined with anisotropic thermal parameters. H atoms in all structures were refined in calculated positions in a rigid group model. One of two solvent molecules CHCl₃ in **9** and a mixture of solvent molecules CH₂Cl₂/CHCl₃/CH₃CN in **6** are highly disordered in a general position and around an inversion center, respectively. These disordered solvent molecules were treated by SQUEEZE.² The corrections of the X-ray data by SQUEEZE are 232 and 208 electron/cell; the required values are 232 electron/cell for four CHCl₃ in **9**. The disordered solvent

molecules in **6** were not resolved and they have not been included into the final formula of the compound given in the CIF file. Thermal parameters for terminal *t*-Bu groups in **6** and **9** are significantly elongated. The crystal structure of **9** was treated as a racemic twin; the Flack parameter is 0.28(3). X-ray diffraction for crystals of **9** at high angles is very weak due to strong disorder in the structure. As a result the structure of **9** is not very precisely determined. All calculations were performed by the Bruker SHELXL-2014 package.³

Low-temperature X-ray diffraction data for **8** were collected on a Rigaku XtaLAB Synergy diffractometer coupled to a Rigaku HyPix detector with Cu K α radiation ($\lambda = 1.54184 \text{ \AA}$) from a PhotonJet micro-focus X-ray source at 100 K. The diffraction images were processed and scaled using the CrysAlisPro software.⁴ The structures were solved through intrinsic phasing using SHELXT³ and refined against F^2 on all data by full-matrix least squares with SHELXL⁵ following established refinement strategies.⁶ All non-hydrogen atoms were refined anisotropically. All hydrogen atoms bound to carbon were included in the model at geometrically calculated positions and refined using a riding model. The isotropic displacement parameters of all hydrogen atoms were fixed to 1.2 times the U_{eq} value of the atoms they are linked to (1.5 times for methyl groups).

Crystallographic Data for 5-Mes: $\text{C}_{43}\text{H}_{33}\text{Cl}_3\text{O}_4\text{S}_2$, $M = 784.16$, $0.06 \times 0.04 \times 0.02 \text{ mm}$, $T = 173(2) \text{ K}$, Triclinic, space group $P-1$, $a = 8.1459(3) \text{ \AA}$, $b = 9.0608(4) \text{ \AA}$, $c = 13.562(5) \text{ \AA}$, $\alpha = 75.860(2)^\circ$, $\beta = 73.582(2)^\circ$, $\gamma = 84.176(2)^\circ$, $V = 930.52(6) \text{ \AA}^3$, $Z = 1$, $Z' = 0.5$, $D_c = 1.399 \text{ Mg/m}^3$, $\mu(\text{Cu}) = 3.628 \text{ mm}^{-1}$, $F(000) = 406$, $2\theta_{\text{max}} = 133.05^\circ$, 8785 reflections, 3229 independent reflections [$R_{\text{int}} = 0.0463$], $R1 = 0.0530$, $wR2 = 0.1387$ and $\text{GOF} = 1.077$ for 3229 reflections (255 parameters) with $I > 2\sigma(I)$, $R1 = 0.0566$, $wR2 = 0.1411$ and $\text{GOF} =$

1.077 for all reflections, max/min residual electron density +0.662/−0.451 eÅ^{−3}. CCDC 1995028.

Crystallographic Data for 6: C₄₈H₄₄O₄S₂, M = 748.95, 0.06 x 0.03 x 0.01 mm, T = 173(2) K, Triclinic, space group *P*-1, *a* = 13.0977(14) Å, *b* = 15.0775(16) Å, *c* = 15.4634(15) Å, $\alpha = 115.901(3)^\circ$, $\beta = 94.740(3)^\circ$, $\gamma = 112.307(3)^\circ$, *V* = 2425.5(4) Å³, *Z* = 2, *Z'* = 1, *D*_c = 1.025 Mg/m³, $\mu(\text{Mo}) = 0.146 \text{ mm}^{-1}$, *F*(000) = 792, $2\theta_{\text{max}} = 56.32^\circ$, 17634 reflections, 8491 independent reflections [*R*_{int} = 0.0485], *R*1 = 0.0848, *wR*2 = 0.2035 and *GOF* = 1.002 for 8491 reflections (487 parameters) with *I* > 2σ(*I*), *R*1 = 0.1468, *wR*2 = 0.2237 and *GOF* = 1.002 for all reflections, max/min residual electron density +0.465/−0.389 eÅ^{−3}. CCDC 1995030.

Crystallographic Data for 8: C₅₆H₅₂N₂O₄S₂, C₅₂H₄₆O₄S₂•2(CH₃CN), M = 881.11, 0.136 x 0.058 x 0.047 mm³, T = 100.00(2) K, Triclinic, space group *P*-1, *a* = 7.62440(10) Å, *b* = 10.3907(2) Å, *c* = 15.0797(3) Å, $\alpha = 92.525(2)^\circ$, $\beta = 97.786(2)^\circ$, $\gamma = 98.462(2)^\circ$, *V* = 1168.26(4) Å³, *Z* = 1, *D*_c = 1.252 Mg/m³, $\mu(\text{Cu}) = 1.418 \text{ mm}^{-1}$, *F*(000) = 466, $2\theta_{\text{max}} = 74.503^\circ$, 24859 reflections, 4765 independent reflections [*R*(int) = 0.0318], *R*1 = 0.0470, *wR*2 = 0.1063 and *GOF* = 1.020 for all reflections, max/min residual electron density +0.397/−0.464 eÅ^{−3}. CCDC 1994473.

Crystallographic Data for 9: C₅₄H₄₈Cl₆N₂O₄S₂, M = 1065.76, 0.14 x 0.06 x 0.02 mm, T = 173(2) K, Monoclinic, space group *Cc*, *a* = 11.949(3) Å, *b* = 25.877(6) Å, *c* = 16.528(5) Å, $\beta = 98.21(2)^\circ$, *V* = 5058(2) Å³, *Z* = 4, *Z'* = 0.5, *D*_c = 1.400 Mg/m³, $\mu(\text{Cu}) = 4.257 \text{ mm}^{-1}$, *F*(000) = 2208, $2\theta_{\text{max}} = 135.86^\circ$, 17136 reflections, 6906 independent reflections [*R*_{int} = 0.0827], *R*1 = 0.0719, *wR*2 = 0.1746 and *GOF* = 1.052 for 6906 reflections (578

parameters) with $I > 2\sigma(I)$, $R1 = 0.0972$, $wR2 = 0.2030$ and $GOF = 1.052$ for all reflections, $Flack = 0.28(3)$, max/min residual electron density $+0.277/-0.348 \text{ e}\text{\AA}^{-3}$. CCDC 1995029.

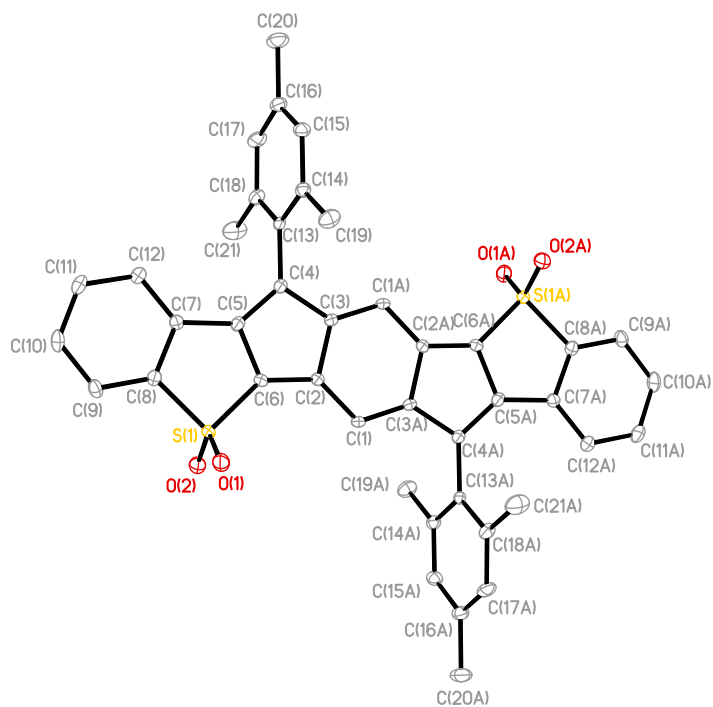


Figure C13. Molecular structure of IDBT-S 5-Mes.

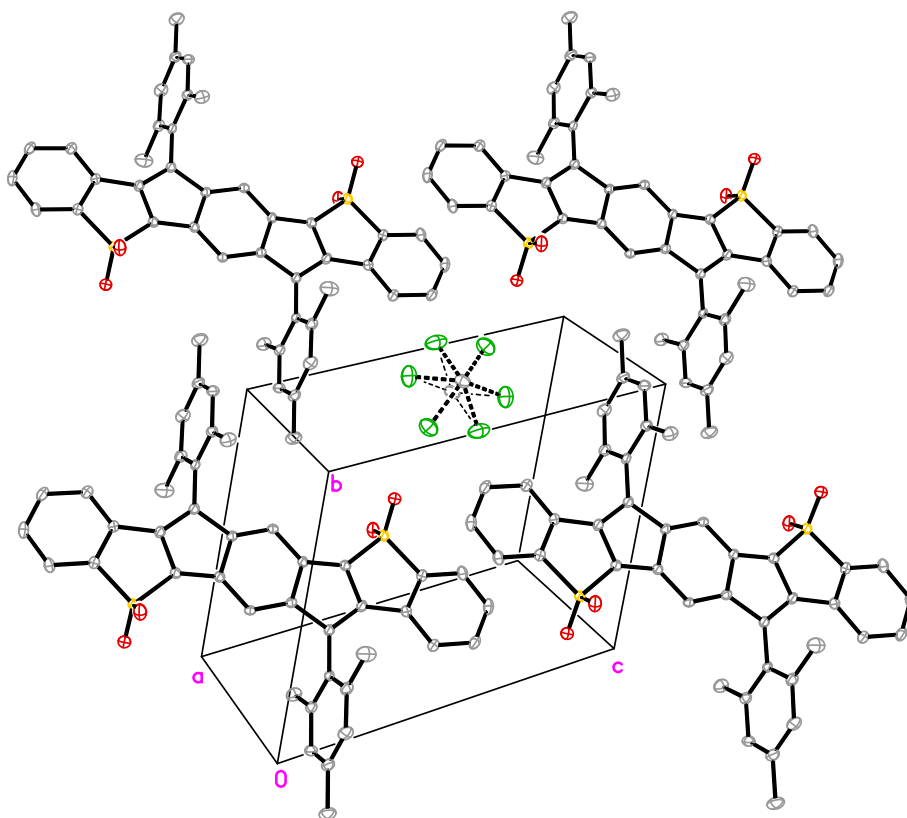


Figure C14. Molecular packing of IDBT-S 5-Mes with disordered solvent molecule.

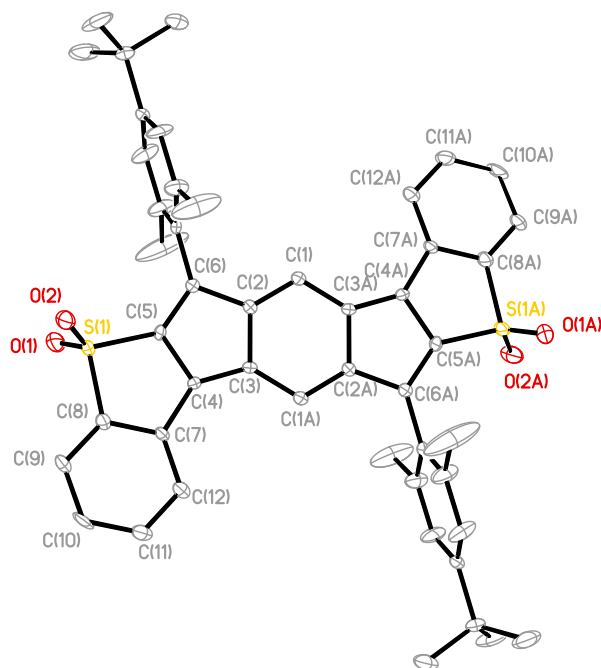


Figure C15. Molecular structure of IDBT-S 6.

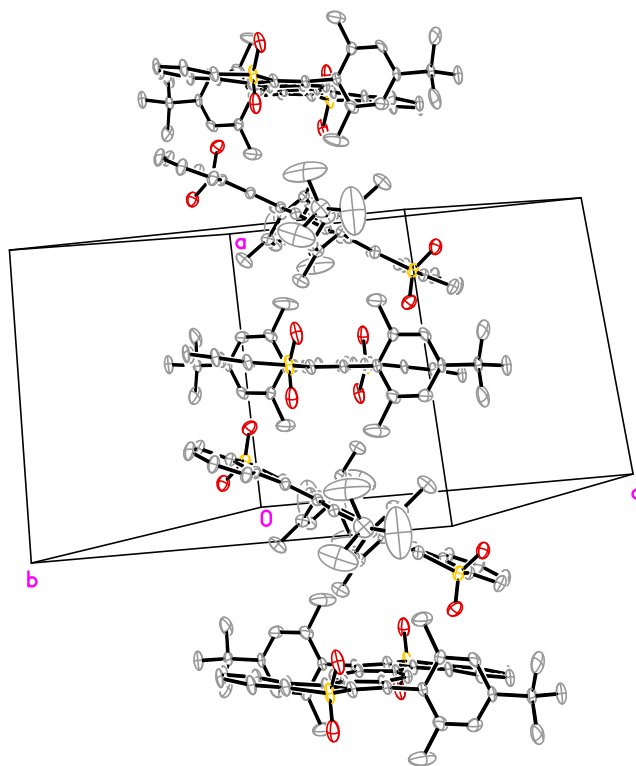


Figure C16. Molecular packing of IDBT-S 6.

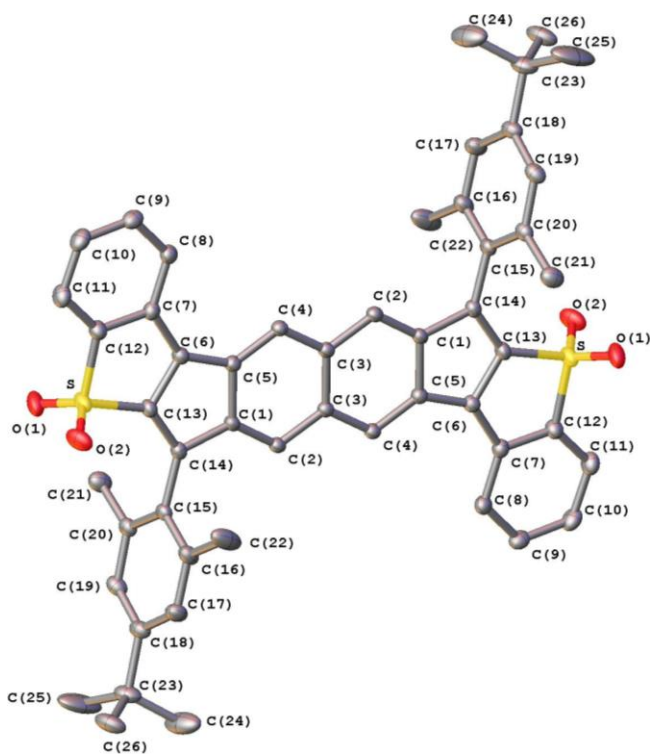


Figure C17. Molecular structure of IDBT-S 8.

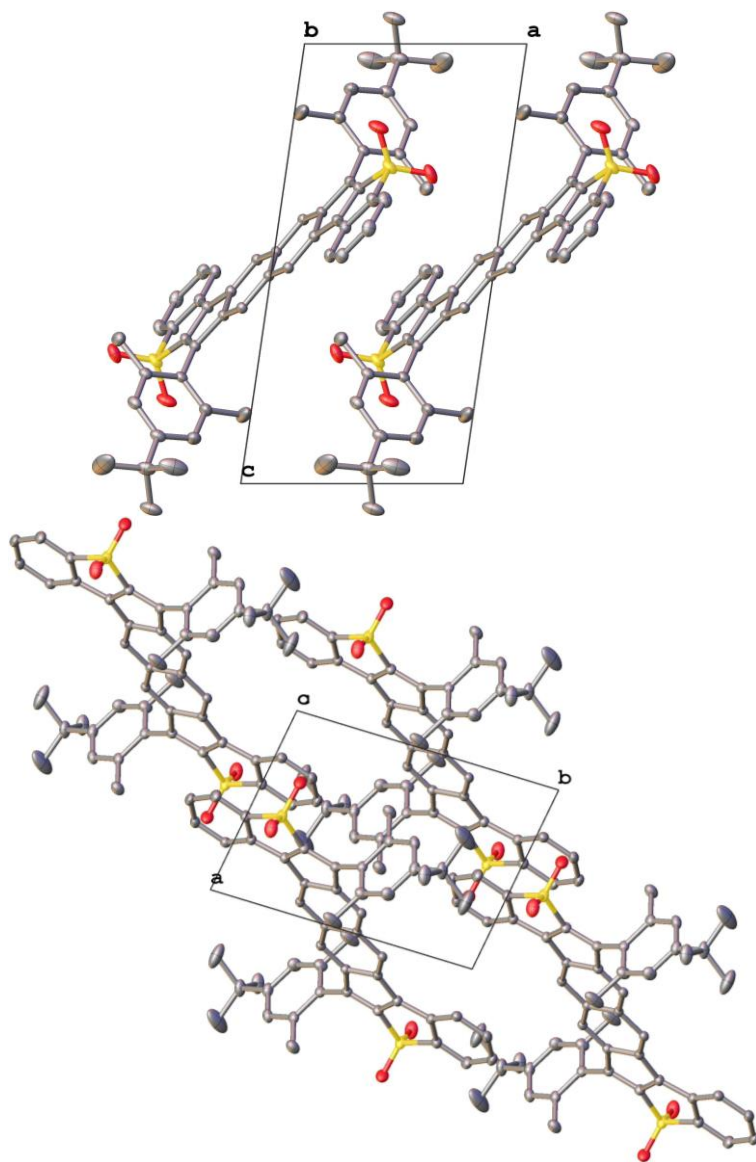


Figure C18. Molecular packing of IDBT-S 8.

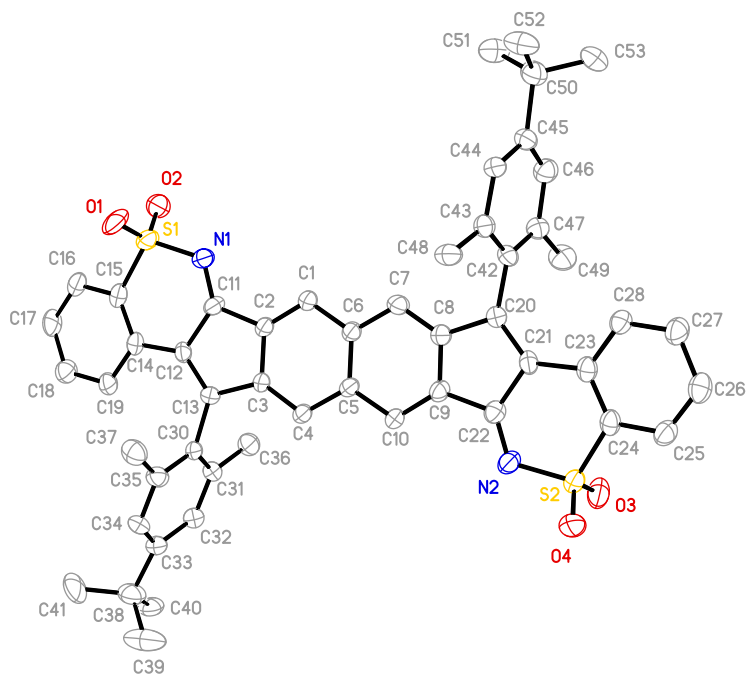


Figure C19. Molecular structure of decomposition product **9**.

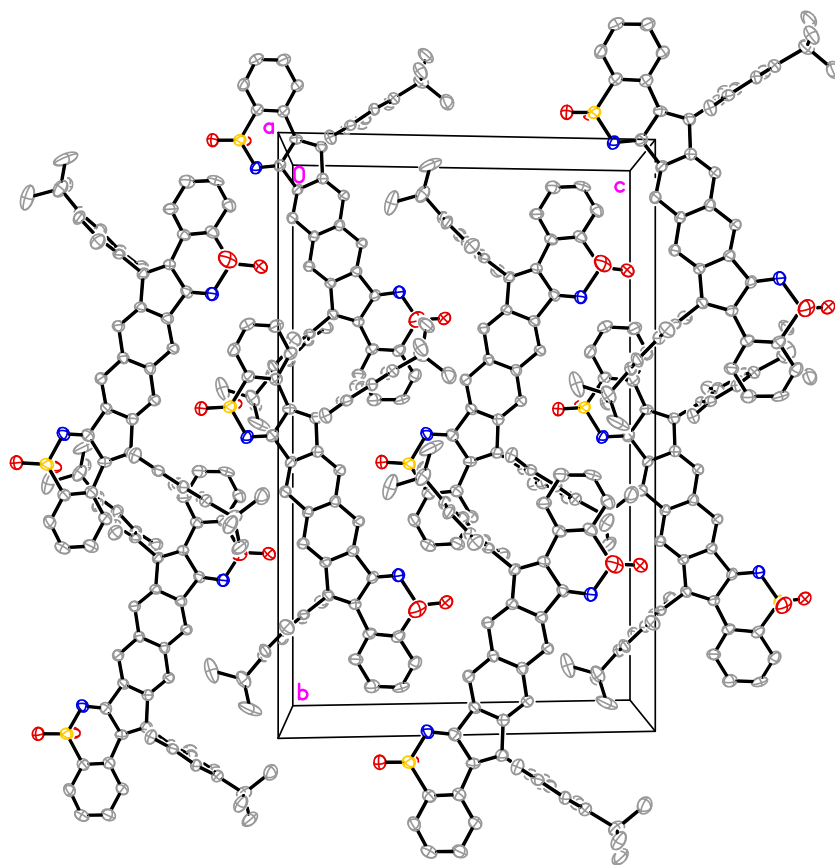


Figure C20. Molecular packing of decomposition product **9**.

7. Computational Details

7.1 NICS-XY scan details

All calculations related to the NICS-XY scans were performed using Gaussian 09.⁷ Geometries were optimized using B3LYP/6-311++G** level of theory and the structures were verified to be minima by frequency calculation. NICS-XY scans were carried out with the Aroma package⁸ at the B3LYP/6-311++G** level of theory using the sigma-only model.⁹ For the sake of computational efficiency calculations were performed on the hydrocarbon parent molecules for each compound. Previous computational studies in our group have shown that due to their nearly orthogonal orientation relative to the plane of the indacene core, removal of the pendant aryl groups on the apical carbons has little to no effect on NICS-XY scan calculations.

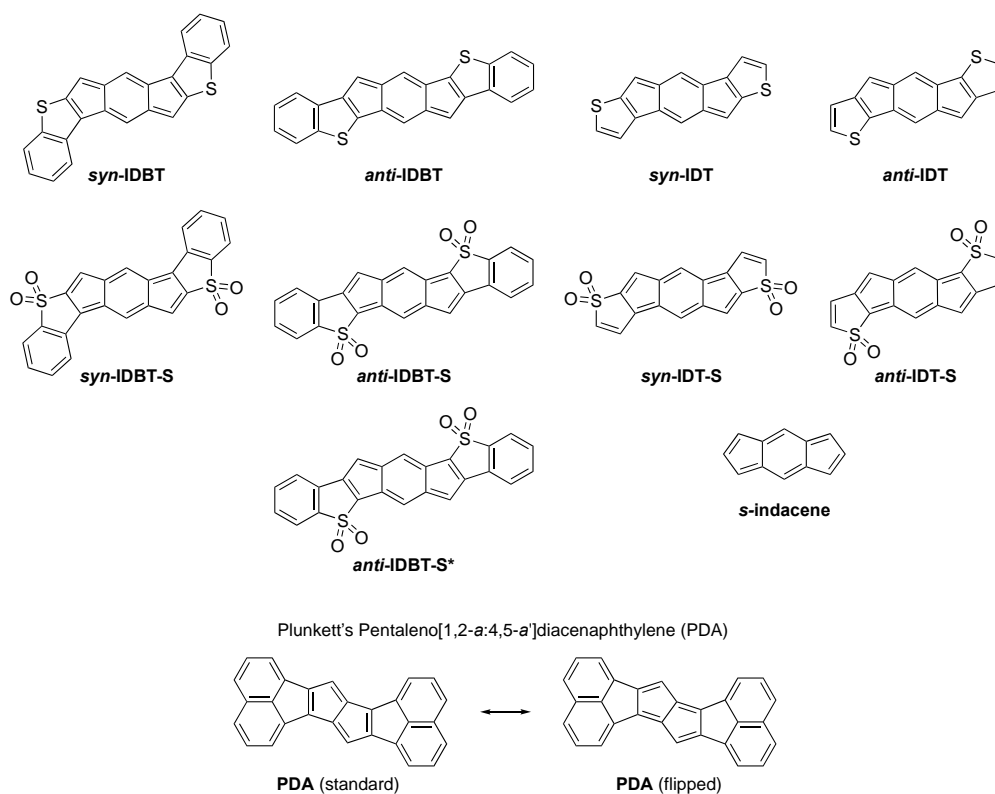


Figure C21. Simplified structures used for the NICS-XY scan calculations.

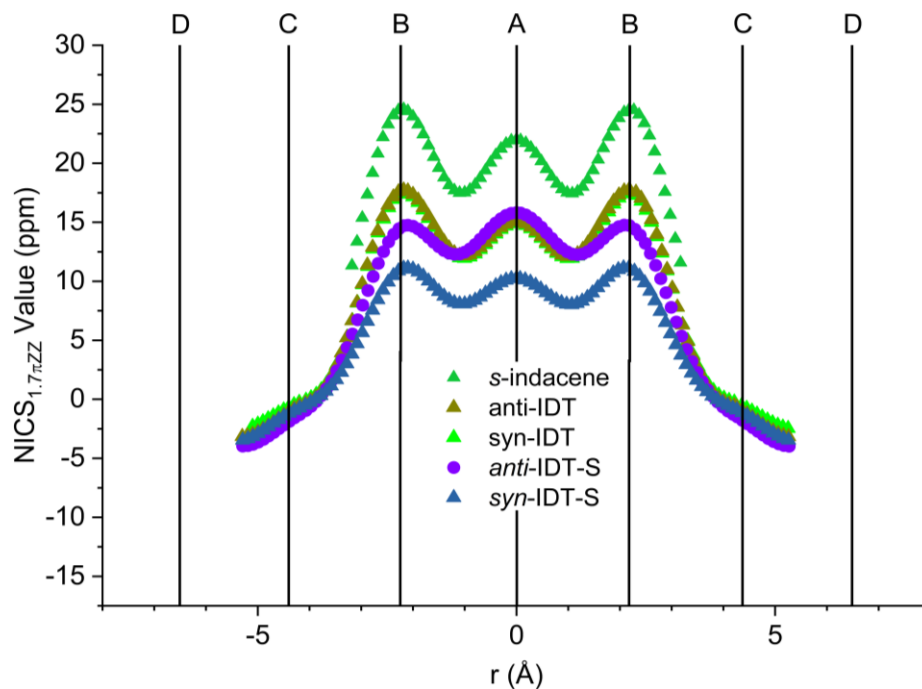


Figure C22. NICS-XY scans of IDTs and IDT-sulfones (IDT-S) from most to least paratropic.

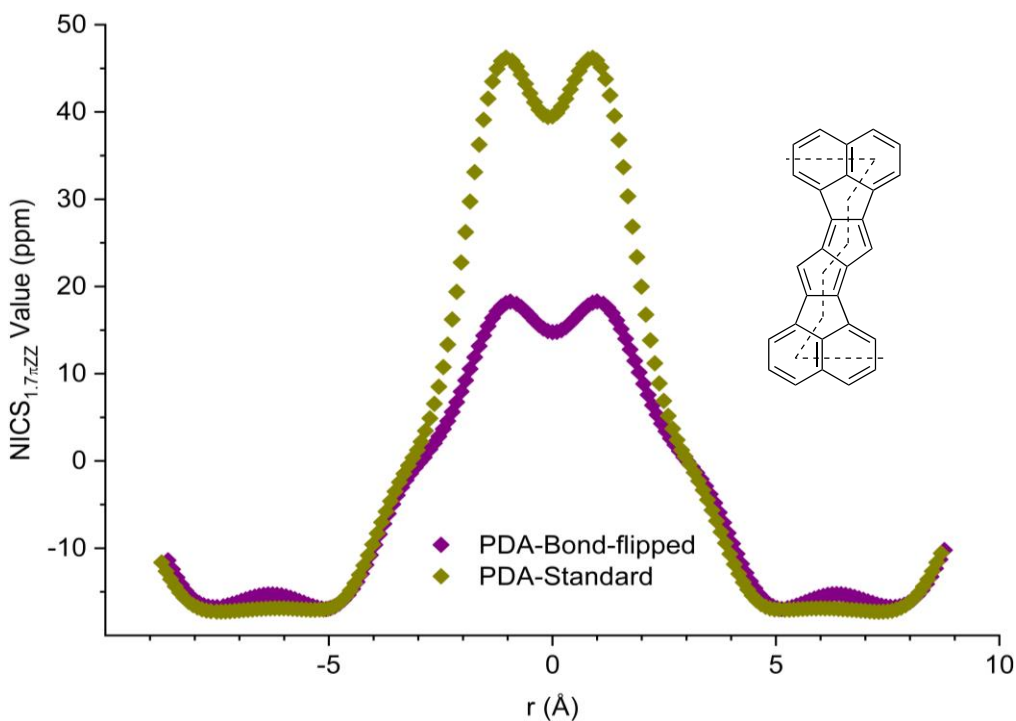


Figure C23. NICS-XY scans (left) of **PDA** with standard bond alternation vs. **PDA** with flipped bond alternation along with a depiction of the scan pathway (right). Like the sulfones, the observed bonding pattern is due to the minimization of paratropicity in the pentalene core of the PDAs. It is worth noting that the “standard” geometry is 10.8 kcal mol⁻¹ higher in energy than the “flipped” geometry.

Calculated Geometries for NICS-XY Scan Structures

s-indacene

Zero-point correction= 0.155426 (Hartree/Particle)
Thermal correction to Energy= 0.163727
Thermal correction to Enthalpy= 0.164671
Thermal correction to Gibbs Free Energy= 0.122995
Sum of electronic and zero-point Energies= -461.984810

H	-2.5102810000	0.3004220000	0.0000000000
H	-2.4745840000	-2.6117090000	0.0000000000
H	-1.8282260000	3.1575890000	0.0000000000
C	-1.4300430000	0.1833990000	0.0000000000
C	-1.4152820000	-2.3879420000	0.0000000000
C	-0.8486790000	-1.1094930000	0.0000000000
C	-0.8486790000	2.6984970000	0.0000000000
C	-0.5912530000	1.2773850000	0.0000000000
H	-0.5068920000	-4.4309980000	0.0000000000
C	-0.3648030000	-3.3598230000	0.0000000000
C	0.3648030000	3.3598230000	0.0000000000
H	0.5068920000	4.4309980000	0.0000000000
C	0.5912530000	-1.2773850000	0.0000000000
C	0.8486790000	1.1094930000	0.0000000000
C	0.8486790000	-2.6984970000	0.0000000000
C	1.4152820000	2.3879420000	0.0000000000
C	1.4300430000	-0.1833990000	0.0000000000
H	1.8282260000	-3.1575890000	0.0000000000
H	2.4745840000	2.6117090000	0.0000000000
H	2.5102810000	-0.3004220000	0.0000000000

anti-IDBT (1)

Zero-point correction= 0.276505 (Hartree/Particle)
Thermal correction to Energy= 0.295053
Thermal correction to Enthalpy= 0.295997
Thermal correction to Gibbs Free Energy= 0.230158
Sum of electronic and zero-point Energies= -1718.131387

H	-6.1286300000	-3.8515800000	0.0000000000
H	-5.8051950000	-6.3091470000	0.0000000000
C	-5.1300770000	-4.2730740000	0.0000000000
C	-4.9428860000	-5.6527350000	0.0000000000
S	-4.0178190000	-1.6725420000	0.0000000000
C	-4.0062750000	-3.4519740000	0.0000000000

C	-3.6510580000	-6.1963720000	0.0000000000
H	-3.5247130000	-7.2730020000	0.0000000000
C	-2.6900680000	-3.9801160000	0.0000000000
C	-2.5316060000	-5.3738130000	0.0000000000
C	-2.2858450000	-1.6429150000	0.0000000000
H	-2.1736340000	1.2944130000	0.0000000000
C	-1.7111180000	-2.9239560000	0.0000000000
H	-1.5366610000	-5.8048880000	0.0000000000
C	-1.2466520000	0.7287100000	0.0000000000
C	-1.2466520000	-0.6490180000	0.0000000000
H	-0.4313600000	3.5747470000	0.0000000000
C	-0.2953890000	-2.7729320000	0.0000000000
C	-0.0044970000	1.4034920000	0.0000000000
C	0.0044970000	-1.4034920000	0.0000000000
C	0.2953890000	2.7729320000	0.0000000000
H	0.4313600000	-3.5747470000	0.0000000000
C	1.2466520000	-0.7287100000	0.0000000000
C	1.2466520000	0.6490180000	0.0000000000
H	1.5366610000	5.8048880000	0.0000000000
C	1.7111180000	2.9239560000	0.0000000000
H	2.1736340000	-1.2944130000	0.0000000000
C	2.2858450000	1.6429150000	0.0000000000
C	2.5316060000	5.3738130000	0.0000000000
C	2.6900680000	3.9801160000	0.0000000000
H	3.5247130000	7.2730020000	0.0000000000
C	3.6510580000	6.1963720000	0.0000000000
C	4.0062750000	3.4519740000	0.0000000000
S	4.0178190000	1.6725420000	0.0000000000
C	4.9428860000	5.6527350000	0.0000000000
C	5.1300770000	4.2730740000	0.0000000000
H	5.8051950000	6.3091470000	0.0000000000
H	6.1286300000	3.8515800000	0.0000000000

syn-IDBT (2)

Zero-point correction=	0.276857 (Hartree/Particle)
Thermal correction to Energy=	0.295366
Thermal correction to Enthalpy=	0.296310
Thermal correction to Gibbs Free Energy=	0.230524
Sum of electronic and zero-point Energies=	-1718.129179

H	-7.5190140000	-2.6827280000	0.0000000000
H	-6.8201300000	-0.3069460000	0.0000000000

C	-6.4642940000	-2.4333600000	0.0000000000
C	-6.0661100000	-1.0856680000	0.0000000000
H	-5.8282160000	-4.4909360000	0.0000000000
C	-5.5193320000	-3.4520420000	0.0000000000
C	-4.7245740000	-0.7416500000	0.0000000000
H	-4.4309630000	0.3011920000	0.0000000000
C	-4.1676710000	-3.1098100000	0.0000000000
C	-3.7405750000	-1.7495270000	0.0000000000
S	-2.8145630000	-4.2456770000	0.0000000000
C	-2.3147730000	-1.6615170000	0.0000000000
H	-2.1777890000	1.2834010000	0.0000000000
C	-1.6920510000	-2.9080290000	0.0000000000
C	-1.2558300000	0.7114710000	0.0000000000
C	-1.2558300000	-0.6576730000	0.0000000000
H	-0.4561280000	3.5603190000	0.0000000000
C	-0.2720290000	-2.7607780000	0.0000000000
C	-0.0051050000	1.3954320000	0.0000000000
C	0.0051050000	-1.3954320000	0.0000000000
C	0.2720290000	2.7607780000	0.0000000000
H	0.4561280000	-3.5603190000	0.0000000000
C	1.2558300000	-0.7114710000	0.0000000000
C	1.2558300000	0.6576730000	0.0000000000
C	1.6920510000	2.9080290000	0.0000000000
H	2.1777890000	-1.2834010000	0.0000000000
C	2.3147730000	1.6615170000	0.0000000000
S	2.8145630000	4.2456770000	0.0000000000
C	3.7405750000	1.7495270000	0.0000000000
C	4.1676710000	3.1098100000	0.0000000000
H	4.4309630000	-0.3011920000	0.0000000000
C	4.7245740000	0.7416500000	0.0000000000
C	5.5193320000	3.4520420000	0.0000000000
H	5.8282160000	4.4909360000	0.0000000000
C	6.0661100000	1.0856680000	0.0000000000
C	6.4642940000	2.4333600000	0.0000000000
H	6.8201300000	0.3069460000	0.0000000000
H	7.5190140000	2.6827280000	0.0000000000

anti-IDBT-sulfone (bond 'flipped', 5)

Zero-point correction=	0.293661 (Hartree/Particle)
Thermal correction to Energy=	0.316228
Thermal correction to Enthalpy=	0.317172
Thermal correction to Gibbs Free Energy=	0.241864
Sum of electronic and zero-point Energies=	-2018.916229

H	-4.7226432920	-6.5591048234	0.0000000000
H	-4.3881243537	-4.1092432870	0.0000000000
C	-3.7166097002	-6.1557452115	0.0000000000
C	-3.5330952354	-4.7752135921	0.0000000000
H	-3.4074056047	-1.3545659945	0.0000000000
H	-2.7901258152	-8.1009186597	0.0000000000
C	-2.6252790079	-7.0301222815	0.0000000000
C	-2.3573134435	-1.6100211588	0.0000000000
C	-2.2356373255	-4.2549018589	0.0000000000
H	-2.1848123947	1.2955113474	0.0000000000
C	-1.8020124868	-2.8622231565	0.0000000000
C	-1.3223339272	-6.5307535724	0.0000000000
C	-1.2647514722	0.7211516873	0.0000000000
C	-1.2645943701	-0.6454755841	0.0000000000
O	-1.1568279502	4.5351093400	-1.2607199992
O	-1.1568279502	4.5351093400	1.2607199992
C	-1.1568279502	-5.1562054549	0.0000000000
H	-0.4671896224	-7.1960500286	0.0000000000
S	-0.4454342896	4.3080059083	0.0000000000
C	-0.3584305682	-2.7142111748	0.0000000000
C	-0.0002735789	-1.3883911340	0.0000000000
C	0.0002735789	1.3883911340	0.0000000000
C	0.3584305682	2.7142111748	0.0000000000
S	0.4454342896	-4.3080059083	0.0000000000
H	0.4671896224	7.1960500286	0.0000000000
O	1.1568279502	-4.5351093400	-1.2607199992
O	1.1568279502	-4.5351093400	1.2607199992
C	1.1568279502	5.1562054549	0.0000000000
C	1.2645943701	0.6454755841	0.0000000000
C	1.2647514722	-0.7211516873	0.0000000000
C	1.3223339272	6.5307535724	0.0000000000
C	1.8020124868	2.8622231565	0.0000000000
H	2.1848123947	-1.2955113474	0.0000000000
C	2.2356373255	4.2549018589	0.0000000000
C	2.3573134435	1.6100211588	0.0000000000
C	2.6252790079	7.0301222815	0.0000000000
H	2.7901258152	8.1009186597	0.0000000000
H	3.4074056047	1.3545659945	0.0000000000
C	3.5330952354	4.7752135921	0.0000000000
C	3.7166097002	6.1557452115	0.0000000000
H	4.3881243537	4.1092432870	0.0000000000
H	4.7226432920	6.5591048234	0.0000000000

anti-IDBT-sulfone (regular geometry, 5*)

Zero-point correction= 0.293098 (Hartree/Particle)
Thermal correction to Energy= 0.315801
Thermal correction to Enthalpy= 0.316745
Thermal correction to Gibbs Free Energy= 0.240492
Sum of electronic and zero-point Energies= -2018.913837

H	-8.5866580000	0.6443890000	0.0000000000
H	-7.5395030000	2.8816740000	0.0000000000
C	-7.5070990000	0.7352990000	0.0000000000
H	-7.1628970000	-1.4056840000	0.0000000000
C	-6.9134730000	1.9968970000	0.0000000000
C	-6.7148040000	-0.4192040000	0.0000000000
C	-5.5233710000	2.1411690000	0.0000000000
C	-5.3444540000	-0.2569470000	0.0000000000
H	-5.0770810000	3.1289790000	0.0000000000
C	-4.7209540000	1.0018010000	0.0000000000
O	-4.1499210000	-2.3415690000	1.2601950000
O	-4.1499210000	-2.3415690000	-1.2601950000
S	-4.1115690000	-1.5944110000	0.0000000000
C	-3.2621510000	0.8839370000	0.0000000000
C	-2.7817060000	-0.4086570000	0.0000000000
H	-2.1784640000	2.8570720000	0.0000000000
C	-2.1357180000	1.7760970000	0.0000000000
C	-1.3452760000	-0.4036100000	0.0000000000
C	-0.9730070000	1.0068630000	0.0000000000
H	-0.6711700000	-2.4451340000	0.0000000000
C	-0.3957150000	-1.3957970000	0.0000000000
C	0.3957150000	1.3957970000	0.0000000000
H	0.6711700000	2.4451340000	0.0000000000
C	0.9730070000	-1.0068630000	0.0000000000
C	1.3452760000	0.4036100000	0.0000000000
C	2.1357180000	-1.7760970000	0.0000000000
H	2.1784640000	-2.8570720000	0.0000000000
C	2.7817060000	0.4086570000	0.0000000000
C	3.2621510000	-0.8839370000	0.0000000000
S	4.1115690000	1.5944110000	0.0000000000
O	4.1499210000	2.3415690000	1.2601950000
O	4.1499210000	2.3415690000	-1.2601950000
C	4.7209540000	-1.0018010000	0.0000000000

H	5.0770810000	-3.1289790000	0.0000000000
C	5.3444540000	0.2569470000	0.0000000000
C	5.5233710000	-2.1411690000	0.0000000000
C	6.7148040000	0.4192040000	0.0000000000
C	6.9134730000	-1.9968970000	0.0000000000
H	7.1628970000	1.4056840000	0.0000000000
C	7.5070990000	-0.7352990000	0.0000000000
H	7.5395030000	-2.8816740000	0.0000000000
H	8.5866580000	-0.6443890000	0.0000000000

***syn*-IDBT-sulfone (6)**

Zero-point correction=	0.293669 (Hartree/Particle)
Thermal correction to Energy=	0.316214
Thermal correction to Enthalpy=	0.317158
Thermal correction to Gibbs Free Energy=	0.241323
Sum of electronic and zero-point Energies=	-2018.922157

H	-7.4283550000	2.7154620000	0.0000060000
H	-7.3050770000	0.2245250000	0.0000060000
C	-6.4643230000	2.2208310000	0.0000040000
C	-6.4030190000	0.8246870000	0.0000040000
H	-5.3572340000	4.0636520000	0.0000010000
O	-5.3108340000	-2.1501520000	-1.2606670000
O	-5.3108280000	-2.1501530000	1.2606690000
C	-5.2914510000	2.9819560000	0.0000010000
C	-5.1552650000	0.2324390000	0.0000010000
S	-4.8539310000	-1.5602150000	0.0000000000
C	-4.0405680000	2.3719600000	-0.0000020000
C	-3.9554900000	0.9729500000	-0.0000020000
H	-3.1436250000	2.9782500000	-0.0000050000
C	-3.0957390000	-1.2872070000	-0.0000040000
C	-2.7848020000	0.1170310000	-0.0000040000
C	-1.9578650000	-2.0461040000	-0.0000100000
H	-1.8858990000	-3.1240450000	-0.0000120000
C	-1.3845660000	0.2369970000	-0.0000090000
H	-0.8934970000	2.3636770000	-0.0000140000
C	-0.8481290000	-1.1161370000	0.0000030000
C	-0.5107070000	1.3492330000	-0.0000130000
C	0.5107070000	-1.3492330000	0.0000120000
C	0.8481290000	1.1161370000	-0.0000040000
H	0.8934970000	-2.3636770000	0.0000130000
C	1.3845660000	-0.2369970000	0.0000080000

H	1.8858990000	3.1240450000	0.0000090000
C	1.9578650000	2.0461040000	0.0000080000
C	2.7848020000	-0.1170310000	0.0000030000
C	3.0957390000	1.2872070000	0.0000030000
H	3.1436250000	-2.9782500000	0.0000040000
C	3.9554900000	-0.9729500000	0.0000010000
C	4.0405680000	-2.3719600000	0.0000020000
S	4.8539310000	1.5602150000	0.0000000000
C	5.1552650000	-0.2324390000	-0.0000010000
C	5.2914510000	-2.9819560000	0.0000000000
O	5.3108290000	2.1501530000	-1.2606690000
O	5.3108330000	2.1501520000	1.2606680000
H	5.3572340000	-4.0636520000	0.0000000000
C	6.4030190000	-0.8246870000	-0.0000030000
C	6.4643230000	-2.2208310000	-0.0000030000
H	7.3050770000	-0.2245250000	-0.0000050000
H	7.4283550000	-2.7154620000	-0.0000050000

anti-IDT

Zero-point correction=	0.183298 (Hartree/Particle)
Thermal correction to Energy=	0.196273
Thermal correction to Enthalpy=	0.197217
Thermal correction to Gibbs Free Energy=	0.143954
Sum of electronic and zero-point Energies=	-1410.849992

H	-2.9971940000	-1.9723270000	0.0000000000
H	-2.3955180000	0.8233690000	0.0000000000
H	-2.2393570000	-5.1295720000	0.0000000000
C	-1.9154660000	-2.0066860000	0.0000000000
C	-1.3626090000	0.4886840000	0.0000000000
S	-1.2848410000	4.1870810000	0.0000000000
C	-1.2848410000	-4.6198380000	0.0000000000
C	-1.1099680000	-3.2042400000	0.0000000000
C	-1.0704230000	-0.9081250000	0.0000000000
C	-0.3226960000	1.3749190000	0.0000000000
C	-0.2344780000	2.8213190000	0.0000000000
H	-0.0911600000	6.3436260000	0.0000000000
C	-0.0888250000	-5.2795770000	0.0000000000
C	0.0888250000	5.2795770000	0.0000000000
H	0.0911600000	-6.3436260000	0.0000000000
C	0.2344780000	-2.8213190000	0.0000000000
C	0.3226960000	-1.3749190000	0.0000000000

C	1.0704230000	0.9081250000	0.0000000000
C	1.1099680000	3.2042400000	0.0000000000
C	1.2848410000	4.6198380000	0.0000000000
S	1.2848410000	-4.1870810000	0.0000000000
C	1.3626090000	-0.4886840000	0.0000000000
C	1.9154660000	2.0066860000	0.0000000000
H	2.2393570000	5.1295720000	0.0000000000
H	2.3955180000	-0.8233690000	0.0000000000
H	2.9971940000	1.9723270000	0.0000000000

syn-IDT

Zero-point correction=	0.183355 (Hartree/Particle)
Thermal correction to Energy=	0.196302
Thermal correction to Enthalpy=	0.197247
Thermal correction to Gibbs Free Energy=	0.144083
Sum of electronic and zero-point Energies=	-1410.852469

H	-2.7653050000	-2.2924930000	0.0000000000
H	-2.6067720000	3.6700130000	0.0000000000
H	-2.4680710000	0.5582100000	0.0000000000
C	-1.6874200000	-2.2051470000	0.0000000000
C	-1.5350130000	3.8191340000	0.0000000000
H	-1.4568800000	6.0256140000	0.0000000000
C	-1.4048570000	0.3379260000	0.0000000000
C	-0.9600550000	5.0672500000	0.0000000000
C	-0.9600550000	-1.0176220000	0.0000000000
S	-0.7833760000	-5.0164130000	0.0000000000
C	-0.7480980000	-3.2818890000	0.0000000000
C	-0.5626310000	2.7902320000	0.0000000000
C	-0.4680090000	1.3334880000	0.0000000000
C	0.4680090000	-1.3334880000	0.0000000000
C	0.5626310000	-2.7902320000	0.0000000000
C	0.7480980000	3.2818890000	0.0000000000
S	0.7833760000	5.0164130000	0.0000000000
C	0.9600550000	-5.0672500000	0.0000000000
C	0.9600550000	1.0176220000	0.0000000000
C	1.4048570000	-0.3379260000	0.0000000000
H	1.4568800000	-6.0256140000	0.0000000000
C	1.5350130000	-3.8191340000	0.0000000000
C	1.6874200000	2.2051470000	0.0000000000
H	2.4680710000	-0.5582100000	0.0000000000
H	2.6067720000	-3.6700130000	0.0000000000

H	2.7653050000	2.2924930000	0.0000000000
---	--------------	--------------	--------------

***anti*-IDT-sulfone**

Zero-point correction=	0.183300 (Hartree/Particle)
Thermal correction to Energy=	0.196273
Thermal correction to Enthalpy=	0.197217
Thermal correction to Gibbs Free Energy=	0.142964
Sum of electronic and zero-point Energies=	-1410.849990

H	-3.2707130000	1.6703290000	0.0000000000
H	-2.8320730000	4.8257230000	0.0000000000
H	-2.2995320000	-1.0858680000	0.0000000000
C	-2.2005550000	1.8216340000	0.0000000000
C	-1.8220110000	4.4335320000	0.0000000000
O	-1.5275260000	-4.4583190000	-1.2616400000
O	-1.5275260000	-4.4583190000	1.2616400000
C	-1.5275260000	3.0112940000	0.0000000000
C	-1.3300870000	-0.5997800000	0.0000000000
C	-1.2012990000	0.7579550000	0.0000000000
S	-0.8070740000	-4.2731500000	0.0000000000
C	-0.7322510000	5.2189140000	0.0000000000
H	-0.6653900000	6.2970170000	0.0000000000
C	-0.1312640000	-1.3841590000	0.0000000000
C	-0.1004370000	2.7330210000	0.0000000000
C	0.1004370000	-2.7330210000	0.0000000000
C	0.1312640000	1.3841590000	0.0000000000
H	0.6653900000	-6.2970170000	0.0000000000
C	0.7322510000	-5.2189140000	0.0000000000
S	0.8070740000	4.2731500000	0.0000000000
C	1.2012990000	-0.7579550000	0.0000000000
C	1.3300870000	0.5997800000	0.0000000000
O	1.5275260000	4.4583190000	-1.2616400000
O	1.5275260000	4.4583190000	1.2616400000
C	1.5275260000	-3.0112940000	0.0000000000
C	1.8220110000	-4.4335320000	0.0000000000
C	2.2005550000	-1.8216340000	0.0000000000
H	2.2995320000	1.0858680000	0.0000000000
H	2.8320730000	-4.8257230000	0.0000000000
H	3.2707130000	-1.6703290000	0.0000000000

***syn*-IDT-sulfone**

Zero-point correction= 0.183352 (Hartree/Particle)
 Thermal correction to Energy= 0.196302
 Thermal correction to Enthalpy= 0.197246
 Thermal correction to Gibbs Free Energy= 0.144074
 Sum of electronic and zero-point Energies= -1410.852466

H	-2.9974210000	-3.1920250000	0.0000000000
H	-2.5301400000	2.6514700000	0.0000000000
H	-2.5207810000	-0.2584490000	0.0000000000
H	-2.2645050000	-5.7074210000	0.0000000000
C	-1.9691160000	-3.5331990000	0.0000000000
C	-1.6265860000	-4.8351550000	0.0000000000
C	-1.4714450000	2.4368130000	0.0000000000
C	-1.4425210000	-0.1365370000	0.0000000000
C	-0.8678590000	1.1089430000	0.0000000000
C	-0.8329970000	-2.6395520000	0.0000000000
O	-0.5831520000	5.7011430000	-1.2622700000
O	-0.5831520000	5.7011430000	1.2622700000
C	-0.5831520000	-1.2693760000	0.0000000000
C	-0.4403490000	3.3237980000	0.0000000000
S	-0.1681710000	5.0869040000	0.0000000000
S	0.1681710000	-5.0869040000	0.0000000000
C	0.4403490000	-3.3237980000	0.0000000000
O	0.5831520000	-5.7011430000	-1.2622700000
O	0.5831520000	-5.7011430000	1.2622700000
C	0.5831520000	1.2693760000	0.0000000000
C	0.8329970000	2.6395520000	0.0000000000
C	0.8678590000	-1.1089430000	0.0000000000
C	1.4425210000	0.1365370000	0.0000000000
C	1.4714450000	-2.4368130000	0.0000000000
C	1.6265860000	4.8351550000	0.0000000000
C	1.9691160000	3.5331990000	0.0000000000
H	2.2645050000	5.7074210000	0.0000000000
H	2.5207810000	0.2584490000	0.0000000000
H	2.5301400000	-2.6514700000	0.0000000000
H	2.9974210000	3.1920250000	0.0000000000

PDA-Standard

Zero-point correction= 0.320129 (Hartree/Particle)
 Thermal correction to Energy= 0.338424
 Thermal correction to Enthalpy= 0.339368
 Thermal correction to Gibbs Free Energy= 0.273840

Sum of electronic and zero-point Energies= -1075.284484

H	-7.277380000	0.9066240000	-0.0000050000
H	-6.913166000	-1.7608810000	-0.0000070000
H	-6.207597000	3.1148090000	-0.0000010000
C	-6.195460000	0.9841280000	-0.0000030000
C	-5.849250000	-1.5482230000	-0.0000050000
C	-5.588332000	2.2245160000	-0.0000010000
C	-5.394516000	-0.1977700000	-0.0000030000
H	-5.302142000	-3.6099510000	-0.0000060000
C	-4.937126000	-2.5888840000	-0.0000040000
C	-4.173568000	2.3852410000	0.0000010000
C	-4.013682000	-0.0117290000	-0.0000010000
H	-3.754421000	3.3857060000	0.0000030000
C	-3.533709000	-2.3705570000	-0.0000020000
C	-3.371014000	1.2609710000	0.0000020000
C	-3.059931000	-1.0715750000	0.0000000000
H	-2.862171000	-3.2220680000	-0.0000020000
C	-1.944173000	0.9626600000	0.0000040000
C	-1.760295000	-0.4165070000	0.0000020000
C	-0.639517000	1.6329880000	0.0000070000
H	-0.485201000	2.7043930000	0.0000080000
C	-0.322217000	-0.6612310000	0.0000040000
C	0.322217000	0.6612310000	0.0000040000
H	0.485201000	-2.7043930000	0.0000080000
C	0.639517000	-1.6329880000	0.0000070000
C	1.760295000	0.4165070000	0.0000020000
C	1.944173000	-0.9626600000	0.0000040000
H	2.862171000	3.2220680000	-0.0000020000
C	3.059931000	1.0715750000	0.0000000000
C	3.371014000	-1.2609710000	0.0000020000
C	3.533709000	2.3705570000	-0.0000020000
H	3.754421000	-3.3857060000	0.0000030000
C	4.013682000	0.0117290000	-0.0000010000
C	4.173568000	-2.3852410000	0.0000010000
C	4.937126000	2.5888840000	-0.0000040000
H	5.302142000	3.6099510000	-0.0000060000
C	5.394516000	0.1977700000	-0.0000030000
C	5.588332000	-2.2245160000	-0.0000010000
C	5.849250000	1.5482230000	-0.0000050000
C	6.195460000	-0.9841280000	-0.0000030000
H	6.207597000	-3.1148090000	-0.0000010000
H	6.913166000	1.7608810000	-0.0000070000
H	7.277380000	-0.9066240000	-0.0000050000

PDA-Bond-flipped

Zero-point correction=	0.321003 (Hartree/Particle)
Thermal correction to Energy=	0.339015
Thermal correction to Enthalpy=	0.339959
Thermal correction to Gibbs Free Energy=	0.275158
Sum of electronic and zero-point Energies=	-1075.300781
Sum of electronic and thermal Energies=	-1075.282769
Sum of electronic and thermal Enthalpies=	-1075.281825
Sum of electronic and thermal Free Energies=	-1075.346626

H	-7.2212060000	0.8393980000	0.0000010000
H	-6.8162160000	-1.8036280000	0.0000010000
H	-6.2055850000	3.0700410000	0.0000010000
C	-6.1412190000	0.9401090000	0.0000010000
C	-5.7548260000	-1.5789410000	0.0000010000
C	-5.5628090000	2.1964010000	0.0000010000
C	-5.3234120000	-0.2239320000	0.0000000000
H	-5.1897960000	-3.6349600000	0.0000000000
C	-4.8323190000	-2.6110910000	0.0000000000
C	-4.1587590000	2.3907150000	0.0000000000
C	-3.9330210000	-0.0128830000	0.0000000000
H	-3.7561520000	3.3970910000	0.0000000000
C	-3.4355170000	-2.3807090000	0.0000000000
C	-3.3318880000	1.2830800000	0.0000000000
C	-2.9778880000	-1.0753780000	0.0000000000
H	-2.7504660000	-3.2204310000	0.0000000000
C	-1.8953430000	1.0556230000	-0.0000010000
C	-1.6733430000	-0.4395710000	-0.0000010000
C	-0.6979220000	1.7017140000	-0.0000010000
H	-0.5241060000	2.7680520000	0.0000000000
C	-0.3298590000	-0.6616700000	-0.0000010000
C	0.3298590000	0.6616700000	-0.0000010000
H	0.5241060000	-2.7680520000	0.0000000000
C	0.6979220000	-1.7017140000	-0.0000010000
C	1.6733430000	0.4395710000	-0.0000010000
C	1.8953430000	-1.0556230000	-0.0000010000
H	2.7504660000	3.2204310000	0.0000000000
C	2.9778880000	1.0753780000	0.0000000000
C	3.3318880000	-1.2830800000	0.0000000000
C	3.4355170000	2.3807090000	0.0000000000
H	3.7561520000	-3.3970910000	0.0000000000
C	3.9330210000	0.0128830000	0.0000000000
C	4.1587590000	-2.3907150000	0.0000000000
C	4.8323190000	2.6110910000	0.0000000000
H	5.1897960000	3.6349600000	0.0000000000
C	5.3234120000	0.2239320000	0.0000000000
C	5.5628090000	-2.1964010000	0.0000010000

C	5.7548260000	1.5789410000	0.0000010000
C	6.1412190000	-0.9401090000	0.0000010000
H	6.2055850000	-3.0700410000	0.0000010000
H	6.8162160000	1.8036280000	0.0000010000
H	7.2212060000	-0.8393980000	0.0000010000

7.2 Calculated HOMO/LUMO Energy Levels with TD-DFT Calculations for Predicted UV-Vis Spectra

The same geometries used above for the NICS-XY scans were used to predict UV-vis spectra and calculate optical energy gaps for the IDBTs and IDBT sulfones. Optical values were calculated with TD-B3LYP/6-311++G** for the IDBTs and IDBT-sulfones, and with TD-B3LYP/6-311+G* for the IIDBTs and IIDBT-sulfones. HOMO-LUMO levels were generated using B3LYP/6-311++G** for the IDBTs and IDBT-sulfones, and using B3LYP/6-311+G* for the IIDBTs and IIDBT-sulfones.

Table C1. Calculated optical data and HOMO-LUMO energy gaps for compounds **1-8**.

	λ_{\max} (nm)	f	configuration	Optical Gap (eV)	HOM O (eV)	LUMO (eV)	E_{gap} (eV)
<i>anti</i> -IDBT (1)	597	0.3685	HOMO-1→LUMO (93%)	2.05	-5.297	-3.336	1.96 1
<i>anti</i> -IDBT-S (5)	550	0.1528	HOMO-1→LUMO (75%)	2.20	-6.179	-4.339	1.84 0
<i>syn</i> -IDBT (2)	608	0.5578	HOMO-1→LUMO (94%)	1.99	-5.292	-3.455	1.83 7
<i>syn</i> -IDBT-S (6)	603	0.7178	HOMO→LUMO (99%)	2.04	-6.347	-4.393	1.95 4
<i>anti</i> -IIDBT (3)	702	0.5576	HOMO→LUMO (95%)	1.78	-4.983	-3.378	1.60 5
<i>anti</i> -IIDBT-S (7)	639	0.4487	HOMO→LUMO (93%)	1.94	-6.198	-4.387	1.81 1
<i>syn</i> -IIDBT (4)	730	0.7576	HOMO→LUMO (100%)	1.71	-5.100	-3.572	1.52 8
<i>syn</i> -IIDBT-S (8)	716	0.8410	HOMO→LUMO (100%)	1.75	-5.888	-4.368	1.52 0

anti-IIDBT (3)

Zero-point correction= 0.323156 (Hartree/Particle)
Thermal correction to Energy= 0.344386
Thermal correction to Enthalpy= 0.345330
Thermal correction to Gibbs Free Energy= 0.272772
Sum of electronic and zero-point Energies= -1871.733601

H	-9.5125540000	-1.1169460000	1.7421150000
H	-8.6458070000	0.1993580000	3.6537040000
C	-8.5662770000	-0.5940130000	1.6519960000
H	-8.2326090000	-1.2479210000	-0.3761170000
C	-8.0747920000	0.1509030000	2.7323870000
C	-7.8511110000	-0.6708640000	0.4597140000
C	-6.8650350000	0.8275090000	2.6363270000
C	-6.6394540000	0.0084530000	0.3674080000
H	-6.4917300000	1.4022090000	3.4780620000
C	-6.1243450000	0.7673650000	1.4476350000
S	-5.5738950000	0.0415450000	-1.0579430000
C	-4.8606620000	1.3715880000	1.1025560000
C	-4.4509890000	1.0620710000	-0.2130050000
H	-3.9089390000	2.6072290000	2.7013740000
C	-3.8831670000	2.2012560000	1.6981390000
C	-3.1994840000	1.6922710000	-0.4794700000
C	-2.8573620000	2.4122140000	0.7519140000
H	-2.6010050000	1.2061400000	-2.4827870000
C	-2.3566120000	1.7361440000	-1.5655590000
C	-1.6713360000	3.1404340000	0.8110000000
H	-1.4063680000	3.6784190000	1.7179880000
C	-1.1462870000	2.4770740000	-1.5105080000
C	-0.8036260000	3.1924380000	-0.2908060000
H	-0.5435460000	1.9910940000	-3.5193020000
C	-0.2785770000	2.5290780000	-2.6123140000
C	0.4066980000	3.9333690000	-0.2357550000
H	0.6510910000	4.4633730000	0.6814730000
C	0.9074480000	3.2572990000	-2.5532280000
C	1.2495700000	3.9772410000	-1.3218440000
C	1.9332540000	3.4682570000	-3.4994530000
H	1.9590260000	3.0622830000	-4.5026880000
C	2.5010750000	4.6074410000	-1.5883090000
C	2.9107490000	4.2979250000	-2.9038710000
S	3.6239810000	5.6279680000	-0.7433720000
C	4.1744310000	4.9021470000	-3.2489490000
H	4.5418170000	4.2673040000	-5.2793760000

C	4.6895400000	5.6610600000	-2.1687230000
C	4.9151220000	4.8420030000	-4.4376420000
C	5.9011980000	6.3403770000	-2.2610280000
C	6.1248780000	5.5186100000	-4.5337010000
H	6.2826950000	6.9174340000	-1.4251970000
C	6.6163630000	6.2635260000	-3.4533100000
H	6.6958940000	5.4701550000	-5.4550190000
H	7.5626400000	6.7864590000	-3.5434290000

anti-IIDBT-sulfone (7)

Zero-point correction=	0.339841 (Hartree/Particle)
Thermal correction to Energy=	0.365195
Thermal correction to Enthalpy=	0.366139
Thermal correction to Gibbs Free Energy=	0.283946
Sum of electronic and zero-point Energies=	-2172.523676

H	0.7904070000	-2.5882160000	-4.2387010000
H	1.2079160000	-0.3307170000	-3.3162780000
C	1.4921500000	-1.9274980000	-4.7366780000
C	1.7247320000	-0.6553950000	-4.2133120000
H	1.9533120000	-3.3560940000	-6.2815710000
H	2.0640750000	2.3740730000	-2.6822540000
C	2.1476690000	-2.3635350000	-5.8902900000
C	2.6276180000	0.1939650000	-4.8544440000
C	2.7482730000	2.4912020000	-3.5122650000
C	3.0332690000	1.5546110000	-4.5023340000
C	3.0549270000	-1.5265470000	-6.5453400000
H	3.0661390000	5.0778740000	-2.2415520000
C	3.2732890000	-0.2691900000	-6.0127170000
C	3.5315670000	3.6595570000	-3.7859870000
H	3.5710160000	-1.8519660000	-7.4419040000
C	3.6423540000	4.8720650000	-3.1396410000
O	3.9266070000	1.4585330000	-7.9954720000
C	3.9840220000	2.1166330000	-5.3944730000
O	4.0125570000	10.9691190000	-1.8896540000
H	4.0462040000	7.2999880000	-2.0865180000
C	4.3195900000	3.4128160000	-4.9914200000
S	4.4035410000	0.9779260000	-6.6948210000
C	4.5149600000	5.8789830000	-3.6371620000
C	4.6298050000	7.1119770000	-2.9828020000
C	5.1798270000	4.3925350000	-5.4904370000
C	5.2946720000	5.6255280000	-4.8360770000
S	5.4060910000	10.5265850000	-1.7784170000

C	5.4900420000	8.0916960000	-3.4818180000
H	5.7634280000	4.2045230000	-6.3867200000
O	5.7970750000	0.5353930000	-6.5835850000
C	5.8256100000	9.3878780000	-3.0787650000
O	5.8830250000	10.0459780000	-0.4777660000
C	6.1672780000	6.6324460000	-5.3335970000
H	6.2386160000	13.3564770000	-1.0313350000
C	6.2780650000	7.8449550000	-4.6872520000
C	6.5363430000	11.7737010000	-2.4605220000
H	6.7434930000	6.4266370000	-6.2316860000
C	6.7547040000	13.0310590000	-1.9278990000
C	6.7763630000	9.9499000000	-3.9709050000
C	7.0613590000	9.0133090000	-4.9609740000
C	7.1820140000	11.3105470000	-3.6187950000
C	7.6619630000	13.8680470000	-2.5829490000
H	7.7455570000	9.1304380000	-5.7909850000
H	7.8563190000	14.8606060000	-2.1916680000
C	8.0849000000	12.1599070000	-4.2599270000
C	8.3174820000	13.4320100000	-3.7365610000
H	8.6017160000	11.8352280000	-5.1569610000
H	9.0192240000	14.0927270000	-4.2345380000

***syn*-IIDBT (4)**

Zero-point correction=	0.323198 (Hartree/Particle)
Thermal correction to Energy=	0.344397
Thermal correction to Enthalpy=	0.345341
Thermal correction to Gibbs Free Energy=	0.272835
Sum of electronic and zero-point Energies=	-1871.734022

H	-8.5812330000	-1.4340420000	2.1361090000
S	-7.6803850000	0.5772850000	0.0681060000
C	-7.5261770000	-1.2063080000	2.2463990000
H	-7.2470360000	-2.5240180000	3.9154730000
C	-6.8997280000	-0.3000220000	1.3942560000
C	-6.7725680000	-1.8159420000	3.2442980000
H	-6.3105990000	2.7649410000	-2.0394960000
C	-6.1615990000	1.3588980000	-0.3128840000
C	-5.7180480000	2.2948280000	-1.2660310000
C	-5.5156500000	0.0121130000	1.5230940000
C	-5.4072020000	-1.5235200000	3.3897660000
C	-5.1090210000	0.9640190000	0.5374080000
H	-4.8365800000	-2.0094480000	4.1742710000
C	-4.7812320000	-0.6220660000	2.5432110000

C	-4.3434290000	2.5082910000	-1.0230830000
C	-3.9327220000	1.6803820000	0.1103350000
H	-3.7258030000	-0.4051500000	2.6665600000
H	-3.7146970000	3.9443570000	-2.5041520000
C	-3.4110560000	3.3282000000	-1.6613630000
C	-2.6300110000	1.7147090000	0.5404190000
H	-2.2993730000	1.1096140000	1.3798480000
C	-2.0799730000	3.3689980000	-1.2286890000
C	-1.6700740000	2.5494090000	-0.1055150000
H	-1.4506740000	4.8087940000	-2.7140520000
C	-1.1200360000	4.2036980000	-1.8746230000
C	-0.3389920000	2.5902090000	0.3271600000
H	-0.0353500000	1.9740510000	1.1699480000
H	-0.0242460000	6.3235640000	-4.0007590000
C	0.1826740000	4.2380260000	-1.4445390000
C	0.5933820000	3.4101170000	-0.3111210000
C	1.0311830000	6.5404800000	-3.8774100000
H	1.0865300000	7.9278660000	-5.5084670000
C	1.3589740000	4.9543910000	-1.8716110000
C	1.6571520000	7.4419360000	-4.7239630000
C	1.7656010000	5.9062990000	-2.8572940000
C	1.9680020000	3.6235760000	-0.0681750000
C	2.4115520000	4.5595100000	-1.0213200000
H	2.5605530000	3.1534620000	0.7052880000
C	3.0225190000	7.7343580000	-4.5784950000
C	3.1496790000	6.2184350000	-2.7284570000
H	3.4969860000	8.4424350000	-5.2496690000
C	3.7761280000	7.1247220000	-3.5805980000
S	3.9303370000	5.3411250000	-1.4023080000
H	4.8311840000	7.3524560000	-3.4703070000

***syn*-IIDBT-sulfone (8)**

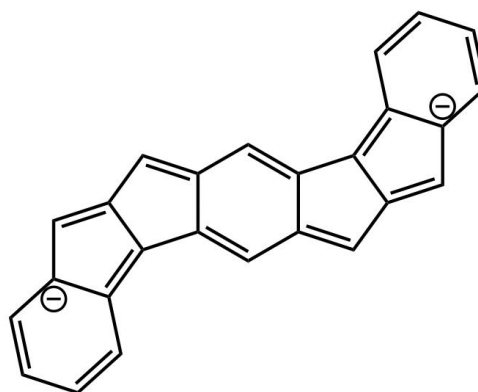
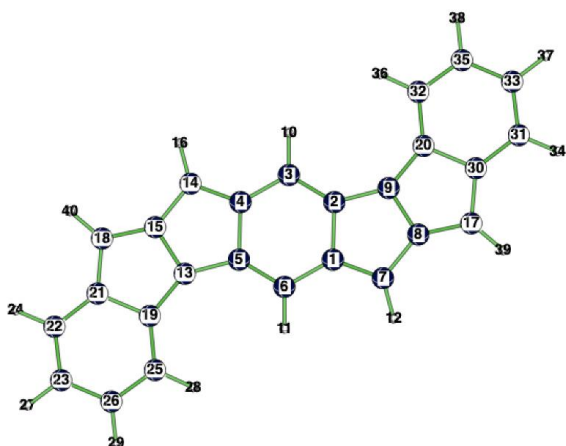
Zero-point correction=	0.340273 (Hartree/Particle)
Thermal correction to Energy=	0.365517
Thermal correction to Enthalpy=	0.366461
Thermal correction to Gibbs Free Energy=	0.284546
Sum of electronic and zero-point Energies=	-2172.526341

O	0.9799490000	1.4332070000	-0.5345300000
H	1.4923090000	-1.5697660000	0.8772780000
H	2.1228980000	-3.8675570000	0.1340150000
C	2.1711300000	-1.7169130000	0.0444140000
S	2.3794920000	1.1049740000	-0.2518740000

C	2.5286140000	-3.0015470000	-0.3772050000
C	2.7091060000	-0.6407170000	-0.6324510000
O	2.9365410000	1.4557930000	1.0569280000
C	3.4046530000	-3.1728380000	-1.4522670000
C	3.4527560000	1.6228770000	-1.5789430000
C	3.5951490000	-0.7813070000	-1.7203660000
H	3.6125480000	3.8134120000	-1.8063720000
H	3.6730830000	-4.1752680000	-1.7682560000
C	3.8804910000	2.8147520000	-2.1220160000
C	3.9397570000	-2.0772380000	-2.1258850000
C	4.0133930000	0.5012670000	-2.2530640000
H	4.6175470000	-2.2333860000	-2.9572310000
C	4.7616410000	2.4684790000	-3.2014420000
C	4.8428330000	1.0111900000	-3.2810240000
H	5.4126830000	4.3369860000	-4.0286630000
C	5.4697020000	3.2531440000	-4.0838200000
C	5.6421770000	0.4198850000	-4.2569300000
H	5.7177770000	-0.6603470000	-4.3352690000
C	6.2865510000	2.6569430000	-5.0810550000
C	6.3682820000	1.2095630000	-5.1616850000
H	6.9370560000	4.5268530000	-5.9074700000
C	7.0126560000	3.4466210000	-5.9858100000
C	7.1851310000	0.6133620000	-6.1589200000
H	7.2421500000	-0.4704800000	-6.2140770000
C	7.8120010000	2.8553160000	-6.9617150000
C	7.8931920000	1.3980270000	-7.0412980000
H	8.0372850000	6.0998920000	-7.2855100000
C	8.6414400000	3.3652390000	-7.9896760000
C	8.7150760000	5.9437440000	-8.1168550000
C	8.7743430000	1.0517540000	-8.1207240000
H	8.9817500000	8.0417740000	-8.4744840000
H	9.0422850000	0.0530940000	-8.4363680000
C	9.0596840000	4.6478130000	-8.5223740000
C	9.2020780000	2.2436290000	-8.6637970000
C	9.2501800000	7.0393440000	-8.7904730000
O	9.7182940000	2.4107130000	-11.2996670000
C	9.9457270000	4.5072230000	-9.6102890000
C	10.1262190000	6.8680530000	-9.8655350000
S	10.2753420000	2.7615320000	-9.9908650000
C	10.4837030000	5.5834190000	-10.2871540000
H	10.5319350000	7.7340630000	-10.3767550000
H	11.1625240000	5.4362720000	-11.1200170000
O	11.6748850000	2.4333000000	-9.7082090000

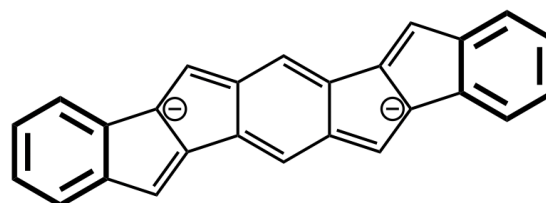
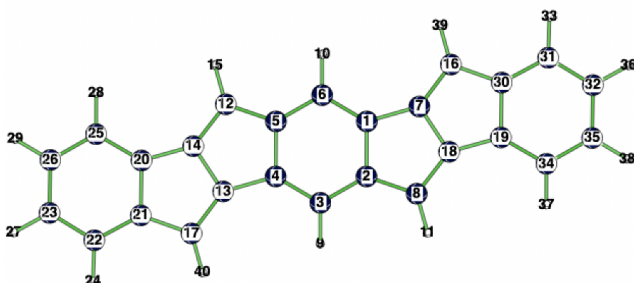
7.3 Clar Sextet-Effects in *syn*- and *anti*-IDBT Fused *s*-Indacenes

Geometries for the dianion hydrocarbon reference compounds that are isoelectronic with the benzothiophene-fused *s*-indacenes (i.e., *syn*-IDBT **2** and *anti*-IDBT **1**) were optimized at B3LYP/6-311++G(d,p) using the Gaussian16 program.¹⁰ Vibrational frequency analyses verified the nature of the stationary points. Natural Lewis structure (NLS) analyses were performed at the same level of theory using the NBO 7.0 program¹¹ to identify the major Lewis structures of the dianion hydrocarbon references and illustrate the “Clar sextet-effect”. The NLS procedure finds and prints out a representation of the best possible Lewis structure for a given molecular wavefunction. According to the recognized Lewis structure, atom numbers specified in the “LONE” string indicate the locations of lone pairs, and the pairs of atom numbers specified in the “BOND” string indicate the locations of single (S) and double (D) bonds. The NLS-recognized Lewis structures for the *syn*-IDBT dianion reference (Figure C24, note absence of Clar sextets in the suggested Lewis structure) and the *anti*-IDBT dianion reference (Figure C25, note two Clar sextets in the suggested Lewis structure) are shown below.



```
LONE 21 1 30 1 END
BOND S 1 2 S 1 6 D 1 7 D 2 3 S 2 9 S 3 4 S 3 10 S 4 5 D 4 14 D 5 6 S 5 13 S 6 11
S 7 8 S 7 12 S 8 9 D 8 17 D 9 20 S 13 15 D 13 19 S 14 15 S 14 16 D 15 18 S 17 30
S 17 39 S 18 21 S 18 40 S 19 21 S 19 25 S 20 30 S 20 32 S 21 22 D 22 23 S 22 24
S 23 26 S 23 27 D 25 26 S 25 28 S 26 29 S 30 31 D 31 33 S 31 34 D 32 35 S 32 36
S 33 35 S 33 37 S 35 38 END
```

Figure C24. NLS output string, atom numbering, and Lewis structure for the isoelectronic dianion hydrocarbon reference structure of *syn*-IDBT **2**. Note the absence of formal Clar sextets in the NLS-recognized Lewis structure.



```
LONE 14 1 18 1 END
BOND S 1 2 D 1 6 S 1 7 S 2 3 D 2 8 D 3 4 S 3 9 S 4 5 S 4 13 S 5 6 D 5 12 S 6 10
D 7 16 S 7 18 S 8 11 S 8 18 S 12 14 S 12 15 S 13 14 D 13 17 S 14 20 S 16 30
S 16 39 S 17 21 S 17 40 S 18 19 S 19 30 D 19 34 S 20 21 D 20 25 D 21 22 S 22 23
S 22 24 D 23 26 S 23 27 S 25 26 S 25 28 S 26 29 D 30 31 S 31 32 S 31 33 D 32 35
S 32 36 S 34 35 S 34 37 S 35 38 END
```

Figure C25. NLS output string, atom numbering, and Lewis structure for the isoelectronic dianion hydrocarbon reference of *anti*-IDBT **1**. Note two Clar sextets in the NLS-recognized Lewis structure.

Dianion hydrocarbon reference for syn-IDBT

Zero-point correction = 0.300441 (Hartree/Particle)

Thermal correction to Energy=	0.318324
Thermal correction to Enthalpy=	0.319268
Thermal correction to Gibbs Free Energy=	0.255528
Sum of electronic and zero-point Energies=	-999.106521
Sum of electronic and thermal Energies=	-999.088638
Sum of electronic and thermal Enthalpies=	-999.087694
Sum of electronic and thermal Free Energies=	-999.151434

C	-1.21563	-0.71236	0.00000
C	0.08738	-1.44016	0.00000
C	1.25475	-0.72300	0.00000
C	1.21563	0.71236	0.00000
C	-0.08738	1.44016	0.00000
C	-1.25475	0.72300	0.00000
C	-2.24077	-1.63873	0.00000
C	-1.66505	-2.97157	0.00000
C	-0.24335	-2.85115	0.00000
H	2.21961	-1.22511	0.00000
H	-2.21961	1.22511	0.00000
H	-3.29874	-1.39651	0.00000
C	0.24335	2.85115	0.00000
C	2.24077	1.63873	0.00000
C	1.66505	2.97157	0.00000
H	3.29874	1.39651	0.00000
C	-2.04406	-4.32378	0.00000
C	2.04406	4.32378	0.00000
C	-0.30257	4.15775	0.00000
C	0.30257	-4.15775	0.00000
C	0.83646	5.09040	0.00000
C	0.59496	6.47253	0.00000
C	-0.71222	6.96357	0.00000
H	1.43374	7.16788	0.00000
C	-1.60801	4.68994	0.00000
C	-1.80641	6.06930	0.00000
H	-0.89115	8.03619	0.00000
H	-2.46615	4.02267	0.00000
H	-2.81977	6.46520	0.00000
C	-0.83646	-5.09040	0.00000
C	-0.59496	-6.47253	0.00000
C	1.60801	-4.68994	0.00000
C	0.71222	-6.96357	0.00000

H	-1.43374	-7.16788	0.00000
C	1.80641	-6.06930	0.00000
H	2.46615	-4.02267	0.00000
H	0.89115	-8.03619	0.00000
H	2.81977	-6.46520	0.00000
H	-3.04957	-4.72936	0.00000
H	3.04957	4.72936	0.00000

Dianion hydrocarbon reference for anti-IDBT

Zero-point correction=	0.300573 (Hartree/Particle)
Thermal correction to Energy=	0.318394
Thermal correction to Enthalpy=	0.319338
Thermal correction to Gibbs Free Energy=	0.255827
Sum of electronic and zero-point Energies=	-999.116178
Sum of electronic and thermal Energies=	-999.098357
Sum of electronic and thermal Enthalpies=	-999.097413
Sum of electronic and thermal Free Energies=	-999.160924

C	1.32434	-0.50996	0.00000
C	1.05838	0.93491	0.00000
C	-0.27567	1.40840	0.00000
C	-1.32434	0.50996	0.00000
C	-1.05838	-0.93491	0.00000
C	0.27567	-1.40840	0.00000
C	2.77145	-0.65617	0.00000
C	2.29366	1.62068	0.00000
H	-0.46731	2.48072	0.00000
H	0.46731	-2.48072	0.00000
H	2.39749	2.70122	0.00000
C	-2.29366	-1.62068	0.00000
C	-2.77145	0.65617	0.00000
C	-3.34159	-0.67087	0.00000
H	-2.39749	-2.70122	0.00000
C	3.79684	-1.60948	0.00000
C	-3.79684	1.60948	0.00000
C	3.34159	0.67087	0.00000
C	4.76641	0.53792	0.00000
C	-4.76641	-0.53792	0.00000
C	-5.04347	0.90003	0.00000
C	-6.37908	1.33356	0.00000

C	-7.42410	0.40615	0.00000
H	-6.60373	2.39914	0.00000
C	-5.83561	-1.44203	0.00000
C	-7.15511	-0.97809	0.00000
H	-8.45473	0.75410	0.00000
H	-5.64163	-2.51281	0.00000
H	-7.97879	-1.68805	0.00000
C	5.04347	-0.90003	0.00000
C	6.37908	-1.33356	0.00000
C	7.42410	-0.40615	0.00000
H	6.60373	-2.39914	0.00000
C	5.83561	1.44203	0.00000
C	7.15511	0.97809	0.00000
H	8.45473	-0.75410	0.00000
H	5.64163	2.51281	0.00000
H	7.97879	1.68805	0.00000
H	3.69514	-2.68852	0.00000
H	-3.69514	2.68852	0.00000

7.4 Charge-Effects in IDT and IDT-S Fused *s*-Indacenes

When the two terminal benzene rings of IDBT and IDBT-S are removed, both thiophene (IDT) and thiophene-dioxide (IDT-S) fused *s*-indacenes exhibit a more paratropic *anti*-isomer. In these systems, the “Clar sextet-effect,” arising from differences in the dominant resonance forms of the outer benzenoid rings is absent, and a “charge-effect” (i.e., topological charge stabilization) dominates. Computed NPA charges for the *s*-indacene core show that carbons 2 and 6 display the most negative charges (see Figure 4.4 in Chapter IV). In the *syn*-forms, the S and SO₂ groups stabilize negative charges at carbons 2 and 6, resulting in larger HOMO-LUMO gaps (S: 2.29 eV, SO₂: 2.27 eV) and decreased paratropicity. In the *anti*-forms, the S and SO₂ groups destabilize charges at carbons 2 and 6, resulting in smaller HOMO-LUMO gaps (S: 1.35 eV, SO₂: 1.28 eV) and increased paratropicity.

Geometries for IDT and IDT-S were optimized at B3LYP/6-311++G(d,p) using the Gaussian16 program.¹⁰ Optimized Cartesian coordinates are included in Section 7.1 of Appendix C. Natural Population Analyses (NPA) analyses were performed at the same level of theory using the NBO 7.0 program¹¹ as implemented in Gaussian16. HOMO-LUMO gaps were computed as vertical excitation energies from the HOMO to the LUMO orbitals at TD-B3LYP/6-311++G(d,p).

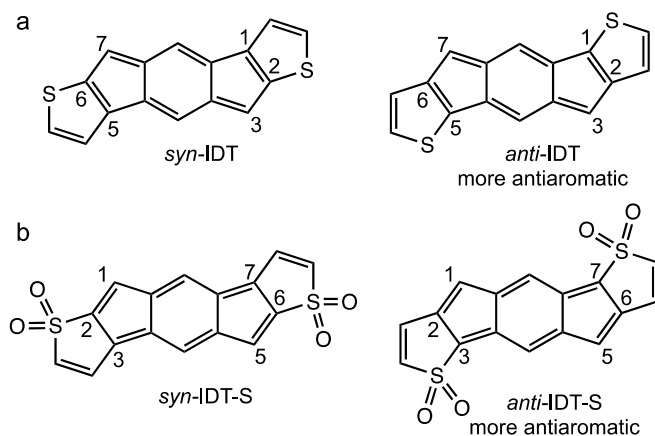


Figure C26. Structures for (a) IDT (shown in “normal” bonding pattern) and (b) IDT-S (shown in “flipped” bonding pattern). Both systems show a more paratropic *anti*- form, as expected by a “charge-effect” (i.e., topological charge stabilization; see Figure S25). Electronegative groups stabilize the *s*-indacene core when attached to positions 2 and 6 (*syn*-), and destabilize the *s*-indacene core when attached to positions 1 and 5 or 3 and 7 (*anti*-).

7.5 Optimized Geometries and Calculated γ and ΔE_{ST} Values

Geometry optimization and frequency analysis calculations for the singlet and triplet states were performed at the RB3LYP and UB3LYP levels, respectively, using the 6-311G* basis set. Vertical and adiabatic ΔE_{ST} values were evaluated at the SF-NC-TDDFT PBE50/6-311G* level,¹² where zero-point vibrational energy (ZPVE) corrections for the singlet and triplet states were estimated from the results of the frequency analysis calculations at the RB3LYP and UB3LYP levels, respectively. Diradical character γ for the singlet state was evaluated at the PUHF/6-311G* level. Quantum chemical calculations were performed using Gaussian 09¹³ and Q-Chem 5¹⁴ program packages. Calculation results were visualized using DrawMol package.¹⁵

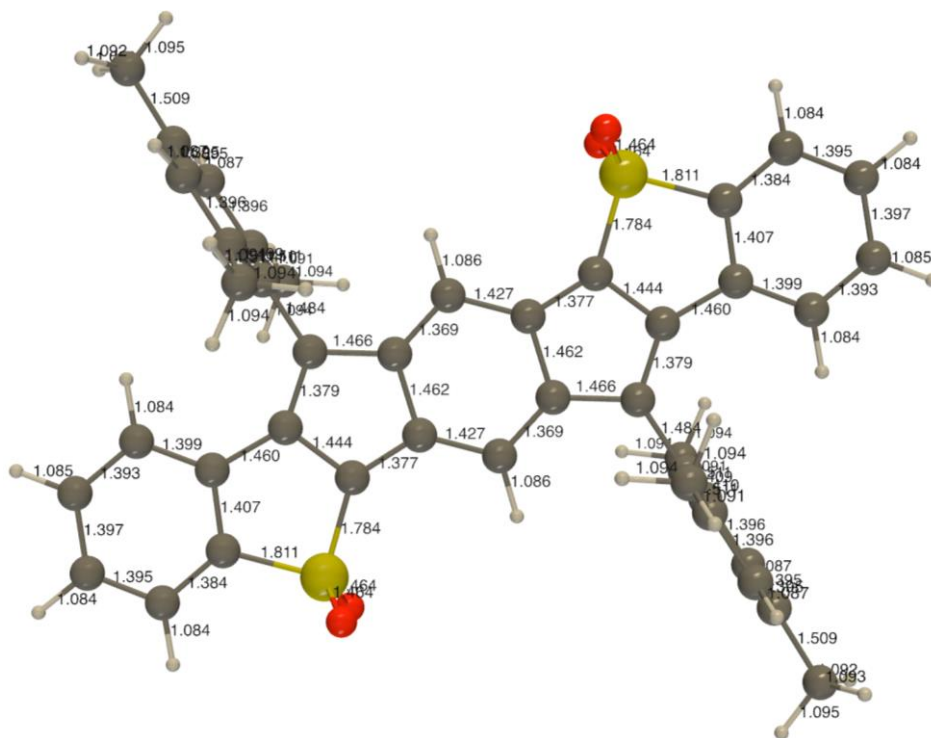


Figure C27. Optimized geometry of *anti*-IDBT-sulfone **5**.

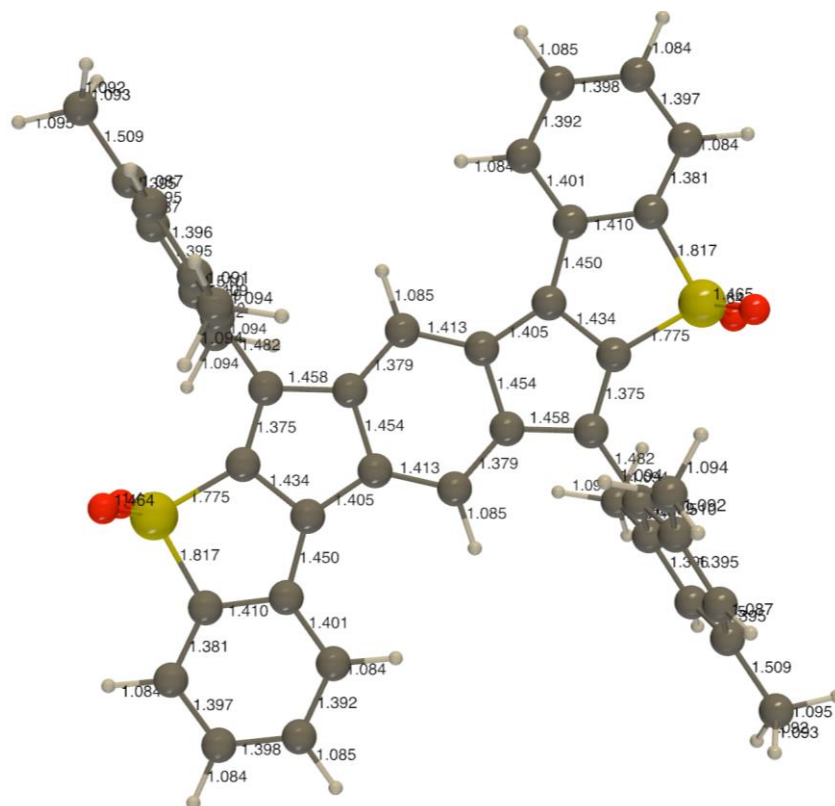


Figure C28. Optimized geometry of *syn*-IDBT-sulfone **6**.

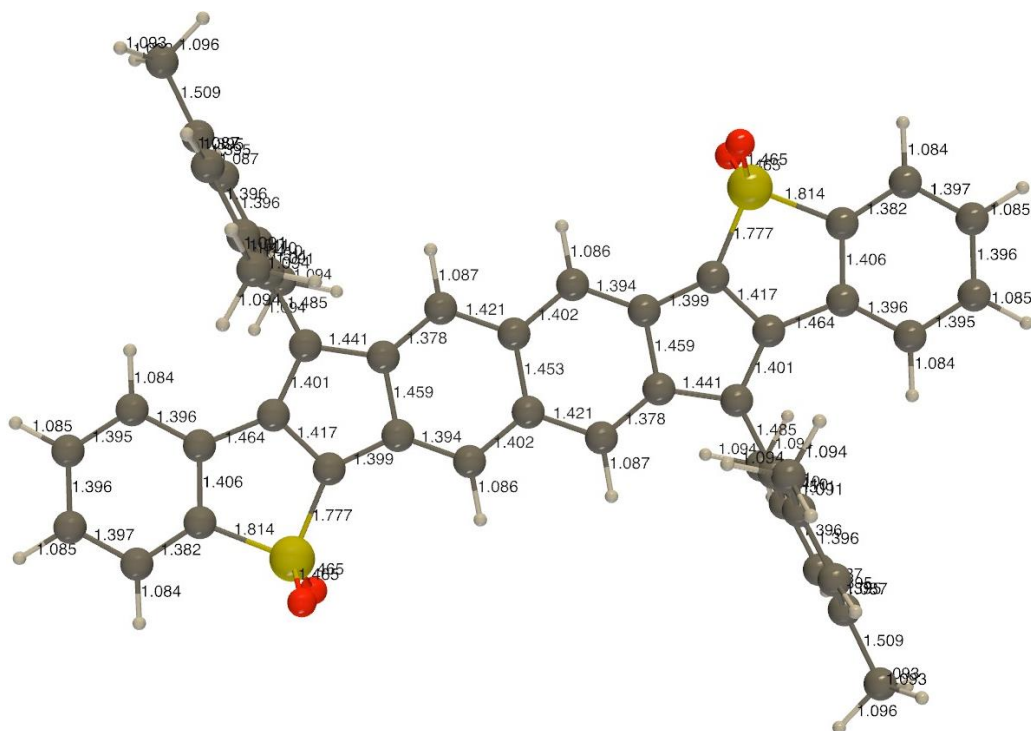


Figure C29. Optimized geometry of *anti*-IIDBT-sulfone **7**.

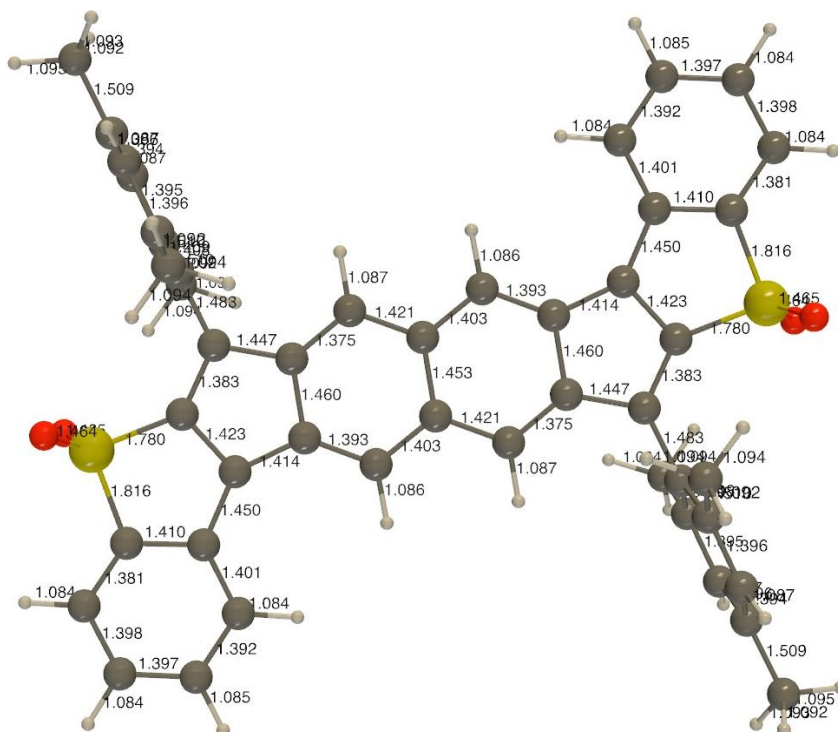


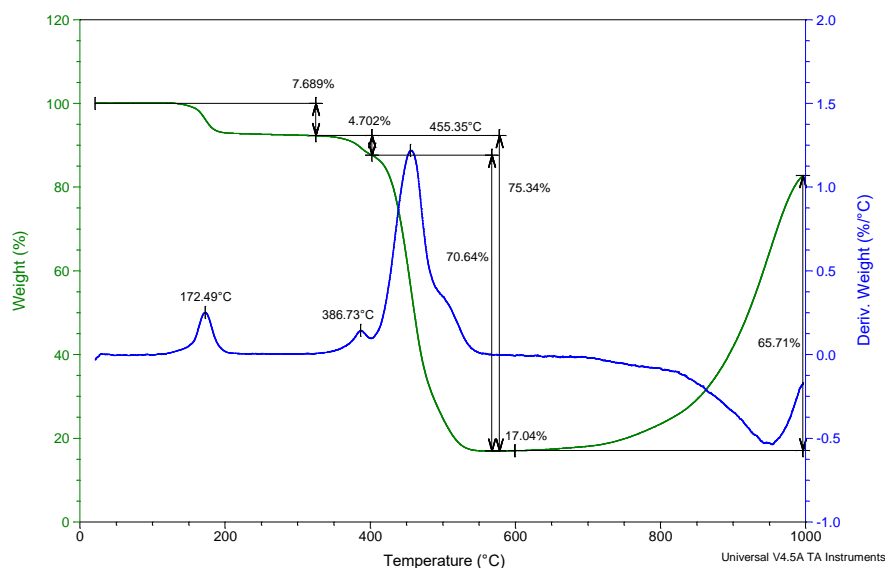
Figure C30. Optimized geometry of *syn*-IIDBT-sulfone **8**.

Table C2. Summary of calculation results.

	IIDBT		IIDBT-sulfone	
	<i>anti</i> (3)	<i>syn</i> (4)	<i>anti</i> (7)	<i>syn</i> (8)
χ (PUHF) [-]	0.613	0.658	0.601	0.652
Vert. ΔE_{ST} (kcal mol ⁻¹)	-11.65	-11.09	-13.59	-11.26
Adia. ΔE_{ST} (kcal mol ⁻¹)	-9.37	-8.84	-10.72	-9.33
Adia. ΔE_{ST} (+ZPVE) (kcal mol ⁻¹)	-8.77	-8.06	-9.65	-8.29
ΔE_{ST} (exp) (kcal mol ⁻¹)	-8.3	-7.1	n.a.	-6.5

8. SQUID Details and TGA Analysis

Magnetic susceptibility measurements were performed with a Quantum Design MPMS-XL-5 SQUID susceptometer in the 300-580 K temperature range with an applied field of 0.5 T using a sample space oven with the sample ($m = 4.528$ mg) inserted in a 1.5 mm diameter aluminum foil cylinder. The susceptibility data were corrected for the same sample holder previously measured using the same conditions and for the diamagnetic contributions of the compound as deduced by using Pascal's constant tables.¹⁶ The magnetic measurements were fitted using the classical Bleaney-Bowers model for an antiferromagnetic $S = 1/2$ dimer plus a monomeric $S = 1/2$ impurity.¹⁷

**Figure C31.** TGA data for *syn*-IIDBT-S 8. Weight loss at ~170 °C corresponds to loss of residual 1,2-dichlorobenzene solvent (or possibly loss of a *t*-butyl group).

9. References

1. Sheldrick, G. M. *Bruker/Siemens Area Detector Absorption Correction Program*, Bruker AXS, Madison, WI, 1998.
2. van der Sluis, P.; Spek, A. L. *Acta Cryst., Sect. A* **1990**, *A46*, 194–201.
3. Sheldrick, G. M. *Acta Cryst.* **2015**, *C71*, 3–8.
4. CrysAlisPro; Rigaku OD, The Woodlands, TX, 2015.
5. Sheldrick, G. M. *Acta Cryst.* **2008**, *A64*, 112–122.
6. Müller, P. *Crystallogr. Rev.* **2009**, *15*, 57–83.
7. Frisch, M. J.; Trucks, G. W.; Schlegel, H. B.; Scuseria, G. E.; Robb, M. A.; Cheeseman, J. R.; Scalmani, G.; Barone, V.; Mennucci, B.; Petersson, G. A.; Nakatsuji, H.; Caricato, M.; Li, X.; Hratchian, H. P.; Izmaylov, A. F.; Bloino, J.; Zheng, G.; Sonnenberg, J. L.; Hada, M.; Ehara, M.; Toyota, K.; Fukuda, R.; Hasegawa, J.; Ishida, M.; Nakajima, T.; Honda, Y.; Kitao, O.; Nakai, H.; Vreven, T.; Montgomery, Jr., J. A.; Peralta, J. E.; Ogliaro, F.; Bearpark, M.; Heyd, J. J.; Brothers, E.; Kudin, K. N.; Staroverov, V. N.; Keith, T.; Kobayashi, R.; Normand, J.; Raghavachari, K.; Rendell, A.; Burant, J. C.; Iyengar, S. S.; Tomasi, J.; Cossi, M.; Rega, N.; Millam, J. M.; Klene, M.; Knox, J. E.; Cross, J. B.; Bakken, V.; Adamo, C.; Jaramillo, J.; Gomperts, R.; Stratmann, R. E.; Yazyev, O.; Austin, A. J.; Cammi, R.; Pomelli, C.; Ochterski, J. W.; Martin, R. L.; Morokuma, K.; Zakrzewski, V. G.; Voth, G. A.; Salvador, P.; Dannenberg, J. J.; Dapprich, S.; Daniels, A. D.; Farkas, O.; Foresman, J. B.; Ortiz, J. V.; Cioslowski, J.; and Fox, D. J. *Gaussian 09*, Revision E.01; Gaussian, Inc.: Wallingford CT, 2013.
8. Rahalkar, A.; Stanger, A. http://schulich.technion.ac.il/Amnon_Stanger.htm

9. (a) Stanger, A. *J. Org. Chem.* **2006**, *71*, 883–893; (b) Stanger, A. *J. Org. Chem.* **2010**, *75*, 2281–2288; (c) Gershoni-Poranne, R.; Stanger, A. *Chem.–Eur. J.* **2014**, *20*, 5673–5688.
10. Frisch, M. J., Trucks, G. W., Schlegel, H. B., Scuseria, G. E., Robb, M. A., Cheeseman, J. R., Scalmani, G., Barone, V., Petersson, G. A., Nakatsuji, H., Li, X., Caricato, M., Marenich, A. V., Bloino, J., Janesko, B. G., Gomperts, R., Mennucci, B., Hratchian, H. P., Ortiz, J. V., Izmaylov, A. F., Sonnenberg, J. L., Williams-Young, D., Ding, F., Lipparini, F., Egidi, F., Goings, J., Peng, B., Petrone, A., Henderson, T., Ranasinghe, D., Zakrzewski, V. G., Gao, J., Rega, N., Zheng, G., Liang, W., Hada, M., Ehara, M., Toyota, K., Fukuda, R., Hasegawa, J., Ishida, M., Nakajima, T., Honda, Y., Kitao, O., Nakai, H., Vreven, T., Throssell, K., Montgomery, J. A., Jr., Peralta, J. E., Ogliaro, F., Bearpark, M. J., Heyd, J. J., Brothers, E. N., Kudin, K. N., Staroverov, V. N., Keith, T. A., Kobayashi, R., Normand, J., Raghavachari, K., Rendell, A. P., Burant, J. C., Iyengar, S. S., Tomasi, J., Cossi, M., Millam, J. M., Klene, M., Adamo, C., Cammi, R., Ochterski, J. W., Martin, R. L., Morokuma, K., Farkas, O., Foresman, J. B., Fox, D. J. *Gaussian 16, Revision C.01*; Gaussian, Inc.: Wallingford CT, 2016.
11. Glendening, E. D.; Badenhoop, J. K.; Reed, A. E.; Carpenter, J. E.; Bohmann, J. A.; Morales, C. M.; Karafiloglou, P.; Landis, C. R.; Weinhold, F. *NBO 7.0*, Theoretical Chemistry Institute, University of Wisconsin, Madison, 2018.
12. (a) Shao, Y.; Head-Gordon, M.; Krylov, A. I. *J. Chem. Phys.* **2003**, *118*, 4807–4818. (b) Wang, F.; Ziegler, T. *J. Chem. Phys.* **2004**, *121*, 12191–12196. (c) Wang, F.; Ziegler, T. *J. Chem. Phys.* **2005**, *122*, 074109–1-9. c) Wang, F.; Ziegler, T. *Int. J. Quantum Chem.* **2006**, *106*, 2545–2550.

13. Frisch, M. J.; Trucks, G. W.; Schlegel, H. B.; Scuseria, G. E.; Robb, M. A.; Cheeseman, J. R.; Scalmani, G.; Barone, V.; Mennucci, B.; Petersson, G. A.; Nakatsuji, H.; Caricato, M.; Li, X.; Hratchian, H. P.; Izmaylov, A. F.; Bloino, J.; Zheng, G.; Sonnenberg, J. L.; Hada, M.; Ehara, M.; Toyota, K.; Fukuda, R.; Hasegawa, J.; Ishida, M.; Nakajima, T.; Honda, Y.; Kitao, O.; Nakai, H.; Vreven, T.; Montgomery, J. A., J.; Peralta, J. E.; Ogliaro, F.; Bearpark, M.; Heyd, J. J.; Brothers, E.; Kudin, K. N.; Staroverov, V. N.; Kobayashi, R.; Normand, J.; Raghavachari, K.; Rendell, A.; Burant, J. C.; Iyengar, S. S.; Tomasi, J.; Cossi, M.; Rega, N.; Millam, J. M.; Klene, M.; Knox, J. E.; Cross, J. B.; Bakken, V.; Adamo, C.; Jaramillo, J.; Gomperts, R.; Stratmann, R. E.; Yazyev, O.; Austin, A. J.; Cammi, R.; Pomelli, C.; Ochterski, J. W.; Martin, R. L.; Morokuma, K.; Zakrzewski, V. G.; Voth, G. A.; Salvador, P.; Dannenberg, J. J.; Dapprich, S.; Daniels, A. D.; Farkas, Ö.; Foresman, J. B.; Ortiz, J. V.; Cioslowski, J.; Fox, D. J. Gaussian 09, Revision D.01; Gaussian, Inc.: Wallingford CT, 2009.

14. Shao, Y.; Gan, Z.; Epifanovsky, E.; Gilbert, A. T. B.; Wormit, M.; Kussmann, J.; Lange, A. W.; Behn, A.; Deng, J.; Feng, X.; Ghosh, D.; Goldey, M.; Horn, P. R.; Jacobson, L. D.; Kaliman, I.; Khaliullin, R. Z.; Kuš, T.; Landau, A.; Liu, J.; Proynov, E. I.; Rhee, Y. M.; Richard, R. M.; Rohrdanz, M. A.; Steele, R. P.; Sundstrom, E. J.; Woodcock, H. L.; Zimmerman, P. M.; Zuev, D.; Albrecht, B.; Alguire, E.; Austin, B.; Beran, G. J. O.; Bernard, Y. A.; Berquist, E.; Brandhorst, K.; Bravaya, K. B.; Brown, S. T.; Casanova, D.; Chang, C.-M.; Chen, Y.; Chien, S. H.; Closser, K. D.; Crittenden, D. L.; Diedenhofen, M.; DiStasio, R. A.; Do, H.; Dutoi, A. D.; Edgar, R. G.; Fatehi, S.; Fusti-Molnar, L.; Ghysels, A.; Golubeva-Zadorozhnaya, A.; Gomes, J.; Hanson-Heine, M. W. D.; Harbach, P.H.P.; Hauser, A. W. ; Hohenstein, E. G.; Holden, Z. C.; Jagau, T.-C.; Ji, H.; Kaduk, B.n;

Khistyayev, K.; Kim, J.; Kim, J.; King, R. A.; Klunzinger, P.; Kosenkov, D.; Kowalczyk, T.; Krauter, C. M.; Lao, K. U.; Laurent, A. D.; Lawler, K. V.; Levchenko, S. V.; Lin, C. Y.; Liu, F.; Livshits, E.; Lochan, R. C.; Luenser, A.; Manohar, P.; Manzer, S. F.; Mao, S.-P.; Mardirossian, N.; Marenich, A. V.; Maurer, S. A.; Mayhall, N. J.; Neuscamman, E.; Oana, C. M.; Olivares-Amaya, R.; O'Neill, D. P.; Parkhill, J. A.; Perrine, T. M.; Peverati, R.; Prociuk, A.; Rehn, D. R.; Rosta, E.; Russ, N. J.; Sharada, S. M.; Sharma, S.; Small, D. W.; Sodt, A.; Stein, T.; Stück, D.; Su, Y.-C.; Thom, A. J. W.; Tsuchimochi, T.; Vanovschi, V.; Vogt, L.; Vydrov, O.; Wang, T.; Watson, M. A.; Wenzel, J.; White, A.; Williams, C. F.; Yang, J.; Yeganeh, S.; Yost, S. R.; You, Z.-Q.; Zhang, I. Y.; Zhang, X.; Zhao, Y.; Brooks, B. R.; Chan, G. K. L.; Chipman, D. M.; Cramer, C. J.; Goddard, W. A.; Gordon, M. S.; Hehre, W. J.; Klamt, A.; Schaefer, H. F.; Schmidt, M. W.; Sherrill, C. D.; Truhlar, D. G.; Warshel, A.; Xu, X.; Aspuru-Guzik, A.; Baer, R.; Bell, A. T.; Besley, N. A.; Chai, J.-D.; Dreuw, A.; Dunietz, B. D.; Furlani, T. R.; Gwaltney, S. R.; Hsu, C.-P.; Jung, Y.; Kong, J.; Lambrecht, D. S.; Liang, W.; Ochsenfeld, C.; Rassolov, V. A.; Slipchenko, L. V.; Subotnik, J. E.; Voorhis, T. V.; Herbert, J. M.; Krylov, A. I.; Gill, P. M. W.; Head-Gordon, M. *Mol. Phys.* **2015**, *113*, 184–215.

15. Liegeois, V. DrawMol ver. 1.5, UNamur, www.unamur.be/drawmol.

16. Bain, G. A.; Berry, J. F. *J. Chem. Educ.* **2008**, *85*, 532–536.

17. Bleaney, B.; Bowers, K. D. *Proc. R. Soc. Lond. A.* **1952**, *214*, 451–465.

APPENDIX D

SUPPLEMENTARY INFORMATION FOR CHAPTER IV

Appendix D is the supplementary information for Chapter V of this dissertation. It includes experimental details, other experimental data, spectra, and computational details relevant to the content in Chapter V.

Computational Details

General. Geometry optimization and frequency analysis for the neutral singlet were performed at the RB3LYP and UB3LYP levels, respectively, using the 6-311G* basis set. We employed the UB3LYP functional for geometry optimization of radical cations and anions. Vertical and adiabatic ΔE_{ST} values were evaluated at the spin-flip noncollinear (SF-NC-)TDDFT PBE50/6-311G* level,¹ where zero-point vibrational energy (ZPVE) corrections for the singlet and triplet states were estimated from the results of the frequency analysis calculations at the RB3LYP and UB3LYP levels, respectively. CASCI(2,2) calculations for the estimations of VCI parameters were performed using the molecular orbitals obtained at the tuned-LC-RBLYP/6-311G* level, where an optimal range-separating parameter μ for each system was determined by IP-tuning scheme for N -electron system.² Diradical characters y were evaluated at the PUHF/6-311G* [denoted as $y(\text{PUHF})$]³ and tuned-LC-RBLYP-CASCI(2,2)/6-311G* [denoted as $y(\text{CASCI})$] levels. The results are given in Table S1.

Nucleus-independent chemical shift (NICS)⁴ calculations as well as the aromaticity of induced current density (AICD)⁵ analyses were performed at the GIAO- and CSGT-

tuned-LC-UBLYP/6-311G* level where we employed the same μ values for the neutral species. Excitation properties were evaluated at the time-dependent tuned-LC-UBLYP/6-311G* level. These calculations were performed using Gaussian 09 (geometry optimization and TD-DFT excitation energy),⁶ GAMESS-US (CASCI),⁷ and Q-Chem 4 and 5 (ΔE_{ST})⁸ program packages. DrawMol package⁹ was used for the visualizations of molecular modeling and spatial distributions of MOs and odd-electron densities.

The tendencies of PUHF/SF-TDDFT results for γ and ST gaps are qualitatively in agreement with those of CASCI results within DBFF (linear vs. syn vs. anti) and TBFF. The tendency of γ for FF vs. linear-DBFF at the PUHF was not in agreement with that at the CASCI. This may be due to the limitation of the present estimation scheme of tuned-LC-CASCI including orbital parameter tuning. We have also checked the effect of aryl groups on the calculation results as listed in Table S2. Substituent effects on several diradical properties discussed here are expected to be very slight and negligible.

Table D1. Summary of calculation results

	FF 1 ^a	<i>lin.</i> -DBFF 2	<i>syn</i> -DBFF 3	<i>anti</i> -DBFF 4	TBFF 5
<i>y</i> (PUHF) (–)	0.492	0.512	0.559	0.595	0.629
Vertical ΔE_{ST} (kcal mol ⁻¹)	-17.46	-17.52	-15.32	-13.68	-12.68
Adiabatic ΔE_{ST} (kcal mol ⁻¹)	-11.44	-11.31	-10.67	-9.62	-9.19
Adiabatic ΔE_{ST} (+ZPVE) (kcal mol ⁻¹)	-10.25	-10.03	-9.63	-8.61	-7.90
Tuned value of μ (bohr ⁻¹)	0.1546	0.1413	0.1411	0.1409	0.1321
<i>y</i> (CASCI) (–)	0.151	0.133	0.158	0.166	0.182
Vertical ΔE_{ST} (CASCI) (kcal mol ⁻¹)	-27.9	-28.8	-24.3	-22.4	-20.2
$ t_{ab} $ (eV)	1.163	1.143	1.055	1.012	0.960
$f_{ST}(y)$ (–)	-0.894	-1.006	-0.854	-0.815	-0.740
$U/2 = K_{gu}^M$ (eV)	1.446	1.315	1.352	1.336	1.349
$(U/2)f_{ST}(y)$ (eV)	-1.293	-1.323	-1.154	-1.089	-0.998
J_{gg}^M (eV)	4.566	4.102	4.373	4.165	4.201
J_{uu}^M (eV)	4.667	4.423	4.495	4.425	4.424
J_{gu}^M (eV)	4.535	4.189	4.332	4.179	4.189
$2K_{ab}$ (eV)	0.082	0.073	0.102	0.116	0.123

^aResults taken from reference 10.**Table D2.** Effects of aryl species Ar on the calculation results of *y* and ΔE_{ST} .

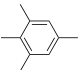
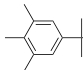
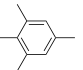
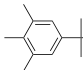
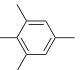
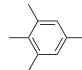
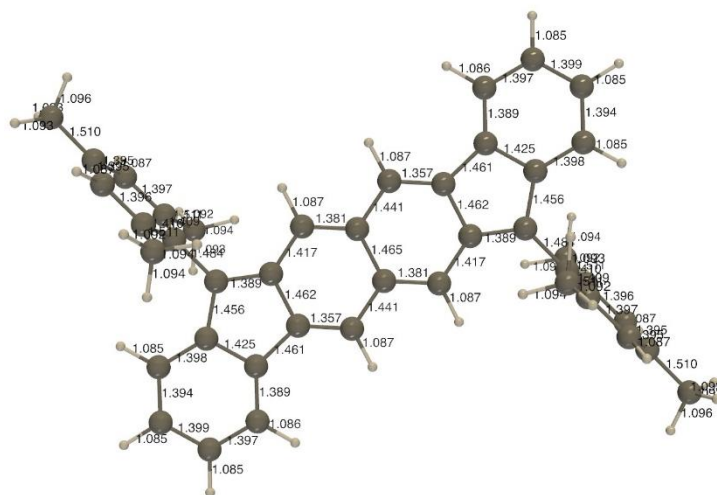
Ar	<i>syn</i> -DBFF		<i>anti</i> -DBFF		TBFF	
						
<i>y</i> (PUHF) (–)	0.559	0.555	0.595	0.594	0.629	0.628
Vertical ΔE_{ST} (kcal mol ⁻¹)	-15.32	-15.33	-13.68	-13.70	-12.68	-12.69
Adiabatic ΔE_{ST} (kcal mol ⁻¹)	-10.67	-10.79	-9.62	-9.61	-9.19	-9.07
Adiabatic ΔE_{ST} +ZPVE (kcal mol ⁻¹)	-9.63	-9.64	-8.61	-8.40	-7.90	-8.10

Table S3. Comparison of physical parameters calculated at the tuned-LC-CASCI/6-311G* for FF/DBFF and DIAn/DBDIAn (central anthracene core is substituted by CCSiMe₃ groups).

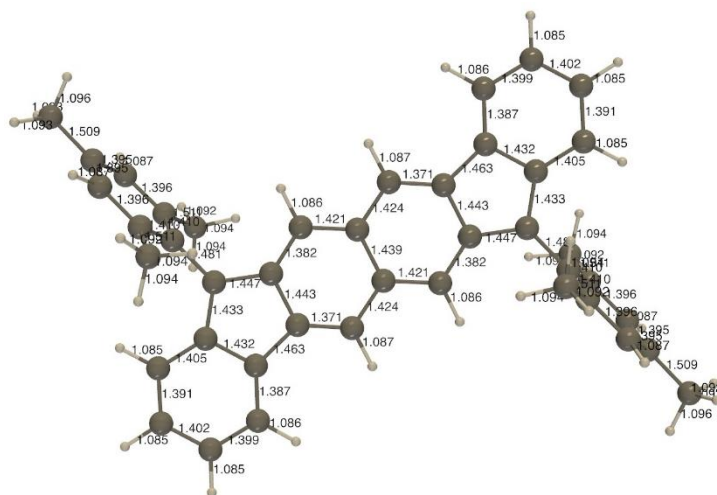
	FF core	<i>linear</i> -DBFF	<i>syn</i> -DBFF	<i>anti</i> -DBFF
$U/2$ (eV)	1.446	1.315	1.352	1.336
$ t_{ab} $ (eV)	1.163	1.143	1.055	1.012
$U/ t_{ab} $ (-)	2.487	2.301	2.563	2.640

	DIAn core	<i>linear</i> -DBDIAn	<i>syn</i> -DBDIAn	<i>anti</i> -DBDIAn
$U/2$ (eV)	1.435	1.348	1.378	1.377
$ t_{ab} $ (eV)	0.916	0.905	0.818	0.781
$U/ t_{ab} $ (-)	3.133	2.979	3.369	3.526

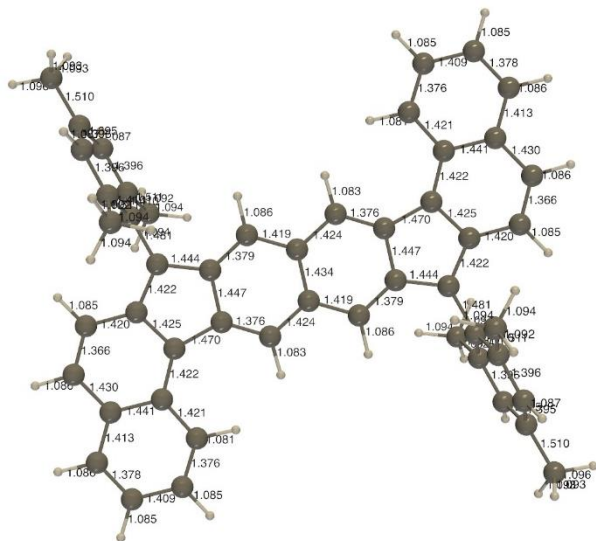


FF 1

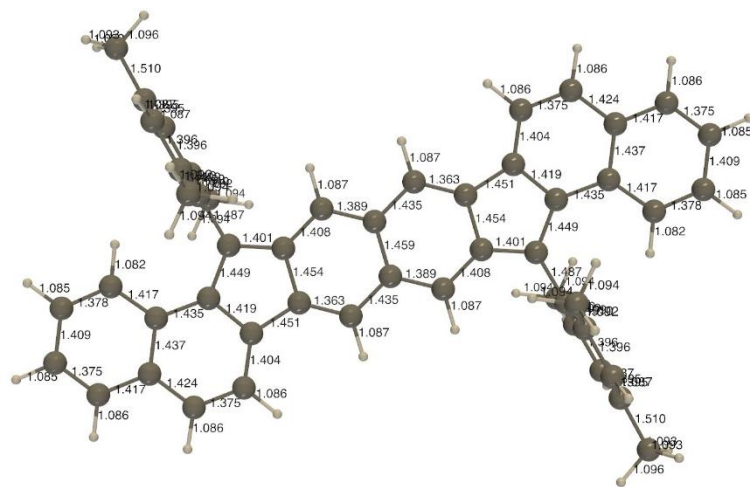
Singlet



Triplet

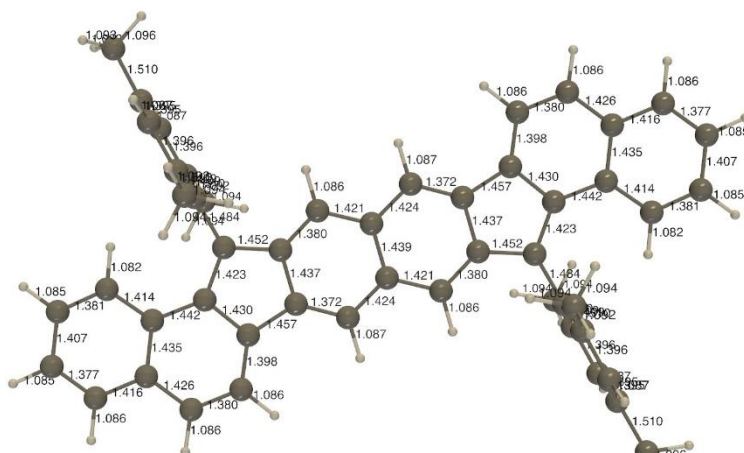


Triplet



Singlet

anti-
DBFF
4



Triplet

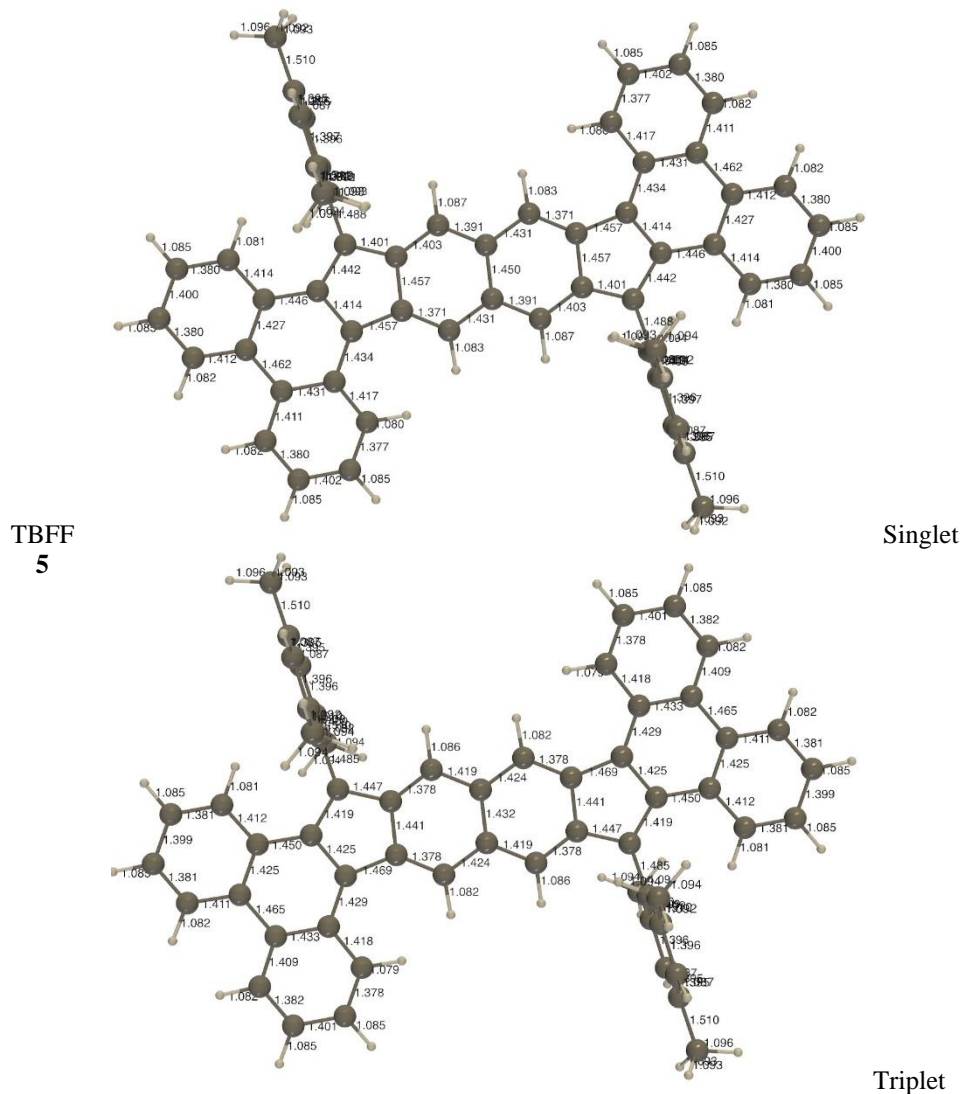


Figure D1. Optimized bond lengths (Å) of calculated FFs **1-5** at the singlet (upper) and triplet (lower) states.

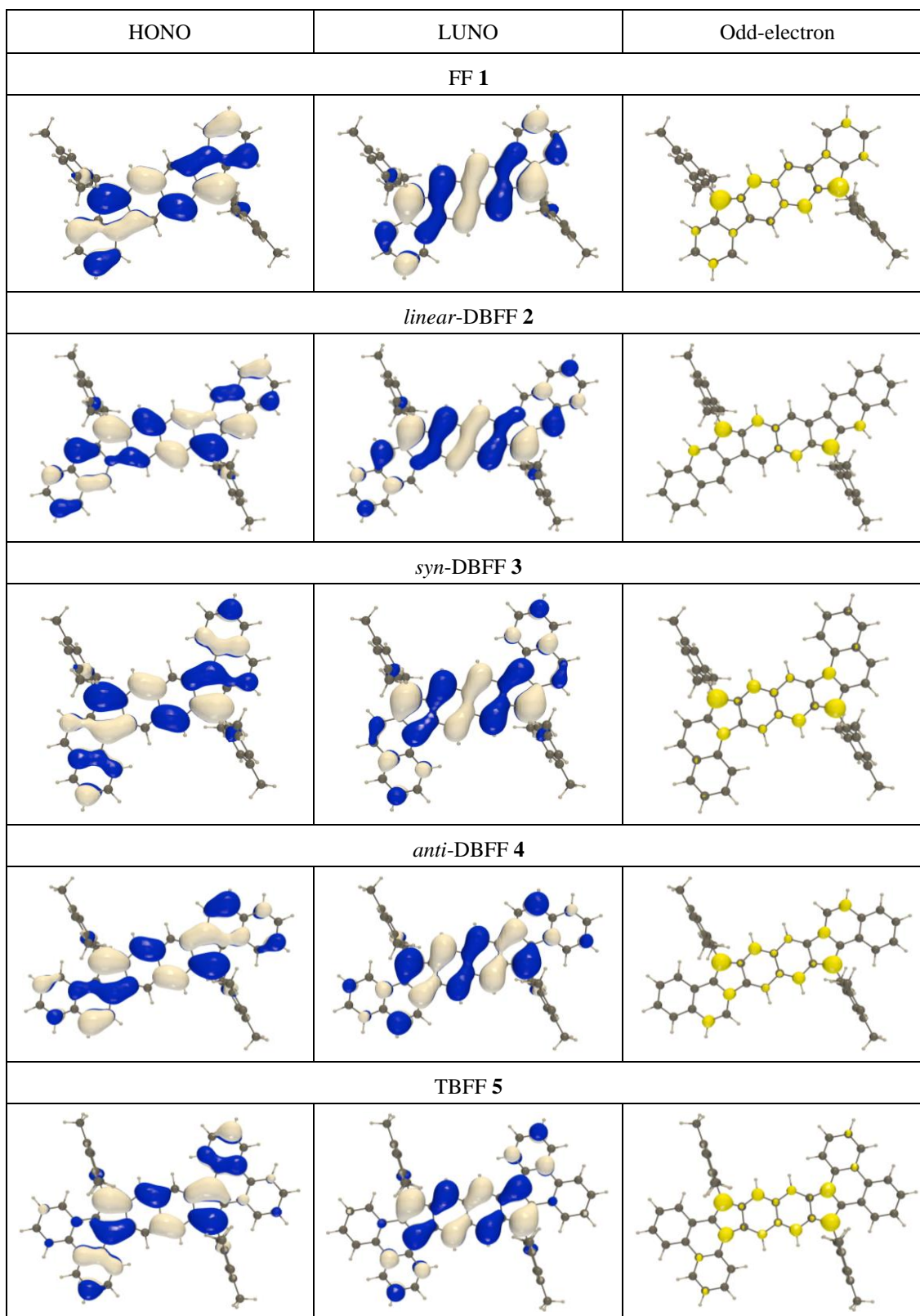


Figure D2. Maps of HONO, LUNO and odd-electron density distributions for neutral species of FFs **1-5** calculated at the tuned-LC-RBLYP CASCI/6-311G* level.

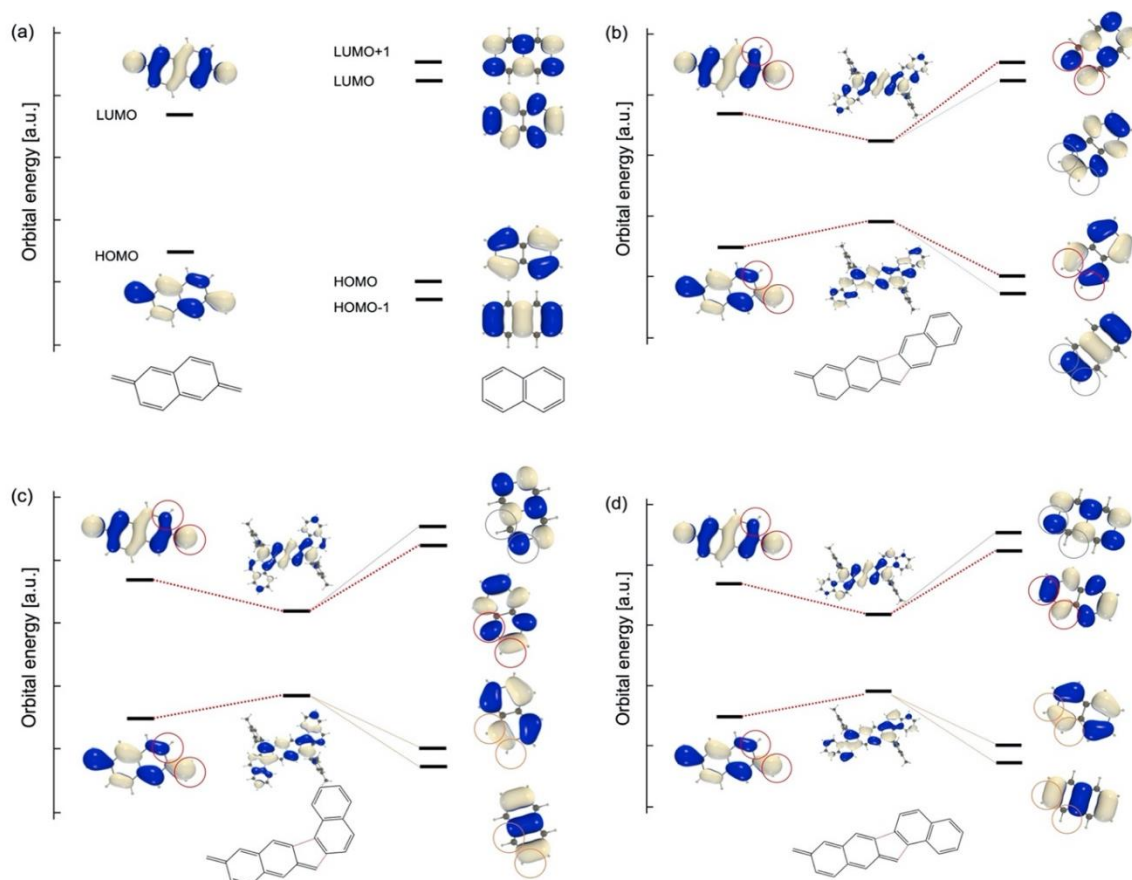


Figure D3. Frontier MO levels of 2,6-dimethylene-2,6-dihydronaphthalene and naphthalene (a), and correlation diagrams for HOMO and LUMO of **2** (b), **3** (c) and **4** (d), where only the interaction with one side of the outer fragments is shown. MO levels are evaluated at the tuned-LC-RBLYP/6-311G**/RB3LYP/6-311G* level. Phases of MOs are sometimes reversed in the correlation diagrams so that they are in consistent with their orbital interactions.

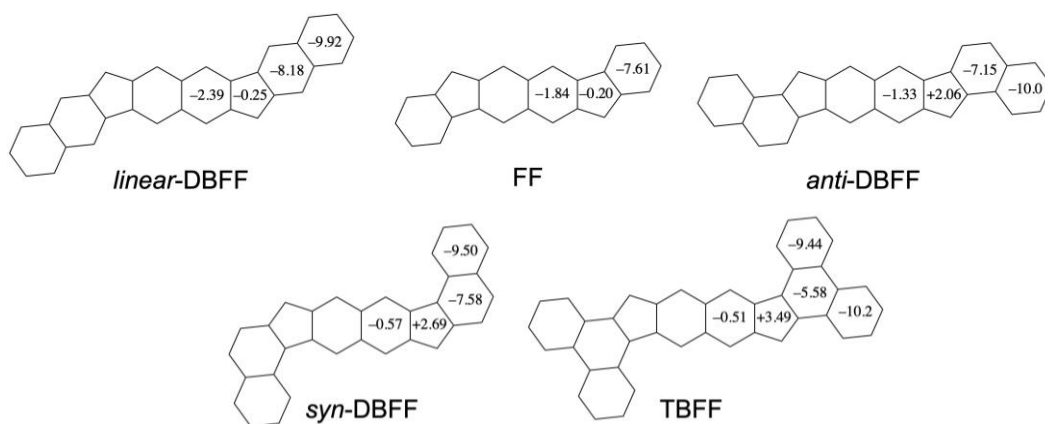


Figure D4. Calculation results of NICS(1) values (ppm) for the neutral singlet species of **1-5** that include the two Mes substituents (not shown above).

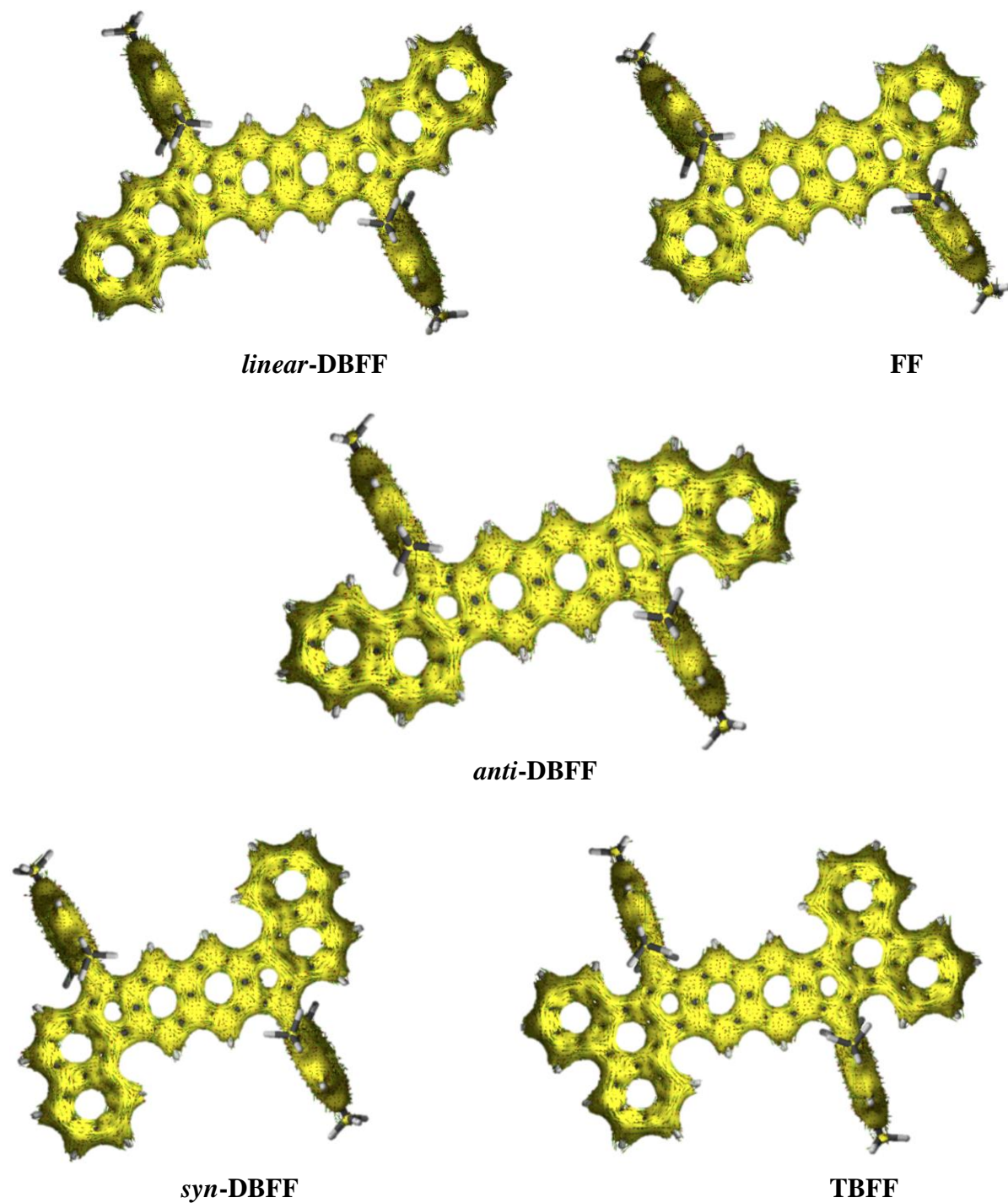


Figure D5. Calculation results of AICD plots for neutral singlet species.

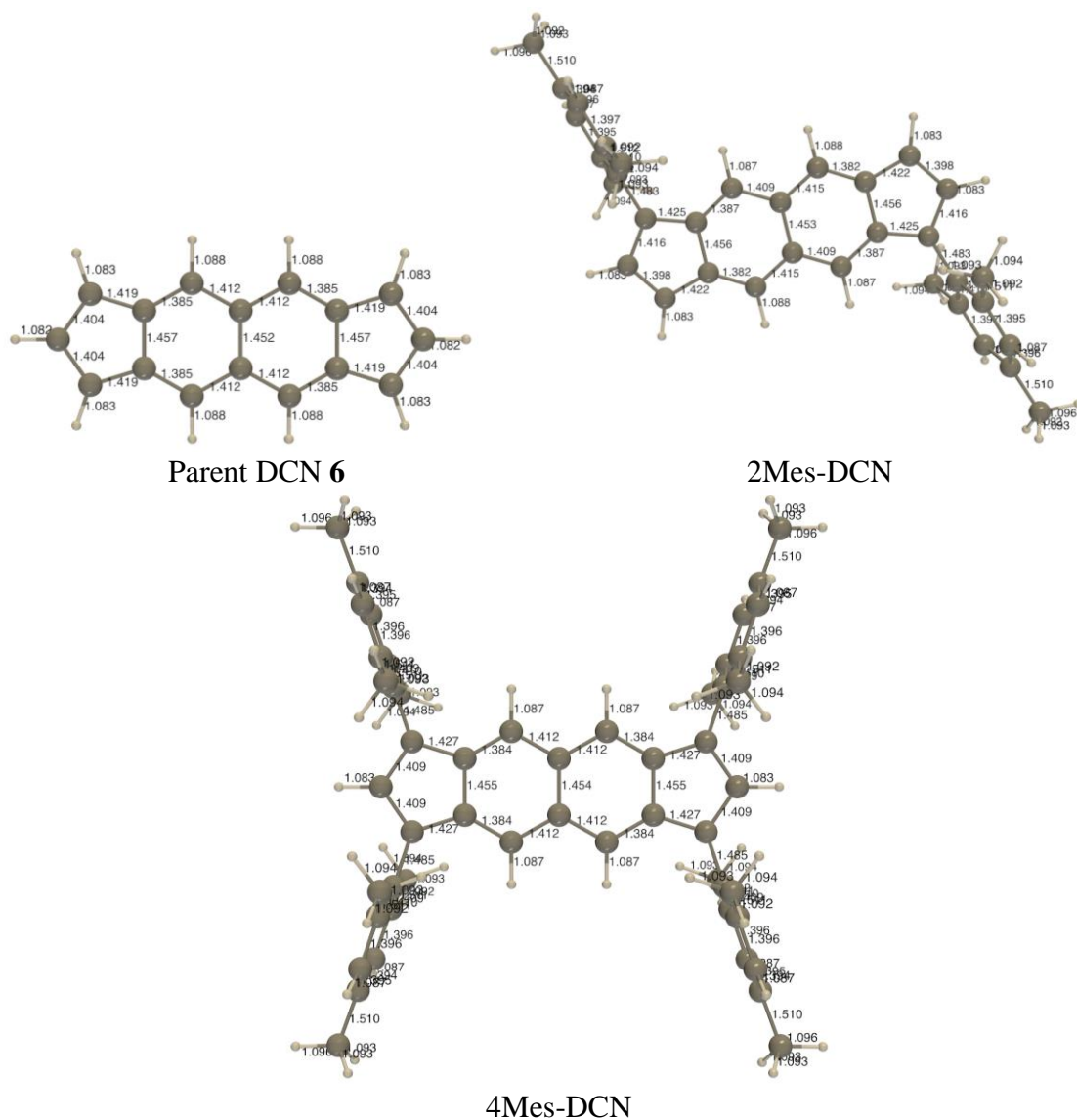


Figure D6. Optimized bond lengths (Å) of neutral singlet **6** (DCN) with differing number of mesityl substituents.

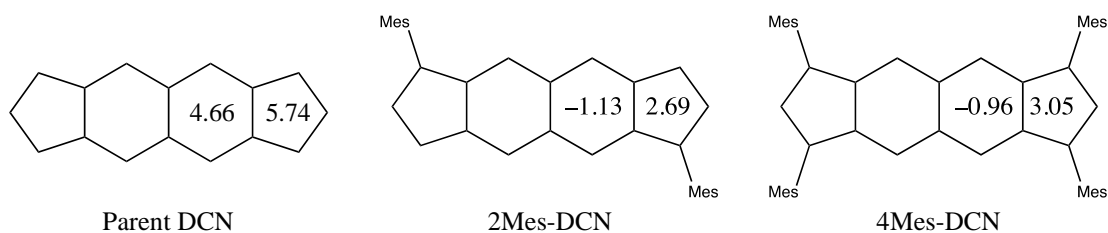


Figure D7. Calculated NICS(1) values (ppm) for neutral singlet **6** (DCN) with differing number of mesityl substituents.

Table D4. Summary of computational results for DCN derivatives with differing number of mesityl substituents.

	Parent DCN	2Mes-DCN	4Mes-DCN
y (PUHF) (–)	0.623	0.657	0.651
Vertical ΔE_{ST} (kcal mol ⁻¹)	-12.97	-12.33	-11.45
Adiabatic ΔE_{ST} (kcal mol ⁻¹)	-10.97	-10.27	-9.49
Adiabatic ΔE_{ST} (+ ZPVE) (kcal mol ⁻¹)	-9.80	-9.36	-9.37
<hr/>			
Tuned value of μ (bohr ⁻¹)	0.2212	0.1746	0.1487
y (CASCI) (–)	0.214	0.224	0.242
Vertical ΔE_{ST} (CASCI) (kcal mol ⁻¹)	-20.45	-19.54	-18.47
$ t_{ab} $ (eV)	1.130	1.084	1.059
$f_{ST}(y)$ (–)	-0.617	-0.587	-0.532
$U/2 = K_{gu}^M$ (eV)	1.780	1.760	1.824
$(U/2)f_{ST}(y)$ (eV)	-1.098	-1.033	-0.971
J_{gg}^M (eV)	5.319	5.092	5.099
J_{uu}^M (eV)	5.210	5.071	5.035
J_{gu}^M (eV)	5.054	4.896	4.897
$2K_{ab}$ (eV)	0.211	0.186	0.170

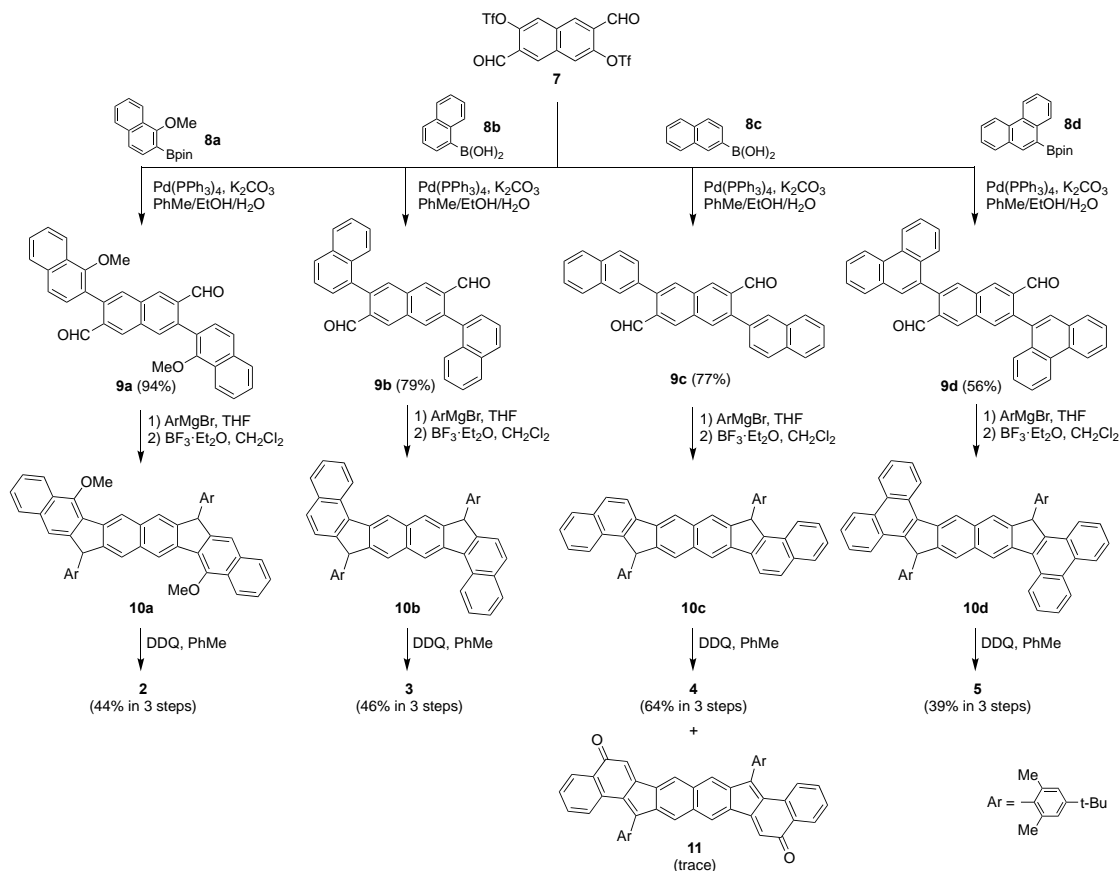
2. Experimental Details

General. 2-Bromo-1-methoxynaphthalene,¹¹ bistriflate **7**,¹² boronate **8d**,¹³ dione **S1**,¹⁴ and bistriflate **S2**¹⁵ were prepared according to literature procedures. In Japan, all air-sensitive manipulations were carried out under an inert atmosphere using standard Schlenk technique. For moisture sensitive reactions, super-dehydrated grade THF, toluene, and CH₂Cl₂ were used. Silica gel (240-300 mesh) was used for column chromatography. All other reagents were purchased and used as received. NMR spectra were recorded on a JEOL ECS-400 (¹H: 400 MHz, ¹³C: 100 MHz) or JEOL ECA-600 (¹H: 600 MHz, ¹³C: 151 MHz) NMR spectrometer at room temperature (unless otherwise noted). ¹H and ¹³C NMR chemical shifts (δ) are expressed in ppm relative to the residual non-deuterated solvent reference (CDCl₃: ¹H 7.26 ppm, ¹³C 77.16 ppm). UV-Vis-NIR spectra were recorded on a SHIMADZU UV-2550 UV-Vis or JASCO V-670 UV-Vis-NIR spectrometer in HPLC grade CH₂Cl₂. High-resolution mass spectra (HRMS) were measured on a Thermo Fisher

Scientific LTQ Orbitrap XL or JEOL JMS-700 spectrometer. Elemental analysis was performed in A Rabbit Science Japan Co., Ltd.

In Oregon, all air-sensitive manipulations were carried out under an inert atmosphere using standard Schlenk technique. For moisture sensitive reactions, THF and toluene were dried on a solvent system and stored over molecular sieves. Silica gel (240-300 mesh) was used for column chromatography. All other reagents were purchased and used as received. NMR spectra were recorded on a Bruker Avance III HD 500 equipped with a Prodigy multinuclear cryoprobe (^1H : 500 MHz, ^2D : 77 MHz) or Bruker Avance III HD 600 equipped with a Prodigy multinuclear cryoprobe (^1H : 600 MHz, ^{13}C : 151 MHz) NMR spectrometer at room temperature (unless otherwise noted). ^1H and ^{13}C NMR chemical shifts (δ) are expressed in ppm relative to the residual non-deuterated solvent reference (CDCl_3 : ^1H 7.26 ppm, ^{13}C 77.16 ppm; CD_2Cl_2 : ^1H 5.32 ppm, ^{13}C 53.84 ppm; $\text{DMSO-}d_6$: ^1H 2.50 ppm, ^{13}C 39.52 ppm). HRMS were recorded on a Waters XEVO G2-XS TOF mass spectrometer.

Scheme D1. Synthesis of *linear*-DBFF **2, *syn*-DBFF **3**, *anti*-DBFF **4**, and TBFF **5**.**



Boronate 8a. To 2-bromo-1-methoxynaphthalene (0.50 g, 2.11 mmol) in THF (45 mL) was added dropwise a solution of *n*-BuLi (1.1 mL, 3.16 mmol, 2.76 M in hexane) at -70 °C under N₂ atmosphere. After stirring at room temperature for 30 min, the reaction was cooled to -70 °C and 2-isopropoxy-4,4,5,5-tetramethyl-1,3,2-dioxaborolane (0.87 mL, 4.22 mmol) was added. After stirring at room temperature for 12 h, the resulting mixture was poured into water and extracted with CH₂Cl₂. The combined organic phase was washed with water and brine, dried over Na₂SO₄, and evaporated under reduced pressure. The residue was purified by column chromatography (SiO₂, CH₂Cl₂/hexane = 1:2) to give **8a** (302 mg, 1.06 mmol, 50%) as a white solid. Mp 86 °C; ¹H NMR (400 MHz, CDCl₃): δ 8.24 (d, *J* = 6.8 Hz, 1H), 7.82 (dd, *J* = 7.1, 1.8 Hz, 1H), 7.75 (d, *J* = 8.3 Hz, 1H), 7.58 (d, *J*

= 8.2 Hz, 1H), 7.52 (td, $J = 7.1, 1.8$ Hz, 1H), 7.48 (td, $J = 7.1, 1.8$ Hz, 1H), 4.01 (s, 3H), 1.39 (s, 12H); ^{13}C NMR (100 MHz, CDCl_3): δ 164.23, 137.22, 132.03, 128.35, 128.12, 127.65, 126.11, 123.37, 83.83, 63.75, 24.75 (11 signals out of 13 expected); HR-ESI-MS (FTMS, positive): m/z calcd for $\text{C}_{17}\text{H}_{21}\text{O}_3\text{BNa}^+$ 307.1476, found 307.1479 $[(\text{M}+\text{Na})^+]$.

General Procedure A for Synthesis of Compounds 9a-9d. A solution of triflate **7**, boronic acid or boronic acid ester **8**, and K_2CO_3 in toluene/EtOH/ H_2O (95:5:5) was purged with N_2 for 30 min. $\text{Pd}(\text{PPh}_3)_4$ was added to the solution, and the resulting mixture was heated at 95 °C for 2 h. The organic phase was separated, washed with water, dried over Na_2SO_4 , and evaporated under reduced pressure. After the residue was dissolved with CH_2Cl_2 , the resulting solution was filtered through a short silica plug, and the filtrate was evaporated under reduced pressure. The residue was purified by column chromatography to give the desired product.

Aldehyde 9a. Triflate **7** (100 mg, 208 μmol) and 1-methoxy-2-naphthaleneboronic acid pinacolate ester (**8a**, 177 mg, 624 μmol) were reacted in the presence of $\text{Pd}(\text{PPh}_3)_4$ (24 mg, 21 μmol) and K_2CO_3 (172 mg, 1.25 mmol) in toluene/EtOH/ H_2O (25 mL/3 mL/3 mL) according to general procedure A. The obtained material was subjected to column chromatography (SiO_2 , CH_2Cl_2 /hexane 3:1) to give aldehyde **9a** (97 mg, 195 μmol , 94%) as a yellow solid. Mp 282 °C (decomp.); ^1H NMR (400 MHz, CDCl_3): δ 10.02 (s, 2H), 8.70 (s, 2H), 8.25 (d, $J = 9.6$ Hz, 2H), 8.21 (s, 2H), 7.97 (d, $J = 9.4$ Hz, 2H), 7.85 (d, $J = 8.5$ Hz, 2H), 7.65–7.59 (m, 6H), 3.48 (s, 6H); ^{13}C NMR (100 MHz, CDCl_3): δ 192.71, 153.92, 138.24, 135.61, 134.63, 134.18, 132.42, 129.04, 128.71, 128.47, 128.13, 127.51, 127.23, 126.02, 125.37, 122.94, 61.08; UV–vis (CH_2Cl_2): $\lambda_{\text{max}}^{\text{abs}}$ (relative intensity) 276

(1.00), 384 (0.03) nm; HR-ESI-MS (FTMS, positive): m/z calcd for $C_{34}H_{24}O_4Na^+$ 519.1566, found 519.1564 [(M+Na)⁺].

Aldehyde 9b. Triflate **7** (300 mg, 625 μ mol) and 1-naphthaleneboronic acid (**8b**, 321 mg, 1.87 mmol) were reacted in the presence of Pd(PPh₃)₄ (73 mg, 63 μ mol) and K₂CO₃ (520 mg, 3.76 mmol) in toluene/EtOH/H₂O (75 mL/9 mL/9 mL) according to general procedure A. The obtained material was subjected to column chromatography (SiO₂, CH₂Cl₂/hexane 2:1) to give aldehyde **9b** (217 mg, 498 μ mol, 79%) as a yellow solid. Mp. 283 °C (decomp.); ¹H NMR (400 MHz, CDCl₃): δ 9.74 (s, 2H), 8.69 (s, 2H), 8.19 (s, 2H), 8.04–7.97 (m, 4H), 7.64 (t, J = 7.0 Hz, 2H), 7.57–7.51 (m, 6H), 7.48–7.42 (m, 2H); ¹³C NMR (100 MHz, CDCl₃): δ 192.56, 140.48, 135.49, 134.80, 133.84, 133.30, 133.27, 133.07, 129.42, 129.17, 128.99, 128.79, 127.48, 126.78, 125.95, 125.69; UV–vis (CH₂Cl₂): $\lambda_{\max}^{\text{abs}}$ (relative intensity) 262 (1.00), 297 (0.72), 395 (0.05) nm; HR-ESI-MS (FTMS, positive): m/z calcd for $C_{32}H_{20}O_2Na^+$ 459.1336, found 459.1354 [(M+Na)⁺].

Aldehyde 9c. Triflate **7** (100 mg, 208 μ mol) and 2-naphthaleneboronic acid (**8c**, 107 mg, 625 μ mol) were reacted in the presence of Pd(PPh₃)₄ (24 mg, 21 μ mol) and K₂CO₃ (172 mg, 1.25 mmol) in toluene/EtOH/H₂O (28.2 mL/3.4 mL/3.4 mL) according to general procedure A. The obtained material was subjected to column chromatography (SiO₂, CH₂Cl₂/hexane 2:1) to give aldehyde **9c** (70 mg, 161 μ mol, 77%) as a yellow solid. Mp 282 °C (decomp.); ¹H NMR (400 MHz, CDCl₃): δ 10.21 (s, 2H), 8.67 (s, 2H), 8.22 (s, 2H), 8.02 (d, J = 8.5 Hz, 2H), 7.98–7.94 (m, 6H), 7.64 (dd, J = 8.4, 1.6 Hz, 2H), 7.61–7.59 (m, 4H); ¹³C NMR (100 MHz, CDCl₃): δ 192.46, 141.82, 135.17, 134.58, 134.08, 133.42, 133.07, 132.05, 129.90, 129.57, 128.66, 128.41, 128.07, 127.96, 127.20, 127.04; UV–vis (CH₂Cl₂): $\lambda_{\max}^{\text{abs}}$ (relative intensity) 273 (1.00), 393 (0.03) nm; HR-FAB-MS (3-

nitrobenzyl alcohol, positive): m/z calcd for $C_{32}H_{21}O_2^+$ 437.1542, found 437.1554 [(M+H)⁺].

Aldehyde 9d. Triflate **7** (100 mg, 208 μ mol) and 9-phenanthreneboronic acid pinacolate ester (**8d**, 190 mg, 625 μ mol) in the presence of Pd(PPh₃)₄ (24 mg, 21 μ mol) and K₂CO₃ (172 mg, 1.25 mmol) in toluene/EtOH/H₂O (28.2 mL/3.4 mL/3.4 mL) according to general procedure A. The obtained material was successively washed with CH₂Cl₂/hexane and hexane to give aldehyde **9d** (52 mg, 97 μ mol, 46%) as a yellow solid. The mother liquor was evaporated under reduced pressure, and the residue was purified by column chromatography (SiO₂, CH₂Cl₂/hexane 2:1) to give **9d** (11 mg, 21 μ mol, total 56%) as a yellow solid. Mp >300 °C; ¹H NMR (400 MHz, CDCl₃, mixture of atropisomers): δ 9.83 (s, 2H), 8.86 (d, J = 8.4 Hz, 2H), 8.81 (d, J = 8.1 Hz, 2H), 8.73 (s, 2H), 8.28 (s, 2H), 7.98 (d, J = 8.0 Hz, 2H), 7.87 (d, J = 4.4 Hz, 2H), 7.80–7.76 (m, 2H), 7.73–7.69 (m, 4H), 7.57–7.55 (m, 4H); ¹³C NMR (100 MHz, CDCl₃): δ 192.48, 140.55, 135.68, 135.02, 134.34, 133.10, 132.52, 132.49, 131.52, 130.89, 130.75, 129.80, 129.28, 129.26, 127.87, 127.75, 127.54, 127.03, 123.63, 123.13; UV–vis (CH₂Cl₂): $\lambda_{\max}^{\text{abs}}$ (relative intensity) 301 (1.00), 353 (0.73) nm; HR-FAB-MS (3-nitrobenzyl alcohol, positive): m/z calcd for C₄₀H₂₄O₂Na⁺ 559.1674, found 559.1673 [(M+Na)⁺].

General Procedure B for Synthesis of DBFFs and TBFF. A Grignard reagent mixture was prepared from 2-bromo-5-*t*-butyl-1,3-dimethylbenzene (740 mg, 3.07 mmol), 1,2-dibromoethane (26 μ L, 307 μ mol), Mg (96 mg, 3.99 mmol), I₂ (3 mg, 11 μ mol) in THF (5 mL). To a THF solution of aldehyde (0.02 M) was added the freshly prepared Grignard reagent at room temperature under N₂ atmosphere, and the resulting solution was stirred for 12 h. After addition of aqueous HCl (1 M), the organic phase was separated, and the

aqueous phase was extracted with CH₂Cl₂. The combined organic phase was washed with brine, dried over Na₂SO₄, and concentrated under reduced pressure. The residue was subjected to column chromatography to give crude alcohol, which was used without further purification.

To a CH₂Cl₂ solution (~0.02 M) of crude alcohol was added BF₃·OEt₂ (~40 equiv.) at room temperature under N₂ atmosphere. After stirring the mixture at room temperature for 10 min, aqueous NaHSO₃ (10 wt.%) was added. The organic phase was separated, and the aqueous phase was extracted with CH₂Cl₂. The combined organic phase was dried over Na₂SO₄ and evaporated under reduced pressure to give the crude dihydro intermediate which was used without further purification.

The dihydro intermediate was dissolved with toluene (~0.003 M) by heating and then 2,3-dichloro-5,6-dicyano-*p*-benzoquinone (DDQ, ~2.5 equiv) was added at room temperature under N₂ atmosphere. After heating the mixture at 70 °C for 1.5 h, the mixture was cooled and then evaporated under reduced pressure. The residue was subjected to filtration over a short silica plug or column chromatography. The obtained material was washed with EtOH and hexane to give the desired product.

linear-DBFF (2). According to general procedure B, aldehyde **9a** (97 mg, 195 μmol) in THF (15 mL) was reacted with freshly prepared Grignard reagent (1.95 mmol). The obtained material was filtered through a short silica plug to give crude alcohol (157 mg), which was subjected to Friedel–Crafts cyclization with BF₃·OEt₂ (0.97 mL, 7.65 mmol). The crude dihydro intermediate **10a** (99 mg) was oxidized with DDQ (75 mg, 327 μmol). The obtained material was purified according to the general procedure to give **2** (64 mg,

82 μmol , 44% in 3 steps) as a violet solid. Analytically pure **10a** and **2** were obtained by recycling GPC eluting with CHCl_3 .

10a: $\text{Mp} > 300\text{ }^\circ\text{C}$; $^1\text{H NMR}$ (400 MHz, CDCl_3 , diastereomer mixture): δ 8.62, 8.59 (2s, 2H), 8.29, 8.27 (2s, 2H), 7.84, 7.80 (2s, 2H), 7.76 (d, $J = 7.8\text{ Hz}$, 2H) 7.54 (t, $J = 8.0\text{ Hz}$, 2H), 7.47–7.43 (4H, m), 7.29 (s, 2H), 6.88, 6.87 (2s, 2H), 5.97 (s, 2H), 4.18 (2s, 6H), 2.86, 2.85 (2s, 6H), 1.37, 1.36 (2s, 18H), 1.23, 1.21 (2s, 6H) ppm; $^{13}\text{C NMR}$ (100 MHz, CDCl_3): δ 152.34, 149.95, 149.90, 147.44, 145.55, 145.47, 138.00, 137.92, 137.53, 137.44, 135.85, 135.81, 135.54, 133.88, 133.83, 129.88, 129.80, 128.42, 128.21, 127.49, 127.41, 126.37, 125.71, 125.30, 125.25, 123.34, 123.12, 123.04, 122.52, 119.29, 61.34, 48.99, 34.15, 31.30, 22.11, 19.75; UV–vis (CH_2Cl_2): $\lambda_{\text{max}}^{\text{abs}}$ (relative intensity) 267 (1.00), 290 (1.00), 359 (0.79), 365 (0.77) nm; HR-APCI-MS (FTMS, positive): m/z calcd for $\text{C}_{58}\text{H}_{57}\text{O}_2^+$ 785.4353, found 785.4338 [(M+H) $^+$].

2: $\text{Mp} > 300\text{ }^\circ\text{C}$; $^1\text{H NMR}$ (400 MHz, CDCl_3): δ 8.11 (d, $J = 7.9\text{ Hz}$, 2H), 7.76 (s, 2H), 7.68–7.63 (m, 2H), 7.41 (t, $J = 7.0\text{ Hz}$, 2H), 7.37 (t, $J = 7.0\text{ Hz}$, 2H), 7.26 (s, 4H), 7.10 (s, 2H), 7.05 (s, 2H), 4.13 (s, 6H), 2.18 (s, 12H), 1.43 (s, 18H); $^{13}\text{C NMR}$ (100 MHz, CDCl_3): δ 152.60, 151.26, 143.45, 140.99, 138.18, 137.48, 136.46, 136.11, 133.78, 130.80, 129.24, 128.46, 126.89, 126.41, 126.01, 125.24, 124.89, 124.38, 123.15, 117.51, 61.04, 34.45, 31.39, 20.58; UV–vis–NIR (CH_2Cl_2): $\lambda_{\text{max}}^{\text{abs}}$ (ϵ) 342 (95300), 361 (104400), 595 (53600), 629 (58900) nm; HR-APCI-MS (FTMS, positive): m/z calcd for $\text{C}_{58}\text{H}_{55}\text{O}_2^+$ 783.4197, found 783.4196 [(M+H) $^+$].

syn-DBFF (3). According to general procedure B, aldehyde **9b** (134 mg, 307 μmol) in THF (5.9 mL) was reacted with freshly prepared Grignard reagent (3.07 mmol). The obtained material was filtered through a short silica plug to give crude alcohol (157 mg),

which was subjected to Friedel–Crafts cyclization with $\text{BF}_3 \cdot \text{OEt}_2$ (1.5 mL, 11.6 mmol). The crude dihydro intermediate **10b** (169 mg) was oxidized with DDQ (132 mg, 583 μmol). The obtained material was purified according to the general procedure to give **3** (102 mg, 141 μmol , 46% in 3 steps) as a violet solid. Analytically pure **10b** and **3** were obtained by recycling GPC eluting with CHCl_3 .

10b: Mp >300 °C; ^1H NMR (400 MHz, CDCl_3 , diastereomer mixture): δ 8.95 (2d, $J = 8.1$ Hz, 2H), 8.80 (d, $J = 9.2$ Hz, 2H), 7.96 (2d, $J = 9.4$ Hz, 4H), 7.81 (d, $J = 8.3$ Hz, 2H), 7.69 (t, $J = 6.8$ Hz, 2H), 7.56 (t, $J = 7.4$ Hz, 2H), 7.42 (2d, $J = 8.2$ Hz, 2H), 6.99 (s, 4H), 6.85–6.81 (m, 2H), 5.82 (s, 2H), 2.86 (2s, 6H), 1.35 (2s, 18H), 1.13 (2s, 6H); ^{13}C NMR (100 MHz, CDCl_3 , diastereomer mixture): δ 149.5, 149.5, 147.4, 147.4, 146.1, 146.0, 140.7, 137.6, 137.5, 137.4, 134.9, 134.8, 134.3, 134.2, 133.7, 132.4, 132.4, 129.9, 129.5, 129.2, 129.0, 128.4, 127.1, 127.1, 127.0, 127.0, 125.4, 125.3, 125.2, 125.2, 124.2, 123.0, 122.9, 122.8, 121.4, 49.8, 34.7, 31.7, 31.5, 22.5, 22.5, 19.5, 19.4 ppm (43 signals out of 52 expected); UV–vis (CH_2Cl_2): $\lambda_{\text{max}}^{\text{abs}}$ (relative intensity) 300 (0.41), 369 (0.97), 389 (1.00) nm; HR-FAB-MS (3-nitrobenzyl alcohol, positive): m/z calcd for $\text{C}_{56}\text{H}_{53}^+$ 725.4142, found 725.4135 [(M+H) $^+$].

3: Mp >300 °C; ^1H NMR (400 MHz, CDCl_3): δ 8.36 (d, $J = 9.1$ Hz, 2H), 7.88 (s, 2H), 7.70 (d, $J = 8.2$ Hz, 2H), 7.45–7.40 (m, 4H), 7.32 (t, $J = 7.5$ Hz, 2H), 7.21 (s, 4H), 7.06 (s, 2H), 6.96 (d, $J = 8.3$ Hz, 2H), 2.20 (s, 12H), 1.41 (s, 18H); ^{13}C NMR (100 MHz, CDCl_3): δ 151.20, 144.20, 143.35, 138.08, 137.25, 135.77, 134.48, 132.59, 130.97, 130.84, 130.67, 130.55, 129.91, 128.80, 127.62, 125.68, 124.88, 124.18, 121.44, 34.41, 31.36, 20.61; UV–vis–NIR (CH_2Cl_2): $\lambda_{\text{max}}^{\text{abs}}$ (ϵ) 376 (53000), 392 (53200), 488 (4600), 638 (21500), 688

(35600) nm; HR-FAB-MS (3-nitrobenzyl alcohol, positive): m/z calcd for $C_{56}H_{51}^+$ 723.3985, found 723.3994 [(M+H)⁺].

anti-DBFF (4). According to general procedure B, aldehyde **8** (32 mg, 74 μ mol) in THF (3 mL) was reacted with freshly prepared Grignard reagent (0.74 mmol). The obtained material was filtered through a short silica plug to give crude alcohol (44 mg), which was subjected to Friedel–Crafts cyclization with $BF_3 \cdot OEt_2$ (375 μ L, 2.96 mmol). The crude dihydro intermediate **12** (42 mg) was oxidized with DDQ (40 mg, 175 μ mol). The obtained material was subjected to column chromatography (SiO_2 , CH_2Cl_2 /hexane 2:1 to CH_2Cl_2) to give **4** (34 mg, 47 μ mol, 64% in 3 steps) as a violet solid as well as diketone **11** (trace) as a purple solid. Analytically pure **10c**, **4**, and **dione 11** were obtained by recycling GPC eluting with $CHCl_3$.

10c: M.p. >300 °C; 1H NMR (400 MHz, $CDCl_3$, diastereomer mixture): δ 8.22 (2 s, 2H), 8.02 (2d, J = 8.4 Hz, 2H), 7.91 (t, J = 8.0 Hz, 4H), 7.81–7.75 (m, 2H), 7.52 (d, J = 8.3 Hz, 2H), 7.42–7.37 (m, 2H), 7.31 (2d, J = 7.6 Hz, 4H), 6.74 (dd, J = 9.4, 1.7 Hz, 2H), 5.96 (s, 2H), 2.95 (2s, 6H), 1.32 (2s, 18H), 1.06 (2s, 6H); ^{13}C NMR (100 MHz, $CDCl_3$, diastereomer mixture): δ 149.80, 149.72, 145.54, 145.48, 144.35, 144.30, 140.54, 138.57, 138.53, 137.70, 137.63, 136.49, 136.42, 135.75, 135.74, 134.04, 133.99, 133.43, 131.18, 129.34, 128.69, 127.55, 127.51, 126.88, 125.85, 125.74, 124.53, 123.08, 123.05, 119.36, 118.05, 49.14, 49.10, 34.10, 31.28, 22.46, 22.42, 18.91, 18.84; UV–vis (CH_2Cl_2): λ_{max}^{abs} (relative intensity) 274 (1.00), 354 (0.79), 362 (0.70), 373 (0.75) nm; HR-APCI-MS (FT, positive): m/z calcd for $C_{56}H_{53}^+$ 725.4142, found 725.4136 [(M+H)⁺].

4: Mp >300 °C. 1H NMR (400 MHz, $CDCl_3$): δ 7.67 (d, J = 7.9 Hz, 2H), 7.60 (d, J = 8.3 Hz, 2H), 7.51 (d, J = 8.5 Hz, 2H), 7.46 (s, 2H), 7.23 (s, 4H), 7.18 (d, J = 8.3 Hz, 2H),

7.08 (ddd, $J = 8.0, 6.6, 1.1$ Hz, 2H), 6.93 (s, 2H), 2.15 (s, 12H), 1.44 (s, 18H); ^{13}C NMR (100 MHz, CDCl_3): δ 151.36, 149.08, 144.54, 138.86, 137.11, 136.84, 135.81, 134.68, 133.14, 130.93, 130.53, 130.04, 129.29, 128.53, 127.64, 127.36, 125.78, 124.89, 123.71, 119.66, 34.45, 31.43, 20.53; UV-vis-NIR (CH_2Cl_2): $\lambda_{\text{max}}^{\text{abs}}$ (ϵ) 365 (75200), 381 (84100), 697 (50000) nm; HR-FAB-MS (3-nitrobenzyl alcohol, positive): m/z calcd for $\text{C}_{56}\text{H}_{50}^+$ 722.3913, found 722.3893 [M^+].

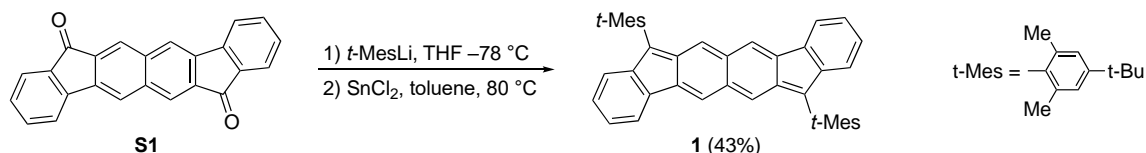
11: Mp >300 °C; ^1H NMR (400 MHz, CDCl_3): δ 8.17 (dd, $J = 7.8, 1.3$ Hz, 2H), 7.80 (s, 2H), 7.34 (td, $J = 7.8, 1.3$ Hz, 2H), 7.27 (s, 4H), 7.25 (td, $J = 7.0, 1.3$ Hz, 2H), 7.08 (s, 2H), 6.99 (dd, $J = 7.0, 1.3$ Hz, 2H), 6.91 (s, 2H), 2.17 (s, 12H), 1.44 (s, 18H) ppm; ^{13}C NMR (100 MHz, CDCl_3): δ 186.3, 152.0, 151.8, 149.8, 143.4, 135.8, 135.4, 135.1, 133.5, 133.1, 131.4, 130.9, 130.1, 128.5, 127.5, 125.4, 124.6, 123.2, 122.8, 120.0, 34.8, 31.6, 20.3 ppm; UV-vis-NIR (CH_2Cl_2): $\lambda_{\text{max}}^{\text{abs}}$ (ϵ) 357 (62500), 374 (57400), 461 (10200), 489 (13000), 561 (11000), 697 (3600) nm; HR-FAB-MS (3-nitrobenzyl alcohol, positive): m/z calcd for $\text{C}_{56}\text{H}_{49}\text{O}_2^+$ 753.3733, found 753.3736 [($\text{M}+\text{H}$) $^+$].

TBFF 5. According to the general procedure B, aldehyde **10** (54 mg, 101 μmol) in THF (10 mL) was reacted with freshly prepared Grignard reagent (1.01 mmol). The obtained material was filtered through a short silica plug to give crude alcohol (61 mg), which was subjected to Friedel-Crafts cyclization with $\text{BF}_3 \cdot \text{OEt}_2$ (0.4 mL, 3.2 mmol). The crude dihydro intermediate **15** (71 mg) was oxidized with DDQ (41 mg, 178 μmol). The obtained material was purified according to the general procedure to give **TBFF 5** (33 mg, 40 μmol , 39% in 3 steps) as a violet solid. Analytically pure **15** and **TBFF 5** were obtained by recycling GPC eluting with CHCl_3 .

10d: Mp >300 °C; ¹H NMR (400 MHz, CDCl₃): δ 9.04 (d, *J* = 8.0 Hz, 2H), 8.80 (d, *J* = 8.3 Hz, 2H), 8.67–8.65 (m, 4H), 7.82 (t, *J* = 7.4 Hz, 2H), 7.78 (s, 2H), 7.74 (t, *J* = 7.5 Hz, 2H), 7.59 (d, *J* = 8.1 Hz, 2H), 7.51 (t, *J* = 7.5 Hz, 2H), 7.39–7.34 (m, 4H), 6.69 (s, 2H), 5.84 (s, 2H), 3.03 (s, 6H), 1.31 (s, 18H), 1.04 (s, 6H); ¹³C NMR (150 MHz, CDCl₃): δ 149.4, 145.4, 144.7, 140.9, 137.3, 136.0, 135.8, 134.0, 132.4, 131.1, 130.7, 129.8, 129.4, 127.5, 127.19, 127.05, 126.6, 126.2, 125.6, 125.2, 124.9, 123.8, 123.3, 122.8, 121.1, 49.5, 34.4, 31.6, 23.0, 19.3 ppm; UV–vis (CH₂Cl₂): λ_{max}^{abs} (relative intensity) 256 (1.00), 276 (0.87), 352 (0.44), 370 (0.84), 393 (0.97) nm; HR-APCI-MS (FTMS, positive): *m/z* calcd for C₆₄H₅₇⁺ 825.4460, found 825.4441 [(M+H)⁺].

5: M.p. >300 °C; ¹H NMR (600 MHz, CDCl₃): δ 8.55 (d, *J* = 7.2 Hz, 2H), 8.52 (dd, *J* = 8.1, 1.2 Hz, 4H), 7.96 (s, 2H), 7.55 (t, *J* = 7.5 Hz, 2H), 7.51 (t, *J* = 7.2 Hz, 2H), 7.44 (t, *J* = 7.5 Hz, 2H), 7.33 (dd, *J* = 7.2, 1.2 Hz, 2H), 7.27 (s, overlapped by the solvent peak), 7.18 (t, *J* = 8.2, 1.2 Hz, 2H), 6.96 (s, 2H), 2.20 (s, 12H), 1.48 (s, 18H) ppm; the ¹³C NMR spectrum could not be obtained due to low solubility; UV–vis–NIR (CH₂Cl₂): λ_{max}^{abs} (ε) 383 (49800), 404 (62400), 499 (41600), 679 (14700), 738 (40300); HR-APCI-MS (FTMS, positive): *m/z* calcd for C₆₄H₅₅⁺ 823.4298, found 823.4296 [(M+H)⁺].

Scheme D2. Synthesis of Fluoreno[3,2-*b*]fluorene 1

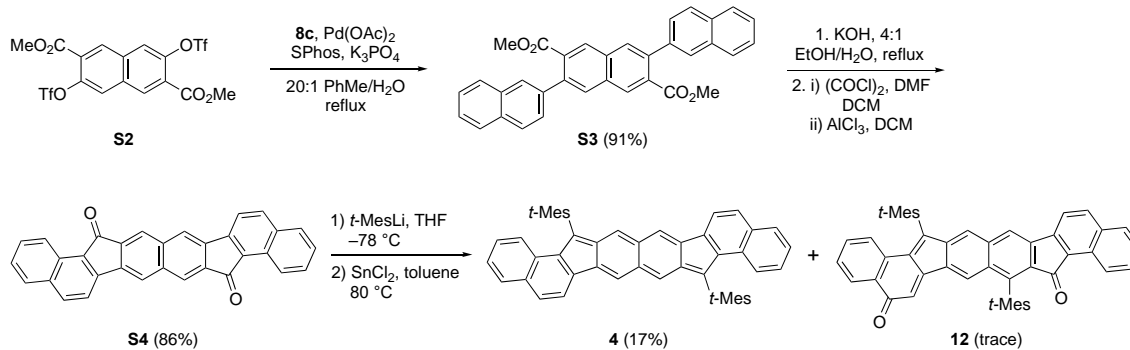


FF 1. In an oven-dried round bottom flask, a suspension of dione **S1** (0.140 g, 0.420 mmol, 1 equiv.) in dry THF (20 mL) was cooled to –78 °C under a N₂ atmosphere. In a separate oven-dried round bottom flask, 2-bromo-5-*tert*-butyl-1,3-dimethylbenzene

(0.813 g, 3.37 mmol, 8 equiv.) was dissolved in dry THF (20 mL), cooled to $-78\text{ }^{\circ}\text{C}$ under a N_2 atmosphere, and *n*-BuLi (1.6 M in hexanes, 1.97 mL, 3.15 mmol, 7.5 equiv.) was added dropwise. After stirring the mixture at $-78\text{ }^{\circ}\text{C}$ for 1 h, the aryl lithiate was transferred via cannula to the flask containing the dione. This reaction mixture was stirred for 4 h at $-78\text{ }^{\circ}\text{C}$, then slowly warmed to room temperature overnight with stirring. The reaction was then quenched with a saturated aq. NH_4Cl solution and extracted with CH_2Cl_2 (3 \times). The combined organic layer was washed with brine, dried (MgSO_4) and concentrated in vacuo. The resulting crude residue was passed through a silica plug eluting with hexanes, followed by a CH_2Cl_2 wash, to provide the desired diol that was carried onto the reductive dearomatization step without further purification.

In a single-neck round-bottom flask the crude diol (0.147 g, 0.22 mmol, 1 equiv.) and SnCl_2 (0.162 g, 0.88 mmol, 4 equiv.) were dissolved in dry degassed toluene (60 mL). Trifluoroacetic acid (5 drops) was added and this mixture was then vigorously stirred at $80\text{ }^{\circ}\text{C}$. The reaction was monitored via TLC (9:1 hexanes/ CH_2Cl_2). After 4 h, the mixture was poured over a silica plug and washed with CH_2Cl_2 . The filtrate was concentrated, triturated with acetonitrile, and filtered to yield FF **1** as a deep blue solid (114 mg, 43% from dione **S1**). ^1H NMR (600 MHz, CD_2Cl_2) δ 7.60 (d, $J = 7.3\text{ Hz}$, 2H), 7.43 (s, 2H), 7.22 (s, 4H), 7.12 (t, $J = 7.3\text{ Hz}$, 2H), 7.09 (t, $J = 7.3\text{ Hz}$, 2H), 6.97 (s, 2H), 6.84 (d, $J = 7.4\text{ Hz}$, 2H), 2.14 (s, 12H), 1.39 (s, 18H); ^{13}C NMR (151 MHz, CD_2Cl_2) δ 151.31, 144.38, 142.39, 138.00, 137.37, 137.22, 135.25, 132.10, 130.71, 128.13, 127.13, 125.30, 125.10, 122.49, 121.22, 34.90, 31.70, 20.93; HRMS (ASAP) (m/z) calculated for $\text{C}_{48}\text{H}_{47}$ ($\text{M}+\text{H}$) $^+$ 623.3678, found 623.3681.

Scheme D3. Alternative Synthesis of *anti*-DBFF 4 via Dione S4



Diester S3. A two-neck round-bottom flask fitted with a condenser was charged with bistriflate **S2** (0.500 g, 0.925 mmol, 1 equiv.), 2-naphthaleneboronic acid (**8c**, 0.350 g, 2.03 mmol, 2.2 equiv.), K₃PO₄ (0.589 g, 2.78 mmol, 3 equiv.), Pd(OAc)₂ (8.3 mg, 0.037 mmol, 0.04 equiv.), and SPhos (30.4 mg, 0.074 mmol, 0.08 equiv.). These solids were then placed under N₂ atmosphere and dissolved in toluene (40 mL) and H₂O (1 mL) that had been sparged with N₂ for 1.5 h. After refluxing overnight and cooling to room temperature, the reaction was quenched with H₂O and poured over filter paper. The precipitate was washed with hexanes and water to yield diester **S3** (0.419 g, 91%) as a grey solid. ¹H NMR (500 MHz, CDCl₃) δ 8.50 (s, 2H), 8.08 (s, 2H), 7.96–7.92 (m, 8H), 7.57–7.54 (m, 6H), 3.70 (s, 6H); ¹³C NMR (126 MHz, CDCl₃) δ 168.90, 139.77, 138.62, 133.53, 132.75 (d, *J* = 5.6 Hz), 131.69, 130.95, 130.80, 128.30, 127.92, 127.73, 127.16 (d, *J* = 5.6 Hz), 126.53, 126.31, 52.46; HRMS (ES⁺) (*m/z*), calculated for C₃₄H₂₄O₄ (M)⁺ 496.1675, found 496.1654.

***anti*-DBFF Dione S4.** A round-bottom flask fitted with a condenser was charged with diester **S3** (0.400 g, 0.805 mmol, 1 equiv.), KOH (0.730 g, 12.88 mmol, 16 equiv.), EtOH (60 mL), and H₂O (15 mL). After refluxing the flask overnight, the reaction was cooled and the EtOH evaporated. Concentrated HCl was slowly added to the aqueous solution and

a precipitate formed, which was isolated and washed with H₂O to yield the diacid intermediate as a yellow solid (0.335 g, 89%) that was carried on without further purification.

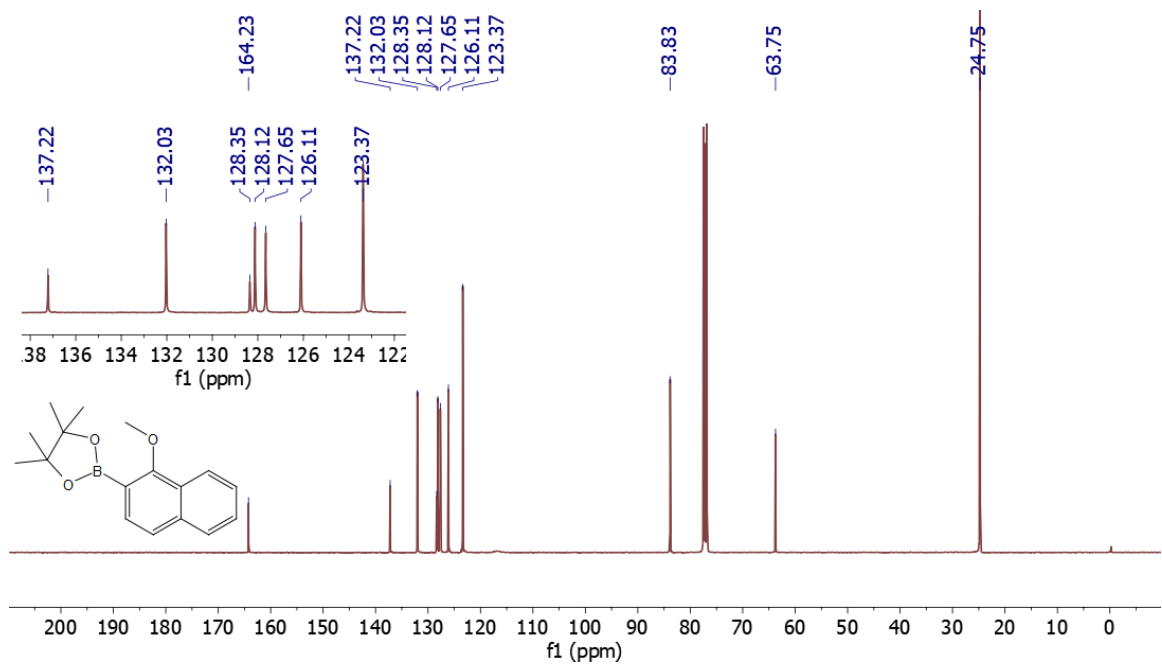
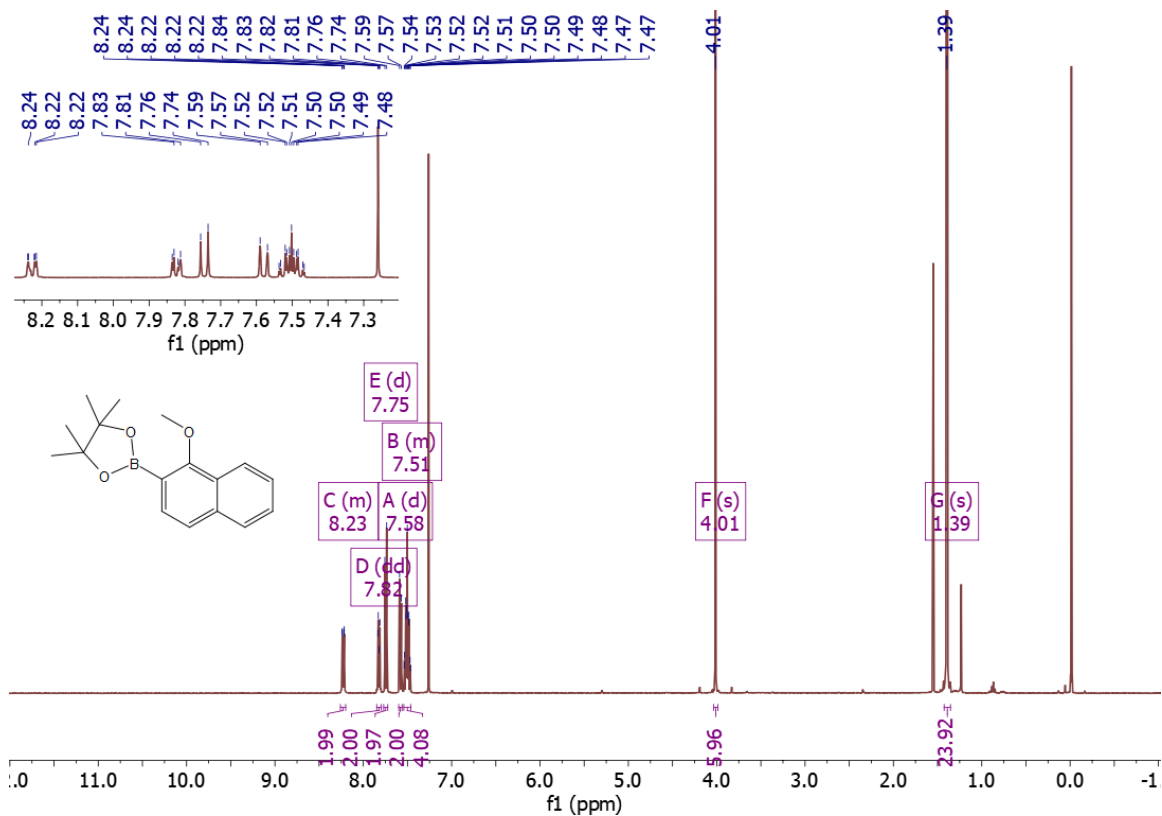
To a suspension of the diacid (0.250 g, 0.534 mmol, 1 equiv.) in CH₂Cl₂ (40 mL) was added DMF (0.082 mL, 1.07 mmol, 2 equiv.) followed by oxalyl chloride (0.18 mL, 2.14 mmol, 4.0 equiv.). After 12 h, the volatiles were removed under reduced pressure. The crude acid chloride was dissolved in CH₂Cl₂ (40 mL) and solid AlCl₃ (0.356 g, 2.67 mmol, 5 equiv.) was added to the flask. The reaction was stirred overnight and then poured into an HCl-ice mixture, precipitating the dione. The solid was filtered and washed successively with H₂O, CH₂Cl₂ and acetone to afford dione **S4** as a purple solid (0.198 g, 86%) that was too insoluble to obtain NMR spectra. HRMS (ES⁺) (*m/z*), calculated for C₃₂H₁₆O₂ (M)⁺ 433.1223, found 433.1225.

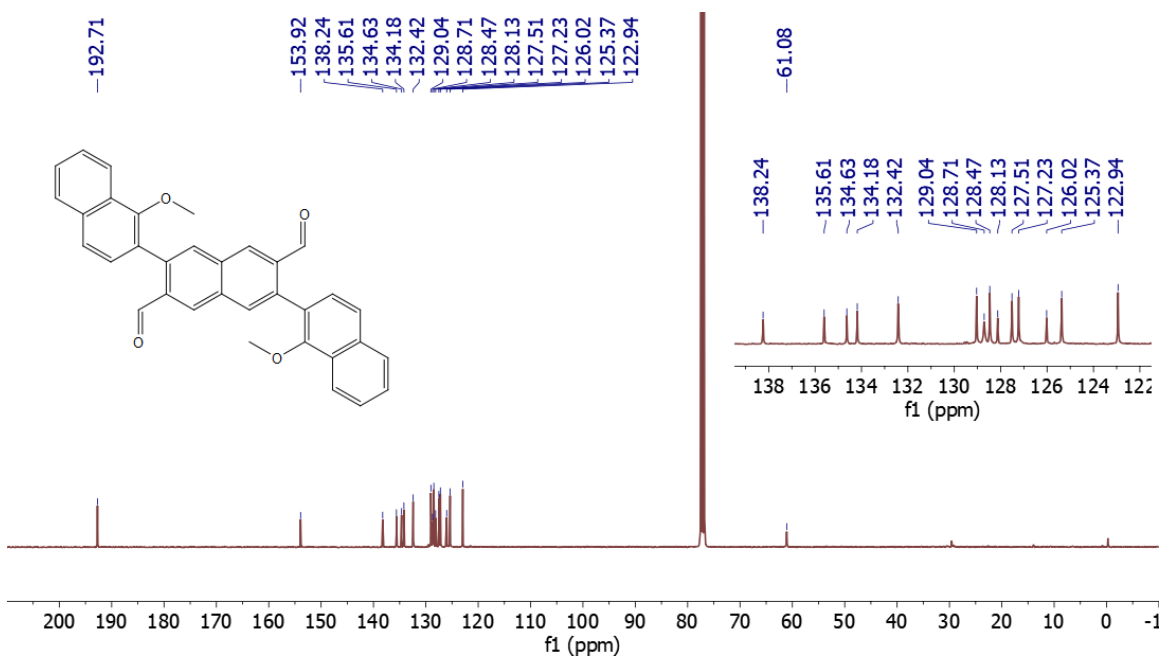
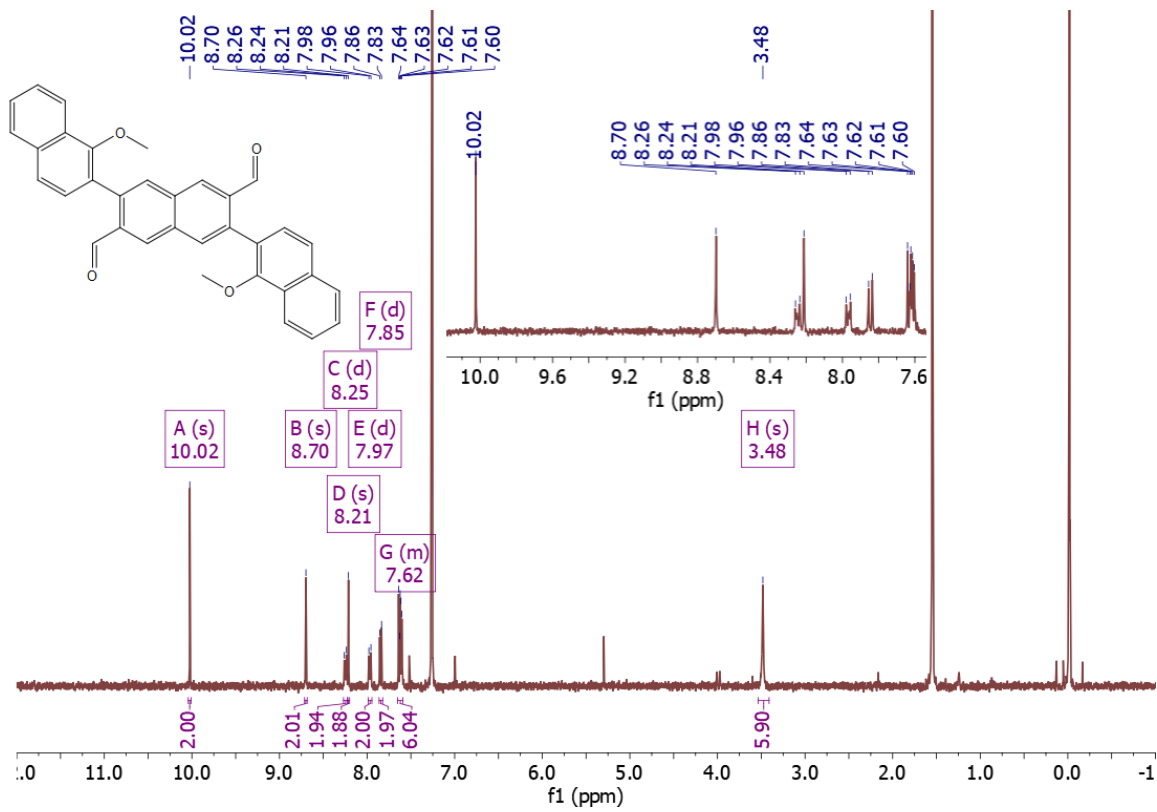
anti-DBFF 4. In an oven-dried round bottom flask, a suspension of dione **S4** (0.112 g, 0.259 mmol, 1 equiv.) in dry THF (20 mL) was cooled to -78 °C under a N₂ atmosphere. In a separate oven-dried round bottom flask, 2-bromo-5-*t*-butyl-1,3-dimethylbenzene (0.625 g, 2.59 mmol, 10 equiv.) was dissolved in dry THF (20 mL), cooled to -78 °C under a N₂ atmosphere, and *n*-BuLi (2.5 M in hexanes, 0.984 mL, 2.46 mmol, 9.5 equiv.) was added dropwise. After stirring the mixture at -78 °C for 1 h, the aryl lithiate was transferred via cannula to the flask containing the dione. This reaction mixture was stirred for 4 h at -78 °C, then slowly warmed to room temperature overnight with stirring. The reaction was then quenched with a saturated aq. NH₄Cl solution and extracted with CH₂Cl₂ (3×). The combined organic layer was washed with brine, dried (MgSO₄) and concentrated in vacuo. The resulting crude residue was passed through a silica plug eluting with hexanes, followed

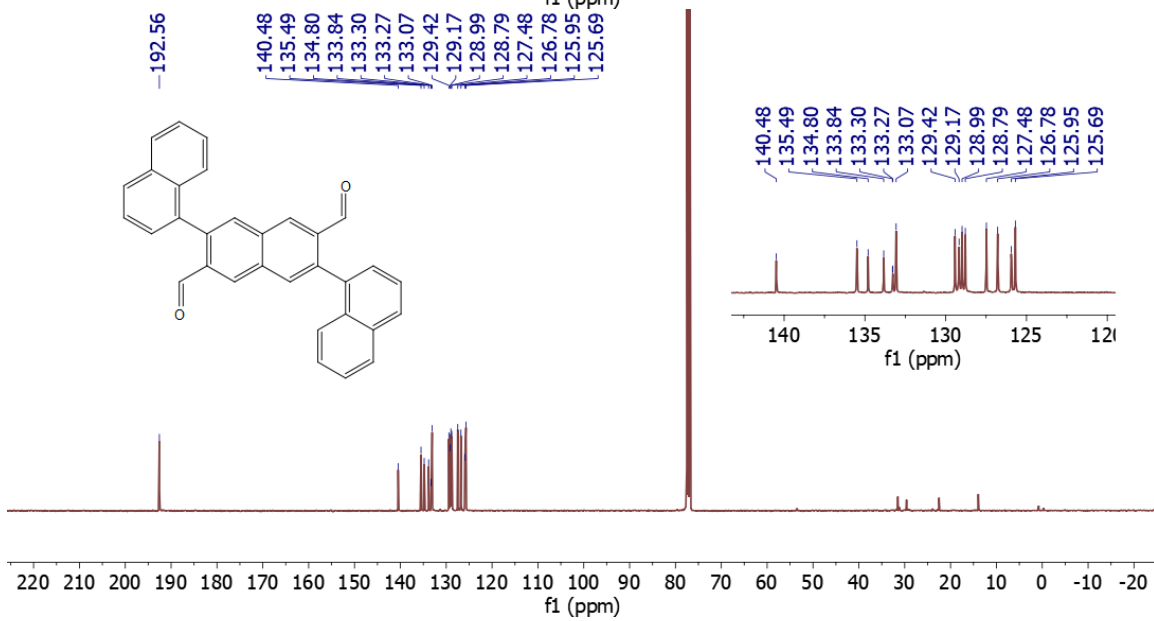
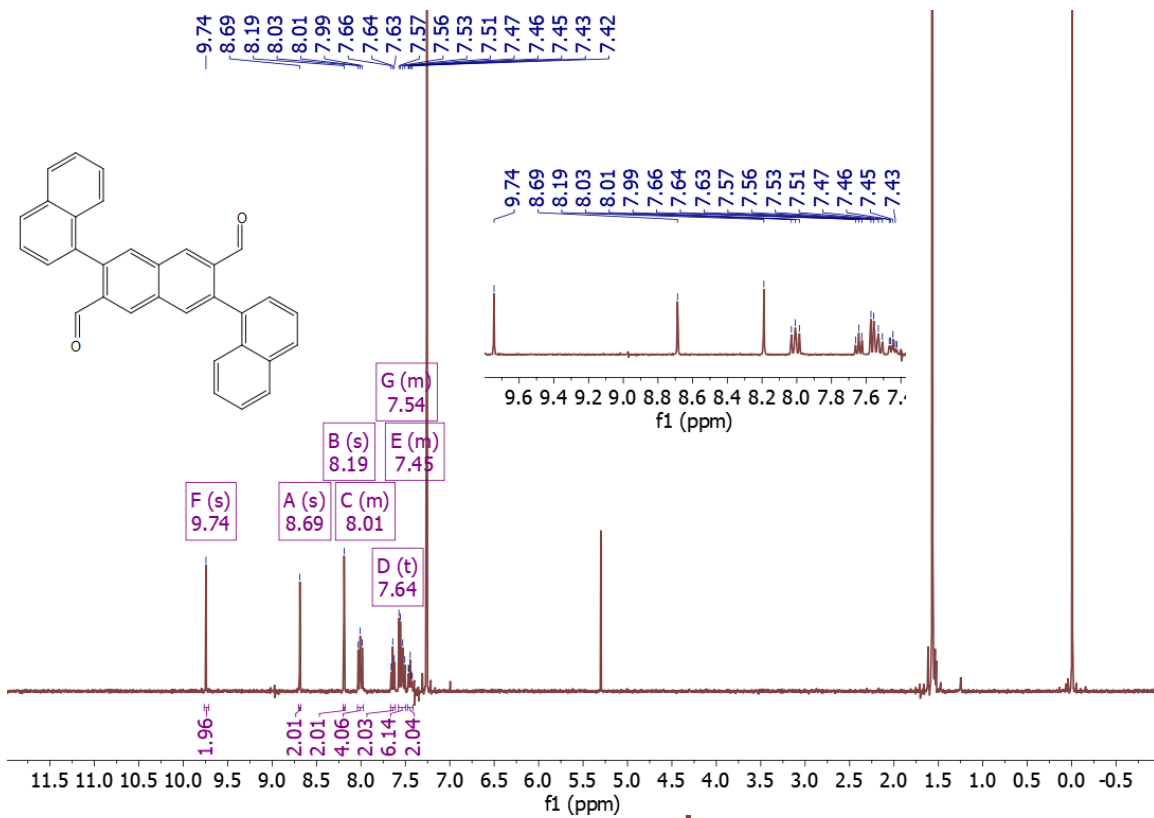
by a CH₂Cl₂ wash, to provide the desired diol that was carried onto the reductive dearomatization step without further purification.

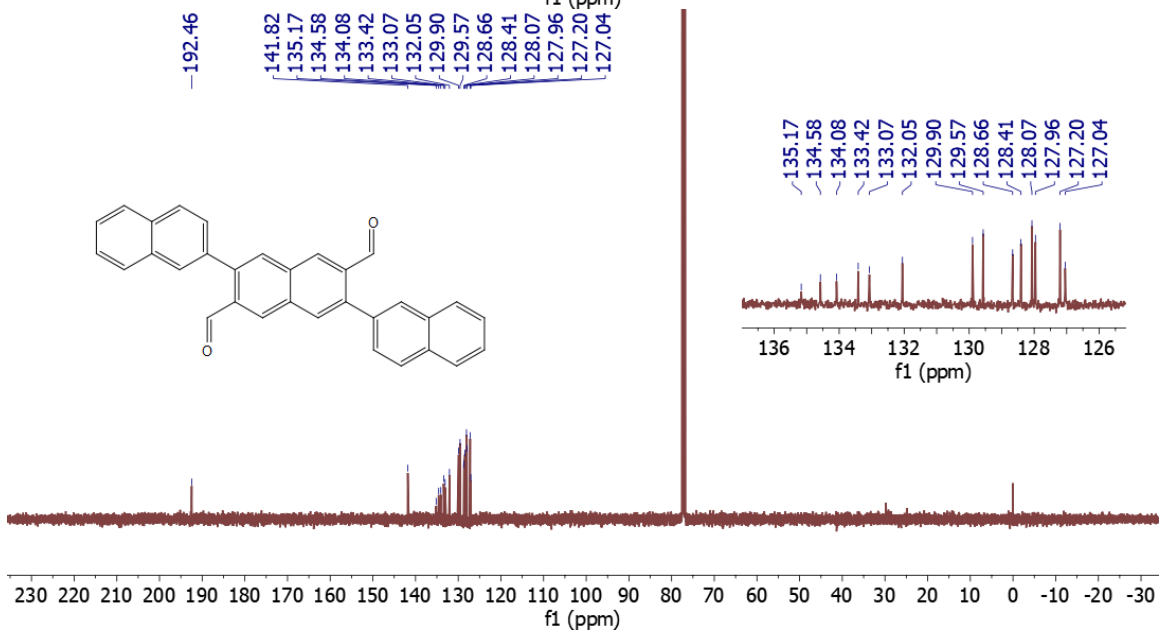
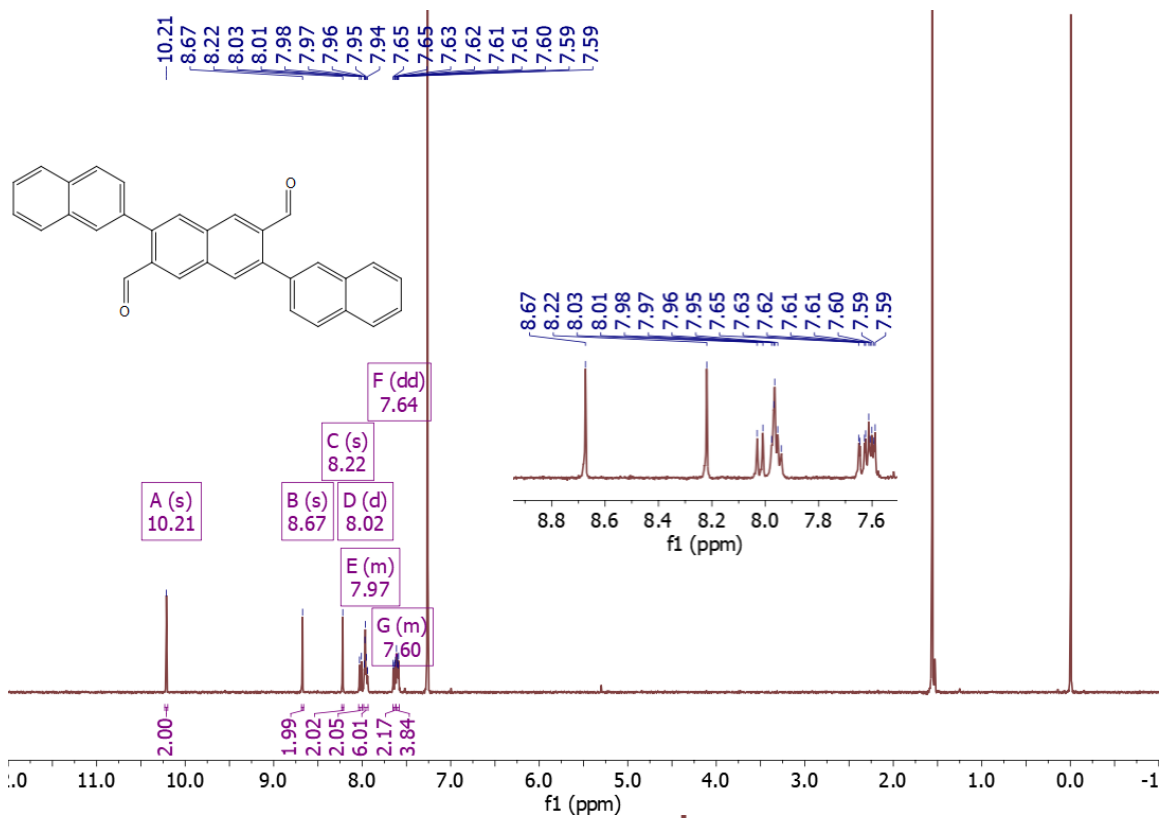
In a single-neck round-bottom flask the crude diol (0.197 g, 0.17 mmol, 1 equiv.) and anhydrous SnCl₂ (0.191 g, 0.68 mmol, 4 equiv.) were dissolved in dry degassed toluene (60 mL). Trifluoroacetic acid (5 drops) was added and this mixture was then vigorously stirred. The reaction was monitored via TLC (9:1 hexanes/CH₂Cl₂). After 4 h, the reaction was filtered through a pad of celite. The filtrate was concentrated, triturated with MeCN, and filtered to yield *anti*-DBFF **4** as a deep blue solid (34 mg, 17% from **S4**). Spectroscopic data were the same as described above for **4**. *anti*-DBFF-dione **12** was also obtained in such trace amounts that it precluded spectroscopic analysis. Further attempts to increase the yield of this side-product were unsuccessful.

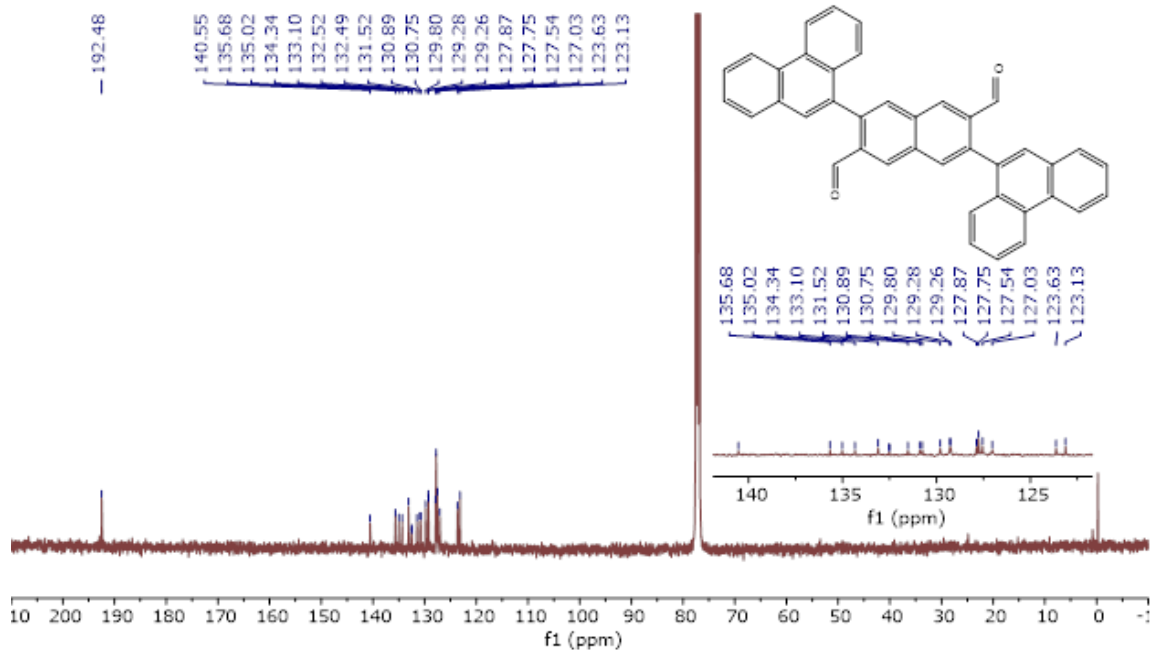
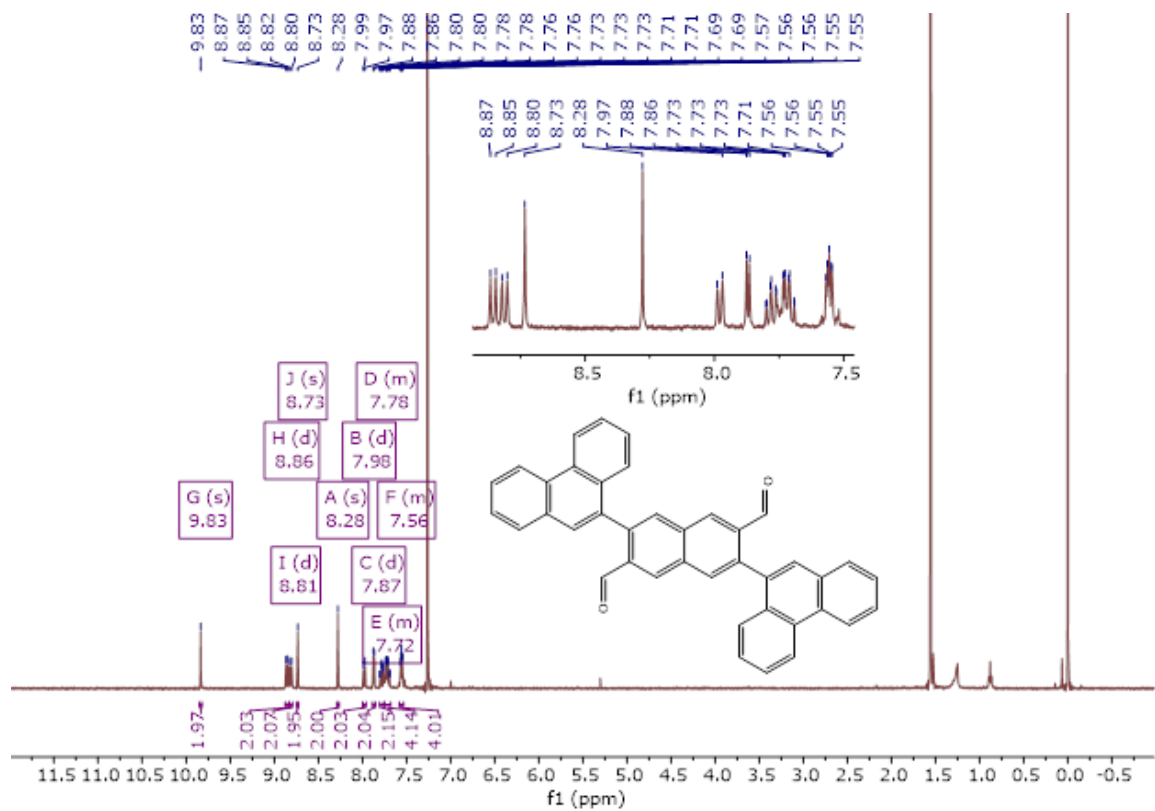
3. Copies of NMR Spectra

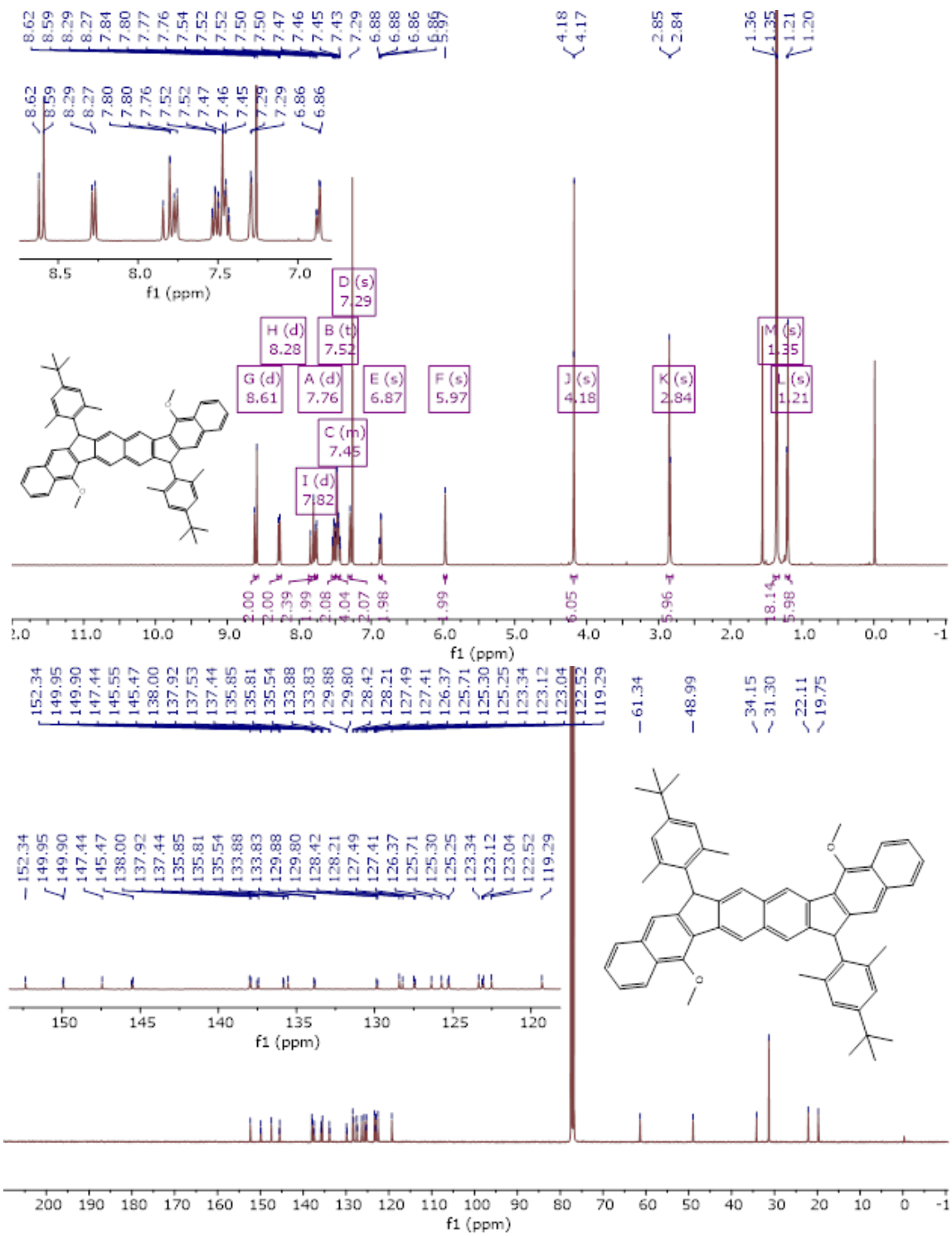


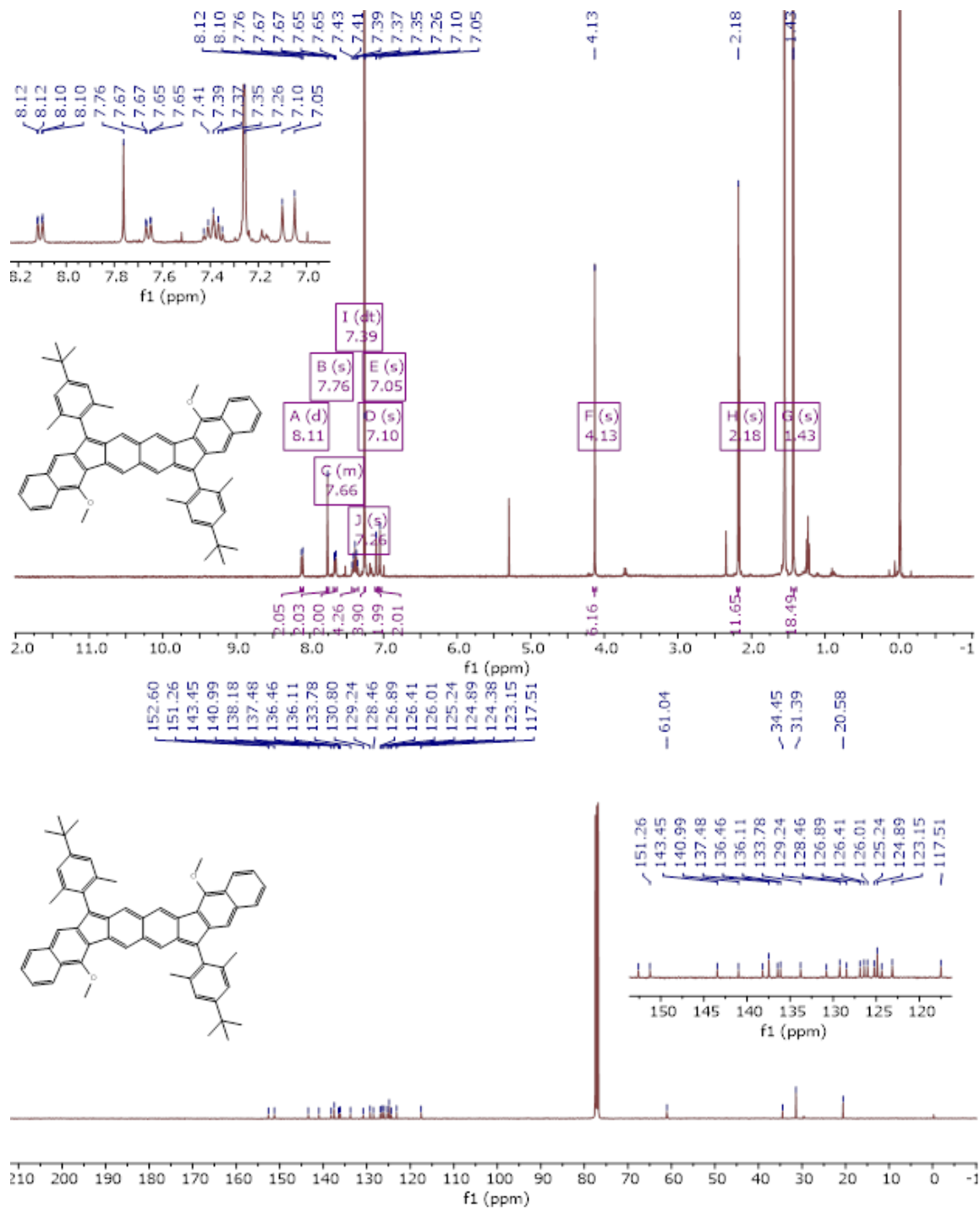


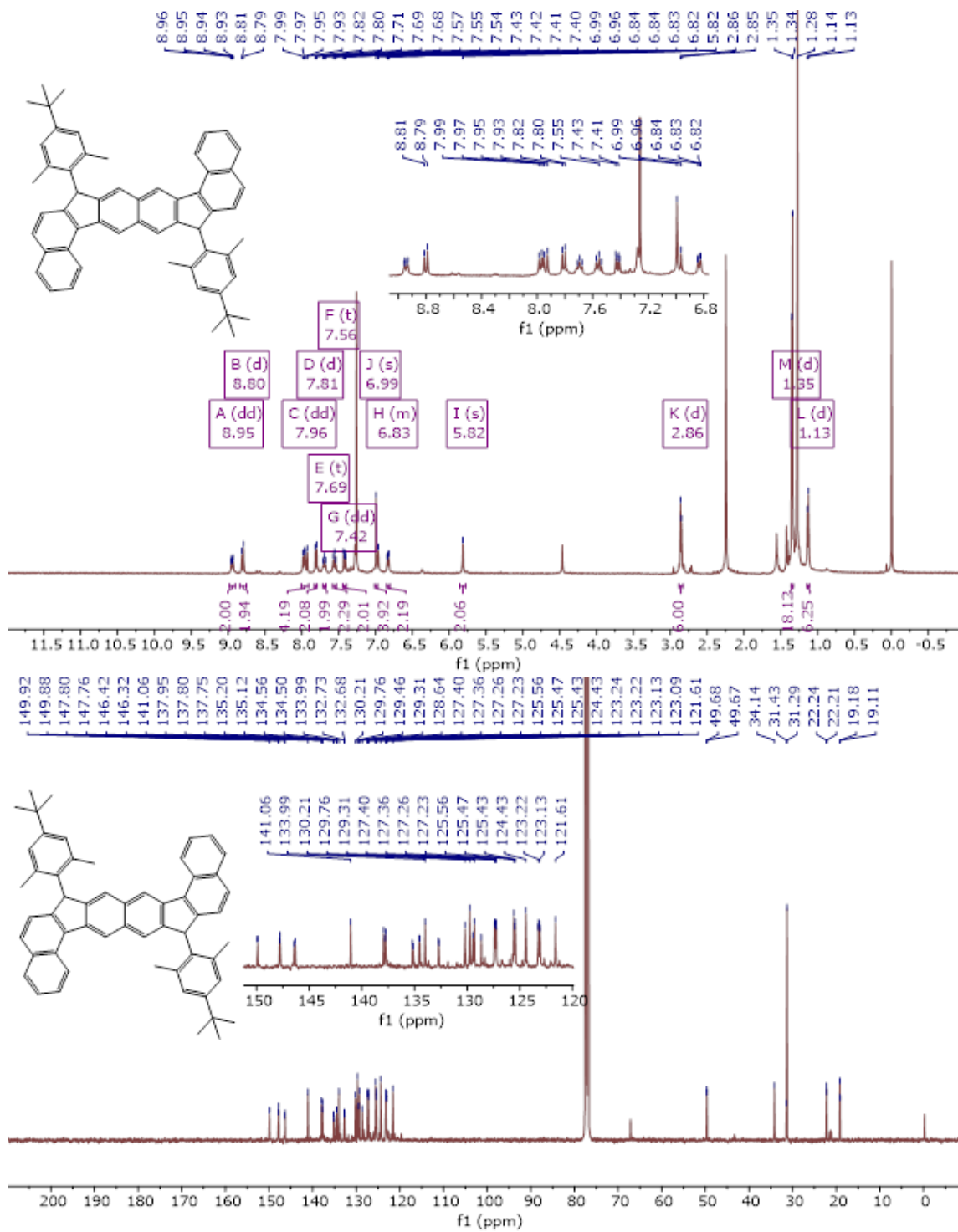


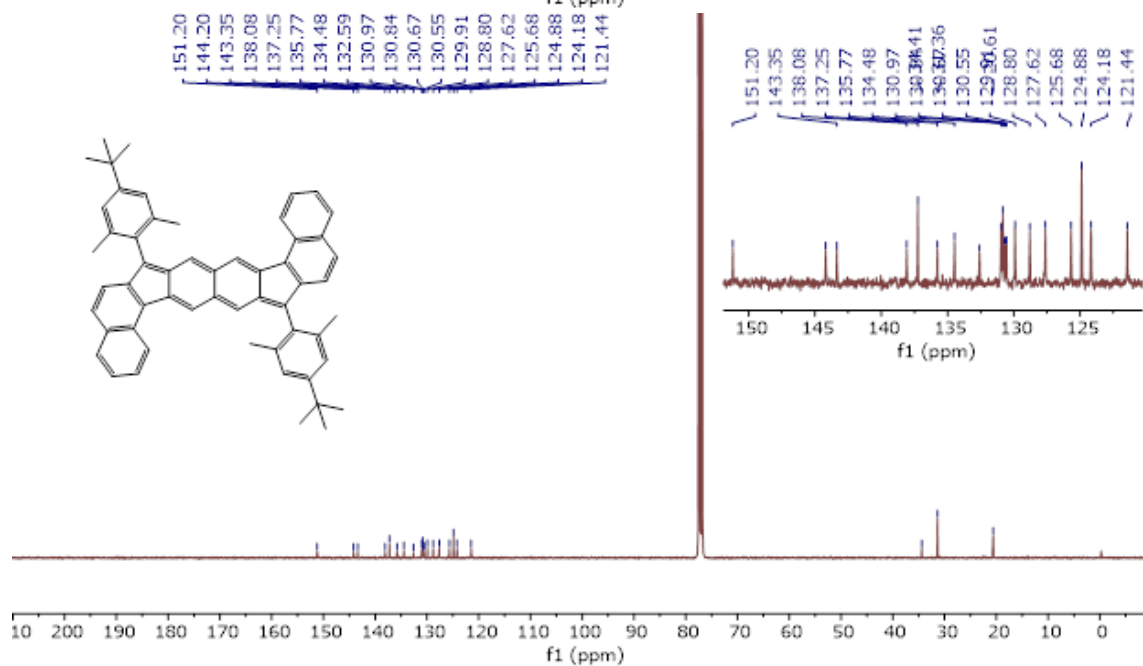
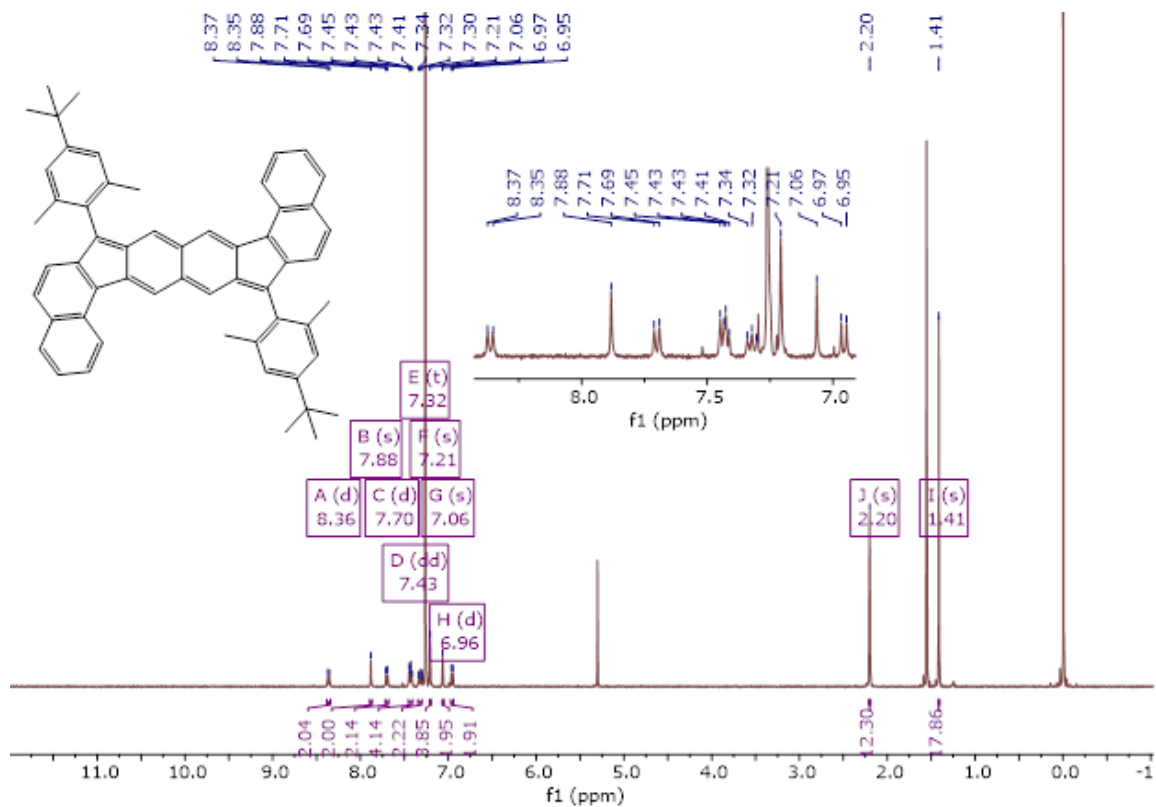


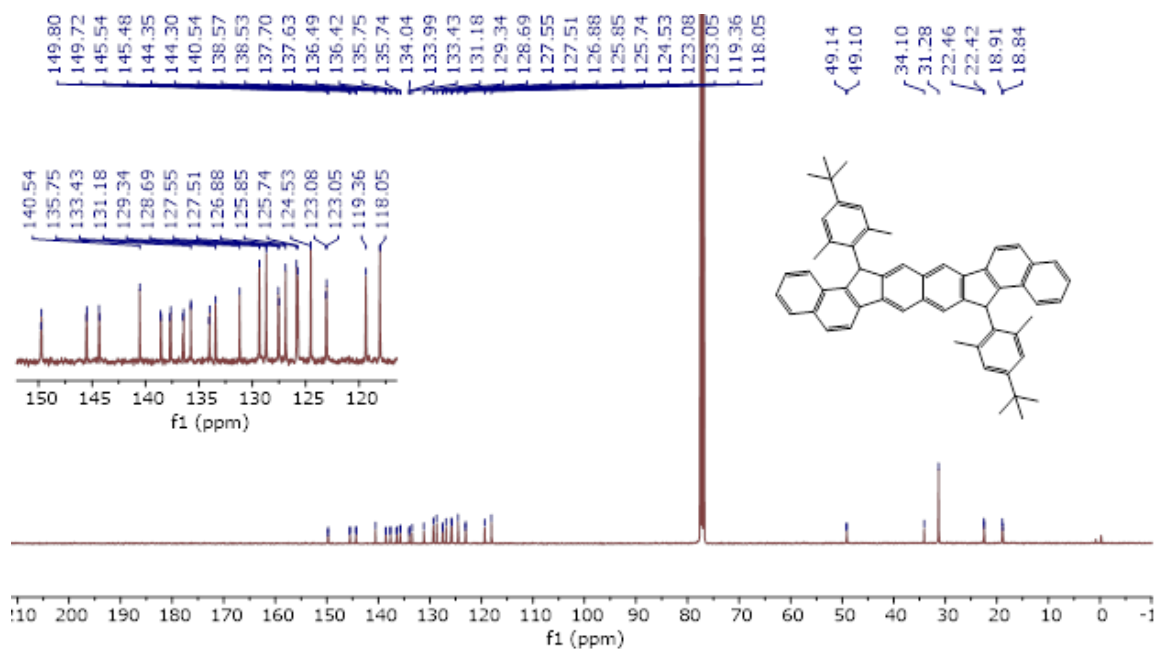
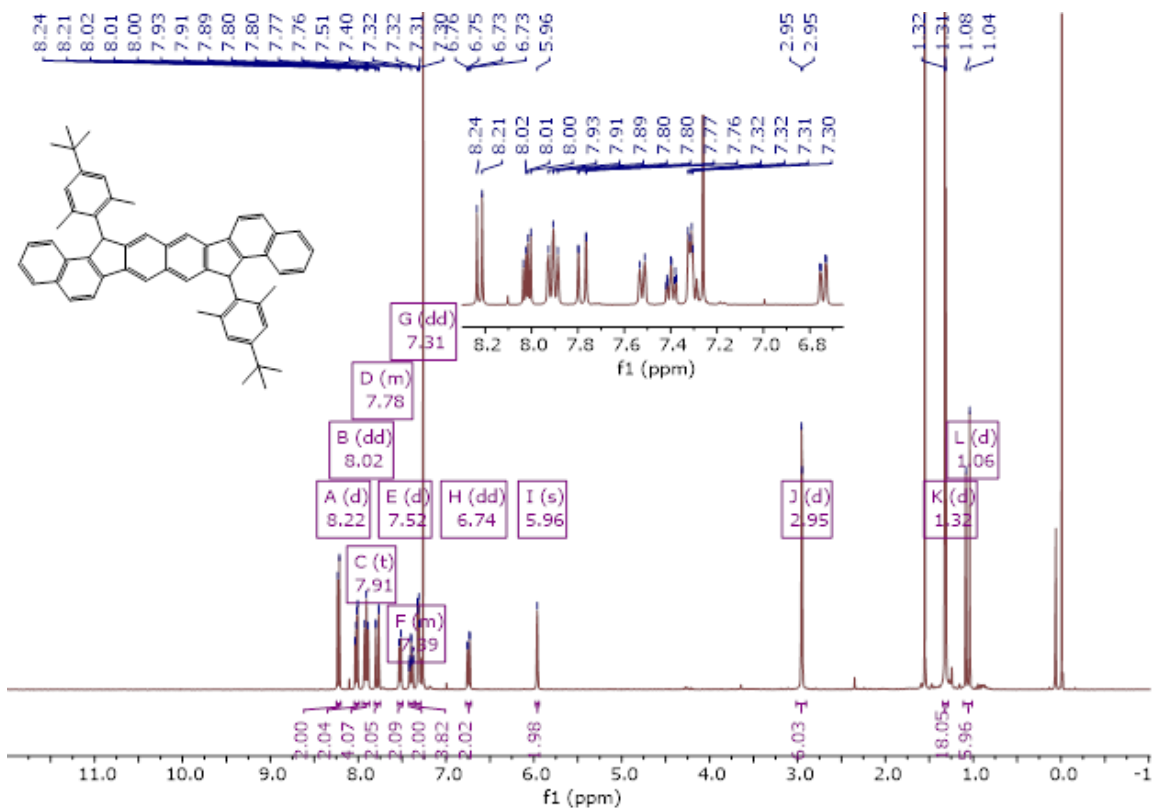


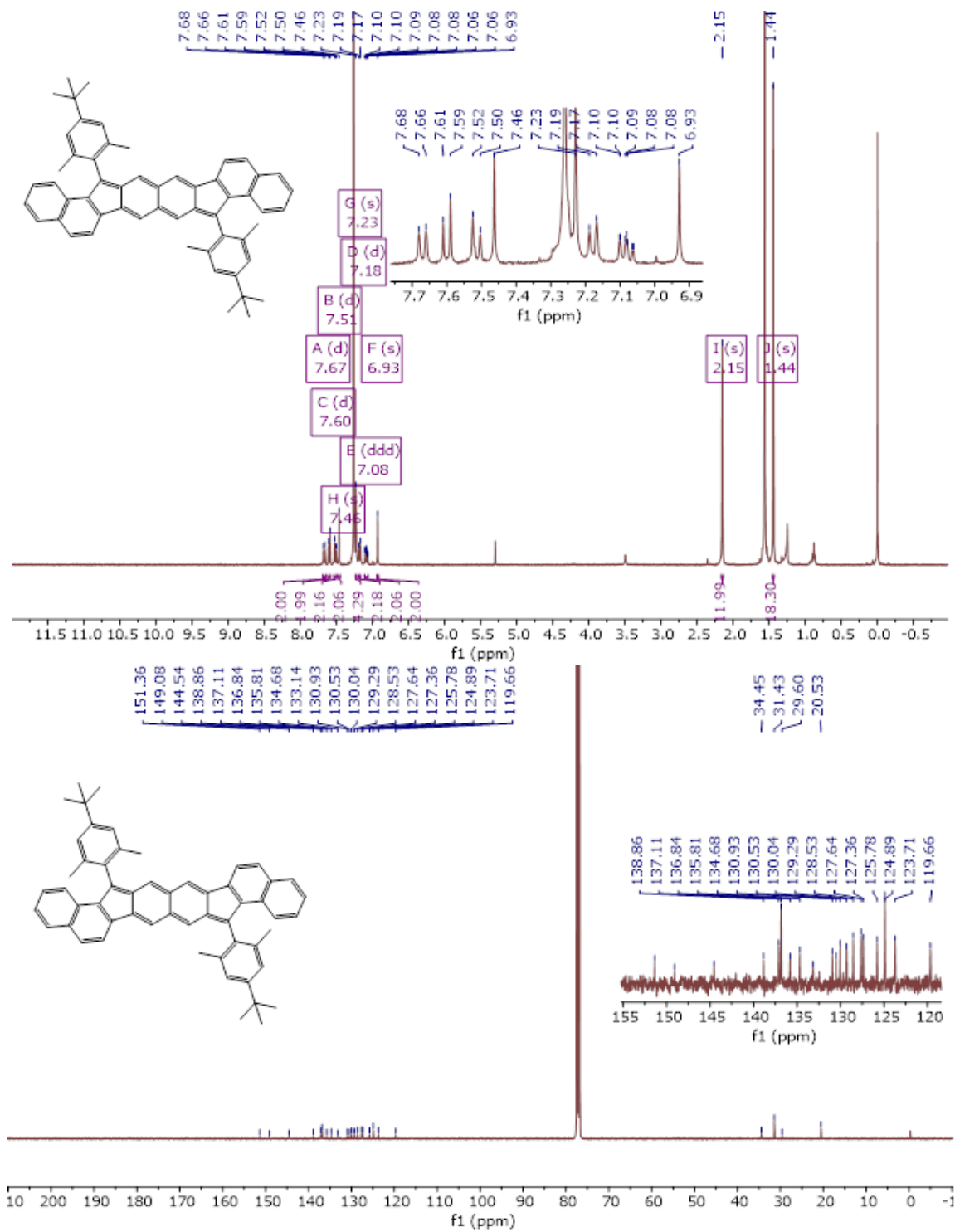


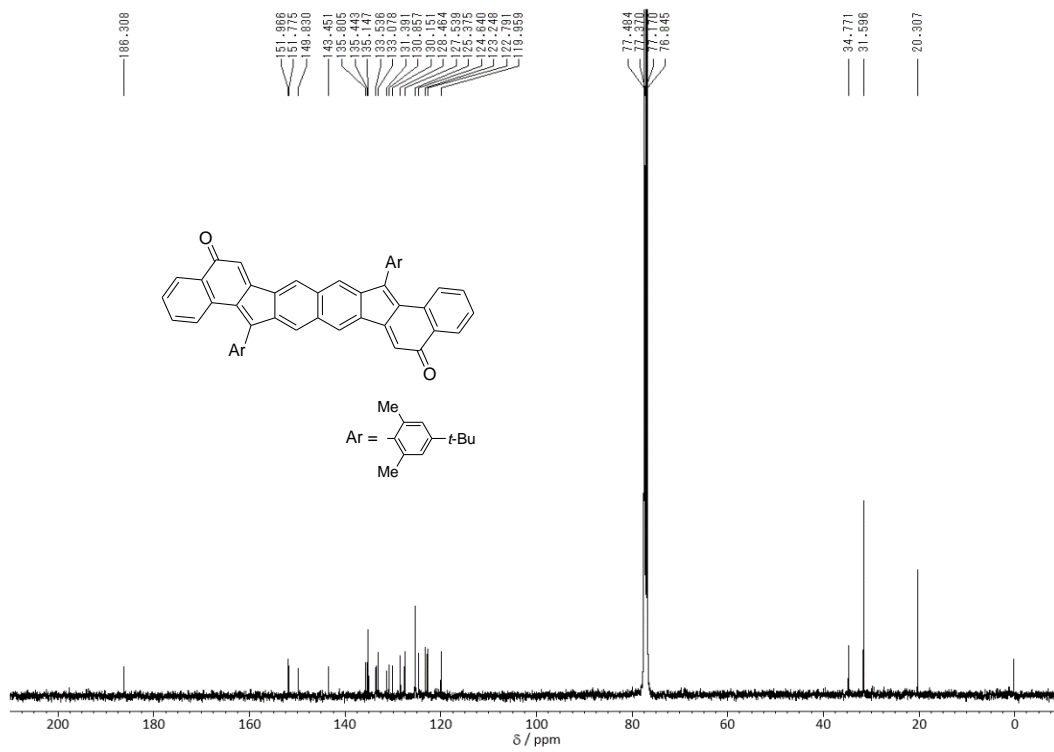
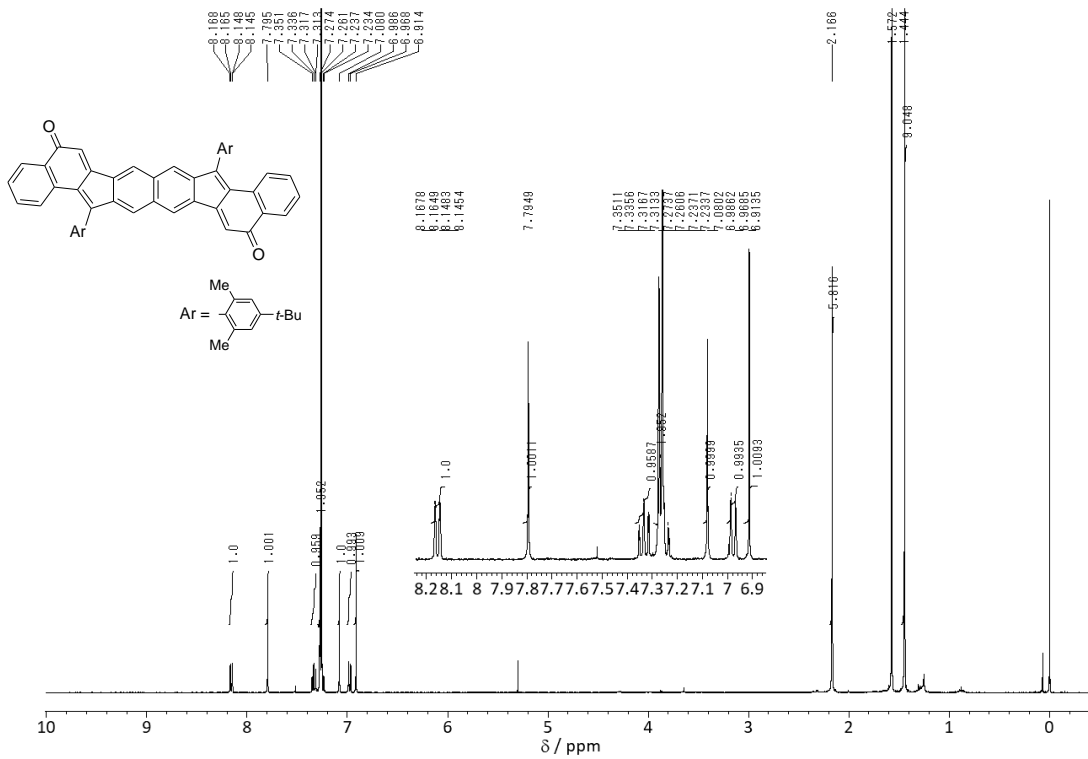


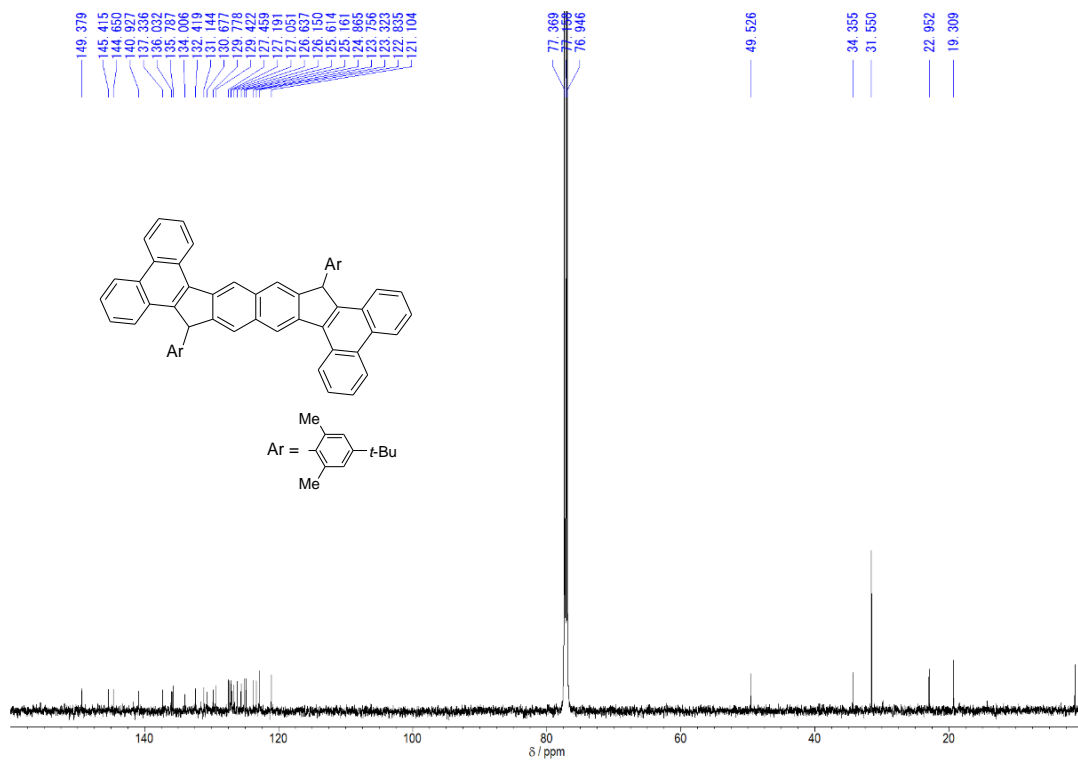
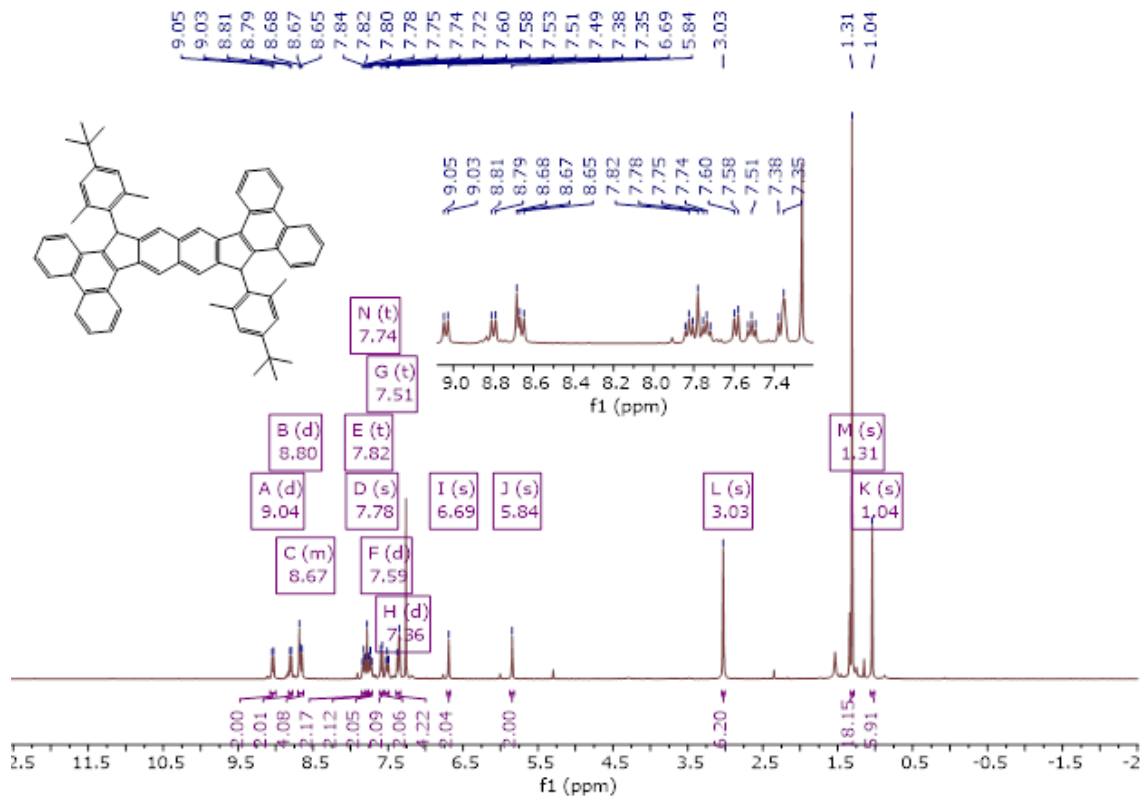


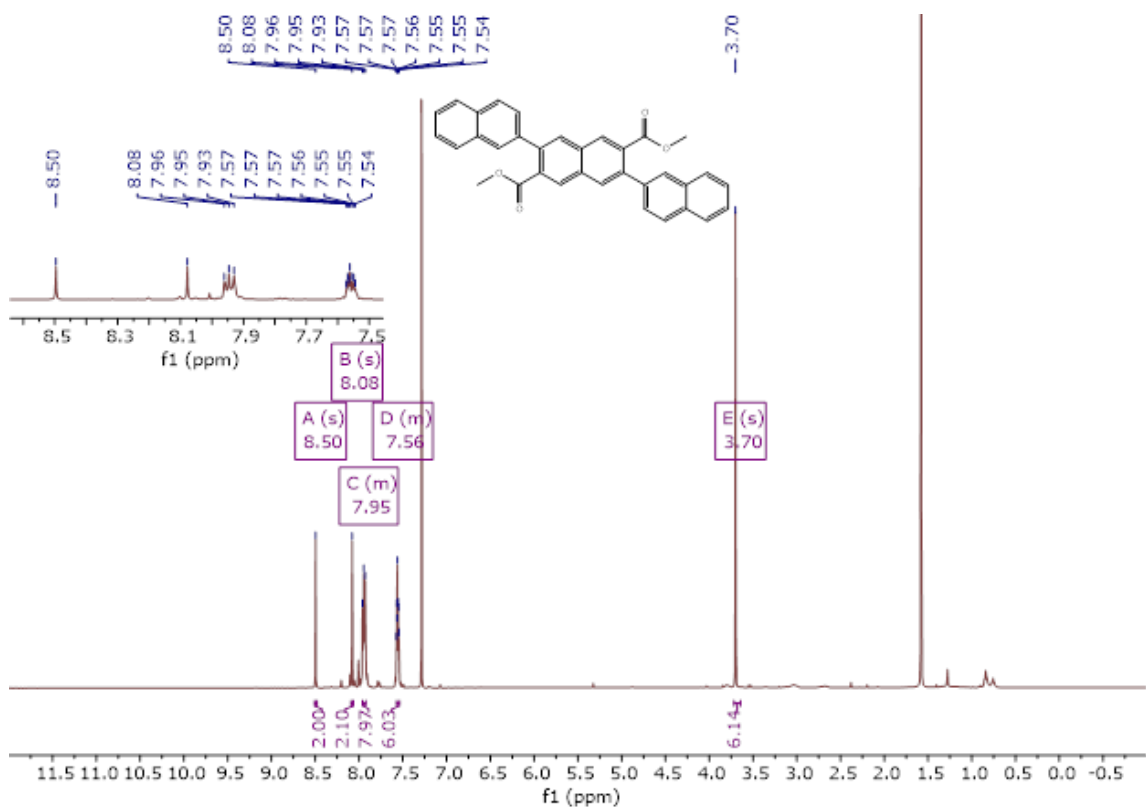
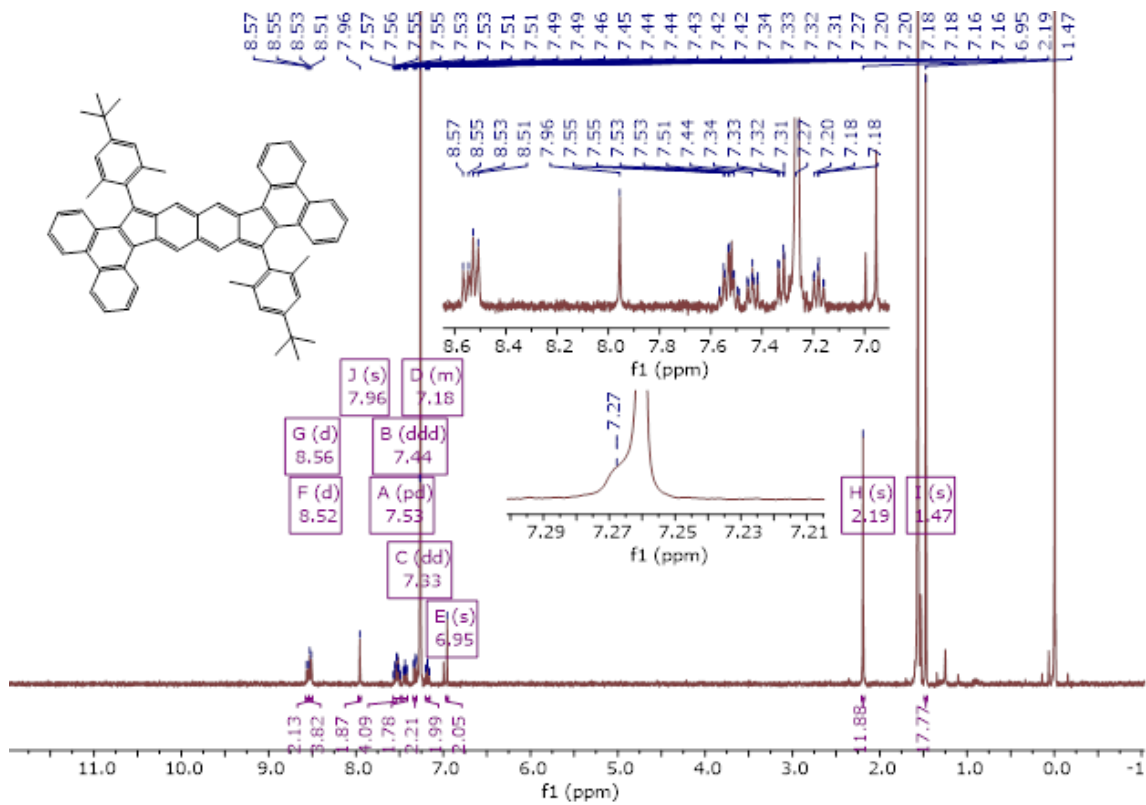


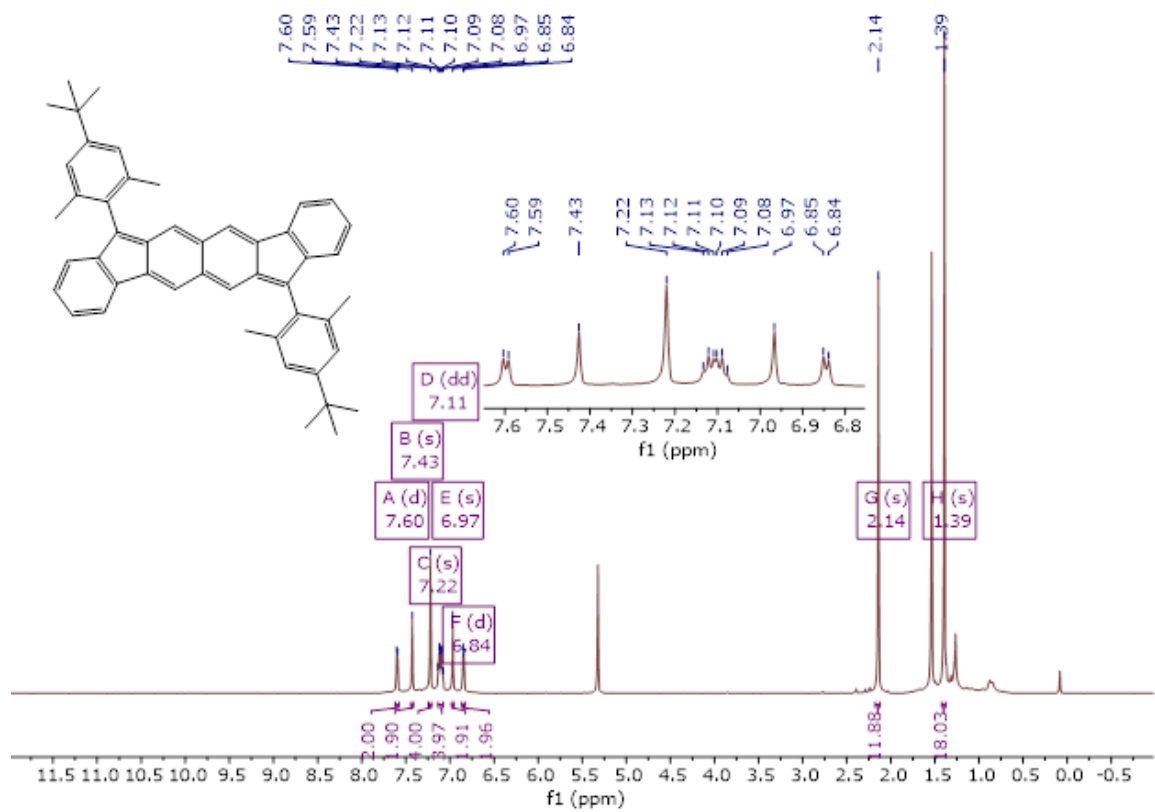
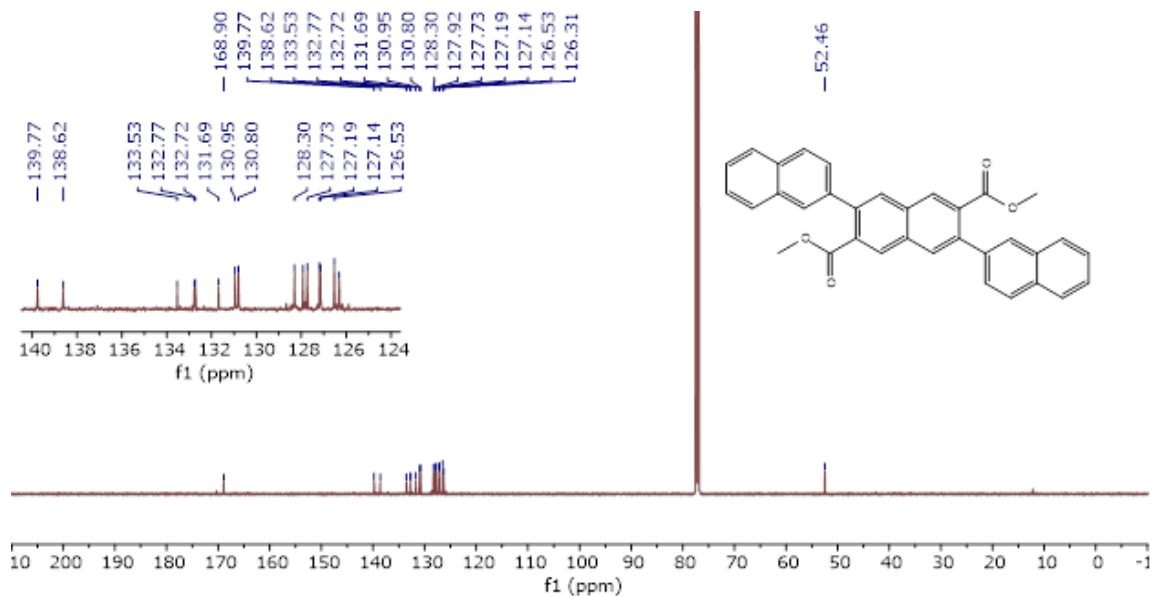


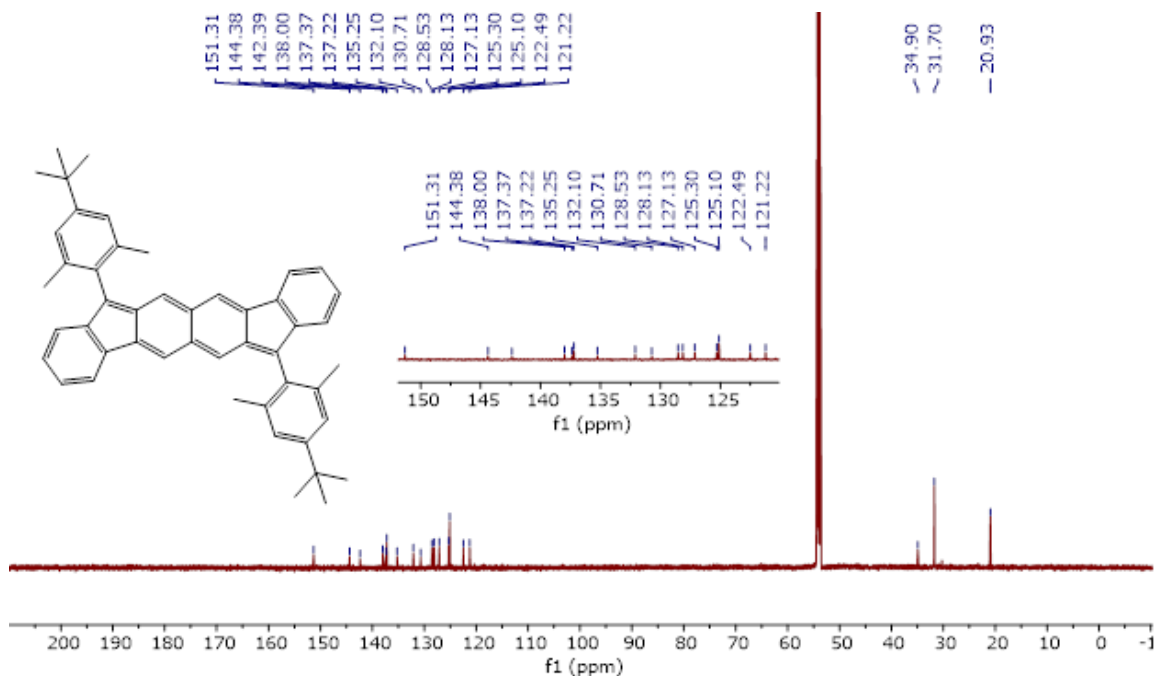








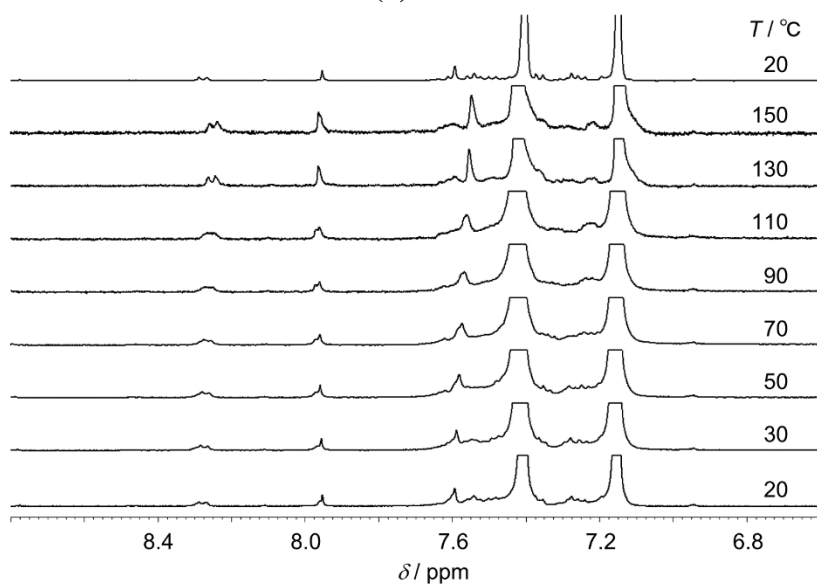




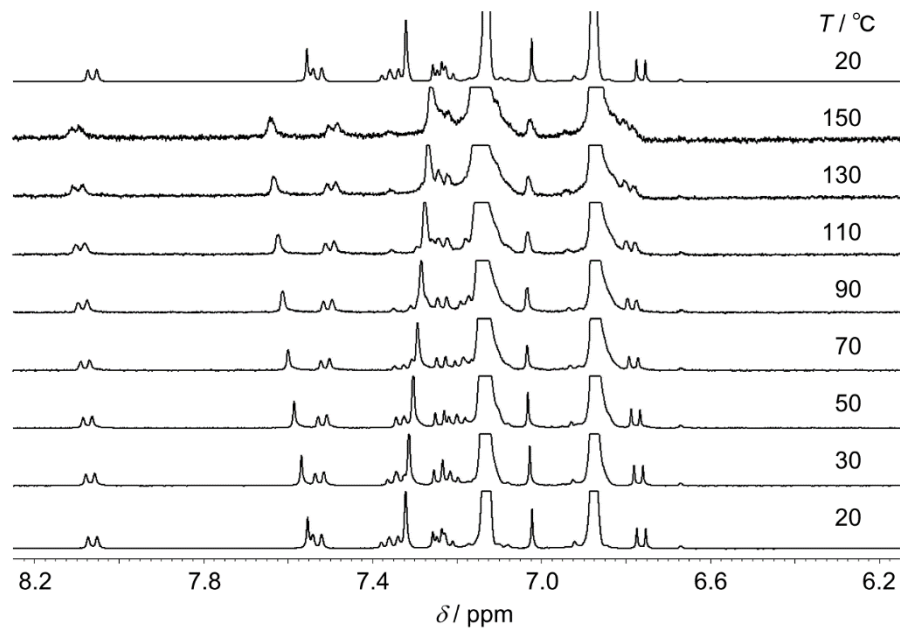
4. Variable Temperature Proton NMR Experiments

General. Approximately 3 mg of each FF derivative was dissolved in 1,2-dichlorobenzene- d_4 , or 1,1,2,2-tetrachloroethane- d_4 and transferred to an NMR tube. Proton NMR spectra were acquired in a JEOL ECS 400 or 600 MHz spectrometer that was heated to 30, 50, 70, 90, 110, 130, 150 and then back to 20 °C.

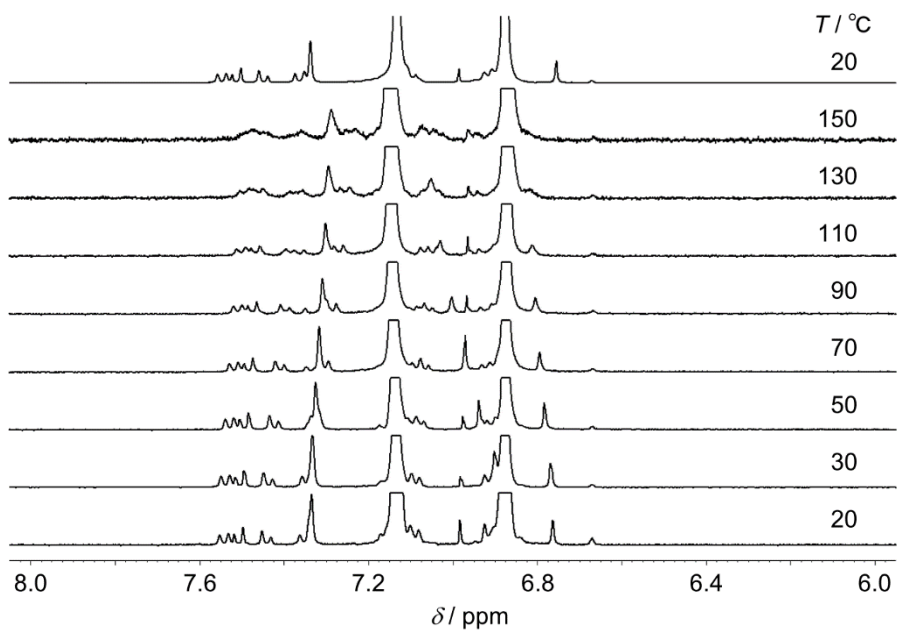
VT-NMR for *linear-DBFF* (2)



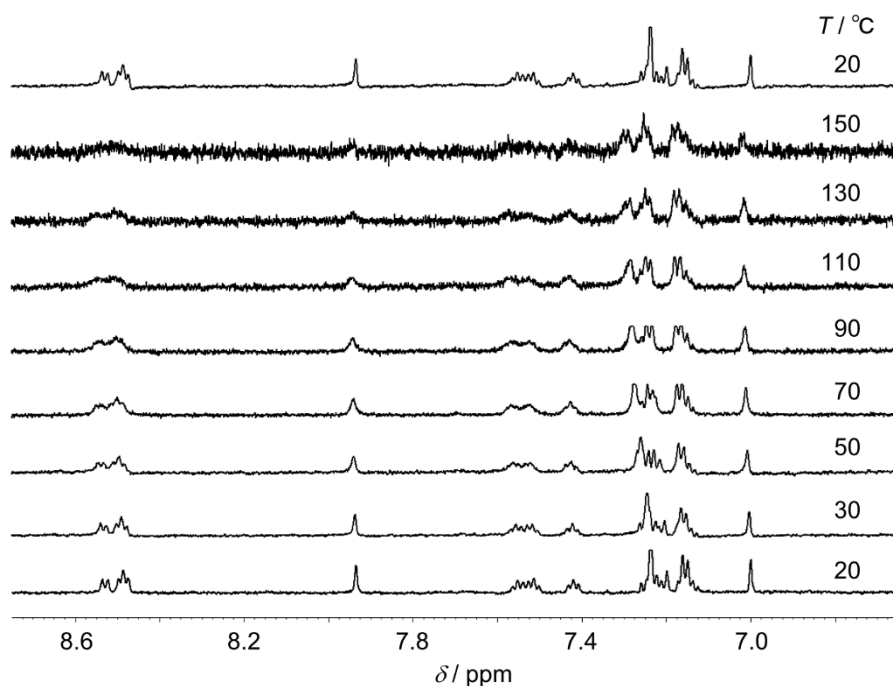
VT-NMR for *syn*-DBFF (3)



VT-NMR for *anti*-DBFF (4)



VT-NMR for TBFF (5)



5. X-ray Structure Details

General. Low-temperature X-ray diffraction data for FFs **1-4**, dione **11** and radical cation $\mathbf{3}^+\cdot\mathbf{SbCl}_6^-$ were collected on a Rigaku AFC10 diffractometer coupled to a Rigaku AFC HyPix-6000 or Saturn724 detector with Mo $K\alpha$ radiation ($\lambda = 0.71073 \text{ \AA}$), from a FR-E+ X-ray source, while the data for dione **12** were collected on a Rigaku XtaLAB Synergy diffractometer coupled to a Rigaku HyPix detector with Cu $K\alpha$ radiation ($\lambda = 1.54184 \text{ \AA}$), from a PhotonJet micro-focus X-ray source. The diffraction images were processed and spaced using the CrysAlisPro software¹⁶ for FFs **1-3**, diones **11** and **12**, and radical cation $\mathbf{3}^+\cdot\mathbf{SbCl}_6^-$ as well as the CrystalClear software¹⁷ for FF **4**. The structures were solved through intrinsic phasing using SHELXT¹⁸ and refined against F^2 on all data by full-matrix least squares with SHELXL¹⁹ following established refinement strategies.²⁰ All non-hydrogen atoms were refined anisotropically. All hydrogen atoms bound to carbon were included in the model at geometrically calculated positions and refined using a riding

model. The isotropic displacement parameters of all hydrogen atoms were fixed to 1.2 times the U_{eq} value of the atoms they are linked to (1.5 times for methyl groups).

Diketone 11: crystal data at 123 K, $C_{56}H_{48}O_2$, $M_r = 752.97$, Triclinic, space group $P-1$, $D_{calcd} = 1.096 \text{ g/cm}^3$, $Z = 2$, $a = 9.9954(7) \text{ \AA}$, $b = 10.6728(7) \text{ \AA}$, $c = 11.9853(8) \text{ \AA}$, $\alpha = 111.991(6)^\circ$, $\beta = 103.830(6)^\circ$, $\gamma = 91.681(5)^\circ$, $V = 1141.11(14) \text{ \AA}^3$; Mo- $K\alpha$ radiation, $\lambda = 0.71075 \text{ \AA}$, $\mu = 0.065 \text{ mm}^{-1}$. A purple crystal was obtained from CH_2Cl_2 /hexane solution at 5°C . Numbers of measured and unique reflections were 16749 and 5224, respectively. Final $R(F) = 0.0644$ for 267 parameters and 5224 reflections with $I > 2\sigma(I)$ (for all data, $R(F)$ and $wR(F^2)$ values are 0.0863 and 0.1621, respectively). CCDC-2016990.

Diketone 12: $C_{60}H_{54}N_2O_2$, $C_{56}H_{48}O_2S_2 \cdot 2(\text{MeCN})$, $M = 835.05$, $0.123 \times 0.112 \times 0.071 \text{ mm}^3$, $T = 100.00(10) \text{ K}$, Triclinic, space group $P-1$, $a = 10.0059(2) \text{ \AA}$, $b = 12.3784(2) \text{ \AA}$, $c = 20.1959(2) \text{ \AA}$, $\alpha = 91.1170(10)^\circ$, $\beta = 102.5650(10)^\circ$, $\gamma = 109.1090(10)^\circ$, $V = 2295.96(7) \text{ \AA}^3$, $Z = 2$, $D_c = 1.208 \text{ Mg/m}^3$, $\mu(\text{Cu}) = 0.556 \text{ mm}^{-1}$, $F(000) = 888$, $2\theta_{\max} = 67.738^\circ$, 96197 reflections, 8302 independent reflections [$R(\text{int}) = 0.0413$], $R1 = 0.0706$, $wR2 = 0.2174$ and $\text{GOF} = 1.042$ for all reflections, max/min residual electron density $+0.681/-0.516 \text{ e\AA}^{-3}$. CCDC-2016622.

FF 1: crystal data at 100 K, $C_{48}H_{46}$, $M_r = 622.85$, Monoclinic, space group $C2/c$, $D_{calcd} = 1.103 \text{ g/cm}^3$, $Z = 4$, $a = 39.8191(10) \text{ \AA}$, $b = 7.1078(2) \text{ \AA}$, $c = 13.2632(4) \text{ \AA}$, $\alpha = \gamma = 90^\circ$, $\beta = 92.057(2)^\circ$, $V = 3751.41(18) \text{ \AA}^3$; Mo- $K\alpha$ radiation, $\lambda = 0.71075 \text{ \AA}$, $\mu = 0.062 \text{ mm}^{-1}$. A dark purple crystal was obtained from THF/EtOH solution at 5°C . Numbers of measured and unique reflections were 51323 and 4307, respectively. Final $R(F) = 0.0458$ for 222 parameters and 4307 reflections with $I > 2\sigma(I)$ (for all data, $R(F)$ and $wR(F^2)$ values are 0.0500 and 0.1204, respectively). CCDC-2016986.

linear-DBFF 2: crystal data at 123 K, $C_{58}H_{54}O_2$, $M_r = 783.01$, Triclinic, space group $P-1$, $D_{\text{calcd}} = 1.043 \text{ g/cm}^3$, $Z = 1$, $a = 9.6155(5) \text{ \AA}$, $b = 12.5278(7) \text{ \AA}$, $c = 12.5966(8) \text{ \AA}$, $\alpha = 115.337(6)^\circ$, $\beta = 105.190(5)^\circ$, $\gamma = 100.350(5)^\circ$, $V = 1247.27(16) \text{ \AA}^3$; Mo- $K\alpha$ radiation, $\lambda = 0.71075 \text{ \AA}$, $\mu = 0.061 \text{ mm}^{-1}$. A purple crystal was obtained from CH_2Cl_2 /hexane solution at 5°C . Numbers of measured and unique reflections were 20192 and 5735, respectively ($R_{\text{int}} = 0.0329$). Final $R(F) = 0.0441$ for 277 parameters and 5735 reflections with $I > 2\sigma(I)$ (for all data, $R(F)$ and $wR(F^2)$ values are 0.0608 and 0.1205, respectively). The contribution to the scattering arising from the presence of the disordered solvents in the crystals was removed by use of the utility “solvent mask”²¹ in the Olex2 software package.²² CCDC-2016987.

syn-DBFF 3: crystal data at 123 K, $C_{56}H_{50}$, $M_r = 722.39$, Triclinic, space group $P-1$, $D_{\text{calcd}} = 1.199 \text{ g/cm}^3$, $Z = 2$, $a = 9.1789(10) \text{ \AA}$, $b = 11.6468(9) \text{ \AA}$, $c = 11.9710(10) \text{ \AA}$, $\alpha = 66.929(7)^\circ$, $\beta = 76.102(8)^\circ$, $\gamma = 88.471(7)^\circ$, $V = 1139.67(19) \text{ \AA}^3$; Mo- $K\alpha$ radiation, $\lambda = 0.71075 \text{ \AA}$, $\mu = 0.068 \text{ mm}^{-1}$. A dark purple crystal was obtained from CH_2Cl_2 /hexane solution at 5°C . Numbers of measured and unique reflections were 18203 and 5220, respectively. Final $R(F) = 0.0834$ for 258 parameters and 5220 reflections with $I > 2\sigma(I)$ (for all data, $R(F)$ and $wR(F^2)$ values are 0.1126 and 0.2292, respectively). CCDC-2016989.

anti-DBFF 4: crystal data at 123 K, $C_{56}H_{50}$, $M_r = 722.39$, Triclinic, space group $P-1$, $D_{\text{calcd}} = 1.014 \text{ g/cm}^3$, $Z = 2$, $a = 9.710(4) \text{ \AA}$, $b = 9.881(4) \text{ \AA}$, $c = 13.545(6) \text{ \AA}$, $\alpha = 103.172(7)^\circ$, $\beta = 100.516(8)^\circ$, $\gamma = 104.692(6)^\circ$, $V = 1183.4(8) \text{ \AA}^3$; Mo- $K\alpha$ radiation, $\lambda = 0.71075 \text{ \AA}$, $\mu = 0.570 \text{ mm}^{-1}$. A dark purple crystal was obtained from CH_2Cl_2 /hexane solution at 5°C . Numbers of measured and unique reflections were 16871 and 5404,

respectively. Final $R(F) = 0.1013$ for 258 parameters and 5404 reflections with $I > 2\sigma(I)$ (for all data, $R(F)$ and $wR(F^2)$ values are 0.1250 and 0.2510, respectively). The contribution to the scattering arising from the presence of the disordered solvents in the crystals was removed by use of the utility SQUEEZE in the PLATON software package.²³ CCDC-2016988.

syn-DBFF 3⁺·SbCl₆⁻: crystal data at 123 K, C₅₆H₅₀Cl₆Sb, $M_r = 1057.41$, Triclinic, space group $P-1$, $D_{\text{calcd}} = 1.434 \text{ g/cm}^3$, $Z = 1$, $a = 10.2867(8) \text{ \AA}$, $b = 10.3877(9) \text{ \AA}$, $c = 13.2088(11) \text{ \AA}$, $\alpha = 103.921(7)^\circ$, $\beta = 108.432(7)^\circ$, $\gamma = 103.472(7)^\circ$, $V = 1224.31(19) \text{ \AA}^3$; Mo- $K\alpha$ radiation, $\lambda = 0.71075 \text{ \AA}$, $\mu = 0.928 \text{ mm}^{-1}$. A black crystal was obtained from CH₂Cl₂/hexane solution at 5 °C. Numbers of measured and unique reflections were 14069 and 5299, respectively. Final $R(F) = 0.0711$ for 291 parameters and 5299 reflections with $I > 2\sigma(I)$ (for all data, $R(F)$ and $wR(F^2)$ values are 0.1012 and 0.1343, respectively). CCDC-2023797.

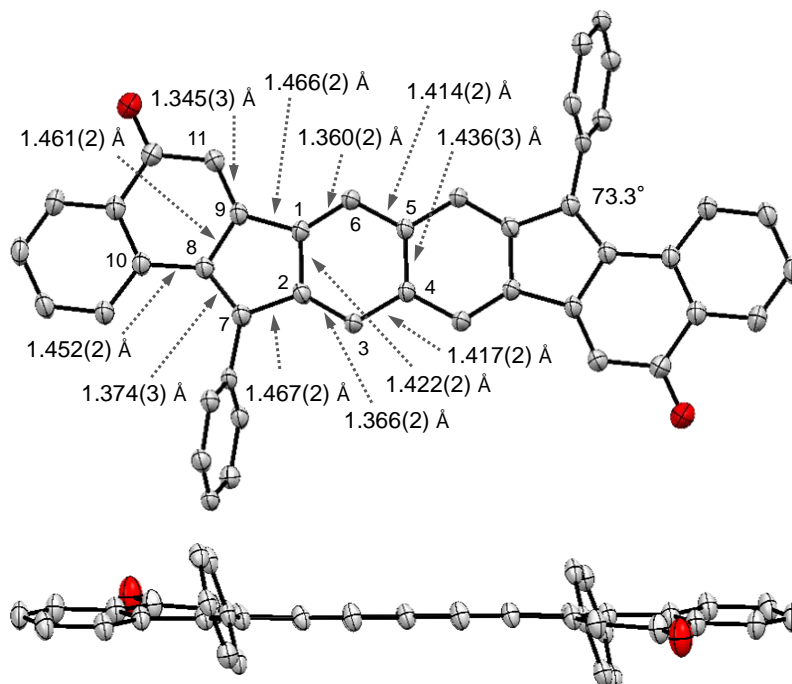


Figure D8. Molecular structure of diketone **11** with thermal ellipsoids at 50% probability. Hydrogen atoms, Me, and *t*-Bu groups are omitted for clarity.

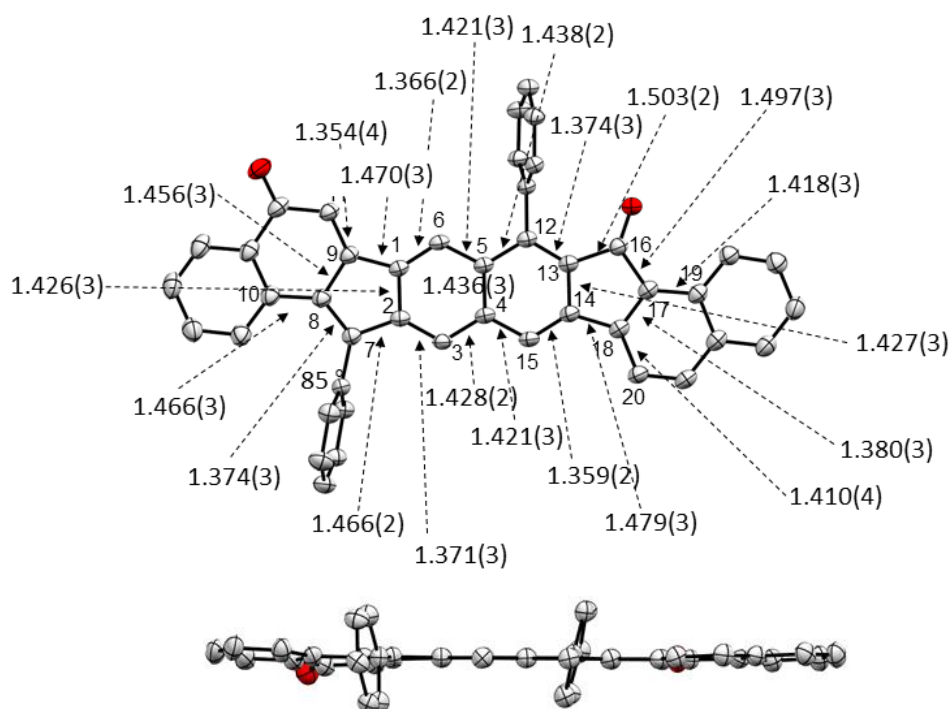


Figure D9. Molecular structure of diketone **12** with thermal ellipsoids at 50% probability. Hydrogen atoms, Me, and *t*-Bu groups are omitted for clarity.

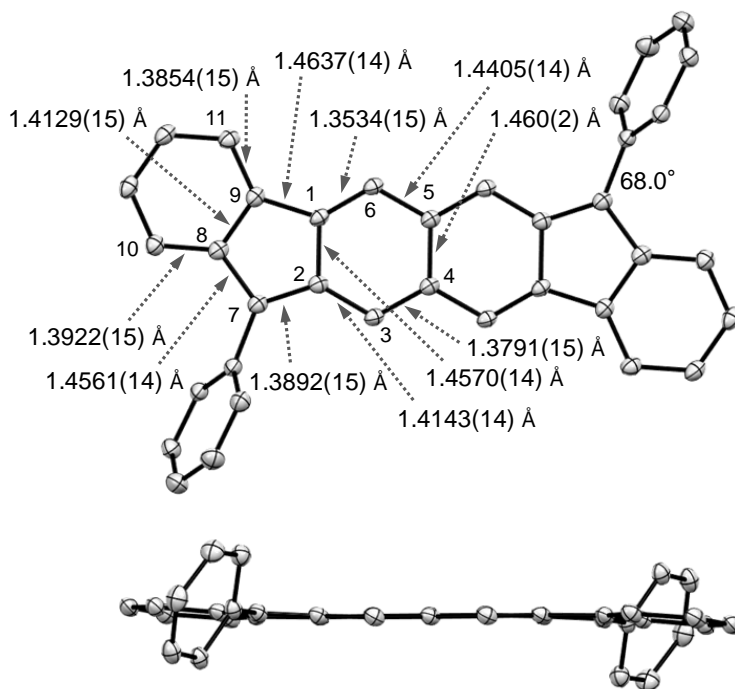


Figure D10. Molecular structure of **FF 1** with thermal ellipsoids at 50% probability. Hydrogen atoms, Me, and *t*-Bu groups are omitted for clarity.

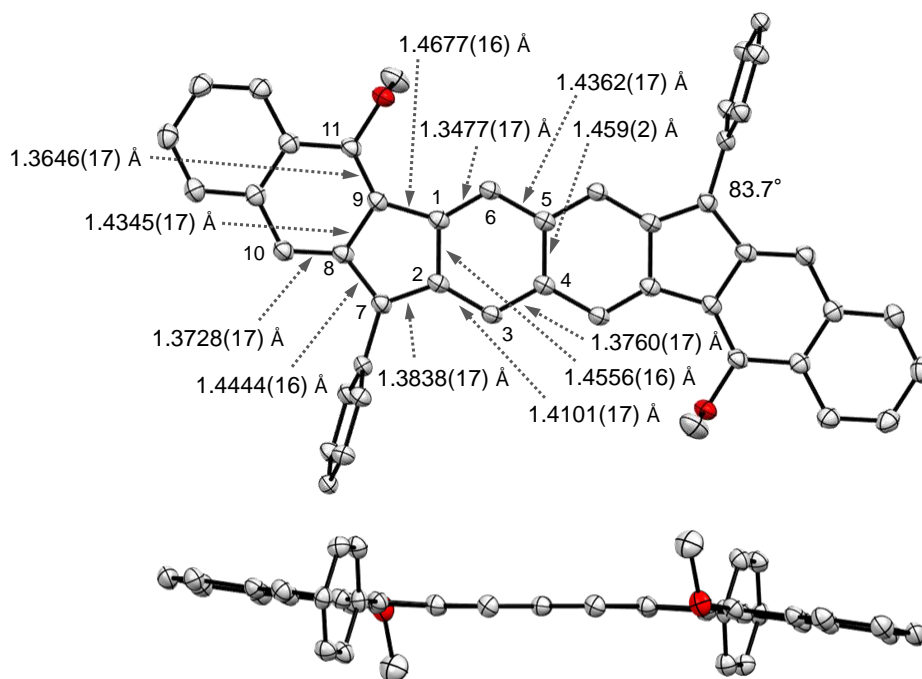


Figure D11. Molecular structure of *linear*-**DBFF 2** with thermal ellipsoids at 50% probability. Hydrogen atoms, Me, and *t*-Bu groups are omitted for clarity.

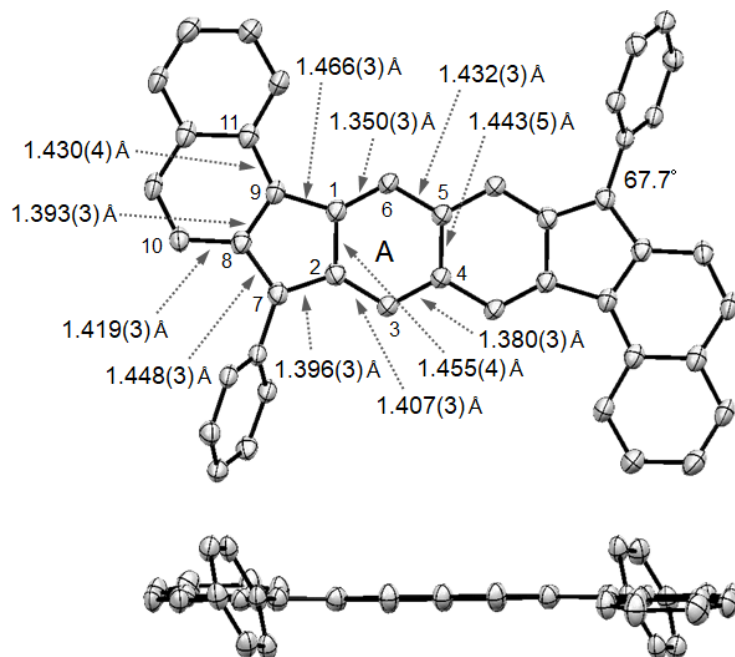


Figure D12. Molecular structure of *syn*-DBFF **3** with thermal ellipsoids at 50% probability. Hydrogen atoms and Me and *t*-Bu groups are omitted for clarity.

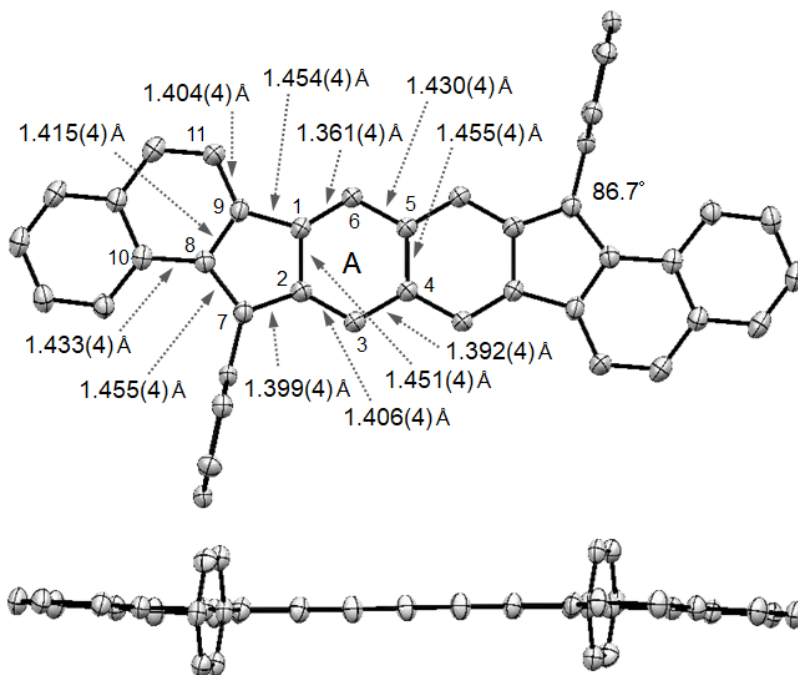


Figure D13. Molecular structure of *anti*-DBFF **4** with thermal ellipsoids at 50% probability. Hydrogen atoms, Me, and *t*-Bu groups are omitted for clarity.

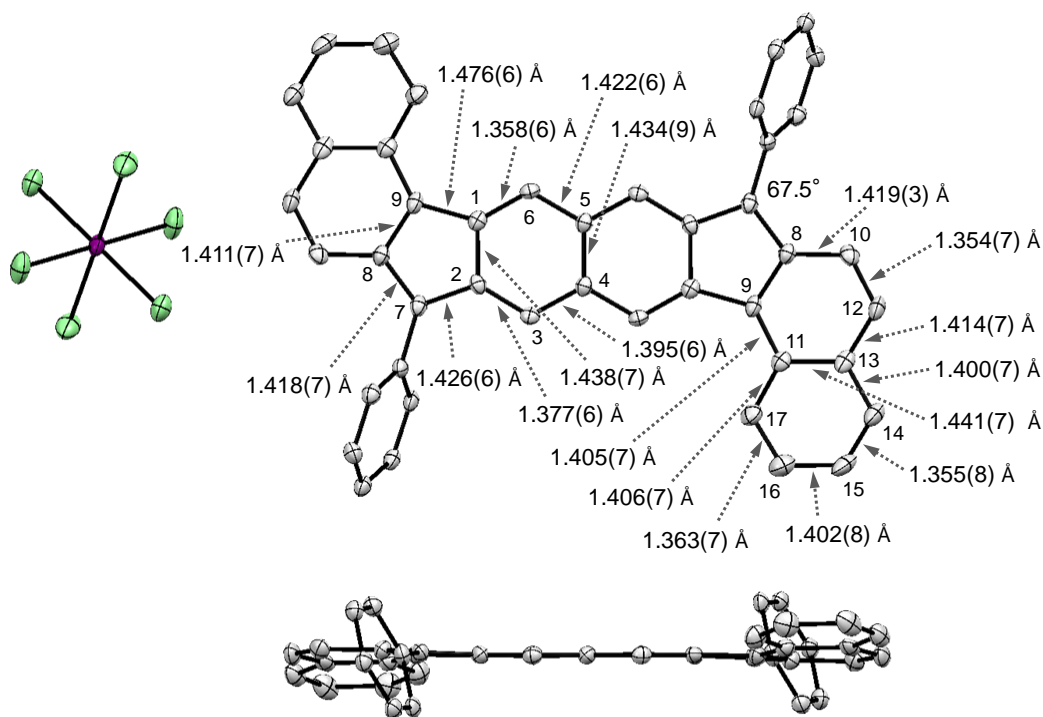


Figure D14. Molecular structure of *syn*-DBFF $3^{3+} \cdot SbCl_6^{-}$ with thermal ellipsoids at 50% probability. Hydrogen atoms and Me and *t*-Bu groups are omitted for clarity.

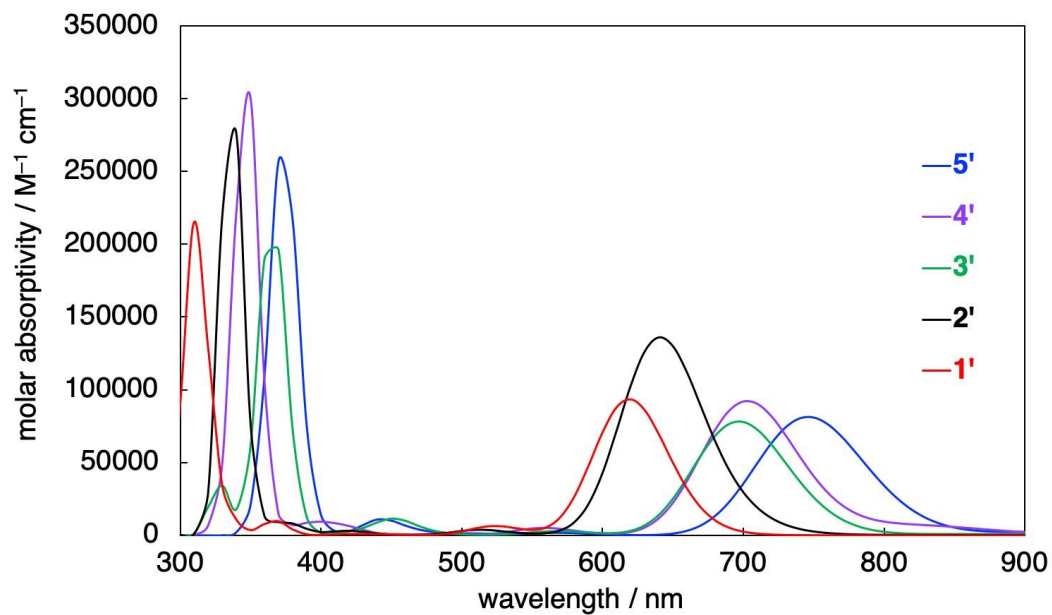


Figure D15. Calculated UV-vis-NIR spectra for FF $1'-5'$ at the TD-tuned-LC-UBLYP/6-311G*// RB3LYP/6-311G* level (gas-phase). Half-width at half-height (HWHH) value for the Gaussian line-shape is set to 0.1 eV.

6. Raman Details

Raman spectra of FF **2-5** were measured using a Bruker Senterra Raman microscope by averaging spectra during 50 min with a resolution of $3\text{--}5\text{ cm}^{-1}$. Three Raman excitations wavelengths at 532, 633, and 785 nm were used. The Raman spectra were collected by using the 1×1 camera of a CCD camera operating at $-50\text{ }^{\circ}\text{C}$. Spectra of the dihydrogenated precursors **10a** and **10c** (due to strong fluorescence) were analyzed by using the RAMII FT-Raman module of a VERTEX 70 FT-IR spectrometer. A continuous-wave Nd-YAG laser working at 1064 nm was employed for excitation, at a laser power in the sample not exceeding 30 mW. Raman scattering radiation was collected in a back-scattering configuration with a standard spectral resolution of 4 cm^{-1} . 2000 scans were averaged for each spectrum.

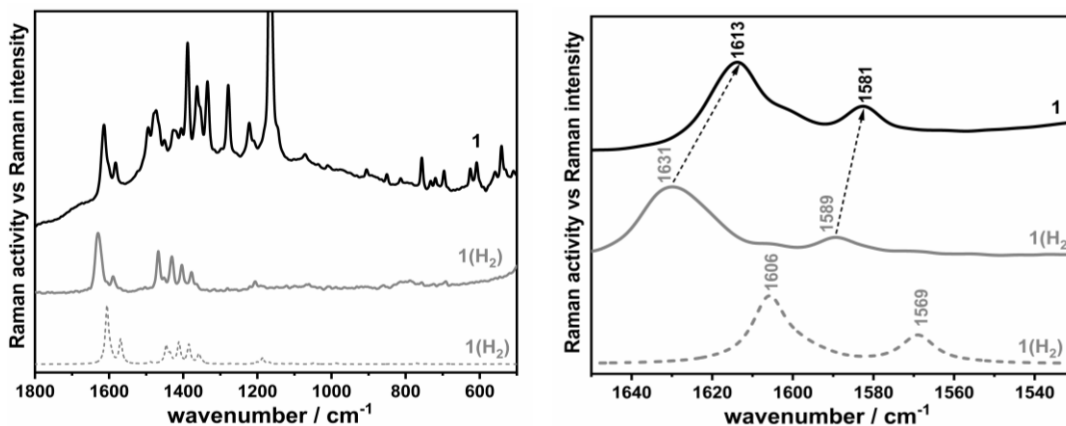


Figure D16. (left) Comparison of the B3LYP/6-31G** theoretical spectrum of **1(H₂)** dotted line, its experimental spectrum, grey solid line and the experimental Raman spectrum of **1**, solid black line. (right) Zoomed in the region of the CC stretching modes.

Unfortunately, it is well known that DFT calculations on singlet diradicals do not provide reliable Raman spectra. The BS symmetry approach works well for relative energies but not for wavefunction and geometric properties and, by extrapolation Raman intensities (and spectra) are unreliable. Therefore, we cannot support our assignment and discussion based on the theoretical Raman spectra of the diradicaloid compounds. To solve

this, we have carried out quantum chemical calculations of the Raman spectra on the dihydrogenated analogues taken as an example the dihydrogenated *linear*-DBFF **1**, or **1(H₂)** which displays closed-shell structure and therefore the theoretical Raman spectra are meaningful. The experimental and B3LYP/6-31G** theoretical Raman spectra of **1(H₂)** are shown in Figure S16. The comparison is very good and allows us to make accurate assignments based on the theoretical vibrational eigenvectors (Figure S17). The bands at 1606 and 1569 cm⁻¹ in the theoretical spectrum of **1(H₂)** can be associated with the experimental Raman bands of **1(H₂)** at 1631 and 1589 cm⁻¹, respectively.

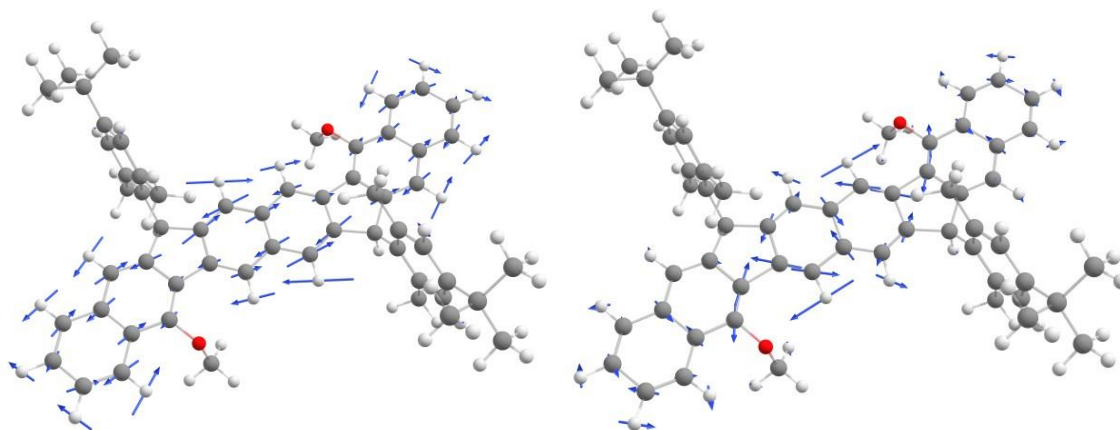


Figure D17. B3LYP/6-31G** vibrational eigenvectors associated with the main Raman bands in the region of 1650-1500 cm⁻¹ of the theoretical spectrum of **1(H₂)**. (left) vibrational eigenvector of the 1606 cm⁻¹ theoretical Raman band (associated with the experimental one at 1631 cm⁻¹). (right) Vibrational eigenvector of the 1569 cm⁻¹ theoretical Raman band (associated with the experimental one at 1589 cm⁻¹).

Based on their vibrational eigenvectors in Figure S17, the theoretical band at 1569 cm⁻¹ (experimentally at 1589 cm⁻¹) corresponds to motions mostly containing CC stretching vibrations of the central naphthalene. On the other hand, the band at 1606 cm⁻¹ (experimentally at 1631 cm⁻¹) is due mostly to CC stretching modes of the external naphthalenes (mixed to a certain extent with the CC stretching motions of the central naphthalene). Obviously, vibrational mixing of the CC stretching modes of the two

naphthalene aromatic groups unavoidably occurs. However, this mixing is expected to be smaller or minorized in the diradical compound **1** as the central anthracene is partially quinoidal. Assuming that the number of normal modes in **1** and **1(H₂)** should be similar in this 1700-1500 cm⁻¹ region, a one-to-one correspondence between the Raman bands of the two can be made such as proposed in Figure S15 (arrows). From this correspondence, the band at 1581 cm⁻¹ of **1** can be described as a naphthalene based CC stretching, or $\nu_{\text{naphth}}(\text{CC})$.

7. Magnetic Measurements/SQUID

General. Magnetic susceptibility measurements were performed with a Quantum Design MPMS-XL-7 SQUID susceptometer equipped with a sample space oven. The measurements were performed with an applied DC field of 1 T in the temperature range 300-620 K for compounds **3-5** and 300-670 K for compounds **1** and **2** with the samples inserted in a 1.5 mm diameter aluminum foil cylinder. The measurements were performed in a heating-cooling cycle with very similar behaviors in both scans, confirming the thermal stability of all the samples in the measured temperature range. The susceptibility data were corrected for the same sample holder previously measured using the same conditions and the diamagnetic contributions of the compound as deduced by using Pascal's constant tables.²⁴ The magnetic measurements were fitted using the classical Bleaney-Bowers model for an antiferromagnetic $S = \frac{1}{2}$ dimer.²⁵ This model reproduces satisfactorily the magnetic properties with $g = 2.0(1)$ and paramagnetic $S = \frac{1}{2}$ impurities (ρ) of *ca.* 0.5-1.0%. In all cases the paramagnetic impurities likely come from a small fraction of mono-radical present in the sample. Given the low magnetic signal, the J value obtained presents an uncertainty of around 10%, as this error corresponds to the error in the $\chi_m T$ values (and,

therefore in the g values that are directly related to them). For the estimated ΔE_{ST} values from the fit to the Bleaney-Bowers model, however, the ΔE_{ST} value mainly depends on the curvature of the plot as T increases; thus, the error in ΔE_{ST} can be evaluated to be around $0.2 \text{ kcal mol}^{-1}$, which is more like 2-3%.

8. TGA Measurements

General. Thermogravimetric Analysis (TGA) was performed from 20-450 °C on samples of FFs **1-5** using a Rigaku Thermo Plus TG 8120 instrument. The measurements were performed under an oxygen-free dry N_2 flow.

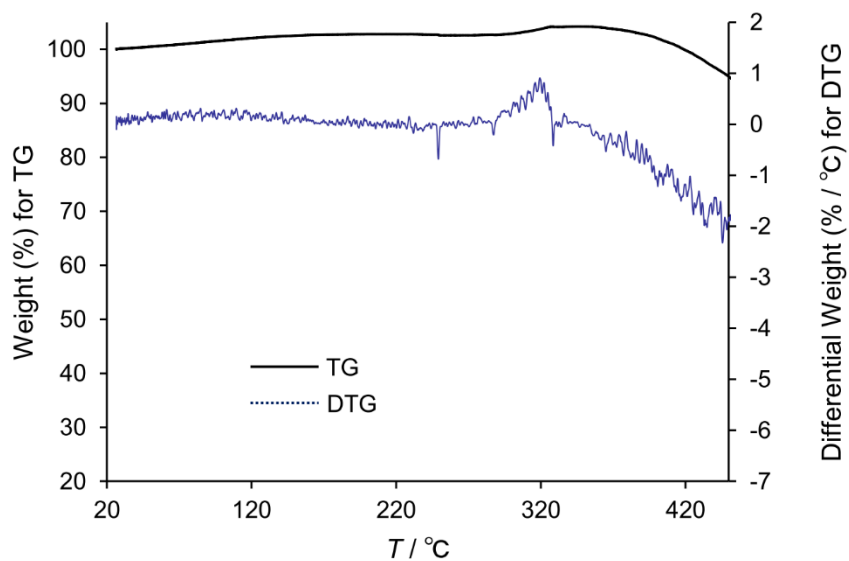


Figure D18. TGA plot for FF 1.

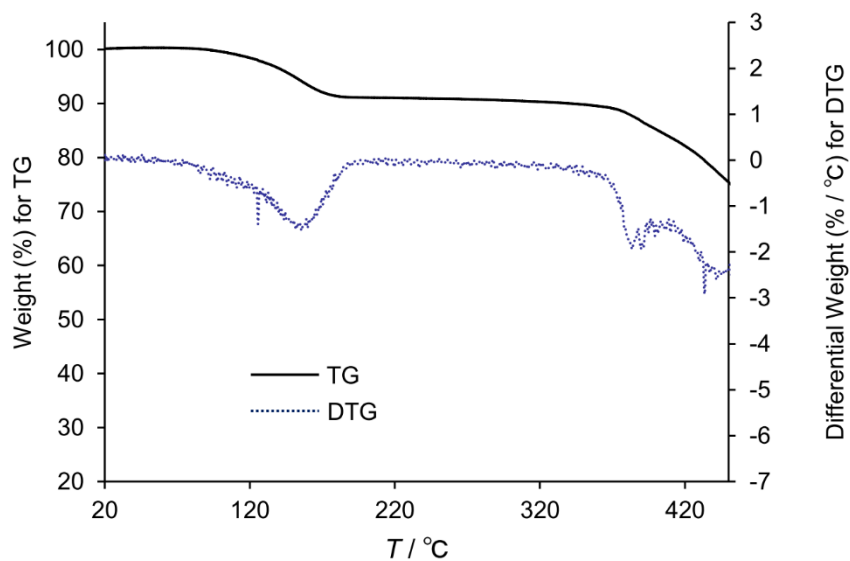


Figure D19. TGA plot for *linear*-DBFF **2**. The initial weight loss corresponds to hexane. Based on the X-ray crystallographic analysis, hexane solvent is included in the solid sample.

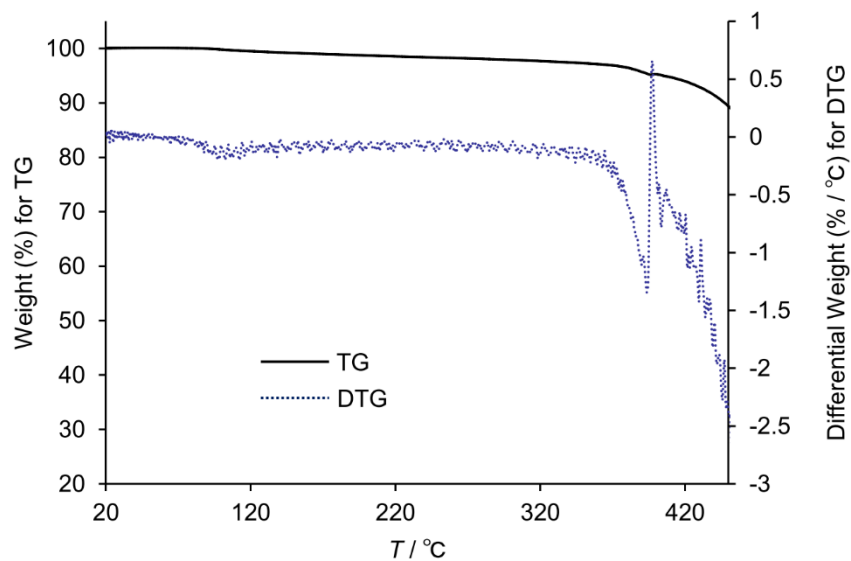


Figure D20. TGA plot for *syn*-DBFF **3**.

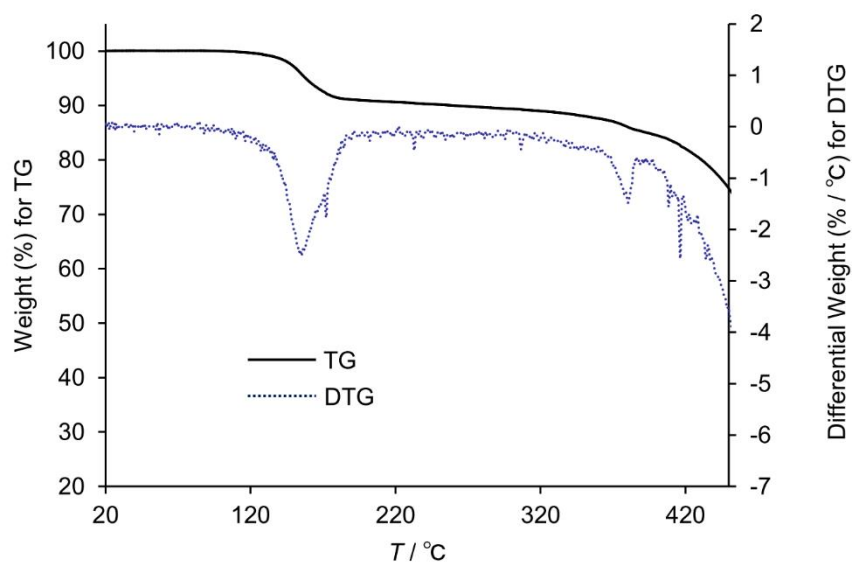


Figure D21. TGA plot for *anti*-DBFF 4. The initial weight loss corresponds to hexane solvent judging from the ^1H NMR spectrum of the analytical sample. Based on the X-ray crystallographic analysis, hexane solvent is included in the solid sample.

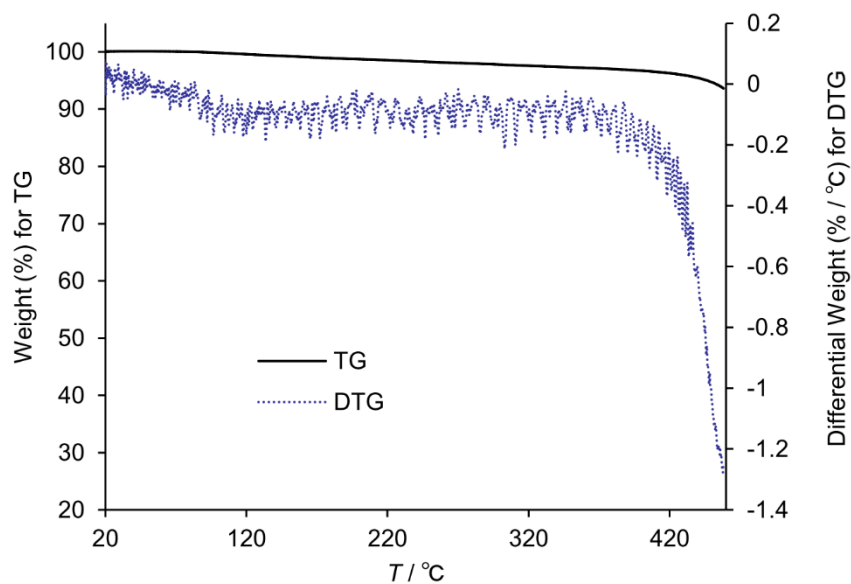


Figure D22. TGA plot for TBFF 5.

9. Characterization of the Redox Species: Electrochemistry, Spectroelectrochemistry and Theoretical Calculations

A. Electrochemical details. All electrochemical experiments were conducted with traditional 3-electrode geometry using a Biologic SP-50 or EC Frontier ECstat-100 potentiostat. Electrolyte solutions (0.1 M) were prepared from anhydrous, degassed HPLC grade CH_2Cl_2 and anhydrous Bu_4NPF_6 . The working electrode was a glassy carbon electrode (3-mm diameter), with a Pt-coil counter electrode and a Ag wire pseudo reference. The ferrocene/ferrocenium (Fc/Fc^+) couple was used as an internal standard following each experiment. CV experiments were conducted in a three-neck flask that had been purged with nitrogen. Voltammograms were recorded at a sweep rates of 100 mV s^{-1} . $E_{1/2}$ values were calculated assuming $E_{1/2} \approx E_{o'} = (E_{\text{anodic}} + E_{\text{cathodic}})/2$ based on these observations for reversible couples; for irreversible couples the $E_{o'}$ value is estimated as the potential at peak current. Analyte concentrations were ca. 1-5 mM.

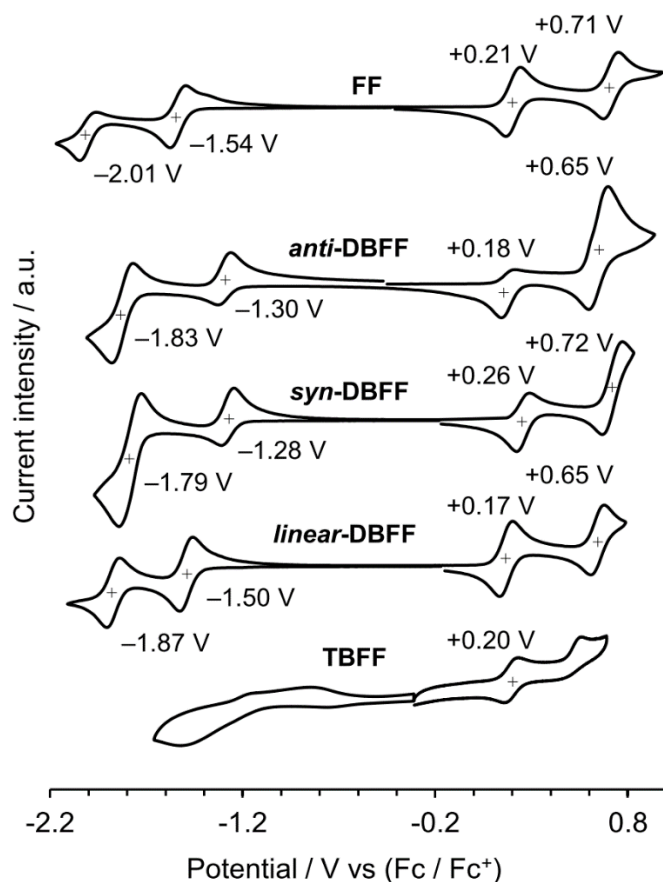


Figure D23. Cyclic voltammograms of FFs **1-5** in CH_2Cl_2 containing 0.1 mol L^{-1} $n\text{-Bu}_4\text{NPF}_6$ as a supporting electrolyte at a scan rate of 100 mV s^{-1} .

Table D5. Redox potentials (V) for compounds **1-5** analyzed by cyclic voltammetry and the corresponding CV and optically-determined energy gaps (eV). ^a The electrochemical gap is defined as the potential difference between the first oxidation and first reduction potential. ^b The optical gap is defined as the energy corresponding to the longest wavelength absorption maximum.

Compound	E^1_{red} (V)	E^2_{red} (V)	E^1_{oxd} (V)	E^2_{oxd} (V)	E^3_{oxd} (V)	CV E_{gap} (eV) ^a	Optical E_{gap} (eV) ^b
1 ³	-1.54	-2.01	0.21	0.71	—	1.75	2.07
2	-1.50	-1.87	0.17	0.65	1.31	1.67	1.97
3	-1.28	-1.79	0.26	0.72	—	1.54	1.80
4	-1.30	-1.83	0.18	0.65	—	1.48	1.78
5	-0.75	—	0.20	—	—	0.95	1.68

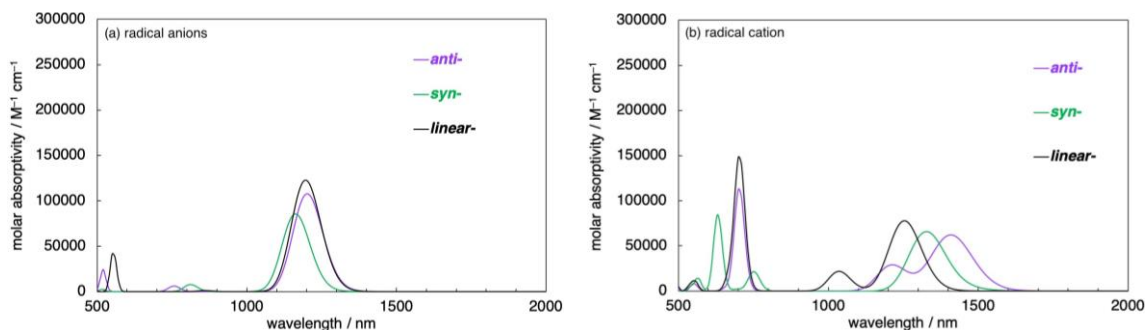


Figure D24. TD-DFT/tuned-LC-URBLYP/6-311G* theoretical electronic absorption spectra of gas-phase (a) radical anions and (b) radical cations of **2'**, **3'**, and **4'**. Half-width at half-height (HWHH) value for the Gaussian line-shape is set to 0.05 eV.

B. NICS-XY scans of the redox species. NICS-XY scans were carried out using the Aroma package described by Stanger and co-workers following established procedures.²⁶

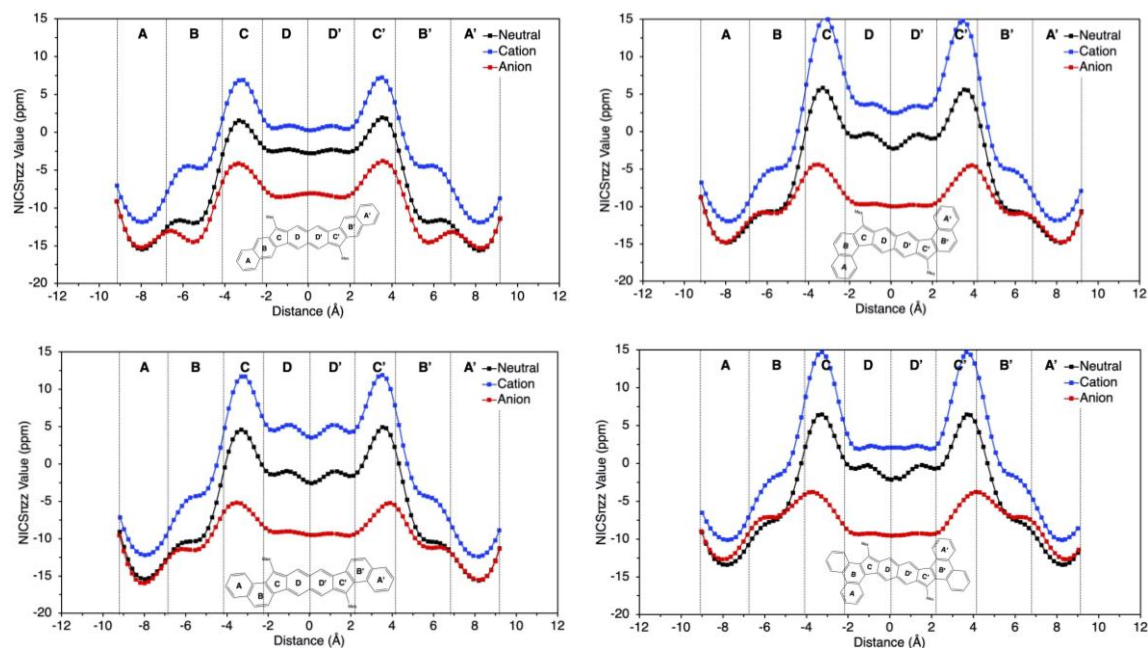


Figure D25. NICS π_{zz} (1.7) scans performed with Gaussian 09 at the tuned-LC-UBLYP/6-311G**//R(U)B3LYP/6-311G** level for cation, anion and neutral **2'** (top left), **3'** (top right), **4'** (bottom left) and **5'** (bottom right).

C. Synthesis and Characterization of *syn*-DBFF radical cation ($3'^+\text{SbCl}_6^-$, Scheme S4). To a solution of *syn*-DBFF **3** (20.0 mg, 27.6 μmol) in CH_2Cl_2 (10 mL) was added “magic blue” (22.6 mg, 27.6 μmol) at room temperature under N_2 atmosphere. The mixture

was stirred at room temperature for 30 min and then concentrated under reduced pressure. The residue was washed with Et₂O and pentane to give **3^{•+}SbCl₆⁻** (20.4 mg, 19.3 μmol, 70%) as a black solid. ¹H NMR (400 MHz, CD₂Cl₂): NMR silent; UV-vis-NIR (CH₂Cl₂): λ_{max}^{abs} (ε) 264 (39200), 326 (19100), 395 (50700), 487 (8000), 584 (8800), 730 (44700), 1275 (8400) nm; HR-ESI-MS (positive): *m/z* calcd for C₅₆H₅₀ 722.3907, found 722.3905 [(M-SbCl₆)⁺]; HR-ESI-MS (negative): *m/z* calcd for SbCl₆ 330.7175, found 330.7174 [(M-C₅₆H₅₀)⁻]; elemental analysis calcd (%) for C₅₆H₅₀Cl₆Sb: C 63.60 H 4.77; found : C 63.53, H 4.72.

Scheme D4. Synthesis of the radical cation of *syn*-DBFF **3**

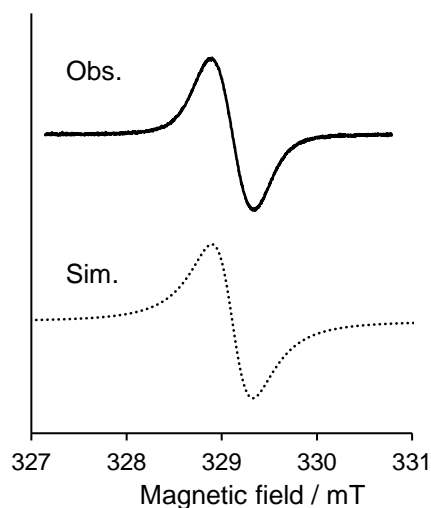
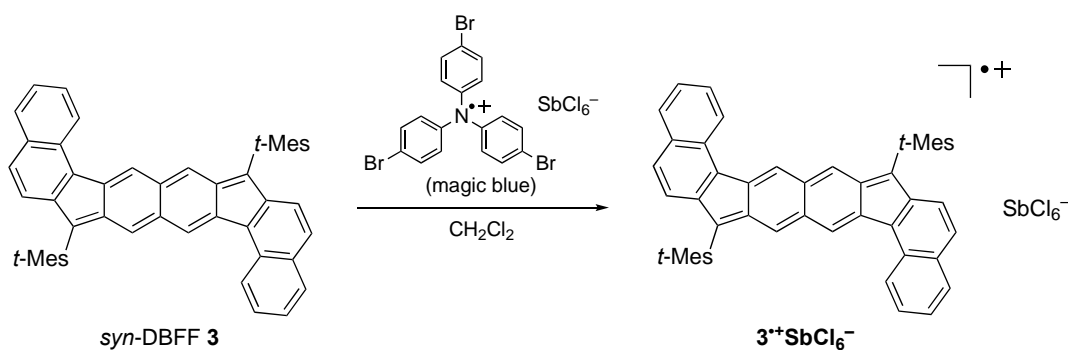


Figure D26. Experimentally observed ESR spectrum of **3^{•+}SbCl₆⁻** in CH₂Cl₂ (*g* = 2.003) and the simulated spectrum.

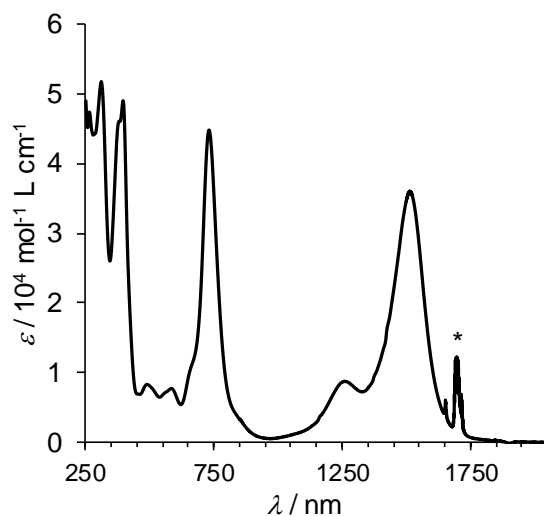


Figure D27. UV-vis-NIR spectrum of $3^{+\bullet}\text{SbCl}_6^-$ in CH_2Cl_2 . *Solvent peaks.

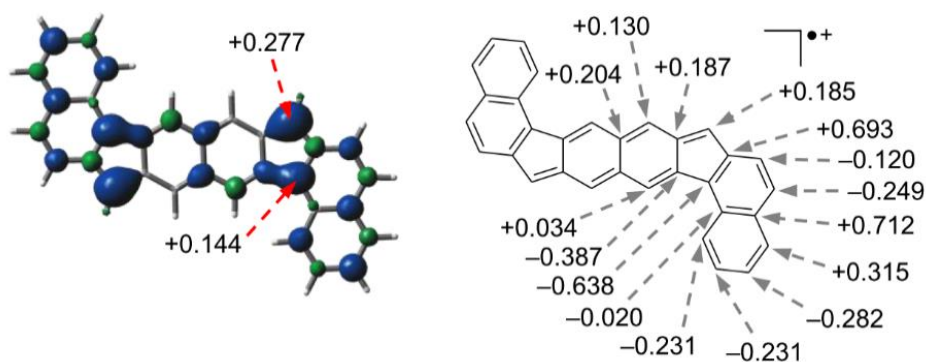


Figure D28. Mulliken spin density map and charge of $3^{+\bullet}$, in which the 4-*tert*-butyl-2,6-dimethylphenyl groups of *syn*-DBFF **3** were replaced with the H groups, calculated at the DFT/UB3LYP/6-31+G(d) level of theory.

D. UV-Vis-NIR Spectroelectrochemical Details. UV-Vis-NIR spectroelectrochemical studies were conducted on a Cary 5000 spectrophotometer. A C3 epsilon potentiostat from BASi was used for the electrolysis using a thin layer cell from a demountable omni cell from Specac. In this cell a three-electrodes system was coupled to conduct in situ spectroelectrochemistry. A Pt gauze was used as the working electrode, a Pt wire was used as the counter electrode, and an Ag wire was used as the pseudo-reference electrode. The spectra were collected a constant potential electrolysis and the potentials were changed in

interval of 15 mV. The electrochemical medium used was 0.1 M TBAPF₆ in freshly distilled CH₂Cl₂ at room temperature with sample concentrations of 10⁻³ M.

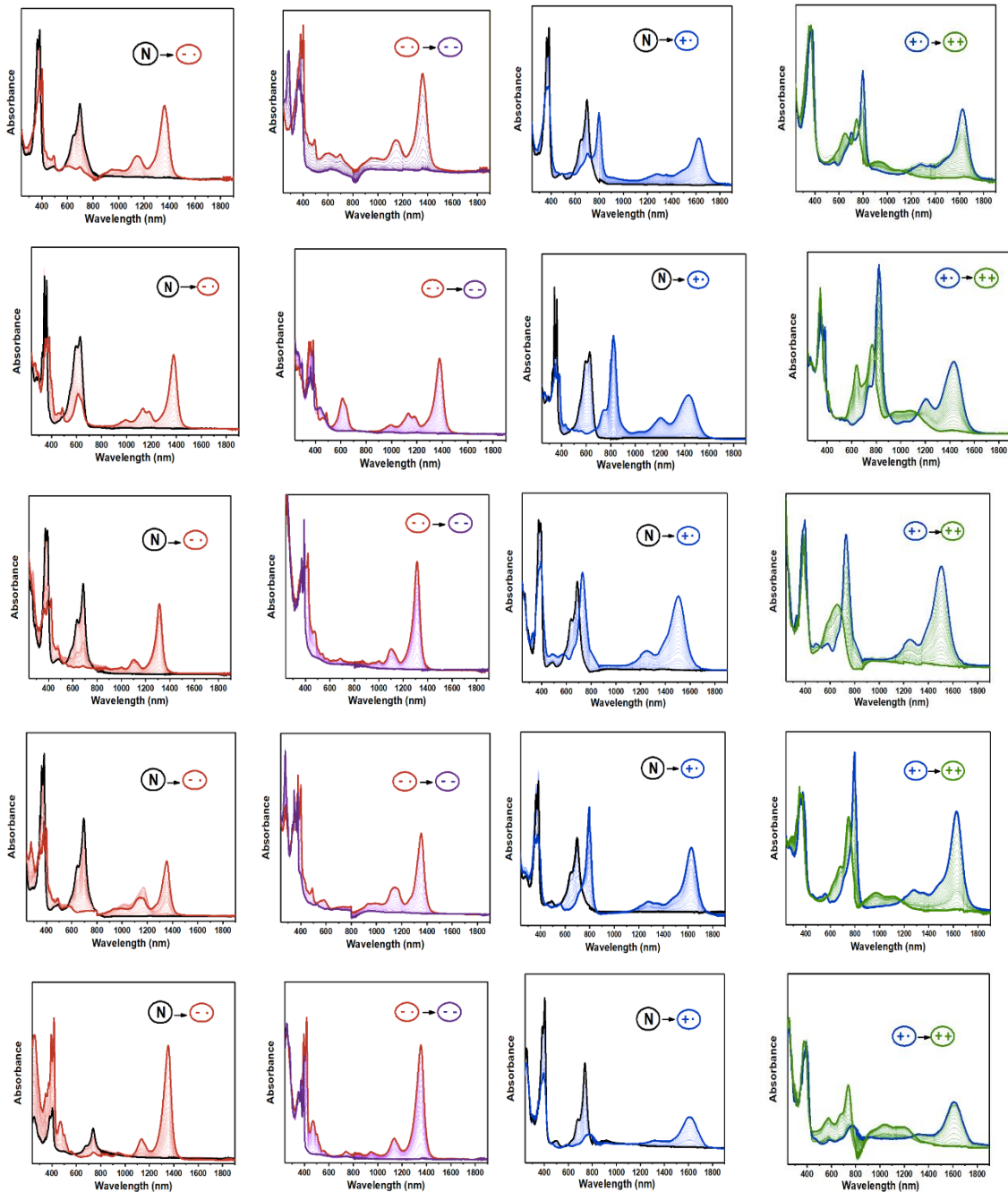


Figure D29. UV-Vis-NIR spectroelectrochemical data of FFs **1**, **2**, **3**, **4** and **5** (from top to bottom) recorded in 0.1 M TBAPF₆/CH₂Cl₂ solution at room temperature. From the left: conversion from the neutral to the radical anion, from the radical anion to the dianion, from the neutral to the radical cation and from the radical cation to the dication.

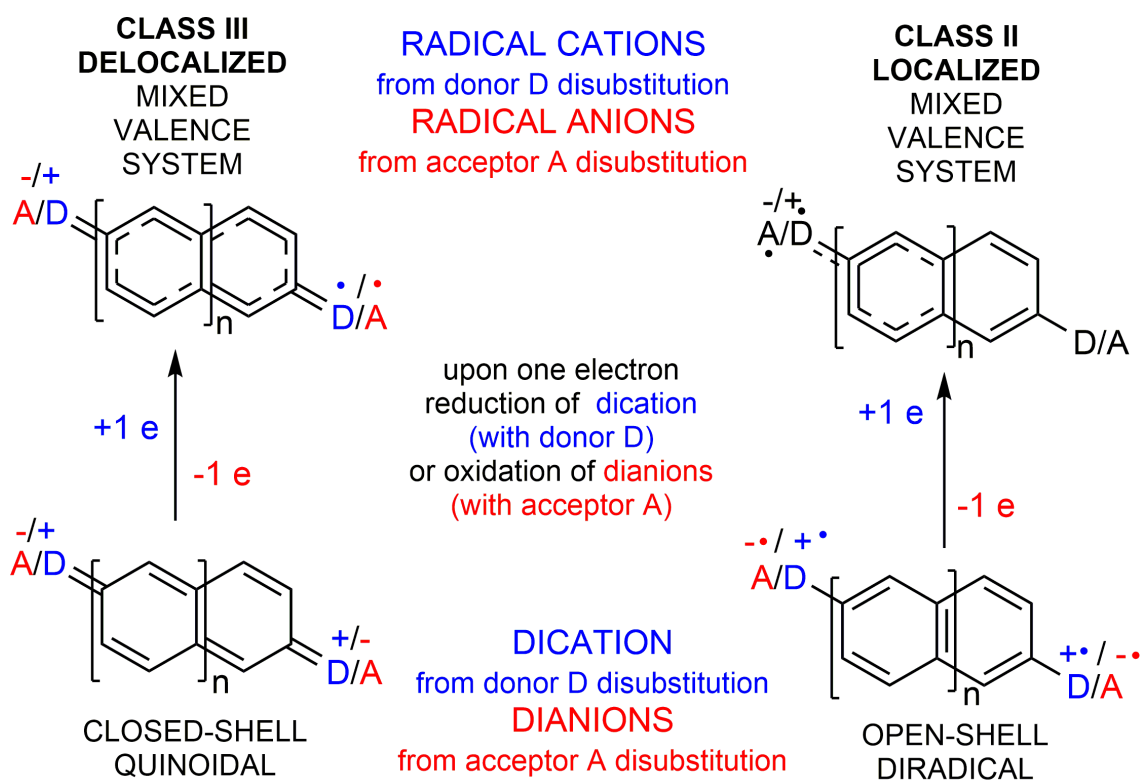


Figure D30. Examples of disubstituted donor dications and acceptor dianions with open-shell diradicaloid and closed-shell species.

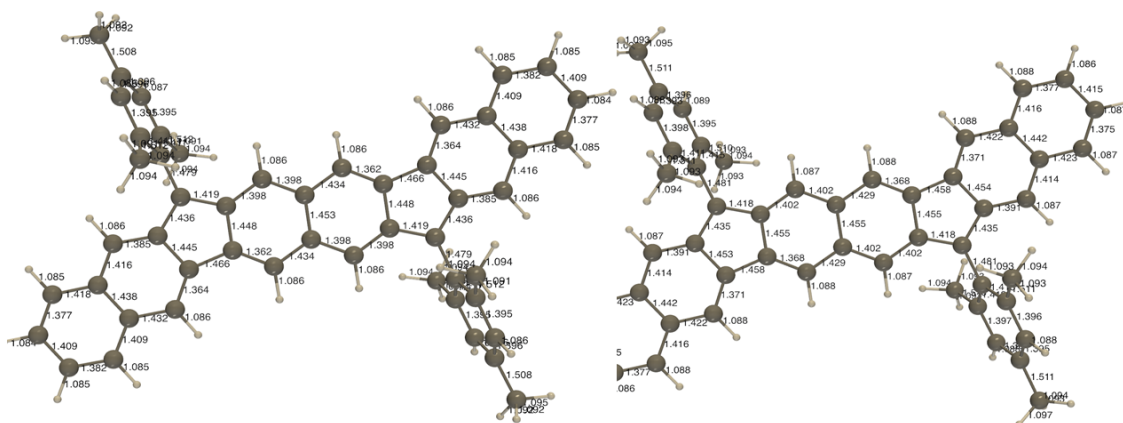


Figure D31. Gas phase DFT/UB3LYP/6-311G* optimized bond lengths (Å) of cationic (left) and anionic (right) species of *linear-DBFF 2*.

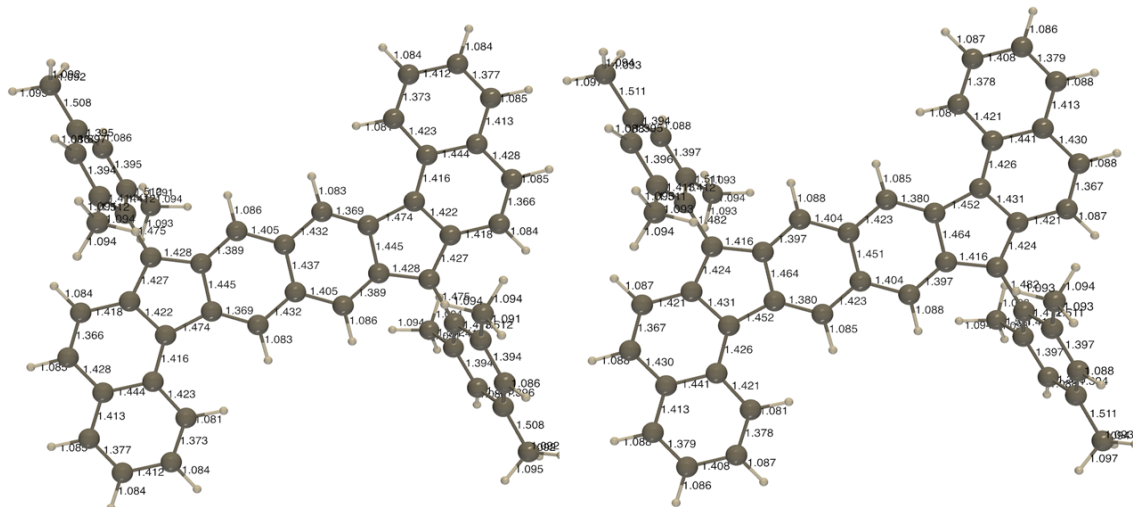


Figure D32. Gas phase DFT/UB3LYP/6-311G* optimized bond lengths (Å) of cationic (left) and anionic (right) species of *syn*-DBFF **3**.

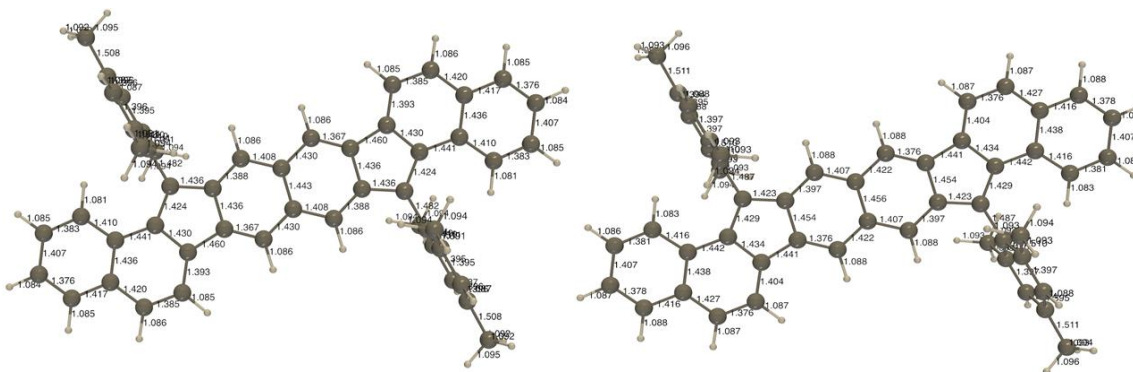


Figure D33. Gas phase DFT/UB3LYP/6-311G* optimized bond lengths (Å) of cationic (left) and anionic (right) species of *anti*-DBFF **4**.

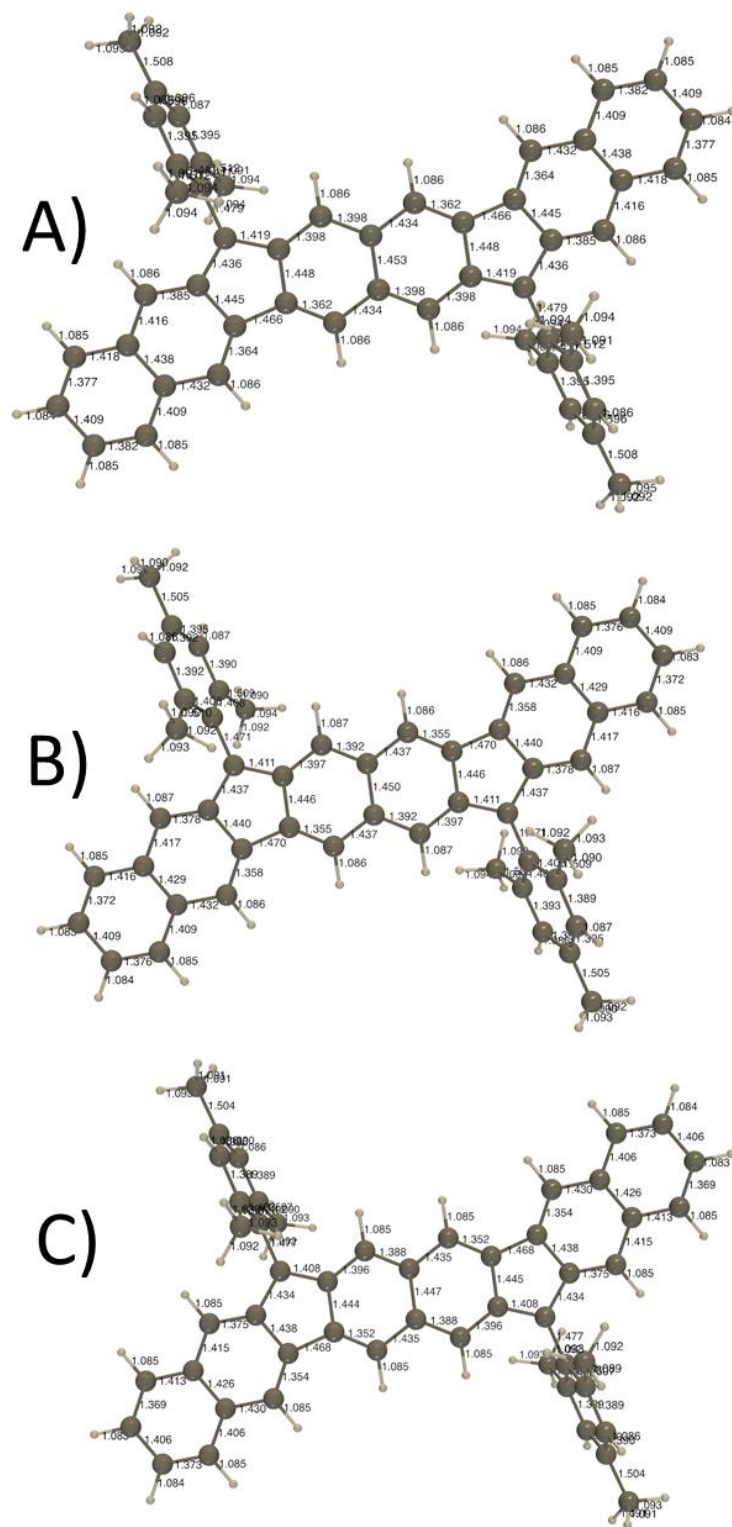


Figure D34. Optimized bond lengths (\AA) of cationic *linear*-DBFF **2** at the (A) UB3LYP/6-311G* (20% of HF exchange), (B) UM06-2X/6-311G* (54% of HF exchange), and (C) UCAM-B3LYP/6-311G* (Range-separating hybrid, 54% of HF exchange at the long-range limit) levels of theory.

10. References

- (1) (a) Shao, Y.; Head-Gordon, M.; Krylov, A. I. *J. Chem. Phys.* **2003**, *118*, 4807–4818.
(b) Wang, F.; Ziegler, T. *J. Chem. Phys.* **2004**, *121*, 12191–12196. (c) Wang, F.; Ziegler, T. *J. Chem. Phys.* **2005**, *122*, 074109. (d) Wang, F.; Ziegler, T. *Int. J. Quantum Chem.* **2006**, *106*, 2545–2550.
- (2) Stein, T.; Eisenberg, H.; Kronik, L.; Baer, R. *Phys. Rev. Lett.* **2010**, *105*, 266802.
- (3) (a) Hayes, E. F.; Siu, A. K. Q. *J. Am. Chem. Soc.* **1971**, *93*, 2090–2091. (b) Yamaguchi, K. *Chem. Phys. Lett.* **1975**, *33*, 330–335.
- (4) Chen, Z.; Wannere, C. S.; Corminboeuf, C.; Puchta, R.; Schleyer, P. v. R. *Chem. Rev.* **2005**, *105*, 3842–3882.
- (5) Geuenich, D.; Hess, K.; Köhler, F.; Herges, R. *Chem. Rev.* **2005**, *105*, 3758–3772.
- (6) Frisch, M. J.; Trucks, G. W.; Schlegel, H. B.; Scuseria, G. E.; Robb, M. A.; Cheeseman, J. R.; Scalmani, G.; Barone, V.; Mennucci, B.; Petersson, G. A.; Nakatsuji, H.; Caricato, M.; Li, X.; Hratchian, H. P.; Izmaylov, A. F.; Bloino, J.; Zheng, G.; Sonnenberg, J. L.; Hada, M.; Ehara, M.; Toyota, K.; Fukuda, R.; Hasegawa, J.; Ishida, M.; Nakajima, T.; Honda, Y.; Kitao, O.; Nakai, H.; Vreven, T.; Montgomery, J. A., Jr.; Peralta, J. E.; Ogliaro, F.; Bearpark, M.; Heyd, J. J.; Brothers, E.; Kudin, K. N.; Staroverov, V. N.; Kobayashi, R.; Normand, J.; Raghavachari, K.; Rendell, A.; Burant, J. C.; Iyengar, S. S.; Tomasi, J.; Cossi, M.; Rega, N.; Millam, J. M.; Klene, M.; Knox, J. E.; Cross, J. B.; Bakken, V.; Adamo, C.; Jaramillo, J.; Gomperts, R.; Stratmann, R. E.; Yazyev, O.; Austin, A. J.; Cammi, R.; Pomelli, C.; Ochterski, J. W.; Martin, R. L.; Morokuma, K.; Zakrzewski, V. G.; Voth, G. A.; Salvador, P.; Dannenberg, J. J.; Dapprich, S.; Daniels, A. D.; Farkas, Ö.;

Foresman, J. B.; Ortiz, J. V.; Cioslowski, J.; Fox, D. J. *Gaussian 09*; Revision D.01; Gaussian, Inc.: Wallingford CT, 2009.

(7) Schmidt, M. W.; Baldridge, K. K.; Boatz, J. A.; Elbert, S. T.; Gordon, M. S.; Jensen, J. H.; Koseki, S.; Matsunaga, N.; Nguyen, K. A.; Su, S.; Windus, T. L.; Dupuis, M.; Montgomery, J. A. *J. Comput. Chem.* **1993**, *14*, 1347.

(8) Shao, Y.; Gan, Z.; Epifanovsky, E.; Gilbert, A. T. B.; Wormit, M.; Kussmann, J.; Lange, A. W.; Behn, A.; Deng, J.; Feng, X.; Ghosh, D.; Goldey, M.; Horn, P. R.; Jacobson, L. D.; Kaliman, I.; Khaliullin, R. Z.; Kuś, T.; Landau, A.; Liu, J.; Proynov, E. I.; Rhee, Y. M.; Richard, R. M.; Rohrdanz, M. A.; Steele, R. P.; Sundstrom, E. J.; Woodcock, H. L.; Zimmerman, P. M.; Zuev, D.; Albrecht, B.; Alguire, E.; Austin, B.; Beran, G. J. O.; Bernard, Y. A.; Berquist, E.; Brandhorst, K.; Bravaya, K. B.; Brown, S. T.; Casanova, D.; Chang, C.-M.; Chen, Y.; Chien, S. H.; Closser, K. D.; Crittenden, D. L.; Diedenhofen, M.; DiStasio, R. A.; Do, H.; Dutoi, A. D.; Edgar, R. G.; Fatehi, S.; Fusti-Molnar, L.; Ghysels, A.; Golubeva-Zadorozhnaya, A.; Gomes, J.; Hanson-Heine, M. W. D.; Harbach, P.H.P.; Hauser, A. W. ; Hohenstein, E. G.; Holden, Z. C.; Jagau, T.-C.; Ji, H.; Kaduk, B.n; Khistyayev, K.; Kim, J.; Kim, J.; King, R. A.; Klunzinger, P.; Kosenkov, D.; Kowalczyk, T.; Krauter, C. M.; Lao, K. U.; Laurent, A. D.; Lawler, K. V.; Levchenko, S. V.; Lin, C. Y.; Liu, F.; Livshits, E.; Lochan, R. C.; Luenser, A.; Manohar, P.; Manzer, S. F.; Mao, S.-P.; Mardirossian, N.; Marenich, A. V.; Maurer, S. A.; Mayhall, N. J.; Neuscammann, E.; Oana, C. M.; Olivares-Amaya, R.; O'Neill, D. P.; Parkhill, J. A.; Perrine, T. M.; Peverati, R.; Prociuk, A.; Rehn, D. R.; Rosta, E.; Russ, N. J.; Sharada, S. M.; Sharma, S.; Small, D. W.; Sodt, A.; Stein, T.; Stück, D.; Su, Y.-C.; Thom, A. J. W.; Tsuchimochi, T.; Vanovschi, V.; Vogt, L.; Vydrov, O.; Wang, T.; Watson, M. A.; Wenzel, J.; White, A.; Williams, C.

F.; Yang, J.; Yeganeh, S.; Yost, S. R.; You, Z.-Q.; Zhang, I. Y.; Zhang, X.; Zhao, Y.; Brooks, B. R.; Chan, G. K. L.; Chipman, D. M.; Cramer, C. J.; Goddard, W. A.; Gordon, M. S.; Hehre, W. J.; Klamt, A.; Schaefer, H. F.; Schmidt, M. W.; Sherrill, C. D.; Truhlar, D. G.; Warshel, A.; Xu, X.; Aspuru-Guzik, A.; Baer, R.; Bell, A. T.; Besley, N. A.; Chai, J.-D.; Dreuw, A.; Dunietz, B. D.; Furlani, T. R.; Gwaltney, S. R.; Hsu, C.-P.; Jung, Y.; Kong, J.; Lambrecht, D. S.; Liang, W.; Ochsenfeld, C.; Rassolov, V. A.; Slipchenko, L. V.; Subotnik, J. E.; Voorhis, T. V.; Herbert, J. M.; Krylov, A. I.; Gill, P. M. W.; Head-Gordon, M. *Mol. Phys.* **2015**, *113*, 184.

(9) Liegeois, V. DrawMol ver. 1.5, UNamur, www.unamur.be/drawmol.

(10) Dressler, J. J.; Teraoka, M.; Espejo, G.; Kishi, R.; Takamuku, S.; Gómez-García, C. J.; Zakharov, L. N.; Nakano, M.; Casado, J.; Haley, M. M. Thiophene and its sulfur inhibit indenoindenodibenzothiophene diradicals from low-energy lying thermal triplets. *Nat. Chem.* **2018**, 1134-1140.

(11) Bentley, K. W.; Nam, Y. G.; Murphy, J. M.; Wolf, C. *J. Am. Chem. Soc.* **2013**, *135*, 18052–18055.

(12) (a) Mitsui, C.; Soeda, J.; Miwa, K.; Shoyama, K.; Ota, Y.; Tsuji, H.; Takeya, J.; Nakamura, E. *Bull. Chem. Soc. J.* **2015**, *88*, 776–783. (b) Hu, P.; Lee, S.; Park, K. H.; Das, S.; Heng, T. S.; Gonçalves, T. P.; Huang, K.-W.; Ding, J.; Kim, D.; Wu, J. *J. Org. Chem.* **2016**, *81*, 2911–2919.

(13) Wu, Z.; Li, A.; Fan, B.; Xue, F.; Adachi, C.; Ouyang, J. *Sol. Energy Mater. Sol. Cells* **2011**, *95*, 2516–2523.

(14) Barker, J. E.; Frederickson, C. K.; Jones, M. H.; Zakharov, L. N.; Haley, M. M. *Org. Lett.* **2017**, *19*, 5312–5315.

- (15) Knall, A.-C.; Ashraf, R. S.; Nikolka, M.; Nielsen, C. B.; Purushothaman, B.; Sadhanala, A.; Hurhangee, M.; Broch, K.; Harkin, D. J.; Novák, J.; Neophytou, M.; Hayoz, P.; Siringhaus, H.; McCulloch, I. *Adv. Funct. Mater.* **2016**, *26*, 6961–6969.
- (16) CrysAlisPro; Rigaku OD, The Woodlands, TX, 2015.
- (17) CrystalClear; Rigaku Co. Ltd., 2015.
- (18) Sheldrick, G. M. *Acta Crystallogr., Sect. A* **2015**, *71*, 3–8.
- (19) Sheldrick, G.M. *Acta Crystallogr., Sect. A* **2008**, *64*, 112–122.
- (20) Müller, P. *Crystallogr. Rev.* **2009**, *15*, 57–83.
- (21) van der Sluis, P.; Spek, A. L. *Acta Crystallogr., Sect. A* **1990**, *46*, 194–201.
- (22) Dolomanov, O. V.; Bourhis, L. J.; Gildea, R. J.; Howard, J. A. K.; Puschmann, H. *J. Appl. Cryst.* **2009**, *42*, 339–341.
- (23) Squeeze-Platon; Spek, A. L. PLATON, A Multipurpose Crystallographic Tool, Utrecht, The Netherlands, 2005
- (24) Bain, G. A.; Berry, J. F. *J. Chem. Educ.* **2008**, *85*, 532–536.
- (25) Bleaney, B.; Bowers, K. D. *Proc. R. Soc. Lond. A* **1952**, *214*, 451–465.
- (26) (a) Gershoni-Poranne, R.; Stanger, A. *Chem.–Eur. J.* **2014**, *20*, 5673–5688. (b) Stanger, A. *J. Org. Chem.* **2006**, *71*, 883–893. (c) Stanger, A. *J. Org. Chem.* **2010**, *75*, 2281–2288.

APPENDIX E

SUPPLEMENTARY INFORMATION FOR CHAPTER VI

Appendix E is the supplementary information for Chapter VI of this dissertation. It includes experimental details, other experimental data, spectra, and computational details relevant to the content in Chapter VI.

1. Experimental Details

General. All air-sensitive manipulations were carried out under an inert atmosphere using standard Schlenk technique. For moisture sensitive reactions, THF and toluene were refluxed with Na benzophenone ketyl for 24 h prior to distillation and use. Silica gel (240-300 mesh) was used for column chromatography. All other reagents were purchased and used as received. NMR spectra were recorded on a Bruker Avance III HD 500 equipped with a Prodigy multinuclear cryoprobe (^1H : 500 MHz, ^{13}C : 126 MHz) or Bruker Avance III HD 600 equipped with a Prodigy multinuclear cryoprobe (^1H : 600 MHz, ^{13}C : 151 MHz) NMR spectrometer at room temperature (unless otherwise noted). ^1H and ^{13}C NMR chemical shifts (δ) are expressed in ppm relative to the residual non-deuterated solvent reference (CDCl_3 : ^1H 7.26 ppm, ^{13}C 77.16 ppm; CD_2Cl_2 : ^1H 5.32 ppm, ^{13}C 53.84 ppm). UV-Vis spectra were recorded on an Agilent Technologies Cary 60 UV-Vis spectrometer in HPLC grade CH_2Cl_2 . HRMS were recorded on a Waters XEVOG2-XS TOF mass spectrometer. Bistriflate **11** was prepared as previously described.^[1]

General Procedure for Suzuki Cross-Coupling for Diesters 14-17. A two-neck round-bottom flask fitted with a condenser was charged with either diethyl 2,5-dibromoterephthalate (**10**) or bistriflate **11** (1.0 equiv.), benzofuran-3-boronic acid or

benzofuran-2-boronic acid (2.5-4.0 equiv.), K_3PO_4 (4 equiv.), $Pd(OAc)_2$ (0.04 equiv.), and SPhos (0.08 equiv.). These solids were then placed under N_2 atmosphere and dissolved in a 20:1 solution of toluene and water (0.09 M) that had been degassed by sparging with N_2 . After refluxing overnight and cooling to room temperature, the reaction was quenched with H_2O and extracted with CH_2Cl_2 (3×20 mL). The organics were washed with brine (1×30 mL), dried ($MgSO_4$), filtered, and concentrated under vacuum. The residue was triturated with hexanes and filtered to yield diesters **14-17**.

Diester 14. Diester **10** (500 mg, 1.32 mmol, 1.0 equiv.), benzofuran-3-boronic acid (470 mg, 2.90 mmol, 2.2 equiv.), K_3PO_4 (700 mg, 2.30 mmol, 2.5 equiv.), $Pd(OAc)_2$ (12.0 mg, 0.053 mmol, 0.04 equiv.), SPhos (44.0 mg, 0.106 mmol, 0.08 equiv.) gave diester **14** (561 mg, 94%) as a light yellow solid. 1H NMR (500 MHz, CD_2Cl_2) δ 8.05 (s, 2H), 7.81 (s, 2H), 7.58 (d, $J = 8.3$ Hz, 2H), 7.46 (d, $J = 7.7$ Hz, 2H), 7.37 (t, $J = 8.3$ Hz, 2H), 7.29 (t, $J = 7.9$ Hz, 2H), 4.07 (q, $J = 7.1$ Hz, 4H), 0.93 (t, $J = 7.1$ Hz, 6H); ^{13}C NMR (151 MHz, CD_2Cl_2) δ (ppm) 167.49, 155.58, 142.90, 135.08, 133.59, 131.50, 128.23, 125.21, 123.62, 121.31, 120.42, 112.18, 62.16, 13.89; HRMS (ASAP) (m/z), calculated for $C_{28}H_{23}O_6$ ($M+H$)⁺ 455.1495, found 455.1468.

Diester 15. Diester **10** (500 mg, 1.32 mmol, 1.0 equiv.), benzofuran-2-boronic acid (1.06 g, 6.58 mmol, 5 equiv.), K_3PO_4 (1.397 g, 6.58 mmol, 5 equiv.), $Pd(OAc)_2$ (12.0 mg, 0.053 mmol, 0.04 equiv.), SPhos (44.0 mg, 0.106 mmol, 0.08 equiv.) gave diester **15** (518 mg, 86%) as a light yellow solid. 1H NMR (500 MHz, $CDCl_3$) δ 8.11 (s, 2H), 7.63 (d, $J = 7.6$ Hz, 2H), 7.50 (d, $J = 8.2$ Hz, 2H), 7.33 (t, $J = 8.3$ Hz, 2H), 7.27 (t, $J = 7.0$ Hz, 4H), 7.08 (d, $J = 1.9$ Hz, 2H), 4.37 (q, $J = 7.1$ Hz, 4H), 1.22 (t, $J = 7.1$ Hz, 6H); ^{13}C NMR (126 MHz, CD_2Cl_2) δ 168.26, 155.74, 153.68, 133.75, 130.09, 129.65, 129.31, 125.71, 123.80,

122.03, 111.70, 106.26, 62.58, 14.42; HRMS (ASAP) (m/z), calculated for $C_{28}H_{22}O_6$ (M)⁺ 454.1396, found 454.1416.

Diester 16 (*syn-IIDBF*). Bistriflate **11** (350 mg, 0.647 mmol, 1.0 equiv.), benzofuran-3-boronic acid (230 mg, 1.42 mmol, 2.2 equiv.), K_3PO_4 (343 mg, 1.62 mmol, 2.5 equiv.), $Pd(OAc)_2$ (6.0 mg, 0.0259 mmol, 0.04 equiv.), SPhos (21.0 mg, 0.0518 mmol, 0.08 equiv.) gave diester **16** (270 mg, 88%) as a light yellow solid. 1H NMR (500 MHz, $CDCl_3$) δ 8.50 (s, 2H), 8.09 (s, 2H), 7.82 (s, 2H), 7.59 (d, $J = 8.3$ Hz, 2H), 7.46 (d, $J = 7.7$ Hz, 2H), 7.36 (t, $J = 7.2$ Hz, 2H), 7.28 (t, $J = 7.7$ Hz, 2H), 3.65 (s, 6H); ^{13}C NMR (126 MHz, $CDCl_3$) δ 168.29, 155.20, 142.16, 133.15, 131.89, 131.21, 131.02, 129.13, 127.96, 124.75, 123.20, 121.51, 119.87, 111.96, 52.57; HRMS (ASAP) (m/z), calculated for $C_{30}H_{20}O_6$ (M)⁺ 476.1260, found 476.1261.

Diester 17 (*anti-IIDBF*). Bistriflate **11** (750 mg, 1.39 mmol, 1.0 equiv.), benzofuran-2-boronic acid (1.123 g, 6.94 mmol, 5.0 equiv.), K_3PO_4 (1.473 g, 6.94 mmol, 5.0 equiv.), $Pd(OAc)_2$ (12.0 mg, 0.0556 mmol, 0.04 equiv.), SPhos (46.0 mg, 0.111 mmol, 0.08 equiv.) gave diester **17** (521 mg, 79%) as a light yellow solid. 1H NMR (500 MHz, $CDCl_3$) δ 8.32 (s, 2H), 8.31 (s, 2H), 7.65 (d, $J = 7.6$ Hz, 2H), 7.53 (d, $J = 8.1$ Hz, 2H), 7.34 (t, $J = 7.1$ Hz, 2H), 7.28 (t, $J = 7.2$ Hz, 2H), 7.05 (s, 2H), 3.90 (s, 6H); ^{13}C NMR (126 MHz, $CDCl_3$) δ 168.89, 155.42, 154.28, 132.82, 130.99, 130.49, 129.14, 129.04, 128.02, 125.01, 123.28, 121.15, 111.30, 105.18, 52.94; HRMS (ASAP) (m/z), calculated for $C_{30}H_{20}O_6$ (M)⁺ 476.1260, found 476.1263.

General Procedure for Diones 18-21. A round-bottom flask fitted with a condenser was charged with a diester (1 equiv.), KOH (10 equiv.), and a 4:1 solution of EtOH and H_2O (0.10 M). After refluxing the mixture overnight, the reaction was cooled and the EtOH

evaporated. Concentrated HCl was slowly added to the aqueous solution and a precipitate formed, which was isolated and washed with H₂O to yield the diacid intermediate as a yellow solid that was carried on without further purification.

To a suspension of the diacid (1 equiv.) in CH₂Cl₂ (0.05 M) was added DMF (2 equiv.) followed by oxalyl chloride (4 equiv.). After 12 h, the volatiles were removed under reduced pressure. The crude acid chloride was dissolved in CH₂Cl₂ (40 mL) and solid AlCl₃ (5 equiv.) was added to the flask. The reaction was stirred overnight and then poured into an HCl-ice mixture, precipitating the dione. The solid was filtered and washed successively with H₂O, acetone, and CH₂Cl₂ to afford dione **5** as colorful solid that was too insoluble to obtain NMR spectra.

syn-IDBF dione 18. Diester **14** (495 mg, 1.09 mmol, 1 equiv.) and KOH (566 mg, 10.09 mmol, 10 equiv.) afforded the crude diacid (433 mg, 96%). The *syn*-IDBF diacid (433 mg, 1.05 mmol, 1 equiv.) was reacted with (COCl)₂ (533 mg, 0.358 ml, 4.20 mmol, 4 equiv.), DMF (153 mg, 0.162 ml, 2.10 mmol, 2 equiv.), and AlCl₃ (700 mg, 5.25 mmol, 5 equiv.) to furnish dione **18** (97 mg, 24%) as a green powder. HRMS (ASAP) (*m/z*), calculated for C₂₄H₁₀O₄ (M)⁺ 362.0579, found 362.0583.

anti-IDBF dione 19. Diester **15** (518 mg, 1.14 mmol, 1 equiv.) and KOH (640 mg, 11.4 mmol, 10 equiv.) afforded the crude diacid (400 mg, 88%). The *anti*-IDBF diacid (360 mg, 0.904 mmol, 1 equiv.) was reacted with (COCl)₂ (458 mg, 0.308 ml, 3.61 mmol, 4 equiv.), DMF (132 mg, 0.139 ml, 1.81 mmol, 2 equiv.), and AlCl₃ (603 mg, 4.52 mmol, 5 equiv.) to furnish dione **19** (253 mg, 78%) as a dark blue powder. HRMS (ASAP) (*m/z*), calculated for C₂₄H₁₀O₄ (M)⁺ 362.0579, found 362.0580.

syn-IIDBF dione 20. Diester **16** (440 mg, 0.925 mmol, 1 equiv.) and KOH (519 mg,

9.25 mmol, 10 equiv.) afforded the crude diacid (410 mg, 99%). The *syn*-IIDBF diacid (410 mg, 0.914 mmol, 1 equiv.) was reacted with (COCl)₂ (465 mg, 0.312 ml, 3.66 mmol, 4 equiv.), DMF (134 mg, 0.141 ml, 1.83 mmol, 2 equiv.), and AlCl₃ (610 mg, 4.57 mmol, 5 equiv.) to furnish dione **20** (293 mg, 78%) as an olive-brown powder. HRMS (ASAP) (*m/z*), calculated for C₂₈H₁₂O₄ (M)⁺ 412.0736, found 412.0740.

***anti*-IIDBF dione 21.** Diester **17** (521 mg, 1.09 mmol, 1 equiv.) and KOH (611 mg, 9.25 mmol, 10 equiv.) afforded the crude diacid (484 mg, 99%). The *anti*-IIDBF diacid (484 mg, 1.08 mmol, 1 equiv.) was reacted with (COCl)₂ (548 mg, 0.368 ml, 4.32 mmol, 4 equiv.), DMF (158 mg, 0.167 ml, 2.16 mmol, 2 equiv.), and AlCl₃ (720 mg, 5.40 mmol, 5 equiv.) to furnish dione **21** (353 mg, 79%) as a bright red powder. HRMS (ASAP) (*m/z*), calculated for C₂₈H₁₂O₄ (M)⁺ 412.0736, found 412.0741.

General Synthesis for IDBFs 6-7 and IIDBFs 8-9. In an oven-dried round bottom flask, a suspension of dione (1 equiv.) in dry THF was cooled to -78 °C under a N₂ atmosphere. In a separate oven-dried round bottom flask, 2-bromomesitylene or 2-bromo-5-*tert*-butyl-1,3-dimethylbenzene (8 equiv.) was dissolved in dry THF (0.25 M), cooled to -78 °C under a N₂ atmosphere, and *n*-BuLi (7.5 equiv.) was added dropwise. After stirring the mixture at -78 °C for 1 h, the aryl lithiate was transferred via cannula to the flask containing the dione suspended in THF (0.05 M). This reaction mixture was stirred for 4 h at -78 °C, then slowly warmed to room temperature overnight with stirring. The reaction was then quenched with a saturated aq. NH₄Cl solution and extracted with CH₂Cl₂ (3×). The combined organic layer was washed with brine, dried (MgSO₄) and concentrated in vacuo. The resulting crude residue was passed through a silica plug eluting with hexanes, followed by a CH₂Cl₂ wash, to provide the desired diol that was carried onto the reductive

dearomatization step without further purification.

In a single-neck round-bottom flask the crude diol (1 equiv.) and anhydrous SnCl₂ (4 equiv.) were dissolved in dry degassed toluene (0.005 M). The reaction solution was then heated to 80 °C for 3-4 h. After cooling, the reaction mixture was filtered through a plug of silica and the solvent was evaporated. The resulting solid was redissolved in minimal CHCl₃ and MeCN was layered over the solution to furnish the IDBF/IIDBF.

***syn*-IDBF (6).** Dione **18** (90 mg, 0.239 mmol, 1.0 equiv.), MesBr (380 mg, 0.292 mL, 1.91 mmol, 8.0 equiv.), *n*-BuLi (0.716 mL, 2.5 M, 7.5 equiv.) yielded the crude diol (134 mg, 91 %) as a light brown solid. Diol (134 mg, 0.223 mmol, 1.0 equiv.) and SnCl₂ (165 mg, 0.868 mmol, 4.0 equiv.) furnished **6** (53 mg, 38% from the dione) as a deep blue solid. ¹H NMR (500 MHz, CD₂Cl₂) δ 7.09 (d, *J* = 7.7 Hz, 2H), 7.06 (d, *J* = 7.7 Hz, 2H), 7.03-6.96 (m, 4H), 6.96 (s, 4H), 5.60 (s, 2H), 2.42 (s, 12H), 2.32 (s, 6H); ¹³C NMR (126 MHz, CD₂Cl₂) δ 166.86, 162.54, 140.24, 139.02, 137.60, 137.32, 131.19, 129.01, 128.67, 127.87, 127.35, 125.53, 124.39, 124.21, 120.44, 112.83, 21.42, 20.95; UV-Vis (CHCl₃): λ_{max}^{abs} (ε) 313 nm (14,410), 642 nm (12,780); HRMS (ASAP) (*m/z*), calculated for C₄₂H₃₂O₂ (M)⁺ 568.2402, found 568.2436.

***anti*-IDBF (7)/bis(enone) 22.** Dione **19** (300 mg, 0.828 mmol, 1.0 equiv.), MesBr (1.318 g, 6.62 mmol, 8 equiv.), *n*-BuLi (3.93 mL, 1.6 M, 7.6 equiv.) yielded the crude diol (397 mg, 79 %) as a light brown solid. Diol (200 mg, 0.271 mmol, 1.0 equiv.) and SnCl₂ (206 mg, 1.11 mmol, 4.0 equiv.) furnished **7** as a crude material that quickly ring-opened/hydrolyzed to give **22** (210 mg, 42% from the dione) as a red solid. Compound **7**: ¹H NMR (500 MHz, CD₂Cl₂) δ 7.11 (d, *J* = 8.1 Hz, 2H), 7.01 (t, *J* = 7.3 Hz, 2H), 6.96 (s, 4H), 6.93 (t, *J* = 7.3 Hz, 2H), 6.72 (d, *J* = 7.0 Hz, 2H), 6.14 (s, 2H), 2.35 (s, 12H), 2.33 (s,

6H); a ^{13}C spectrum was obtained but the compound was too crude to assign peaks to **7** vs. impurities; HRMS (ASAP⁺) (m/z), calculated for $\text{C}_{42}\text{H}_{33}\text{O}_2$ ($\text{M}+\text{H}$)⁺ 569.2481, found 569.2491. Compound **22**: ^1H NMR (500 MHz, CD_2Cl_2) δ 7.23 (s, 2H), 7.15 (t, $J = 8.3$ Hz, 2H), 6.97 (s, 4H), 6.89 (d, $J = 8.2$ Hz, 2H), 6.87 (s, 2H), 6.81 (d, $J = 7.8$ Hz, 2H), 6.66 (t, $J = 7.5$ Hz, 2H), 2.33 (s, 6H), 2.12 (s, 12H); ^{13}C NMR (126 MHz, CD_2Cl_2) δ 199.42, 159.34, 154.37, 148.90, 139.61, 135.80, 135.53, 133.64, 131.17, 130.72, 129.51, 128.90, 121.02, 119.37, 119.03, 116.59, 21.46, 20.40; HRMS (ASAP⁺) (m/z), calculated for $\text{C}_{42}\text{H}_{35}\text{O}_4$ ($\text{M}+\text{H}$)⁺ 603.2535, found 603.2536.

syn-IIDBF (8). Dione **20** (306 mg, 0.142 mmol, 1.0 equiv.), 2-bromo-5-*tert*-butyl-1,3-dimethylbenzene (1.42 g, 5.90 mmol, 8 equiv.), *n*-BuLi (2.23 mL, 2.5 M, 7.5 equiv.) yielded the crude diol (261 mg, 47 %) as a light brown solid. Diol (261 mg, 0.340 mmol, 1.0 equiv.) and SnCl_2 (262 mg, 1.42 mmol, 4.0 equiv.) furnished **8** (114 mg, 23% from the dione) as a teal solid. ^1H NMR (500 MHz, CD_2Cl_2) δ 7.47 (d, $J = 6.6$ Hz, 2H), 7.21–7.13 (m, 6H), 7.19 (s, 4H), 6.95 (s, 2H), 6.54 (s, 2H), 2.33 (s, 12H), 1.37 (s, 18H); ^{13}C NMR (151 MHz, CD_2Cl_2) δ 166.15, 163.62, 151.89, 139.16, 137.51, 133.63, 131.42, 129.89, 128.84, 128.16, 128.04, 127.36, 126.99, 125.33, 124.60, 124.44, 121.37, 112.73, 34.92, 31.62, 21.28; UV-Vis (CHCl_3): $\lambda_{\text{max}}^{\text{abs}}$ (ϵ) 365 nm (80,400), 753 nm (103,800); HRMS (ES^+) (m/z), calculated for $\text{C}_{52}\text{H}_{46}\text{O}_2$ (M)⁺ 702.3498, found 702.3521.

anti-IIDBF (9)/bis(enone) 23. Dione **21** (253 mg, 0.613 mmol, 1.0 equiv.), 2-bromo-5-*tert*-butyl-1,3-dimethylbenzene (1.478 g, 6.13 mmol, 10.0 equiv.), *n*-BuLi (3.63 mL, 1.6 M, 5.80 mmol, 9.5 equiv.) yielded the crude diol (210 mg, 46 %) as a light brown solid. Diol (210 mg, 0.285 mmol, 1.0 equiv.) and SnCl_2 (210 mg, 1.14 mmol, 4.0 equiv.) did not furnish **9** but rather the ring-opened/hydrolyzed product **23** (110 mg, 24% from the dione)

as a deep red solid. ^1H NMR (500 MHz, CDCl_3) δ 8.27 (s, 2H), 7.84 (s, 2H), 7.16 (t, $J = 8.5$ Hz, 2H), 7.14 (s, 4H), 7.04 (s, 2H), 6.98 (d, $J = 7.3$ Hz, 2H), 6.74 (dd, $J = 7.9, 1.5$ Hz, 2H), 6.59 (t, $J = 8.0$ Hz, 2H), 2.14 (s, 12H), 1.36 (s, 18H); ^{13}C NMR (151 MHz, CD_2Cl_2) δ 199.12, 161.48, 154.73, 152.64, 142.67, 138.57, 137.79, 135.44, 132.17, 131.26, 130.63, 129.29, 125.74, 125.26, 123.87, 120.84, 119.77, 119.46, 34.97, 31.58, 20.70; HRMS (ASAP⁺) (m/z), calculated for $\text{C}_{52}\text{H}_{49}\text{O}_4$ ($\text{M}+\text{H}$)⁺ 737.3631, found 737.3611.

Additional Attempts to Synthesize *anti*-IDBF 7. According to the general procedure described above for synthesis of the IDBFs samples of the diol addition product of dione **19** and mesityllithium was subjected to a reductive dearomatization in dry, degassed toluene. Table S1 shows the results of each of these attempts along with additives used.

Table S1. Attempts to synthesize **7** using different additives.

Additive	% Yield of 7	% Yield of 22
5 drops of trifluoroacetic acid	trace	61
K_2CO_3	0	XX
3 Å molecular sieves	0	Observed as the only product, not isolated
No additive	trace	42

Variable Temperature NMR Studies. Approximately 5 mg of *syn*-IIDBF (**8**) was placed in an NMR tube and dissolved in 1,1,2,2-tetrachloroethane- d_2 . Spectra were acquired from 25-95 °C (the operational limit of the cryoprobe) in 10 °C intervals using a Bruker Avance III HD 600 equipped with a Prodigy multinuclear cryoprobe (^1H : 600 MHz, ^{13}C : 151 MHz) NMR spectrometer.

Electrochemistry. All electrochemical experiments were conducted with traditional 3-electrode geometry using a Biologic SP-50 potentiostat. Electrolyte solutions (0.1 M)

were prepared from anhydrous, degassed HPLC grade CH_2Cl_2 and anhydrous Bu_4NPF_6 . The working electrode was a glassy carbon electrode (3-mm diameter), with a Pt-coil counter electrode and a Ag wire pseudo reference. The ferrocene/ferrocenium (Fc/Fc⁺) couple was used as an internal standard following each experiment. Potential values were re-referenced to SCE using a value of 0.46 (V vs. SCE) for the Fc/Fc⁺ couple in CH_2Cl_2 . LUMO and HOMO levels were approximated using SCE = -4.68 eV vs. vacuum. CV experiments were conducted in a three-neck flask that had been evacuated and backfilled with nitrogen for three cycles using standard Schlenk-line technique. Voltammograms were recorded at a sweep rates of 100 mV s^{-1} . $E_{1/2}$ values were calculated assuming $E_{1/2} \approx E_{o'} = (E_{\text{anodic}} + E_{\text{cathodic}})/2$ based on these observations for reversible couples; for irreversible couples the $E_{o'}$ value is estimated as the potential at peak current. Analyte concentrations were ca. 1-5 mM.

SQUID. Magnetic susceptibility measurements of **8** were performed with a Quantum Design MPMS-XL-5 SQUID susceptometer in the 300-700 K temperature range with an applied field of 0.1 T using a sample space oven with the sample ($m = 3.868$ mg) inserted in a 1.5 mm diameter aluminum foil cylinder. The susceptibility data were corrected for the same sample holder previously measured using the same conditions and for the diamagnetic contributions of the compound as deduced by using Pascal's constant tables.^[2] The magnetic measurements were fitted using the classical Bleaney-Bowers model (with a fixed g value of 2.0) for an antiferromagnetic $S = 1/2$ dimer plus a monomeric $S = 1/2$ impurity.^[3]

TGA measurements. Thermogravimetric Analysis (TGA) was performed from 25-1000 °C on a sample of **8** using a TGA Q500 V6.7 Build 203 instrument. The

measurements were performed under an oxygen-free dry N₂ flow.

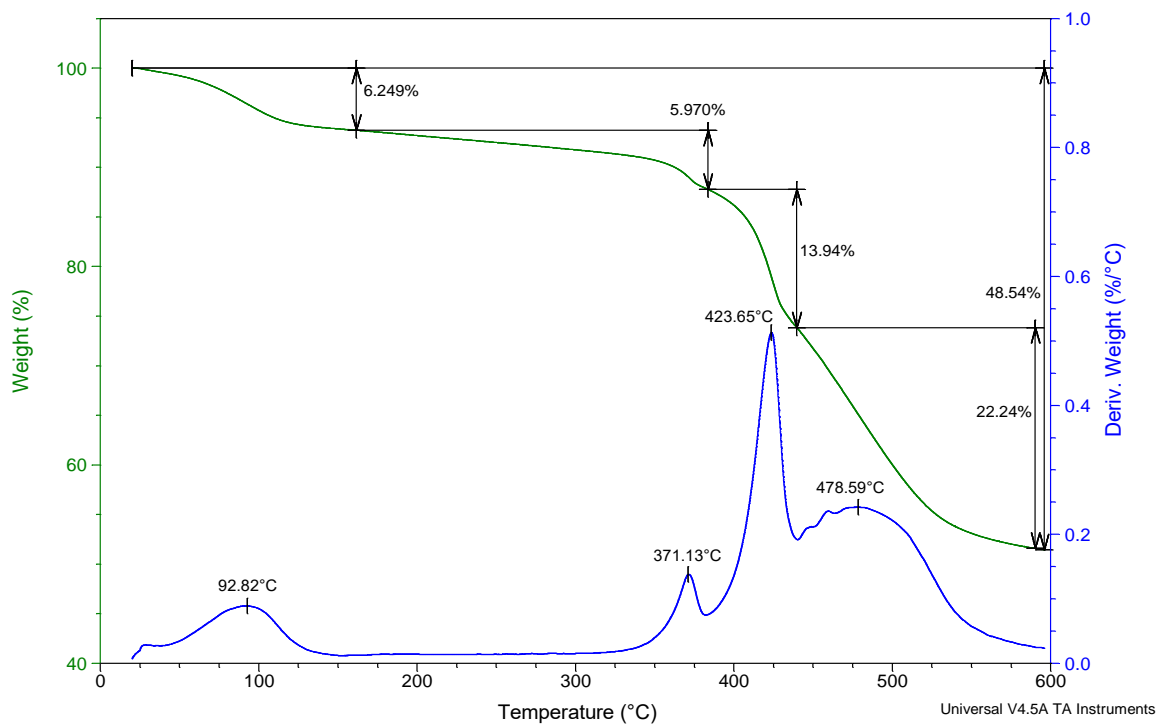


Figure E1. TGA data for *syn*-IIDBF **8**. Weight loss at ~90 °C corresponds to loss of residual toluene solvent.

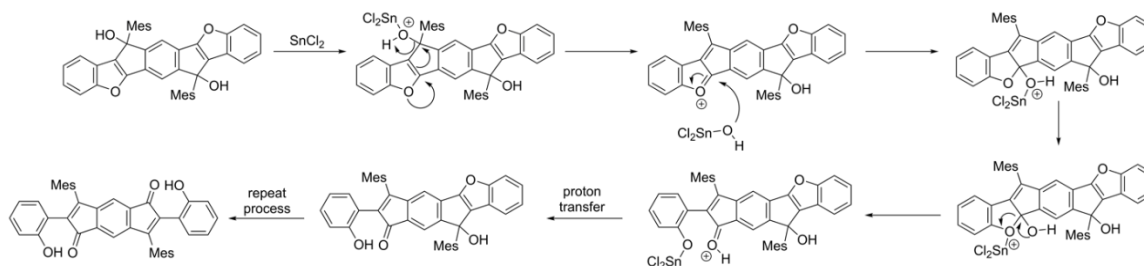


Figure E2. Plausible mechanism for the decomposition of the *anti*-IDBF/IIDBF diols represented with the diol precursor to **7/22**.

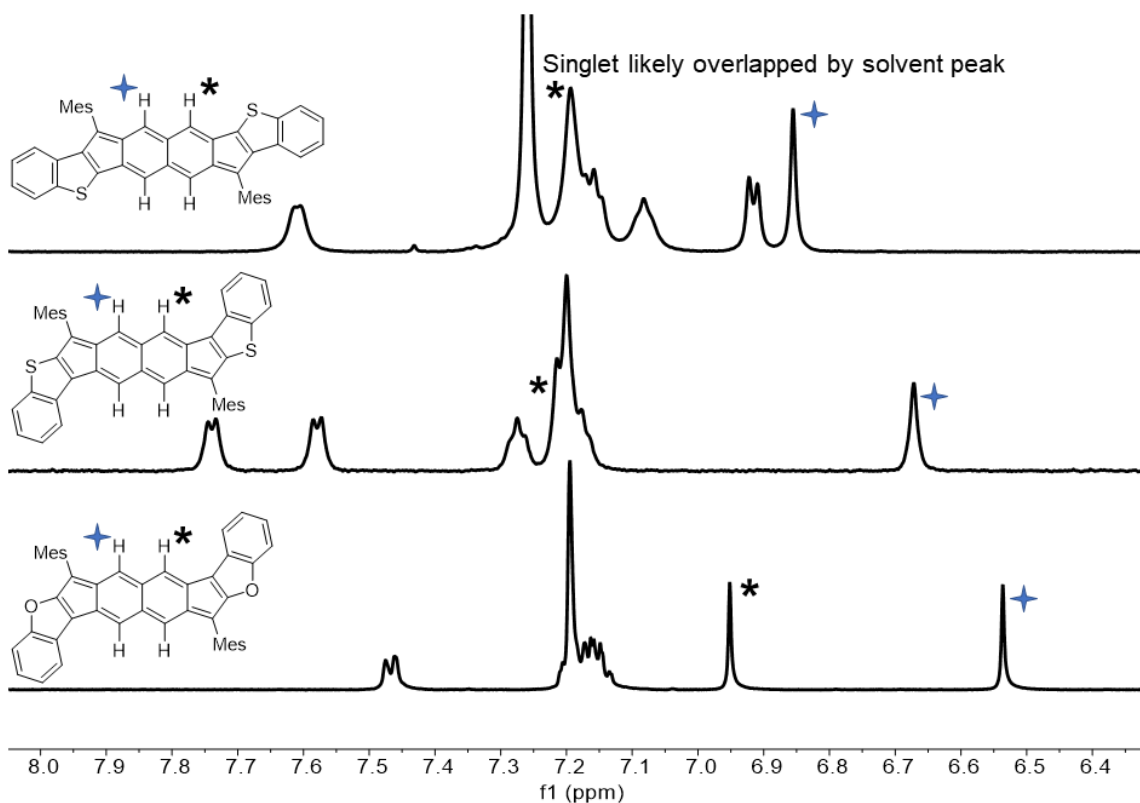
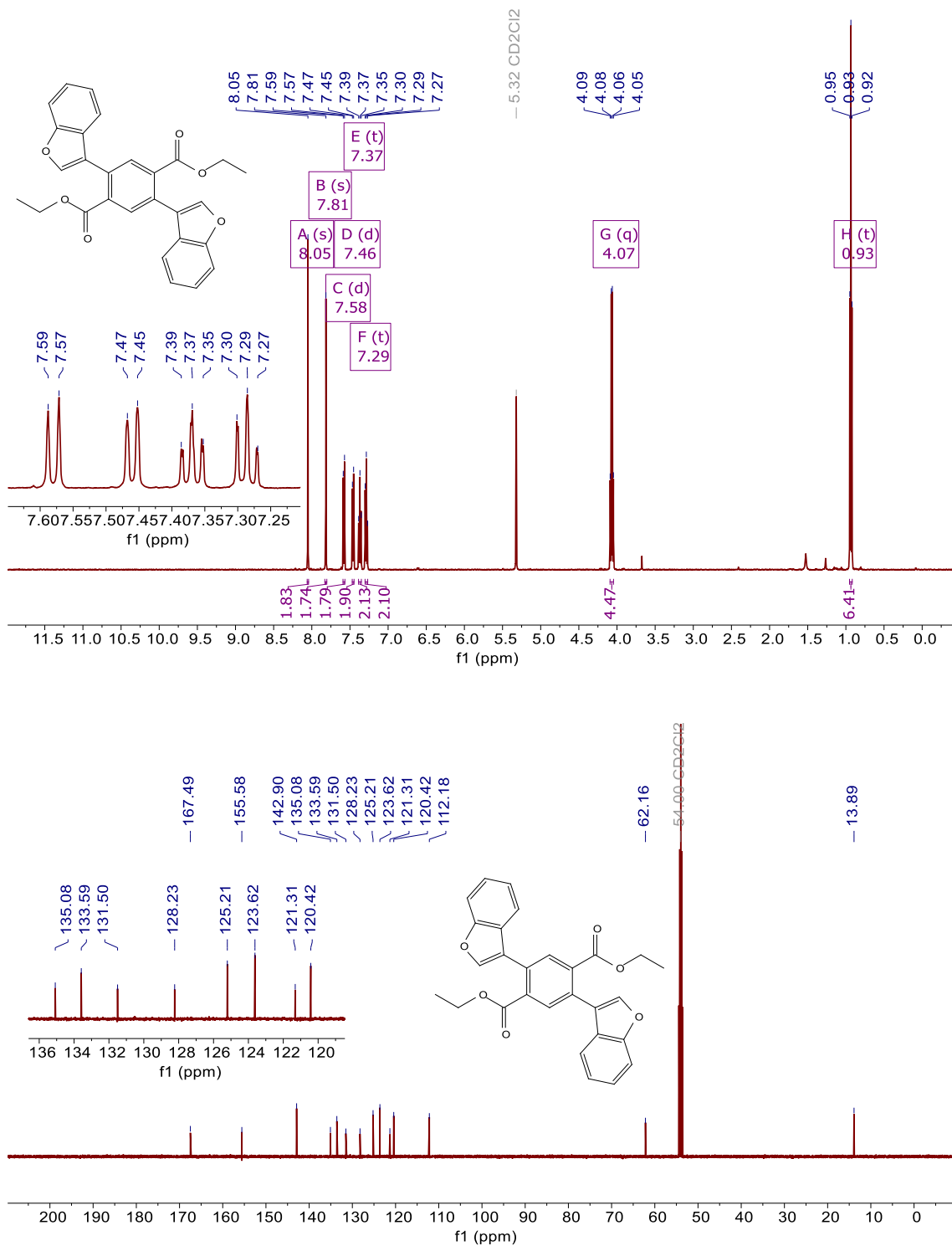
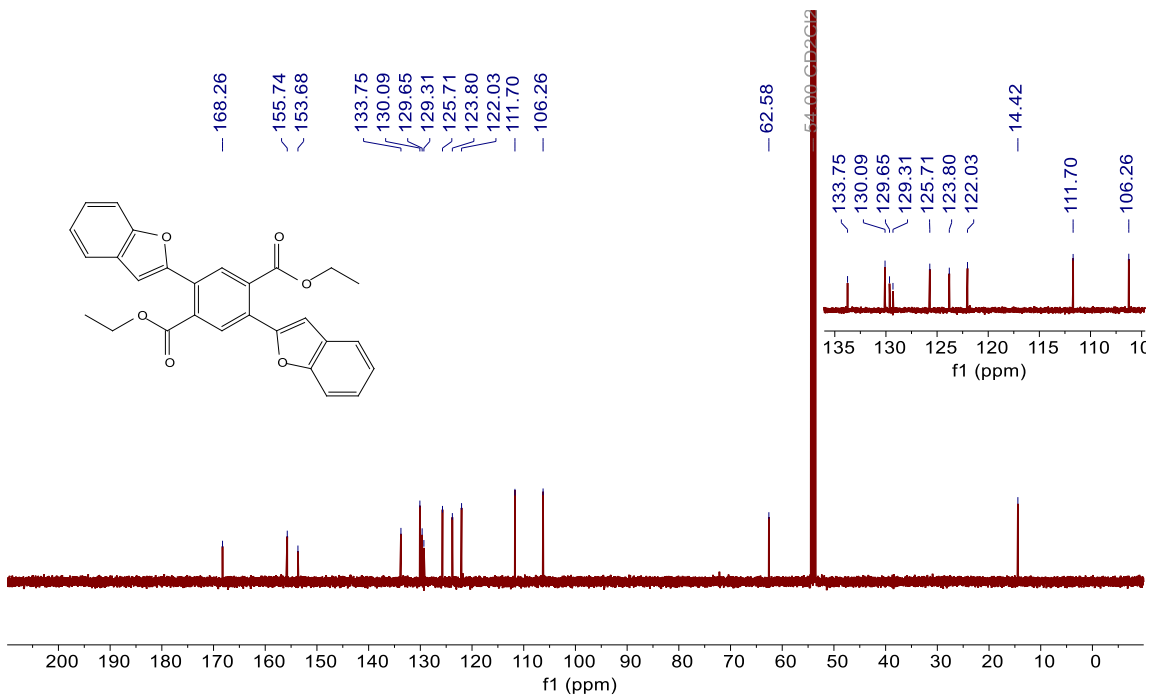
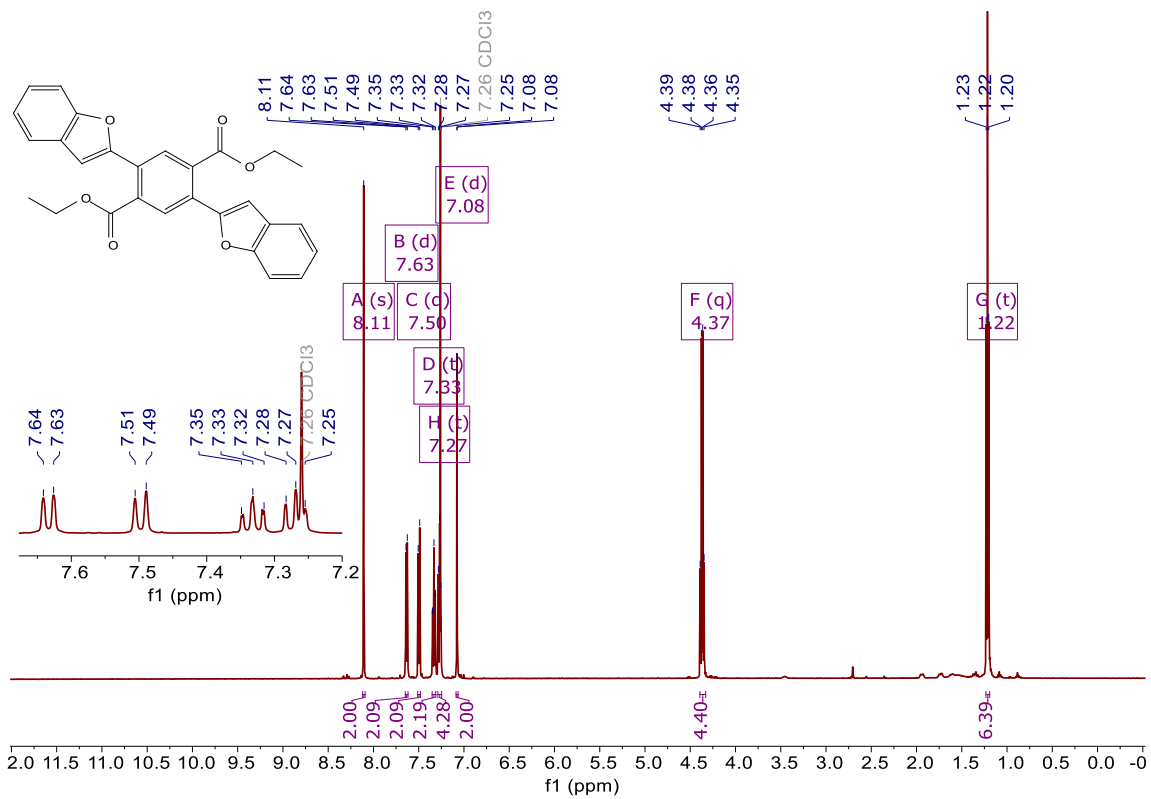
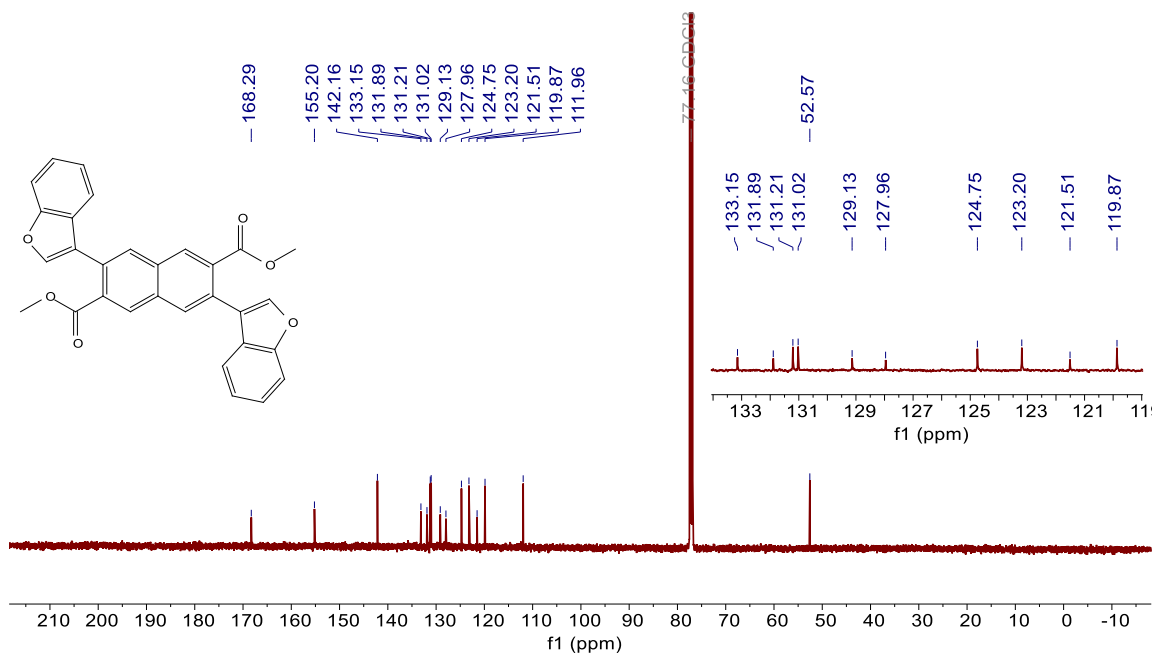
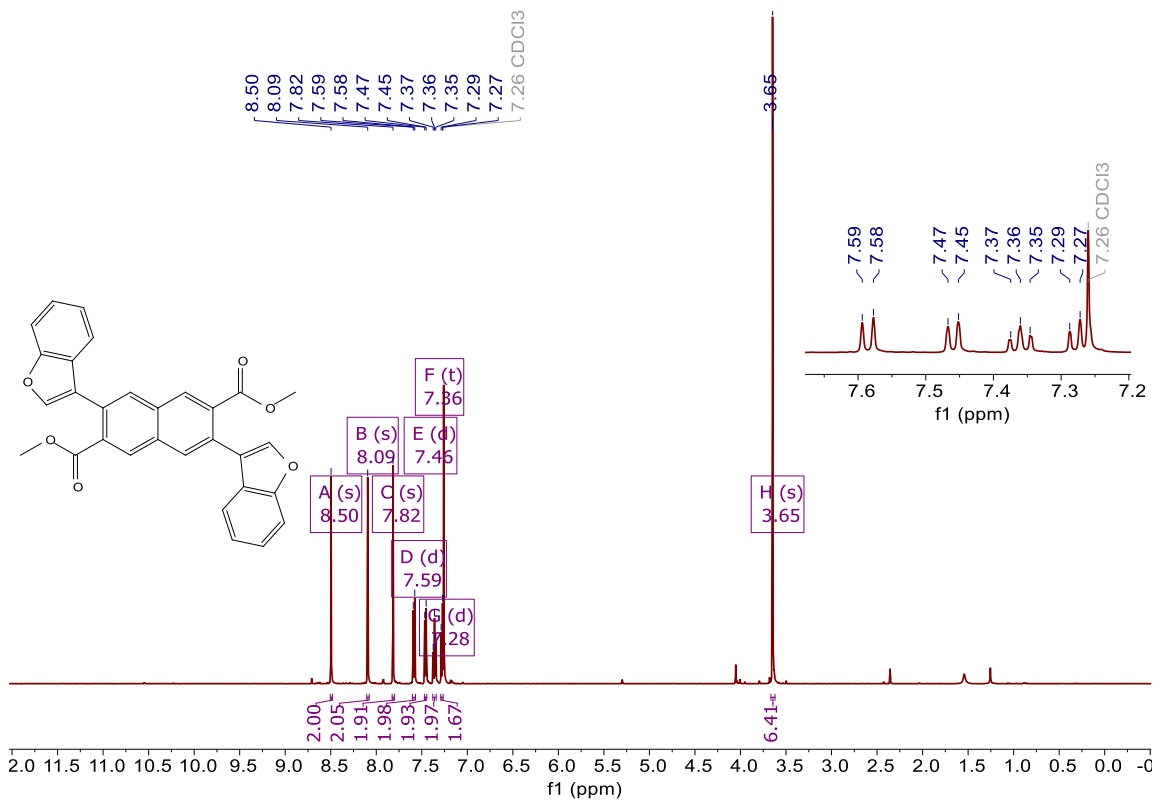


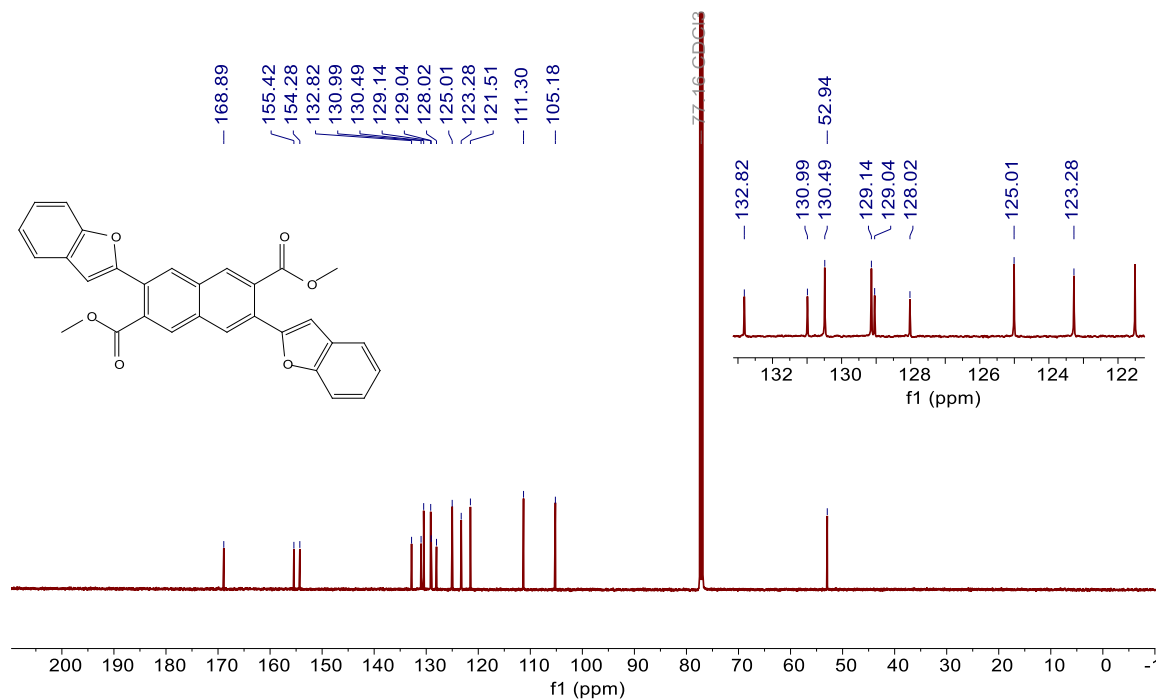
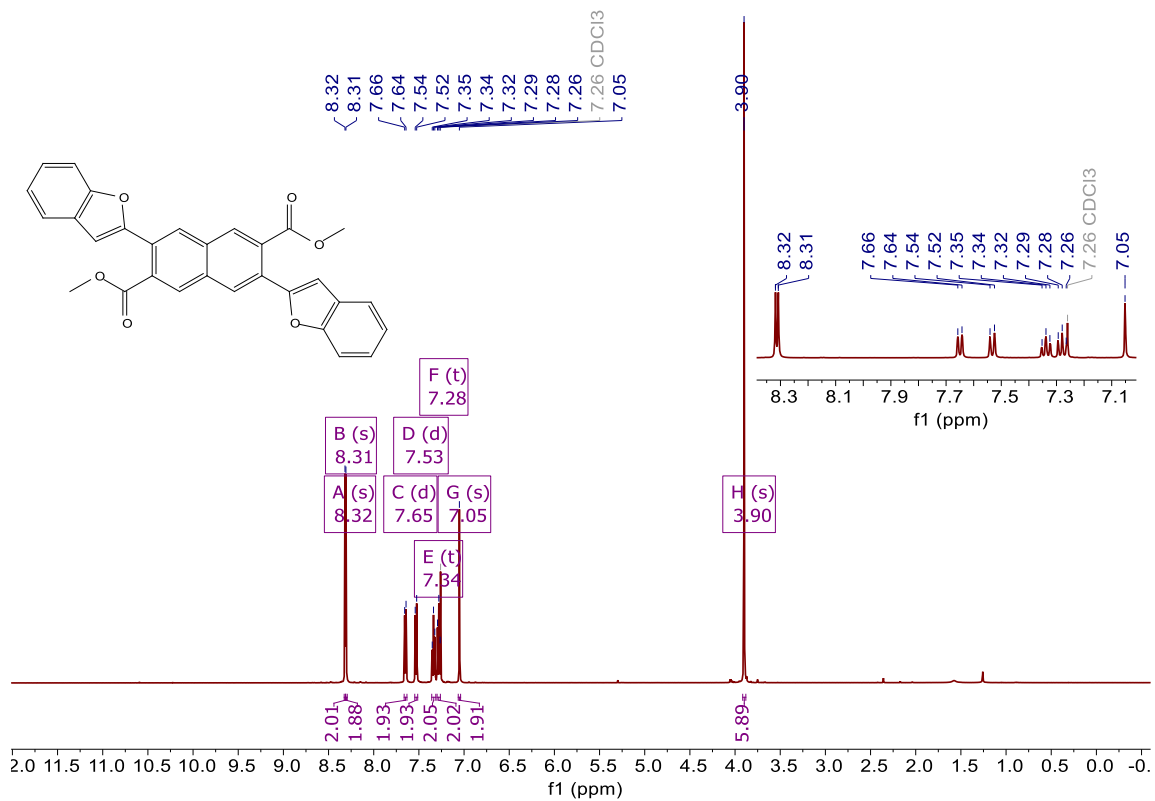
Figure E3. Stacked NMR spectra of the IIDBTs and syn-IIDBF showing upfield shifting proton resonances as the dicyclopenta[*b,g*]naphthalene core becomes more paratropic.

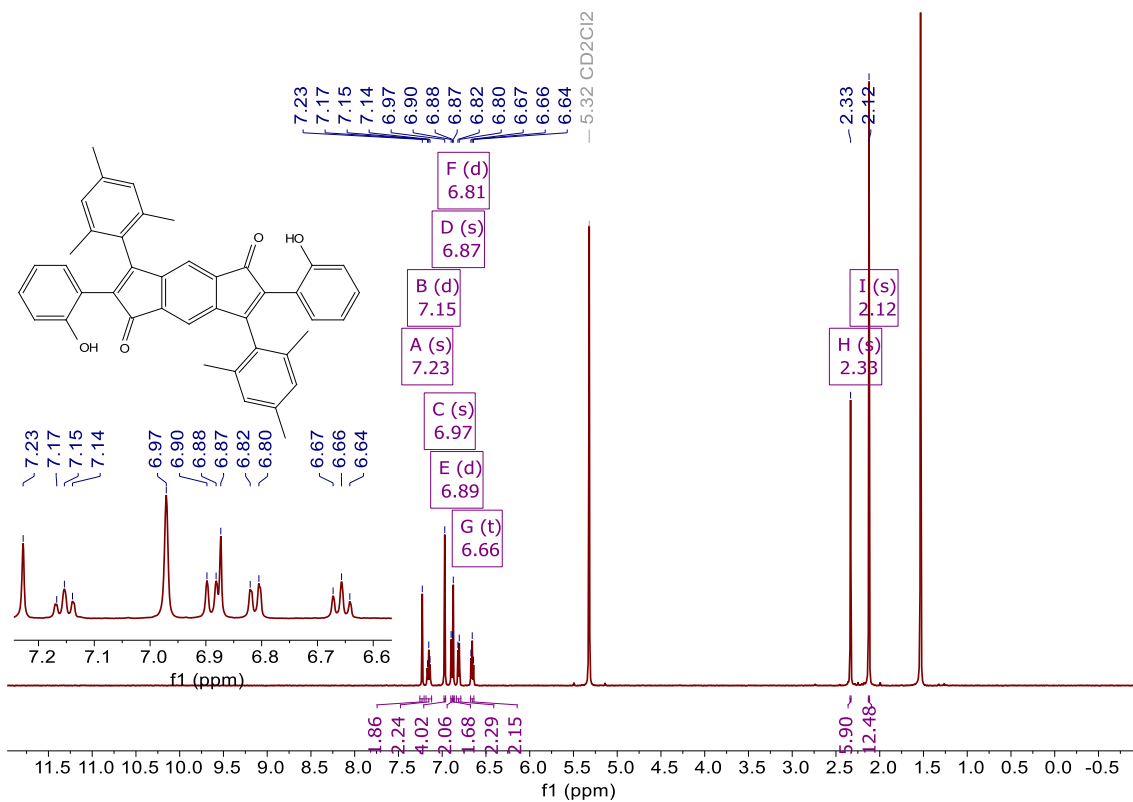
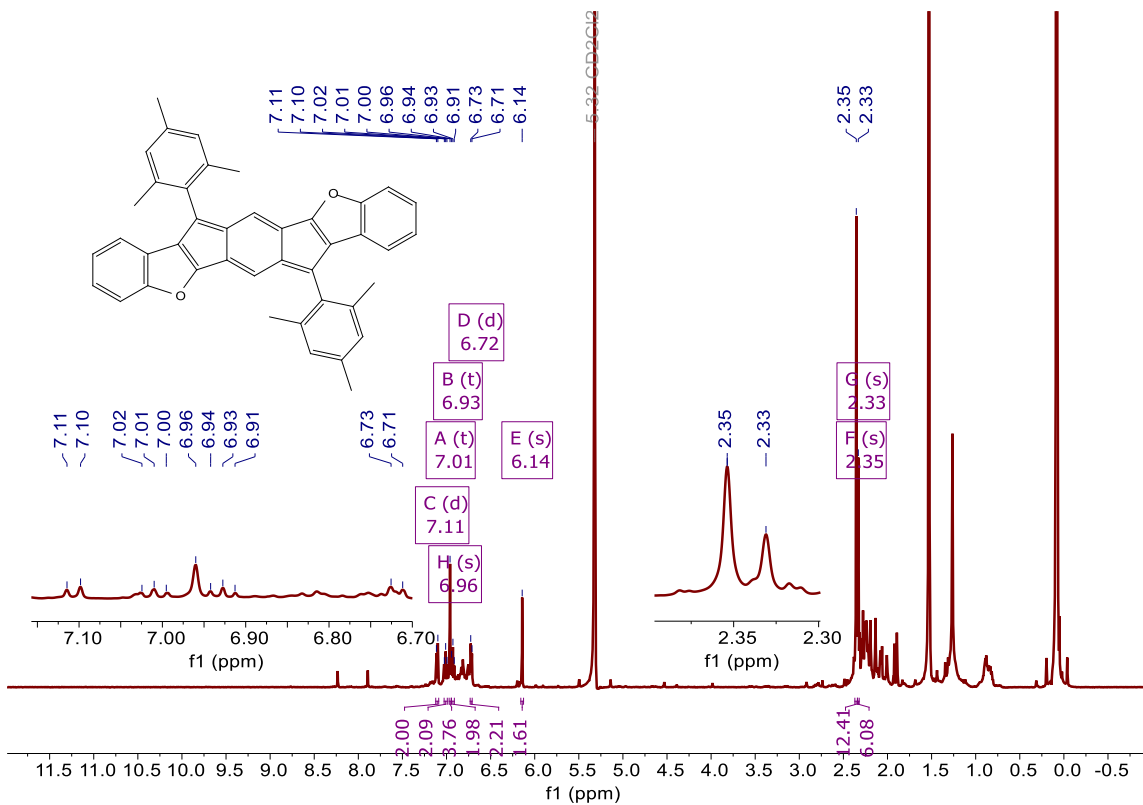
2. Copies of NMR Spectra

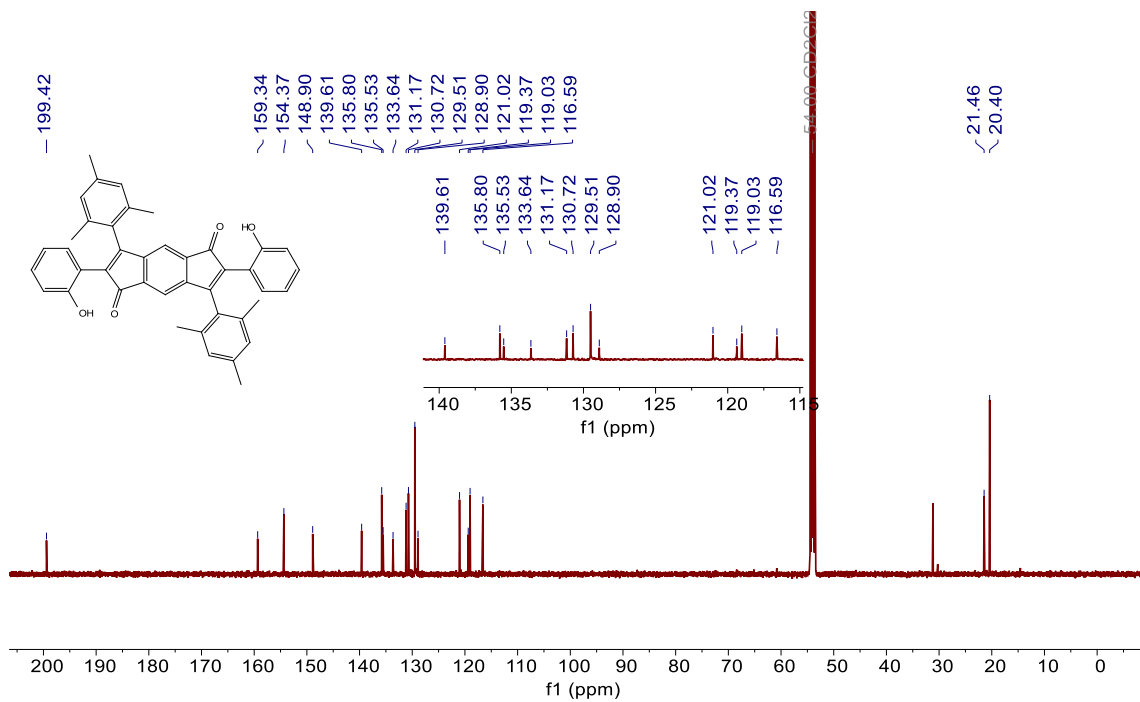


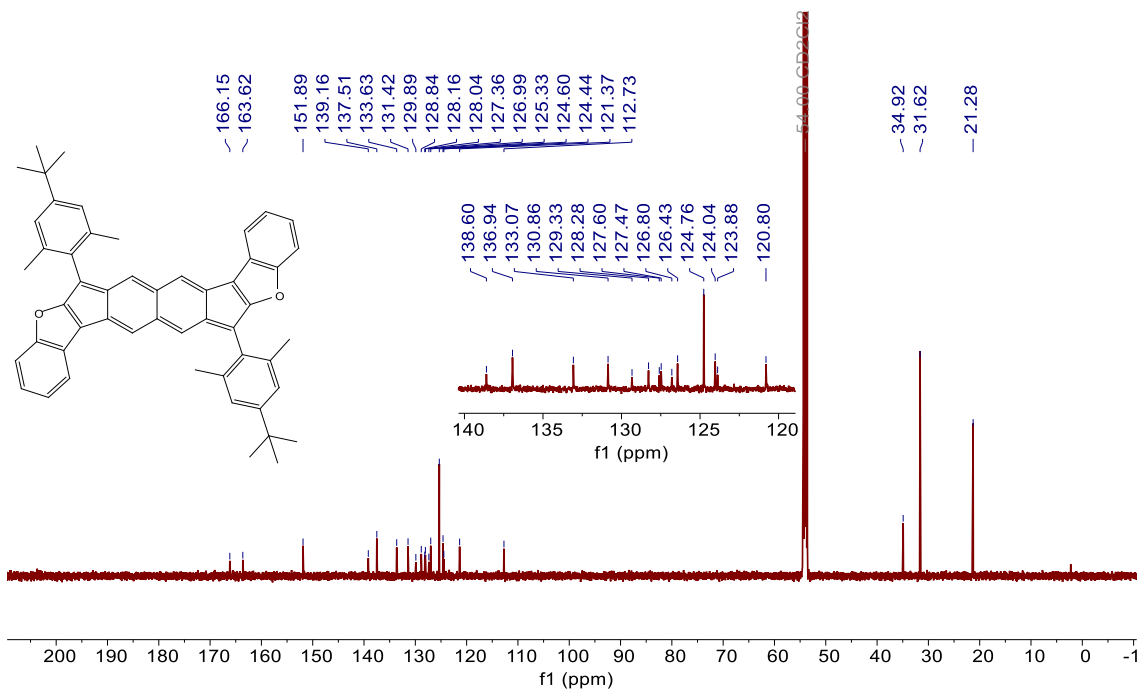
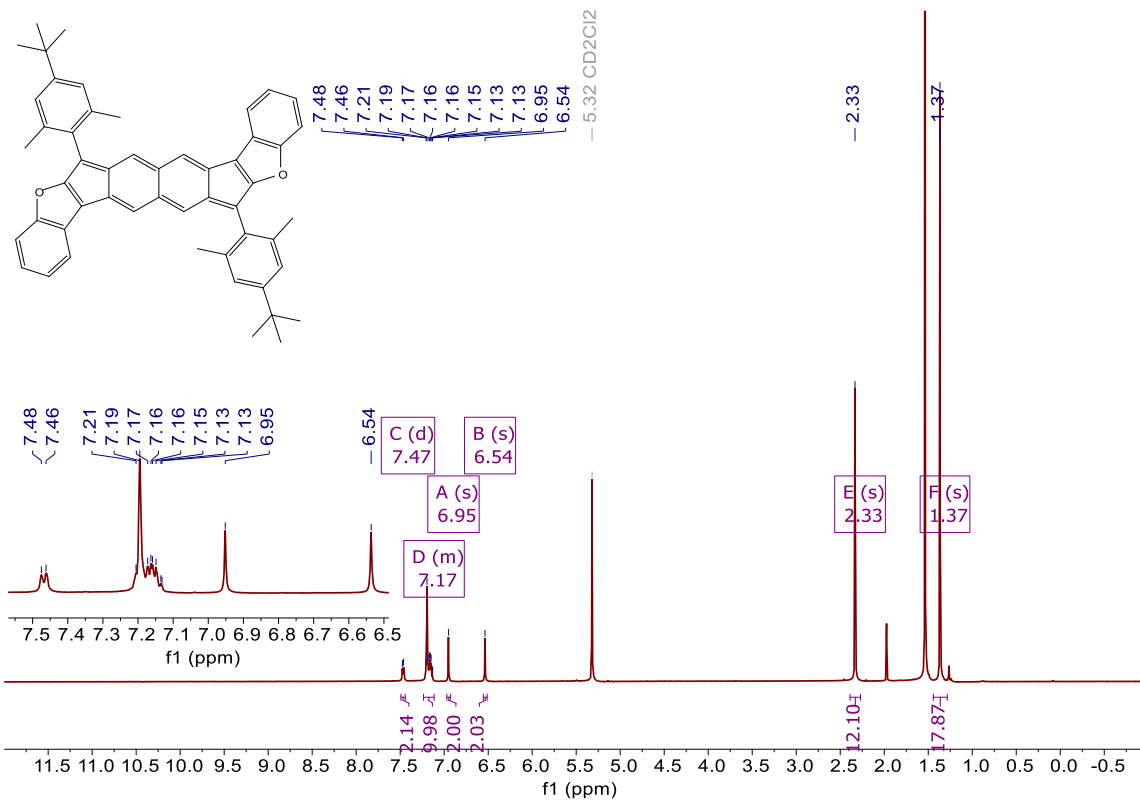


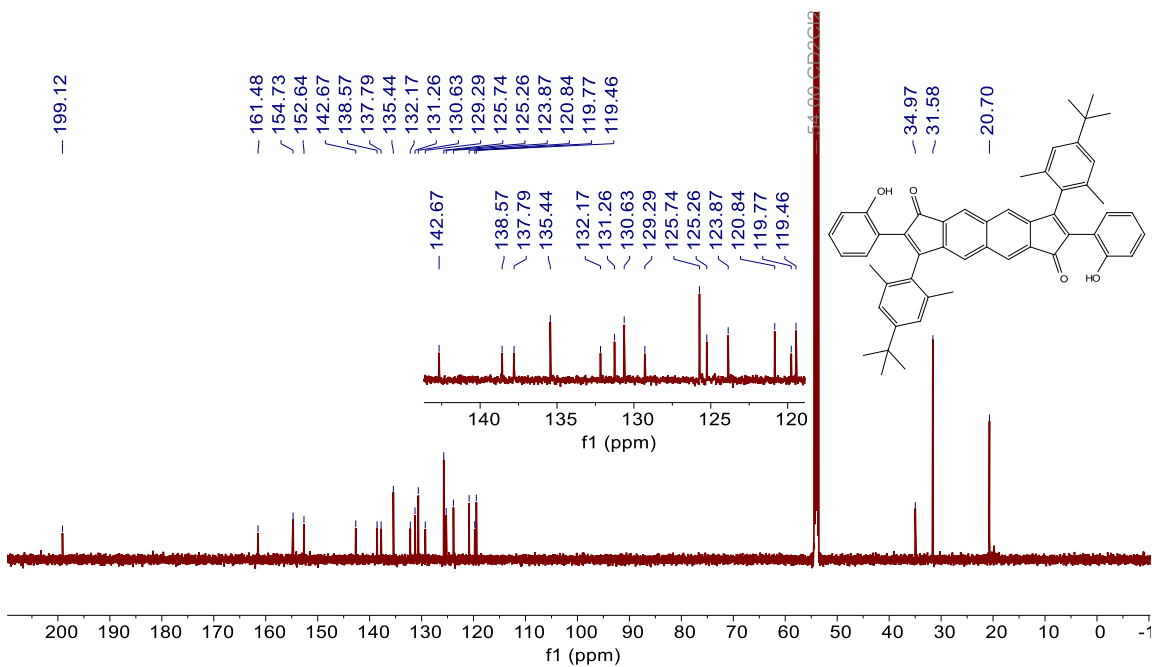
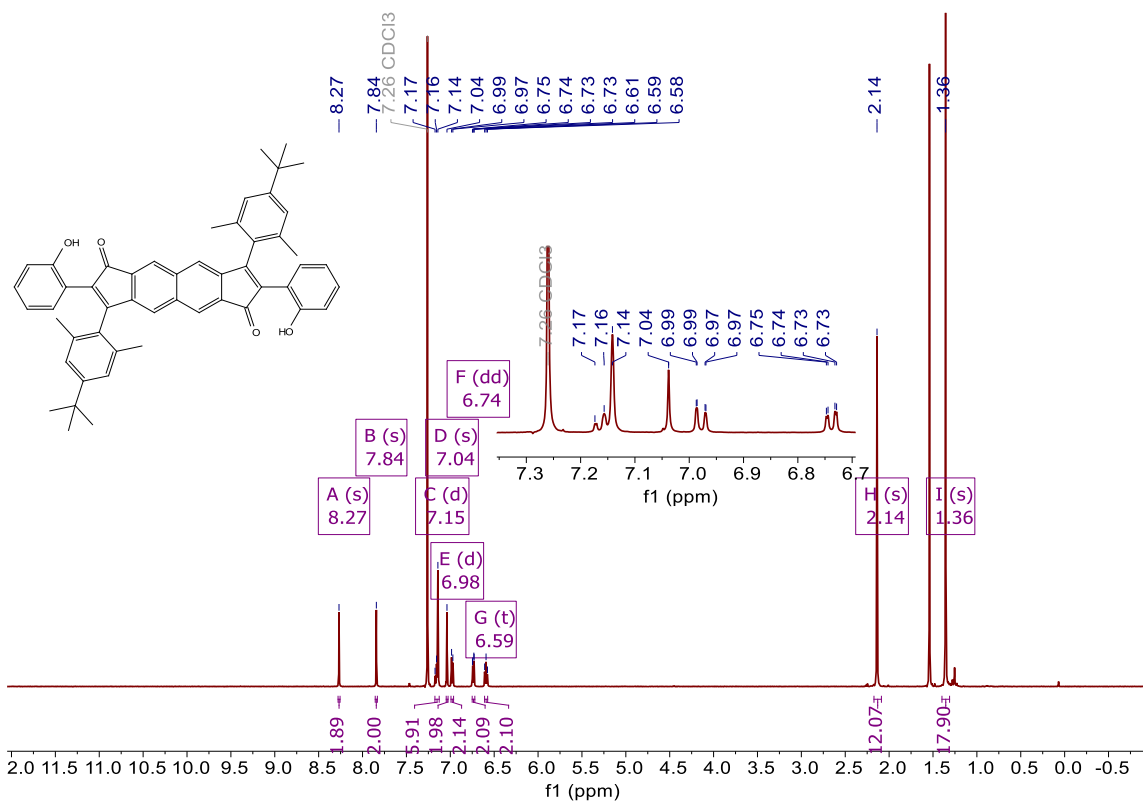












3. X-ray Crystallography

General. At Cornell, low-temperature X-ray diffraction data for **6**, **8**, **22** and **23** were collected on a Rigaku XtaLAB Synergy diffractometer coupled to a Rigaku Hypix detector

with Cu K α radiation ($\lambda = 1.54184 \text{ \AA}$) from a PhotonJet micro-focus X-ray source at 100 K (**6** and **22**), 200 K (**23**) and 253 K (**8**). The diffraction images were processed and scaled using the CrysAlisPro software.^[4] The structures were solved through intrinsic phasing using SHELXT^[5] and refined against F^2 on all data by full-matrix least squares with SHELXL^[6] following established refinement strategies.^[7] All non-hydrogen atoms were refined anisotropically. All hydrogen atoms bound to carbon were included in the model at geometrically calculated positions and refined using a riding model. Hydrogen atoms bound to oxygen were located in the difference Fourier synthesis and subsequently refined semi-freely with the help of distance restraints. The isotropic displacement parameters of all hydrogen atoms were fixed to 1.2 times the U_{eq} value of the atoms they are linked to (1.5 times for methyl groups). Compound **23** contains disordered MeOH solvent molecules that were included in the unit cell but could not be satisfactorily modeled. Therefore, those solvents were treated as diffuse contributions to the overall scattering without specific atom positions using the solvent mask routine in Olex2.^[8]

At Oregon, diffraction intensities for **7** were collected at 173 K on a Bruker Apex2 CCD diffractometer using CuK α radiation, $\lambda = 1.54178 \text{ \AA}$. Space group was determined based on intensity statistics. Absorption correction was applied by SADABS.^[9] Structure was solved by direct methods and Fourier techniques and refined on F^2 using full matrix least-squares procedures. All non-H atoms were refined with anisotropic thermal parameters. H atoms were refined in calculated positions in a rigid group model. Besides the centro-symmetrical main molecules, the crystal structure includes CHCl₃ solvent molecules. All calculations were performed by the Bruker SHELXL-2014 package.^[10]

Crystallographic Data for 6: C₄₂H₃₂O₂, M = 568.67, 0.181 x 0.116 x 0.045 mm³, T

= 100.00(10) K, Monoclinic, space group $P2_1/c$, $a = 9.89240(10)$ Å, $b = 10.35090(10)$ Å, $c = 14.74380(10)$ Å, $\alpha = 90^\circ$, $\beta = 100.5160(10)^\circ$, $\gamma = 90^\circ$, $V = 1484.34(2)$ Å³, $Z = 2$, $D_c = 1.272$ Mg/m³, $\mu(\text{Cu}) = 0.593$ mm⁻¹, $F(000) = 600$, $2\theta_{\text{max}} = 78.048^\circ$, 6081 reflections, 3174 independent reflections [$R(\text{int}) = 0.0387$], $R1 = 0.0449$, $wR2 = 0.1183$ and $\text{GOF} = 1.067$ for all reflections, max/min residual electron density $+0.477/-0.291$ eÅ⁻³. CCDC 2077068.

Crystallographic Data for 7: $\text{C}_{44}\text{H}_{34}\text{Cl}_6\text{O}_2$, $M = 807.41$, $0.09 \times 0.09 \times 0.11$ mm, $T = 173(2)$ K, Triclinic, space group $P-1$, $a = 8.0002(3)$ Å, $b = 9.6492(3)$ Å, $c = 12.4646(3)$ Å, $\alpha = 96.257(2)^\circ$, $\beta = 93.872(2)^\circ$, $\gamma = 92.522(2)^\circ$, $V = 953.02(5)$ Å³, $Z = 1$, $Z' = 0.5$, $D_c = 1.407$ Mg/m³, $\mu(\text{Cu}) = 4.410$ mm⁻¹, $F(000) = 416$, $2\theta_{\text{max}} = 133.37^\circ$, 10660 reflections, 3716 independent reflections [$R_{\text{int}} = 0.0306$], $R1 = 0.0698$, $wR2 = 0.2051$ and $\text{GOF} = 1.013$ for 3716 reflections (235 parameters) with $I > 2\sigma(I)$, $R1 = 0.0769$, $wR2 = 0.2185$ and $\text{GOF} = 1.013$ for all reflections, max/min residual electron density $+0.642/-0.792$ eÅ⁻³. CCDC 2076414.

Crystallographic Data for 8: $\text{C}_{54}\text{H}_{48}\text{Cl}_6\text{O}_2$, $\text{C}_{52}\text{H}_{46}\text{O}_2 \cdot 2(\text{CHCl}_3)$, $M = 941.62$, $0.168 \times 0.058 \times 0.053$ mm³, $T = 252.99(10)$ K, Triclinic, space group $P-1$, $a = 9.7456(3)$ Å, $b = 11.3374(4)$ Å, $c = 12.4630(4)$ Å, $\alpha = 66.041(3)^\circ$, $\beta = 71.335(3)^\circ$, $\gamma = 84.798(3)^\circ$, $V = 1190.97(8)$ Å³, $Z = 1$, $D_c = 1.313$ Mg/m³, $\mu(\text{Cu}) = 3.605$ mm⁻¹, $F(000) = 490$, $2\theta_{\text{max}} = 70.074^\circ$, 24592 reflections, 4510 independent reflections [$R(\text{int}) = 0.0517$], $R1 = 0.0831$, $wR2 = 0.2301$ and $\text{GOF} = 1.069$ for all reflections, max/min residual electron density $+0.469/-0.419$ eÅ⁻³. CCDC 2077067.

Crystallographic Data for 22: $\text{C}_{44}\text{H}_{36}\text{Cl}_6\text{O}_4$, $\text{C}_{42}\text{H}_{34}\text{O}_4 \cdot 2(\text{CHCl}_3)$, $M = 841.43$, $0.255 \times 0.170 \times 0.143$ mm³, $T = 99.9(6)$ K, Triclinic, space group $P-1$, $a = 9.5657(2)$ Å, $b = 10.4522(3)$ Å, $c = 10.7320(2)$ Å, $\alpha = 105.068(2)^\circ$, $\beta = 96.763(2)^\circ$, $\gamma = 94.099(2)^\circ$, $V =$

1023.06(4) Å³, $Z = 1$, $D_c = 1.366 \text{ Mg/m}^3$, $\mu(\text{Cu}) = 4.167 \text{ mm}^{-1}$, $F(000) = 434$, $2\theta_{\text{max}} = 77.143^\circ$, 22268 reflections, 4304 independent reflections [$R(\text{int}) = 0.0447$], $R1 = 0.0453$, $wR2 = 0.1194$ and $\text{GOF} = 1.085$ for all reflections, max/min residual electron density $+0.805/-0.780 \text{ e}\text{\AA}^{-3}$. CCDC 207707.

Crystallographic Data for 23: $\text{C}_{58}\text{H}_{66}\text{Cl}_6\text{O}_8$, $\text{C}_{52}\text{H}_{48}\text{O}_4 \cdot 4(\text{MeOH}) \cdot 2\text{CHCl}_3$, $M = 1103.80$, $0.291 \times 0.115 \times 0.043 \text{ mm}^3$, $T = 200.00(10) \text{ K}$, Triclinic, space group P-1, $a = 9.68960(10) \text{ \AA}$, $b = 12.5880(2) \text{ \AA}$, $c = 13.1120(2) \text{ \AA}$, $\alpha = 110.0970(10)^\circ$, $\beta = 108.0540(10)^\circ$, $\gamma = 95.2180(10)^\circ$, $V = 1392.63(4) \text{ \AA}^3$, $Z = 1$, $D_c = 1.316 \text{ Mg/m}^3$, $\mu(\text{Cu}) = 3.241 \text{ mm}^{-1}$, $F(000) = 580$, $2\theta_{\text{max}} = 67.739^\circ$, 55846 reflections, 5053 independent reflections [$R(\text{int}) = 0.0487$], $R1 = 0.0905$, $wR2 = 0.27094$ and $\text{GOF} = 1.084$ for all reflections, max/min residual electron density $+0.811/-1.235 \text{ e}\text{\AA}^{-3}$. CCDC 2077069.

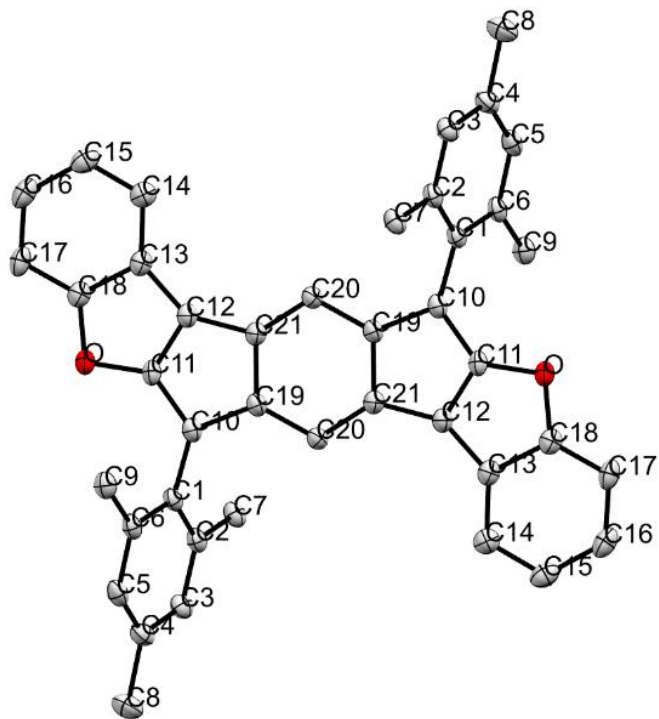


Figure E4. Molecular structure of *syn*-IDBF **6**; ellipsoids drawn at the 50% probability level.

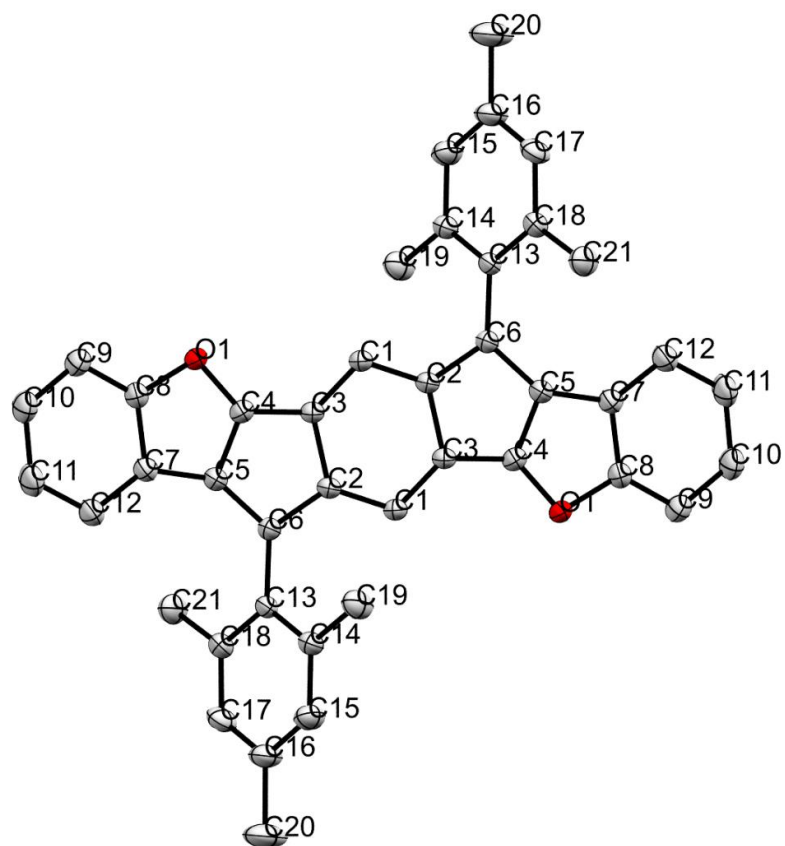


Figure E5. Molecular structure of *anti*-IDBF 7; ellipsoids drawn at the 50% probability level.

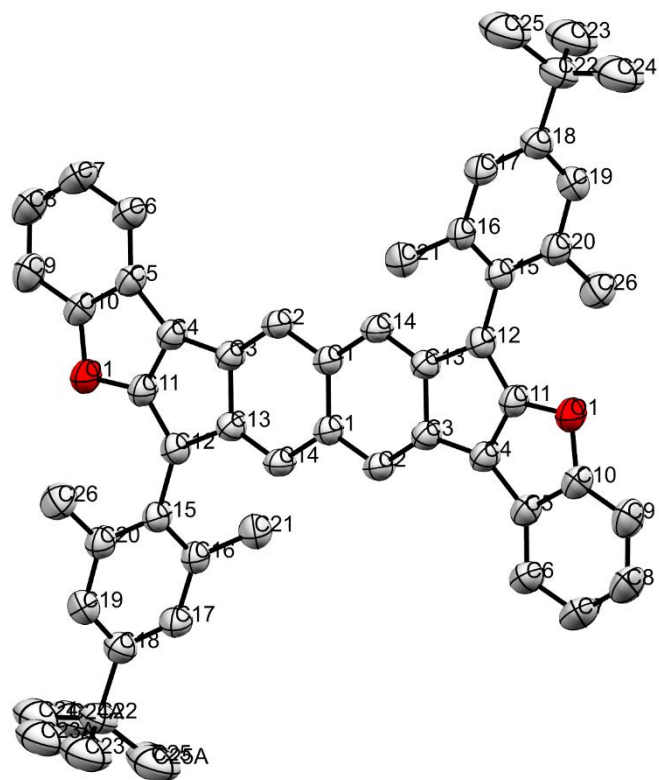


Figure E6. Molecular structure of *syn*-IIDBF **8**; ellipsoids drawn at the 50% probability level.

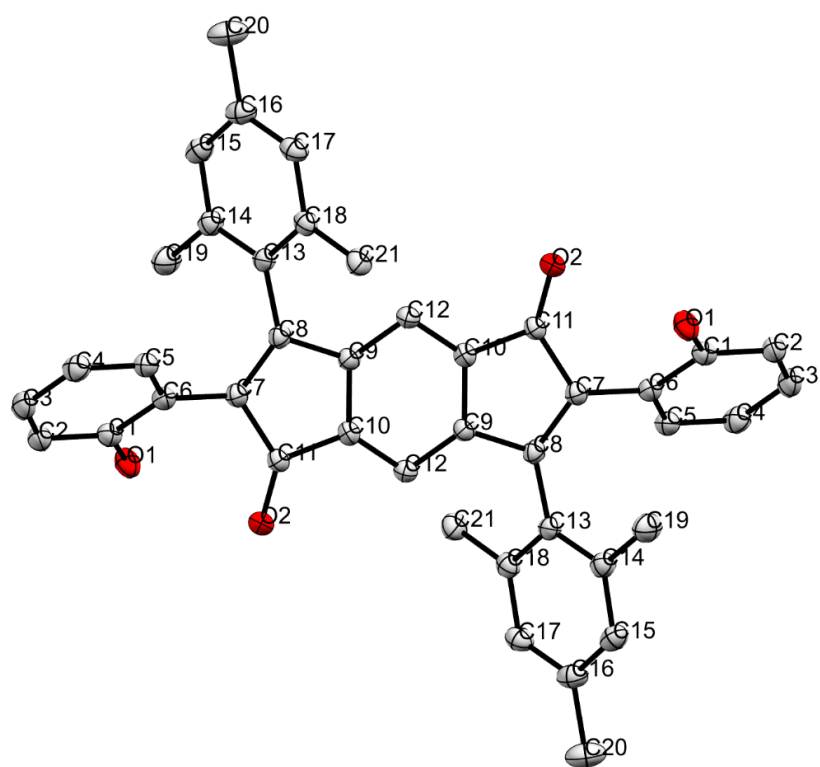


Figure E7. Molecular structure of ring-opened product **22**; ellipsoids drawn at the 50% probability level.

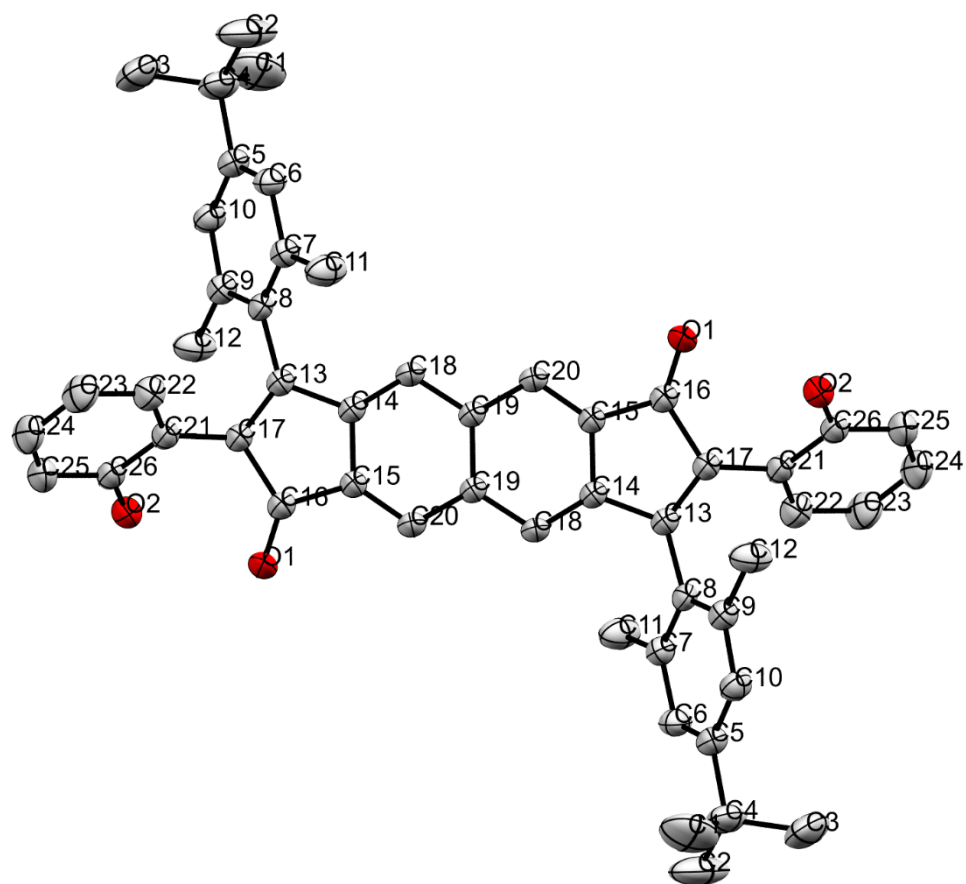


Figure E8. Molecular structure of ring-opened product **23**; ellipsoids drawn at the 50% probability level.

4. Computational Details

4.1 NICS-XY Scan Calculations. All calculations related to the NICS-XY scans were performed using Gaussian 09.^[11] For the IDBFs, geometries were optimized using B3LYP/6-311++G** level of theory. For the IIDBFs and dicyclopenta[*b,g*]naphthalene (DCN), geometries were optimized using B3LYP/6-311+G*. All the structures were verified to be minima by frequency calculation. NICS-XY scans were carried out with the Aroma package^[12] at the B3LYP/6-311++G** level of theory for the IDBFs and the B3LYP/6-31+G* level of theory for the IIDBFs and DCN using the sigma-only model.^[13] For the sake of computational efficiency calculations were performed on the hydrocarbon parent molecules for each compound. Previous computational studies in our group have shown that due to their nearly orthogonal orientation relative to the plane of the indacene core, removal of the pendant aryl groups on the apical carbons has little to no effect on NICS-XY scan calculations. NICS-XY data for *s*-indacene, *syn*-IDBT, and *anti*-IDBT have been previously reported.^[14]

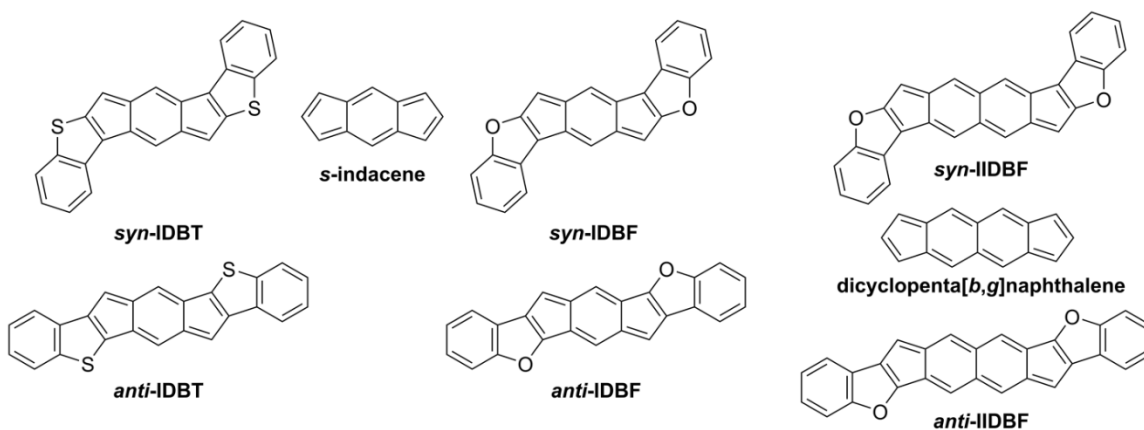


Figure E9. Simplified structures used for the NICS-XY scan calculations.

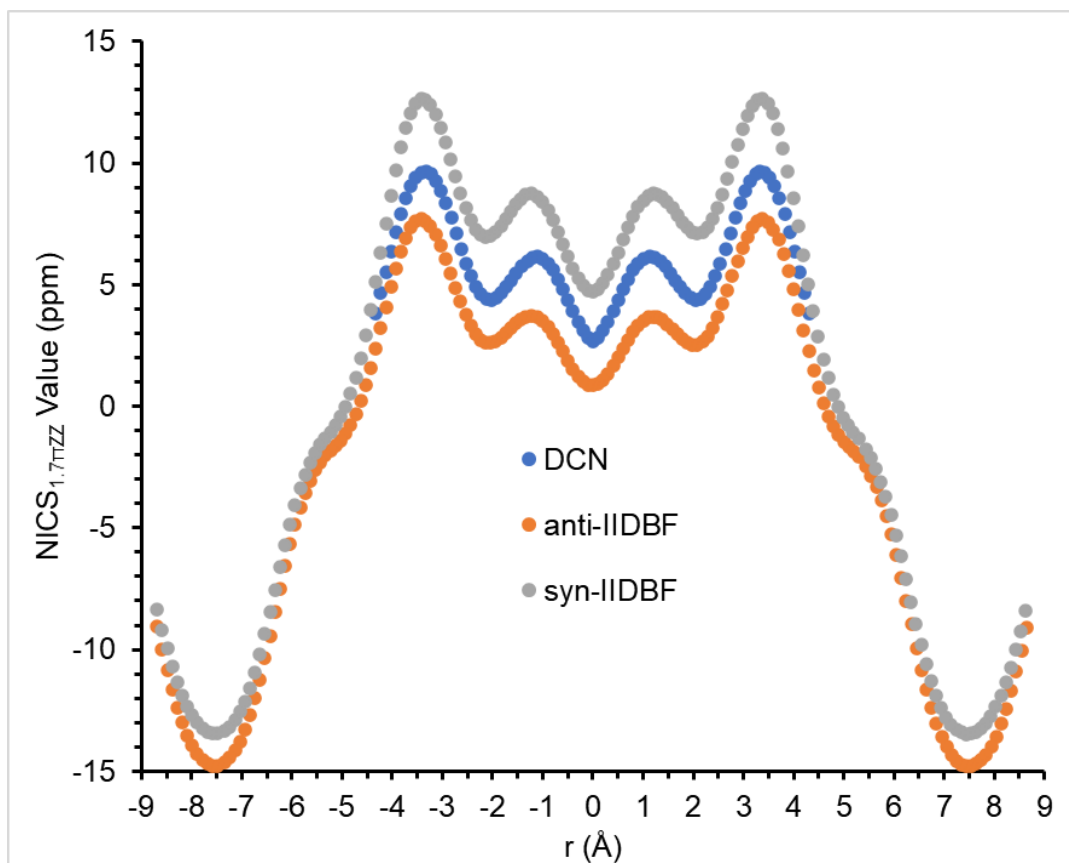


Figure E10. NICS-XY scans of the IIDBFs and dicyclopenta[*b,g*]naphthalene (DCN) calculated at the B3LYP/6-31+G* level of theory

Calculated Geometries for NICS-XY Scan Structures

syn-IIDBF (6')

Zero-point correction= 0.282548 (Hartree/Particle)
 Thermal correction to Energy= 0.299845
 Thermal correction to Enthalpy= 0.300789
 Thermal correction to Gibbs Free Energy= 0.237872
 Sum of electronic and zero-point Energies= -1072.144671

H	-7.1207170000	-3.7826280000	0.0000000000
H	-7.0376400000	-1.3179510000	0.0000000000
C	-6.1588500000	-3.2834650000	0.0000000000
C	-6.1098860000	-1.8783500000	0.0000000000
H	-5.0174720000	-5.1310410000	0.0000000000
C	-4.9936920000	-4.0485440000	0.0000000000
C	-4.8993450000	-1.1981990000	0.0000000000
H	-4.8761410000	-0.1150010000	0.0000000000
C	-3.7931860000	-3.3596950000	0.0000000000
C	-3.7066620000	-1.9398040000	0.0000000000

O	-2.5476870000	-3.9467300000	0.0000000000
C	-2.3042760000	-1.6608750000	0.0000000000
H	-2.1783340000	1.2804160000	0.0000000000
C	-1.6719280000	-2.8958860000	0.0000000000
C	-1.2515930000	0.7151980000	0.0000000000
C	-1.2515930000	-0.6568980000	0.0000000000
H	-0.4611890000	3.5800750000	0.0000000000
C	-0.2636630000	-2.7786410000	0.0000000000
C	-0.0062920000	1.3999970000	0.0000000000
C	0.0062920000	-1.3999970000	0.0000000000
C	0.2636630000	2.7786410000	0.0000000000
H	0.4611890000	-3.5800750000	0.0000000000
C	1.2515930000	-0.7151980000	0.0000000000
C	1.2515930000	0.6568980000	0.0000000000
C	1.6719280000	2.8958860000	0.0000000000
H	2.1783340000	-1.2804160000	0.0000000000
C	2.3042760000	1.6608750000	0.0000000000
O	2.5476870000	3.9467300000	0.0000000000
C	3.7066620000	1.9398040000	0.0000000000
C	3.7931860000	3.3596950000	0.0000000000
H	4.8761410000	0.1150010000	0.0000000000
C	4.8993450000	1.1981990000	0.0000000000
C	4.9936920000	4.0485440000	0.0000000000
H	5.0174720000	5.1310410000	0.0000000000
C	6.1098860000	1.8783500000	0.0000000000
C	6.1588500000	3.2834650000	0.0000000000
H	7.0376400000	1.3179510000	0.0000000000
H	7.1207170000	3.7826280000	0.0000000000

anti-IDBF (7')

Zero-point correction=	0.282526 (Hartree/Particle)
Thermal correction to Energy=	0.299789
Thermal correction to Enthalpy=	0.300733
Thermal correction to Gibbs Free Energy=	0.238001
Sum of electronic and zero-point Energies=	-1072.146113

H	-2.8094780000	2.2971220000	0.0000000000
H	-2.5021830000	5.7736600000	0.0000000000
H	-2.4902810000	-6.2099590000	0.0000000000
H	-2.4689120000	-0.5570270000	0.0000000000
C	-1.7302460000	2.2297400000	0.0000000000
O	-1.4587130000	-3.6686000000	0.0000000000
H	-1.4318200000	8.0076950000	0.0000000000
C	-1.4220910000	5.8618850000	0.0000000000
C	-1.4108210000	-6.1258630000	0.0000000000
C	-1.4108210000	-0.3145080000	0.0000000000

H	-1.023790000	-8.238301000	0.000000000
C	-0.983385000	1.012944000	0.000000000
C	-0.814202000	7.116980000	0.000000000
C	-0.813143000	3.289734000	0.000000000
C	-0.788076000	-4.894860000	0.000000000
C	-0.614486000	4.721446000	0.000000000
C	-0.579351000	-7.250088000	0.000000000
C	-0.486112000	-2.732241000	0.000000000
C	-0.446557000	-1.322161000	0.000000000
C	0.446557000	1.322161000	0.000000000
C	0.486112000	2.732241000	0.000000000
C	0.579351000	7.250088000	0.000000000
C	0.614486000	-4.721446000	0.000000000
C	0.788076000	4.894860000	0.000000000
C	0.813143000	-3.289734000	0.000000000
C	0.814202000	-7.116980000	0.000000000
C	0.983385000	-1.012944000	0.000000000
H	1.023790000	8.238301000	0.000000000
C	1.410821000	6.125863000	0.000000000
C	1.410821000	0.314508000	0.000000000
C	1.422091000	-5.861885000	0.000000000
H	1.431820000	-8.007695000	0.000000000
O	1.458713000	3.668600000	0.000000000
C	1.730246000	-2.229740000	0.000000000
H	2.468912000	0.557027000	0.000000000
H	2.490281000	6.209959000	0.000000000
H	2.502183000	-5.773660000	0.000000000
H	2.809478000	-2.297122000	0.000000000

***syn-II*DBF (8')**

Zero-point correction=	0.329167 (Hartree/Particle)
Thermal correction to Energy=	0.349088
Thermal correction to Enthalpy=	0.350032
Thermal correction to Gibbs Free Energy=	0.280553
Sum of electronic and zero-point Energies=	-1225.751937

H	-8.294394000	-2.188877000	0.926019000
H	-8.215175000	-2.138855000	3.423563000
C	-7.553241000	-1.600766000	1.454691000
C	-7.497334000	-1.563524000	2.848818000
C	-6.615715000	-0.849684000	0.770134000
C	-6.530850000	-0.796521000	3.519487000
O	-6.523991000	-0.769247000	-0.604765000
H	-6.517556000	-0.791653000	4.604275000
C	-5.624237000	-0.062564000	1.416065000
C	-5.594029000	-0.045916000	2.819168000

C	-5.4706470000	0.0718910000	-0.8372890000
H	-5.1031630000	0.3765590000	-3.0124750000
C	-4.8801140000	0.5364400000	0.3512260000
H	-4.8527960000	0.5422280000	3.3492760000
C	-4.8509850000	0.5721380000	-1.9798450000
C	-3.8017480000	1.3984650000	-0.0347370000
C	-3.7998010000	1.4078850000	-1.5007600000
C	-2.8701630000	2.1377170000	0.6572640000
H	-2.8595530000	2.1403170000	1.7440950000
C	-2.8543670000	2.1655610000	-2.1803920000
H	-2.8442810000	2.1794210000	-3.2675510000
C	-1.9007910000	2.9145730000	-0.0327080000
C	-1.8982440000	2.9243770000	-1.4790770000
H	-0.9547530000	3.6595280000	1.7557660000
C	-0.9446700000	3.6733920000	0.6686070000
H	-0.9394830000	3.6986350000	-3.2558800000
C	-0.9288700000	3.7012300000	-2.1690490000
C	0.0007650000	4.4310660000	-0.0110240000
C	0.0027140000	4.4404840000	-1.4770480000
C	1.0519610000	5.2667980000	0.4680600000
H	1.0537300000	5.2967600000	-4.8610610000
C	1.0810710000	5.3025200000	-1.8630110000
H	1.3041470000	5.4623680000	1.5006900000
C	1.6716100000	5.7670610000	-0.6744960000
C	1.7949650000	5.8849040000	-4.3309530000
C	1.8251830000	5.9015390000	-2.9278500000
H	2.7184740000	6.6306620000	-6.1160590000
O	2.7249480000	6.6082070000	-0.9070190000
C	2.7317760000	6.6355190000	-5.0312720000
C	2.8166610000	6.6886570000	-2.2819190000
C	3.6982610000	7.4025210000	-4.3606020000
C	3.7541780000	7.4397510000	-2.9664750000
H	4.4160940000	7.9778620000	-4.9353470000
H	4.4953320000	8.0278610000	-2.4378040000

anti-IIDBF (9')

Zero-point correction=	0.329390 (Hartree/Particle)
Thermal correction to Energy=	0.349292
Thermal correction to Enthalpy=	0.350236
Thermal correction to Gibbs Free Energy=	0.280852
Sum of electronic and zero-point Energies=	-1225.747522

H	-9.2767330000	-1.1956930000	1.1926170000
H	-8.7082050000	-0.2275110000	3.3906890000
C	-8.3535750000	-0.6381090000	1.3087530000
C	-8.0294100000	-0.0878620000	2.5559470000
H	-7.7447030000	-0.9013390000	-0.7623040000

C	-7.507330000	-0.481564000	0.208349000
C	-6.852366000	0.634354000	2.742435000
H	-6.612680000	1.055439000	3.713049000
C	-6.345859000	0.237521000	0.414206000
C	-5.987166000	0.806323000	1.657912000
O	-5.390144000	0.491812000	-0.564969000
C	-4.718070000	1.455744000	1.418745000
C	-4.431345000	1.219267000	0.060368000
C	-3.666088000	2.213112000	1.965890000
H	-3.572148000	2.565638000	2.984416000
C	-3.204089000	1.805237000	-0.314264000
H	-2.818675000	1.413753000	-2.390923000
C	-2.724494000	2.441042000	0.924002000
C	-2.463797000	1.883363000	-1.477558000
C	-1.516653000	3.120782000	0.905842000
C	-1.232880000	2.576230000	-1.495600000
H	-1.143988000	3.597558000	1.809230000
H	-0.839843000	2.186687000	-3.580364000
C	-0.750951000	3.208015000	-0.275534000
C	-0.467179000	2.663464000	-2.676976000
C	0.479965000	3.900882000	-0.293576000
C	0.740662000	3.343204000	-2.695136000
H	0.834843000	4.370493000	0.619789000
C	1.220257000	3.979008000	-1.456870000
H	1.588317000	3.218608000	-4.755550000
C	1.682257000	3.571134000	-3.737025000
C	2.447514000	4.564979000	-1.831502000
C	2.734239000	4.328501000	-3.189879000
O	3.406313000	5.292434000	-1.206166000
C	4.003335000	4.977922000	-3.429046000
C	4.362028000	5.546724000	-2.185340000
H	4.628848000	4.728807000	-5.484183000
C	4.868535000	5.149891000	-4.513570000
C	5.523499000	6.265809000	-1.979483000
H	5.760872000	6.685585000	-1.008830000
C	6.045578000	5.872107000	-4.327081000
C	6.369743000	6.422354000	-3.079887000
H	6.724373000	6.011756000	-5.161823000
H	7.292901000	6.979938000	-2.963751000

Dicyclopenta[*b,g*]naphthalene

Zero-point correction=	0.202207 (Hartree/Particle)
Thermal correction to Energy=	0.213072
Thermal correction to Enthalpy=	0.214016
Thermal correction to Gibbs Free Energy=	0.166352
Sum of electronic and zero-point Energies=	-615.597066

H	-2.5079050000	1.2190590000	0.0000000000
H	-2.5079050000	-1.2190530000	0.0000000000
H	-2.1717660000	-4.1356330000	0.0000000000
H	-2.1717650000	4.1356390000	0.0000000000
C	-1.4203360000	-1.2300650000	0.0000000000
C	-1.4203350000	1.2300690000	0.0000000000
C	-1.1465790000	3.7872980000	0.0000000000
C	-1.1465790000	-3.7872900000	0.0000000000
C	-0.7284950000	2.4304470000	0.0000000000
C	-0.7284950000	-2.4304460000	0.0000000000
C	-0.7263040000	-0.0000010000	0.0000000000
H	-0.0000090000	-5.6813580000	0.0000000000
C	-0.0000040000	-4.5989100000	0.0000000000
C	0.0000040000	4.5989100000	0.0000000000
H	0.0000090000	5.6813580000	0.0000000000
C	0.7263040000	0.0000010000	0.0000000000
C	0.7284950000	2.4304460000	0.0000000000
C	0.7284950000	-2.4304470000	0.0000000000
C	1.1465790000	3.7872900000	0.0000000000
C	1.1465790000	-3.7872980000	0.0000000000
C	1.4203350000	-1.2300690000	0.0000000000
C	1.4203360000	1.2300650000	0.0000000000
H	2.1717650000	-4.1356390000	0.0000000000
H	2.1717660000	4.1356330000	0.0000000000
H	2.5079050000	1.2190530000	0.0000000000
H	2.5079050000	-1.2190590000	0.0000000000

4.2 TD-DFT Calculations for UV-Vis Spectra. The same geometries used above for the NICS-XY scans were used to calculate the vertical transitions for the IDBFs and *syn*-IIDBF. Calculations were performed at the TD-B3LYP/6-311++G** level for the IDBFs and TD-B3LYP/ 6-311+G* for *syn*-IIDBF. HOMO-LUMO levels in Table E2 were generated from the ground state geometry using B3LYP/6-311++G** for the IDBFs and B3LYP/6-311+G* for *syn*-IIDBF.

Table E2. Calculated optical data and HOMO-LUMO energy gaps for compounds **6-8**

	λ_{max} (nm)	f	configuration	HOMO (eV)	LUMO (eV)	E_{gap} (eV)
<i>syn</i> -IDBF (6')	552	0.2741	H-1→L (87%)	-5.273	-3.272	2.001
			H→L+1 (12%)			
<i>anti</i> -IDBF (7')	617	0.6299	H-1→L (97%)	-5.291	-3.513	1.778
<i>syn</i> -IIDBF (8')	729	0.8236	H→L (100%)	-5.076	-3.590	1.486

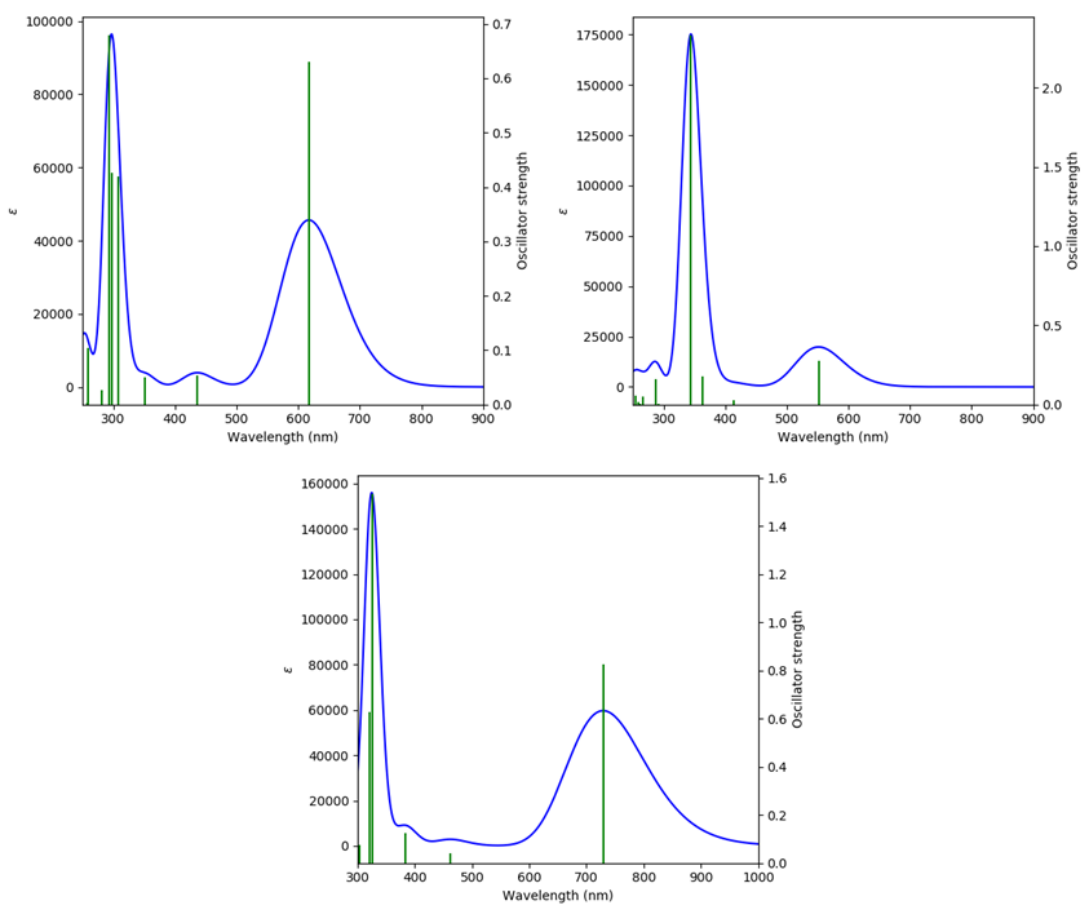


Figure E11. TD-DFT predicted UV-Vis spectra for (top-left) *syn*-IDBF (**6'**), (top-right) *anti*-IDBF (**7'**), and (bottom) *syn*-IIDBF (**8'**).

4.3 Diradical Character (y_0) and ΔE_{ST} Calculations. Geometry optimization and frequency analysis for the singlet and triplet states were performed at the RB3LYP and UB3LYP levels, respectively, using the 6-311G* basis set. Vertical and adiabatic ΔE_{ST} values were evaluated at the SF-NC-TDDFT PBE50/6-311G* level, where ZPVE corrections for the singlet and triplet states were estimated from the results of the frequency analysis calculations at the RB3LYP and UB3LYP levels, respectively. CASCI(2,2) calculations for the estimations of VCI parameters were performed using the molecular orbitals obtained at the tuned-LC-RBLYP/6-311G* level, where an optimal range-separating parameter μ for each system was determined by IP-tuning scheme for N -electron system. Diradical characters y were evaluated at the PUHF/6-311G* [denoted as $y(\text{PUHF})$] and tuned-LC-RBLYP-CASCI(2,2)/6-311G* [denoted as $y(\text{CASCI})$] levels.

Table E3. Summary of calculation results for *anti/syn*-IIDBTs and IIDBFs.

	<i>anti</i> -IIDBT ^a	<i>syn</i> -IIDBT ^a	<i>anti</i> -IIDBF	<i>syn</i> -IIDBF
<i>y</i> (PUHF) [-]	0.613	0.658	0.623	0.682
Vertical ΔE_{ST} [kcal mol ⁻¹]	-11.65	-11.09	-11.99	-10.32
Adiabatic ΔE_{ST} [kcal mol ⁻¹]	-9.37	-8.84	-9.91	-8.56
Adiabatic ΔE_{ST} (+ZPVE) [kcal mol ⁻¹]	-8.77	-8.06	-9.10	-7.68
Tuned value of μ [bohr ⁻¹]	0.1444	0.1434	0.1479	0.1465
<i>y</i> (CASCI) [-]	0.203	0.210	0.216	0.218
Vertical ΔE_{ST} (CASCI) [kcal mol ⁻¹]	-19.8	-17.5	-20.1	-16.1
$ t_{ab} $ [eV]	1.031	0.905	1.058	0.865
$f_{ST}(y)$ [-]	-0.655	-0.632	-0.611	-0.603
$U/2 = K_{gu}^M$ [eV]	1.563	1.404	1.677	1.380
$(U/2)f_{ST}(y)$ [eV]	-1.025	-0.887	-1.024	-0.833
J_{gg}^M [eV]	4.417	4.225	4.701	4.119
J_{uu}^M [eV]	4.755	4.394	4.807	4.314
J_{gu}^M [eV]	4.420	4.179	4.603	4.084
$2K_{ab}$ [eV]	0.165	0.130	0.076	0.066

^aData from reference [15].

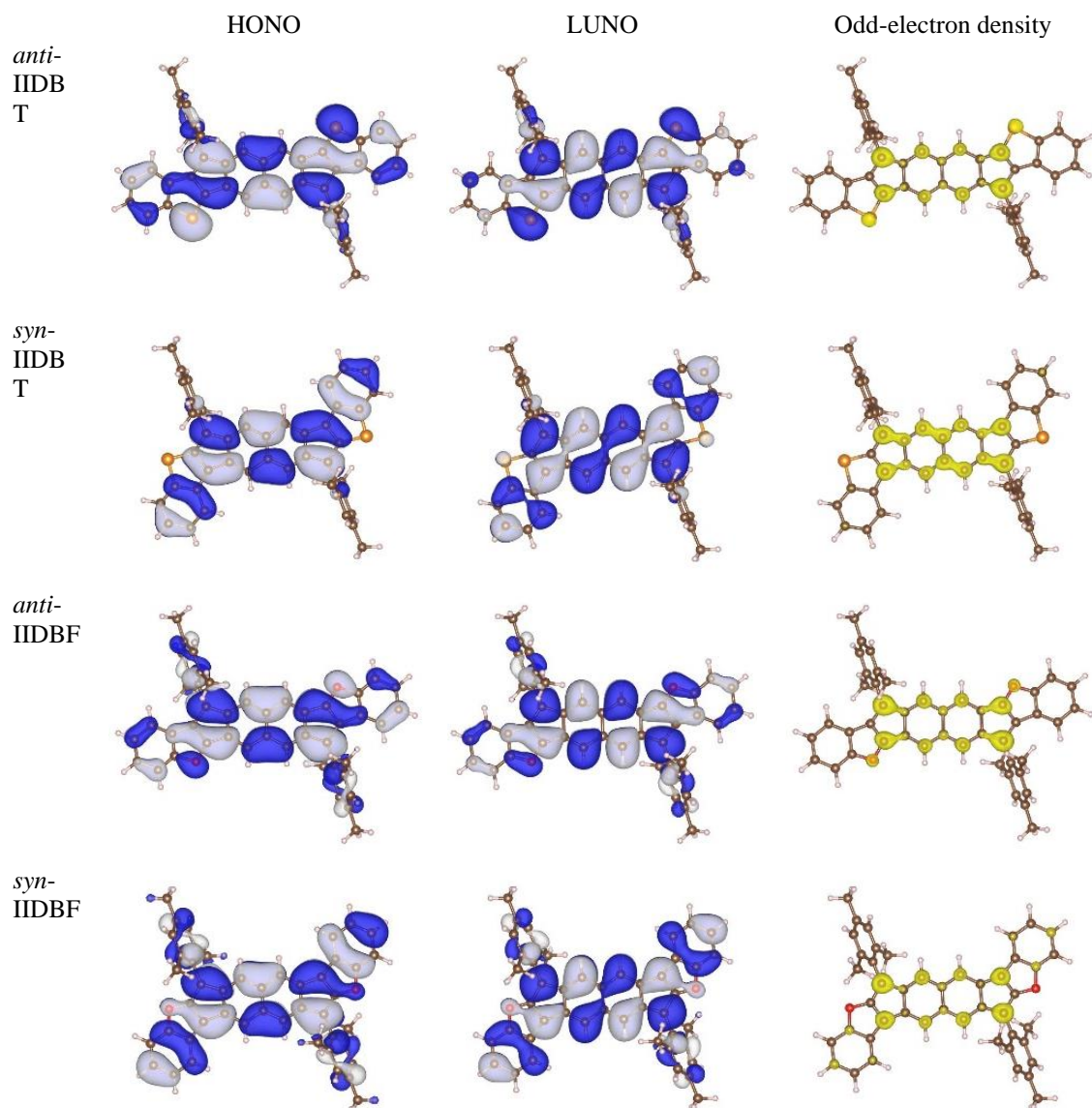
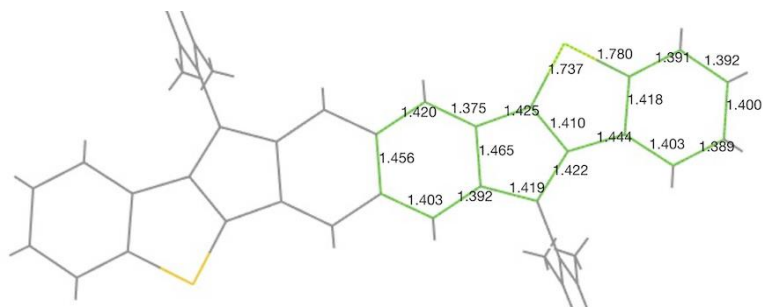
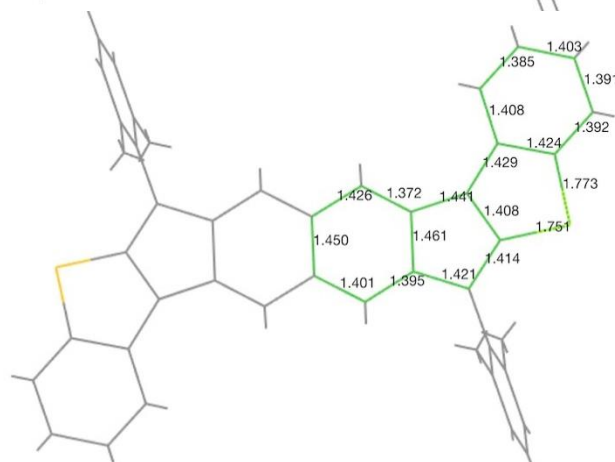


Figure E12. Spatial distributions of natural orbitals (NOs) and odd-electron density calculated at the tuned-LC-RBLYP-CASCI(2,2)/6-311G* level. White and blue meshes for NO maps represent the isosurfaces with the contour values of ± 0.01 a.u. Yellow mesh for odd-electron density maps represents the isosurface with the contour value of 0.001 a.u.

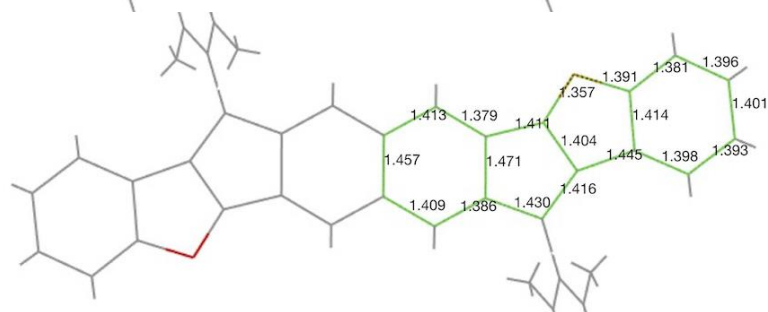
anti-IIDBT



syn-IIDBT



anti-IIDBF



syn-IIDBF

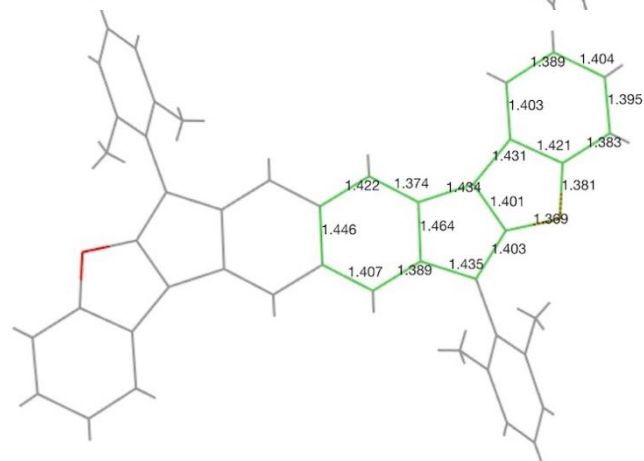


Figure E13. Bond lengths (Å) of selected bonds for the singlet state calculated at the RB3LYP/6-311G* level.

7. References

- [1] Knall, A.-C.; Ashraf, R. S.; Nikolka, M.; Nielsen, C. B.; Purushothaman, B.; Sadhanala, A.; Hurhangee, M.; Broch, K.; Harkin, D. J.; Novák, J.; Neophytou, M.; Hayoz, P.; Siringhaus, H.; McCulloch, I. *Adv. Funct. Mater.* **2016**, *26*, 6961–6969.
- [2] Bain, G. A.; Berry, J. F. *J. Chem. Educ.* **2008**, *85*, 532–536.
- [3] Bleaney, B.; Bowers, K. D. *Proc. R. Soc. Lond. A* **1952**, *214*, 451–465.
- [4] CrysAlisPro; Rigaku OD, The Woodlands, TX, 2015.
- [5] Sheldrick, G. M. *Acta Cryst.* **2015**, *A71*, 3–8.
- [6] Sheldrick, G.M. *Acta Cryst.* **2008**, *A64*, 112–122.
- [7] Müller, P. *Crystallography Reviews* **2009**, *15*, 57–83.
- [8] Dolomanov, O. V.; Bourhis, L. J.; Gildea, R. J.; Howard, J. A. K.; Puschmann, H. J. *Appl. Cryst.* **2009**, *42*, 339–341.
- [9] Sheldrick, G. M. *Bruker/Siemens Area Detector Absorption Correction Program*, Bruker AXS, Madison, WI, 1998.
- [10] Sheldrick, G. M. *Acta Cryst.* **2015**, *C71*, 3–8.
- [11] Frisch, M. J.; Trucks, G. W.; Schlegel, H. B.; Scuseria, G. E.; Robb, M. A.; Cheeseman, J. R.; Scalmani, G.; Barone, V.; Mennucci, B.; Petersson, G. A.; Nakatsuji, H.; Caricato, M.; Li, X.; Hratchian, H. P.; Izmaylov, A. F.; Bloino, J.; Zheng, G.; Sonnenberg, J. L.; Hada, M.; Ehara, M.; Toyota, K.; Fukuda, R.; Hasegawa, J.; Ishida, M.; Nakajima, T.; Honda, Y.; Kitao, O.; Nakai, H.; Vreven, T.; Montgomery, Jr., J. A.; Peralta, J. E.; Ogliaro, F.; Bearpark, M.; Heyd, J. J.; Brothers, E.; Kudin, K. N.; Staroverov, V. N.; Keith, T.; Kobayashi, R.; Normand, J.; Raghavachari, K.; Rendell, A.; Burant, J. C.; Iyengar, S. S.; Tomasi, J.; Cossi, M.; Rega, N.; Millam, J. M.; Klene, M.; Knox, J. E.; Cross, J. B.; Bakken, V.; Adamo, C.; Jaramillo, J.; Gomperts, R.; Stratmann, R. E.; Yazyev, O.; Austin, A. J.; Cammi, R.; Pomelli, C.; Ochterski, J. W.; Martin, R. L.; Morokuma, K.; Zakrzewski, V. G.; Voth, G. A.; Salvador, P.; Dannenberg, J. J.; Dapprich, S.; Daniels, A.

D.; Farkas, O.; Foresman, J. B.; Ortiz, J. V.; Cioslowski, J.; and Fox, D. J. Gaussian 09, Revision E.01; Gaussian, Inc.: Wallingford CT, 2013.

[12] Rahalkar, A.; Stanger, A. http://schulich.technion.ac.il/Amnon_Stanger.htm

[13] (a) Stanger, A. *J. Org. Chem.* **2006**, *71*, 883–893; (b) Stanger, A. *J. Org. Chem.* **2010**, *75*, 2281–2288; (c) Gershoni-Poranne, R.; Stanger, A. *Chem.–Eur. J.* **2014**, *20*, 5673–5688.

[14] Marshall, J. L.; Uchida, K.; Frederickson, C. K.; Schütt, C.; Zeidell, A. M.; Goetz, K. P.; Finn, T. W.; Jarolimek, K.; Zakharov, L. N.; Risko, C.; Herges, R.; Jurchescu, O. D.; Haley, M. M. *Chem. Sci.* **2016**, *7*, 5547–5558.

[15] Barker, J. E.; Dressler, J. J.; Cárdenas Valdivia, A.; Kishi, R.; Strand, E. T.; Zakharov, L. N.; MacMillan, S. N.; Gómez-García, C. J.; Nakano, M.; Casado, J.; Haley, M. M. *J. Am. Chem. Soc.* **2020**, *142*, 1548–1555.

REFERENCES CITED

Chapter I.

1. Chase, D. T.; Rose, B. D.; McClintock, S. P.; Zakharov, L. N.; Haley, M. M. Indeno[1,2-b]Fluorenes: Fully Conjugated Antiaromatic Analogues of Acenes. *Angew. Chem. Int. Ed.* **2011**, *50*, 1127–1130.
2. Frederickson, C. K.; Rose, B. D.; Haley, M. M. Explorations of the Indenofluorenes and Expanded Quinoidal Analogues. *Acc. Chem. Res.* **2017**, *50*, 977–987.
3. Fix, A. G.; Deal, P. E.; Vonnegut, C. L.; Rose, B. D.; Zakharov, L. N.; Haley, M. M. Indeno[2,1-*c*]Fluorene: A New Electron-Accepting Scaffold for Organic Electronics. *Org. Lett.* **2013**, *15*, 1362–1365.
4. Shimizu, A.; Tobe, Y. Indeno[2,1-*a*]Fluorene: An Air-Stable Ortho-Quinodimethane Derivative. *Angew. Chem. Int. Ed.* **2011**, *50*, 6906–6910.
5. Shimizu, A.; Kishi, R.; Nakano, M.; Shiomi, D.; Sato, K.; Takui, T.; Hisaki, I.; Miyata, M.; Tobe, Y. Indeno[2,1-*b*]Fluorene: A 20- π -Electron Hydrocarbon with Very Low-Energy Light Absorption. *Angew. Chem. Int. Ed.* **2013**, *52*, 6076–6079.
6. Dressler, J. J.; Zhou, Z.; Marshall, J. L.; Kishi, R.; Takamuku, S.; Wei, Z.; Spisak, S. N.; Nakano, M.; Petrukhina, M. A.; Haley, M. M. Synthesis of the Unknown Indeno[1,2-*a*]Fluorene Regioisomer: Crystallographic Characterization of Its Dianion. *Angew. Chem. Int. Ed.* **2017**, *56*, 15363–15367.
7. Zhou, Q.; Carroll, P. J.; Swager, T. M. Synthesis of Diacetylene Macrocycles Derived from 1,2-Diethynyl Benzene Derivatives: Structure and Reactivity of the Strained Cyclic Dimer. *J. Org. Chem.* **1994**, *59*, 1294–1301.
8. Deuschel, W. Fluorenacene und Fluorenaphene. Synthesen in der Indenofluorenreihe. II. Endo-*cis*-Fluorenaphen (Indeno-(2,1:1, 2)-fluoren) und *trans*-Fluorenacen (Indeno-(1,2:2, 3)-fluoren). *Helv. Chim. Acta* **1951**, *34*, 2403–2416.
9. Ebel, F.; Deuschel, W. *trans*-Fluorenacendion, ein neues, verküpbares Diketon. *Chem. Ber.* **1956**, *89*, 2794–2799.
10. Merlet, S.; Birau, M.; Wang, Z. Y. Synthesis and Characterization of Highly Fluorescent Indenofluorenes. *Org. Lett.* **2002**, *4*, 2157–2159.
11. Rose, B. D.; Vonnegut, C. L.; Zakharov, L. N.; Haley, M. M. Fluoreno[4,3-*c*]Fluorene: A Closed-Shell, Fully Conjugated Hydrocarbon. *Org. Lett.* **2012**, *14*, 2426–2429.

12. Rudebusch, G. E.; Zafra, J. L.; Jorner, K.; Fukuda, K.; Marshall, J. L.; Arrechea-Marcos, I.; Espejo, G. L.; Ponce Ortiz, R.; Gómez-García, C. J.; Zakharov, L. N.; Nakano, M.; Ottosson, H.; Casado, J.; Haley, M. M. Diindeno-Fusion of an Anthracene as a Design Strategy for Stable Organic Biradicals. *Nature Chem* **2016**, *8*, 753–759.
13. Frederickson, C. K.; Zakharov, L. N.; Haley, M. M. Modulating Paratropicity Strength in Diareno-Fused Antiaromatics. *J. Am. Chem. Soc.* **2016**, *138*, 16827–16838.
14. Young, B. S.; Chase, D. T.; Marshall, J. L.; Vonnegut, C. L.; Zakharov, L. N.; Haley, M. M. Synthesis and Properties of Fully-Conjugated Indacenedithiophenes. *Chem. Sci.* **2014**, *5*, 1008–1014.
15. Marshall, J. L.; Uchida, K.; Frederickson, C. K.; Schütt, C.; Zeidell, A. M.; Goetz, K. P.; Finn, T. W.; Jarolimek, K.; Zakharov, L. N.; Risko, C.; Herges, R.; Jurchescu, O. D.; Haley, M. M. Indacenodibenzothiophenes: Synthesis, Optoelectronic Properties and Materials Applications of Molecules with Strong Antiaromatic Character. *Chem. Sci.* **2016**, *7*, 5547–5558.
16. Gershoni-Poranne, R.; Stanger, A. The NICS-XY-Scan: Identification of Local and Global Ring Currents in Multi-Ring Systems. *Chem. Eur. J.* **2014**, *20*, 5673–5688.
17. Barker, J. E.; Frederickson, C. K.; Jones, M. H.; Zakharov, L. N.; Haley, M. M. Synthesis and Properties of Quinoidal Fluorenofluorenes. *Org. Lett.* **2017**, *19*, 5312–5315.
18. Frederickson, C.; Barker, J.; Dressler, J.; Zhou, Z.; Hanks, E.; Bard, J.; Zakharov, L.; Petrukhina, M.; Haley, M. Synthesis and Characterization of a Fluorescent Dianthraceno-indacene. *Synlett* **2018**, *29*, 2562–2566.
19. Hafner, K.; Stowasser, B.; Krimmer, H.-P.; Fischer, S.; Böhm, M. C.; Lindner, H. J. Synthesis and Properties of 1,3,5,7-Tetra-Tert-Butyl-s-Indacene. *Angew. Chem. Int. Ed. Engl.* **1986**, *25*, 630–632.
21. Dunitz, J. D.; Krüger, C.; Irgartinger, H.; Maverick, E. F.; Wang, Y.; Nixdorf, M. Equilibrium Structure, Stabilized Transition State, or Disorder in the Crystal? Studies of the Antiaromatic Systems Tetra-Tert-Butyl-s-Indacene and Tetra-Tert-Butylcyclobutadiene by Low-Temperature Crystal Structure Analysis. *Angew. Chem. Int. Ed. Engl.* **1988**, *27*, 387–389.
21. Nendel, M.; Goldfuss, B.; Houk, K. N.; Hafner, K. S-Indacene, a Quasi-Delocalized Molecule with Mixed Aromatic and Anti-Aromatic Character. *Journal of Molecular Structure: THEOCHEM* **1999**, *461–462*, 23–28.

22. Hertwig, R. H.; Holthausen, M. C.; Koch, W.; Maksi, Z. B. S-Indacene: A Delocalized, Formally Antiaromatic 12π Electron System. *Angew. Chem. Int. Ed. Engl.* **1994**, *33*, 1192–1194.
23. Soriano Jartín, R.; Ligabue, A.; Soncini, A.; Lazzeretti, P. Ring Currents and Magnetic Properties of *s*-Indacene, an Archetypal Paratropic, Non-Antiaromatic Molecule. *J. Phys. Chem. A* **2002**, *106*, 11806–11814.
24. There has been disagreement among former graduate students in and adjacent to the Haley group as to who first proposed the IDBTDOs. Regardless, the work was excellently completed and reported in reference 25 by Justin Dressler and rotation student Hannah Hashimoto.
25. Barker, J. E.; Price, T. W.; Karas, L. J.; Kishi, R.; MacMillan, S. N.; Zakharov, L. N.; Gómez-García, C. J.; Wu, J. I.; Nakano, M.; Haley, M. M. A Tale of Two Isomers: Enhanced Antiaromaticity/Diradical Character versus Deleterious Ring-Opening of Benzofuran-fused *s*-Indacenes and Dicyclopenta[*b,g*]naphthalenes. *Angew. Chem. Int. Ed.* **2021**, *submitted*.
26. Dressler, J. J.; Barker, J. E.; Karas, L. J.; Hashimoto, H. E.; Kishi, R.; Zakharov, L. N.; MacMillan, S. N.; Gómez-García, C. J.; Nakano, M.; Wu, J. I.; Haley, M. M. Late-Stage Modification of Electronic Properties of Antiaromatic and Diradicaloid Indeno[1,2-*b*]fluorene Analogues via Sulfur Oxidation. *J. Org. Chem.* **2020**, *85*, 10846–10857.
27. Warren, G. I.; Barker, J. E.; Zakharov, L. N.; Haley, M. M. Enhancing the Antiaromaticity of *s*-Indacene Through Naphthothiophene Fusion. *Org. Lett.* **2021**, *submitted*.
28. *The IUPAC Compendium of Chemical Terminology: The Gold Book*, 4th ed.; Gold, V., Ed.; International Union of Pure and Applied Chemistry (IUPAC): Research Triangle Park, NC, 2019. <https://doi.org/10.1351/goldbook>.
29. Nakano, M.; Kishi, R.; Nitta, T.; Kubo, T.; Nakasuji, K.; Kamada, K.; Ohta, K.; Champagne, B.; Botek, E.; Yamaguchi, K. Second Hyperpolarizability (γ) of Singlet Diradical System: Dependence of γ on the Diradical Character. *J. Phys. Chem. A* **2005**, *109*, 885–891.
30. Nakano, M. Open-Shell-Character-Based Molecular Design Principles: Applications to Nonlinear Optics and Singlet Fission. *Chem. Rec.* **2016**, *17*, 27–62.
31. Muhammad, S.; Nakano, M.; Al-Sehemi, A. G.; Kitagawa, Y.; Irfan, A.; Chaudhry, A. R.; Kishi, R.; Ito, S.; Yoneda, K.; Fukuda, K. Role of a singlet diradical character in carbon nanomaterials: a novel hot spot for efficient nonlinear optical materials. *Nanoscale*, **2016**, *8*, 17998–18020.

32. Huang, Y.; Egap, E. Open-shell organic semiconductors: an emerging class of materials with novel properties. *Polym. J.* **2018**, *50*, 603-614.
33. Dressler, J. J.; Teraoka, M.; Espejo, G. L.; Kishi, R.; Takamuku, S.; Gómez-García, C. J.; Zakharov, L. N.; Nakano, M.; Casado, J.; Haley, M. M. *Nat. Chem.* **2018**, *10*, 1134-1140.
34. Zeng, Z.; Shi, X.; Chi, C.; López Navarrete, J. T.; Casado, J.; Wu, J. Pro-Aromatic and Anti-Aromatic π -Conjugated Molecules: An Irresistible Wish to Be Diradicals. *Chem. Soc. Rev.* **2015**, *44*, 6578–6596.
35. Barker, J. E.; Dressler, J. J.; Cárdenas Valdivia, A.; Kishi, R.; Strand, E. T.; Zakharov, L. N.; MacMillan, S. N.; Gómez-García, C. J.; Nakano, M.; Casado, J.; Haley, M. M. Molecule Isomerism Modulates the Diradical Properties of Stable Singlet Diradicaloids. *J. Am. Chem. Soc.* **2020**, *142*, 1548–1555.
36. Hiyashi, H.; Barker, J. E.; Valdivia, A. C.; Kishi, R.; MacMillan, S. N.; Gómez-García, C. J.; Miyauchi, H.; Nakamura, Y.; Nakano, M.; Kato, S.; Haley, M. M.; Casado, J. *J. Am. Chem. Soc.* **2020**, *142*, 20444-20445.
37. Dressler, J. J.; Cárdenas Valdivia, A.; Kishi, R.; Rudebusch, G. E.; Ventura, A. M.; Chastain, B. E.; Gómez-García, C. J.; Zakharov, L. N.; Nakano, M.; Casado, J.; Haley, M. M. Diindenoanthracene Diradicaloids Enable Rational, Incremental Tuning of Their Singlet-Triplet Energy Gaps. *Chem* **2020**, *6*, 1353–1368.

Chapter II.

1. Anthony, J. E.; Facchetti, A.; Heeney, M.; Marder, S. R.; Zhan, X. *Adv. Mater.* **2010**, *22*, 3876–3892.
2. Rosenberg, M.; Dahlstrand, C.; Kilsa, K.; Ottosson, H. *Chem. Rev.* **2014**, *114*, 5379–5425.
3. (a) Nishinaga, T.; Ohmae, T.; Araa, K.; Takase, M.; Iyoda, M.; Atai, T.; Kunugi, Y. *Chem. Commun.* **2013**, *49*, 5354–5356. (b) Cao, J.; London, G.; Dumele, O.; von Wantoch Rekowski, M.; Trapp, N.; Ruhlmann, L.; Boudon, C.; Stanger, A.; Diederich, F. *J. Am. Chem. Soc.* **2015**, *137*, 7178–7188. (c) Jin, Z.; Teo, Y. C.; Zulaybar, N. G.; Smith, M. D.; Xia, Y. *J. Am. Chem. Soc.* **2017**, *139*, 1806–1809.
4. (a) Chase, D. T.; Rose, B. D.; McClintock, S. P.; Zakharov, L. N.; Haley, M. M. *Angew. Chem., Int. Ed.* **2011**, *50* 1127–1130. (b) Chase, D. T.; Fix, A. G.; Rose, B. D.; Weber, C. D.; Nobusue, S.; Stockwell, C. E.; Zakharov, L. N.; Lonergan, M. C.; Haley, M. M. *Angew. Chem., Int. Ed.* **2011**, *50*, 11103–11106. (c) Chase, D. T.; Fix, A. G.; Kang, S. J.; Rose, B. D.; Weber, C. D.; Zhong, Y.; Zakharov, L. N.; Lonergan, M. C.; Nuckolls, C.; Haley, M. M. *J. Am. Chem. Soc.* **2012**, *134*, 10349–10352.

5. Frederickson, C. K.; Rose, B. D.; Haley, M. M. *Acc. Chem. Res.* **2017**, *50*, 977–987.
6. (a) Fix, A. G.; Deal, D. E.; Vonnegut, C. L.; Rose, B. D.; Zakharov, L. N.; Haley, M. M. *Org. Lett.* **2013**, *15*, 1362–1365. (b) Shimizu, A.; Tobe, Y. *Angew. Chem., Int. Ed.* **2011**, *50*, 6906–6910. (c) Shimizu, A.; Kishi, T.; Nakano, M.; Shiomi, D.; Sato, K.; Takui, T.; Hisaki, I.; Miyata, M.; Tobe, Y. *Angew. Chem., Int. Ed.* **2013**, *52*, 6076–6079.
7. Frederickson, C. K.; Zakharov, L. N.; Haley, M. M. *J. Am. Chem. Soc.* **2016**, *138*, 16827–16838.
8. (a) Young, B. S.; Chase, D. T.; Marshall, J. L.; Vonnegut, C. L.; Zakharov, L. N.; Haley, M. M. *Chem. Sci.* **2014**, *5*, 1008–1014. (b) Rudebusch, G. E.; Fix, A. G.; Henthorn, H. A.; Vonnegut, C. L.; Zakharov, L. N.; Haley, M. M. *Chem. Sci.* **2014**, *5*, 3627–3633. (c) Marshall, J. L.; Uchida, K.; Frederickson, C. F.; Schütt, C.; Zeidell, A. M.; Goetz, K. P.; Finn, T. W.; Jarolimek, K.; Zakharov, L. N.; Risko, C.; Herges, R.; Jurchescu, O. D.; Haley, M. M. *Chem. Sci.* **2016**, *7*, 5547–5558.
9. (a) Rudebusch, G. E.; Zafra, J. L.; Jorner, K.; Fukuda, K.; Marshall, J. L.; Arrechea-Marcos, I.; Espejo, G.L.; Ortiz, R. P.; Gómez-García, C. J.; Zakharov, L. N.; Nakano, M.; Ottosson, H.; Casado, J.; Haley, M. M. *Nat. Chem.* **2016**, *8*, 753–759. (b) Hu, P.; Lee, S.; Herng, T. S.; Aratani, N.; Goncalves, T. P.; Qi, Q.; Shi, X.; Yamada, H.; Huang, K.-W.; Ding, J.; Kim, D.; Wu, J. *J. Am. Chem. Soc.* **2016**, *138*, 1065–1077. (c) Miyoshi, H.; Nobusue, S.; Shimizu, A.; Hisaki, I.; Miyata, M.; Tobe, Y. *Chem. Sci.* **2014**, *5*, 163–168.
10. Rose, B. D.; Vonnegut, C. L.; Zakharov, L. N.; Haley, M. M. *Org. Lett.* **2012**, *14*, 2426–2429.
11. Fukuda, K.; Nagami, T.; Fujiyoshi, J.-Y.; Nakano, M. *J. Phys. Chem. A* **2015**, *119*, 10620–10627.
12. Miyoshi, H.; Miki, M.; Hirano, S.; Shimizu, A.; Kishi, R.; Fukuda, K.; Shiomi, D.; Sato, K.; Takui, T.; Hisaki, I.; Nakano, M.; Tobe, Y. *J. Org. Chem.* **2017**, *82*, 1380–1388.
13. Liu, J.; Ma, J.; Zhang, K.; Ravat, P.; Machata, P.; Avdoshenko, S.; Hennersdorf, F.; Komber, H.; Pisula, W.; Weigand, J. J.; Popov, A. A.; Berger, R.; Müllen, K.; Feng, X. *J. Am. Chem. Soc.* **2017**, *139*, 7513–7521.
14. Kubo, T.; Shimizu, A.; Uruichi, M.; Yakushi, K.; Nakano, M.; Shiomi, D.; Sato, K.; Takui, T.; Morita, Y.; Nakasuji, K. *Org. Lett.* **2007**, *9*, 81–84.

15. (a) Shinamura, S.; Osaka, I.; Miyazaki, E.; Nakao, A.; Yamagishi, M.; Takeya, J.; Takimiya, K. *J. Am. Chem. Soc.* **2011**, *133*, 5024–5035. (b) Hu, P.; Lee, S.; Park, K. H.; Das, S.; Heng, T. S.; Goncalves, T. P.; Huang, K.-W.; Ding, J.; Kim, D.; Wu, J. *J. Org. Chem.* **2016**, *81*, 2911–2919. (c) Dong, S.; Heng, T.-S.; Gopalakrishna, T. Y.; Phan, H.; Lim, Z. L.; Hu, P.; Webster, R. D.; Ding, J.; Chi, C. *Angew. Chem., Int. Ed.* **2016**, *55*, 9316–9320.
16. Knall, A.-C.; Ashraf, R. S.; Nikolka, M.; Nielsen, C. B.; Purushothaman, B.; Sadhanala, A.; Hurhangee, M.; Broch, K.; Harkin, D. J.; Novák, J.; Neophytou, M.; Hayoz, P.; Siringhaus, H.; McCulloch, I. *Adv. Funct. Mater.* **2016**, *26*, 6961–6969.
17. Anton, U.; Adam, M.; Wagner, M.; Qi-Lin, Z.; Müllen, K. *Chem. Ber.* **1993**, *126*, 517–521.
18. Frisch, M. J.; Trucks, G. W.; Schlegel, H. B.; Scuseria, G. E.; Robb, M. A.; Cheeseman, J. R.; Scalmani, G.; Barone, V.; Men-nucci, B.; Petersson, G. A.; Nakatsuji, H.; Caricato, M.; Li, X.; Hratchian, H. P.; Izmaylov, A. F.; Bloino, J.; Zheng, G.; Son-nenberg, J. L.; Hada, M.; Ehara, M.; Toyota, K.; Fukuda, R.; Hasegawa, J.; Ishida, M.; Nakajima, T.; Honda, Y.; Kitao, O.; Nakai, H.; Vreven, T.; Montgomery, J. A., Jr.; Peralta, J. E.; Ogliaro, F.; Bearpark, M.; Heyd, J. J.; Brothers, E.; Kudin, K. N.; Staroverov, V. N.; Kobayashi, R.; Normand, J.; Raghavachari, K.; Rendell, A.; Burant, J. C.; Iyengar, S. S.; Tomasi, J.; Cossi, M.; Rega, N.; Millam, N. J.; Klene, M.; Knox, J. E.; Cross, J. B.; Bakken, V.; Adamo, C.; Jaramillo, J.; Gomperts, R.; Stratmann, R. E.; Yazyev, O.; Austin, A. J.; Cammi, R.; Pomelli, C.; Ochterski, J. W.; Martin, R. L.; Morokuma, K.; Zakrzewski, V. G.; Voth, G. A.; Salvador, P.; Dannenberg, J. J.; Dapprich, S.; Daniels, A. D.; Farkas, Ö.; Foresman, J. B.; Ortiz, J. V.; Cioslowski, J.; Fox, D. J. Gaussian 09, revision D.01; Gaussian Inc.: Wallingford, CT, 2010.
19. (a) Zeng, Z.; Shi, X.; Chi, C.; López Navarrete, J. T.; Casado, J.; Wu, J. *Chem. Soc. Rev.* **2015**, *44*, 6578–6596. (b) Di Motta, S.; Negri, F.; Fazzi, D.; Castiglioni, C.; Canesi, E. V. *J. Phys. Chem. Lett.* **2010**, *1*, 3334–3339.
20. (a) Rahalkar, A.; Stanger, A. Aroma; <http://chemistry.technion.ac.il/members/amnon-stanger/> (accessed 08/15/17). (b) Stanger, A. *J. Org. Chem.* **2006**, *71*, 883–893. (c) Stanger, A. *J. Org. Chem.* **2010**, *75*, 2281–2288. (d) Gershoni-Poranne R; Stanger, A. *Chem. Eur. J.* **2014**, *20*, 5673–5688.
21. All γ values were calculated with the long range correlation correction method LC-UBLYP/6-311+G(d,p) with range separating parameter μ of 0.33 bohr⁻¹, as described in reference 11.

Chapter III

1. Clar, E. *Polycyclic Hydrocarbons, Vols. 1 and 2*; John Wiley: New York, 1964.

2. Dediu, V. A.; Hueso, L. E.; Bergenti, I.; Taliani, C. Spin route to organic electronics. *Nat. Mater.* **2009**, *8*, 707–716.
3. Abe, M., Diradicals. *Chem. Rev.* **2013**, *113*, 7011–7088.
4. (a) Muhammad, S.; Nakano, M.; Al-Sehemi, A. G.; Kitagawa, Y.; Irfan, A.; Chaudhry, A. R.; Kishi, R.; Ito, S; Yoneda, K.; Fukuda, K. Role of a singlet diradical character in carbon nanomaterials: a novel hot spot for efficient nonlinear optical materials. *Nanoscale* **2016**, *8*, 17998–18020. b) Nakano, M. Open-Shell-Character-Based Molecular Design Principles: Applications to Nonlinear Optics and Singlet Fission. *Chem. Rec.* **2017**, *17*, 27–62. (c) Huang, Y.; Egap, E. Open-shell organic semiconductors: An emerging class of materials with novel properties. *Polym. J.* **2018**, *50*, 603–614.
5. (a) Zeng, Z.; Shi, X.; Chi, C.; Lopez Navarrete, J. T.; Casado, J.; Wu, J. Pro-aromatic and anti-aromatic π -conjugated molecules: an irresistible wish to be diradicals. *Chem. Soc. Rev.* **2015**, *44*, 6578–6596. (b) Shi, X.; Chi, C. Heterocyclic Quinodimethanes. *Top. Curr. Chem.* **2017**, *375*, 169–207. (c) Casado, J. Para-Quinodimethanes: A Unified Review of the Quinoidal-Versus-Aromatic Competition and its Implications. *Top. Curr. Chem.* **2017**, *375*, 209–248. (d) Tobe, Y. Quinodimethanes Incorporated in Non-Benzenoid Aromatic or Antiaromatic Frameworks. *Top. Curr. Chem.* **2017**, *375*, 107–168. (e) Gopalakrishna, T. Y.; Zeng, W.; Lu, X.; Wu, J. From open-shell singlet diradicaloids to polyradicaloids. *Chem. Commun.* **2018**, *54*, 2186–2199.
6. (a) Nakano, M.; Kishi, R.; Ohta, S.; Takahashi, H.; Kubo, T.; Kamada, K.; Ohta, K.; Botek, E.; Champagne, B. Relationship between Third-Order Nonlinear Optical Properties and Magnetic Interactions in Open-Shell Systems: A New Paradigm for Nonlinear Optics. *Phys. Rev. Lett.* **2007**, *99*, 033001-1–033001-4. (b) Nakano, M.; Champagne, B. Diradical character dependences of the first and second hyperpolarizabilities of asymmetric open-shell singlet systems. *J. Chem. Phys.* **2013**, *138*, 244306-1–244306-13.

7. (a) Nakano, M.; Minami, T.; Yoneda, K.; Muhammad, S.; Kishi, R.; Shigeta, Y.; Kubo, T.; Rougier, L.; Champagne, B.; Kamada, K.; Ohta, K. Giant Enhancement of the Second Hyperpolarizabilities of Open-Shell Singlet Polyaromatic Diphenalenyl Diradicaloids by an External Electric Field and Donor-Acceptor Substitution. *J. Phys. Chem. Lett.* **2011**, *2*, 1094–1098. (b) Zeng, Z.; Ishida, M.; Zafra, J. L.; Zhu, X.; Sung, Y. M.; Bao, N.; Webster, R. D.; Lee, B. S.; Li, R.-W.; Zeng, W.; Li, Y.; Chi, C.; López Navarrete, J. T.; Ding, J.; Casado, J.; Kim, D.; Wu, J. Pushing Extended *p*-Quinodimethanes to the Limit: Stable Tetracyano-oligo(*N*-annulated perylene)quinodimethanes with Tunable Ground States. *J. Am. Chem. Soc.* **2013**, *135*, 6363–6371. (c) Zeng, Z.; Lee, S.; Zafra, J. L.; Ishida, M.; Bao, N.; Webster, R. D.; López Navarrete, J. T.; Ding, J.; Casado, J.; Kim, D.-H.; Wu, J. Turning on the biradical state of tetracyano-perylene and quaterrylenequinodimethanes by incorporation of additional thiophene rings. *Chem. Sci.* **2014**, *5*, 3072–3080. (d) Zeng, Z.; Lee, S.; Son, M.; Fukuda, K.; Mayorga Burrezo, P.; Zhu, X.; Qi, Q.; Li, R.-W.; López Navarrete, J. T.; Ding, J.; Casado, J.; Nakano, M.; Kim, D.; Wu, J. Push-Pull Type Oligo(*N*-annulated perylene)quinodimethanes: Chain Length and Solvent-Dependent Ground States and Physical Properties. *J. Am. Chem. Soc.* **2015**, *137*, 8572–8583.
8. Zeng, Z.; Sung, Y. M.; Bao, N.; Tan, D.; Lee, R.; Zafra, J. L.; Lee, B. S.; Ishida, M.; Ding, J.; López Navarrete, J. T.; Li, Y.; Zeng, W.; Kim, D.; Huang, K.-W.; Webster, R. D.; Casado, J.; Wu, J. Stable Tetrabenzo-Chichibabin's Hydrocarbons: Tunable Ground State and Unusual Transition between Their Closed-Shell and Open-Shell Resonance Forms. *J. Am. Chem. Soc.* **2012**, *134*, 14513–14525.
9. Dressler, J. J.; Teraoka, M.; Espejo, G. L.; Kishi, R.; Takamuku, S.; Gómez-García, C. J.; Zakharov, L. N.; Nakano, M.; Casado, J.; Haley, M. M. Thiophene and its sulfur inhibit indenoindenodibenzothiophene diradicals from low-energy lying thermal triplets. *Nat. Chem.* **2018**, *10*, 1134–1140.

10. Examples of quinoidal/diradicaloid constitutional isomers, *inter alia*: (a) Tukada, H. *p*-Phenylene-2,2'-bis(1,1:3,3-di-2,2'-biphenyl-enepropenyl): A Stable Non-Kekule Molecule as a Ground-State Singlet. *J. Am. Chem. Soc.* **1991**, *113*, 8991–8992. (b) Tukada, H.; Mutai, K. A Stable Triplet Non-Kekulé Molecule; *m*-Phenylene-2,2'-bis(1,1:3,3-di-2,2'-biphenylenepropenyl). *Tetrahedron Lett.* **1992**, *33*, 6665–6668. (c) Kubo, T.; Sakamoto, M.; Nakasuji, K. Biradicaloid Character of Phenalenyl-Based Aromatic Compounds with a Small HOMO–LUMO Gap. *Polyhedron* **2005**, *24*, 2522–2527. (d) Sun, Z.; Lee, S.; Hyung, K.; Zhu, X.; Zhang, W.; Zheng, B.; Hu, P.; Zeng, Z.; Das, S.; Li, Y.; Chi, C.; Li, R.W.; Huang, K.W.; Ding, J.; Kim, D.; Wu, J. Dibenzoheptazethrene Isomers with Different Biradical Characters: An Exercise of Clar's Sextets Rule in Singlet Biradicaloids. *J. Am. Chem. Soc.* **2013**, *135*, 18229–18236. (e) Hu, P.; Lee, S.; Park, K. H.; Das, S.; Heng, T. S.; Gonçalves, T. P.; Huang, K.-W.; Ding, J.; Kim, D.; Wu, J. Octazethrene and Its Isomer with Different Diradical Characters and Chemical Reactivity: The Role of the Bridge Structure. *J. Org. Chem.* **2016**, *81*, 2911–2919. (f) Sun, Z.; Zheng, B.; Hu, P.; Huang, K.-W.; Wu, J. Highly Twisted 1,2:8,9-Dibenzozethrenes: Synthesis, Ground State, and Physical Properties. *ChemPlusChem* **2014**, *79*, 1549–1553. (g) Yadav, P.; Das, S.; Phan, H.; Heng, T. S.; Ding, J.; Wu, J. Kinetically Blocked Stable 5,6:12,13-Dibenzozethrene: A Laterally π -Extended Zethrene with Enhanced Diradical Character. *Org. Lett.* **2016**, *18*, 2886–2889. (h) Rudebusch, G. E.; Zafra, J. L.; Jorner, K.; Fukuda, K.; Marshall, J. L.; Arrechea-Marcos, I.; Espejo, G. L.; Ponce-Ortiz, C. J.; Gomez-Garcia, C. J.; Zakharov, L. N.; Nakano, M.; Ottosson, H.; Casado, J.; Haley, M. M. Diindeno-Fusion of an Anthracene as a Design Strategy for Stable Organic Biradicals. *Nat. Chem.* **2016**, *8*, 753–759. (i) Majewski, M. A.; Chmielewski, P. J.; Chien, A.; Hong, Y.; Lis, T.; Witwicki, M.; Kim, D.; Zimmerman, P. M.; Stępień, M. 5,10-Dimesityldiindeno[1,2-*a*:2',1'-*i*]phenanthrene: A Stable Biradicaloid Derived from Chichibabin's Hydrocarbon. *Chem. Sci.* **2019**, *10*, 3413–3420. (j) Lu, R.-Q.; Wu, S.; Yang, L.-L.; Gao, W.-B.; Qu, H.; Wang, X.-Y.; Chen, J.-B.; Tang, C.; Shi, H.-Y.; Cao, X.-Y. Stable Diindeno-Fused Corannulene Regioisomers with Open-Shell Singlet Ground States and Large Diradical Characters. *Angew. Chem. Int. Ed.* **2019**, *58*, 7600–7605. (k) Miyoshi, H.; Miki, M.; Hirano, S.; Shimizu, A.; Kishi, R.; Fukuda, K.; Shiomi, D.; Sato, K.; Takui, T.; Hisaki, I.; Nakano, M.; Tobe, Y. Fluoreno[2,3-*b*]fluorene vs Indeno[2,1-*b*]fluorene: Unusual Relationship between the Number of π Electrons and Excitation Energy in *m*-Quinodimethane-Type Singlet Diradicaloids. *J. Org. Chem.* **2017**, *82*, 1380–1387. (l) Barker, J. E.; Frederickson, C. K.; Jones, M. H.; Zakharov, L. N.; Haley, M. M. Synthesis and Properties of Quinoidal Fluorenofluorenes. *Org. Lett.* **2017**, *19*, 5312–5315. (m) Hacker, A. S.; Pavano, M.; Wood II, J. E.; Hashimoto, H.; D'Ambrosio, K. M.; Frederickson, C. K.; Zafra, J. L.; Gómez-García, C. J.; Postils, V.; McDonald, A. R.; Casanova, D.; Frantz, D. K.; Casado, J. Fluoreno[2,1-*a*]fluorene: an *ortho*-Naphthoquinodimethane-Based System with Partial Diradical Character. *Chem. Commun.* **2019**, *55*, 14186–14189. (n) Melidonie, J.; Dmitrieva, E.; Zhang, K.; Fu, Y.; Popov, A. A.; Pisula, W.; Berger, R.; Liu, J.; Feng, X. Dipyrene-Fused Dicyclopenta[*a,f*]naphthalenes. *J. Org. Chem.* **2019**, in press (DOI: 10.1021/acs.joc.9b02626).

11. (a) Chase, D. T.; Rose, B. D.; McClintock, S. P.; Zakharov, L. N.; Haley, M. M. Indeno[1,2-*b*]fluorenes: Fully conjugated Antiaromatic Analogues of Acenes. *Angew. Chem., Int. Ed.* **2011**, *50*, 1127–1130. (b) Shimizu, A.; Tobe, Y. Indeno[2,1-*a*]fluorene: An Air-stable Orthoquinodimethane Derivative. *Angew. Chem., Int. Ed.* **2011**, *50*, 6906–6910. (c) Fix, A. G.; Deal, P. E.; Vonnegut, C. L.; Rose, B. D.; Zakharov, L. N.; Haley, M. M. Indeno[2,1-*c*]fluorene: A New Electron-Accepting Scaffold for Organic Electronics. *Org. Lett.* **2013**, *15*, 1362–1365. (d) Shimizu, A.; Kishi, R.; Nakano, M.; Shiomi, D.; Sato, K.; Takui, T.; Hisaki, I.; Miyata, M.; Tobe, Y. Indeno[2,1-*b*]fluorene: A 20- π -Electron Hydrocarbon with Very Low-Energy Light Absorption. *Angew. Chem. Int. Ed.* **2013**, *52*, 6076–6079. (e) Dressler, J. J.; Zhou, Z.; Marshall, J. L.; Kishi, R.; Takamuku, S.; Wei, Z.; Spisak, S. N.; Nakano, M.; Petrukhina, M. A.; Haley, M. M. Synthesis of the Unknown Indeno[1,2-*a*]fluorene Regioisomer: Crystallographic Characterization of Its Dianion. *Angew. Chem., Int. Ed.* **2017**, *56*, 15363–15367.
12. (a) Tobe, Y. Non-Alternant Non-Benzenoid Aromatic Compounds: Past, Present, and Future. *Chem. Rec.* **2015**, *15*, 86–96; (b) Frederickson, C. K.; Rose, B. D.; Haley, M. M. Explorations of the Indenofluorenes and Expanded Quinoidal Analogues. *Acc. Chem. Res.* **2017**, *50*, 977–987.
13. Nakano, M. Electronic Structure of Open-Shell Singlet Molecules: Diradical Character Viewpoint. *Top. Curr. Chem.* **2017**, *375*, 1–67.
14. *Inter alia*: (a) Gilroy, J. B.; McKinnon, S. D. J.; Kennepohl, P.; Zsombor, M. S.; Ferguson, M. J.; Thompson, L. K.; Hicks, R. G. Probing Electronic Communication in Stable Benzene-Bridged Verdazyl Diradicals. *J. Org. Chem.* **2007**, *72*, 8062–8069. (b) Caneschi, A.; Chiesi, P.; David, L.; Ferraro, F.; Gatteschi, D.; Sessoli, R. Crystal Structure and Magnetic Properties of Two Nitronyl Nitroxide Biradicals and of Their Copper(II) Complexes. *Inorg. Chem.* **1993**, *32*, 1445–1453.
15. (a) Hubbard, J. Electron correlations in narrow energy bands. *Proc. R. Soc. A* **1963**, *276*, 238–257. (b) Fazekas, P. *Lecture Notes on Electron Correlation and Magnetism*; World Scientific: Singapore, 1999.
16. Gebhard, F. *The Mott Metal-Insulator Transition, Models and Methods*; Springer: Heidelberg, Germany, 1997.
17. Knall, A.-C.; Ashraf, R. S.; Nikolka, M.; Nielsen, C. B.; Purushothaman, B.; Sadhanala, A.; Hurhangee, M.; Broch, K.; Harkin, D. J.; Novák, J.; Neophytou, M.; Hayoz, P.; Siringhaus, H.; McCulloch, I. Naphthacenodithiophene Based Polymers—New Members of the Acenodithiophene Family Exhibiting High Mobility and Power Conversion Efficiency. *Adv. Funct. Mater.* **2016**, *26*, 6961–6969.

18. Nakagawa, H.; Kawai, S.; Nakashima, T.; Kawai, T. Synthesis and Photochemical Reactions of Photochromic Terarylene Having a Leaving Methoxy Group. *Org. Lett.* **2009**, *11*, 1475–1478.
19. Kubo, T.; Shimizu, A.; Sakamoto, M.; Uruichi, M.; Yakushi, K.; Nakano, M.; Shiomi, D.; Sato, K.; Takui, T.; Morita, Y.; Nakasuji, K. Synthesis, Intermolecular Interaction, and Semiconductive Behavior of a Delocalized Singlet Biradical Hydrocarbon. *Angew. Chem., Int. Ed.* **2005**, *44*, 6564–6568.
20. Shimizu, A.; Kubo, T.; Uruichi, M.; Yakushi, K.; Nakano, M.; Shiomi, D.; Sato, K.; Takui, T.; Hirao, Y.; Matsumoto, K.; Kurata, H.; Morita, Y.; Nakasuji, K. Alternating Covalent Bonding Interactions in a One-Dimensional Chain of a Phenalenyl-Based Singlet Biradical Molecule Having Kekulé Structures. *J. Am. Chem. Soc.* **2010**, *132*, 14421–14428.
21. Bleaney, B.; Bowers, K. D. Anomalous Paramagnetism of Copper Acetate. *Proc. R. Soc. Lond. A.* **1952**, *214*, 451–465.
22. Shimizu, A.; Hirao, Y.; Matsumoto, K.; Kurata, H.; Kubo, T.; Uruichi, M.; Yakushi, K. Aromaticity and π -bond covalency: prominent intermolecular covalent bonding interaction of a Kekulé hydrocarbon with very significant singlet biradical character. *Chem. Commun.* **2012**, *48*, 5629–5631.

Chapter IV

1. Giri, G.; Verploegen, E.; Mannsfeld, S. C. B.; Atahan-Evrenk, S.; Kim, D. H.; Lee, S. Y.; Becerril, H. A.; Aspuru-Guzik, A.; Toney, M. F.; Bao, Z. Tuning Charge Transport in Solution-Sheared Organic Semiconductors Using Lattice Strain. *Nature* **2011**, *480*, 504–508.
2. Payne, M. M.; Parkin, S. R.; Anthony, J. E. Functionalized Higher Acenes: Hexacene and Heptacene. *J. Am. Chem. Soc.* **2005**, *127*, 8028–8029.
3. Fudickar, W.; Linker, T. Why Triple Bonds Protect Acenes from Oxidation and Decomposition. *J. Am. Chem. Soc.* **2012**, *134*, 15071–15082.
4. Anthony, J. E. The Larger Acenes: Versatile Organic Semiconductors. *Angew. Chem. Int.* **2008**, *47*, 452–483.
5. Zade, S. S.; Zamoshchik, N.; Reddy, A. R.; Fridman-Marueli, G.; Sheberla, D.; Bendikov, M. Products and Mechanism of Acene Dimerization. A Computational Study. *J. Am. Chem. Soc.* **2011**, *133*, 10803–10816.
6. Schleyer, P. v. R.; Manoharan, M.; Jiao, H.; Stahl, F. The Acenes: Is There a Relationship between Aromatic Stabilization and Reactivity? *Org. Lett.* **2001**, *3*, 3643–3646.

7. Chen, W.; Yu., F.; Xu, Q.; Zhou, G.; Zhang, Q. Recent Progress in High Linearly Fused Polycyclic Conjugated Hydrocarbons (PCHs, $n > 6$) with Well-Defined Structures. *Adv. Sci.* **2020**, 1903766 (DOI: 10.1002/advs.201903766)
8. Breslow, R.; Brown, J.; Gajewski, J. J. Antiaromaticity of Cyclopropenyl Anions. *J. Am. Chem. Soc.* **1967**, 89, 4383–4390.
9. Breslow, R. Antiaromaticity. *Acc. Chem. Res.* **1973**, 6, 393–398.
10. Krygowski, T. M.; Cyrański, M. K.; Czarnocki, Z.; Häfelinger, G.; Katritzky, A. R. Aromaticity: A Theoretical Concept of Immense Practical Importance. *Tetrahedron* **2000**, 56, 1783–1791.
11. Wiberg, K. B. Antiaromaticity in Monocyclic Conjugated Carbon Rings. *Chem Rev.* **2001**, 101, 1317–1332.
12. Chen, Z.; Wannere, C. S.; Corminboeuf, C.; Puchta, R.; Schleyer, P. v. R. Nucleus-Independent Chemical Shifts (NICS) as an Aromaticity Criterion. *Chem Rev.* **2005**, 105, 3842–3888.
13. Mills, N. S.; Llagostera, K. B. Summation of Nucleus Independent Chemical Shifts as a Measure of Aromaticity. *J. Org. Chem.* **2007**, 72, 9163–9169.
14. Kawase, T.; Fujiwara, T.; Kitamura, C.; Konishi, A.; Hirao, Y.; Matsumoto, K.; Kurata, H.; Kubo, T.; Shinamura, S.; Mori, H.; Miyazaki, E.; Takimiya, K. Dinaphthopentalenes: Pentalene Derivatives for Organic Thin-Film Transistors. *Angew. Chem. Int. Ed.* **2010**, 49, 7728–7732.
15. Dai, G.; Chang, J.; Shi, X.; Zhang, W.; Zheng, B.; Huang, K.-W.; Chi, C. Thienoacene-Fused Pentalenes: Syntheses, Structures, Physical Properties and Applications for Organic Field-Effect Transistors. *Chem. Eur. J.* **2015**, 21, 2019–2028.
16. Oshima, H.; Fukazawa, A.; Yamaguchi, S. Facile Synthesis of Polycyclic Pentalenes with Enhanced Hückel Antiaromaticity. *Angew. Chem. Int. Ed.* **2017**, 56, 3270–3274.
17. Konishi, A.; Okada, Y.; Nakano, M.; Sugisaki, K.; Sato, K.; Takui, T.; Yasuda, M. Synthesis and Characterization of Dibenzo[*a,f*]pentalene: Harmonization of the Antiaromatic and Singlet Biradical Character. *J. Am. Chem. Soc.* **2017**, 139, 15248–15287.
18. Konishi, A.; Okada, Y.; Kishi, R.; Nakano, M.; Yasuda, M. Enhancement of Antiaromatic Character via Additional Benzoannulation in Dibenzo[*a,f*]pentalene: Synthesis and Properties of Benzo[*a*]naphtho[2,1-*f*]pentalene and Dinaphtho[2,1-*a,f*]pentalene. *J. Am. Chem. Soc.* **2019**, 141, 560–571.

19. Kato, S.; Kuwako, S.; Takahashi, N.; Kijima, T.; Nakamura, Y. Benzo-and Naphthopentalenes: Syntheses, Structures, and Properties. *J. Org. Chem.* **2016**, *81*, 7700–7710.
20. Yuan, B.; Zhuang, J.; Kirmess, K. M.; Bridgmohan, C. N.; Whalley, A. C.; Wang, L.; Plunkett, K. N. Pentaleno[1,2-*a*:4,5']diacenaphthylenes: Uniquely Stabilized Pentalene Derivatives. *J. Org. Chem.* **2016**, *81*, 8312–8318.
21. Cao, J.; London, G.; Dumele, O.; von Wantoch Rekowski, M.; Trapp, N.; Ruhlmann, L.; Boudon, C.; Stanger, A.; Diederich, F. The Impact of Antiaromatic Subunits in $[4n+2]$ π -Systems: Bispentalenes with $[4n+2]$ π -Electron Perimeters and Antiaromatic Character. *J. Am. Chem. Soc.* **2015**, *137*, 7178–7188.
22. Dai, G.; Chang, J.; Zhang, W.; Bai, S.; Huang, K.-W.; Xu, J.; Chi, C. Dianthraceno[*a,e*]pentalenes: Synthesis, Crystallographic Structures and Applications in Organic Field-Effect Transistors. *Chem. Commun.* **2015**, *51*, 23955–26900.
23. Wang, J.; Chu, M.; Fan, J.-X.; Lau, T.-K.; Ren, A.-M.; Lu, X.; Miao, Q. Crystal Engineering of Biphenylene-Containing Acenes for High-Mobility Organic Semiconductors. *J. Am. Chem. Soc.* **2019**, *141*, 3589–3596.
24. Jin, Z.; Teo, Y. C.; Teat, S. J.; Xia, Y. Regioselective Synthesis of [3]Naphthylenes and Tuning of Their Antiaromaticity. *J. Am. Chem. Soc.* **2017**, *139*, 15933–15939.
25. Jin, Z.; Yao, Z.-F.; Barker, K. P.; Pei, J.; Xia, Y. Dinaphthobenz[1,2:4,5]dicyclobutadiene: Antiaromatic and Orthogonally Tunable Electronics and Packing. *Angew. Chem. Int. Ed.* **2019**, *58*, 2034–2039.
26. Teo, Y. C.; Jin, Z.; Xia, Y. Synthesis of Cyclobutadienoid-Fused Phenazines with Strongly Modulated Degrees of Antiaromaticity. *Org. Lett.* **2018**, *20*, 3300–3304.
27. Marshall, J. L.; Uchida, K.; Frederickson, C. K.; Schütt, C.; Zeidell, A. M.; Goetz, K. P.; Finn, T. W.; Jarolimek, K.; Zakharov, L. N.; Risko, C.; Herges, R.; Jurchescu, O. D.; Haley, M. M. Indacenodibenzothiophenes: Synthesis, Optoelectronic Properties and Materials Applications of Molecules with Strong Antiaromatic Character. *Chem. Sci.* **2016**, *7*, 5547–5558.
28. Frederickson, C. K.; Zakharov, L. N.; Haley, M. M. Modulating Paratropicity Strength in Diareno-Fused Antiaromatics. *J. Am. Chem. Soc.* **2016**, *138*, 16827–16838.
29. Frederickson, C. K.; Rose, B. D.; Haley, M. M. Explorations of the Indenofluorenes and Expanded Quinoidal Analogues. *Acc. Chem. Res.* **2017**, *50*, 977–987.

30. Melidonie, J.; Liu, J.; Fu, Y.; Weigand, J. J.; Berger, R.; Feng, X. Pyrene-Fused *s*-Indacene. *J. Org. Chem.* **2018**, *83*, 6633–6639.
31. Broløs, L.; Kilde, M. D.; Hammerich, O.; Nielsen, M. B. Toward Redox-Active Indenofluorene-Extended Tetrathiafulvalene Oligomers—Synthesis and Studies of Dimeric Scaffolds. *J. Org. Chem.* **2020**, *85*, 3277–3286.
32. Ie, Y.; Sato, C.; Yamamoto, K.; Nitani, M.; Aso, Y. A Thiazole-Fused Antiaromatic Compound Containing an *s*-Indacene Chromophore with a High Electron Affinity. *Chem. Lett.* **2018**, *47*, 1534–1537.
33. Jiang, Q.; Tao, T.; Phan, H.; Han, Y.; Gopalakrishna, T. Y.; Heng, T. S.; Li, G.; Yuan, L.; Ding, J.; Chi, C. Diazuleno-*s*-Indacene Diradicaloids: Syntheses, Properties, and Local (Anti)Aromaticity Shift from Neutral to Dicationic State. *Angew. Chem. Int. Ed.* **2018**, *57*, 16737–16741.
34. Breslow, R.; Schneebeli, S. T. Structure-Property Relationships in Molecular Wires. *Tetrahedron* **2011**, *67*, 10171–10178.
35. Breslow, R.; Foss, F. W. Charge Transport in Nanoscale Aromatic and Antiaromatic Systems. *J. Phys. Condens. Matter* **2008**, *20*, 374104.
36. Chen, W.; Li, H.; Widawsky, J. R.; Appayee, C.; Venkataraman, L.; Breslow, R. Aromaticity Decreases Single-Molecule Junction Conductance. *J. Am. Chem. Soc.* **2014**, *136*, 918–920.
37. Mahendran, A.; Gopinath, P.; Breslow, R. Single Molecule Conductance of Aromatic, Nonaromatic, and Partially Antiaromatic Systems. *Tetrahedron Lett.* **2015**, *56*, 4833–4835.
38. Zeidell, A. M.; Jennings, L.; Frederickson, C. K.; Ai, Q.; Dressler, J. J.; Zakharov, L. N.; Risko, C.; Haley, M. M.; Jurchescu, O. D. Organic Semiconductors Derived from Dinaphtho-Fused *s*-Indacenes: How Molecular Structure and Film Morphology Influence Thin-Film Transistor Performance. *Chem. Mater.* **2019**, *31*, 6962–6970.
39. Liu, C.; Xu, S.; Zhu, W.; Zhu, X.; Hu, W.; Li, Z.; Wang, Z. Diaceno[*a,e*]pentalenes: An Excellent Molecular Platform for High-Performance Organic Semiconductors. *Chem. Eur. J.* **2015**, *21*, 17016–17022.
40. Gopalakrishna, T. Y.; Zeng, W.; Lu, X.; Wu, J. From Open-Shell Singlet Diradicaloids to Polyradicaloids. *Chem. Commun.* **2018**, *54*, 2186–2199.

41. Koike, H.; Chikamatsu, M.; Azumi, R.; Tsutsumi, J.; Ogawa, K.; Yamane, W.; Nishiuchi, T.; Kubo, T.; Hasegawa, T.; Kanai, K. Stable Delocalized Singlet Biradical Hydrocarbon for Organic Field-Effect Transistors. *Adv. Funct. Mater.* **2016**, *26*, 277–283.
42. Morita, Y.; Suzuki, S.; Sato, K.; Takui, T. Synthetic Organic Spin Chemistry for Structurally Well-Defined Open-Shell Graphene Fragments. *Nat. Chem.* **2011**, *3*, 197–204.
43. Morita, Y.; Nishida, S.; Murata, T.; Moriguchi, M.; Ueda, A.; Satoh, M.; Arifuku, K.; Sato, K.; Takui, T. Organic Tailored Batteries Materials Using Stable Open-Shell Molecules with Degenerate Frontier Orbitals. *Nat. Mater.* **2011**, *10*, 947–951.
44. Smith, M. B.; Michl, J. Recent Advances in Singlet Fission. *Annu. Rev. Phys. Chem.* **2013**, *64*, 361–386.
45. Minami, T.; Nakano, M. Diradical Character View of Singlet Fission. *J. Phys. Chem. Lett.* **2012**, *3*, 145–150.
46. Ravat, P.; Šolomek, T.; Ribar, P.; Juriček, M. Biradicaloid with a Twist: Lowering the Singlet-Triplet Gap. *Synlett* **2016**, *27*, 1613–1617.
47. Di Motta, S.; Negri, F.; Fazzi, D.; Castiglioni, C.; Canesi, E. V. Biradicaloid and Polyenic Character of Quinoidal Oligothiophenes Revealed by the Presence of a Low-Lying Double-Exciton State. *J. Phys. Chem. Lett.* **2010**, *1*, 3334–3339.
48. Abe, M. Diradicals. *Chem Rev.* **2013**, *113*, 7011–7088.
49. Kubo, T.; Shimizu, A.; Sakamoto, M.; Uruichi, M.; Yakushi, K.; Nakano, M.; Shiomi, D.; Sato, K.; Takui, T.; Morita, Y.; Nakasuji, K. Synthesis, Intermolecular Interaction, and Semiconductive Behavior of a Delocalized Singlet Biradical Hydrocarbon. *Angew. Chem. Int. Ed.* **2005**, *44*, 6564–6568.
50. Shimizu, A.; Kubo, T.; Uruichi, M.; Yakushi, K.; Nakano, M.; Shiomi, D.; Sato, K.; Takui, T.; Hirao, Y.; Matsumoto, K.; Kurata, H.; Morita, Y.; Nakasuji, K. Alternating Covalent Bonding Interactions in a One-Dimensional Chain of a Phenalenyl-Based Singlet Biradical Molecule Having Kekulé Structures. *J. Am. Chem. Soc.* **2010**, *132*, 14421–14428.
51. Shimizu, A.; Hirao, Y.; Matsumoto, K.; Kurata, H.; Kubo, T.; Uruichi, M.; Yakushi, K. Aromaticity and π -Bond Covalency: Prominent Intermolecular Covalent Bonding Interaction of a Kekulé Hydrocarbon with Very Significant Singlet Biradical Character. *Chem. Commun.* **2012**, *48*, 5629–5631.
52. Hu, P.; Wu, J. Modern Zethrene Chemistry. *Can. J. Chem.* **2017**, *95*, 223–233.

53. Zeng, W.; Sun, Z.; Heng, T. S.; Gonçalves, T. P.; Gopalakrishna, T. Y.; Huang, K. W.; Ding, J.; Wu, J. Super-Heptazethrene. *Angew. Chem. Int. Ed.* **2016**, *55*, 8615–8619.
54. Sun, Z.; Lee, S.; Park, K. H.; Zhu, X.; Zhang, W.; Zheng, B.; Hu, P.; Zeng, Z.; Das, S.; Li, Y.; Chi, C.; Li, R. W.; Huang, K. W.; Ding, J.; Kim, D.; Wu, J. Dibenzoheptazethrene Isomers with Different Biradical Characters: An Exercise of Clar's Aromatic Sextet Rule in Singlet Biradicaloids. *J. Am. Chem. Soc.* **2013**, *135*, 18229–18236.
55. Li, Y.; Heng, W. K.; Lee, B. S.; Aratani, N.; Zafra, J. L.; Bao, N.; Lee, R.; Sung, Y. M.; Sun, Z.; Huang, K. W.; Webster, R. D.; Lopez-Navarrete, J. T.; Kim, D.; Osuka, A.; Casado, J.; Ding, J.; Wu, J. Kinetically Blocked Stable Heptazethrene and Octazethrene: Closed-Shell or Open-Shell in the Ground State? *J. Am. Chem. Soc.* **2012**, *134*, 14913–14922.
56. Shimizu, A.; Kishi, R.; Nakano, M.; Shiomi, D.; Sato, K.; Takui, T.; Hisaki, I.; Miyata, M.; Tobe, Y. Indeno[2,1-*b*]fluorene: A 20- π -Electron Hydrocarbon with Very Low-Energy Light Absorption. *Angew. Chem. Int. Ed.* **2013**, *52*, 6076–6079.
57. Dressler, J. J.; Zhou, Z.; Marshall, J. L.; Kishi, R.; Takamuku, S.; Wei, Z.; Spisak, S. N.; Nakano, M.; Petrukhina, M. A.; Haley, M. M. Synthesis of the Unknown Indeno[1,2-*a*]fluorene Regioisomer: Crystallographic Characterization of Its Dianion. *Angew. Chem. Int. Ed.* **2017**, *56*, 15363–15367.
58. Rudebusch, G. E.; Zafra, J. L.; Jorner, K.; Fukuda, K.; Marshall, J. L.; Arrechea-Marcos, I.; Espejo, G. L.; Ponce Ortiz, R.; Gómez-García, C. J.; Zakharov, L. N.; Nakano, M.; Ottosson, H.; Casado, J.; Haley, M. M. Diindeno-Fusion of an Anthracene as a Design Strategy for Stable Organic Biradicals. *Nat. Chem.* **2016**, *8*, 753–759.
59. Miyoshi, H.; Miki, M.; Hirano, S.; Shimizu, A.; Kishi, R.; Fukuda, K.; Shiomi, D.; Sato, K.; Takui, T.; Hisaki, I.; Nakano, M.; Tobe, Y. Fluoreno[2,3-*b*]fluorene vs Indeno[2,1-*b*]fluorene: Unusual Relationship between the Number of π Electrons and Excitation Energy in *m*-Quinodimethane-Type Singlet Diradicaloids. *J. Org. Chem.* **2017**, *82*, 1380–1388.
60. Dressler, J. J.; Teraoka, M.; Espejo, G. L.; Kishi, R.; Takamuku, S.; Gómez-García, C. J.; Zakharov, L. N.; Nakano, M.; Casado, J.; Haley, M. M. Thiophene and Its Sulfur Inhibit Indenoindenodibenzothiophene Diradicals from Low-Energy Lying Thermal Triplets. *Nat. Chem.* **2018**, *10*, 1134–1140.

61. Hacker, A. S.; Pavano, M.; Wood, J. E.; Hashimoto, H.; D'Ambrosio, K. M.; Frederickson, C. K.; Zafra, J. L.; Gómez-García, C. J.; Postils, V.; McDonald, A. R.; Casanova, D.; Frantz, D. K.; Casado, J. Fluoreno[2,1-*a*]fluorene: an *ortho*-naphthoquinodimethane-based system with partial diradical character. *Chem. Commun.* **2019**, *55*, 14186–14189.
62. Barker, J. E.; Dressler, J. J.; Cárdenas Valdivia, A.; Kishi, R.; Strand, E. T.; Zakharov, L. N.; MacMillan, S. N.; Gómez-García, C. J.; Nakano, M.; Casado, J.; Haley, M. M. Molecule Isomerism Modulates the Diradical Properties of Stable Singlet Diradicaloids. *J. Am. Chem. Soc.* **2020**, *142*, 1548–1555.
63. Dressler, J. J.; Cárdenas Valdivia, A.; Kishi, R.; Rudebusch, G. E.; Ventura, A. M.; Chastain, B. E.; Gómez-García, C. J.; Zakharov, L. N.; Nakano, M.; Casado, J.; Haley, M. M. Diindenoanthracene Diradicaloids Enable Rational, Incremental Tuning of Their Singlet-Triplet Energy Gaps. *Chem* **2020**, *6*, 1353–1368.
64. Majewski, M. A.; Chmielewski, P. J.; Chien, A.; Hong, Y.; Lis, T.; Witwicki, M.; Kim, D.; Zimmerman, P. M.; Stępień, M. 5,10-Dimesityldiindeno[1,2-*a*:2',1'-*i*]phenanthrene: A Stable Biradicaloid Derived from Chichibabin's Hydrocarbon. *Chem. Sci.* **2019**, *10*, 3413–3420.
65. Lu, R.-Q.; Wu, S.; Yang, L.-L.; Gao, W.-B.; Qu, H.; Wang, X.-Y.; Chen, J.-B.; Tang, C.; Shi, H.-Y.; Cao, X.-Y. Stable Diindeno-Fused Corannulene Regioisomers with Open-Shell Singlet Ground States and Large Diradical Characters. *Angew. Chem. Int. Ed.* **2019**, *58*, 7600–7605.
66. Zeng, Z.; Shi, X.; Chi, C.; López Navarrete, J. T.; Casado, J.; Wu, J. Pro-Aromatic and Anti-Aromatic π -Conjugated Molecules: An Irresistible Wish to Be Diradicals. *Chem. Soc. Rev.* **2015**, *44*, 6578–6596.
67. Young, B. S.; Chase, D. T.; Marshall, J. L.; Vonnegut, C. L.; Zakharov, L. N.; Haley, M. M. Synthesis and Properties of Fully-Conjugated Indacenedithiophenes. *Chem. Sci.* **2014**, *5*, 1008–1014.
68. Yoshia, T.; Takahashi, K.; Ide, Y.; Kishi, R.; Fujiyoshi, J.-y.; Lee, S.; Hiraoka, Y.; Kim, D.; Nakano, M.; Ikeue, T.; Yamada, H.; Shinokub, H. *Angew. Chem., Int. Ed.* **2018**, *57*, 2209-2213.
69. Wei, S.; Xia, J.; Dell, E. J.; Jiang, Y.; Song, R.; Lee, H.; Rodenbough, P.; Briseno, A. L.; Campos, L. M. Bandgap Engineering through Controlled Oxidation of Polythiophenes. *Angew. Chem. Int. Ed.* **2014**, *53*, 1832–1836.
70. Pappenfus, T. M.; Seidenkranz, D. T.; Lovander, M. D.; Beck, T. L.; Karels, B. J.; Ogawa, K.; Janzen, D. E. Synthesis and Electronic Properties of Oxidized Benzo[1,2-*b*:4,5-*b'*]dithiophenes. *J. Org. Chem.* **2014**, *79*, 9408–9412.

71. Liu, G.; Zhang, H.; Huang, Y.; Han, Z.; Liu, G.; Liu, Y.; Dong, X. Q.; Zhang, X. Efficient Synthesis of Chiral 2,3-Dihydrobenzo[*b*]thiophene 1,1-Dioxides via Rh-Catalyzed Hydrogenation. *Chem. Sci.* **2019**, *10*, 2507–2512.
72. Barbarella, G.; Pudova, O.; Arbizzani, C.; Mastragostino, M.; Bongini, A. Oligothiophene-S,S-Dioxides: A New Class of Thiophene-Based Materials. *J. Am. Chem. Soc.* **1998**, *63*, 1742–1745.
73. Dell, E. J.; Campos, L. M. The Preparation of Thiophene-S,S-Dioxides and Their Role in Organic Electronics. *J. Mater. Chem.* **2012**, *22*, 12945–12952.
74. Gershoni-Poranne, R.; Stanger, A. The NICS-XY-Scan: Identification of Local and Global Ring Currents in Multi-Ring Systems. *Chem. Eur. J.* **2014**, *20*, 5673–5688.
75. Stanger, A. Nucleus-Independent Chemical Shifts (NICS): Distance Dependence and Revised Criteria for Aromaticity and Antiaromaticity. *J. Org. Chem.* **2006**, *71*, 883–893.
76. Even though NBO recognizes the resonance forms we draw for the dianion reference molecules, NRT analyses (which would give us the relative weights for a few of the most important resonance forms) would not finish because of a very large number (1000+) of potential resonance forms.
77. Gimarc, B. M. Topological Charge Stabilization. *J. Am. Chem. Soc.* **1983**, *105*, 1979–1984.
78. Despite multiple efforts, we were unable to obtain a suitable structure for **5** with the *t*-Mes groups. Regardless, our prior studies have shown that use of different bulky aryl groups attached to the apical carbons has minimal effect on the molecular geometry of the π -expanded conjugated system; see references 60 and 62.
79. It is worth noting that no bond-flipped minima structures were found for **1** or **2** as both prefer a “normal” bonding pattern.
80. Bleaney, B.; Bowers, K. D. Anomalous Paramagnetism of Copper Acetate. *Proc. R. Soc. Lond. A* **1952**, *214*, 451–465.
81. Field, J. E.; Hill, T. J.; Venkataraman, D. Bridged Triarylamines: A New Class of Heterohelicenes. *J. Org. Chem.* **2003**, *68*, 6071–6078.

Chapter V

1. Abe, M. Diradicals. *J. Am. Chem. Soc.* **2013**, *113*, 7011–7088.
2. Zeng, Z.; Shi, X.; Chi, C.; Navarrete, J. T. L.; Casado, J.; Wu, J. Pro-aromatic and anti-aromatic π -conjugated molecules: an irresistible wish to be diradicals. *Chem. Soc. Rev.* **2015**, *18*, 6578–6596.

3. Kubo, T. Recent Progress in Quinoidal Singlet Biradical Molecules *Chem. Lett.* **2015**, *44*, 111-122.
4. Gopalakrishna, T. Y.; Zeng, W.; Lu, X.; Wu, J. From open-shell singlet diradicaloids to polyradicaloids. *Chem. Commun.* **2018**, *54*, 2186-2199.
5. Nakano, M.; Champagne, B. Theoretical design of open-shell singlet molecular systems for nonlinear optics. *J. Phys. Chem. Lett.* **2015**, *6*, 3236-3256.
6. Minami, T.; Nakano, M. Diradical character view of singlet fission. *J. Phys. Chem. Lett.* **2012**, *3*, 145-150.
7. Nakano, M.; Kishi, R.; Nitta, T.; Kubo, T.; Nakasuji, K.; Kamada, K.; Ohta, K.; Champagne, B.; Botek, E.; Yamaguchi, K. Second hyperpolarizability (γ) of singlet diradical system: dependence of γ on the diradical character. *J. Phys. Chem. A* **2005**, *109*, 885-891.
8. Morita, Y.; Suzuki, S.; Sato, K.; Takui, T. Synthetic organic spin chemistry for structurally well-defined open-shell graphene fragments. *Nat. Chem.* **2011**, *3*, 297-204.
9. Nakano, M.; Kishi, R.; Ohta, S.; Takahashi, H.; Kubo, T.; Kamada, K.; Ohta, K.; Botek, E.; Champagne, B. Relationship between third-order nonlinear optical properties and magnetic interactions in open-shell systems: a new paradigm for nonlinear optics. *Phys. Rev. Lett.* **2007**, *99*, 033001.
10. Huang, Y.; Egap, E. Open-shell organic semiconductors: an emerging class of materials with novel properties. *Polym. J.* **2018**, *50*, 603-614.
11. Hu, X.; Wang, W.; Wang, D.; Zheng, Y. The electronic applications of stable diradicaloids: present and future. *J. Mater. Chem. C* **2018**, *6*, 11232-11242.
12. Smith, M. B.; Michl, J. Recent advances in singlet fission. *Annu. Rev. Phys. Chem.* **2013**, *64*, 361-386.
13. Varnavsi, O.; Abeyasinghe, N.; Aragó, J.; Serrano-Pérez, J. J.; Ortí, E.; López Navarrete, J. T.; Takimiya, K.; Casanova, D.; Casado, J.; Goodson, T., III. High, yield ultrafast intramolecular singlet exciton fission in a quinoidal bithiophene. *J. Phys. Chem. Lett.* **2015**, *6*, 1375-1384.
14. Kioke, H.; Chikamatsu, M.; Azumi, R.; Tsutsumi, J.; Ogawa, K.; Yamane, W.; Nishiuchi, T.; Kubo, T.; Hasegawa, T.; Kanai, K. Stable delocalized singlet biradical hydrocarbon for organic field-effect transistors. *Adv. Funct. Mater.* **2016**, *26*, 277-283.

15. Ni, Y.; Lee, S.; Son, M.; Aratani, N.; Ishida, M.; Samanta, A.; Yamada, H.; Chang, Y. T.; Furuta, H.; Kim, D.; Wu, J. A diradical approach towards BODIPY-based dyes with intense near-infrared absorption around $\lambda = 1100$ nm. *Angew. Chem. Int. Ed. Engl.* **2016**, *55*, 2815-2819.
16. Lukman, S.; Richter, J. M.; Yang, L.; Hu, P.; Wu, J.; Greenham, N. C.; Musser, A. J. Efficient Singlet Fission and Triplet-Pair Emission in a Family of Zethrene Diradicaloids. *J. Am. Chem. Soc.* **2017**, *139*, 18376-18385.
17. Ravat, P.; Šolomek, T.; Ribar, P.; Juriček, M. Biradicaloid with a twist: lowering the singlet-triplet gap. *Synlett* **2016**, *27* 1613-1617.
18. Kubo, T.; Shimizu, A.; Sakamoto, M.; Uruichi, M.; Yakushi, K.; Nakano, M.; Shiomi, D.; Sato, K.; Takui, T.; Morita, Y.; Nakasuji, K. Synthesis, Intermolecular Interaction, and Semiconductive Behavior of a Delocalized Singlet Biradical Hydrocarbon. *Angew. Chem. Int. Ed.* **2005**, *44*, 6564-6568.
19. Kubo, T.; Shimizu, A.; Uruichi, M.; Yakushi, K.; Nakano, M.; Shiomi, D.; Sato, K.; Takui, T.; Morita, Y.; Nakasuji, K. Singlet Biradical Character of PHenalenyl-Based Kekulé Hydrocarbon with Naphthoquinoid Structure. *Org. Lett.* **2007**, *9*, 81-84.
20. Shimizu, A.; Hirao, Y.; Matsumoto, K.; Kurata, H.; Kubo, T.; Uruichi, M.; Yakushi, K. Aromaticity and π -bond covalency: prominent intermolecular covalent bonding interaction of a Kekulé hydrocarbon with very significant singlet biradical character. *Chem. Commun.* **2012**, *48*, 5629-5631.
21. Chase, D. T.; Rose, B. D.; McClintock, S. P.; Zakharov, L. N.; Haley, M. M. Indeno[1,2-*b*]fluorenes: Fully Conjugated Antiaromatic Analogues of Acenes. *Angew. Chem. Int. Ed.* **2011**, *50*, 1127-1130.
22. Barker, J. E.; Frederickson, C. K.; Jones, M. H.; Zakharov, L. N.; Haley, M. M. Synthesis and Properties of Quinoidal Fluorenofluorenes. *Org. Lett.* **2017**, *19*, 5312-5315.
23. Rudebusch, G. E.; Zafra, J. L.; Jorner, K.; Fukuda, K.; Marshall, J. L.; Arrechea-Marcos, I.; Espejo, G. L.; Ponce-Ortiz, C. J.; Gomez-Garcia, C. J.; Zakharov, L. N.; Nakano, M.; Ottosson, H.; Casado, J.; Haley, M. M. Diindeno-Fusion of an Anthracene as a Design Strategy for Stable Organic Biradicals. *Nat. Chem.* **2016**, *8*, 753-759.
24. Umeda, R.; Hibi, D.; Miki, K.; Tobe, Y. Tetradehydrodinaphtho[10]annulene: A Hitherto Unknown Dehydroannulene and a Viable Precursor to Stable Zethrene Derivatives. *Org. Lett.* **2009**, *11*, 4104-4106.

25. Li, Yuan, Heng, W.-K.; Lee, B. S.; Aratani, N.; Zafra, J. L.; Bao, N.; Lee, R.; Sung, Y. M.; Sun, Z.; Huang, K.-W.; Webster, R. D.; Navarrete, J. T. L.; Kim, D.; Osuka, A.; Casado, J.; Ding, J.; Wu, J. Kinetically Blocked Stable Heptazethrene and Octazethrene: Closed-Shell or Open-Shell in the Ground State? *J. Am. Chem. Soc.* **2012**, *134*, 14913-14922.
26. Sun, Z.; Lee, S.; Hyung, K.; Zhu, X.; Zhang, W.; Zheng, B.; Hu, P.; Zeng, Z.; Das, S.; Li, Y.; Chi, C.; Li, R. W.; Huang, K. W.; Ding, J.; Kim, D.; Wu, J. Dibenzoheptazethrene Isomers with Different Biradical Characters: An Exercise of Clar's Sextets Rule in Singlet Biradicaloids. *J. Am. Chem. Soc.* **2013**, *135*, 18229-18236.
27. Hu, P.; Lee, S.; Park, K. H.; Das, S.; Heng, T. S.; Gonçalves, T. P.; Huang, K.-W.; Ding, J.; Kim, D.; Wu, J. Octazethrene and Its Isomer with Different Diradical Characters and Chemical Reactivity: The Role of the Bridge Structure. *J. Org. Chem.* **2016**, *81*, 2911-2919.
28. Sun, Z.; Zheng, B.; Hu, P.; Huang, K.-W.; Wu, J. Highly Twisted 1,2:8,9-Dibenzozethrenes: Synthesis, Ground State, and Physical Properties. *ChemPlusChem* **2014**, *79*, 1549-1553.
29. Yadav, P.; Das, S.; Phan, H.; Heng, T. S.; Ding, J.; Wu, J. Kinetically Blocked Stable 5,6:12,13-Dibenzozethrene: A Laterally π -Extended Zethrene with Enhanced Diradical Character. *Org. Lett.* **2016**, *18*, 2886-2889.
30. Compare with reference 22: Hacker, A. S.; Pavano, M.; Wood, J. E., II; Hashimoto, H.; D'Ambrosio, K. M.; Frederickson, C. K.; Zafra, J. L.; Gómez-García, C. J.; Postils, V.; McDonald, A. R.; Casanova, D.; Frantz, D. K.; Casado, J. Fluoreno[2,1-a]fluorene: an ortho-Naphthoquinodimethane-Based System with Partial Diradical Character. *Chem. Commun.* **2019**, *55*, 14186-14189.
31. Compare with reference 22: Miyoshi, H.; Miki, M.; Hirano, S.; Shimizu, A.; Kishi, R.; Fukuda, K.; Shiomi, D.; Sato, K.; Takui, T.; Hisaki, I.; Nakano, M.; Tobe, Y. Fluoreno[2,3-b]fluorene vs Indeno[2,1-b]fluorene: Unusual Relationship between the Number of π Electrons and Excitation Energy in *m*-Quinodimethane-Type Singlet Diradicaloids. *J. Org. Chem.* **2017**, *82*, 1380-1387.
32. Compare with reference 23: Majewski, M. A.; Chmielewski, P. J.; Chien, A.; Hong, Y.; Lis, T.; Witwicki, M.; Kim, D.; Zimmerman, P. M.; Stępień, M. 5,10-Dimesityldiindeno[1,2-*a*:2',1'-*i*]phenanthrene: A Stable Biradicaloid Derived from Chichibabin's Hydrocarbon. *Chem. Sci.* **2019**, *10*, 3413-3420.
33. Tukada, H. p-Phenylene-2,2'-bis(1,1:3,3-di-2,2'-biphenylenepropenyl): A Stable Non-Kekule Molecule as a Ground-State Singlet. *J. Am. Chem. Soc.* **1991**, *113*, 8991-8992.

34. Tukada, H.; Mutai, K. A Stable Triplet Non-Kekulé Molecule; m-Phenylene-2,2'-bis(1,1:3,3-di-2,2'-biphenylenepropenyl). *Tetrahedron Lett.* **1992**, *33*, 6665–6668.
35. Kubo, T.; Sakamoto, M.; Nakasuji, K. Biradicaloid Character of Phenalenyl-Based Aromatic Compounds with a Small HOMO–LUMO Gap. *Polyhedron* **2005**, *24*, 2522–2527.
36. Lu, R.-Q.; Wu, S.; Yang, L.-L.; Gao, W.-B.; Qu, H.; Wang, X.-Y.; Chen, J.-B.; Tang, C.; Shi, H.-Y.; Cao, X.-Y. Stable Diindeno-Fused Corannulene Regioisomers with Open-Shell Singlet Ground States and Large Diradical Characters. *Angew. Chem., Int. Ed.* **2019**, *58*, 7600–7605.
37. Shimizu, A.; Tobe, Y. Indeno[2,1-*a*]fluorene: An Air-Stable Ortho-Quinodimethane Derivative. *Angew. Chem., Int. Ed.* **2011**, *50*, 6906–6910.
38. Shimizu, A.; Kishi, R.; Nakano, M.; Shiomi, D.; Sato, K.; Takui, T.; Hisaki, I.; Miyata, M.; Tobe, Y. Indeno[2,1-*b*]fluorene: A 20- π -Electron Hydrocarbon with Very Low-Energy Light Absorption. *Angew. Chem., Int. Ed.* **2013**, *52*, 6076–6079.
39. Fix, A. G.; Deal, P. E.; Vonnegut, C. L.; Rose, B. D.; Zakharov, L. N.; Haley, M. M. Indeno[2,1-*c*]fluorene: A New Electron-Accepting Scaffold for Organic Electronics. *Org. Lett.* **2013**, *15*, 1362–1365.
40. Dressler, J. J.; Zhou, Z.; Marshall, J. L.; Kishi, R.; Takamuku, S.; Wie, Z.; Spisak, S. N.; Nakano, M.; Petrukhina, M. A.; Haley, M. M. Synthesis of the Unknown Indeno[1,2-*a*]fluorene Regioisomer: Crystallographic Characterization of its Dianion. *Angew. Chem. Int. Ed.* **2017**, *56*, 15363–15367.
41. Casado, J. *Para*-Quinodimethanes: A Unified Review of the Quinoidal-Versus-Aromatic Competition and its Implications. *Top. Curr. Chem.* **2017**, *375*, 209–248.
42. Shi, X.; Chi Heterocyclic Quinodimethanes. *Top. Curr. Chem.* **2017**, *375*, 169–207.
43. Tobe, Y. Quinodimethanes, Incorporated in Non-Benzenoid Aromatic or Antiaromatic Frameworks. *Top. Curr. Chem.* **2018**, *375*, 107–168.
44. Dressler, J. J.; Teraoka, M.; Espejo, G.; Kishi, R.; Takamuku, S.; Gómez-García, C. J.; Zakharov, L. N.; Nakano, M.; Casado, J.; Haley, M. M. Thiophene and its sulfur inhibit indenoindenodibenzothiophene diradicals from low-energy lying thermal triplets. *Nat. Chem.* **2018**, 1134–1140.
45. Barker, J. E.; Dressler, J. J.; Valdivia, A. C.; Kishi, R.; Strand, E. T.; Zakharov, L. N.; MacMillan, S. N.; Gómez-García, C. J.; Nakano, M.; Casado, J.; Haley, M. M. Molecule Isomerism Modulates the Diradical Properties of Stable Singlet Diradicaloids. *J. Am. Chem. Soc.* **2020**, *142*, 1548–1555.

46. Dressler, J. J.; Valdivia, A. C.; Kishi, R.; Rudebusch, G. E.; Ventura, A. M.; Chastain, B. E.; Gómez-García, C. J.; Zakharov, L. N.; Nakano, M.; Casado, J.; Haley, M. M. Diindenoanthracene Diradicaloids Enable Rational, Incremental Tuning of Their Singlet-Triplet Energy Gaps. *Chem* **2020**, *6*, 1353–1368.
47. Bleaney, B.; Bowers, K. D. Anomalous Paramagnetism of Copper Acetate. *Proc. R. Soc. Lond. A* **1952**, *214*, 451–465.
48. Rudebusch, G. E.; Espejo, G. Z.; Zafra, J. L.; Pena-Alvarez, M.; Spisak, S. N.; Fukuda, K.; Wei, Z.; Nakano, M.; Petrukhina, M. A.; Casado, J.; Haley, M. M. A Biradical Balancing Act: Redox Amphoterism in a Diindenoanthracene Derivative Results from Quinoidal Acceptor and Aromatic Donor Motifs. *J. Am. Chem. Soc.* **2016**, *138*, 12648–12654.
49. Marcus, R. A. Chemical and Electrochemical Electron-Transfer Theory. *Annu. Rev. Phys. Chem.* **1964**, *15*, 155–196.
50. Heckmann, A.; Lambert, C. Organic Mixed-Valence Compounds: A Playground for Electrons and Holes. *Angew. Chem., Int. Ed.* **2012**, *51*, 326–392.
51. Robin, M. B.; Day, P. Mixed Valence Chemistry: A Survey and Classification. In: Emeleus, H. J. and Sharpe, A. G., Eds., *Advances in Inorganic Chemistry and Radiochemistry*, Vol. 10, Academic Press: New York, 1967, pp. 247–422.
52. González, S. R.; Ie, Y.; Aso, Y.; López Navarrete, J. T.; Casado, J. The Frontiers of Quinoidal Stability in Long Oligothiophenes: Raman Spectra of Dicationic Polaron Pairs. *J. Am. Chem. Soc.* **2011**, *133*, 16350–16353.
53. Mayorga Burrezo, P.; Domínguez, R.; Zafra, J. L.; Pappenfus, T. M.; de la Cruz, P.; Welte, L.; Janzen, D. E.; López Navarrete, J. T.; Langa, F.; Casado, J. Oligomers of Cyclopentadithiophene-Vinylene in Aromatic and Quinoidal Versions and Redox Species with Intermediate Forms. *Chem. Sci.* **2017**, *8*, 8106–8114.
54. Rodríguez González, S.; Caballero, R.; De la Cruz, P.; Langa, F.; López Navarrete, J. T.; Casado, J. Delocalization-to-Localization Charge Transition in Diferrocenyl-Oligothiophenylene-Vinylene Molecular Wires As a Function of the Size By Raman Spectroscopy. *J. Am. Chem. Soc.* **2012**, *134*, 5675–5681.
55. Mayorga Burrezo, P.; Zhu, X.; Zhu, S. F.; Yan, Q.; López Navarrete, J. T.; Tsuji, H.; Nakamura, E.; Casado, J. Planarization, Fusion, and Strain of Carbon-Bridged Phenylenevinylene Oligomers Enhance π -Electron and Charge Conjugation: A Dissectional Vibrational Raman Study. *J. Am. Chem. Soc.* **2015**, *137*, 3834–3843.

56. González-Cano, R. C.; di Motta, S.; Zhu, X.; López Navarrete, J. T.; Tsuji, H.; Nakamura, E.; Negri, F.; Casado, J. Carbon-Bridged Phenylene-Vinylenes: On the Common Diradicaloid Origin of Their Photonic and Chemical Properties. *J. Phys. Chem. C* **2017**, *121*, 23141–23148.
57. Zheng, S.; Barlow, S.; Risko, C.; Kinnibrugh, T. L.; Khrustalev, V. N.; Jones, S. C.; Antipin, M. Yu; Tucker, N. M.; Timofeeva, T. V.; Coropceanu, V. ; Brédas, J.-L.; Marder, S. R. Isolation and Crystal Structures of Two Singlet Bis(Triarylamine) Dications with Nonquinoidal Geometries. *J. Am. Chem. Soc.* **2006**, *128*, 1812–1817.
58. Barlow, S.; Risko, C.; Odom, S. A.; Zheng, S.; Coropceanu, V.; Beverina, L.; Brédas J.-L.; Marder, S. R. Tuning Delocalization in the Radical Cations of 1,4-Bis[4 (diarylamino)styryl]benzenes, 2,5-Bis[4-(diarylamino)styryl]thiophenes, and 2,5-Bis[4-(diarylamino)styryl]pyrroles through Substituent Effects *J. Am. Chem. Soc.* **2012**, *134*, 10146–10155.
59. Barlow, S.; Risko, C.; Chung, S. J.; Tucker, N. M.; Coropceanu, V.; Jones, S. C.; Levi, Z.; Brédas, J. L.; Marder, S. R. Intervalence Transitions in the Mixed-Valence Monocations of Bis(triarylamines) Linked with Vinylene and Phenylene–Vinylene Bridges *J. Am. Chem. Soc.* **2005**, *127*, 16900–16911.
60. Mayorga Burrezo, P.; Lin, N. T.; Nakabayashi, K.; Ohkoshi, S.; Calzado, E. M.; Boj, P. G.; Díaz García, M. A.; Franco, C.; Rovira, C.; Veciana, J.; Moos, M.; Lambert, C.; López Navarrete, J. T.; Tsuji, H.; Nakamura, E.; Casado, J. Bis(Aminoaryl) Carbon-Bridged Oligo(phenylenevinylene)s Expand the Limits of Electronic Couplings. *Angew. Chem., Int. Ed.* **2017**, *56*, 2898–2902.